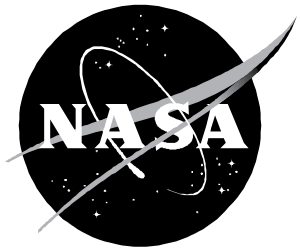

NASA Technical Memorandum 4673

Surface-Pressure and Flow-Visualization Data at Mach Number of 1.60 for Three 65° Delta Wings Varying in Leading-Edge Radius and Camber

S. Naomi McMillin
Langley Research Center • Hampton, Virginia

James E. Byrd
Lockheed Engineering & Sciences Company • Hampton, Virginia

Devendra S. Parmar
Old Dominion University • Norfolk, Virginia

Gaudy M. Bezos-O'Connor and Dana K. Forrest
Langley Research Center • Hampton, Virginia

Susan Bowen
Computer Sciences Corporation • Hampton, Virginia

National Aeronautics and Space Administration
Langley Research Center • Hampton, Virginia 23681-0001

December 1996

The use of trademarks or names of manufacturers in this report is for accurate reporting and does not constitute an official endorsement, either expressed or implied, of such products or manufacturers by the National Aeronautics and Space Administration.

Available electronically at the following URL address: http://techreports.larc.nasa.gov/ltrs/ltrs.html

Printed copies available from the following:

NASA Center for AeroSpace Information
800 Elkridge Landing Road
Linthicum Heights, MD 21090-2934
(301) 621-0390

National Technical Information Service (NTIS)
5285 Port Royal Road
Springfield, VA 22161-2171
(703) 487-4650

Contents

Summary 1
Introduction 1
Symbols 1
Model Description 2
Wind-Tunnel Test Description 3
Test Techniques 4
Surface-Pressure Measurements 4
Vapor-Screen Technique 5
Painted-Oil-Flow Technique 5
Injected-Oil-Flow Technique 6
Liquid-Crystal Technique 6
Results and Discussion 7
Effect of Angle of Attack 8
Upper surface-pressure coefficient data 8
Lower surface-pressure coefficient data 9
Vapor-screen data 9
Painted- and injected-oil-flow data 9
Liquid-crystal data 9
Effect of Longitudinal Position 10
Flow conicity 10
R_x held constant 10
Effect of Reynolds Number 11
Surface-pressure coefficient data 11
Vapor-screen data 12
Painted- and injected-oil-flow data 12
Liquid-crystal data 13
Effect of Transition Grit 13
Surface-pressure coefficient data 13
Painted- and injected-oil-flow data 14
Concluding Remarks 14
Tables 15
Figures 56
Appendix A—Analytical Expressions for Cross-Sectional Shapes of Delta Wing Models 156
Appendix B—Determination of Flow Angle 157
Appendix C—Description of CD-ROM 161
Appendix D—Surface-Pressure Coefficient Data 172
References 262

Summary

An experimental investigation of the effect of leading-edge radius, camber, Reynolds number, and boundary-layer state on the incipient separation of a delta wing at supersonic speeds was conducted at the Langley Unitary Plan Wind Tunnel. The three delta wing models examined had a 65° swept leading edge and varied in cross-sectional shape: a sharp wedge, a 20:1 ellipse, and a 20:1 ellipse with a –9.75° circular camber imposed across the span. The three wings were tested at a Mach number (M) of 1.60 over a free-stream Reynolds number (R) range of 1×10^6 to 5×10^6 ft^{-1}. The wings were tested with and without transition grit applied. Surface-pressure coefficient data were obtained, as well as flow-visualization data. The flow-visualization techniques employed were the vapor-screen, the painted-oil-flow, the injected-oil-flow, and the liquid-crystal techniques. The surface-pressure coefficient data and flow-visualization data are electronically stored on a CD-ROM that accompanies this report.

The data indicated that by rounding the wing leading edge or cambering the wing in the spanwise direction, the onset of leading-edge separation on a delta wing at supersonic speeds can be raised to a higher angle of attack than that observed on a sharp-edged delta wing. Specifically, a 20:1 elliptical cross section increased the angle of attack at which leading-edge separation begins by about 2° over that observed on a sharp-edged delta wing. A cambered elliptical wing, which decreased the local angle of attack at the leading edge by 3.76°, effectively increased the angle of attack at which leading-edge separation begins by 1.5° over that observed on the uncambered elliptical wing.

The application of transition grit on the wing or an increase in R increased the angle of attack at which leading-edge separation began. Fixing transition or increasing R causes the boundary-layer transition to occur closer to the wing apex and leading edge of the wing. A turbulent boundary layer has more energy than a laminar boundary layer and will therefore allow the flow to remain attached at the wing leading edge at higher angles of attack than is possible with a laminar boundary layer

Introduction

A standard configuration for supersonic wing design is that of a highly swept, thin delta wing at moderate angles of attack. Several researchers have experimentally investigated and classified the leeside flow over slender swept wings in supersonic flow. Stanbrook and Squire (ref. 1) originally classified separated and attached leeside flow regimes by using the similarity parameters Mach number normal to the leading edge (M_N) and angle of attack normal to the leading edge (α_N). Whitehead (ref. 2), Szodruch and Ganzer (ref. 3), Szodruch (ref. 4), Miller and Wood (ref. 5), Seshadri and Narayan (ref. 6), and Covell and Wesselmann (ref. 7) extended this work by redefining the separated- and the attached-flow regimes into smaller regimes containing more complex flow structures. The flow structures identified over the leeside of sharp-edged delta wings at supersonic speeds included attached flow, cross-flow shocks, separation bubbles, and a complex vortical system of primary and secondary vortices (ref. 5). The boundaries between the experimentally derived flow regimes have been identified as functions of M_N and α_N.

The aerodynamicist prefers not to be limited to a particular type of flow so that an optimum design may make use of both attached and separated flows. The boundaries between separated- and attached-flow regimes are sensitive to changes in wing leading-edge radius, wing thickness, and Reynolds number (refs. 1, 4, 6, and 8). To take advantage of the sensitivity of the boundaries between flow regimes, it becomes necessary to understand the influence of geometrical and flow parameters on the incipient separation of a delta wing. Incipient separation is defined as the onset of flow separation at the leading edge of the wing.

The present wind-tunnel investigation was conducted to establish a database to improve the understanding of incipient separation on delta wings at supersonic speeds. The effects of leading-edge radius, camber, Reynolds number, and boundary-layer state on the incipient separation on a 65° delta wing at $M = 1.60$ were determined. The three delta wing models tested had a 65° swept leading edge and varied in cross-sectional shape: a sharp wedge, a 20:1 ellipse, and a 20:1 ellipse with a –9.75° circular camber imposed across the span. The three wings were tested in the Langley Unitary Plan Wind Tunnel at an M of 1.60, an R range of 1×10^6 to 5×10^6 ft^{-1}, a nominal angle of attack (α_{nom}) range of 0° to 9°, and an angle of sideslip (β) of 0°. The wings were tested with and without transition grit applied. Extensive surface-pressure coefficient data were obtained at two longitudinal stations. Extensive flow-visualization data were obtained to better understand the flow phenomena associated with incipient separation. The flow-visualization techniques employed were the vapor-screen, the painted-oil-flow, the injected-oil-flow, and the liquid-crystal techniques.

Symbols

AOA	angle of attack
b	wing reference span, in.

b_{to}	wing span with wingtips removed, in.
C_N	normal force coefficient obtained by integrating surface-pressure coefficient data
C_p	surface-pressure coefficient, $(P - P_\infty)/q$
CP#	designation on CD-ROM to denote pressure orifice number
c	wing root chord, in.
ESP	electronic scanning pressure
M	free-stream Mach number
M_N	component of Mach number normal to leading edge, $M\cos\Lambda_{LE}\sqrt{1 + \sin^2\alpha\ \tan^2\Lambda_{LE}}$
n	refractive index of a material
P	local static pressure, lb/ft^2
P_∞	free-stream static pressure, lb/ft^2
q	free-stream dynamic pressure, lb/ft^2
R	free-stream Reynolds number, ft^{-1}
R_x	local Reynolds number based on distance from apex along centerline of wing
r	leading-edge radius, in.
r_c	radius of curvature, in.
S	wing reference area, in^2
s	arc length, in.
T_{aw}	adiabatic wall temperature, °F
T_o	stagnation temperature, °F
t	wing thickness, in.
UPWT	Langley Unitary Plan Wind Tunnel
x, y, z	Cartesian coordinates where origin is at apex of wing, in.
α	corrected angle of attack, deg
α_{ac}	angle of attack as measured by accelerometer, deg
α_{att}	last angle of attack at which attached flow was observed, deg
α_{knu}	pitch of model as set by knuckle, deg
α_N	angle of attack normal to leading edge, deg, $\tan^{-1}(\tan\alpha/\cos\Lambda_{LE})$
α_{nom}	nominal angle of attack, deg
α_{sep}	angle of attack at which leading-edge flow separation is first detected, deg
β	sideslip angle, deg
γ	display monitor parameter which controls contrast and brightness of display
$\Delta\alpha$	change in angle of attack, deg
ζ	z/local semispan
η	y/local semispan
θ_c	angle of spanwise camber, deg
θ_f	angle of wind-tunnel flow, deg
Λ	sweep angle, deg
ϕ	roll angle, deg

Subscripts:

LE	leading edge
l	lower surface of wing
lam	laminar
max	maximum
min	minimum
TE	trailing edge
turb	turbulent
u	upper surface of wing

Tabulated Data Symbols:

ALPHA	α, deg
CP	C_p
ETA	η
FLOW ANGLE	θ_f, deg
MACH	M
PHI	ϕ, deg
PINF	P_∞, lb/ft^2
Q	q, lb/ft^2
R/FT	R, ft^{-1}
X	x, in.

Model Description

A conical 65° delta planform at $M = 1.60$ was chosen as the baseline geometry. The criteria used to select the baseline were M_N and α_N, which are shown in figure 1. As angle of attack increases, the 65° delta planform at $M = 1.6$ traverses the Stanbrook-Squire boundary (ref. 1) that delineates attached-flow and separated-flow regimes. The effects of wing leading-edge radius, wing leading-edge camber, Reynolds number, and boundary layer (laminar or turbulent) on leading-edge flow separation were expected to be most pronounced in the region of the Stanbrook-Squire boundary.

The effect of wing leading-edge radius and wing camber on leading-edge flow separation was examined by varying the cross-sectional shape of the baseline geometry. Details of the three models examined are in figure 2 and table 1. Appendix A contains the analytical expression for each of the cross-sectional shapes. Figure 3 shows the elliptical model installed in the Langley Unitary Plan Wind Tunnel (UPWT).

The baseline geometry was a 65° delta planform with a ratio of centerline thickness to semispan of 0.10. Cross-sectional shape was varied to obtain three wing designs: a sharp wing, an elliptical wing, and a cambered wing. The sharp wing had a wedge-shaped cross section, which is shown in figure 2(a). For machining purposes, the sharp wing had a leading-edge radius of 0.003 in. The elliptical wing, shown in figure 2(b), had a 20:1 elliptical cross section, which yielded a leading-edge radius to local semispan ratio ($r/(b/2)$) of 0.0025 along the length of the leading edge. The elliptical geometry was used as a baseline cross section in examining the effect of camber. A spanwise circular-arc camber was imposed on the elliptical cross section in the cross-flow plane to define the cambered wing. The angle of camber θ_c is defined as the spanwise camber angle at the wing leading edge. The cambered model had an θ_c of –9.75° (fig. 2(c)).

It should be noted in figure 2 that the wingtips of each model could be removed. The left side (viewed upstream from the trailing edge of the model) of the planform shows the wingtips attached and the right side shows the wingtips removed. The models were built with removable wingtips for testing in another facility with a smaller test section than that of the UPWT. The wingtips were attached for this investigation.

Each model was instrumented with pressure orifices on both the upper and the lower surfaces. The orifices were arranged in two spanwise rows at $x = 6$ in. and $x = 12$ in. (measured from the apex along the centerline). The upper surface-pressure orifices were located on the right side (viewed upstream from the trailing edge of the model) of the wing and the lower surface-pressure orifices were located on the left side of the wing. Each orifice on the elliptical and the cambered wings had an inner diameter of 0.01 in. Each orifice on the sharp wing had an inner diameter of 0.015 in. All tubing came out the back of the models as shown in the photographs in figure 3.

Tables 2, 3, and 4 contain the x and the η locations of each pressure orifice, the CP# of each pressure orifice (the CP# is also used in the pressure-listing file on the CD-ROM), and the condition of the orifice. On the elliptical and the cambered wings, the pressure orifice locations range from $\eta \approx 0.10$ to $\eta \approx 0.98$ at both x stations on the upper surface. However, because of the thinness of the sharp wing at the leading edge, the upper surface-pressure orifice locations on the sharp wing range only to $\eta = 0.820$ for the $x = 6$ in. station and to $\eta = 0.899$ for the $x = 12$ in. station. On the lower surface, the pressure orifice locations range from $\eta = 0.200$ to $\eta \approx 0.95$ at both x stations for the elliptical and the cambered wings. For the lower surface of the sharp wing, the pressure orifice locations range to $\eta = 0.802$ for the $x = 6$ in. station and $\eta = 0.901$ for the $x = 12$ in. station.

To minimize any effect of the model support system on the flow over the upper surface of the delta wing, a sting was constructed that attached to the trailing edge of each wing with two bolts. Figure 4 shows the details of the sting.

An electronic accelerometer measured angle of attack during pressure data acquisition. The angle of attack (AOA) sensor was placed in a housing that was attached to the lower surface of the mounting pad of the sting. Thus, the AOA sensor was located directly behind the trailing edge of the delta wing. Because of this location, the AOA sensor was not influenced by sting deflections due to aerodynamic loading. The details of the AOA housing are shown in figure 5. Figure 3(b) shows the assembly of the elliptical wing, sting, and AOA housing components.

Wind-Tunnel Test Description

The wind-tunnel test program was conducted in test section 1 of the UPWT at $M = 1.60$ over a range of R from 1×10^6 ft^{-1} to 5×10^6 ft^{-1}. All data were obtained at stagnation temperature (T_o) of 125°F with the exception of the liquid-crystal data. The liquid-crystal data were obtained at $T_o = 120$°F, 125°F, and 130°F. The test program was conducted under the following test conditions:

Mach number	Stagnation pressure, psf	T_o, °F	R, ft^{-1}
1.60	539	125	1×10^6
1.60	1067	120	2×10^6
1.60	1079	125	2×10^6
1.60	1091	130	2×10^6
1.60	1618	125	3×10^6
1.60	2157	125	4×10^6
1.60	2668	120	5×10^6
1.60	2697	125	5×10^6
1.60	2728	130	5×10^6

Reference 9 contains a detailed description of the wind tunnel and the operating conditions of the wind tunnel.

The dew point was maintained sufficiently low during the pressure tests to prevent condensation in the tunnel. However, at $R = 5 \times 10^6$ ft^{-1}, the dew point was difficult to control and it rose throughout the run. Eventually, a fog appeared in the test section. To control the dew point, it became necessary to manually bleed in dry air. Figure 6 shows the effect of dew point on the surface-pressure measurements for the cambered wing at $R = 5 \times 10^6$ ft^{-1}. Dew point was considered unacceptable when the generally accepted value (from unpublished data based on ref. 9) was not met and/or a fog appeared in the test section.

As discussed in reference 9, flow angularity exists inside the wind-tunnel test section and is illustrated in figure 7. To account for this flow angularity, the model was offset in pitch before data were acquired. This offset is known as the flow angle θ_f where positive flow angularity means the flow is deflected upward. A detailed discussion on the determination of the flow angle is contained in appendix B. The angle of attack correction due to flow angularity was determined to be 0.4°. The corrected angle of attack is referred to as α.

To obtain pressure data, the model was set at $\phi = 0°$ and the angle of attack was measured with the AOA sensor located directly behind the trailing edge of the wing. The angle of attack measured with the AOA sensor is referred to as α_{ac} and is shown in figure 7.

To acquire flow-visualization and liquid-crystal data, the model was set at $\phi = 90°$. Because the AOA sensor could not be used at this roll angle, the angle of attack was set by using the beta angle system of the wind tunnel. (The beta angle system sets the sideslip angle of a model at $\phi = 0°$.) This arrangement sets the pitch angle at the tunnel end of the sting instead of at the base of the model. Thus, sting deflections had to be accounted for when the angle of attack was set. Sting deflections were determined by comparing α_{ac} with a corresponding pitch angle measured at the knuckle α_{knu}. The knuckle is the tunnel hardware in which the sting is installed and is shown in figure 7. Figure 8 shows an example plot of α_{knu} and α_{ac}, which were measured on the elliptical wing without grit at $R = 1 \times 10^6$ ft^{-1}. The line through the data points is a least squares fit and was used to determine the sting deflections. Sting deflections were also obtained at $R = 2 \times 10^6$ and 5×10^6 ft^{-1}.

Transition grit was used to ensure fully turbulent flow over the model when the flow was attached at the wing leading edge. Boundary-layer transition strips of No. 40 (0.0181-in. diameter) sand grit were applied 0.169 in. perpendicular to the leading edge of the delta wing on both the upper and the lower surfaces. The grit was sprinkled on the wing in a strip that was 0.0625 in. wide. The grit size and location were selected by consulting unpublished data that were based on the methods and the data in references 10 to 12.

Shown in figure 9 is the location of the grit with respect to the pressure orifices for each of the three delta wings. The surface-pressure coefficients at the orifices in or near the strip of grit are affected by the presence of the grit (fig. 10). The effect of the grit is more pronounced at the $x = 6$ in. station than at the $x = 12$ in. station. The orifices at the $x = 6$ in. station are spaced closer together than at the $x = 12$ in. station, which can be seen in figure 9(c). Thus, the effect of the grit covers more of the orifices at the $x = 6$ in. station.

For the lower surface, the effect of grit is present over the entire angle of attack range. However, for the upper surface, the effect of grit on the surface-pressure distribution is present only at low angles of attack. This observation can be explained by noting that for attached-flow cases at low angles of attack, the flow moves inboard from the wing leading edge to the transition strip. Whereas, for separated-flow cases at higher angles of attack, the flow approaches the transition strip from the other direction as the flow separates at the leading edge, reattaches inboard of the transition strip, and moves outboard towards the transition strip as shown in figure 11 (from ref. 5).

Test Techniques

The five test techniques used during the test program were surface-pressure measurements, vapor screens, painted oil flows, injected oil flows, and encapsulated liquid crystals.

Surface-Pressure Measurements

Each model had surface-pressure orifices on the upper and the lower surface with the tubing exiting at the rear of the model. The tubing was connected to the electronic scanning pressure (ESP) system located outside the wind-tunnel test section. A valuable feature of the system is the ability to calibrate the ESP modules at anytime during the test. With this feature, changes in temperature or other environmental features can be taken into consideration.

The selection of ESP modules was based on the expected maximum and minimum pressures on the delta wing over the angle of attack range of 0° to 9°. The following is a table of the expected maximum and minimum pressures on the upper and the lower surface of the delta wing for $M = 1.60$ and $T_o = 125$°F:

R, ft^{-1}	$P_{l,\max}$ at $(C_p)_{l,\max} = 0.25$, psi	$P_{l,\max}$ at $(C_p)_{l,\min} = 0.05$, $(C_p)_{u,\max} = 0.05$, psi	$P_{l,\max}$ at $(C_p)_{u,\min} = -0.45$, psi
1×10^6	1.276	0.9597	0.1701
2×10^6	2.553	1.921	0.3417
3×10^6	3.828	2.881	0.5118
4×10^6	5.103	3.840	0.6819
5×10^6	6.381	4.801	0.8535

The expected maximum and minimum pressures were obtained from the computational solutions for the wind-tunnel model geometries at $M = 1.60$ and $T_o = 125°$F. (See ref. 13.)

At the higher Reynolds numbers, the lower surface would likely experience pressures beyond the range of a 5 psi module; so the 15 psi module was used. The upper surface would likely experience pressures ranging from very low values up to 5 psi; therefore, the 5 psi module was selected. In some instances, the upper surface pressures exceeded the range of the 5 psi module—for example, when the wing was subjected to negative angles of attack at $R = 5 \times 10^6$ ft^{-1}. These data were discarded. The 5 psi modules had an accuracy of ±0.0025 psi and the 15 psi module had an accuracy of ±0.0075 psi.

When obtaining surface-pressure measurements, the angle of attack was set and the pressures were allowed to settle before taking measurements. A study of the effect of settling time on the pressure measurements was performed. Figure 12 shows surface-pressure coefficient data taken with a 2 min settling time and with a 7 min settling time at three points. The measurements obtained at the different settling times are the same within the accuracy of the equipment. Based on these results, a settling time of 2 min was allowed between angle of attack changes.

To obtain the pressure data, an α sweep from 0° to 9° in 0.5° increments was performed. When warranted by inspection of the on-line pressure plots, a second α sweep was performed to obtain data over a selected range in 0.25° increments. These two α sweeps were used to determine the repeatability of the pressure data. Figure 13 shows a plot of surface-pressure coefficients with α for both α sweeps. Figure 13 shows that the data repeatability is satisfactory because the surface-pressure coefficients obtained during the second α sweep follow the trend of the surface-pressure coefficients from the first α sweep.

Vapor-Screen Technique

The vapor-screen technique provides qualitative data on the flow field above the leeward surface of the model. Model preparation for the vapor-screen technique consisted of painting one coat of black paint onto the surface of the model. White dots were painted on the model surface centerline at $x = 6$ in. and $x = 12$ in. (the locations of the rows of pressure orifices). Once tunnel start-up was complete, water was added in the diffuser downstream of the test section until a uniform vapor was produced in the test section.

A 4-W argon-ion laser, which emits a blue-green light, was used to create the light sheet across the tunnel test section. Usually, only 2 W of laser power were necessary to produce the desired vapor-screen image. A dual cylindrical lens was used to spread the laser beam. The lens assembly was mounted on a support that could rotate and traverse vertically to the desired orientation. Once a desired orientation was reached, the laser was fixed in place and the model was moved to obtain vapor-screen photographs at various x locations. Still photographs were obtained with 70-mm film and a camera inside the test section. The relative locations of the model, light sheet, and camera are shown in figure 14. Still photographs were obtained at the $x = 12$ in. station only.

One undesirable characteristic of the vapor-screen technique is the reflection of the light sheet off the surface of the model. The use of flat black paint on the surface of the model minimizes this reflection, but does not eliminate it. Another undesirable characteristic of the vapor-screen technique is that the quality of the vapor is more difficult to control in the UPWT at lower Mach numbers such as 1.60. Constant visual monitoring of the vapor and subsequent adjustment of the water input is necessary to ensure an evenly distributed vapor in the test section.

Painted-Oil-Flow Technique

The painted-oil-flow technique provides qualitative data on the flow characteristics of the surface of the model. For the painted-oil-flow technique, the model was painted with one coat of flat black zinc chromate primer. The model surface was then brushed with a mixture of 90W oil and yellow fluorescent powder. During the tunnel start-up period, the model was kept horizontal to prevent the oil from running. The model was rolled 90° (wings vertical) and was illuminated by four ultraviolet lamps that were mounted on the sidewall door. With self-developing film, photographs of the painted oil flows were taken through the window by a camera mounted

outside the tunnel on the sidewall door. After the model was positioned, the oil-flow pattern stabilized in approximately 3 to 4 min.

An undesirable characteristic of this technique was that only 3 or 4 angles of attack could be documented before the oil had to be replaced. The number of angles of attack that can be documented in one setup decreases with increasing Reynolds number.

Injected-Oil-Flow Technique

The injected-oil-flow technique also provides qualitative data on the flow characteristics of the surface of the model. The injected-oil-flow technique differs from the painted-oil-flow technique in that the oil is injected onto the surface through the pressure orifices. The injection was accomplished by the pressure difference between the pressure inside the tunnel and the higher atmospheric pressure outside the tunnel. A peristaltic pump was also used to inject the oil through the orifices. Each upper surface orifice tube was connected to a peristaltic pump module located outside the test section. The oil-flow rate was adjustable as a function of pump speed for all the orifices simultaneously. The oil-flow rate for each orifice was adjustable from 0 to approximately 4 ml/min. The source of oil for each peristaltic pump module was a common container of SAE 10 oil that was mixed with fluorescent powder.

Maintaining constant flow rates between orifices was difficult at times. The difficulty was caused by the fluorescent powder clogging the tubes. The oil and powder mixture had been stirred and filtered beforehand to eliminate large pieces of powder. However, the nonuniform restrictions of each orifice and the associated tubing length of 15 ft allowed small pieces of powder to accumulate and clog some of the tubes. The disparity between orifice flow rates was greater when the pressure difference across the tubes was allowed to be the only motive force of the oil through the tubes. The peristaltic pump provided better uniformity in flow rate among orifices.

The model was prepared and illuminated in the same manner as it was for the painted-oil-flow technique. The oil flows were photographed with an instrumentation camera that had a wide angle lens and 70-mm black and white film. A 30-sec exposure time was generally used.

The flow patterns took less than a minute to settle after a change in α. When a more significant amount of time was needed to obtain a desired change in flow conditions, the oil flow could be slowed by clamping the tubes and removing them from the container of oil and powder mixture. However, after approximately 2 hr, the fluorescent powder caused the paint to flake. Nevertheless, the injected-oil-flow technique allowed many more data points to be obtained than could be obtained with the painted-oil-flow technique. In the painted-oil-flow technique, the oil wore off after 3 to 4 data points (10–20 min) were obtained. However, as the oil on the model is being continually replaced in the injected-oil-flow technique, data points could be taken until the paint started to flake.

Liquid-Crystal Technique

The liquid-crystal technique provides quantitative data on the flow characteristics of the surface of the model. This technique records the data visually with photographs that capture the varying colors of the thermochromic liquid crystals. The thermochromic liquid crystals used in this technique are materials that demonstrate color changes when their temperature is changed. Reference 14 discusses the properties of liquid crystals and how these properties are exploited in measuring temperature. The color of a liquid crystal changes from black to red to blue as the temperature is increased. As a result of this feature, these liquid crystals have been used widely in thermometry and thermography of surfaces.

In their normal state of operation, these liquid crystals are in a viscous fluid state and flow under an applied shear stress (ref. 15). Thus, the liquid crystals do not bind rigidly to the model surface that is exposed to a flow of fluid (ref. 16). To avoid flowing when under shear stress, microdroplets of these liquid crystals are encapsulated in polymer shells (ref. 14). A slurry of the capsules in a water and polymer solution produces a paint that can be sprayed on the model surface with an air brush. When it dries on the model surface, the paint leaves a rigid film of microencapsulated thermochromic liquid-crystal droplets bound rigidly to the surface yet capable of responding to the surface temperature (refs. 14 and 17). The density of the microencapsulated droplets is high enough so that a dry film (approximately 50–100 μm thick) will provide the necessary continuous spread of liquid crystals on the surface. The color pattern on the surface provides information about the temperature distribution on the surface by referring to the calibration of the liquid crystals. The calibration is obtained with the methods in references 15 and 17. The commercially available microencapsulated liquid crystals generally cover a limited temperature range of ≈9°F. This limited range allows one to choose a liquid crystal that is suitable for the desired operation.

To prepare the model for the installation of the liquid crystals, the model surface was thoroughly cleaned with acetone and methanol. The model was then given a black coating compatible with the encapsulated liquid crystals. The black coating (approximately 10 μm) was deposited on the model surface by spraying a flat black paint with an air brush. Unlike many lacquer-based flat black

paints, the black paint used for this test was water soluble and absorbed the light incident on its surface. This absorption meets the necessary condition that the observed reflected light is from the liquid-crystal layer and not from the black coating itself. The paint, being a good thermal insulator, also provides an adequate thermal insulation layer between the liquid crystal and the model surface. After the black coating has completely dried, the encapsulated thermochromic liquid crystal is spray painted on the black coated model to provide a dry uniform film that is approximately 50 μm thick.

In the present experiment, the upper surface of the model was divided into two parts at the centerline. Each side was coated with liquid crystals of different operating ranges of temperature. To gather as much information as possible with these two ranges of temperature, data were obtained with three T_o: 120°F, 125°F, and 130°F. The temperature range of the liquid crystals was selected based on the T_{aw} for a flat plate at $M = 1.60$. (See ref. 18.) The following is a table of the T_{aw} at each temperature for both a laminar and a turbulent boundary layer:

T_o, °F	$T_{aw,\mathrm{lam}}$, °F	$T_{aw,\mathrm{turb}}$, °F
120	90.6	96.4
125	95.3	101.2
130	100.0	106.0

Based on these values, the right side (viewing upstream from the trailing edge of the model) was coated with liquid crystals that had an operating range of 86°F to 95°F. The left side was coated with liquid crystals that had an operating range of 95°F to 104°F.

To obtain photographs of the liquid-crystal data, the model was rolled 90° (wingtips vertical) with angle of attack set by using the beta angle system of the wind tunnel. The model was illuminated by white light lamps mounted on the sidewall door. The light reflected normal to the model surface was recorded by still photographs. An instrumentation camera with a wide angle lens was mounted outside the tunnel on the sidewall door. Color photographs were obtained with 70-mm color film. Data were obtained for the α_{nom} range of 0° to 9° in 0.5° increments. After an angle of attack change, the change in liquid-crystal color due to changes in surface temperature was virtually instantaneous.

The advantage of using the liquid-crystal technique is the ability to gain both qualitative and quantitative data over the entire surface of the model. A possible source of concern in this technique is the interplay of temperature on the lower and the upper surfaces because of conduction of heat through the model. Although the black paint applied on the model is an insulator, it probably does not eliminate the heat transfer completely. One disadvantage of the liquid-crystal technique was that the coating would start to flake away from the model after being in the flow stream for 2 to 4 hr. This problem, however, could probably be avoided by using a sturdier oil-based paint.

Results and Discussion

An experimental investigation of incipient separation on supersonic delta wings was conducted. Three 65° delta wing models were tested in UPWT at $M = 1.60$ over an R range of 1×10^6 ft^{-1} to 5×10^6 ft^{-1} with and without transition grit applied to the surface of the models. The three delta wing models had a 65° swept leading edge and varied in cross-sectional shape: a sharp wedge, a 20:1 ellipse, and a 20:1 ellipse with a –9.75° circular camber imposed across the span. Surface-pressure coefficient, liquid-crystal, and flow-visualization data were obtained for each model. Table 5 summarizes the different data obtained for each configuration. The α_{nom} obtained is also listed in table 5. Presented in tables 6 to 11 are indexes of the angles of attack at which data were obtained during each test technique. The angle of attack data in tables 6 to 11 have been corrected for wind-tunnel flow angularity and sting deflections.

All experimental data obtained from the wind-tunnel test program are on a CD-ROM. The flow-visualization data are stored on the CD-ROM in digital images. Appendix C contains a detailed description of the process used to convert the film negatives or prints to digital images. Appendix C also contains a description of the directory structure and the file formats on the CD-ROM, as well as information on public domain software available to examine the data. The surface-pressure coefficient data are also stored on the CD-ROM in an ASCII file. The surface-pressure coefficient data have been summarized and are plotted in appendix D.

Representative results obtained from the experimental investigation are presented here. The discussion is divided into four sections. The first section discusses the effect of angle of attack on the development of flow structures observed over the leeside of the delta wing models. The second section discusses the effect of longitudinal position on the development of the flow on the delta wing model. The third and the fourth sections discuss the effect of Reynolds number and transition grit on the leeside flow of the delta wing models. Surface-pressure coefficient data are presented for all three wings. However, the majority of the flow-visualization data presented here are for the elliptical wing model.

Effect of Angle of Attack

Upper surface-pressure coefficient data. The effect of angle of attack on the surface-pressure coefficient distribution (hereafter referred to as pressure distribution) on the upper surface for each wing without grit at $x = 12$ in., $M = 1.60$, and $R = 2 \times 10^6$ ft^{-1} is presented in figure 15. For $\alpha < 2.22°$ on the elliptical wing (see fig. 15(b)), the pressure distribution is smooth to the leading edge. This pressure distribution is typical for an attached-flow condition at the wing leading edge. However, for $\alpha \geq 2.22°$, inflections in the pressure distribution over the elliptical wing occur near the leading edge. These inflections are indicative of flow separation at the wing leading edge (referred to hereafter as leading-edge separation). As α increases, the inflections develop into a pressure coefficient distribution typical of a vortex emanating from the wing leading edge (referred to hereafter as leading-edge vortex).

At the onset of leading-edge separation, a separation bubble forms at the wing leading edge. A separation bubble emanating from the wing leading edge (referred to hereafter as a separation bubble) has been defined (refs. 5 and 19) as a leading-edge vortex whose core lies very close to the wing surface so that the reattachment of the induced flow onto the wing surface coincides with the inboard edge of the vortex. As angle of attack increases, the core of the vortical structure lifts off the surface and the reattachment line of the induced flow then occurs slightly inboard of the vortex. Figure 11 (from ref. 5) shows the basic leading-edge vortex characteristics.

As discussed in reference 5, when the energy of the flow normal to the leading edge is not sufficient to negotiate the expansion at the leading edge, the flow will separate at the leading edge and form a region of rotational flow referred to as the primary vortex. The pressure distribution associated with a leading-edge vortex is characterized by a sudden change in the surface-pressure coefficient that occurs over a small range of η with the lower pressures occurring outboard. This characteristic corresponds to the region where the vortex-induced flow reattaches inboard of the vortex. On the inboard side of this reattachment point there is streamwise flow. On the outboard side of the reattachment point, there is outboard spanwise flow, which can induce surface velocities that can decrease the surface pressure relative to the attached-flow pressure distribution (fig. 11).

Figure 16 presents the surface-pressure coefficient distribution for each wing without grit at common nominal angles of attack for $x = 12$ in., $M = 1.60$, and $R = 2 \times 10^6$ ft^{-1}. All three configurations develop a leading-edge vortex as angle of attack increases, which is shown in figures 15 and 16. The data in figure 16 show that wing cross-sectional shape affects the vortex strength as indicated by the sudden change in pressure coefficient near the inboard edge of the vortex. The sharp wing data in figure 16 show a greater increase in pressure coefficient occurring over a smaller range of η than the elliptical and the cambered wings for $\alpha_{nom} = 8°$. This greater increase in pressure indicates a stronger vortex than that observed for the elliptical and the cambered wings. Of the three wings, the cambered wing has the smallest change in pressure coefficient over the largest range of η. Thus, wing leading-edge radius and wing camber appear to weaken the leading-edge vortex. However, note that all three configurations have equivalent values of C_p at the leading edge for $\alpha_{nom} \geq 8°$.

The angle of attack at which leading-edge separation begins is also dependent upon the cross-sectional shape of wing. The data in figures 15 and 16 show that the angle of attack at which the onset of leading-edge separation is first detected α_{sep} is 2.22° for the elliptical wing and 3.72° for the cambered wing. The pressure coefficient distribution inflection that indicates the onset of leading-edge separation occurs at $0.9 < \eta < 1.0$. Note from figures 15 and 16 that the pressure coefficient distribution for the sharp wing ends at $\eta = 0.9$ for the station at $x = 12$ in. The pressure coefficient distribution for the sharp wing for the station at $x = 6$ in. ends at $\eta = 0.82$. Therefore, from the data in figures 15 and 16 and the data for x = 6 in. (not presented here), it is difficult to determine at what α the onset of leading-edge separation occurs for the sharp wing. However, Stanbrook and Squire (ref. 1) observed that increasing wing leading-edge radius increases α_{sep}. Therefore, leading-edge separation on the sharp wing would be expected to occur at a lower angle of attack than the elliptical wing.

The cambered wing has a wing leading-edge geometry that effectively lowers the incidence angle of the flow at the leading edge when compared with the uncambered wings. The geometrical angle of the cambered wing at the leading edge is –9.75° in the cross-flow plane. This angle corresponds to 3.76° in the streamwise direction. Thus the effective angle of flow approaching the leading edge of the elliptical wing is 3.76° higher than that observed for the cambered wing at any given angle of attack. The data in figure 15 show that the incidence of α_{sep} increased only 1.5° from the elliptical wing ($\alpha_{sep} = 2.22°$) to the cambered wing ($\alpha_{sep} = 3.72°$). The elliptical and the cambered wing data in figure 16 show that, at the wing centerline, camber had a much smaller impact on the angle of flow. Thus, the geometrical camber essentially lowers the incidence angle of flow over the cambered wing with a more pronounced effect at the wing leading edge.

Lower surface-pressure coefficient data. Figure 17 presents the effect of angle of attack on the lower surface-pressure coefficient distribution for each wing without grit at $x = 12$ in., $M = 1.60$, and $R = 2 \times 10^6$ ft^{-1}. The data show that for each wing, the flow is attached at the wing leading edge. The surface-pressure coefficient is seen to increase with increasing η and angle of attack.

Vapor-screen data. Presented in figure 18 are vapor-screen photographs for the elliptical wing without grit at $x = 12$ in., $M = 1.60$, and $R = 2 \times 10^6$ ft^{-1}. The effect of angle of attack on the flow structure is illustrated. The vapor-screen data do not show any leading-edge vortical structure until the $\alpha = 3.7°$ condition (fig. 18(f)). However, the surface-pressure coefficient data in figure 15(b) indicate that leading-edge separation is present at $\alpha = 2.22°$. This inconsistency is related to the glare of the laser light sheet off the surface of the wind-tunnel model. At the onset of leading-edge separation ($\alpha_{sep} = 2.22°$ for the elliptical wing), the leading-edge separation is so small and close to the surface of the wing that the glare could obscure the flow structure. At $\alpha = 3.7°$ (fig. 18(f)), there is an inboard region of separation that has been previously observed with leading-edge vortical flows computationally. (See ref. 19.) This region of separation is also evident at the $\alpha = 2.7°$ (fig. 18(d)) condition and could indicate a leading-edge separation that is masked by the glare of the laser sheet off the wind-tunnel model.

For $\alpha \geq 3.7°$, the vortical structure of the leading-edge separation is apparent. For each $\alpha \geq 3.7°$ the inboard edge of the vortex is within the η range of the sudden pressure change in the pressure distribution (fig. 15).

Painted- and injected-oil-flow data. Figure 19 presents painted-oil-flow photographs for the elliptical wing without grit at $\alpha = 3.14°$, 4.17°, 6.26°, and 8.34°, $M = 1.60$, and $R = 2 \times 10^6$ ft^{-1}. Figure 20 presents injected-oil-flow photographs for the elliptical wing without grit at $M = 1.60$, $R = 2 \times 10^6$ ft^{-1}, and $0° \leq \alpha \leq 9.39°$ at approximately 1° increments. The data illustrate the effect of angle of attack on vortex growth. The injected-oil-flow data in figure 20 indicate attached flow on the upper surface of the elliptical wing for $\alpha < 2.08°$. For $\alpha_{nom} = 2°$ and 3° (figs. 19(a), 20(c), and 20(d)), the oil accumulated along the leading edge of the wing, which indicates a narrow leading-edge separation bubble. The injected-oil-flow data (fig. 20(c)) and the surface-pressure coefficient data (fig. 15(b)) indicate similar values of α_{sep}, 2.08° and 2.22°, respectively. In contrast, the vapor-screen data (fig. 18(f)) indicate $\alpha_{sep} = 3.7°$, a greater angle than those observed in the injected-oil-flow and surface-pressure coefficient data.

For each $\alpha_{nom} \geq 4°$, the oil-flow patterns indicate a reattachment line that separates the inboard streamwise flow and the outboard spanwise flow induced by the presence of the leading-edge separation. For $\alpha = 4.17°$ (figs. 19(b) and 20(e)), the location of the flow reattachment point corresponds to the location of the inboard edge of the leading-edge separation bubble, which is shown in the vapor-screen data (fig. 18(g)). Thus, the leading-edge separation at $\alpha = 4.17°$ would be classified as a leading-edge separation bubble. For each $\alpha_{nom} \geq 5°$, the location of the reattachment line as shown in the oil-flow data (figs. 19 and 20) falls slightly inboard of the edge of the leading-edge separation as shown in the corresponding vapor-screen data in figure 18. Thus for $\alpha_{nom} \geq 5°$, the leading-edge separation is defined as a classical leading-edge vortex.

For each $\alpha \geq 4.17°$, the location of the flow reattachment point as shown in the oil-flow data (figs. 19 and 20) lies in the η range over which a sudden pressure change occurs in the corresponding pressure distribution (fig. 15(b)). Also recall that the vapor-screen data in figure 18 showed that the inboard edge of the primary vortex lies in the same η range.

Liquid-crystal data. Figure 21 presents liquid-crystal photographs for the elliptical wing without grit at $M = 1.60$ and $R = 2 \times 10^6$ ft^{-1} for various angles of attack. The photographs provide quantitative and qualitative data about the flow characteristics of the surface of the elliptical wing. The color of the liquid crystals is related to the temperature on the surface of the wind-tunnel model. Figures 21(k) and 21(l) present the color band for the temperature range on the right and the left side of the wing, respectively.

The data in figures 21(a) and 21(b) show that for $\alpha \leq 1.03°$, the temperature on the surface increases suddenly along a line roughly parallel to the leading edge of the wing. At $\alpha = 2.08°$ (fig. 21(c)) the higher temperature extends to the leading edge of the wing. This observation corresponds to the pressure distribution data (fig. 15(b)) and the injected-oil-flow data (fig. 20(c)), which show values of α of 2.22° and 2.08°, respectively. The data in figures 21(d) to 21(j) for $\alpha \geq 3.14°$ also show a distinct line at which the surface temperature changes dramatically. However, this line is not parallel to the wing leading edge, but extends from the wing apex to the wing trailing edge. The angle between this line and the leading edge of the wing increases with increasing angle of attack. The location of this line corresponds to the flow reattachment line evident in the corresponding oil-flow data in figures 19 and 20. This line represents a temperature change on the surface of the model due to reattachment of the leading edge vortical flow to the surface of the wing. (See figs. 19(d), 20(i), and 21(i) for $\alpha_{nom} = 8°$.)

The temperature variation occurring over the wing at $\alpha_{nom} = 0°$ and 1.03° (figs. 21(a) and 21(b)) is believed to be an indication of boundary-layer transition. When the flow separates from the wing leading edge and reattaches inboard, the temperature of the wing surface inboard of the reattachment line is that of the turbulent flow at $\alpha = 0°$. Thus, the flow inboard of the leading-edge separation for $\alpha \geq 2.08°$ is believed to have a turbulent boundary-layer condition. The temperature of the wing surface outboard of the flow reattachment line is that of the laminar flow at $\alpha = 0°$. Also note from the pressure distribution data in figure 15(b) that the flow outboard of the flow reattachment point is in a proverse pressure gradient until the pressure distribution levels to a larger negative value of C_p than that at the centerline of the wing. A proverse pressure gradient is a favorable condition for a laminar boundary layer. Thus, the flow outboard of the reattachment point is believed to have a laminar boundary-layer condition.

Effect of Longitudinal Position

Flow conicity. A comparison of the pressure distributions at two longitudinal positions on the model indicates whether the flow over the wing grows conically down the length of the wing. Figure 22 shows the upper surface-pressure distribution for each wing at $x = 6$ in. and $x = 12$ in. for $M = 1.60$ and $R = 2 \times 10^6$ ft^{-1}. The sharp wing data in figure 22(a) show that the pressure distributions at $x = 6$ in. and $x = 12$ in. are very similar, thus indicating that the flow over the leeside of the sharp wing grows conically down the length of the wing.

The elliptical wing data in figure 22(b) show that the pressure distributions at $x = 6$ in. and $x = 12$ in. vary significantly beginning from $\alpha = 2.22°$ (the angle of attack at which leading-edge separation was first detected in the pressure data) to, but not including, $\alpha = 5.23°$ (the angle of attack at which a classical leading-edge vortex was first detected in the injected-oil-flow data, which is shown in fig. 20(f)). For $1.23° < \alpha < 5.23°$, the inboard edge of the leading-edge separation (denoted by a sudden change in the pressure distribution) occurs at different η conditions for the $x = 6$ in. and $x = 12$ in. stations, which indicates that the flow does not grow conically down the length of the elliptical wing. This observation corresponds to the painted and the injected-oil-flow data for $1° < \alpha_{nom} < 5°$ (figs. 19(a), 19(b), 20(c), 20(d), and 20(e)), which show a leading-edge separation bubble that does not grow conically down the length of the wing.

For $\alpha > 5.23°$, the pressure distributions at the $x = 6$ in. and $x = 12$ in. stations (fig. 22(b)) are similar from the centerline to the flow reattachment point (determined from the oil-flow data), which indicates that the flow grows conically down the length of the wing. This observation corresponds to the injected-oil-flow data for $\alpha_{nom} = 5°$ (fig. 20(f)), which show a conical growth of the leading-edge separation. Outboard of the flow reattachment point for $\alpha = 5.23°$, the pressure distribution levels to a surface-pressure coefficient that is lower at the $x = 12$ in. station than that observed at the $x = 6$ in. station. This observation indicates that, for angles of attack just above the α range of nonconical growth of the flow, the leading-edge vortex grows conically, but varies slightly in strength down the length of the wing. For $\alpha > 5.23°$, the surface-pressure coefficients near the wing leading edge (fig. 22(b)) are essentially the same at the two x stations.

The pressure data in figure 22(c) and the flow-visualization data (not presented here) of the cambered wing show similar trends to the data for the elliptical wing. The flow over the wing is nonconical at $3.18° < \alpha < 7.18°$. Recall that $\alpha_{sep} = 3.72°$ for the cambered wing at $M = 1.60$ and $R = 2 \times 10^6$ ft^{-1}. The vapor-screen data and oil-flow data for the cambered wing (not presented here) show that the leading-edge vortex is first detected at $\alpha_{nom} = 7°$.

Figure 23 shows the upper surface-pressure distribution for each wing without grit at $x = 6$ in. and $x = 12$ in. for $M = 1.60$ and $R = 5 \times 10^6$ ft^{-1}. For the angle of attack range where nonconical growth of the flow was observed at $R = 2 \times 10^6$ ft^{-1} for the elliptical wing and the cambered wing, the $R = 5 \times 10^6$ ft^{-1} data in figures 23(b) and 23(c) show that the pressure distributions at $x = 6$ and 12 in. vary in the η range from the wing leading edge to the sudden pressure change that denotes the inboard edge of the leading-edge separation. However, the variations between the pressure distributions at the $x = 6$ in. and $x = 12$ in. stations are much smaller than was observed at $R = 2 \times 10^6$ ft^{-1}. Thus, Reynolds number affects the conicity of the flow over the 65° swept delta wing.

R_x held constant. The surface-pressure coefficient data presented in figures 22 and 23 show the effect of longitudinal position on the wing at a constant R. The local Reynolds number for each x station R_x changes when R is held constant. For $R = 2 \times 10^6$ ft^{-1} at $x = 6$ in., $R_x = 1 \times 10^6$, and at $x = 12$ in., $R_x = 2 \times 10^6$. Thus, the nonconical growth of the flow could be attributed to Reynolds number effects. Figure 24 shows the upper surface-pressure distributions at $x = 6$ in. and $x = 12$ in. for several wing geometry and constant R_x. The sharp wing data in figure 24(a) show that the longitudinal position on the wing does not have a profound affect on the shape of the pressure distribution when R_x is held constant. The data in figures 24(b) to 24(d) show that in the angle of attack range where nonconical growth of the flow was observed ($1.23° < \alpha < 5.23°$ for the elliptical

wing and $3.18° < \alpha < 7.18°$ for the cambered wing), the pressure distributions at the two x stations agree well. This observation indicates that the nonconical growth of the flow observed on the elliptical and the cambered wings is partially a function of R_x. The sharp wing and elliptical wing data in figures 24(a) to 24(c) also show slightly lower values of C_p across the whole span of the wing at higher R. This trend was not observed in the cambered wing data in figure 24(d).

Effect of Reynolds Number

Surface-pressure coefficient data. Data were obtained over an R range of 1×10^6 ft^{-1} to 5×10^6 ft^{-1} to determine the effect of Reynolds number on the onset of leading-edge separation. Figure 25 presents upper surface-pressure coefficient data obtained at various R_x conditions on the sharp wing model without grit at $x = 12$ in. The data in figure 25 were obtained at $M = 1.60$ over the angle of attack range of 0° to 9°. The pressure data in figure 25 show the development of a leading-edge vortex over the leeside of the sharp wing as the angle of attack increases. The leading-edge vortex influences the pressure distribution so that there is a sudden pressure change over a range of η. The flow reattachment point falls within this range of η. The pressure distribution outboard of this η range levels to a constant C_p near the wing leading edge. The pressure data in figures 25(b) and 25(c) show that the η range over which the sudden pressure change occurs decreases with increasing R_x and the amount of the sudden pressure change increases with increasing R_x. These observations indicate that the strength of the leading-edge vortex increases with increasing R_x. It should be noted that R_x appears to have little affect on the C_p near the centerline or near the leading edge of the sharp wing.

Figure 26 presents upper surface-pressure coefficient data obtained at various R_x conditions on the elliptical wing without grit at $x = 12$ in., $M = 1.60$, and $0° \le \alpha \le 9°$. The data in figure 26 show that Reynolds number has the most effect on the pressure distribution in the range of $1° < \alpha_{nom} < 5°$ where nonconical growth of the flow over the upper surface of the elliptical wing was observed for $R = 2 \times 10^6$ ft^{-1} (fig. 22(b)). At $\alpha_{nom} = 2.0°$, the pressure distribution at $R_x = 1 \times 10^6$ has an inflection near the wing leading edge, which indicates a leading-edge separation bubble. Because the location of the inflection in the pressure distribution at $\alpha_{nom} = 3°$ has moved more inboard than was observed at $\alpha_{nom} = 2.0°$, the leading-edge separation bubble grows larger with an increase in angle of attack. However, for a given angle of attack, the location of the inflection in the pressure distribution moves outboard with increasing R_x. This characteristic is seen more clearly in the surface-pressure coefficient data in figure 27, which presents the pressure distributions at $\Delta\alpha = 0.25°$ increments for the elliptical wing. Thus, the leading-edge separation bubble for $2° \le \alpha_{nom} < 5°$ on the elliptical wing becomes smaller with increasing R_x.

As the leading-edge separation bubble weakens with increasing Reynolds number, the pressure distribution moves to a distribution more typical of an attached flow at the wing leading edge (figs. 26(a), 26(b), and 27). As a result, the surface-pressure coefficient near the leading-edge decreases as Reynolds number increases. The data in figure 27 show that for $R_x = 1 \times 10^6$, the onset of leading-edge separation was first detected at $\alpha_{sep} = 1.97°$. The data for $R_x = 5 \times 10^6$ in figure 27 show that α_{sep} increases to 2.49° where the leading-edge separation is detected by a leveling of the pressure distribution at the leading edge. Thus, α_{sep} increases with increasing R_x.

The pressure data in figures 26(b) and 26(c) indicate that increasing the R_x slightly increases the strength of the leading-edge vortex present over the upper surface of the elliptical wing at the higher angles of attack ($\alpha_{nom} \ge 5°$). However, the pressure data in figures 26(b) and 26(c) also show that the value of C_p near the wing leading edge is insensitive to R_x.

Figure 28 presents upper surface-pressure coefficient data obtained at various R_x conditions on the cambered wing model without grit at $x = 12$ in., $M = 1.60$, and $0° \le \alpha \le 9°$. The cambered wing data in figure 28 show similar trends to those observed in the elliptical wing data. The pressure data in figure 28 show that Reynolds number has the most effect on the pressure distribution in the angle of attack range ($3° < \alpha_{nom} < 7°$) where nonconical growth of the flow over the upper surface of the cambered wing was observed at $R = 2 \times 10^6$ ft^{-1} (fig. 22(c)). As was found on the elliptical wing data, the pressure data for the cambered wing at $3° < \alpha_{nom} < 7°$ (fig. 28) show that as R_x increases, the size of the leading-edge separation bubble decreases and the surface-pressure coefficient near the leading edge decreases. Also the angle of attack at which leading-edge separation begins increases with increasing R_x as shown in figure 29, which presents the pressure distributions for the cambered wing at $\Delta\alpha = 0.5°$ increments. The pressure data in figure 29 show that the angle of attack at which leading-edge separation was first detected on the cambered wing increases from 3.70° for $R_x = 1 \times 10^6$ to 4.20° for $R_x = 5 \times 10^6$.

As seen with the elliptical wing data, the cambered wing data in figure 28 show that Reynolds number has a much smaller influence at $\alpha_{nom} \ge 7°$, where a leading-edge vortex has formed over the cambered wing. The pressure data in figure 28 show that as Reynolds number

increases from 1×10^6 to 5×10^6, the size of the leading-edge vortex is unaffected. However, the strength of the vortex increases slightly with increasing R_x. Also the C_p value near the wing leading edge is unaffected by R_x for $\alpha_{nom} > 7°$.

The R_x affects the onset of leading-edge separation on the leeside of the elliptical and the cambered wings. One explanation for this observation is the effect of R_x on the boundary layer of the model. With an increase in R_x, the boundary layer of the model would be expected to transition from a laminar condition to a turbulent condition closer to the wing apex and the wing leading edge. When a boundary layer is turbulent, the flow is more energetic than when the boundary layer is laminar. Thus, the closer the turbulent boundary layer is to the wing leading edge, the more energy the flow requires to remain attached at the wing leading edge. The onset of leading-edge separation would occur at a higher angle of attack.

The sharp wing data were not affected significantly by increasing R_x. The sharp wing data are available on the CD-ROM and in appendix D. The sharp wing developed a strong leading-edge separation as soon as angle of attack was increased from zero. The state of the boundary layer does not appear to affect flow structures that result from a very strong expansion at the wing leading edge. A strong expansion at the wing leading edge would occur for a sharp-edged wing at any angle of attack and for any wing at high angles of attack.

Vapor-screen data. The effect of Reynolds number on the flow structure over the cambered wing is illustrated in figure 30, which presents vapor-screen photographs for the cambered wing without grit at $x = 12$ in., $\alpha_{nom} = 5°$, $M = 1.60$, and various R_x. The data in figure 30 show a leading-edge separation bubble at $R_x = 1 \times 10^6$. The separation bubble becomes smaller as R_x increases until it finally is hidden by the glare of the laser light sheet off the surface of the model at $R_x = 5 \times 10^6$. This observation is supported by the pressure data in figure 28(b). The pressure data show that for $\alpha_{nom} = 5°$, a leading-edge separation exists at $R_x = 1 \times 10^6$, as indicated by a sudden change in the pressure distribution. The η location of this sudden change in pressure corresponds to the inboard edge of the separation bubble as shown in the vapor-screen data in figure 30(a). As R_x increases, the separation bubble becomes smaller, which is indicated by the outboard movement of the location of inflection in the pressure distribution near the leading edge (fig. 28(b)).

The effect of R_x on the flow over the cambered wing at a higher angle of attack is shown in figure 31. This figure presents vapor-screen photographs for the cambered wing without grit at $M = 1.60$, $x = 12$ in., $\alpha_{nom} = 8°$, and various R_x. The data in figure 31 show that R_x does not significantly impact the size of the leading-edge vortex at $\alpha_{nom} = 8°$. This observation is supported by the surface-pressure coefficient data in figure 28(c).

Painted- and injected-oil-flow data. The painted- and the injected-oil-flow techniques were used to examine the effect of Reynolds number on the flow characteristics of the surface of the wings. Figure 32 presents painted-oil-flow photographs for the cambered wing without grit at $\alpha_{nom} = 4°$, $M = 1.60$, and various R. Figure 33 presents the injected-oil-flow photographs for the same conditions. The oil-flow data in figures 32 and 33 show an accumulation of oil along the leading edge of the wing at $R = 1 \times 10^6$ ft^{-1} for $\alpha_{nom} = 4°$. This accumulation is indicative of a leading-edge separation bubble, which is also evident in the surface-pressure coefficient data in figures 28 and 29. The data in figures 32 and 33 show that as R increases, the accumulation of oil along the leading edge becomes thinner, which indicates a decrease in the size of the separation bubble. Decreasing separation bubble size with increasing Reynolds number is also seen in the surface-pressure coefficient data in figures 28 and 29.

The pressure distribution data for the elliptical and the cambered wings (figs. 27 and 29) showed that increasing Reynolds number increased the angle of attack at which leading-edge separation begins. Recall that figure 20 presents the injected-oil-flow data for the elliptical wing without grit at $M = 1.60$, $R = 2 \times 10^6$, and various angles of attack. Figure 34 presents injected-oil-flow photographs for the elliptical wing without grit at $\alpha_{nom} = 2°$ and 3°, $M = 1.60$, and $R = 5 \times 10^6$ ft^{-1}. For $R_x = 2 \times 10^6$, the oil-flow data in figure 20 show an accumulation of oil along the leading edge (indicating a leading-edge separation bubble) that first occurs at $\alpha = 2.08°$ ($\alpha_{nom} = 2°$, fig. 20(c)). However, the $R_x = 5 \times 10^6$ data in figure 34 do not show a leading-edge separation bubble occurring until $\alpha = 3.25°$ ($\alpha_{nom} = 3°$). This observation corresponds to the pressure data in figure 27, which show that α_{sep} increased from 2.22° ($\alpha_{nom} = 2°$) to 2.49° ($\alpha_{nom} = 2.25°$) as the R_x increased from 2×10^6 to 5×10^6.

The surface-pressure coefficient data in figures 26 and 28 indicated little influence of Reynolds number on the size of the leading-edge vortex at the higher angles of attack where a leading-edge vortex was present. Figure 35 presents injected-oil-flow photographs for the cambered wing without grit at $\alpha_{nom} = 8°$, $M = 1.60$, and various R. The data show that R does not significantly affect the position of the flow reattachment point of the leading-edge vortex. However, the secondary separation

occurring beneath the primary vortex appears to weaken with increasing Reynolds number.

Liquid-crystal data. Liquid-crystal data were obtained at $R = 2 \times 10^6$ ft^{-1} and 5 $\times 10^6$ ft^{-1} to examine the effect of Reynolds number on the flow characteristics of the leeside surface of the model. The liquid-crystal data in figure 21 for the elliptical wing at $R = 2 \times 10^6$ ft^{-1} first detected the onset of leading-edge separation at $\alpha = 2.08°$ ($\alpha_{nom} = 2°$). Figure 36 presents liquid-crystal photographs for the elliptical wing at $M = 1.60$ and $R = 5 \times 10^6$ ft^{-1} for various angles of attack. The data in figure 36 also showed the onset of leading-edge separation occurring at $\alpha = 2.17°$ ($\alpha_{nom} = 2°$). This observation does not correspond to those made in the surface-pressure coefficient data (fig. 27) and injected-oil-flow data (fig. 34) as shown in table 12. Table 12 presents the angle of attack at which leading-edge separation was detected with the surface-pressure, the injected-oil-flow, and the liquid-crystal data. Table 12 also shows the last angle of attack where attached flow was observed α_{att} in each data set. The angle of attack where leading-edge separation begins falls between α_{att} and α_{sep}. The data in table 12 show that the trend of an increase in α_{sep} with an increase in Reynolds number is supported by the pressure and injected-oil-flow data sets. The trend of an increase in α_{sep} with an increase in Reynolds number is not supported by the liquid-crystal data.

However, the liquid-crystal data did indicate a smaller leading-edge separation bubble at the $R = 5 \times 10^6$ ft^{-1} condition than that observed for the $R = 2 \times 10^6$ ft^{-1} condition (figs. 21(c) and 36(c) for $\alpha_{nom} = 2°$). This observation is supported by the surface-pressure coefficient data in figure 27, which show a decrease in the size of the leading-edge separation bubble with an increase in R_x. Because all the data sets indicate that an increase in Reynolds number decreases the size of the leading-edge separation bubble for a given angle of attack, the onset of leading-edge separation occurs at a higher angle of attack as Reynolds number increases. This observation could be explained by noting that increasing the Reynolds number moves the boundary-layer transition location closer to the leading edge. This explanation is supported by the liquid-crystal data for the elliptical wing at $\alpha_{nom} = 0°$ and 1° (figs. 21(a), 21(b), 36(a), and 36(b)). The liquid-crystal data show, inboard of the leading edge, a temperature variation that indicates boundary-layer transition. However, the temperature variation for the $R = 5 \times 10^6$ ft^{-1} condition occurs much closer to the leading edge than that observed for the $R = 2 \times 10^6$ ft^{-1} condition. This observation supports the explanation that boundary-layer condition affects the onset of leading-edge separation.

Effect of Transition Grit

Surface-pressure coefficient data. Data were obtained on the three models with and without grit applied to determine the effect of grit on the onset of flow separation at the wing leading edge. Figure 37 presents upper surface-pressure coefficient data obtained on the sharp wing model at $x = 12$ in. without grit and with transition grit. The data in figure 37 were obtained at $x = 12$ in., $M = 1.60$, and $R_x = 2 \times 10^6$ over the angle of attack range of 0° to 9°. The data in figure 37 show that the application of transition grit appears to have no effect on the development of the vortex over the leeside of the sharp wing with increasing angle of attack. This observation is not unexpected as leading-edge separation occurs on the sharp wing as soon as α is increased from 0°. Thus, the spanwise flow does not encounter the transition strip until it has reattached inboard of the wing leading edge and moves back to the wing leading edge as illustrated in figure 11.

Figure 38 presents a similar set of data for the elliptical wing with and without grit at $x = 12$ in., $M = 1.60$, and $R_x = 2 \times 10^6$ over the α_{nom} range of 0° to 9°. For $\alpha_{nom} \geq 4°$, the application of grit appears to have no significant impact on the leading-edge vortex (figs. 38(b) and 38(c)). For $\alpha_{nom} \geq 4°$, the flow separates at the wing leading edge, reattaches inboard of the leading edge, and does not encounter the transition strip. However, at the angle of attack where leading-edge separation was first detected on the elliptical wing without grit ($\alpha_{sep} = 2.22°$), grit has an effect on the separation bubble emanating from the wing leading edge. The separation bubble influences the upper surface-pressure coefficient distribution so that an inflection appears in the pressure distribution at the inboard edge of the separation bubble. The pressure data in figure 38(a) show that when grit is applied to the model, the location of the inflection moves outboard. Also, with the application of the grit to the model, the pressure distribution moves to a distribution more typical of an attached flow at the wing leading edge (fig. 38(a)). As a result, the surface-pressure coefficient near the leading edge decreases with the application of grit to the model. These trends indicate a weaker leading-edge separation bubble for the case with grit than was observed for the case without grit. These features are seen more clearly in the surface-pressure coefficient data in figure 39, which presents the pressure distributions for the elliptical wing in $\Delta\alpha = 0.5°$ increments at $x = 12$ in., $M = 1.60$, and $R_x = 2 \times 10^6$.

Figure 40 presents surface-pressure coefficient data with and without grit for the cambered wing at $x = 12$ in., $M = 1.60$, and $R_x = 2 \times 10^6$ over α_{nom} range of 0° to 9°. The effect of transition grit on the cambered wing data

was similar to the effect seen in the elliptical wing data (fig. 38). For $\alpha_{nom} \geq 6°$, the application of grit appears to have no significant effect on the leading-edge vortex over the leeside of the cambered wing (figs. 40(b) and 40(c)). However, at $\alpha_{nom} = 4°$ (near the angle of attack where leading-edge separation was first detected on the cambered wing without grit, $\alpha_{sep} = 3.72°$), the presence of transition grit weakens the leading-edge separation bubble. This observation is more clearly evident in the surface-pressure coefficient data in figure 41, which present the pressure distributions for the cambered wing in increments of $\Delta\alpha = 0.5°$ at $x = 12$ in., $M = 1.60$, and $R_x = 2 \times 10^6$.

The surface-pressure coefficient data in figures 38 to 41 indicate that the application of transition grit weakens the leading-edge separation bubble that occurs at low angles of attack on the elliptical and the cambered wings. An explanation for this observation is that the transition grit moves the boundary-layer transition location closer to the wing leading edge than when transition grit was not on the model. Because the flow has more energy in a turbulent boundary layer than in a laminar boundary layer, the cases with grit remain attached at the wing leading edge to a higher angle of attack than the cases without grit. Thus, the cases with grit would have a weaker separation bubble than the cases without grit for an angle of attack where both grit conditions yield leading-edge separation.

Painted- and injected-oil-flow data. The painted- and injected-oil-flow techniques were used to examine the effect of grit on the flow characteristics of the surface of each model. Figure 42 presents the painted-oil-flow photograph for the cambered wing with grit at $\alpha_{nom} = 4°$, $M = 1.60$, and $R = 2 \times 10^6$ ft^{-1}. Figure 43 presents the injected-oil-flow photograph for the same condition. As was observed for the case without grit (figs. 32(b) and 33(b)), the oil-flow data in figures 42 and 43 show an accumulation of oil along the leading edge of the cambered wing at $R = 2 \times 10^6$ ft^{-1} for $\alpha_{nom} = 4°$. However, the accumulation of oil on the leading edge is smaller for the case with grit than that observed for the case without grit. This observation indicates that the leading-edge separation bubble is weaker for the condition with grit. This trend is also evident in the surface-pressure coefficient data in figure 41.

Concluding Remarks

An experimental investigation of the effect of leading-edge radius, camber, Reynolds number, and boundary-layer state on the incipient separation of a delta wing at supersonic speeds was conducted at the Langley Unitary Plan Wind Tunnel. The three delta wing models examined had a 65° swept leading edge and varied in cross-sectional shape: a sharp wedge, a 20:1 ellipse, and a 20:1 ellipse with a –9.75° circular camber imposed across the span. The three wings were tested at a Mach number of 1.60 over a free-stream Reynolds number range of 1×10^6 to 5×10^6 ft^{-1}. The wings were tested with and without transition grit applied. Surface-pressure coefficient data were obtained, as well as flow-visualization data. The flow-visualization techniques employed were the vapor-screen, the painted-oil-flow, the injected-oil-flow, and the liquid-crystal techniques. The surface-pressure coefficient data and flow-visualization data are electronically stored on a CD-ROM that accompanies this report.

The data indicated that by rounding the wing leading edge or cambering the wing in the spanwise direction, the onset of leading-edge separation on a delta wing at supersonic speeds occurs at a higher angle of attack than that observed on a sharp-edged delta wing. Specifically, the 20:1 elliptical cross section increased the angle of attack at which leading-edge separation begins by about 2° over that observed on a sharp-edged delta wing. The cambered elliptical cross section, which decreased the local angle of attack at the wing leading edge by 3.76°, effectively increased the angle of attack at which leading-edge separation begins by 1.5° over that observed on the uncambered elliptical cross section. The data showed that the wing leading-edge radius and/or camber lowers the incidence angle of the flow over the wing with a more pronounced effect on the flow at the wing leading edge.

The application of transition grit on the wing or an increase in free-stream Reynolds number increased the angle of attack at which leading-edge separation began. Fixing transition or increasing free-stream Reynolds number causes the boundary-layer transition to occur closer to the wing apex and leading edge of the wing. A turbulent boundary layer has more energy than a laminar boundary layer and will therefore allow the flow to remain attached at the wing leading edge at higher angles of attack than is possible with a laminar boundary layer.

NASA Langley Research Center
Hampton, VA 23681-0001
December 11, 1995

Table 1. Geometric Characteristics of Delta Wing Models

Overall constants:	
Λ_{LE}, deg	65.00
Λ_{TE}, deg	0
c, in.	18.00
b_{TE}, in.	16.7868
b_{to}, in.	13.9870
S, in^2	151.0812
Aspect ratio	1.8652
t_{max}, in.	0.8394
Sharp wing:	
r, in.	0
θ_c, deg	0
Elliptical wing:	
r, in.	0.0025
θ_c, deg	0
Cambered wing:	
r, in.	0.0025
θ_c, deg	9.75

Table 2. Pressure Orifice Location, CP#, and Condition for Sharp Wing

x, in.	Surface	η	CP#	Condition
6	Upper	0.099	33	
6	Upper	0.199	34	
6	Upper	0.299	35	
6	Upper	0.399	36	
6	Upper	0.499	37	
6	Upper	0.539	38	
6	Upper	0.579	39	
6	Upper	0.620	40	
6	Upper	0.660	41	
6	Upper	0.699	42	Plugged
6	Upper	0.719	43	
6	Upper	0.740	44	
6	Upper	0.759	45	
6	Upper	0.780	46	
6	Upper	0.799	47	
6	Upper	0.820	48	
6	Lower	0.202	1	
6	Lower	0.402	2	
6	Lower	0.498	3	
6	Lower	0.603	4	
6	Lower	0.702	5	
6	Lower	0.802	6	
12	Upper	0.100	49	
12	Upper	0.199	50	
12	Upper	0.301	51	
12	Upper	0.349	52	
12	Upper	0.400	53	
12	Upper	0.450	54	
12	Upper	0.500	55	
12	Upper	0.519	56	
12	Upper	0.539	57	
12	Upper	0.560	58	
12	Upper	0.580	59	
12	Upper	0.599	60	
12	Upper	0.620	61	
12	Upper	0.639	79	
12	Upper	0.660	66	
12	Upper	0.680	67	
12	Upper	0.700	68	
12	Upper	0.720	69	

Table 2. Concluded

x, in.	Surface	η	CP#	Condition
12	Upper	0.740	70	
12	Upper	0.760	71	
12	Upper	0.780	72	
12	Upper	0.800	73	
12	Upper	0.820	74	
12	Upper	0.840	75	
12	Upper	0.859	76	Plugged
12	Upper	0.879	77	
12	Upper	0.899	78	
12	Lower	0.201	9	
12	Lower	0.401	10	
12	Lower	0.451	11	
12	Lower	0.501	12	
12	Lower	0.551	13	
12	Lower	0.601	14	
12	Lower	0.651	15	
12	Lower	0.701	16	
12	Lower	0.751	17	
12	Lower	0.800	18	Plugged
12	Lower	0.850	19	
12	Lower	0.901	20	Plugged

Table 3. Pressure Orifice Location, CP#, and Condition for Elliptical Wing

x, in.	Surface	η	CP#	Condition
6	Upper	0.099	33	
6	Upper	0.199	34	
6	Upper	0.299	35	
6	Upper	0.400	36	
6	Upper	0.499	37	
6	Upper	0.539	38	
6	Upper	0.579	39	
6	Upper	0.619	40	
6	Upper	0.660	41	
6	Upper	0.700	42	
6	Upper	0.720	43	
6	Upper	0.740	44	
6	Upper	0.759	45	
6	Upper	0.781	46	
6	Upper	0.800	47	
6	Upper	0.820	48	
6	Upper	0.840	49	
6	Upper	0.860	50	
6	Upper	0.880	51	
6	Upper	0.899	52	Plugged from run 22
6	Upper	0.920	53	
6	Upper	0.939	54	
6	Upper	0.960	55	Plugged
6	Upper	0.980	56	
6	Lower	0.200	1	
6	Lower	0.400	2	
6	Lower	0.500	3	
6	Lower	0.600	4	
6	Lower	0.700	5	
6	Lower	0.799	6	
6	Lower	0.850	7	
6	Lower	0.900	8	
6	Lower	0.949	9	Plugged
12	Upper	0.100	57	
12	Upper	0.200	58	
12	Upper	0.300	59	
12	Upper	0.350	60	
12	Upper	0.400	61	
12	Upper	0.500	66	
12	Upper	0.520	67	

Table 3. Concluded

x, in.	Surface	η	CP#	Condition
12	Upper	0.540	68	
12	Upper	0.560	69	
12	Upper	0.579	70	
12	Upper	0.599	71	
12	Upper	0.621	72	
12	Upper	0.640	73	
12	Upper	0.660	74	
12	Upper	0.680	75	
12	Upper	0.700	76	
12	Upper	0.720	77	
12	Upper	0.740	78	
12	Upper	0.760	79	
12	Upper	0.780	80	
12	Upper	0.800	81	
12	Upper	0.820	82	
12	Upper	0.840	83	
12	Upper	0.860	84	
12	Upper	0.879	85	
12	Upper	0.899	86	
12	Upper	0.920	87	
12	Upper	0.940	88	
12	Upper	0.960	89	Plugged from run 22
12	Upper	0.981	90	
12	Lower	0.200	12	
12	Lower	0.400	13	
12	Lower	0.450	14	
12	Lower	0.500	15	Plugged
12	Lower	0.550	16	
12	Lower	0.600	17	
12	Lower	0.650	18	
12	Lower	0.700	19	
12	Lower	0.750	20	
12	Lower	0.800	21	
12	Lower	0.850	22	
12	Lower	0.900	23	
12	Lower	0.950	24	Plugged from run 22

Table 4. Pressure Orifice Location, CP#, and Condition for Cambered Wing

x, in.	Surface	η	CP#	Condition
6	Upper	0.099	33	
6	Upper	0.199	34	Slow leak
6	Upper	0.299	35	
6	Upper	0.400	36	
6	Upper	0.499	37	
6	Upper	0.539	38	
6	Upper	0.579	39	
6	Upper	0.619	40	
6	Upper	0.660	41	
6	Upper	0.700	42	
6	Upper	0.720	43	
6	Upper	0.740	44	
6	Upper	0.759	45	
6	Upper	0.781	46	
6	Upper	0.800	47	
6	Upper	0.820	48	
6	Upper	0.840	49	
6	Upper	0.860	50	
6	Upper	0.880	51	
6	Upper	0.899	52	
6	Upper	0.920	53	
6	Upper	0.939	54	Plugged
6	Upper	0.960	55	Plugged
6	Upper	0.980	56	
6	Lower	0.200	1	
6	Lower	0.400	2	
6	Lower	0.500	3	
6	Lower	0.600	4	
6	Lower	0.700	5	
6	Lower	0.799	6	
6	Lower	0.850	7	
6	Lower	0.900	8	
6	Lower	0.949	9	
12	Upper	0.100	57	
12	Upper	0.200	58	
12	Upper	0.300	59	
12	Upper	0.350	60	
12	Upper	0.400	61	
12	Upper	0.450	91	
12	Upper	0.500	66	

Table 4. Concluded

x, in.	Surface	η	CP#	Condition
12	Upper	0.520	67	
12	Upper	0.540	68	
12	Upper	0.560	69	
12	Upper	0.579	70	
12	Upper	0.599	71	
12	Upper	0.621	72	
12	Upper	0.640	73	
12	Upper	0.660	74	
12	Upper	0.680	75	
12	Upper	0.700	76	
12	Upper	0.720	77	
12	Upper	0.740	78	
12	Upper	0.760	79	
12	Upper	0.780	80	
12	Upper	0.800	81	
12	Upper	0.820	82	
12	Upper	0.840	83	
12	Upper	0.860	84	
12	Upper	0.879	85	
12	Upper	0.899	86	
12	Upper	0.920	87	
12	Upper	0.940	88	
12	Upper	0.960	89	
12	Upper	0.981	90	
12	Lower	0.200	12	
12	Lower	0.400	13	
12	Lower	0.450	14	
12	Lower	0.500	15	
12	Lower	0.550	16	
12	Lower	0.600	17	
12	Lower	0.650	18	
12	Lower	0.700	19	
12	Lower	0.750	20	
12	Lower	0.800	21	
12	Lower	0.850	22	
12	Lower	0.900	23	
12	Lower	0.950	24	

Table 5. Summary of Data for Three Models

(a) Sharp wing without transition grit

R, ft^{-1}	Run	T_o	α_{nom}, deg
Surface-pressure data			
1×10^6	40		0, 0.5, 1.0, 1.5, 1.75, 2.0, 2.25, 2.5, 2.75, 3.0, 3.5, 4.0, 4.5, 5.0, 5.5, 5.75, 6.0, 6.25, 6.5, 6.75, 7.0, 7.25, 7.5, 8.0, 8.5, 9.0
2×10^6	41		0, 0.5, 1.0, 1.5, 2.0, 2.5, 3.0, 3.5, 4.0, 4.5, 5.0, 5.5, 6.0, 6.5, 7.0, 7.5, 8.0, 8.5, 9.0
5×10^6	42		0, 0.5, 1.0, 1.5, 1.75, 2.0, 2.25, 2.5, 2.75, 3.0, 3.25, 3.5, 4.0, 4.5, 5.0, 5.5, 5.75, 6.0, 6.25, 6.5, 6.75, 7.0, 7.25, 7.5, 8.0, 8.5, 9.0
Vapor-screen data			
1×10^6			1.0, 2.0, 3.0, 4.0, 5.0, 6.0, 7.0, 8.0, 8.5, 9.0
2×10^6			0, 1.0, 2.0, 2.5, 3.0, 3.5, 4.0, 4.5, 5.0, 5.5, 6.0, 7.0, 8.0, 9.0
Painted-oil-flow data			
2×10^6			4.0, 6.0, 8.0
5×10^6			4.0, 6.0, 8.0
Injected-oil-flow data			
2×10^6			6.0, 7.0, 8.0, 9.0
5×10^6			2.0, 3.0, 4.0, 5.0, 6.0, 7.0, 8.0, 9.0
Liquid-crystal data			
2×10^6		120	0, 1.0, 2.0, 3.0, 4.0, 5.0, 6.0, 7.0, 8.0, 9.0
2×10^6		125	0, 1.0, 2.0, 3.0, 4.0, 5.0, 6.0, 7.0, 8.0, 9.0
2×10^6		130	0, 2.0, 3.0, 4.0, 5.0, 6.0, 7.0, 8.0, 9.0
5×10^6		120	0, 1.0, 2.0, 3.0, 4.0, 5.0, 6.0, 7.0, 8.0, 9.0
5×10^6		125	0, 1.0, 2.0, 3.0, 4.0, 5.0, 6.0, 7.0, 8.0, 9.0
5×10^6		130	0, 1.0, 2.0, 3.0, 4.0, 5.0, 6.0, 7.0, 8.0, 9.0

(b) Sharp wing with transition grit[a]

R, ft^{-1}	Run	α_{nom}, deg
Surface-pressure data		
1×10^6	43	0.0, 0.5, 1.0, 1.5, 1.75, 2.0, 2.25, 2.5, 2.75, 3.0, 3.25, 3.5, 4.0, 4.5, 5.0, 5.5, 5.75, 6.0, 6.25, 6.5, 6.75, 7.0, 7.5, 8.0, 8.5, 9.0
2×10^6	44	0.0, 0.5, 1.0, 1.5, 2.0, 2.5, 3.0, 3.5, 4.0, 4.5, 5.0, 5.5, 6.0, 6.5, 7.0, 7.5, 8.0, 8.5, 9.0
5×10^6	45	0.0, 0.5, 1.0, 2.0, 3.0, 4.0, 5.0, 6.0, 7.0, 8.0, 9.0

[a]Vapor-screen data, painted-oil-flow data, injected-oil-flow data, and liquid-crystal data not applicable.

Table 5. Continued

(c) Elliptical wing without transition grit

R, ft^{-1}	Run	T_o	α_{nom}, deg
Surface-pressure data			
1×10^6	6		0, 0.5, 1.0, 1.5, 1.75, 2.0, 2.25, 2.5, 2.75, 3.0, 3.5, 4.0, 4.5, 5.0, 5.5, 5.75, 6.0, 6.25, 6.5, 6.75, 7.0, 7.25, 7.5, 8.0, 8.5, 9.0
2×10^6	7		0, 0.5, 1.0, 1.5, 2.0, 2.5, 3.0, 3.5, 4.0, 4.5, 5.0, 5.5, 6.0, 6.5, 7.0, 7.5, 8.0, 8.5, 9.0
3×10^6	8		0, 0.5, 1.0, 1.5, 2.0, 2.5, 3.0, 3.5, 4.0, 4.5, 5.0, 5.5, 6.0, 6.5, 7.0, 7.5, 8.0, 8.5, 9.0
4×10^6	10		0, 0.5, 1.0, 1.5, 2.0, 2.5, 3.0, 3.5, 4.0, 4.5, 5.0, 5.5, 6.0, 6.5, 7.0, 7.5, 8.0, 8.5, 9.0
5×10^6	14		0, 0.5, 1.0, 1.5, 1.75, 2.0, 2.25, 2.5, 2.75, 3.0, 3.25, 3.5, 4.0, 4.5, 5.0, 5.5, 5.75, 6.0, 6.5, 7.0, 7.5, 8.0, 8.5, 9.0
Vapor-screen data			
1×10^6			0, 1.0, 2.0, 2.5, 3.0, 3.5, 4.0, 5.0, 6.0, 7.0, 8.0, 9.0
2×10^6			0, 1.0, 2.0, 2.5, 3.0, 3.5, 4.0, 5.0, 6.0, 7.0, 8.0, 9.0
5×10^6			0, 1.0, 2.0, 2.5, 3.0, 3.5, 4.0, 5.0, 6.0, 7.0, 8.0, 9.0
Painted-oil-flow data			
1×10^6			2.0, 3.0, 4.0, 6.0
2×10^6			3.0, 4.0, 6.0, 8.0
5×10^6			4.0, 6.0, 8.0
Injected-oil-flow data			
2×10^6			0, 1.0, 2.0, 3.0, 4.0, 5.0, 6.0, 7.0, 8.0, 9.0
5×10^6			0, 1.0, 2.0, 3.0, 4.0, 5.0, 6.0, 7.0, 8.0
Liquid-crystal data			
2×10^6		120	0, 1.0, 2.0, 3.0, 4.0, 5.0, 6.0, 7.0, 8.0, 9.0
2×10^6		125	0, 1.0, 2.0, 3.0, 4.0, 5.0, 6.0, 7.0, 8.0, 9.0
2×10^6		130	0, 1.0, 2.0, 3.0, 4.0, 5.0, 6.0, 7.0, 8.0, 9.0
5×10^6		120	0, 1.0, 2.0, 3.0, 4.0, 5.0, 6.0, 7.0, 8.0, 9.0
5×10^6		125	0, 1.0, 2.0, 3.0, 4.0, 5.0, 6.0, 7.0, 8.0, 9.0
5×10^6		130	0, 1.0, 2.0, 3.0, 4.0, 5.0, 6.0, 7.0, 8.0, 9.0

Table 5. Continued

(d) Elliptical wing with transition grit[a]

R, ft^{-1}	Run	α_{nom}, deg
Surface-pressure data		
1×10^6	22	0, 0.5, 1.0, 1.5, 1.75, 2.0, 2.25, 2.5, 2.75, 3.0, 3.25, 3.5, 4.0, 4.5, 5.0, 5.5, 5.75, 6.0, 6.25, 6.5, 6.75, 7.0, 7.25, 7.5, 8.0, 8.5, 9.0
2×10^6	25	0, 0.5, 1.0, 1.5, 2.0, 2.5, 3.0, 3.5, 4.0, 4.5, 5.0, 5.5, 6.0, 6.5 7.0, 7.5, 8.0, 8.5, 9.0
3×10^6	28	0, 0.5, 1.0, 1.5, 2.0, 2.5, 3.0, 3.5, 4.0, 4.5, 5.0, 5.5, 6.0, 6.5, 7.0, 7.5, 8.0, 8.5, 9.0
4×10^6	32	0, 0.5, 1.0, 1.5, 2.0, 2.5, 3.0, 3.5, 4.0, 4.5, 5.0, 5.5, 6.0, 6.5, 7.0, 7.5, 8.0, 8.5, 9.0
5×10^6	29	0, 0.5, 1.0, 1.5, 1.75, 2.0, 2.25, 2.5, 2.75, 3.0, 3.25, 3.5, 4.0, 4.5, 5.0, 5.5, 5.75, 6.0, 6.25, 6.5, 6.75, 7.0, 7.25, 7.5, 8.0, 8.5, 9.0
Vapor-screen data		
1×10^6		0, 1.0, 2.0, 2.5, 3.0, 3.5, 4.0, 5.0, 6.0, 7.0, 8.0, 9.0
5×10^6		0, 1.0, 2.0, 2.5, 3.0, 3.5, 4.0, 5.0, 6.0, 7.0, 8.0, 9.0
Painted-oil-flow data		
1×10^6		2.0, 3.0, 4.0, 6.0
2×10^6		2.0, 3.0, 4.0, 6.0
Injected-oil-flow data		
1×10^6		0, 1.0, 2.0, 3.0, 4.0, 5.0, 6.0, 7.0, 8.0, 9.0
2×10^6		0, 1.0, 2.0, 3.0, 4.0, 5.0, 6.0, 7.0, 8.0, 9.0
5×10^6		0, 1.0, 2.0, 3.0, 4.0, 5.0, 6.0, 7.0, 8.0, 9.0

[a]Liquid-crystal data not applicable.

Table 5. Continued

(e) Cambered wing without transition grit

R, ft^{-1}	Run	T_o	α_{nom}, deg
Surface-pressure data			
1×10^6	36		0, 0.5, 1.0, 1.5, 2.0, 2.5, 3.0, 3.5, 4.0, 4.5, 5.0, 5.5, 5.75, 6.0, 6.25, 6.5, 6.75, 7.0, 7.25, 7.5, 8.0, 8.5, 9.0
2×10^6	34		0, 0.5, 1.0, 1.5, 2.0, 2.5, 3.0, 3.5, 4.0, 4.5, 5.0, 5.5, 6.0, 6.5, 7.0, 7.5, 8.0, 8.5, 9.0
5×10^6	35		0, 0.5, 1.0, 1.5, 2.0, 2.5, 3.0, 3.5, 4.0, 4.5, 5.0, 5.5, 5.75, 6.0, 6.25, 6.5, 6.75, 7.0, 7.25, 7.5, 8.0, 8.5, 9.0
Vapor-screen data			
1×10^6			0, 1.0, 2.0, 2.5, 3.0, 3.5, 4.0, 4.5, 5.0, 5.5, 6.0, 6.5, 7.0, 8.0, 9.0
2×10^6			0, 1.0, 2.0, 2.5, 3.0, 3.5, 4.0, 4.5, 5.0, 5.5, 6.0, 6.5, 7.0, 8.0, 9.0
5×10^6			0, 1.0, 2.0, 2.5, 3.0, 3.5, 4.0, 4.5, 5.0, 5.5, 6.0, 6.5, 7.0, 8.0, 9.0
Painted-oil-flow data			
1×10^6			4.0, 5.0, 6.0, 8.0
2×10^6			4.0, 5.0, 6.0, 8.0
5×10^6			4.0, 6.0
Injected-oil-flow data			
1×10^6			0, 1.0, 2.0, 3.0, 4.0, 5.0, 6.0, 7.0, 8.0, 9.0
2×10^6			0, 1.0, 2.0, 4.0, 5.0, 6.0, 7.0, 8.0, 9.0
5×10^6			0, 1.0, 2.0, 3.0, 4.0, 5.0, 6.0, 7.0, 8.0, 9.0
Liquid-crystal data			
2×10^6		120	0, 1.0, 2.0, 3.0, 4.0, 5.0, 6.0, 7.0, 8.0, 9.0
2×10^6		125	0, 1.0, 2.0, 3.0, 4.0, 5.0, 6.0, 7.0, 8.0, 9.0
2×10^6		130	0, 1.0, 2.0, 3.0, 4.0, 5.0, 6.0, 7.0, 8.0, 9.0
5×10^6		120	0, 1.0, 2.0, 3.0, 4.0, 5.0, 6.0, 7.0, 8.0, 9.0
5×10^6		125	0, 1.0, 2.0, 3.0, 4.0, 5.0, 6.0, 7.0, 8.0, 9.0

Table 5. Concluded

(f) Cambered wing with transition grit[a]

R, ft^{-1}	Run	α_{nom}, deg
Surface-pressure data		
1×10^6	37	0, 0.5, 1.0, 1.5, 2.0, 2.5, 3.0, 3.5, 4.0, 4.5, 5.0, 5.5, 5.75, 6.0, 6.25, 6.5, 6.75, 7.0, 7.25, 7.5, 8.0, 8.5, 9.0
2×10^6	38	0, 0.5, 1.0, 1.5, 2.0, 2.5, 3.0, 3.5, 4.0, 4.5, 5.0, 5.5, 6.0, 6.5, 7.0, 7.5, 8.0, 8.5, 9.0
5×10^6	39	0, 0.5, 1.0, 1.5, 2.0, 2.5, 3.0, 3.5, 4.0, 4.5, 5.0, 5.5, 5.75, 6.0, 6.25, 6.5, 6.75, 7.0, 7.25, 7.5, 8.0, 8.5, 9.0
Vapor-screen data		
1×10^6		0, 1.0, 2.0, 2.5, 3.0, 3.5, 4.0, 4.5, 5.0, 5.5, 6.0, 6.5
5×10^6		0, 1.0, 2.0, 2.5, 3.0, 3.5, 4.0, 4.5, 5.0, 5.5, 6.0, 6.5, 7.0,8.0, 9.0
Painted-oil-flow data		
2×10^6		4.0, 5.0, 6.0, 8.0
Injected-oil-flow data		
1×10^6		0, 1.0, 2.0, 3.0, 4.0, 5.0, 6.0, 7.0, 8.0, 9.0
2×10^6		0, 1.0, 2.0, 3.0, 4.0, 5.0, 6.0, 7.0, 8.0, 9.0
5×10^6		0, 1.0, 2.0, 3.0, 4.0, 5.0, 6.0, 7.0, 8.0, 9.0

[a]Liquid-crystal data not applicable.

Table 6. Corrected Angle of Attack Index of Data for Sharp Wing Without Transition Grit

(a) $M = 1.60$, $R = 1 \times 10^6$ ft^{-1}, $\phi = 0°$, and $\theta_f = 0.4°$

α_{nom}, deg	Surface-pressure point number[a]	Surface pressure α, deg	Vapor screen α, deg	Painted oil flow α, deg	Injected oil flow α, deg	Liquid crystal α, deg
0	849 / 868	0.25 / 0.26				
0.50	850	0.75				
1.00	851	1.28	1.1			
1.50	852	1.75				
1.75	869	2.03				
2.00	853	2.29	2.1			
2.25	870	2.50				
2.50	854 / 871	2.76 / 2.74				
2.75	872	3.03				
3.00	855	3.25	3.1			
3.25						
3.50	856	3.75				
3.75						
4.00	857	4.25	4.1			
4.25						
4.50	858	4.75				
4.75						
5.00	859	5.30	5.1			
5.25						
5.50	860	5.77				
5.75	873	6.02				
6.00	861	6.26	6.1			
6.25	874	6.53				
6.50	862	6.79				
6.75	875	7.01				
7.00	863	7.27	7.1			
7.25	876	7.51				
7.50	864	7.76				
7.75						
8.00	865	8.26	8.1			
8.25						
8.50	866	8.75	8.6			
9.00	867	9.27	9.1			

[a]Run 40.

Table 6. Continued

(b) $M = 1.60$, $R = 2 \times 10^6$ ft^{-1}, $\phi = 0°$, and $\theta_f = 0.4°$

α_{nom}, deg	Surface-pressure point number[a]	Surface pressure α, deg	Vapor screen α, deg	Painted oil flow α, deg	Injected oil flow α, deg	Liquid crystal α, deg
0	877 / 896	0.25 / 0.26	0.1			0
0.50	878	0.78				
1.00	879	1.28	1.1			1.03
1.50	880	1.78				
1.75						
2.00	881	2.25	2.1			2.08
2.25						
2.50	882	2.77	2.6			
2.75						
3.00	883	3.28	3.1			3.14
3.25						
3.50	884	3.75	3.6			
3.75						
4.00	885	4.27	4.1	4.17		4.17
4.25						
4.50	886	4.76	4.6			
4.75						
5.00	887	5.25	5.1			5.21
5.25						
5.50	888	5.78	5.6			
5.75						
6.00	889	6.27	6.1	6.26	6.26	6.26
6.25						
6.50	890	6.78				
6.75						
7.00	891	7.26	7.1		7.29	7.29
7.25						
7.50	892	7.76				
7.75						
8.00	893	8.27	8.1	8.34	8.34	8.34
8.25						
8.50	894	8.76				
9.00	895	9.28	9.1		9.39	9.39

[a]Run 41.

Table 6. Concluded

(c) $M = 1.60$, $R = 5 \times 10^6$ ft^{-1}, $\phi = 0°$, and $\theta_f = 0.4°$

α_{nom}, deg	Surface-pressure point number[a]	Surface pressure α, deg	Vapor screen α, deg	Painted oil flow α, deg	Injected oil flow α, deg	Liquid crystal α, deg
0	897 / 916	0.23 / 0.31				0
0.50	898	0.79				
1.00	899	1.28				1.10
1.50	900	1.78				
1.75	917	2.01				
2.00	901	2.29			2.17	2.17
2.25	918	2.52				
2.50	902	2.76				
2.75	919	3.00				
3.00	903	3.28			3.25	3.25
3.25	920	3.51				
3.50	904	3.76				
3.75						
4.00	905	4.25		4.34	4.34	4.34
4.25						
4.50	906	4.76				
4.75						
5.00	907	5.27			5.43	5.43
5.25						
5.50	908	5.75				
5.75	921	6.02				
6.00	909	6.27		6.51	6.51	6.51
6.25	922	6.53				
6.50	910	6.78				
6.75	923	7.00				
7.00	911	7.29			7.60	7.60
7.25	924	7.52				
7.50	912	7.75				
7.75						
8.00	913	8.25		8.68	8.68	8.68
8.25						
8.50	914	8.76				
9.00	915	9.25			9.75	9.75

[a]Run 42.

Table 7. Corrected Angle of Attack Index of Data for Sharp Wing With Transition Grit

(a) $M = 1.60$, $R = 1 \times 10^6$ ft^{-1}, $\phi = 0°$, and $\theta_f = 0.4°$

α_{nom}, deg	Surface-pressure point number[a]	Surface pressure α, deg	Vapor screen α, deg	Painted oil flow α, deg	Injected oil flow α, deg	Liquid crystal α, deg
0	937 / 956	0.23 / 0.24				
0.50	938	0.78				
1.00	939	1.26				
1.50	940	1.78				
1.75	957	2.03				
2.00	941	2.29				
2.25	958	2.49				
2.50	942	2.79				
2.75	959	3.05				
3.00	943	3.24				
3.25	960	3.52				
3.50	944	3.75				
3.75						
4.00	945	4.29				
4.25						
4.50	946	4.76				
4.75						
5.00	947	5.26				
5.25						
5.50	948	5.79				
5.75	961	5.99				
6.00	949	6.25				
6.25	962	6.51				
6.50	950 / 963	6.77 / 6.77				
6.75	964	7.04				
7.00	951	7.22				
7.25						
7.50	952	7.79				
7.75						
8.00	953	8.24				
8.25						
8.50	954	8.74				
9.00	955	9.27				

[a]Run 43.

Table 7. Continued

(b) $M = 1.60$, $R = 2 \times 10^6$ ft^{-1}, $\phi = 0°$, and $\theta_f = 0.4°$

α_{nom}, deg	Surface-pressure point number[a]	Surface pressure α, deg	Vapor screen α, deg	Painted oil flow α, deg	Injected oil flow α, deg	Liquid crystal α, deg
0	965 / 985	0.28 / 0.27				
0.50	966	0.75				
1.00	967	1.29				
1.50	968	1.77				
1.75						
2.00	969	2.29				
2.25						
2.50	970	2.74				
2.75						
3.00	971	3.30				
3.25						
3.50	972	3.76				
3.75						
4.00	973	4.29				
4.25						
4.50	974	4.76				
4.75						
5.00	975	5.25				
5.25						
5.50	976	5.76				
5.75						
6.00	977 / 978	6.28 / 6.28				
6.25						
6.50	979	6.77				
6.75						
7.00	980	7.27				
7.25						
7.50	981	7.77				
7.75						
8.00	982	8.26				
8.25						
8.50	983	8.76				
9.00	984	9.28				

[a]Run 44.

Table 7. Concluded

(c) $M = 1.60$, $R = 5 \times 10^6$ ft^{-1}, $\phi = 0°$, and $\theta_f = 0.4°$

α_{nom}, deg	Surface-pressure point number[a]	Surface pressure α, deg	Vapor screen α, deg	Painted oil flow α, deg	Injected oil flow α, deg	Liquid crystal α, deg
0	986	0.26				
0.50	987	0.78				
1.00	988	1.28				
1.50						
1.75						
2.00	989	2.30				
2.25						
2.50						
2.75						
3.00	990	3.24				
3.25						
3.50						
3.75						
4.00	991 / 992	4.25 / 4.25				
4.25						
4.50						
4.75						
5.00	993	5.29				
5.25						
5.50						
5.75						
6.00	994	6.24				
6.25						
6.50						
6.75						
7.00	995	7.26				
7.25						
7.50						
7.75						
8.00	996	8.30				
8.25						
8.50						
9.00	997	9.29				

[a]Run 45.

Table 8. Corrected Angle of Attack Index of Data for Elliptical Wing Without Transition Grit

(a) $M = 1.60$, $R = 1 \times 10^6$ ft^{-1}, $\phi = 0°$, and $\theta_f = 0.4°$

α_{nom}, deg	Surface-pressure point number[a]	Surface pressure α, deg	Vapor screen α, deg	Painted oil flow α, deg	Injected oil flow α, deg	Liquid crystal α, deg
0	127 / 148	0.23 /0.19	0.2			
0.50	128	0.73				
1.00	129	1.23	1.2			
1.50	130	1.70				
1.75	149	1.97				
2.00	131	2.17	2.2	2.03		
2.25	150	2.47				
2.50	132	2.68	2.7			
2.75	151	2.94				
3.00	133	3.19	3.2	3.05		
3.25						
3.50	134 / 135	3.71 / 3.71	3.7			
3.75						
4.00	136	4.18	4.2	4.06		
4.25						
4.50	137	4.67				
4.75						
5.00	138	5.21	5.2			
5.25						
5.50	139	5.70				
5.75	152	5.97				
6.00	140	6.24	6.2	6.12		
6.25	153	6.45				
6.50	141	6.68				
6.75	154	6.96				
7.00	142	7.23	7.2			
7.25	155	7.43				
7.50	143	7.72				
7.75						
8.00	144 / 145	8.18 / 8.18	8.2			
8.25						
8.50	146	8.69				
9.00	147	9.23	9.2			

[a]Run 6.

Table 8. Continued

(b) $M = 1.60$, $R = 1 \times 10^6$ ft^{-1}, $\phi = 0°$, and $\theta_f = 0°$

α_{nom}, deg	Surface-pressure point number[a]	Surface pressure α, deg	Vapor screen α, deg	Painted oil flow α, deg	Injected oil flow α, deg	Liquid crystal α, deg
–4.00						
–3.00	104	–3.02				
–2.00	105	–2.03				
–1.00	106	–0.99				
0	107	–0.04				
1.00	108	1.02				
2.00	109	2.01				
3.00	110	2.99				
4.00	111	3.99				

[a]Run 4.

(c) $M = 1.60$, $R = 1 \times 10^6$ ft^{-1}, $\phi = 180°$, and $\theta_f = 0°$

α_{nom}, deg	Surface-pressure point number[a]	Surface pressure α, deg	Vapor screen α, deg	Painted oil flow α, deg	Injected oil flow α, deg	Liquid crystal α, deg
–4.00	120	–4.00				
–3.00	119	–2.98				
–2.00	118	–2.03				
–1.00	117	–1.00				
0	116	0.02				
1.00	115	1.03				
2.00	114	1.98				
3.00	113	3.00				
4.00	112	3.99				

[a]Run 5.

Table 8. Continued

(d) $M = 1.60$, $R = 2 \times 10^6$ ft^{-1}, $\phi = 0°$, and $\theta_f = 0.4°$

α_{nom}, deg	Surface-pressure point number[a]	Surface pressure α, deg	Vapor screen α, deg	Painted oil flow α, deg	Injected oil flow α, deg	Liquid crystal α, deg
0	157 / 175	0.19 / 0.19	0.2		0	0
0.50	158	0.71				
1.00	159	1.23	1.2		1.03	1.03
1.50	160	1.75				
1.75						
2.00	161	2.22	2.2		2.08	2.08
2.25						
2.50	162	2.69	2.7			
2.75						
3.00	163	3.24	3.2	3.14	3.14	3.14
3.25						
3.50	176	3.71	3.7			
3.75						
4.00	164	4.25	4.2	4.17	4.17	4.17
4.25						
4.50	165	4.69				
4.75						
5.00	166	5.23	5.2		5.21	5.21
5.25						
5.50	167	5.70				
5.75						
6.00	168	6.23	6.2	6.26	6.26	6.26
6.25						
6.50	169	6.71				
6.75						
7.00	170	7.17	7.2		7.29	7.29
7.25						
7.50	171	7.71				
7.75						
8.00	172	8.18	8.2	8.34	8.34	8.34
8.25						
8.50	173	8.70				
9.00	174	9.22	9.2		9.39	9.39

[a]Run 7.

Table 8. Continued

(e) $M = 1.60$, $R = 3 \times 10^6$ ft^{-1}, $\phi = 0°$, and $\theta_f = 0.4°$

α_{nom}, deg	Surface-pressure point number[a]	Surface pressure α, deg	Vapor screen α, deg	Painted oil flow α, deg	Injected oil flow α, deg	Liquid crystal α, deg
0	194 / 213	0.20 / 0.23				
0.50	195	0.70				
1.00	196	1.21				
1.50	197	1.72				
1.75						
2.00	198	2.19				
2.25						
2.50	199	2.70				
2.75						
3.00	200	3.19				
3.25						
3.50	201	3.73				
3.75						
4.00	202	4.19				
4.25						
4.50	203	4.70				
4.75						
5.00	204	5.22				
5.25						
5.50	205	5.74				
5.75						
6.00	206	6.23				
6.25						
6.50	207	6.72				
6.75						
7.00	208	7.21				
7.25						
7.50	209	7.73				
7.75						
8.00	210	8.21				
8.25						
8.50	211	8.73				
9.00	212	9.18				

[a]Run 8.

Table 8. Continued

(f) $M = 1.60$, $R = 4 \times 10^6$ ft^{-1}, $\phi = 0°$, and $\theta_f = 0.4°$

α_{nom}, deg	Surface-pressure point number[a]	Surface pressure α, deg	Vapor screen α, deg	Painted oil flow α, deg	Injected oil flow α, deg	Liquid crystal α, deg
0	222 / 241	0.25 / 0.21				
0.50	223	0.73				
1.00	224	1.16				
1.50	225	1.69				
1.75						
2.00	226	2.20				
2.25						
2.50	227	2.67				
2.75						
3.00	228	3.23				
3.25						
3.50	229	3.67				
3.75						
4.00	230	4.18				
4.25						
4.50	231	4.73				
4.75						
5.00	232	5.17				
5.25						
5.50	233	5.71				
5.75						
6.00	234	6.19				
6.25						
6.50	235	6.73				
6.75						
7.00	236	7.20				
7.25						
7.50	237	7.71				
7.75						
8.00	238	8.20				
8.25						
8.50	239	8.73				
9.00	240	9.21				

[a]Run 10.

Table 8. Continued

(g) $M = 1.60$, $R = 5 \times 10^6$ ft^{-1}, $\phi = 0°$, and $\theta_f = 0.4°$

α_{nom}, deg	Surface-pressure point number[a]	Surface pressure α, deg	Vapor screen α, deg	Painted oil flow α, deg	Injected oil flow α, deg	Liquid crystal α, deg
0	271 / 290	0.22 / 0.21	0.2		0	0
0.50	272	0.67				
1.00	273	1.21	1.2		1.10	1.10
1.50	274	1.67				
1.75	291	1.96				
2.00	275	2.18	2.2		2.17	2.17
2.25	292	2.49				
2.50	276	2.68	2.7			
2.75	293	2.97				
3.00	277	3.18	3.2		3.25	3.25
3.25	294	3.49				
3.50	278	3.74	3.7			
3.75						
4.00	279	4.24	4.2	4.34	4.34	4.34
4.25						
4.50	280	4.65				
4.75						
5.00	281	5.19	5.2		5.43	5.43
5.25						
5.50	282	5.70				
5.75	295	5.96				
6.00	283	6.22	6.2	6.51	6.51	6.51
6.25						
6.50	284	6.75				
6.75						
7.00	285	7.16	7.2		7.60	7.60
7.25						
7.50	286	7.71				
7.75						
8.00	287	8.21	8.2	8.68	8.68	8.68
8.25						
8.50	288	8.70				
9.00	289	9.22	9.2			9.75

[a]Run 14.

Table 8. Concluded

(h) $M = 1.60$, $R = 5 \times 10^6$ ft^{-1}, $\phi = 0°$, and $\theta_f = 0°$

α_{nom}, deg	Surface-pressure point number[a]	Surface pressure α, deg	Vapor screen α, deg	Painted oil flow α, deg	Injected oil flow α, deg	Liquid crystal α, deg
–4.00						
–3.00						
–2.00						
–1.00	265	–0.97				
0	266	0.05				
1.00	267	1.03				
2.00	268	2.05				
3.00	269	2.99				
4.00	270	3.98				

[a]Run 13.

(i) $M = 1.60$, $R = 5 \times 10^6$ ft^{-1}, $\phi = 180°$, and $\theta_f = 0°$

α_{nom}, deg	Surface-pressure point number[a]	Surface pressure α, deg	Vapor screen α, deg	Painted oil flow α, deg	Injected oil flow α, deg	Liquid crystal α, deg
–4.00						
–3.00						
–2.00						
–1.00	247	–1.06				
0	246	–0.04				
1.00	245	1.05				
2.00	244	2.01				
3.00	243	2.96				
4.00	242	4.02				

[a]Run 11.

Table 9. Corrected Angle of Attack Index of Data for Elliptical Wing With Transition Grit

(a) $M = 1.60$, $R = 1 \times 10^6$ ft^{-1}, $\phi = 0°$, and $\theta_f = 0.4°$

α_{nom}, deg	Surface-pressure point number[a]	Surface pressure α, deg	Vapor screen α, deg	Painted oil flow α, deg	Injected oil flow α, deg	Liquid crystal α, deg
0	408 / 427	0.20 / 0.19	0.2		0	
0.50	409	0.71				
1.00	410	1.19	1.2		1.0	
1.50	411	1.69				
1.75	428	1.93				
2.00	412	2.21	2.2	2.03	2.0	
2.25	429	2.45				
2.50	413	2.71	2.7			
2.75	430	2.93				
3.00	414	3.24	3.2	3.05	3.0	
3.25	431	3.45				
3.50	415	3.65	3.7			
3.75						
4.00	416	4.22	4.2	4.06	4.0	
4.25						
4.50	417	4.72				
4.75						
5.00	418	5.19	5.2		5.0	
5.25						
5.50	419	5.71				
5.75	432	5.95				
6.00	420	6.24	6.2	6.12	6.0	
6.25	433	6.46				
6.50	421	6.74				
6.75	434	6.94				
7.00	422	7.16	7.2		7.0	
7.25	435	7.47				
7.50	423	7.70				
7.75						
8.00	424	8.22	8.2		8.0	
8.25						
8.50	425	8.73				
9.00	426	9.18	9.2		9.0	

[a]Run 22.

Table 9. Continued

(b) $M = 1.60$, $R = 2 \times 10^6$ ft^{-1}, $\phi = 0°$, and $\theta_f = 0.4°$

α_{nom}, deg	Surface-pressure point number[a]	Surface pressure α, deg	Vapor screen α, deg	Painted oil flow α, deg	Injected oil flow α, deg	Liquid crystal α, deg
0	454 / 473	0.22 / 0.21			0	
0.50	455	0.71				
1.00	456	1.22			1.0	
1.50	457	1.74				
1.75						
2.00	458	2.22		2.08	2.0	
2.25						
2.50	459	2.69				
2.75						
3.00	460	3.20		3.14	3.0	
3.25						
3.50	461	3.71				
3.75						
4.00	462	4.18		4.17	4.0	
4.25						
4.50	463	4.69				
4.75						
5.00	464	5.21			5.0	
5.25						
5.50	465	5.71				
5.75						
6.00	466	6.21		6.26	6.0	
6.25						
6.50	467	6.74				
6.75						
7.00	468	7.16			7.0	
7.25						
7.50	469	7.69				
7.75						
8.00	470	8.20			8.0	
8.25						
8.50	471	8.72				
9.00	472	9.20			9.0	

[a]Run 25.

Table 9. Continued

(c) $M = 1.60$, $R = 2 \times 10^6$ ft^{-1}, $\phi = 0°$, and $\theta_f = 0°$

α_{nom}, deg	Surface-pressure point number[a]	Surface pressure α, deg	Vapor screen α, deg	Painted oil flow α, deg	Injected oil flow α, deg	Liquid crystal α, deg
–4.00	436	–4.01				
–3.00	437	–2.98				
–2.00	438	–1.98				
–1.00	439	–1.00				
0	440	0				
1.00	441	1.01				
2.00	442	2.02				
3.00	443	3.04				
4.00	444	3.97				

[a]Run 23.

(d) $M = 1.60$, $R = 2 \times 10^6$ ft^{-1}, $\phi = 180°$, and $\theta_f = 0°$

α_{nom}, deg	Surface-pressure point number[a]	Surface pressure α, deg	Vapor screen α, deg	Painted oil flow α, deg	Injected oil flow α, deg	Liquid crystal α, deg
–4.00	453	–3.99				
–3.00	452	–2.98				
–2.00	451	–1.98				
–1.00	450	–1.02				
0	449	–0.01				
1.00	448	1.00				
2.00	447	2.01				
3.00	446	3.03				
4.00	445	3.99				

[a]Run 24.

Table 9. Continued

(e) $M = 1.60$, $R = 3 \times 10^6$ ft^{-1}, $\phi = 0°$, and $\theta_f = 0.4°$

α_{nom}, deg	Surface-pressure point number[a]	Surface pressure α, deg	Vapor screen α, deg	Painted oil flow α, deg	Injected oil flow α, deg	Liquid crystal α, deg
0	492 / 511	0.22 / 0.22				
0.50	493	0.74				
1.00	494	1.21				
1.50	495	1.74				
1.75						
2.00	496	2.21				
2.25						
2.50	497	2.69				
2.75						
3.00	498	3.23				
3.25						
3.50	499	3.71				
3.75						
4.00	500	4.25				
4.25						
4.50	501	4.71				
4.75						
5.00	502	5.21				
5.25						
5.50	503	5.73				
5.75						
6.00	504	6.23				
6.25						
6.50	505	6.69				
6.75						
7.00	506	7.23				
7.25						
7.50	507	7.73				
7.75						
8.00	508	8.22				
8.25						
8.50	509	8.69				
9.00	510	9.24				

[a]Run 28.

Table 9. Continued

(f) $M = 1.60$, $R = 3 \times 10^6$ ft^{-1}, $\phi = 0°$, and $\theta_f = 0°$

α_{nom}, deg	Surface-pressure point number[a]	Surface pressure α, deg	Vapor screen α, deg	Painted oil flow α, deg	Injected oil flow α, deg	Liquid crystal α, deg
–4.00	474	–3.99				
–3.00	475	–3.00				
–2.00	476	–2.04				
–1.00	477	–1.03				
0	478	0				
1.00	479	0.99				
2.00	480	1.98				
3.00	481	3.00				
4.00	482	4.02				

[a]Run 26.

(g) $M = 1.60$, $R = 3 \times 10^6$ ft^{-1}, $\phi = 180°$, and $\theta_f = 0°$

α_{nom}, deg	Surface-pressure point number[a]	Surface pressure α, deg	Vapor screen α, deg	Painted oil flow α, deg	Injected oil flow α, deg	Liquid crystal α, deg
–4.00	491	–4.01				
–3.00	490	–3.01				
–2.00	489	–2.06				
–1.00	488	–1.02				
0	487	–0.02				
1.00	486	1.04				
2.00	485	1.99				
3.00	484	3.03				
4.00	483	4.00				

[a]Run 27.

Table 9. Continued

(h) $M = 1.60$, $R = 4 \times 10^6$ ft^{-1}, $\phi = 0°$, and $\theta_f = 0.4°$

α_{nom}, deg	Surface-pressure point number[a]	Surface pressure α, deg	Vapor screen α, deg	Painted oil flow α, deg	Injected oil flow α, deg	Liquid crystal α, deg
0	570 / 589	0.16 / 0.20				
0.50	571	0.75				
1.00	572	1.17				
1.50	573	1.73				
1.75						
2.00	574	2.23				
2.25						
2.50	575	2.76				
2.75						
3.00	576	3.26				
3.25						
3.50	577	3.66				
3.75						
4.00	578	4.27				
4.25						
4.50	588	4.70				
4.75						
5.00	579	5.20				
5.25						
5.50	580	5.76				
5.75						
6.00	581	6.20				
6.25						
6.50	582	6.65				
6.75						
7.00	583	7.25				
7.25						
7.50	584	7.71				
7.75						
8.00	585	8.25				
8.25						
8.50	586	8.74				
9.00	587	9.23				

[a]Run 32.

Table 9. Continued

(i) $M = 1.60$, $R = 4 \times 10^6$ ft^{-1}, $\phi = 0°$, and $\theta_f = 0°$

α_{nom}, deg	Surface-pressure point number[a]	Surface pressure α, deg	Vapor screen α, deg	Painted oil flow α, deg	Injected oil flow α, deg	Liquid crystal α, deg
–4.00	552	–3.98				
–3.00	553	–2.95				
–2.00	554	–2.00				
–1.00	555	–1.02				
0	556	–0.03				
1.00	557	1.06				
2.00	558	2.01				
3.00	559	3.06				
4.00	560	3.99				

[a]Run 30.

(j) $M = 1.60$, $R = 4 \times 10^6$ ft^{-1}, $\phi = 180°$, and $\theta_f = 0°$

α_{nom}, deg	Surface-pressure point number[a]	Surface pressure α, deg	Vapor screen α, deg	Painted oil flow α, deg	Injected oil flow α, deg	Liquid crystal α, deg
–4.00	569	–4.00				
–3.00	568	–3.03				
–2.00	567	–2.02				
–1.00	566	–1.04				
0	565	0.04				
1.00	564	1.04				
2.00	563	1.99				
3.00	562	2.96				
4.00	561	3.98				

[a]Run 31.

Table 9. Concluded

(k) $M = 1.60$, $R = 5 \times 10^6$ ft^{-1}, $\phi = 0°$, and $\theta_f = 0.4°$

α_{nom}, deg	Surface-pressure point number[a]	Surface pressure α, deg	Vapor screen α, deg	Painted oil flow α, deg	Injected oil flow α, deg	Liquid crystal α, deg
0	524 / 543	0.22 / 0.21	0.2		0	
0.50	525	0.70				
1.00	526	1.20	1.2		1.0	
1.50	527	1.71				
1.75	544	1.95				
2.00	528	2.17	2.2		2.0	
2.25	545	2.47				
2.50	529	2.72	2.7			
2.75	546	2.94				
3.00	530	3.20	3.2		3.0	
3.25	547	3.48				
3.50	531	3.70	3.7			
3.75						
4.00	532	4.15	4.2		4.0	
4.25						
4.50	533	4.68				
4.75						
5.00	534	5.18	5.2		5.0	
5.25						
5.50	535	5.66				
5.75	548	5.97				
6.00	536	6.18	6.2		6.0	
6.25	549	6.45				
6.50	537	6.75				
6.75	550	6.96				
7.00	538	7.20	7.2		7.0	
7.25	551	7.44				
7.50	539	7.69				
7.75						
8.00	540	8.23	8.2		8.0	
8.25						
8.50	541	8.75				
9.00	542	9.25	9.2		9.0	

[a]Run 29.

Table 10. Corrected Angle of Attack Index of Data for Cambered Wing Without Transition Grit

(a) $M = 1.60$, $R = 1 \times 10^6$ ft^{-1}, $\phi = 0°$, and $\theta_f = 0.4°$

α_{nom}, deg	Surface-pressure point number[a]	Surface pressure α, deg	Vapor screen α, deg	Painted oil flow α, deg	Injected oil flow α, deg	Liquid crystal α, deg
0	683 / 702	0.21 / 0.19	0.2		0	
0.50	684	0.69				
1.00	685	1.18	1.2		1.0	
1.50	686	1.70				
1.75						
2.00	687	2.18	2.2		2.0	
2.25						
2.50	688	2.71	2.7			
2.75						
3.00	689	3.19	3.2		3.0	
3.25						
3.50	690	3.70	3.7			
3.75						
4.00	691	4.21	4.2	4.06	4.0	
4.25						
4.50	692	4.69	4.7			
4.75						
5.00	693	5.20	5.2	5.09	5.0	
5.25						
5.50	694	5.69	5.7			
5.75	703	5.96				
6.00	695	6.21	6.2	6.12	6.0	
6.25	704	6.44				
6.50	696	6.71	6.7			
6.75	705	6.97				
7.00	697	7.19	7.2		7.0	
7.25	706	7.47				
7.50	698	7.72				
7.75						
8.00	699	8.21	8.2	8.15	8.0	
8.25						
8.50	700	8.69				
9.00	701	9.21	9.2		9.0	

[a]Run 36.

Table 10. Continued

(b) $M = 1.60$, $R = 2 \times 10^6$ ft^{-1}, $\phi = 0°$, and $\theta_f = 0.4°$

α_{nom}, deg	Surface-pressure point number[a]	Surface pressure α, deg	Vapor screen α, deg	Painted oil flow α, deg	Injected oil flow α, deg	Liquid crystal α, deg
0	629 / 648	0.21 / 0.20	0.2		0	0
0.50	630	0.74				
1.00	631	1.19	1.2		1.0	1.03
1.50	632	1.74				
1.75						
2.00	633	2.18	2.2		2.0	2.08
2.25						
2.50	634	2.71	2.7			
2.75						
3.00	635	3.18	3.2			3.14
3.25						
3.50	636	3.72	3.7			
3.75						
4.00	637	4.18	4.2	4.17	4.0	4.17
4.25						
4.50	638	4.68	4.7			
4.75						
5.00	639	5.17	5.2	5.21	5.0	5.21
5.25						
5.50	640	5.68	5.7			
5.75						
6.00	641	6.17	6.2	6.26	6.0	6.26
6.25						
6.50	642	6.68	6.7			
6.75						
7.00	643	7.18	7.2		7.0	7.29
7.25						
7.50	644	7.67				
7.75						
8.00	645	8.17	8.2	8.34	8.0	8.34
8.25						
8.50	646	8.70				
9.00	647	9.23	9.2		9.0	9.38

[a]Run 34.

Table 10. Continued

(c) $M = 1.60$, $R = 5 \times 10^6$ ft^{-1}, $\phi = 0°$, and $\theta_f = 0.4°$

α_{nom}, deg	Surface-pressure point number[a]	Surface pressure α, deg	Vapor screen α, deg	Painted oil flow α, deg	Injected oil flow α, deg	Liquid crystal α, deg
0	659 / 678	0.23 / 0.21	0.2		0	0
0.50	660	0.68				
1.00	661	1.21	1.2		1.0	1.10
1.50	662	1.73				
1.75						
2.00	663	2.21	2.2		2.0	2.17
2.25						
2.50	664	2.69	2.7			
2.75						
3.00	665	3.21	3.2		3.0	3.25
3.25						
3.50	666	3.69	3.7			
3.75						
4.00	667	4.20	4.2	4.34	4.0	4.34
4.25						
4.50	668	4.68	4.7			
4.75						
5.00	669	5.19	5.2		5.0	5.43
5.25						
5.50	670	5.71	5.7			
5.75	679	5.96				
6.00	671	6.21	6.2	6.51	6.0	6.51
6.25	680	6.47				
6.50	672	6.70	6.7			
6.75	681	6.96				
7.00	673	7.20	7.2		7.0	7.60
7.25	682	7.47				
7.50	674	7.71				
7.75						
8.00	675	8.22	8.2		8.0	8.68
8.25						
8.50	676	8.69				
9.00	677	9.22	9.2		9.0	9.75

[a]Run 35.

Table 10. Concluded

(d) $M = 1.60$, $R = 5 \times 10^6$ ft^{-1}, $\phi = 0°$, and $\theta_f = 0.4°$ with an unacceptable dew point setting

α_{nom}, deg	Surface-pressure point number[a]	Surface pressure α, deg	Vapor screen α, deg	Painted oil flow α, deg	Injected oil flow α, deg	Liquid crystal α, deg
0	605 / 624	0.20 / 0.21				
0.50	606	0.72				
1.00	607	1.19				
1.50	608	1.74				
1.75						
2.00	609	2.18				
2.25						
2.50	610	2.72				
2.75						
3.00	611	3.22				
3.25						
3.50	612	3.74				
3.75						
4.00	613	4.15				
4.25						
4.50	614	4.67				
4.75						
5.00	615	5.25				
5.25						
5.50	616	5.67				
5.75	625	5.95				
6.00	617	6.19				
6.25	626	6.45				
6.50	618	6.69				
6.75	627	6.95				
7.00	619	7.24				
7.25	628	7.45				
7.50	620	7.67				
7.75						
8.00	621	8.17				
8.25						
8.50	622	8.68				
9.00	623	9.25				

[a]Run 33.

Table 11. Angle of Attack Index of Data for Cambered Wing With Transition Grit

(a) $M = 1.60$, $R = 1 \times 10^6$ ft^{-1}, $\phi = 0°$, and $\theta_f = 0.4°$

α_{nom}, deg	Surface-pressure point number[a]	Surface pressure α, deg	Vapor screen α, deg	Painted oil flow α, deg	Injected oil flow α, deg	Liquid crystal α, deg
0	716 / 735	0.18 / 0.24	0.2		0	
0.50	717	0.72				
1.00	718	1.20	1.2		1.0	
1.50	719	1.70				
1.75						
2.00	720	2.21	2.2		2.0	
2.25						
2.50	721	2.72	2.7			
2.75						
3.00	722	3.20	3.2		3.0	
3.25						
3.50	723	3.72	3.7			
3.75						
4.00	724	4.21	4.2		4.0	
4.25						
4.50	725	4.69	4.7			
4.75						
5.00	726	5.20	5.2		5.0	
5.25						
5.50	727	5.70	5.7			
5.75	736	5.95				
6.00	728	6.19	6.2		6.0	
6.25	737	6.45				
6.50	729	6.69	6.7			
6.75	738	6.95				
7.00	730	7.24			7.0	
7.25	739	7.46				
7.50	731	7.68				
7.75						
8.00	732	8.23			8.0	
8.25						
8.50	733	8.70				
9.00	734	9.23			9.0	

[a]Run 37.

Table 11. Continued

(b) $M = 1.60$, $R = 2 \times 10^6$ ft^{-1}, $\phi = 0°$, and $\theta_f = 0.4°$

α_{nom}, deg	Surface-pressure point number[a]	Surface pressure α, deg	Vapor screen α, deg	Painted oil flow α, deg	Injected oil flow α, deg	Liquid crystal α, deg
0	740 / 759	0.20 / 0.19			0	
0.50	741	0.72				
1.00	742	1.19			1.0	
1.50	743	1.68				
1.75						
2.00	744	2.21			2.0	
2.25						
2.50	745	2.69				
2.75						
3.00	746	3.21			3.0	
3.25						
3.50	747	3.69				
3.75						
4.00	748	4.21		4.17	4.0	
4.25						
4.50	749	4.70				
4.75						
5.00	750	5.21		5.21	5.0	
5.25						
5.50	751	5.71				
5.75						
6.00	752	6.19		6.26	6.0	
6.25						
6.50	753	6.72				
6.75						
7.00	754	7.22			7.0	
7.25						
7.50	755	7.72				
7.75						
8.00	756	8.25		8.34	8.0	
8.25						
8.50	757	8.70				
9.00	758	9.23			9.0	

[a]Run 38.

Table 11. Concluded

(c) $M = 1.60$, $R = 5 \times 10^6$ ft^{-1}, $\phi = 0°$, and $\theta_f = 0.4°$

α_{nom}, deg	Surface-pressure point number[a]	Surface pressure α, deg	Vapor screen α, deg	Painted oil flow α, deg	Injected oil flow α, deg	Liquid crystal α, deg
0	760 / 779	0.18 / 0.21	0.2		0	
0.50	761	0.70				
1.00	762	1.16	1.2		1.0	
1.50	763	1.72				
1.75						
2.00	764	2.21	2.2		2.0	
2.25						
2.50	765	2.74	2.7			
2.75						
3.00	766	3.21	3.2		3.0	
3.25						
3.50	767	3.69	3.7			
3.75						
4.00	768	4.21	4.2		4.0	
4.25						
4.50	769	4.73	4.7			
4.75						
5.00	770	5.22	5.2		5.0	
5.25						
5.50	771	5.72	5.7			
5.75	780	5.96				
6.00	772	6.23	6.2		6.0	
6.25	781	6.43				
6.50	773	6.69	6.7			
6.75	782	6.95				
7.00	774	7.25	7.2		7.0	
7.25	783	7.46				
7.50	775	7.70				
7.75						
8.00	776	8.21	8.2		8.0	
8.25						
8.50	777	8.71				
9.00	778	9.18	9.2		9.0	

[a]Run 39.

Table 12. Values of α_{att} and α_{sep} From Different Data Sets for Elliptical Wing Without Grit at $M = 1.60$

R, ft^{-1}	Surface-pressure data		Injected-oil-flow data		Liquid-crystal data	
	α_{att}, deg	α_{sep}, deg	α_{att}, deg	α_{sep}, deg	α_{att}, deg	α_{sep}, deg
2×10^6	1.75	2.22	1.03	2.08	1.03	2.08
5×10^6	2.18	2.49	2.17	3.25	1.10	2.17

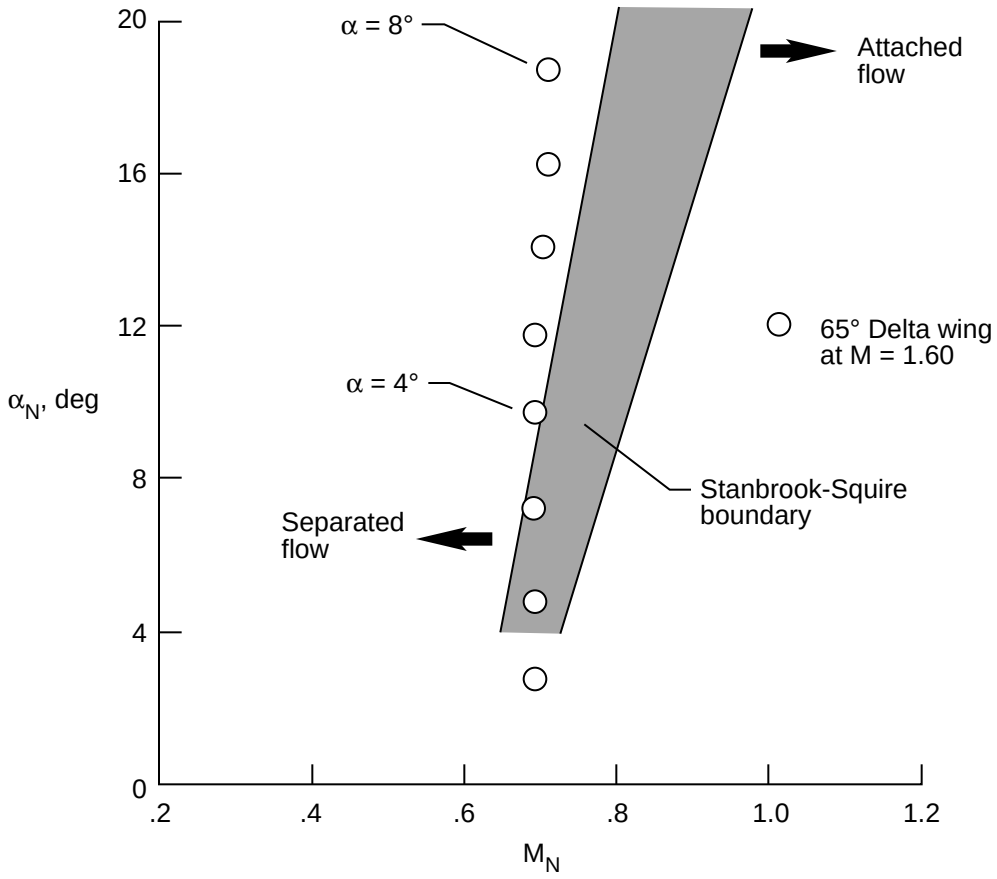

Figure 1. Location of 65° delta wing at *M* = 1.60 with respect to Stanbrook-Squire boundary at various angles of attack.

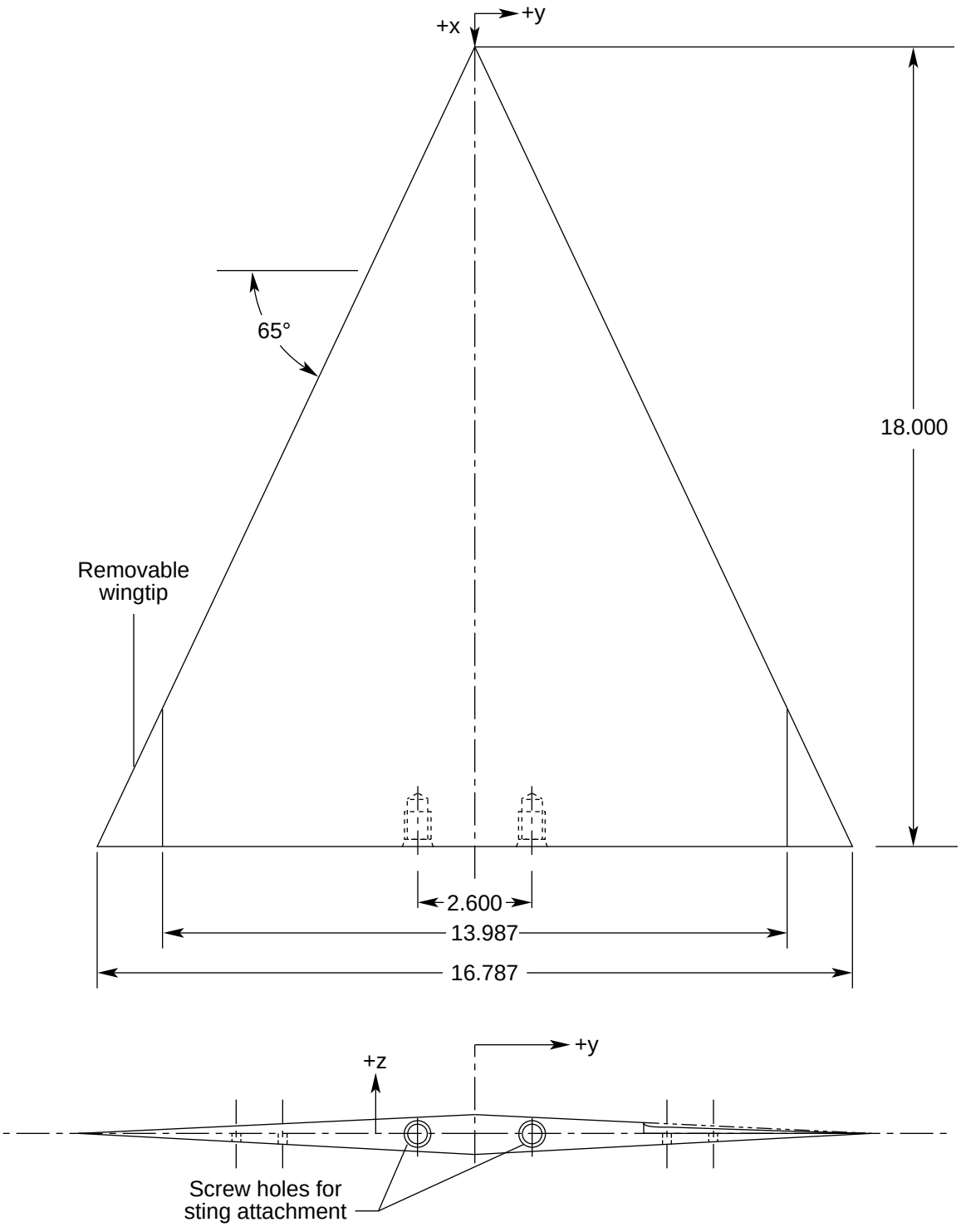

(a) Sharp wing.

Figure 2. Two-view sketches of three delta wing models. All dimensions are in inches unless otherwise noted.

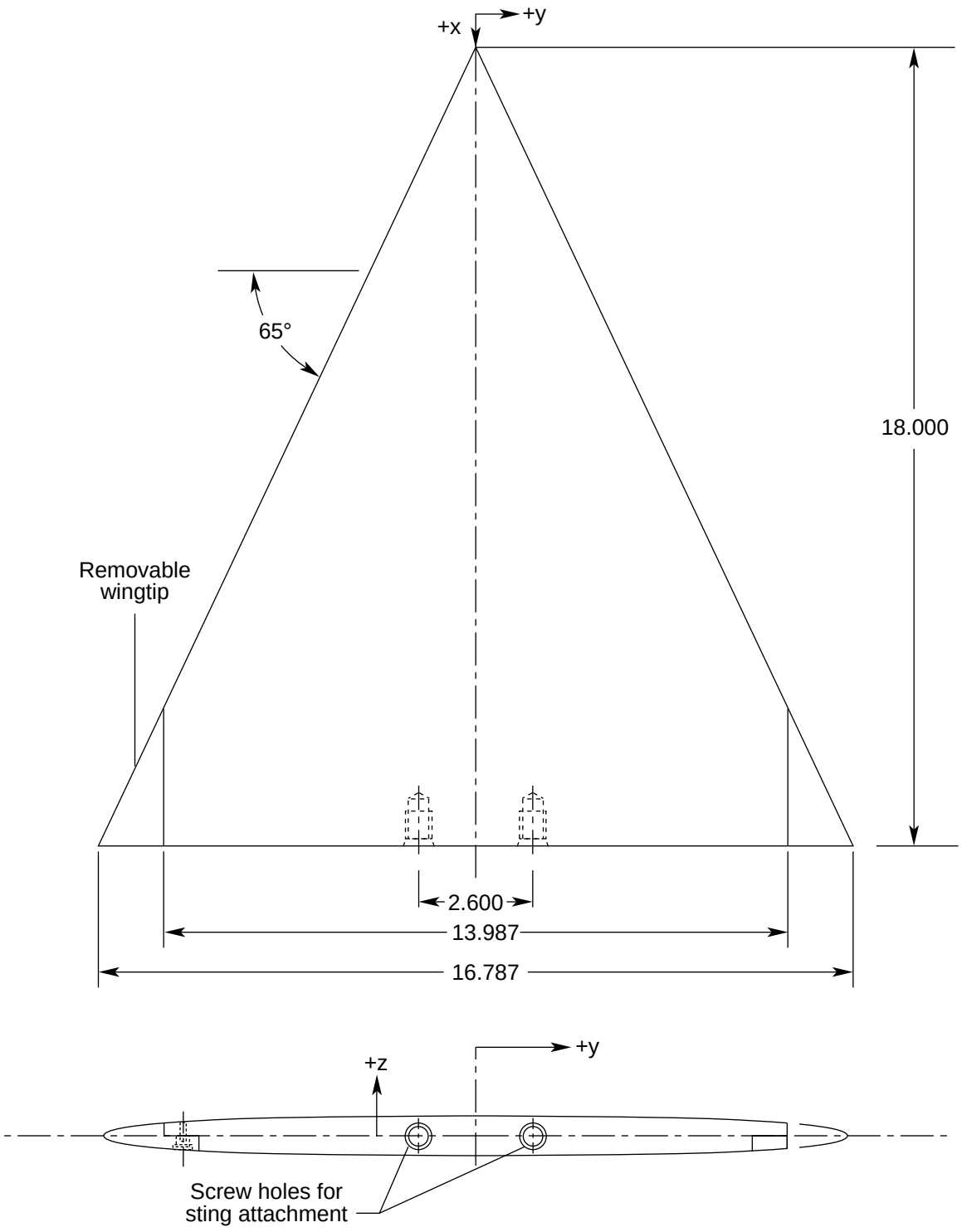

(b) Elliptical wing.

Figure 2. Continued.

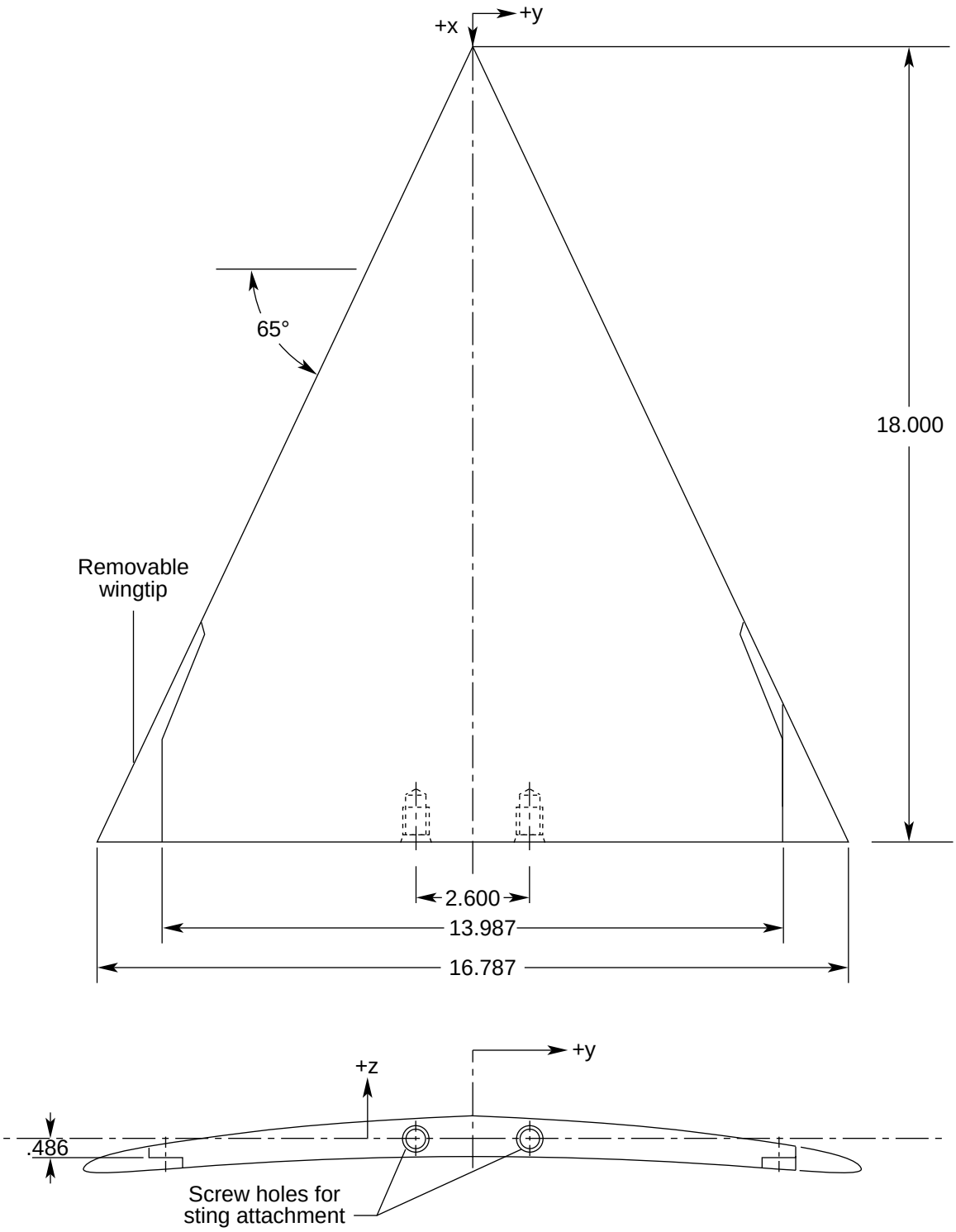

(c) Cambered wing.

Figure 2. Concluded.

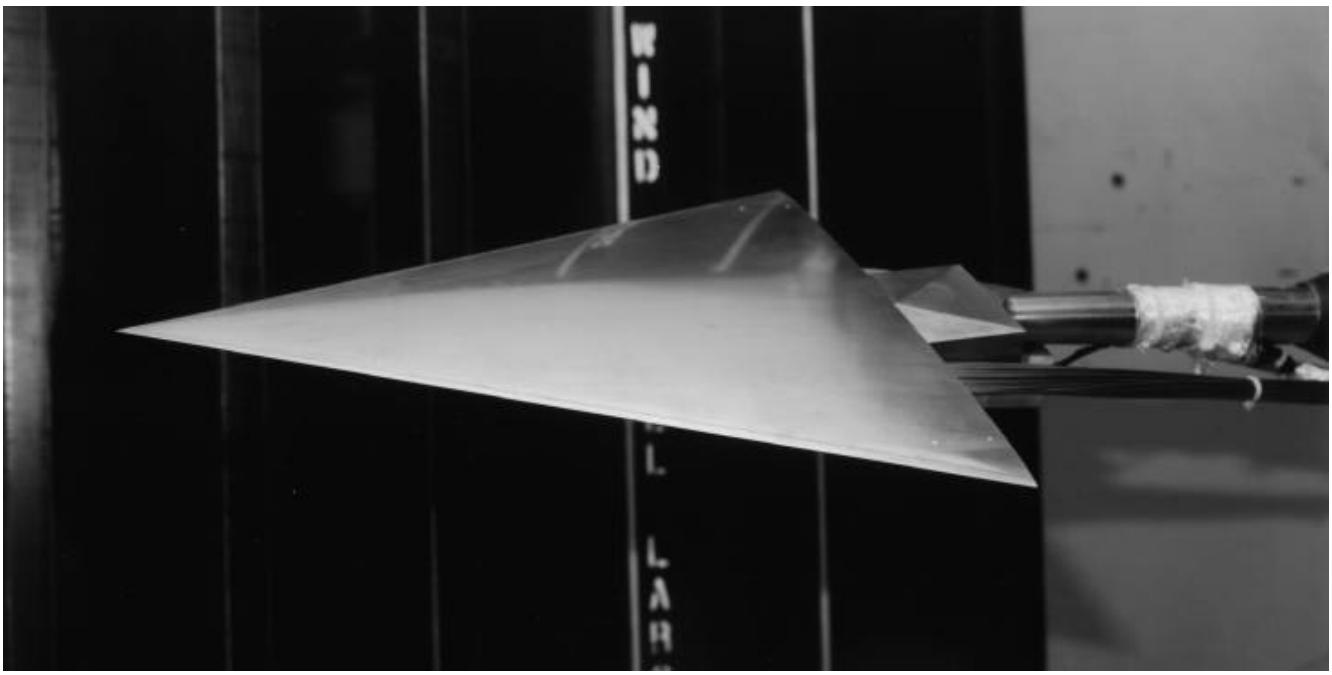

L-90-04477

(a) View of upper surface.

L-90-04479

(b) View of lower surface.

Figure 3. Photographs of elliptical wing model installed in Langley UPWT.

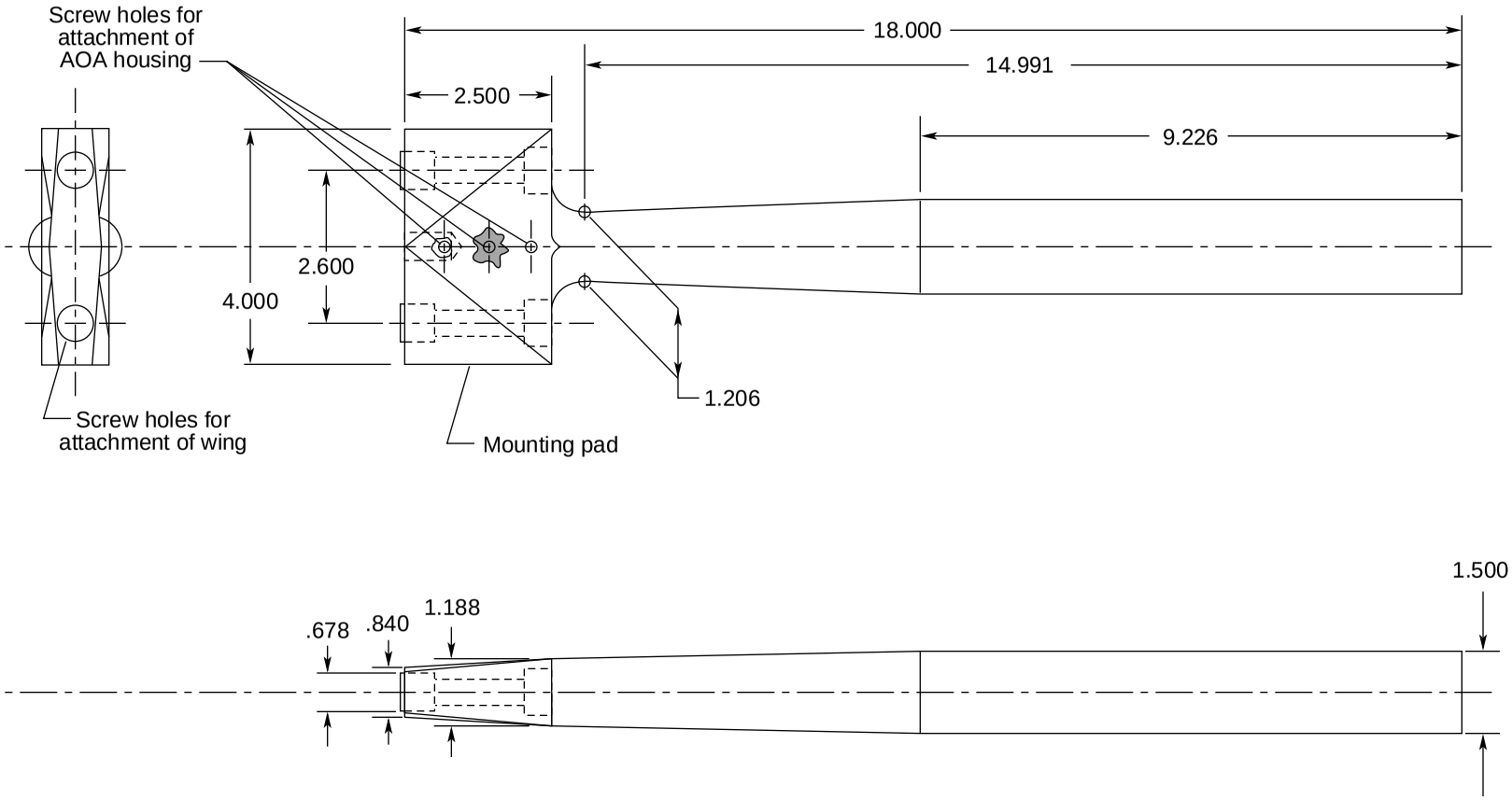

Figure 4. Details of sting. All dimensions are in inches.

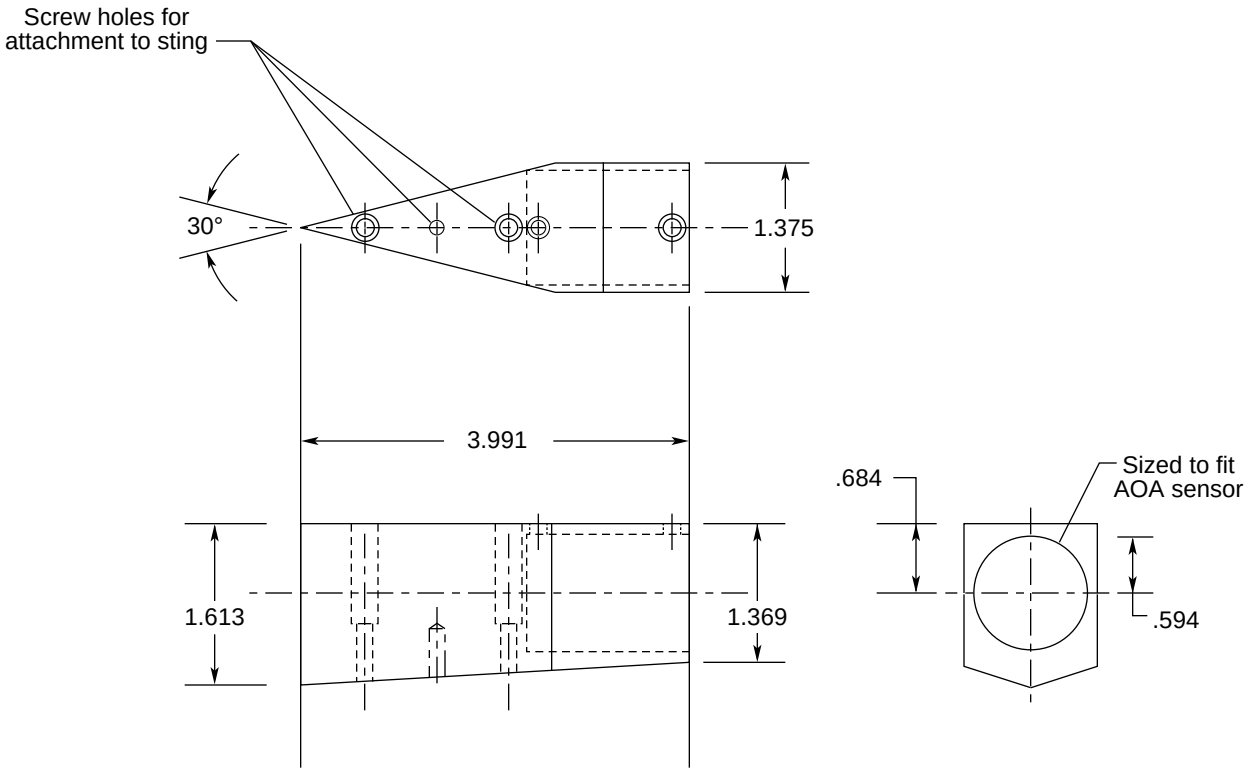

Figure 5. Details of AOA sensor housing. All linear dimensions are in inches.

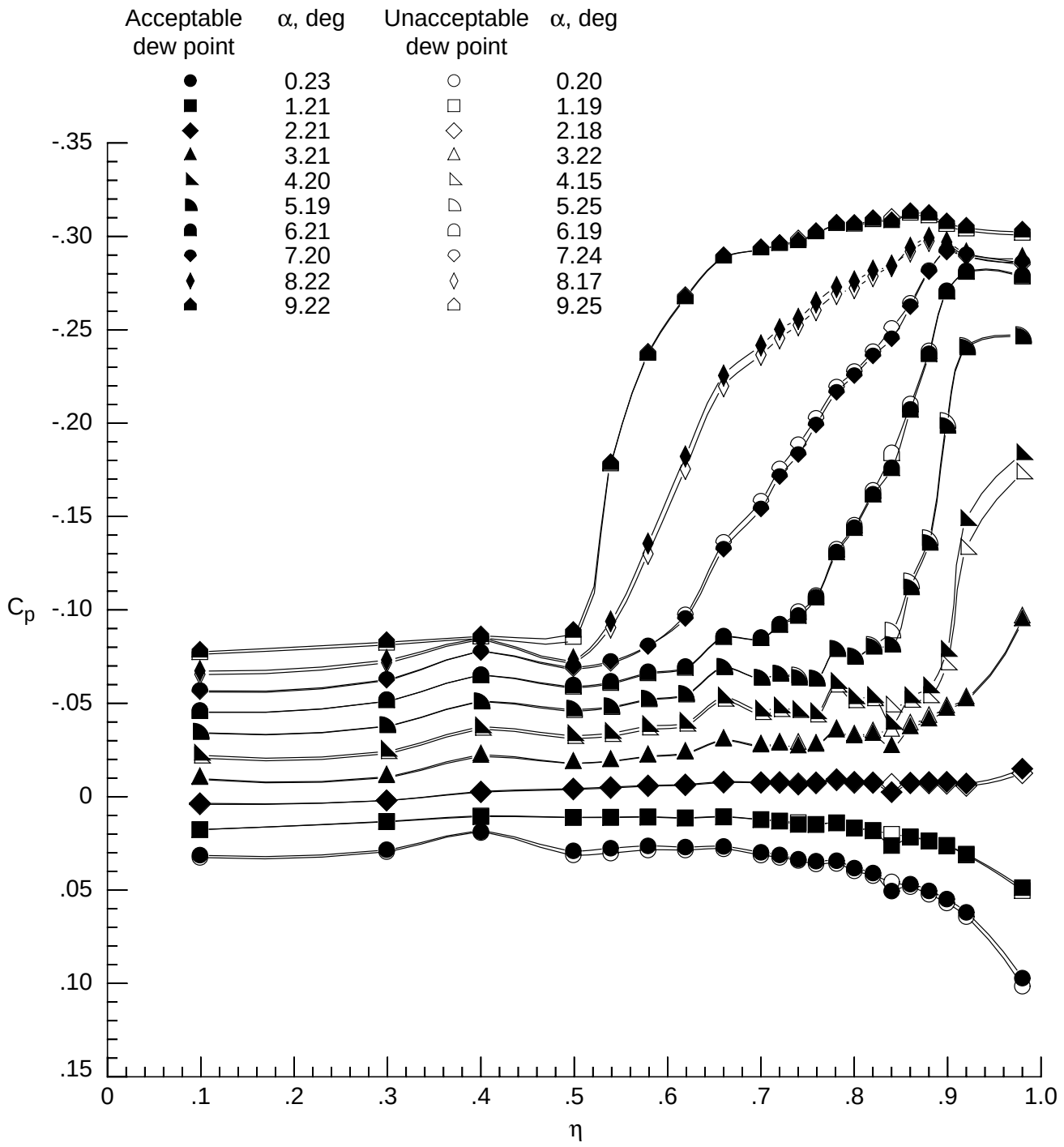

(a) Upper surface at x = 6 in.

Figure 6. Effect of dew point on surface-pressure coefficient data for cambered wing without transition grit at M = 1.60 and $R = 5 \times 10^6$ ft^{-1}.

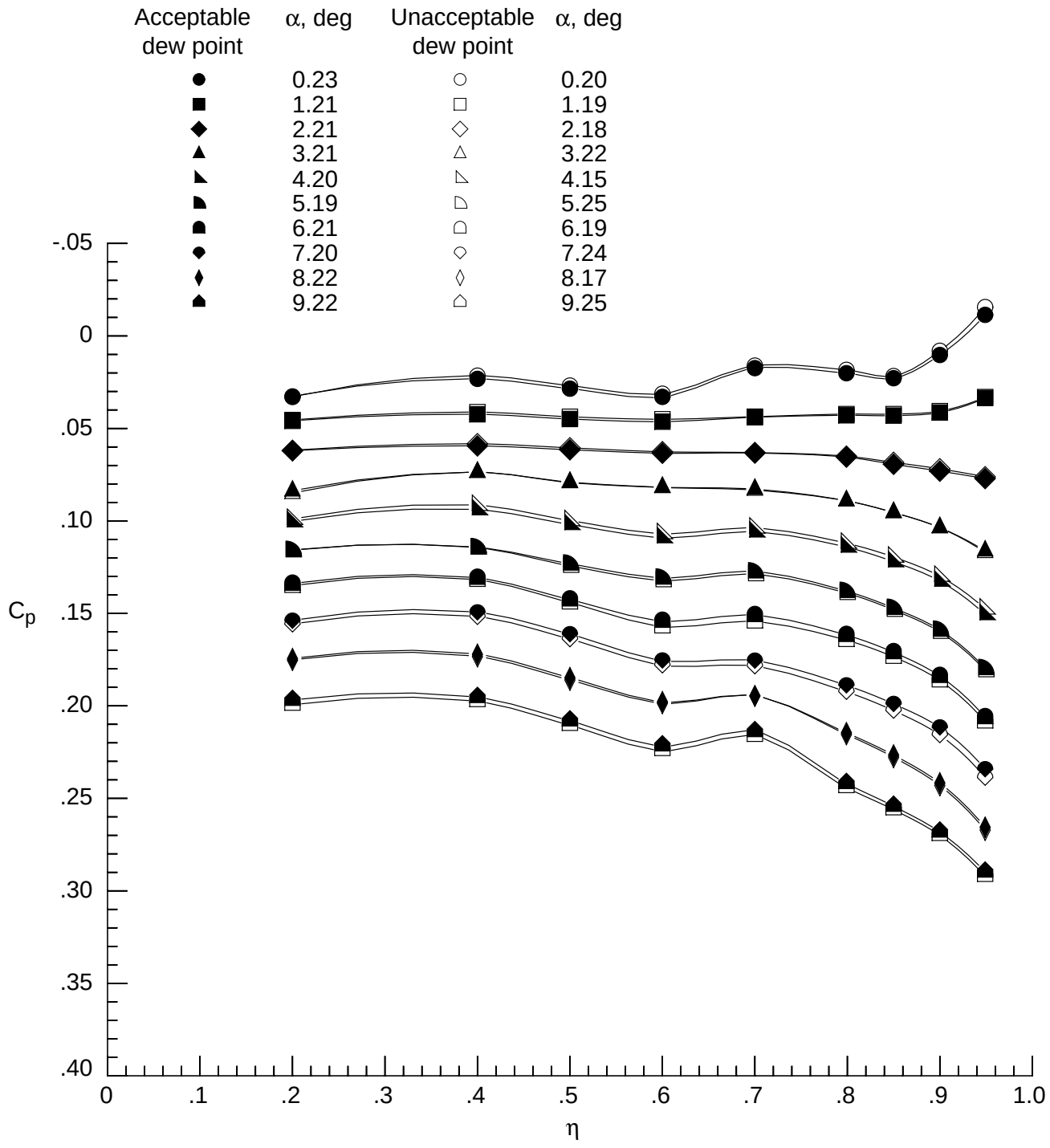

(b) Lower surface at x = 6 in.

Figure 6. Continued.

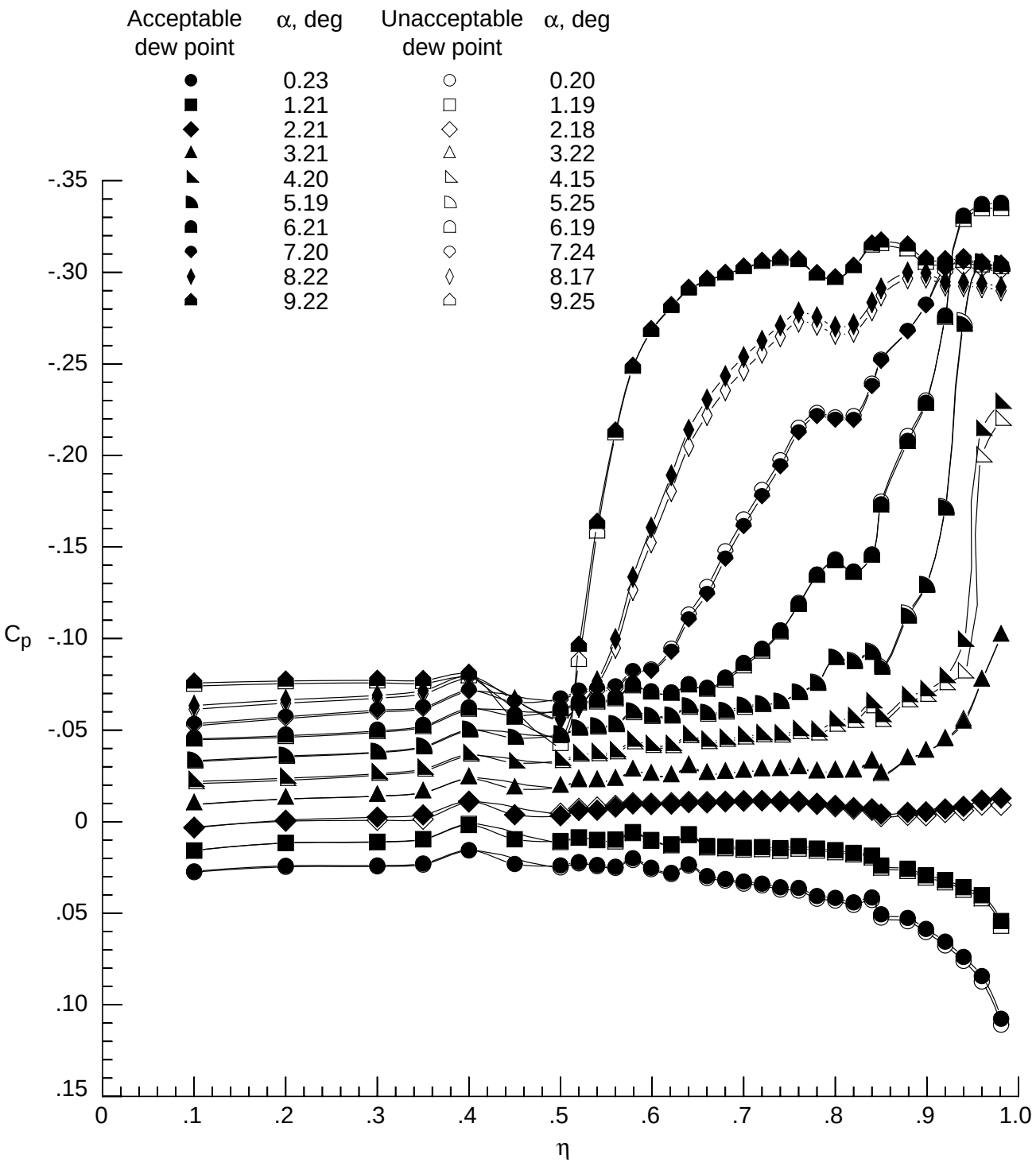

(c) Upper surface at x = 12 in.

Figure 6. Continued.

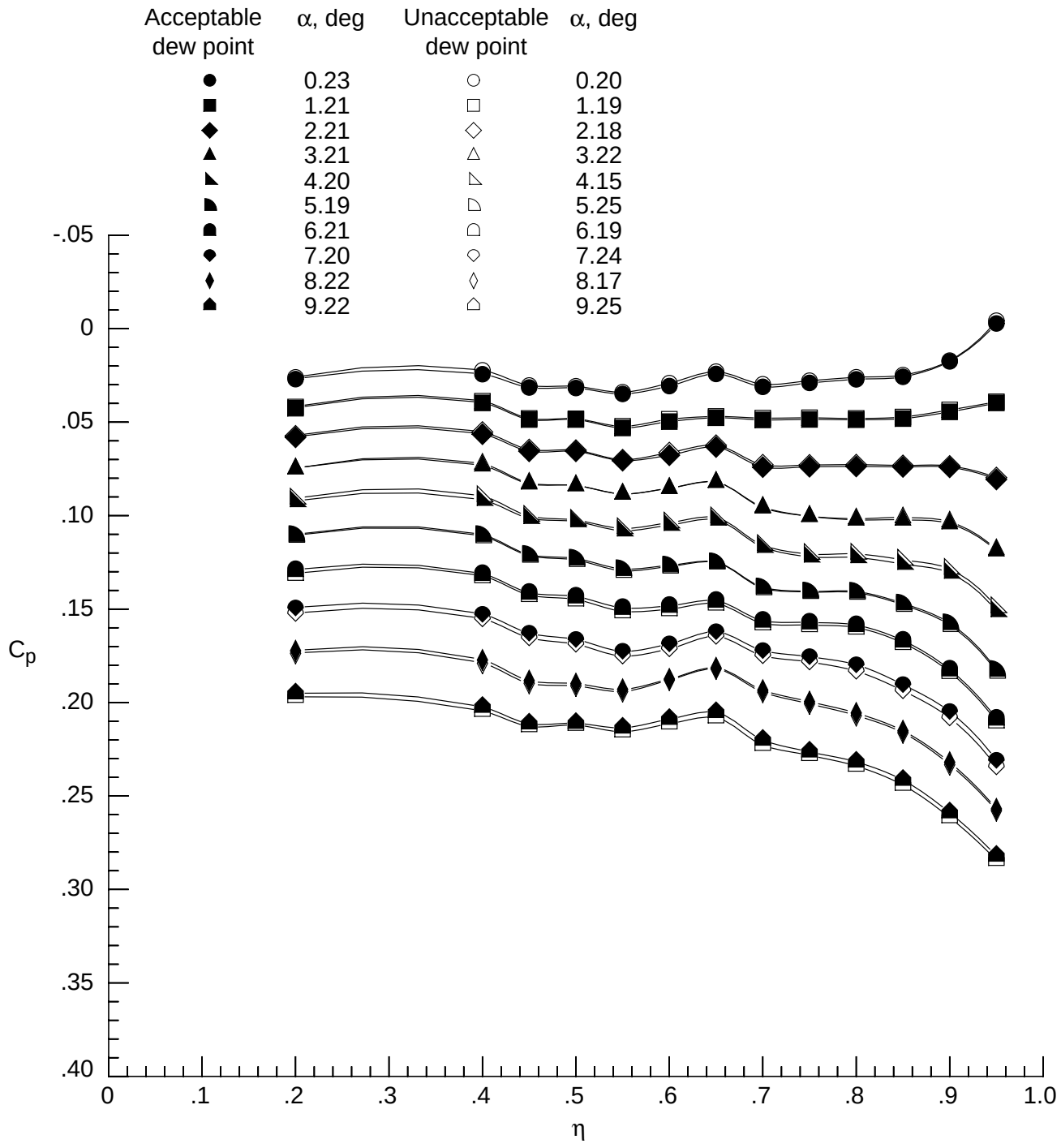

(d) Lower surface at x = 12 in.

Figure 6. Concluded.

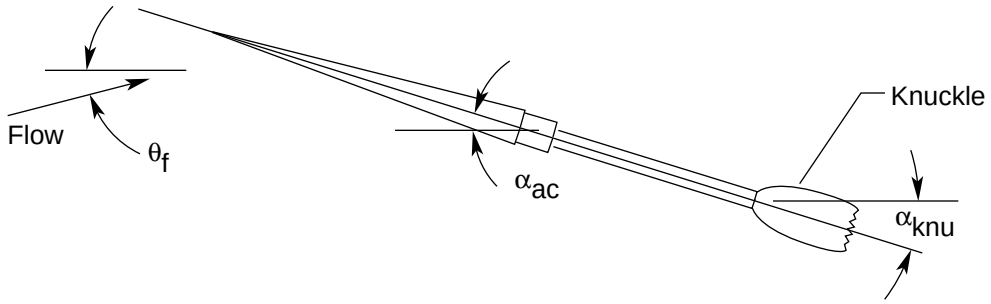

Figure 7. Flow angularity, angle of attack, and knuckle assembly.

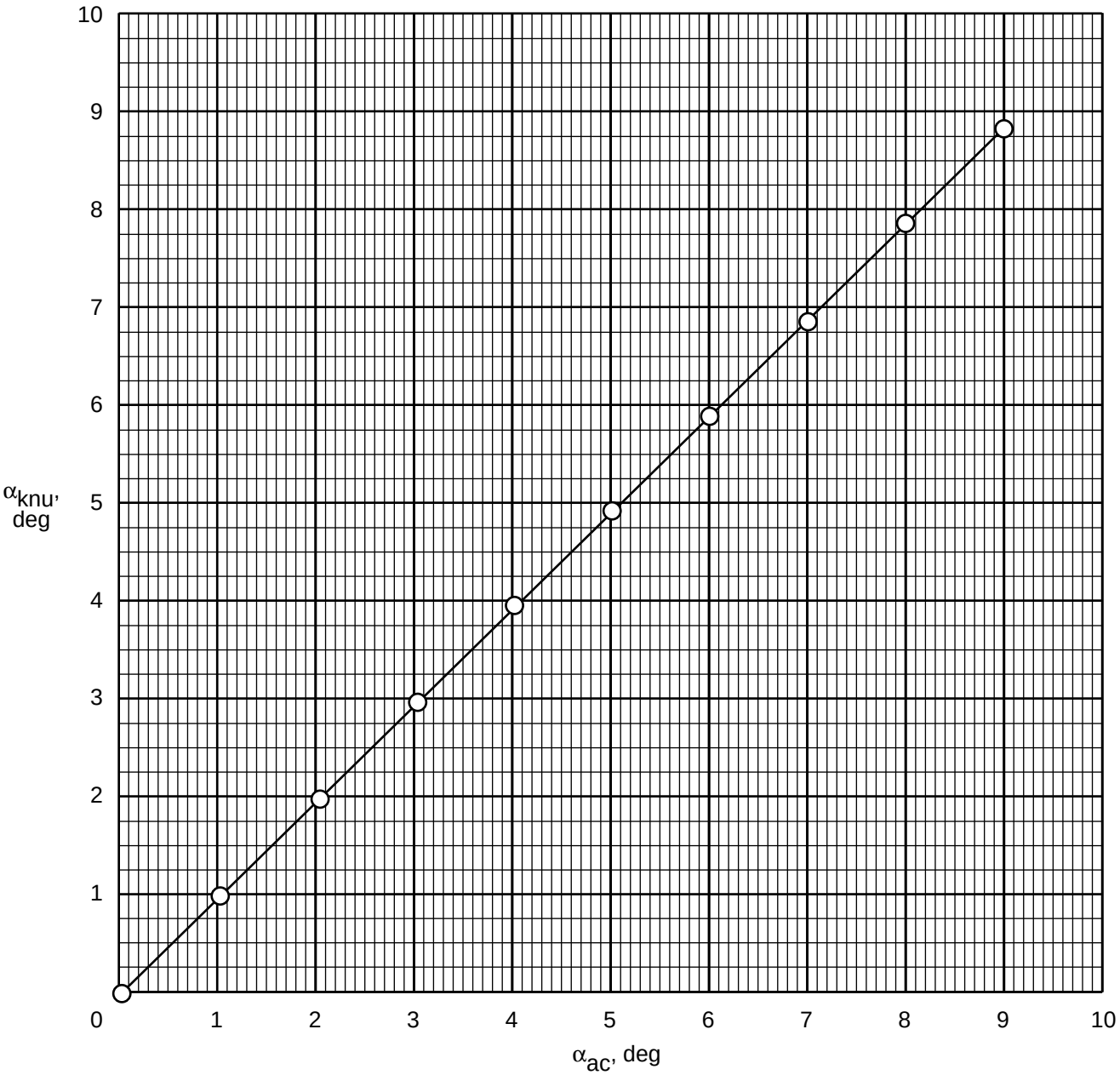

Figure 8. Sting deflections for $R = 1 \times 10^6$ ft^{-1} and $M = 1.60$ from data for elliptical wing without transition grit.

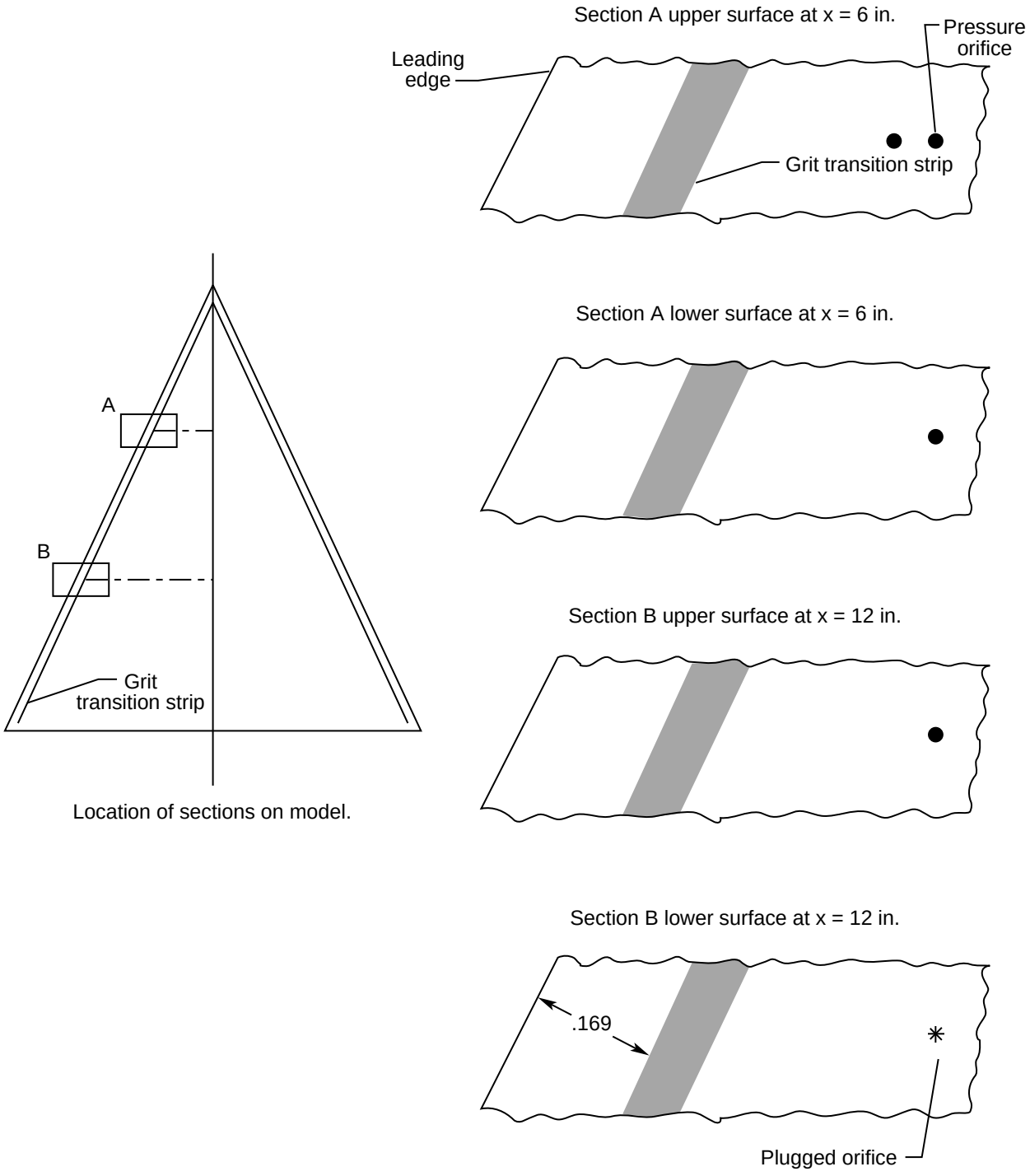

(a) Sharp wing.

Figure 9. Location of transition grit on model with respect to pressure orifices.

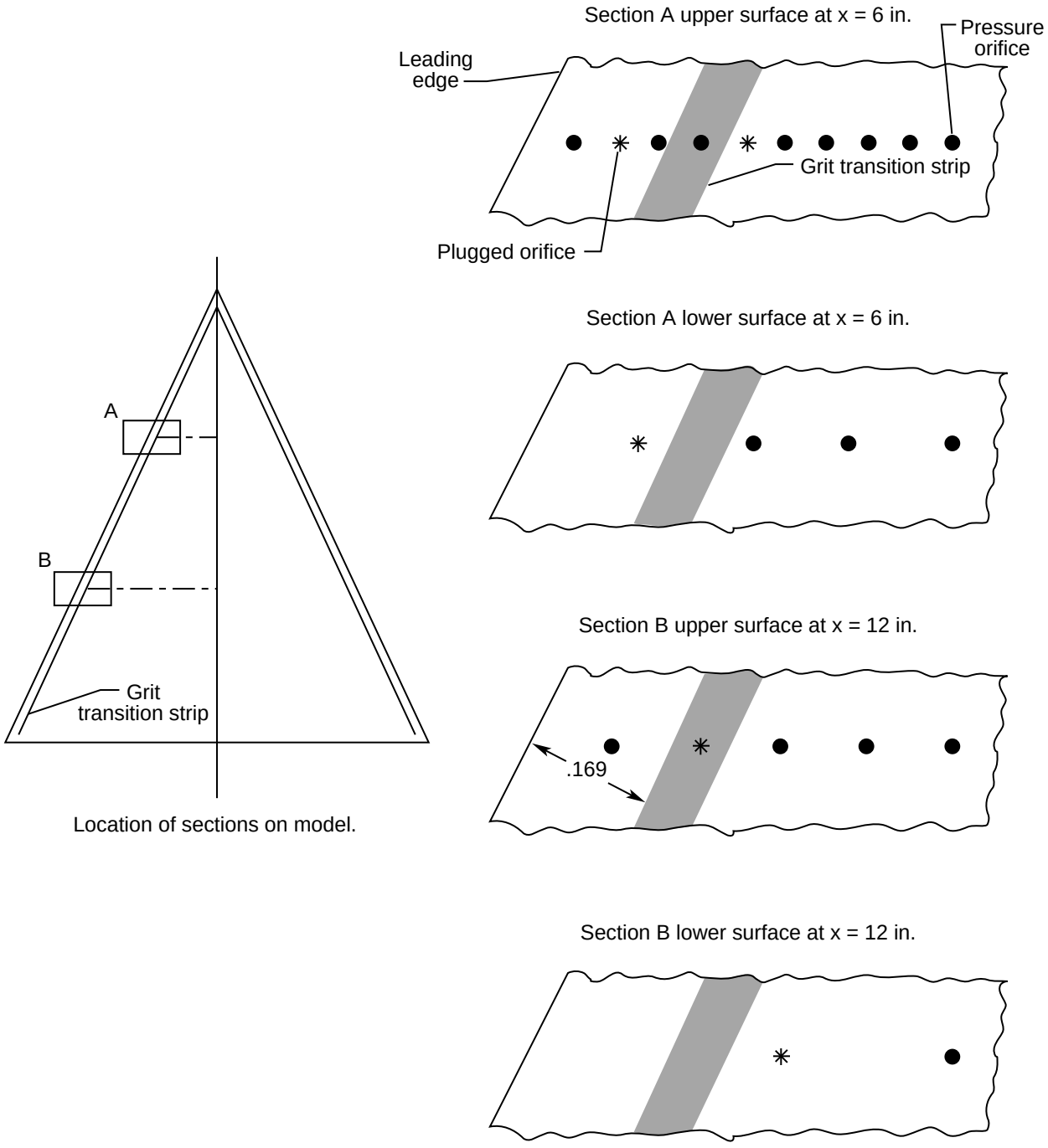

(b) Elliptical wing.

Figure 9. Continued.

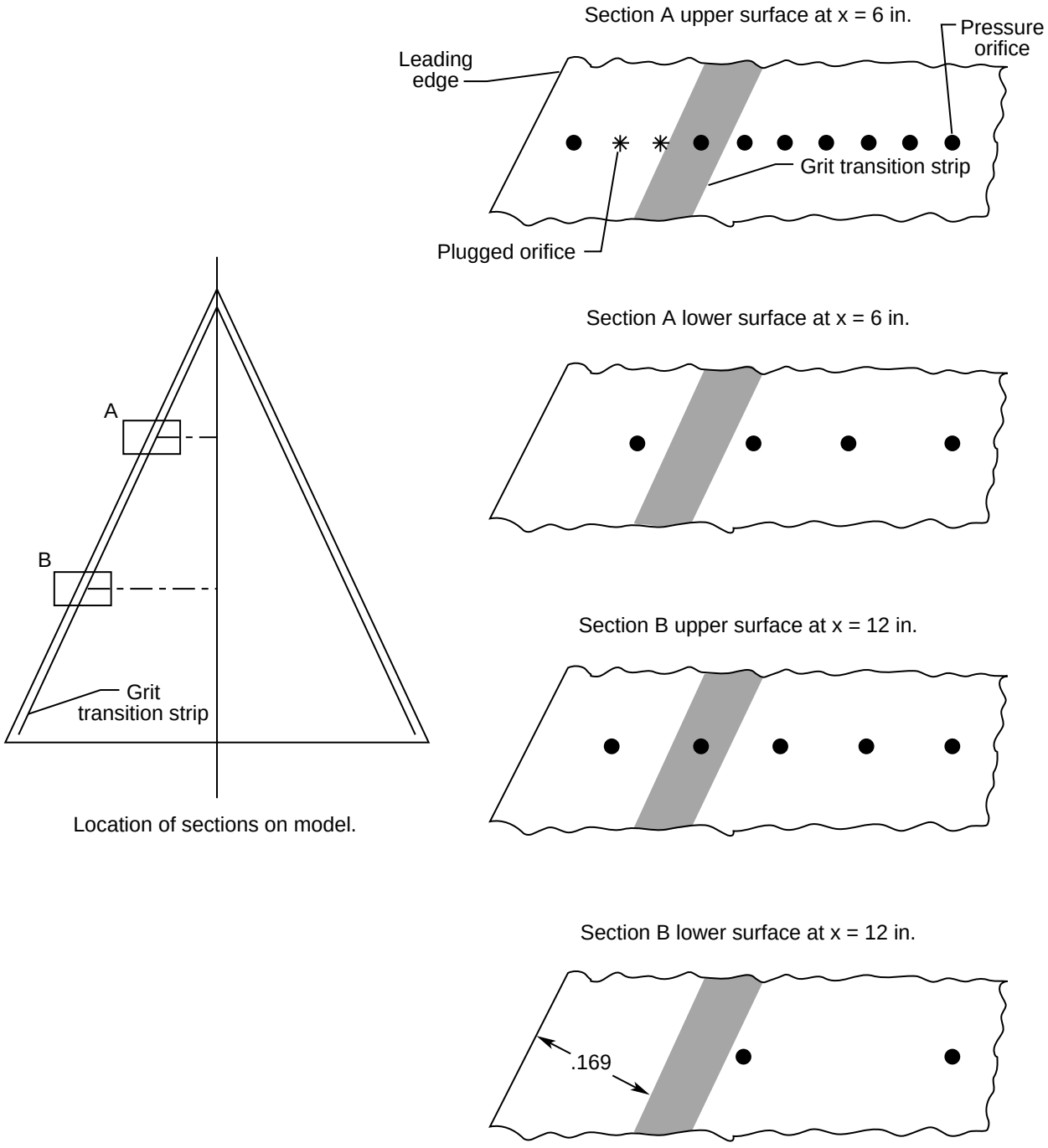

Location of sections on model.

(c) Cambered wing.

Figure 9. Concluded.

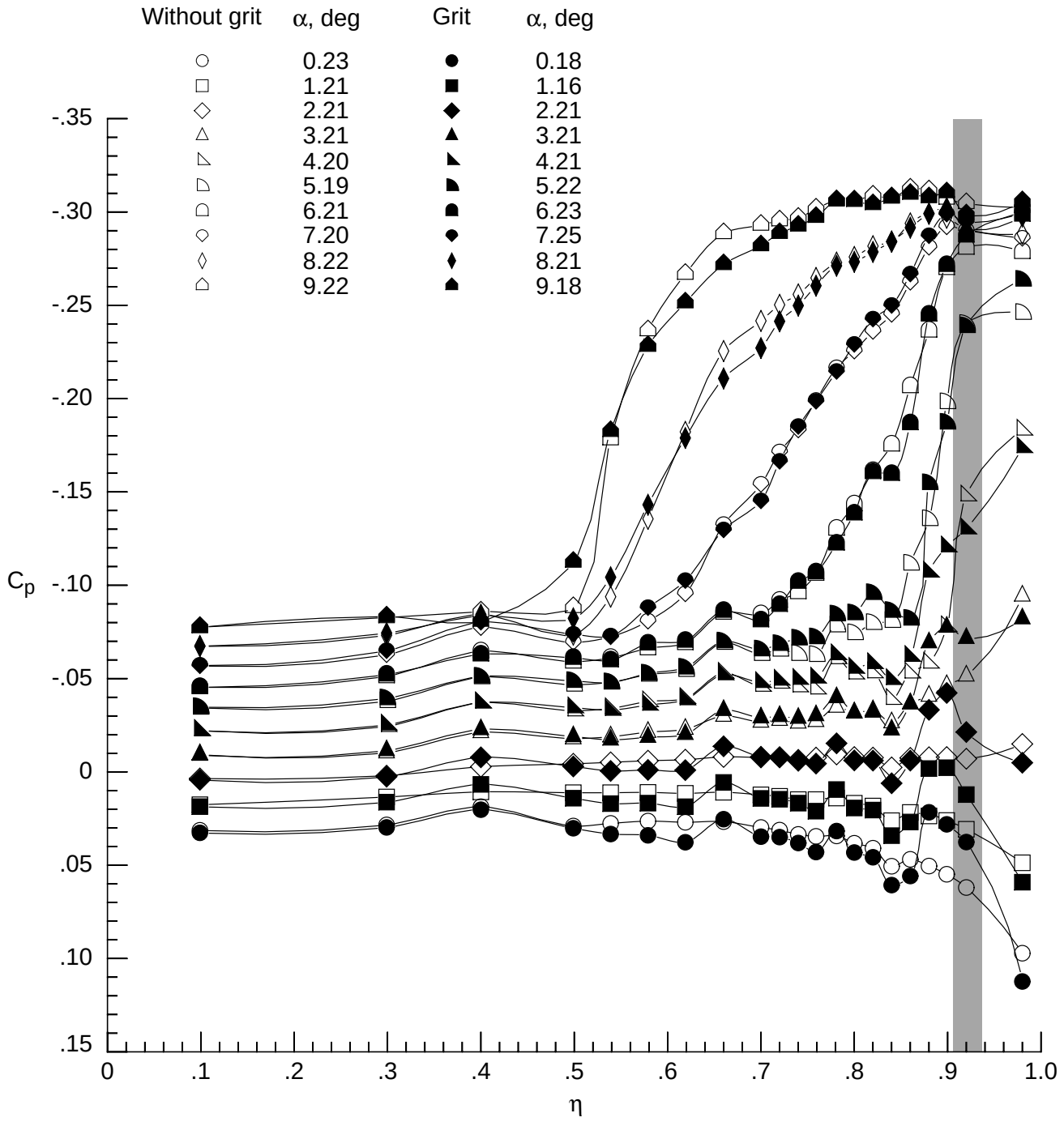

(a) Upper surface at x = 6 in.

Figure 10. Effect of transition grit on surface-pressure coefficient data for cambered wing at $M = 1.60$ and $R = 5 \times 10^6$ ft^{-1}. Shaded area is width and location of transition strip.

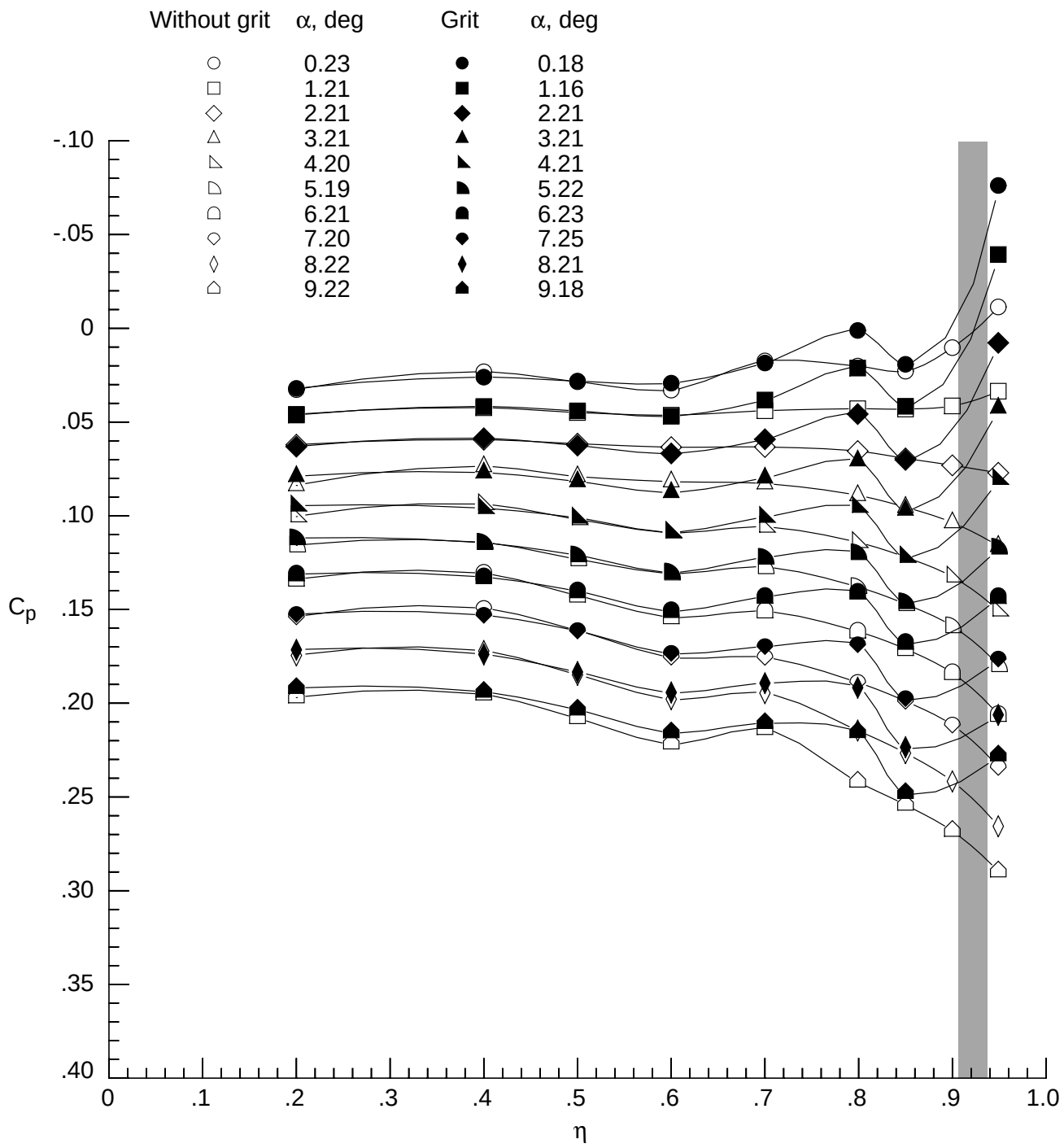

(b) Lower surface at x = 6 in.

Figure 10. Continued.

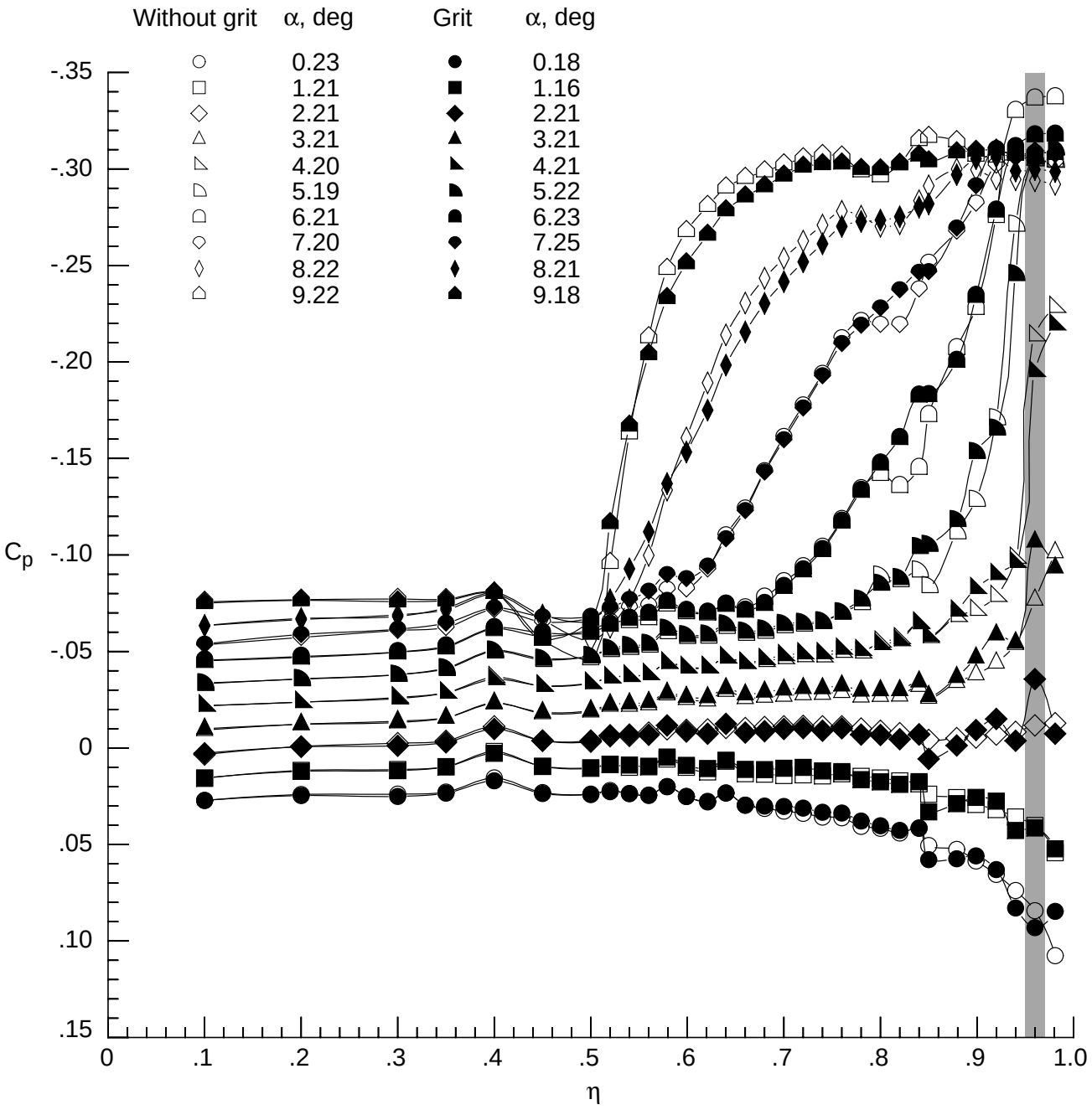

(c) Upper surface at x = 12 in.

Figure 10. Continued.

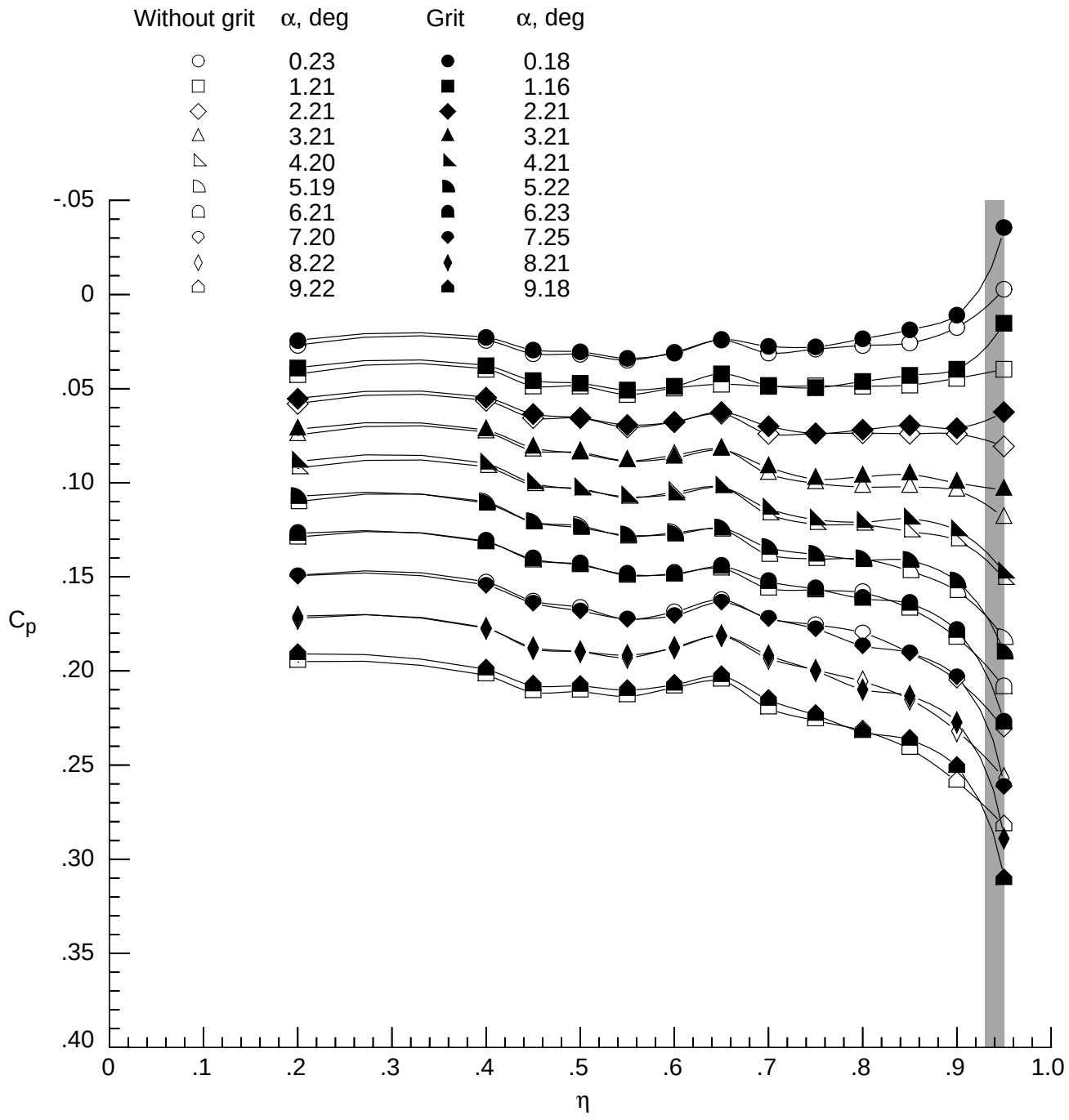

(d) Lower surface at x = 12 in.

Figure 10. Concluded.

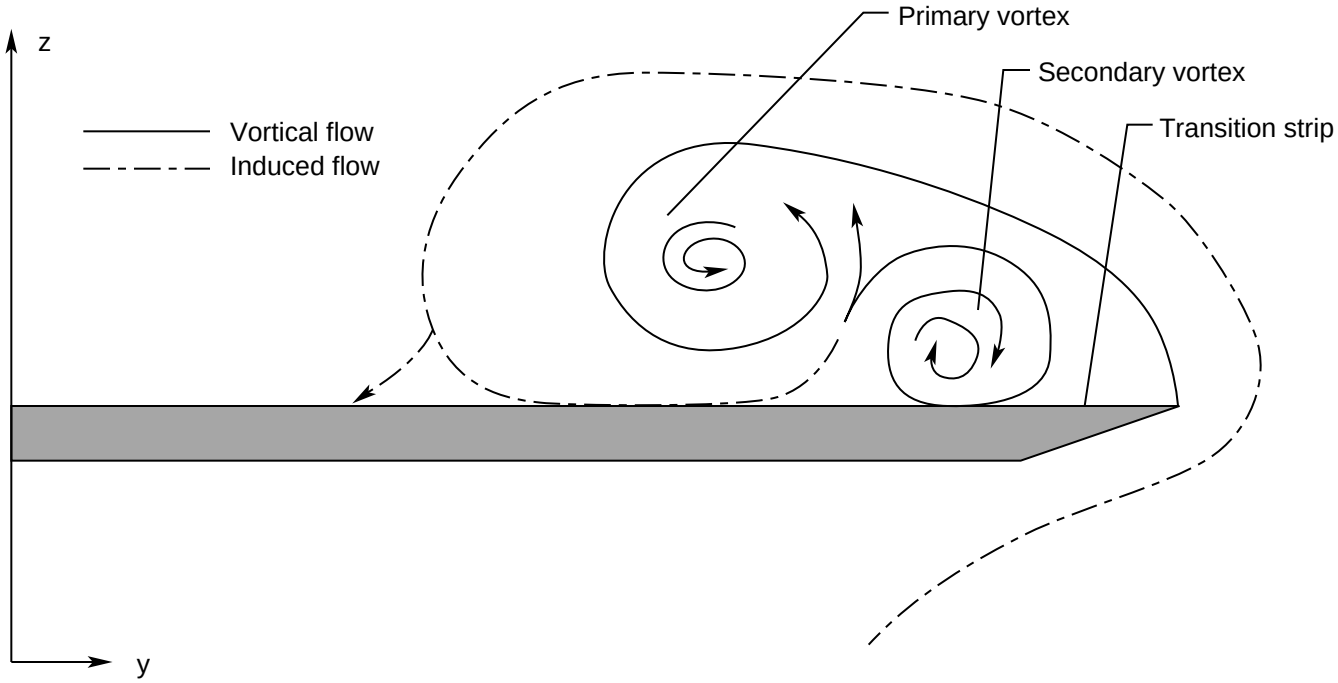

Figure 11. Sketch of vortex emanating from wing leading edge (from ref. 5).

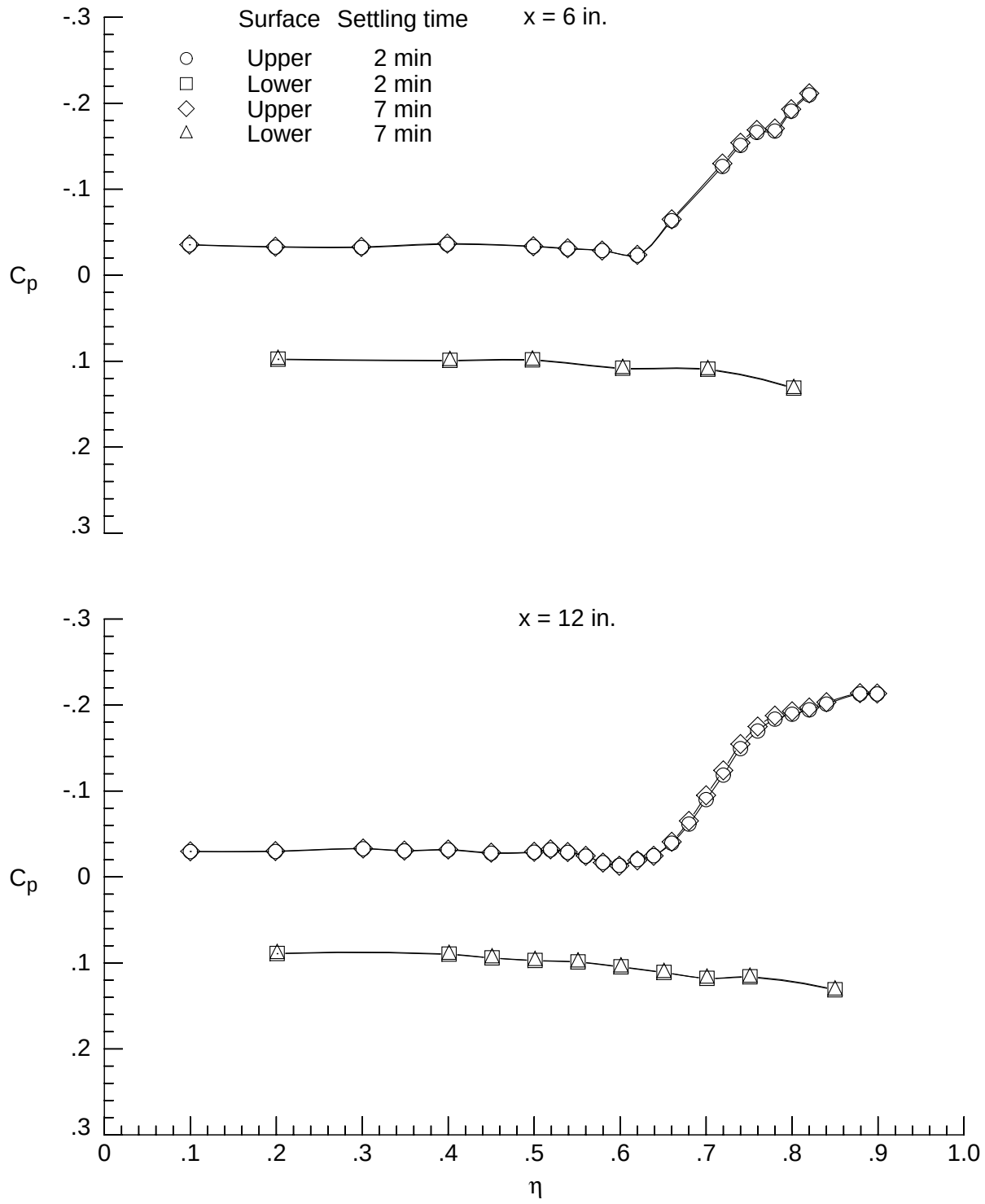

(a) Sharp wing with transition grit at $\alpha = 4.25°$ and $R = 5 \times 10^6$ ft^{-1}.

Figure 12. Effect of settling time on surface-pressure coefficient data for delta wing models at $M = 1.60$.

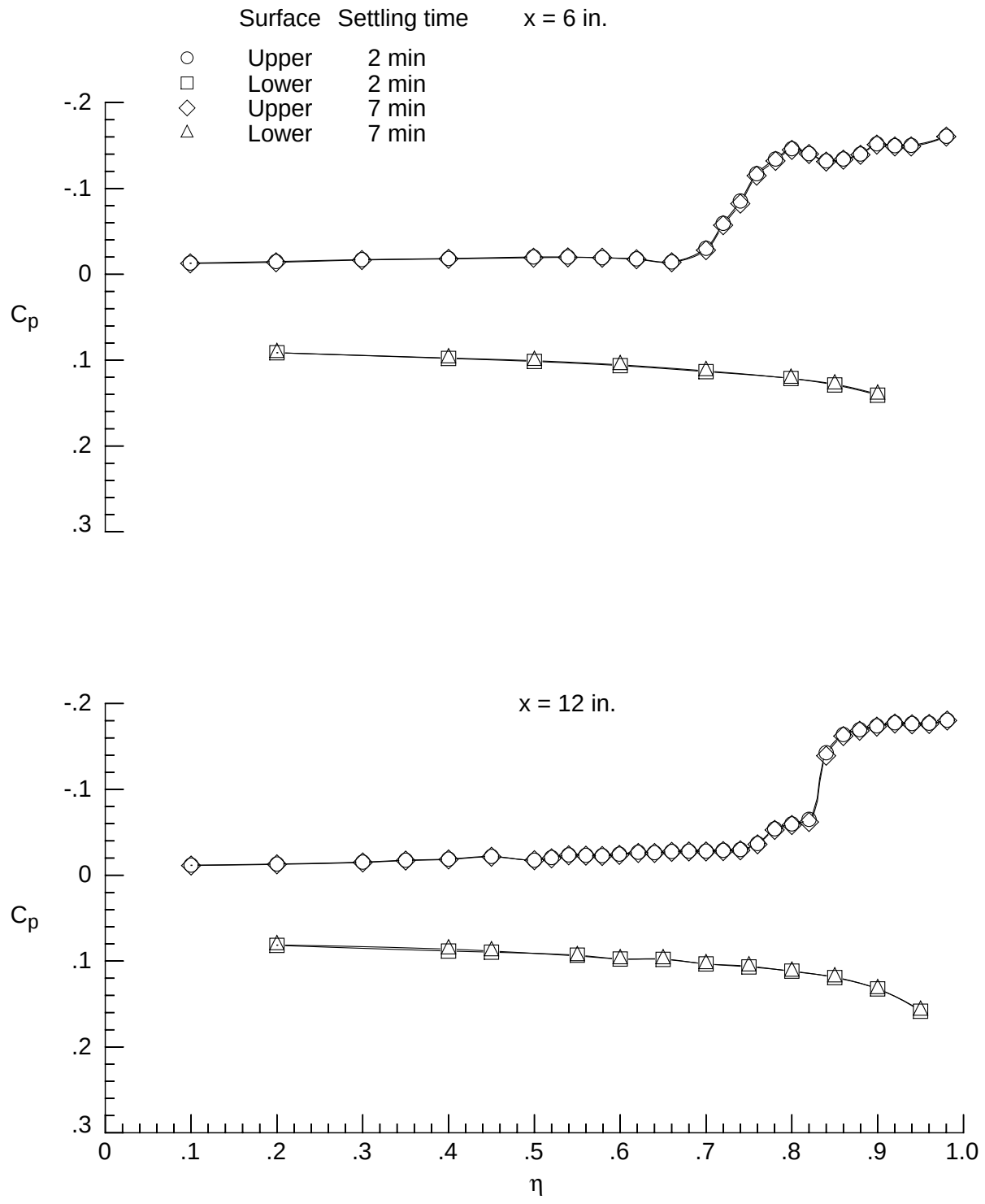

(b) Elliptical wing without transition grit at $\alpha = 3.71°$ and $R = 1 \times 10^6$ ft^{-1}.

Figure 12. Continued.

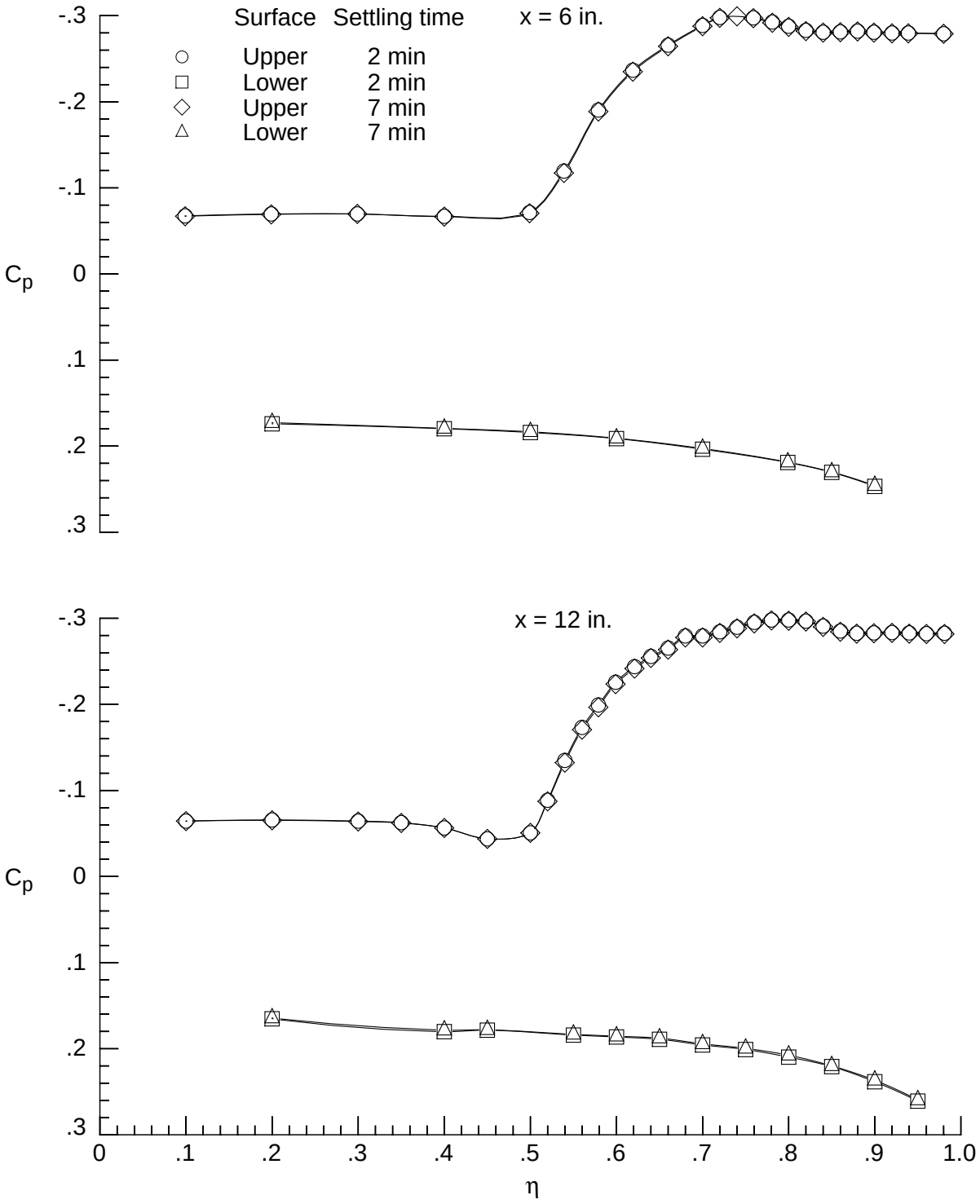

(c) Elliptical wing without transition grit at $\alpha = 8.18°$ and $R = 1 \times 10^6$ ft^{-1}.

Figure 12. Concluded.

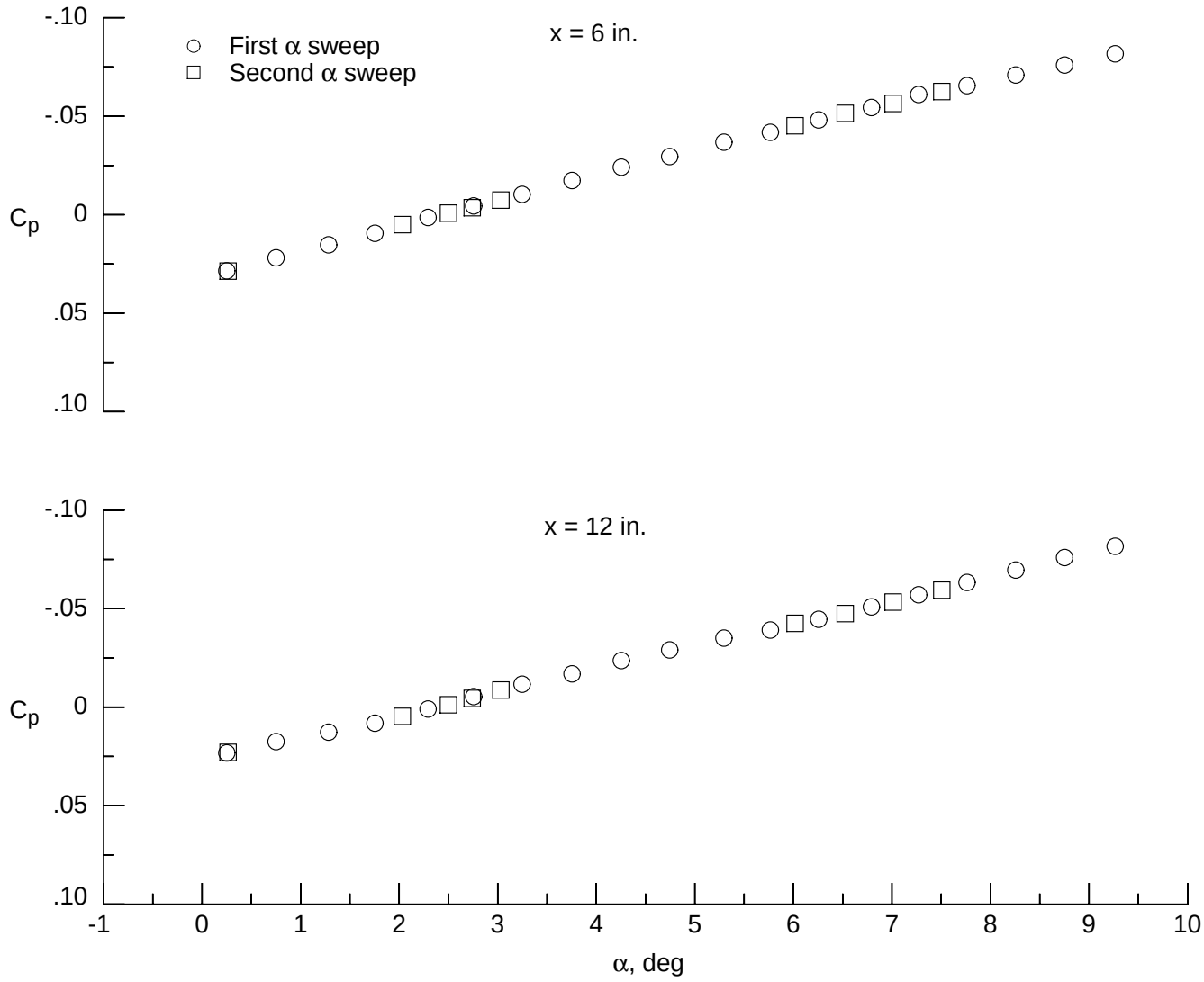

(a) The C_p at $\eta = 0.1$ on upper surface of sharp wing without transition grit at $M = 1.60$ and $R = 1 \times 10^6$ ft^{-1}.

Figure 13. Repeatability of surface-pressure coefficient data.

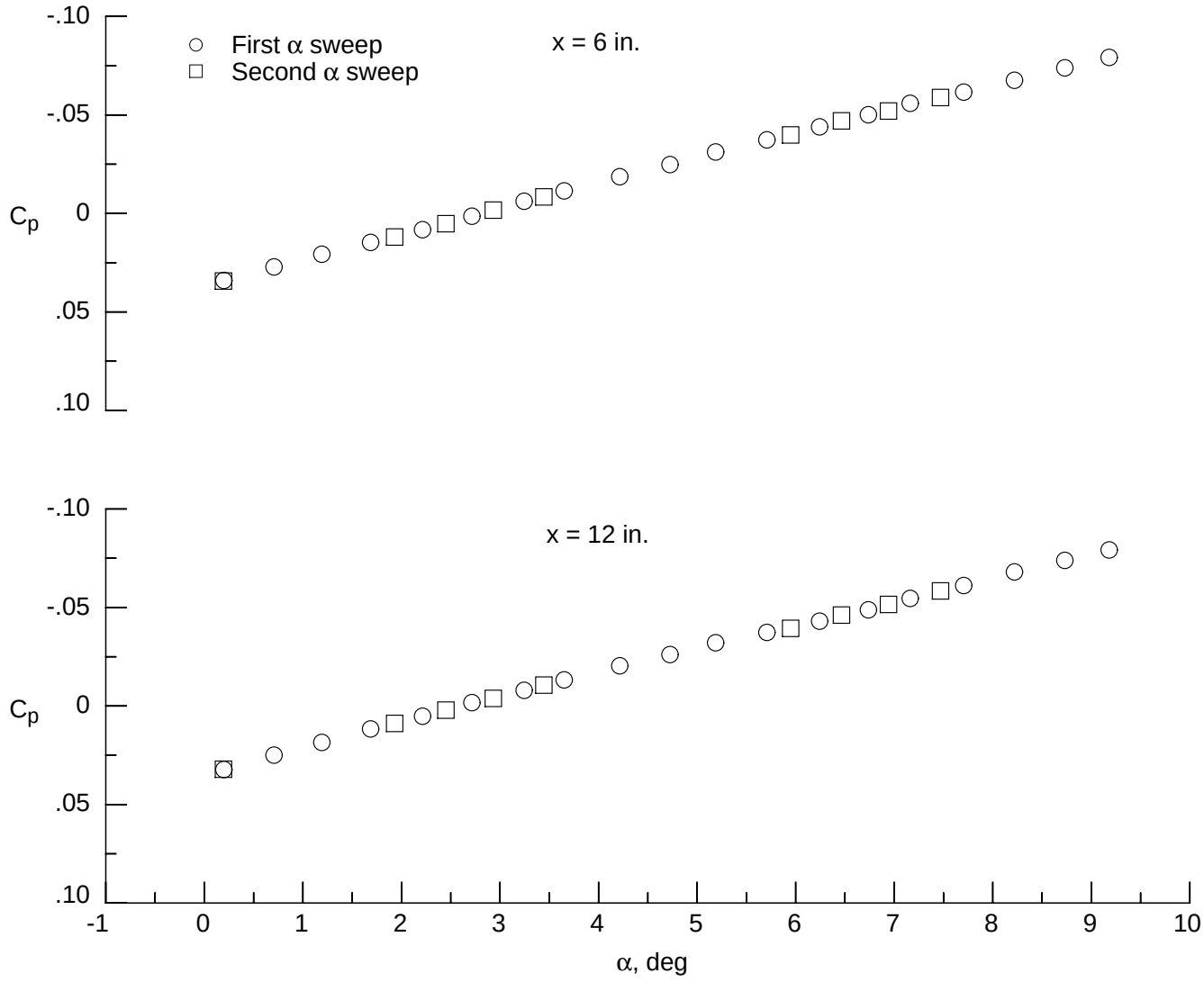

(b) The C_p at $\eta = 0.1$ on upper surface of elliptical wing with transition grit at $M = 1.60$ and $R = 1 \times 10^6$ ft^{-1}.

Figure 13. Continued.

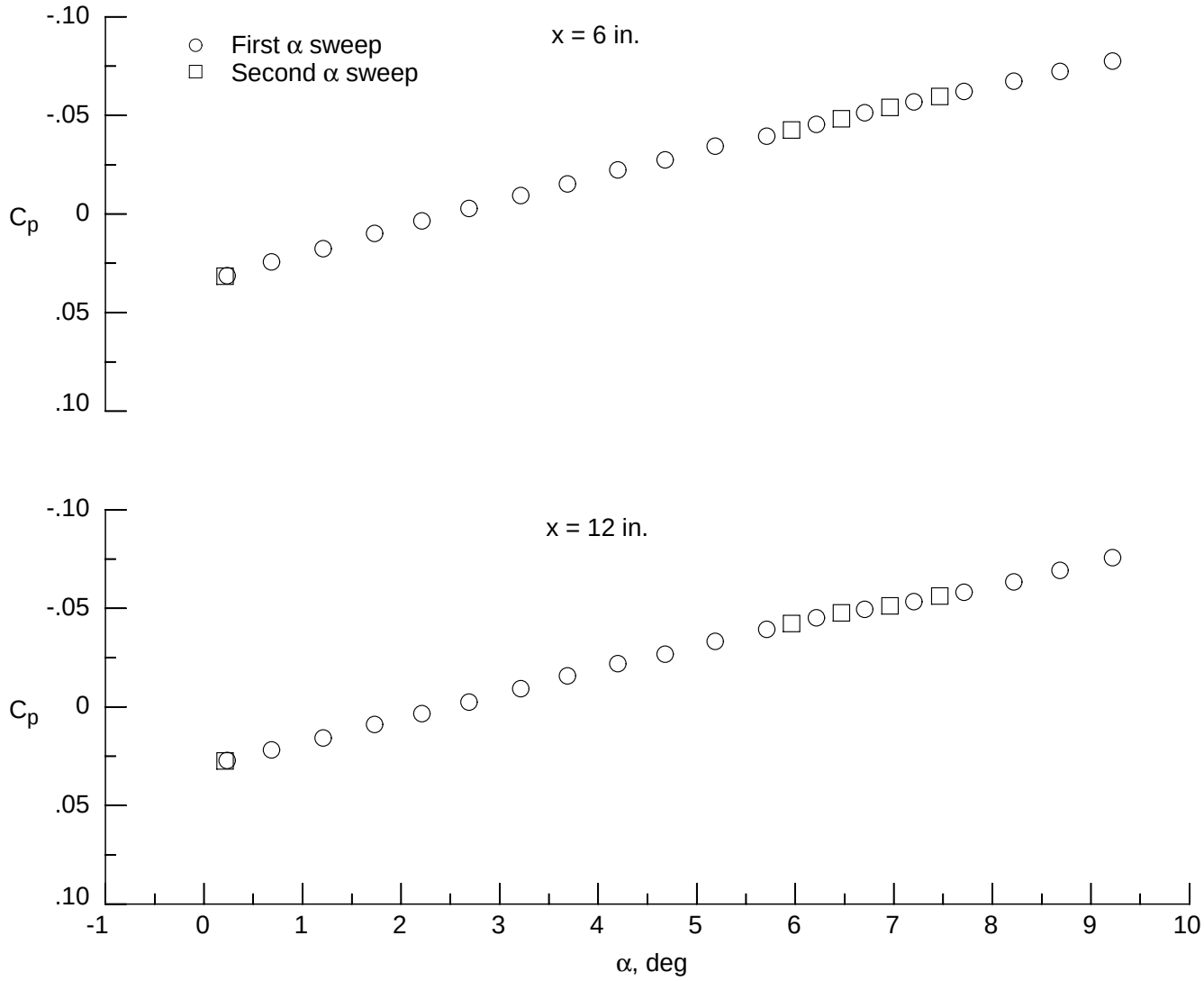

(c) The C_p at $\eta = 0.1$ on upper surface of cambered wing without transition grit at $M = 1.60$ and $R = 5 \times 10^6$ ft^{-1}.

Figure 13. Concluded.

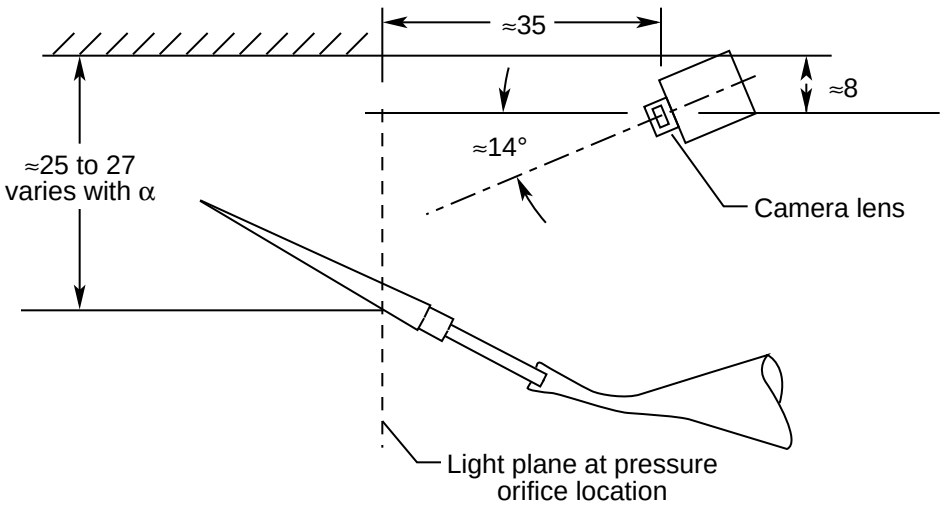

Figure 14. Approximate locations of model, light sheet, and camera for vapor-screen technique. All linear dimensions are in inches.

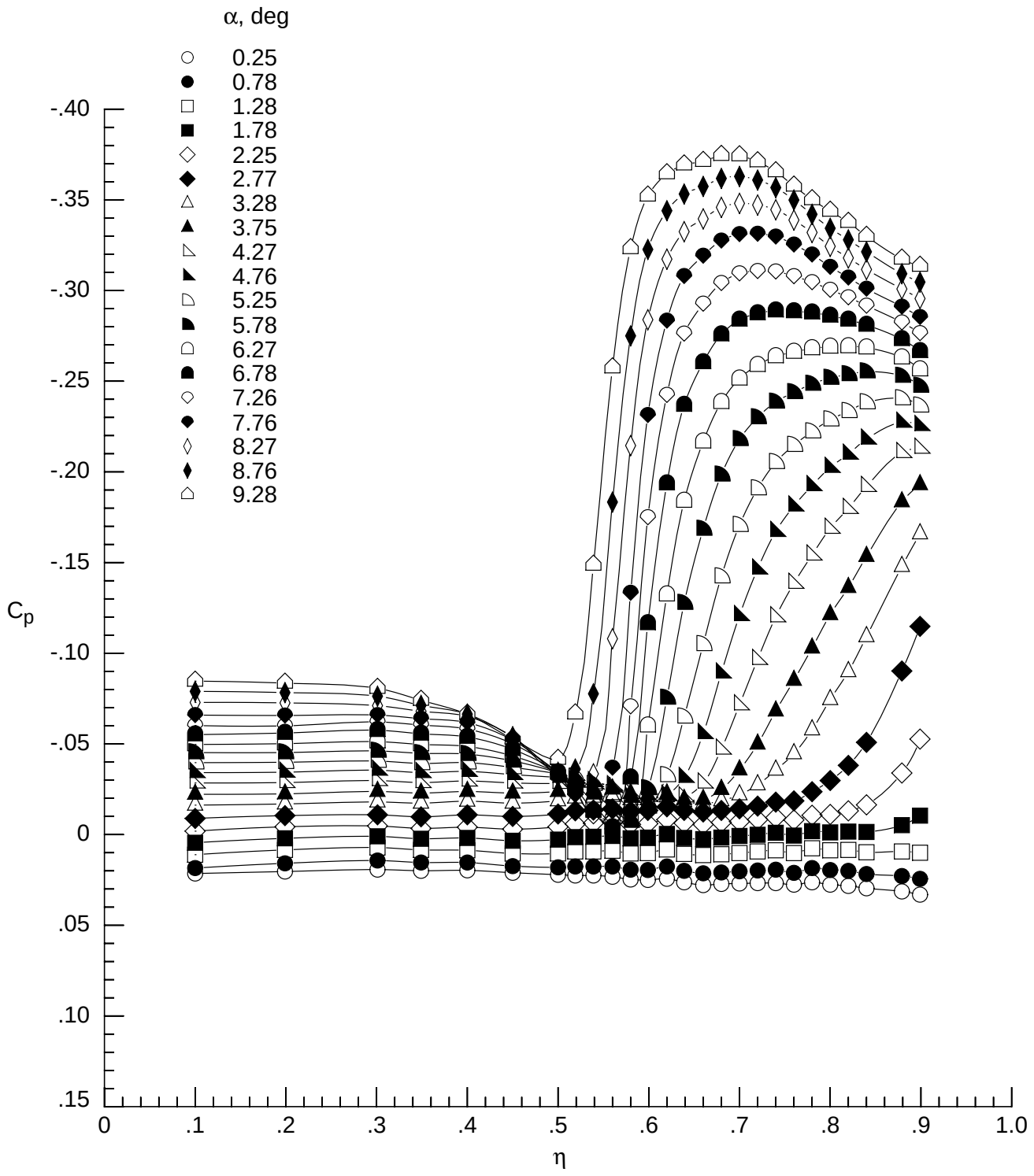

(a) Sharp wing.

Figure 15. Effect of angle of attack on upper surface-pressure coefficient distributions for three delta wings without transition grit at $x = 12$ in., $M = 1.60$, and $R = 2 \times 10^6$ ft^{-1}.

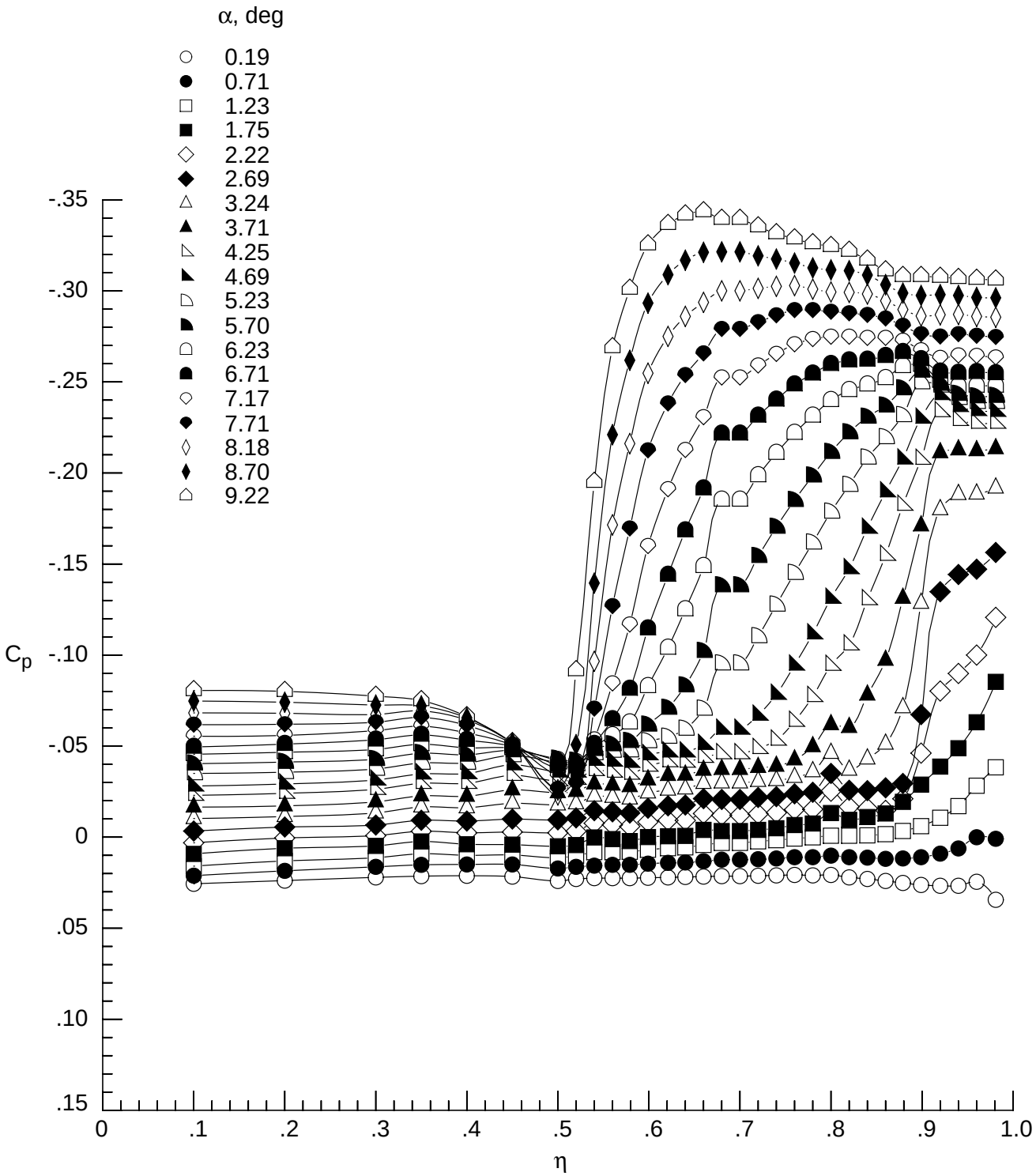

(b) Elliptical wing.

Figure 15. Continued.

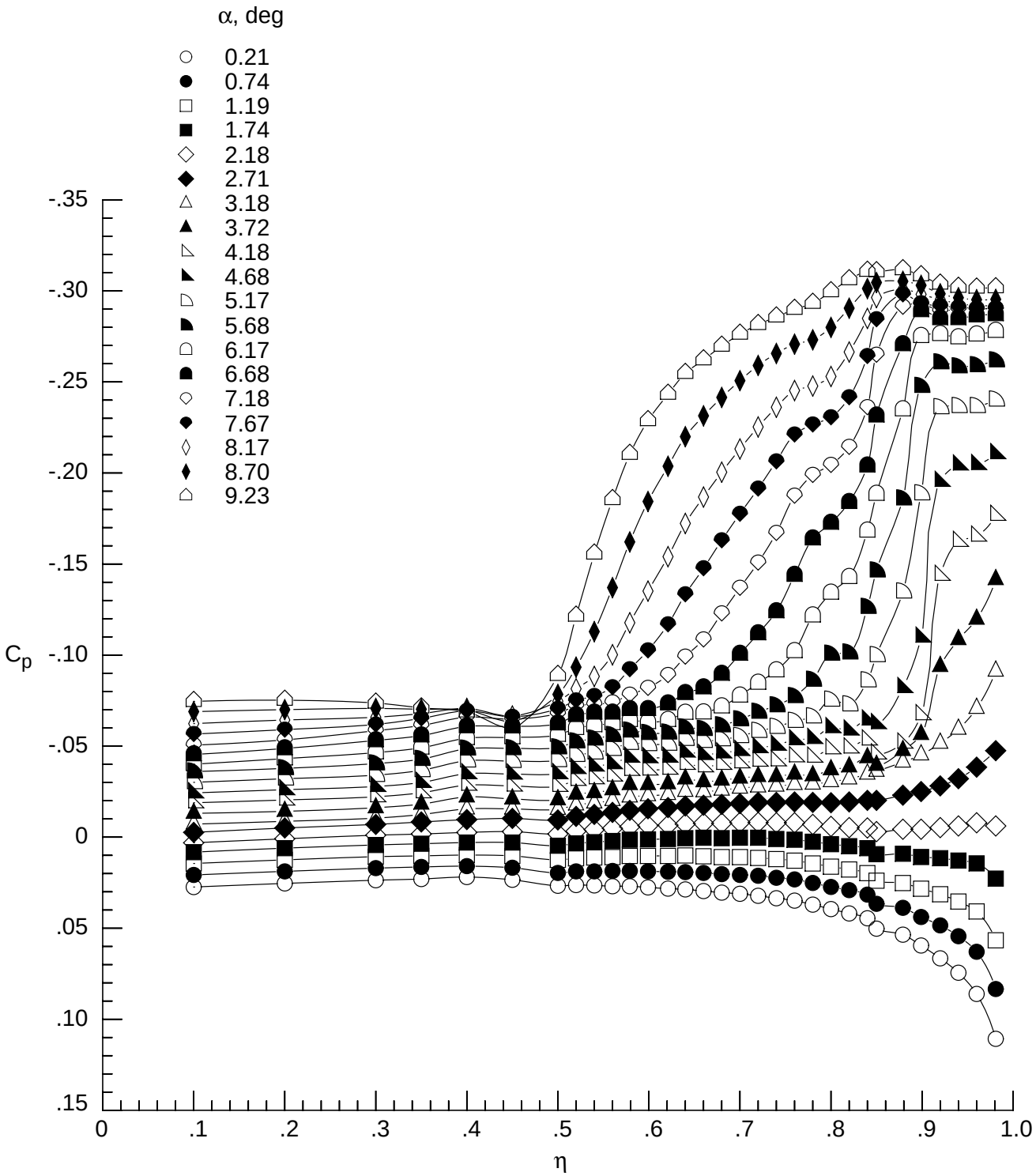

(c) Cambered wing.

Figure 15. Concluded.

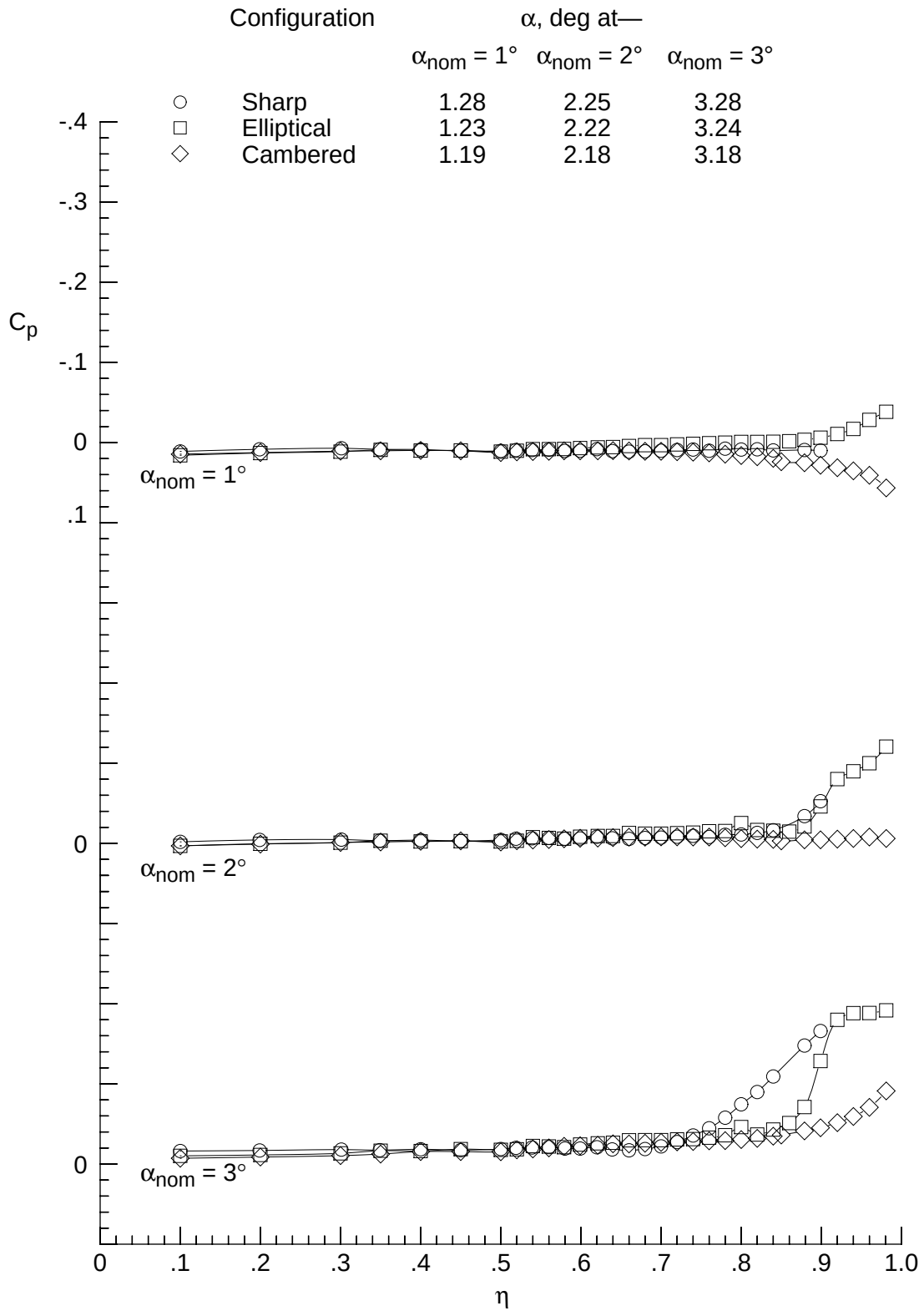

(a) α_{nom} = 1°, 2°, and 3°.

Figure 16. Effect of cross-sectional shape on upper surface-pressure coefficient distribution for delta wing without transition grit at x = 12 in., M = 1.60, and $R = 2 \times 10^6$ ft^{-1}.

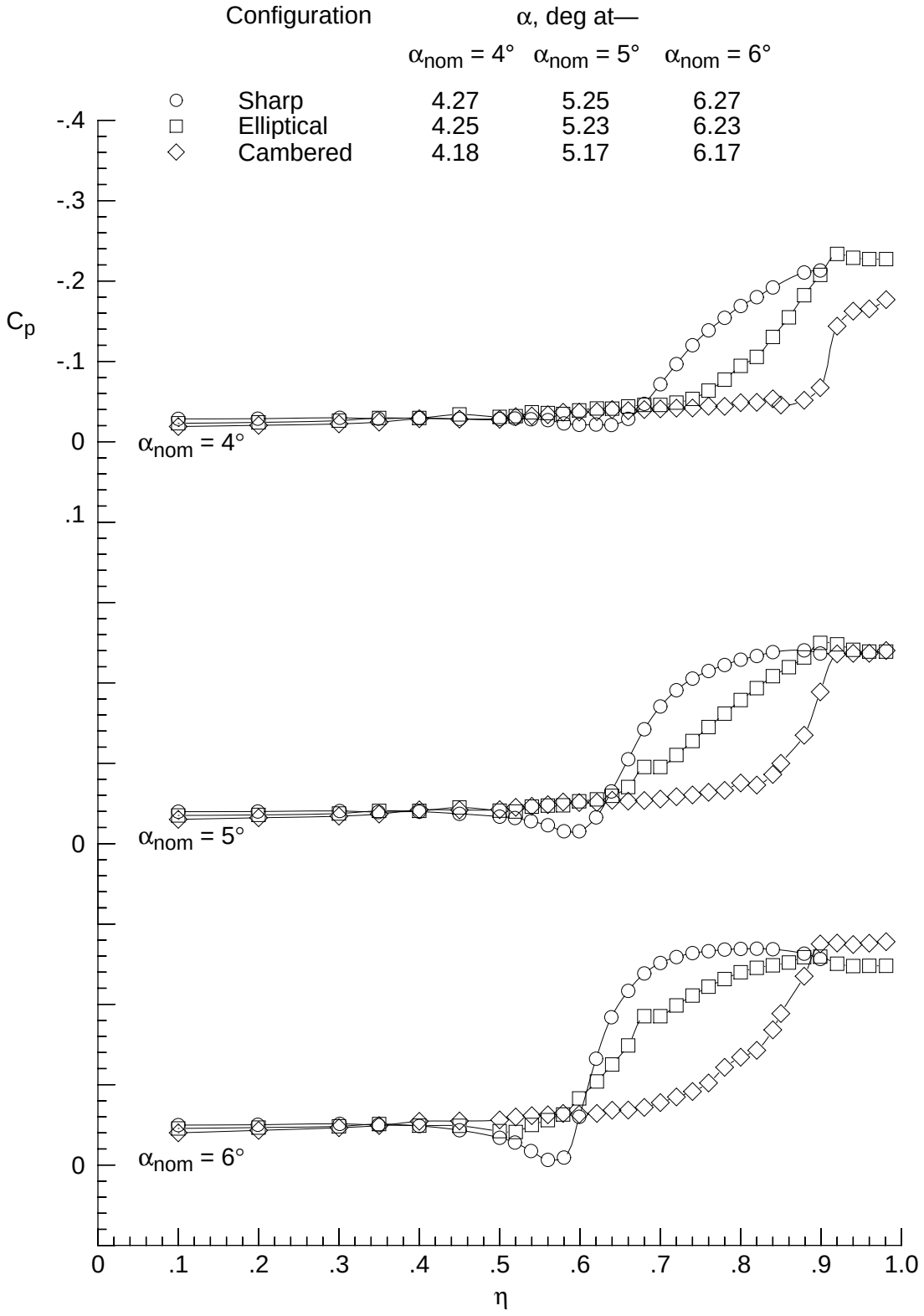

(b) α_{nom} = 4°, 5°, and 6°.

Figure 16. Continued.

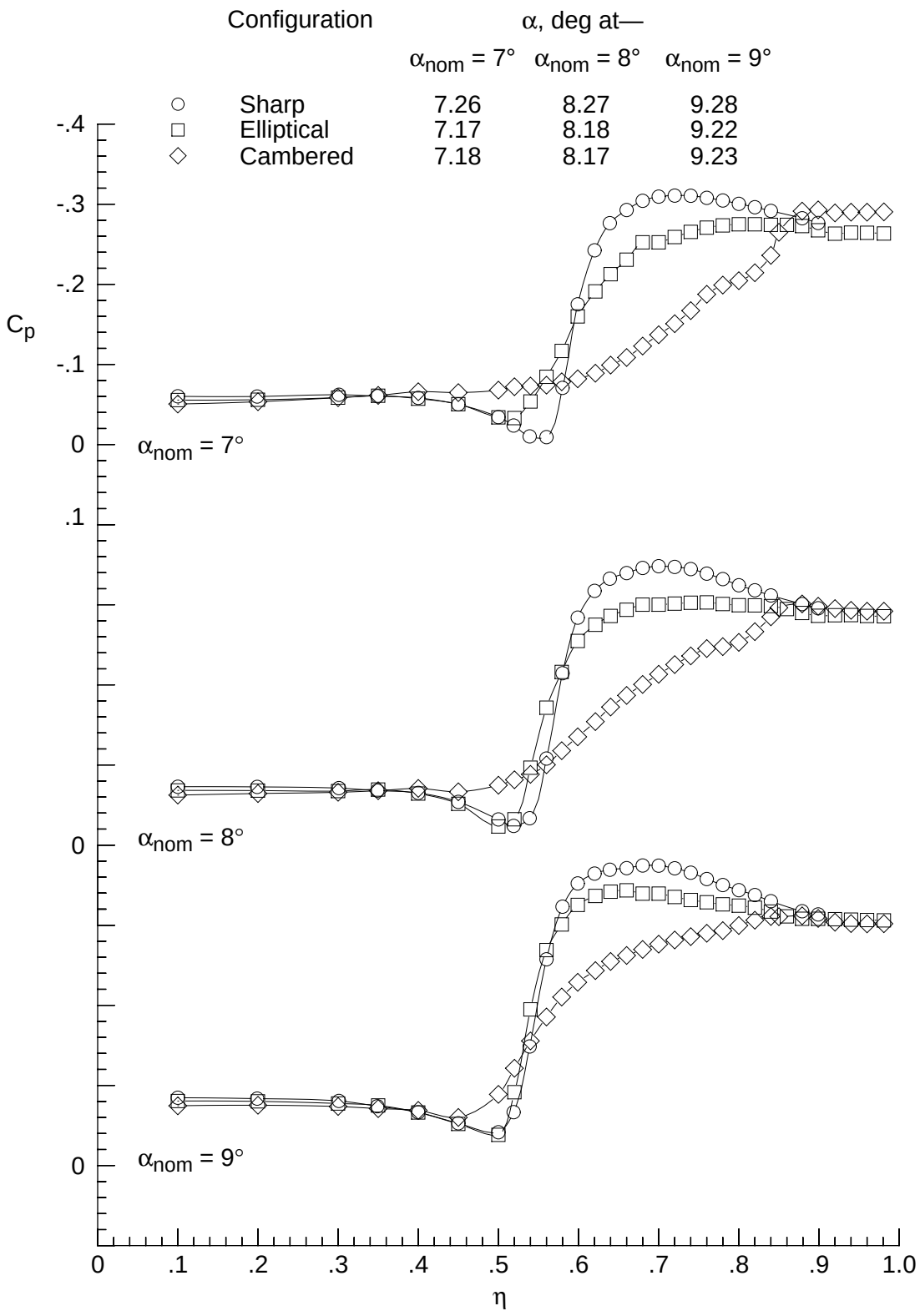

(c) α_{nom} = 7°, 8°, and 9°.

Figure 16. Concluded.

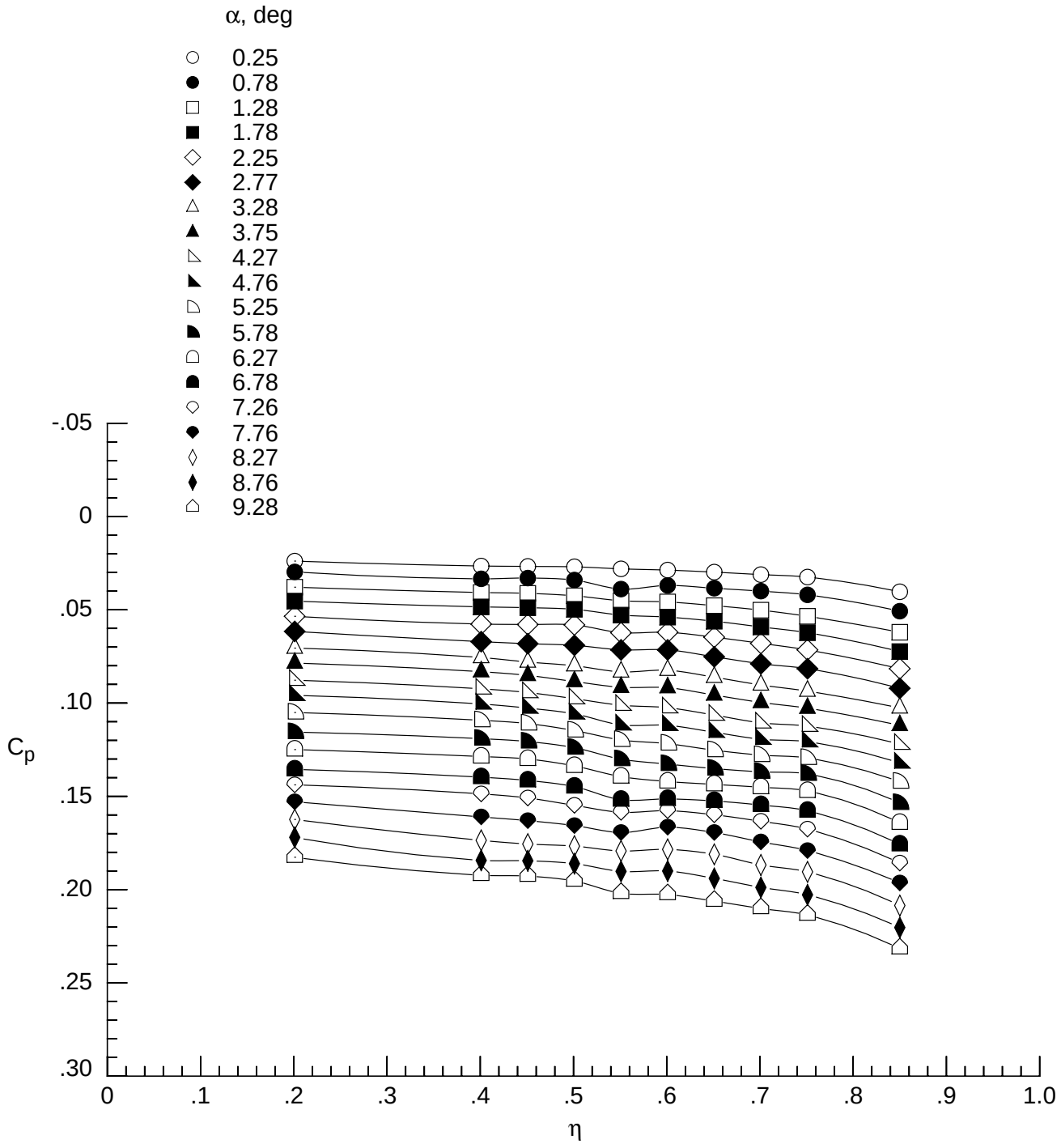

(a) Sharp wing.

Figure 17. Effect of angle of attack on lower surface-pressure coefficient distributions for three delta wings without transition grit at x = 12 in., M = 1.60, and $R = 2 \times 10^6$ ft^{-1}.

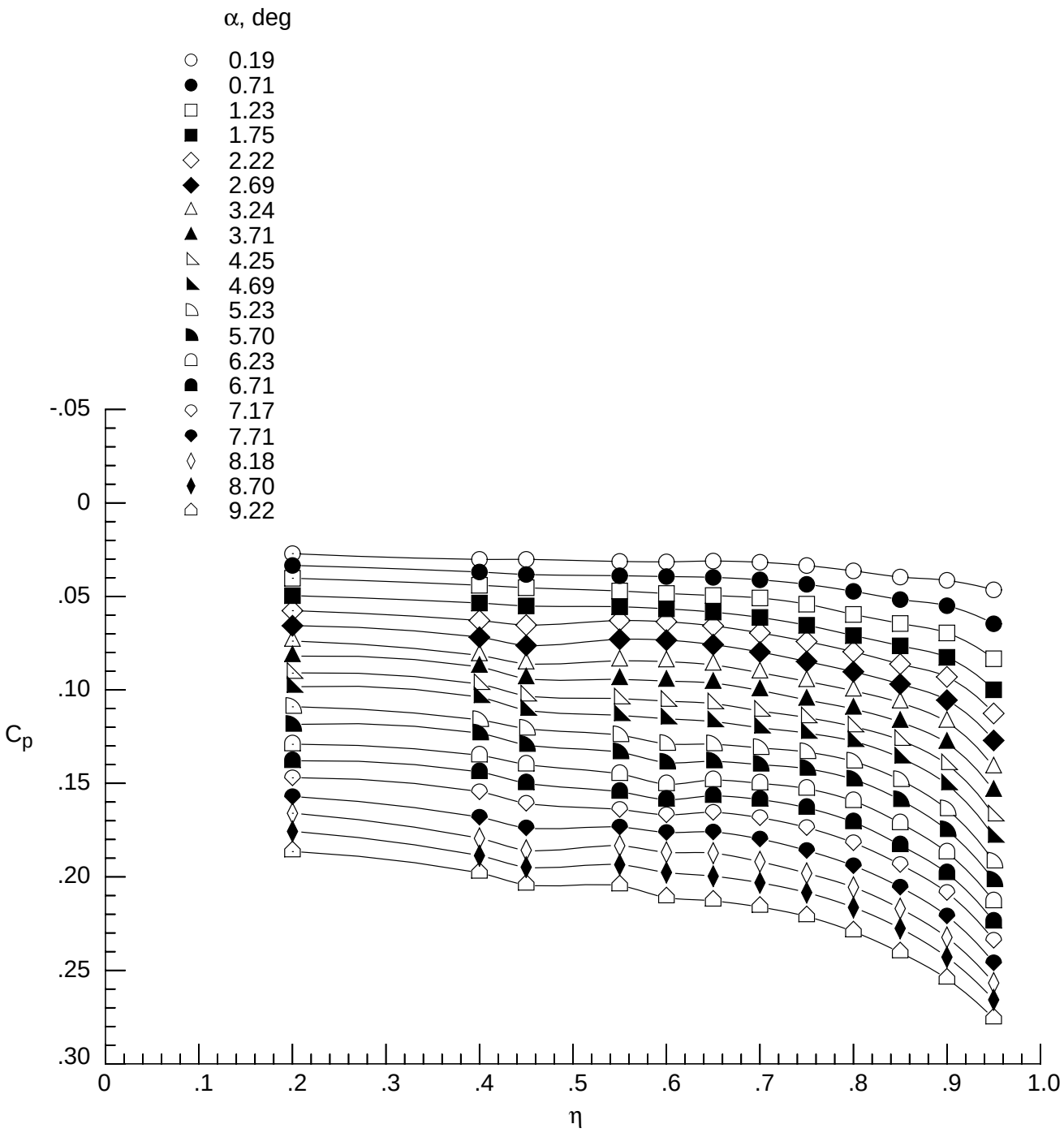

(b) Elliptical wing.

Figure 17. Continued.

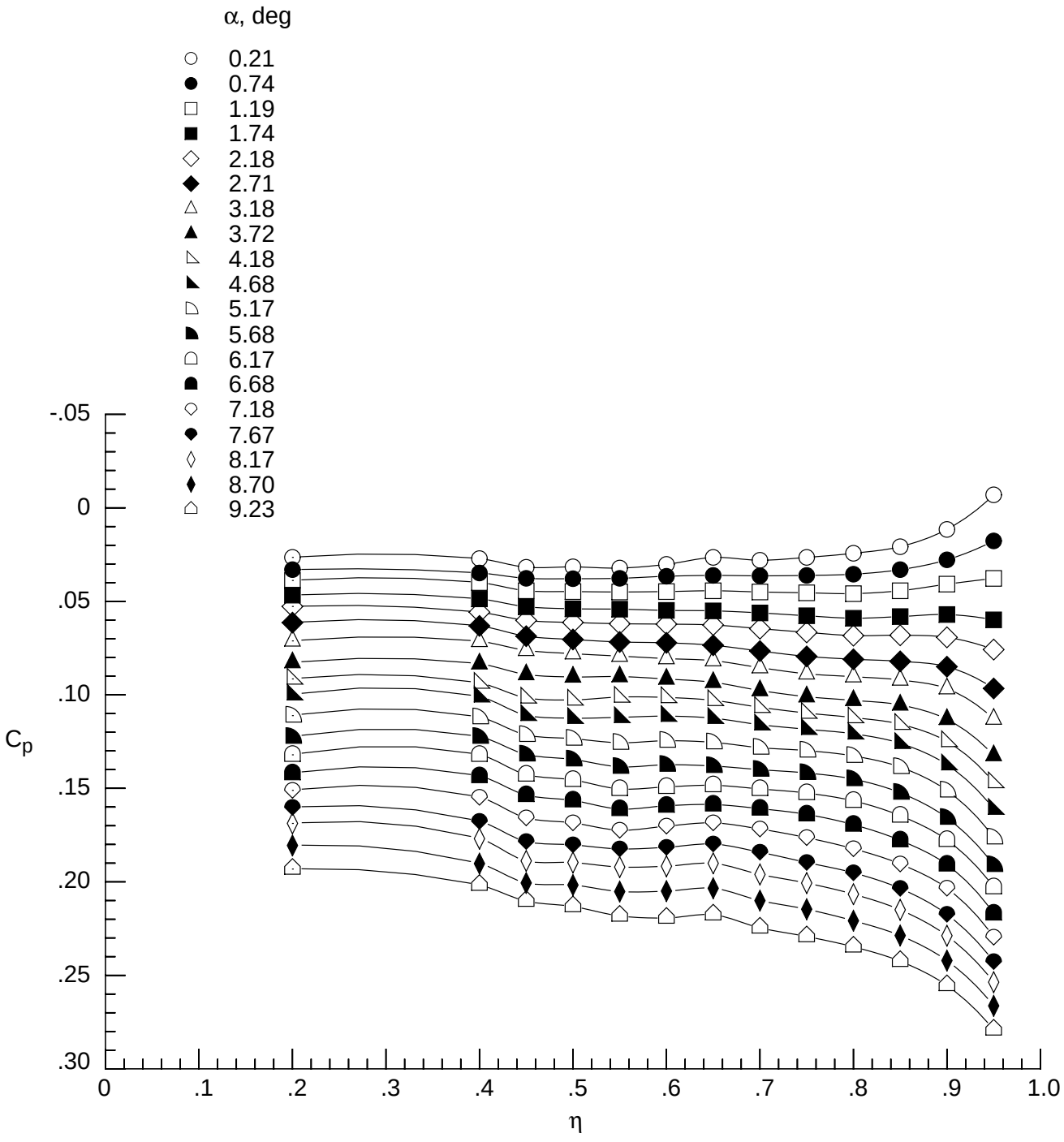

(c) Cambered wing.

Figure 17. Concluded.

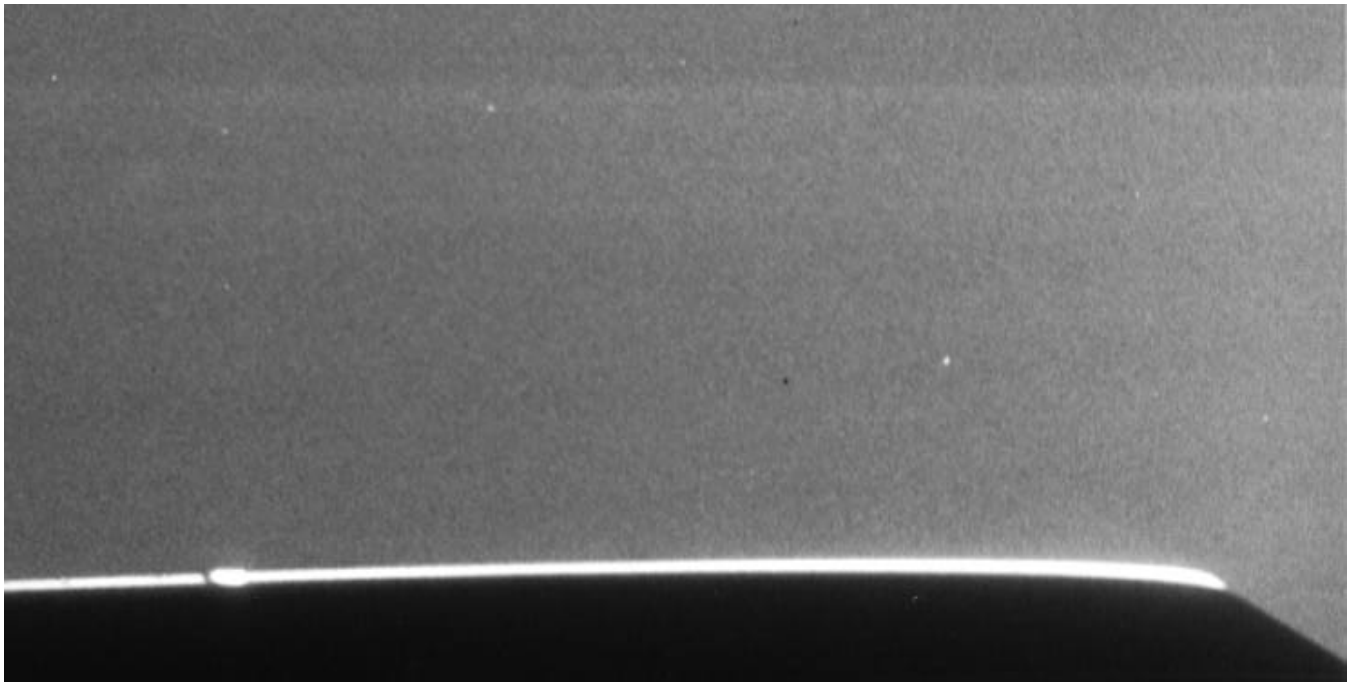

(a) $\alpha = 0.2°$.

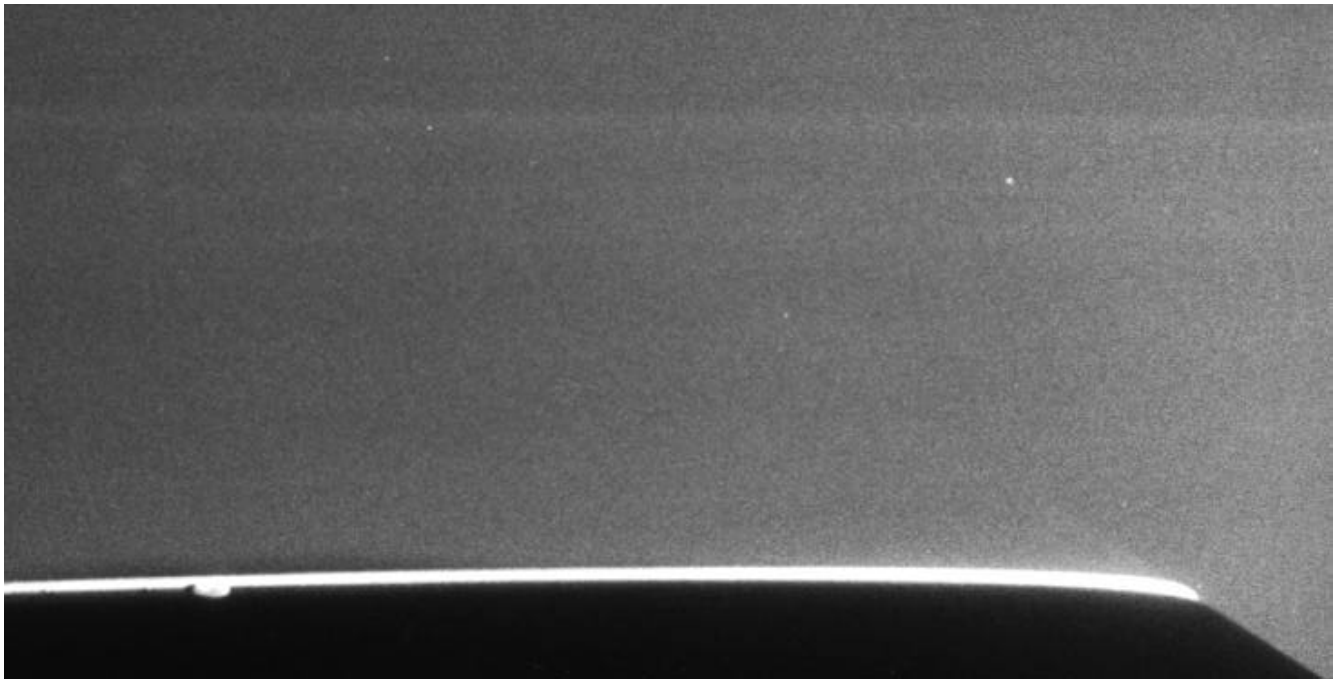

(b) $\alpha = 1.2°$.

Figure 18. Vapor-screen photographs illustrating vortex growth with angle of attack over leeside of elliptical wing without transition grit at $x = 12$ in., $M = 1.60$, and $R = 2 \times 10^6$ ft^{-1}.

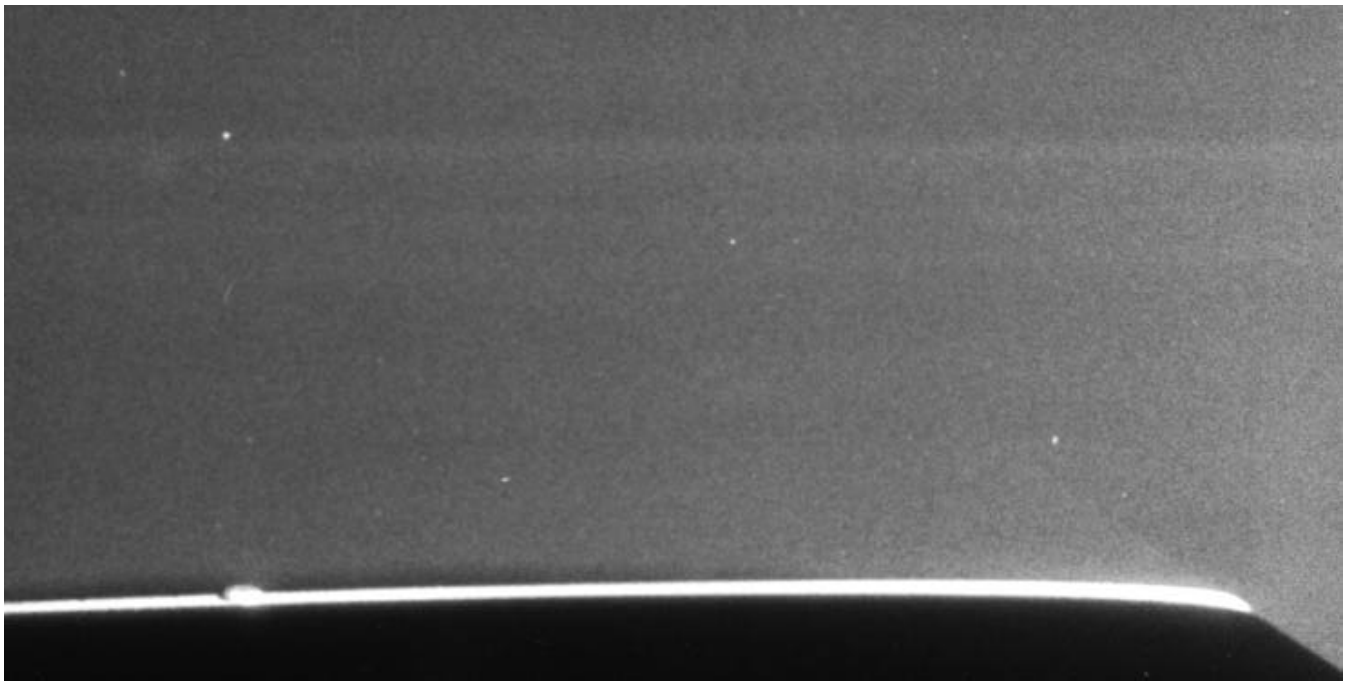

(c) $\alpha = 2.2°$.

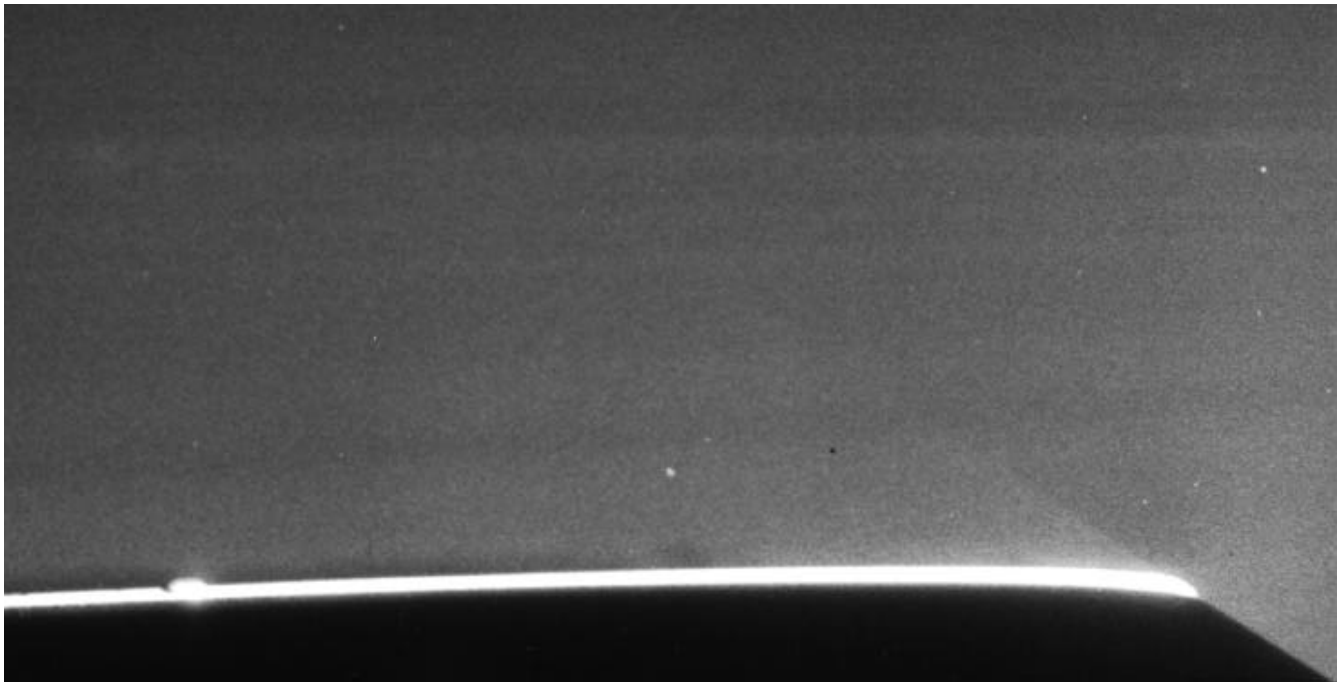

(d) $\alpha = 2.7°$.

Figure 18. Continued.

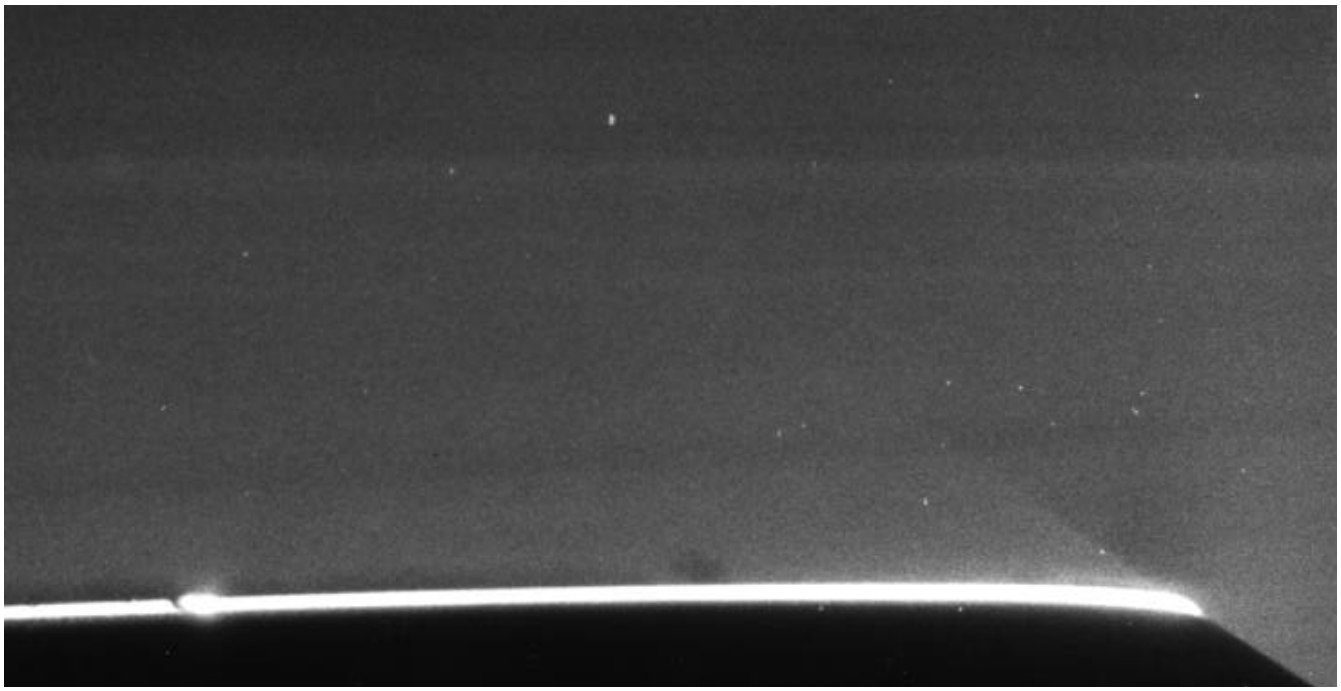

(e) $\alpha = 3.2°$.

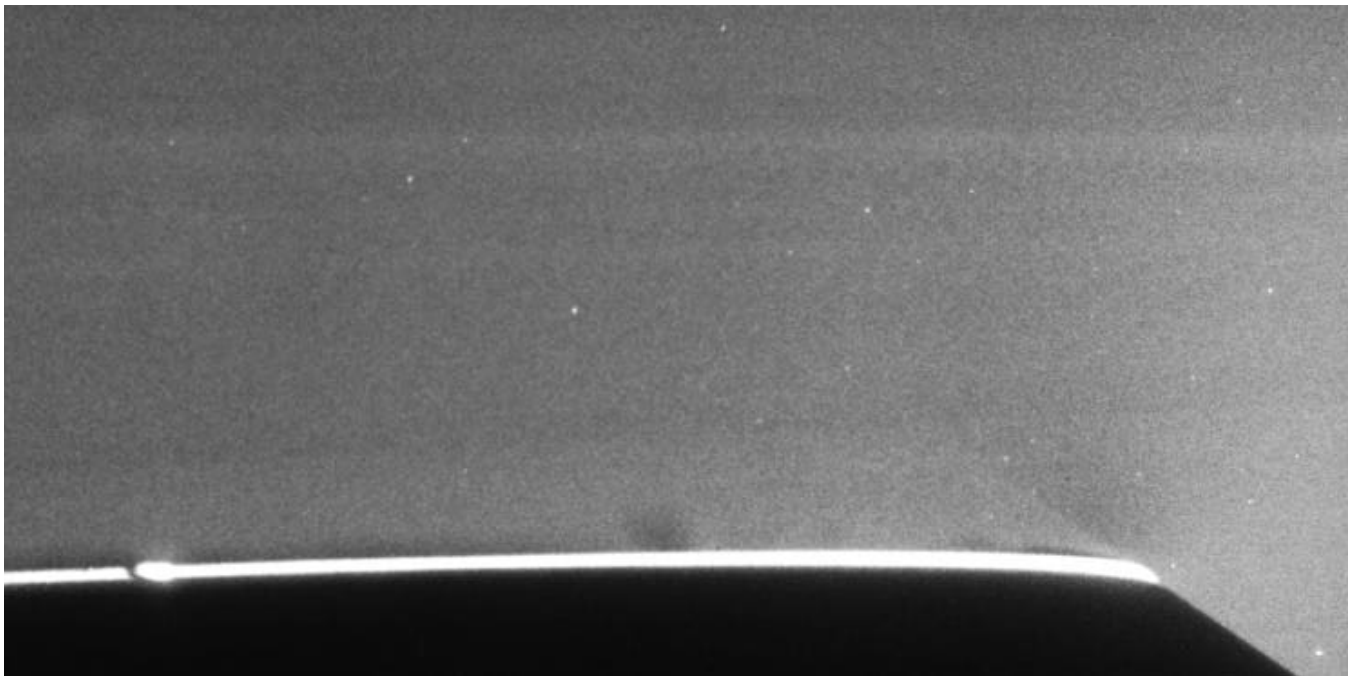

(f) $\alpha = 3.7°$.

Figure 18. Continued.

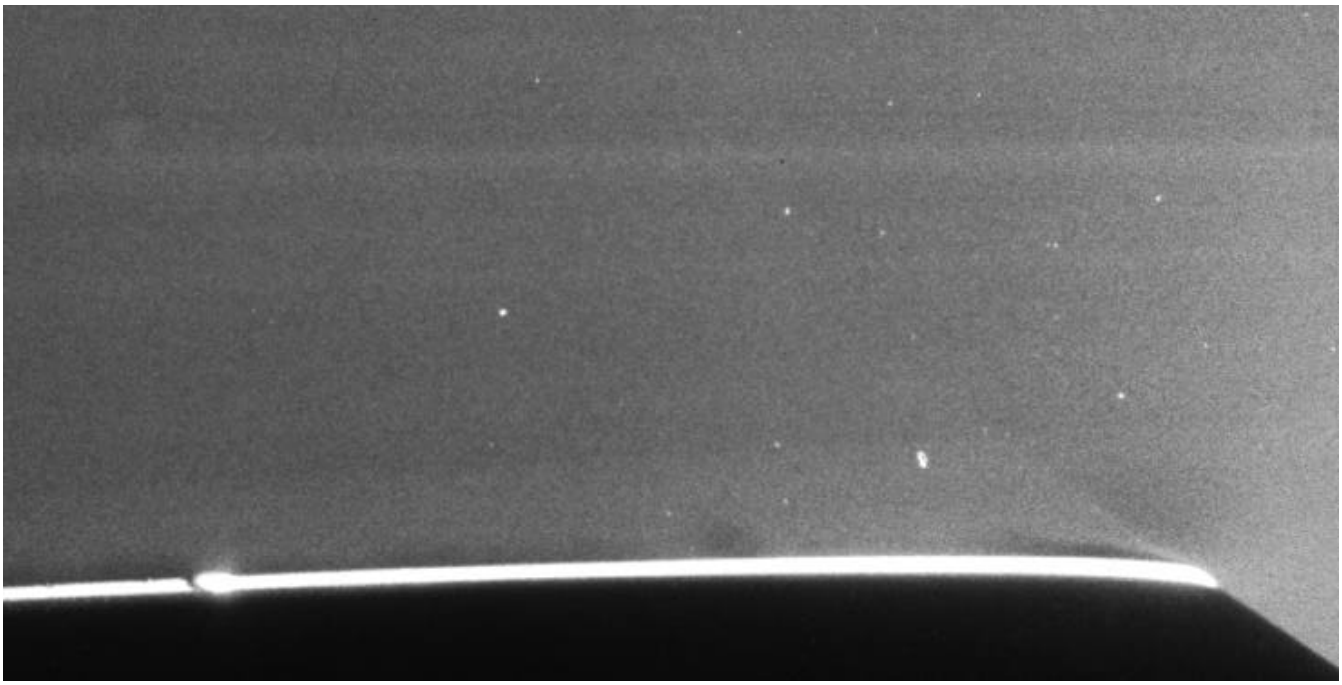

(g) $\alpha = 4.2°$.

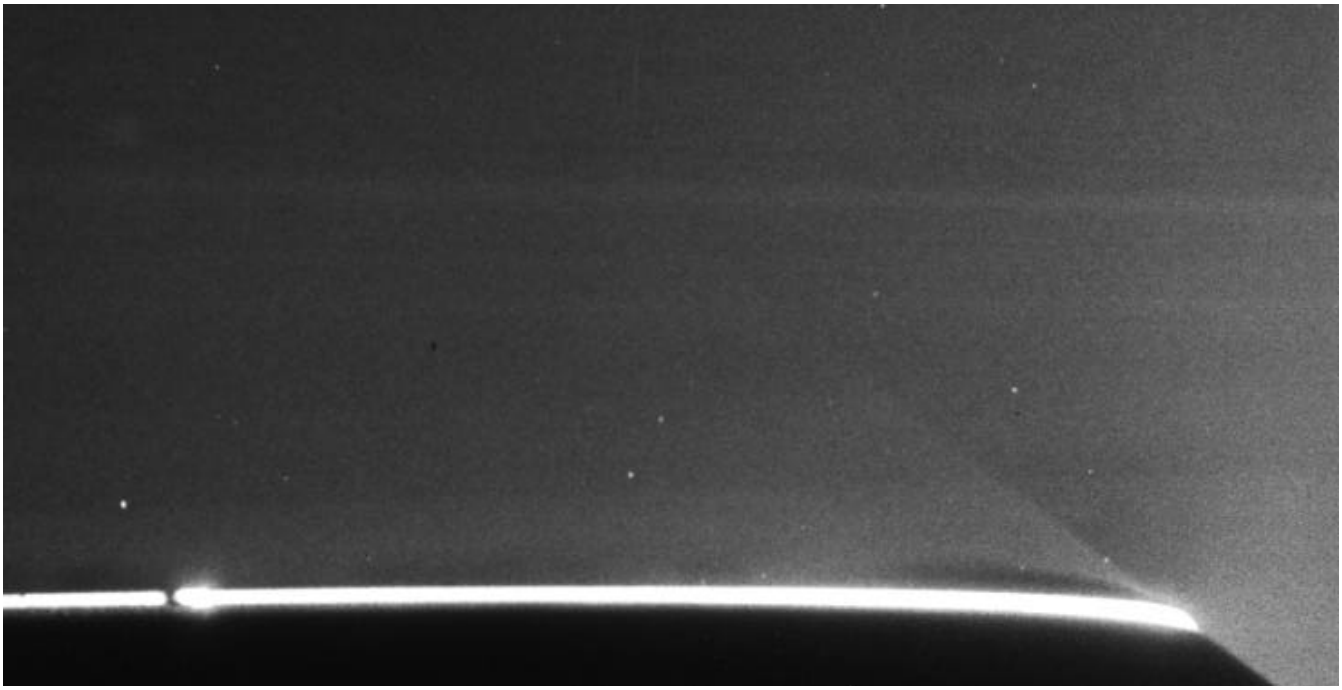

(h) $\alpha = 5.2°$.

Figure 18. Continued.

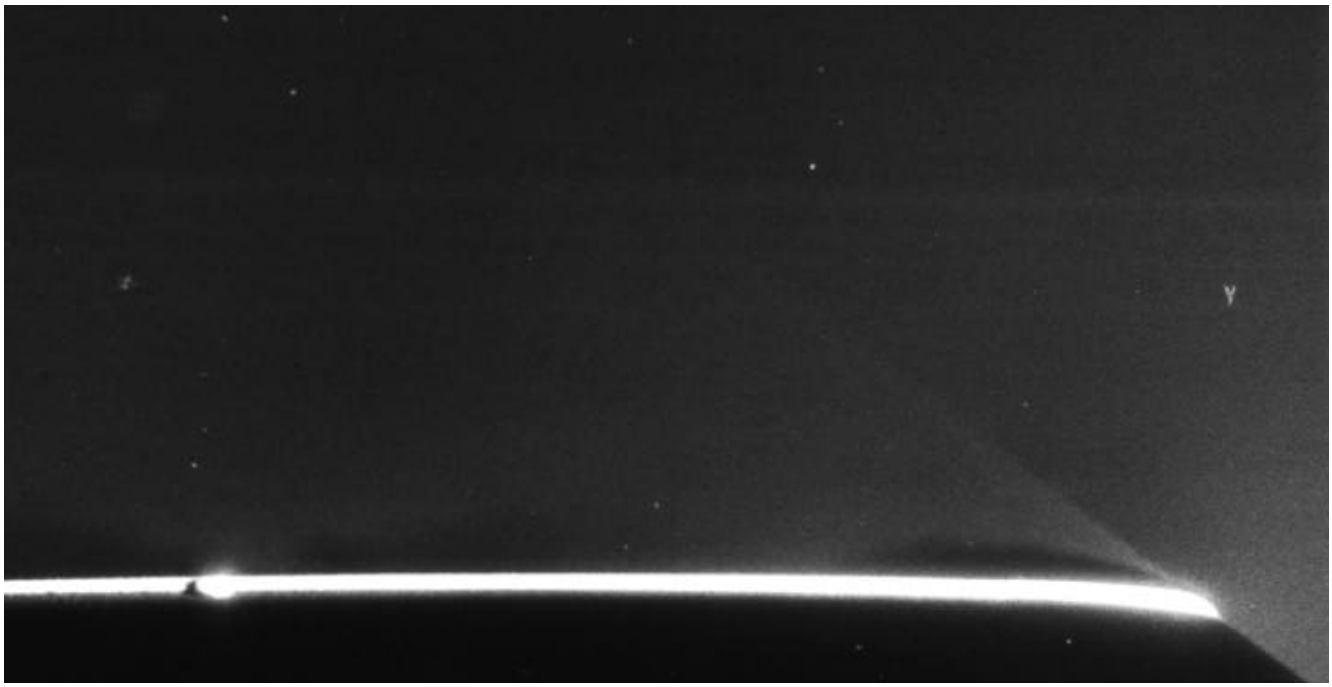

(i) $\alpha = 6.2°$.

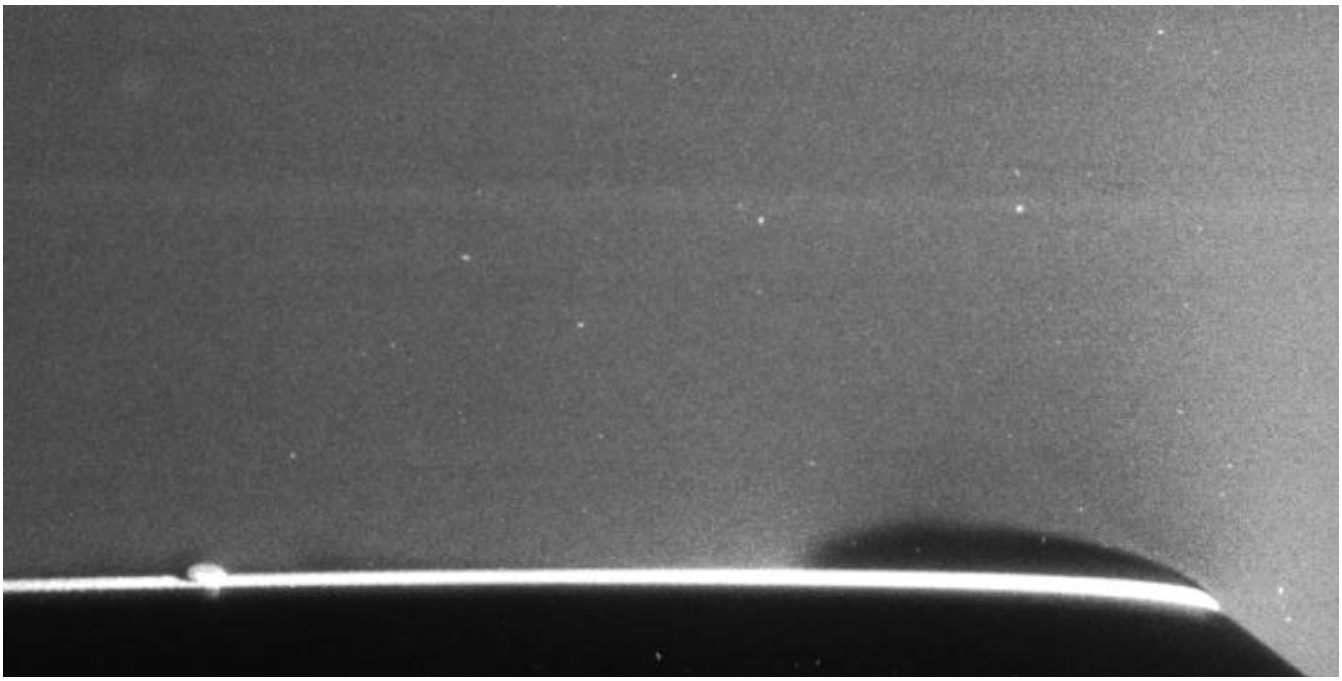

(j) $\alpha = 7.2°$.

Figure 18. Continued.

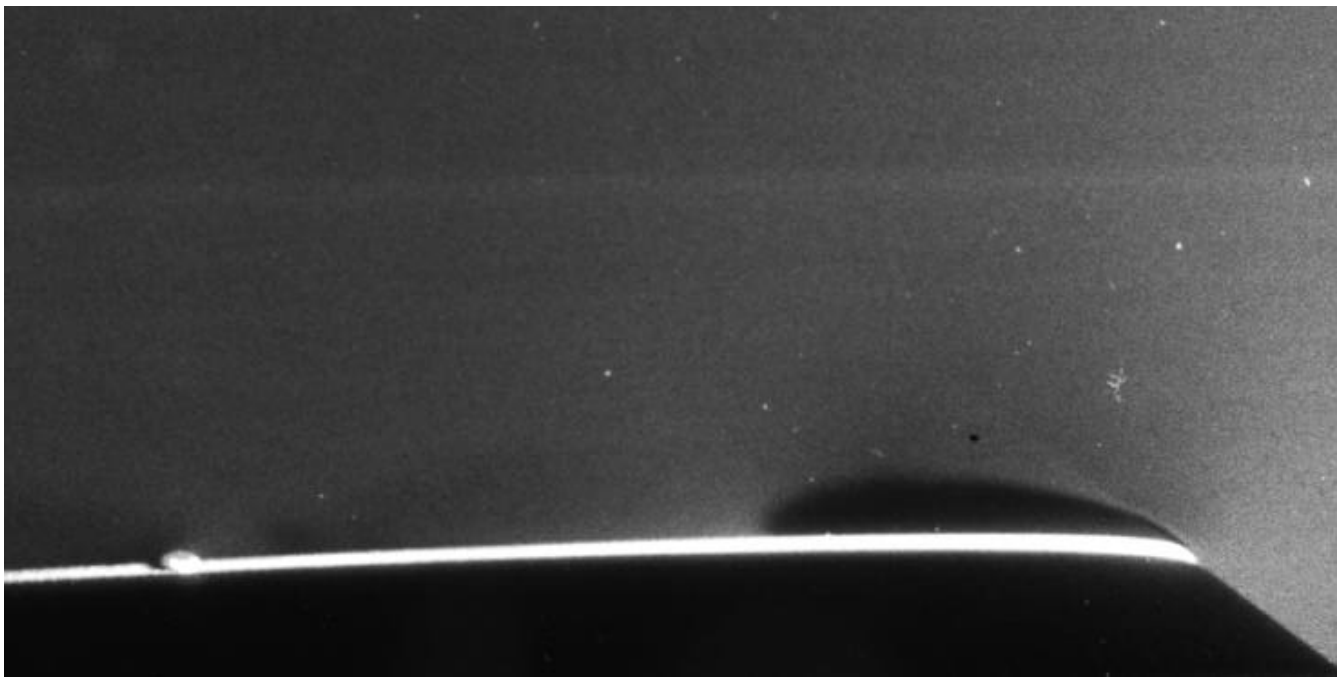

(k) $\alpha = 8.2°$.

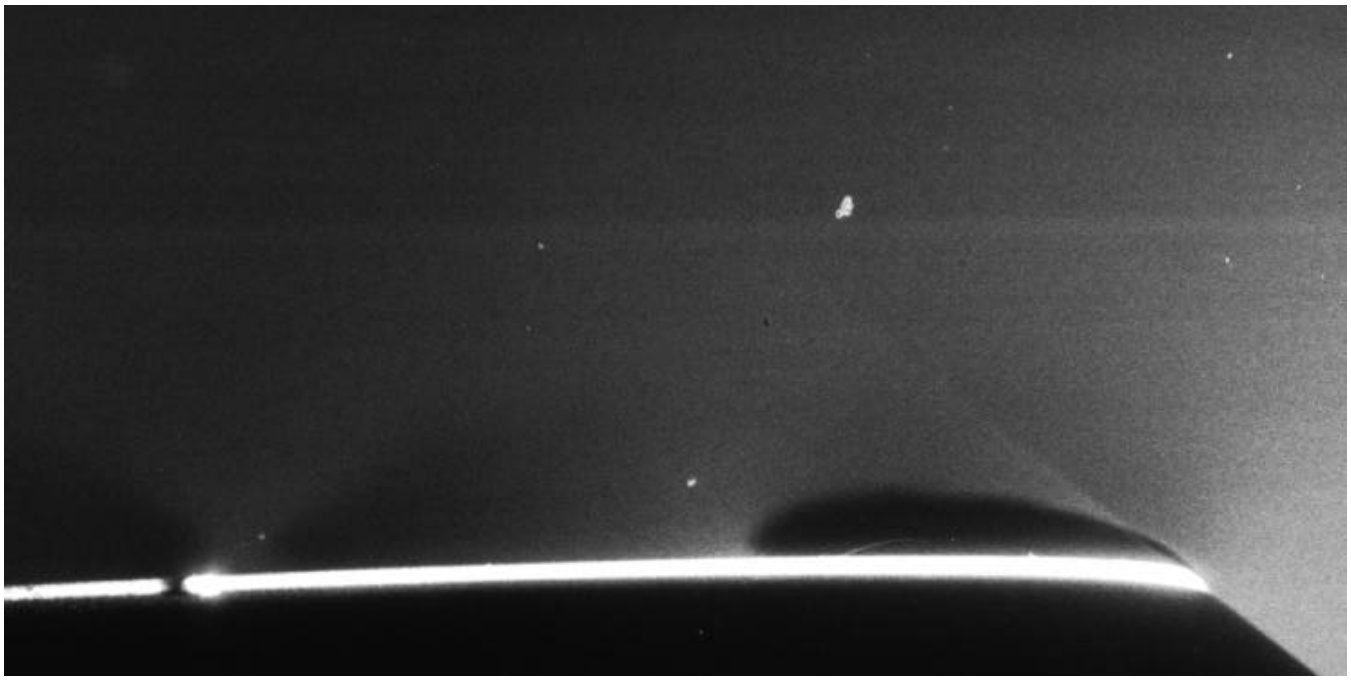

(l) $\alpha = 9.2°$.

Figure 18. Concluded.

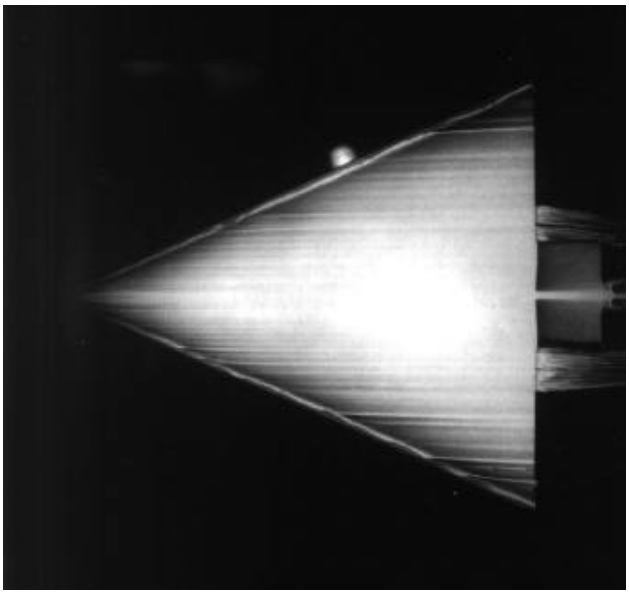

(a) $\alpha = 3.14°$.

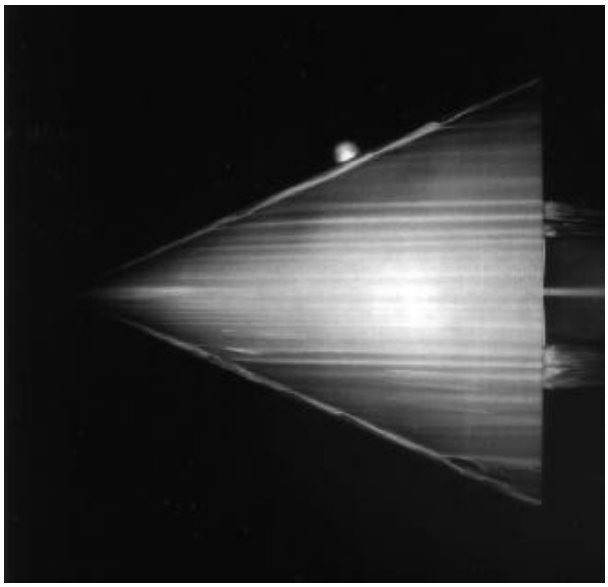

(b) $\alpha = 4.17°$.

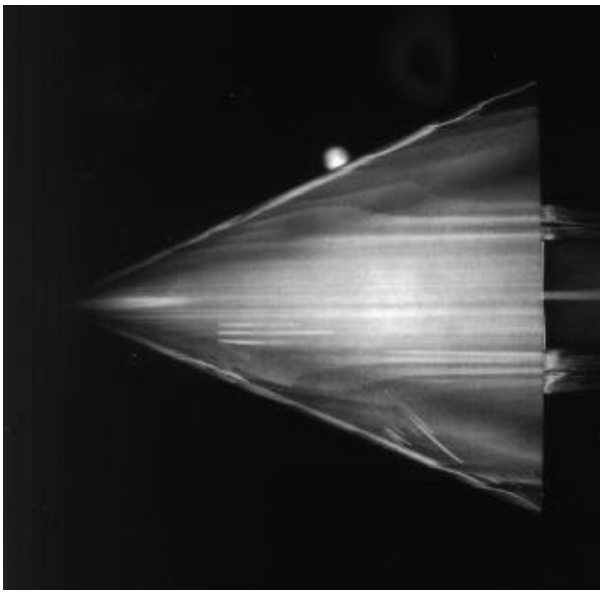

(c) $\alpha = 6.26°$.

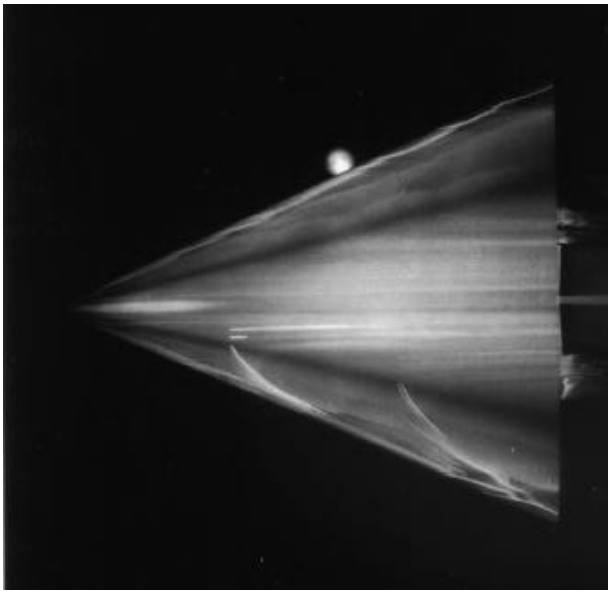

(d) $\alpha = 8.34°$.

Figure 19. Painted-oil-flow photographs illustrating vortex growth with angle of attack on leeside of elliptical wing without transition grit at $M = 1.60$ and $R = 2 \times 10^6$ ft^{-1}.

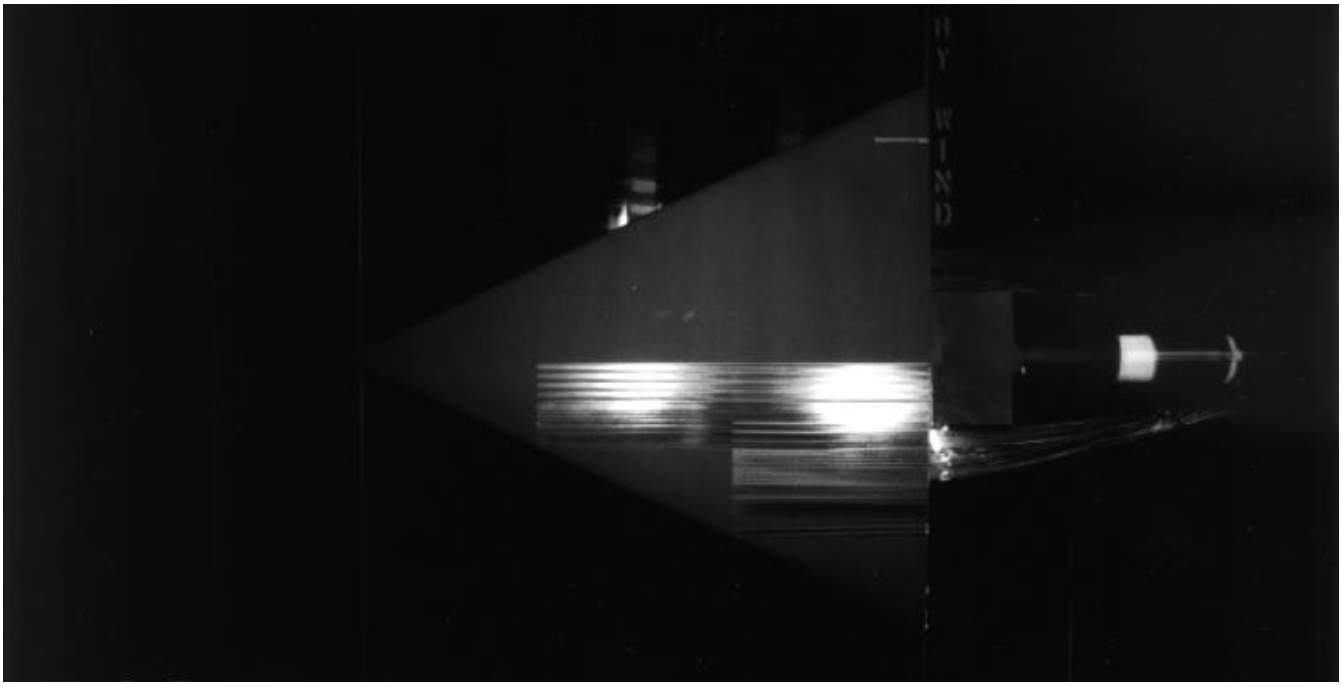

(a) $\alpha = 0°$.

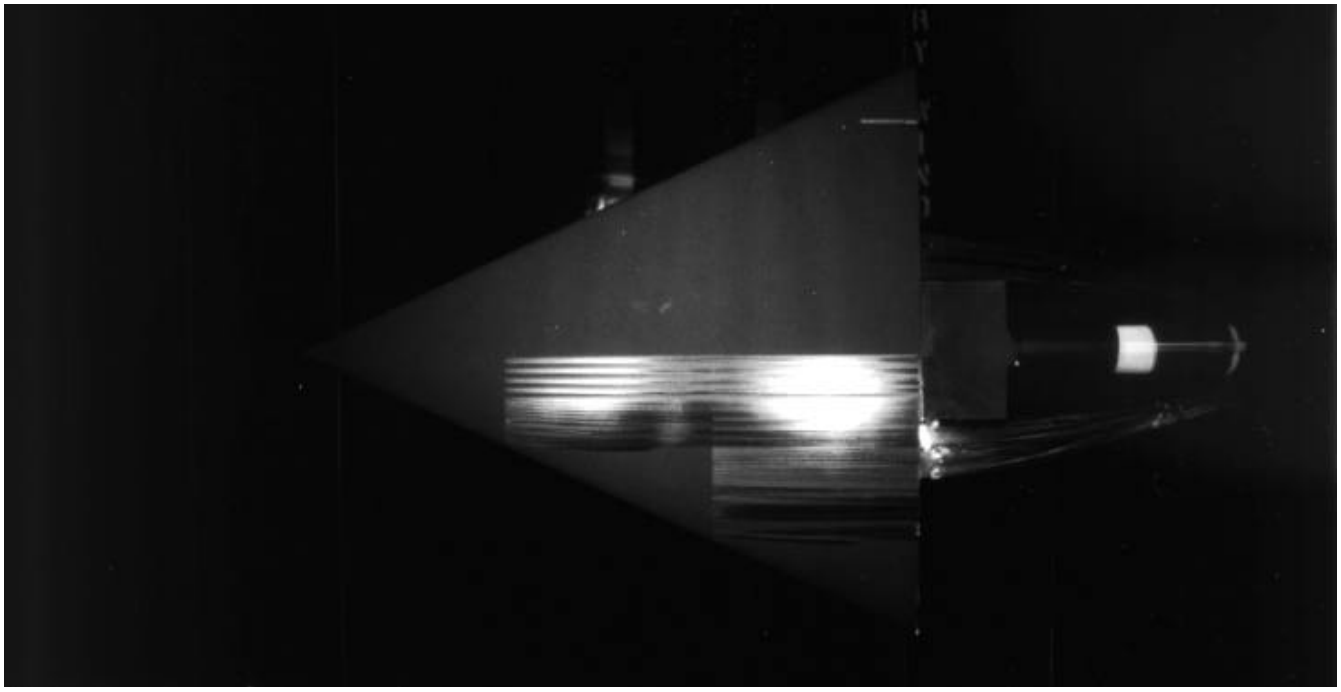

(b) $\alpha = 1.03°$.

Figure 20. Injected-oil-flow photographs illustrating vortex growth with angle of attack on leeside of elliptical wing without transition grit at $M = 1.60$ and $R = 2 \times 10^6$ ft^{-1}.

(c) $\alpha = 2.08°$.

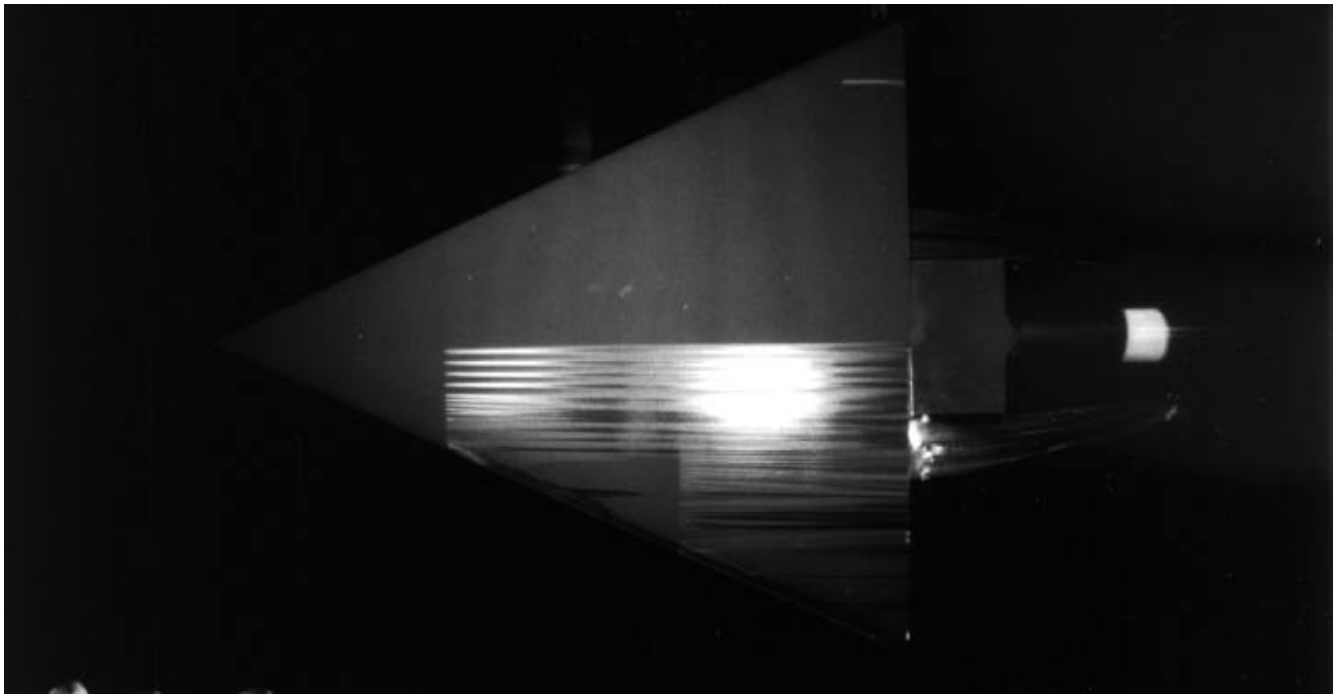

(d) $\alpha = 3.14°$.

Figure 20. Continued.

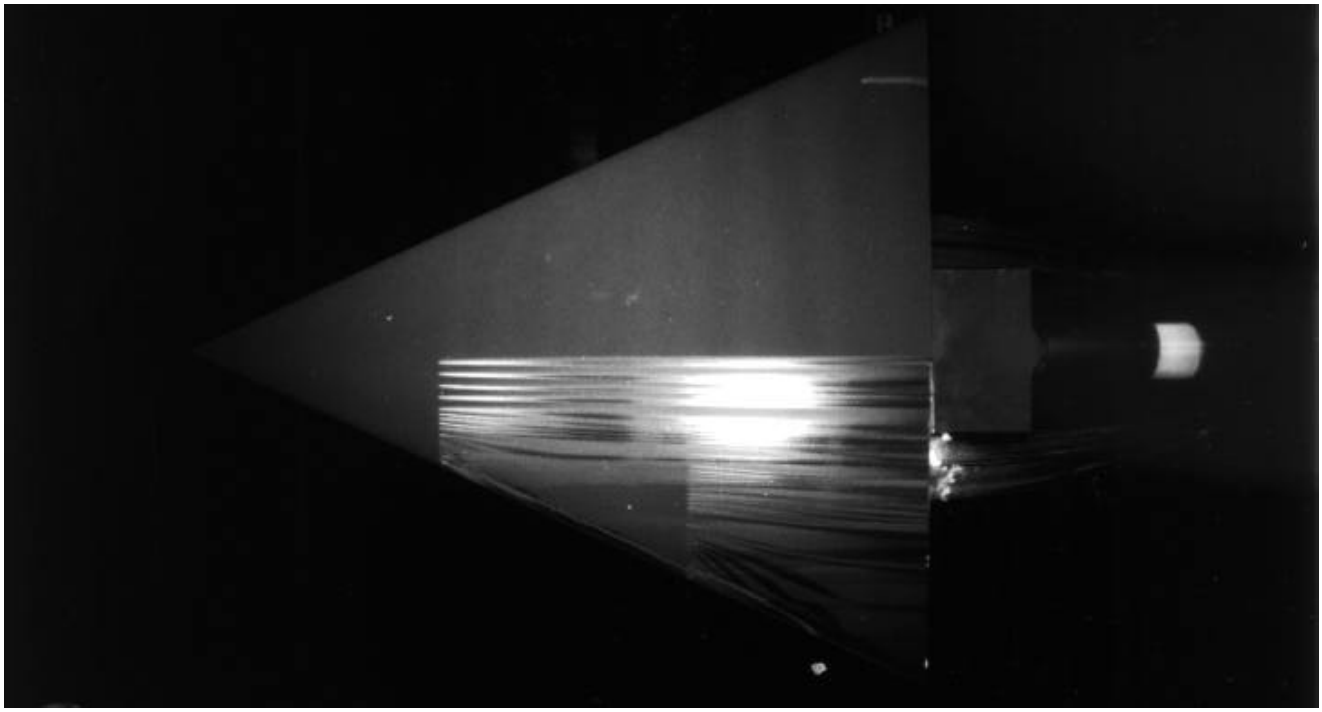

(e) $\alpha = 4.17°$.

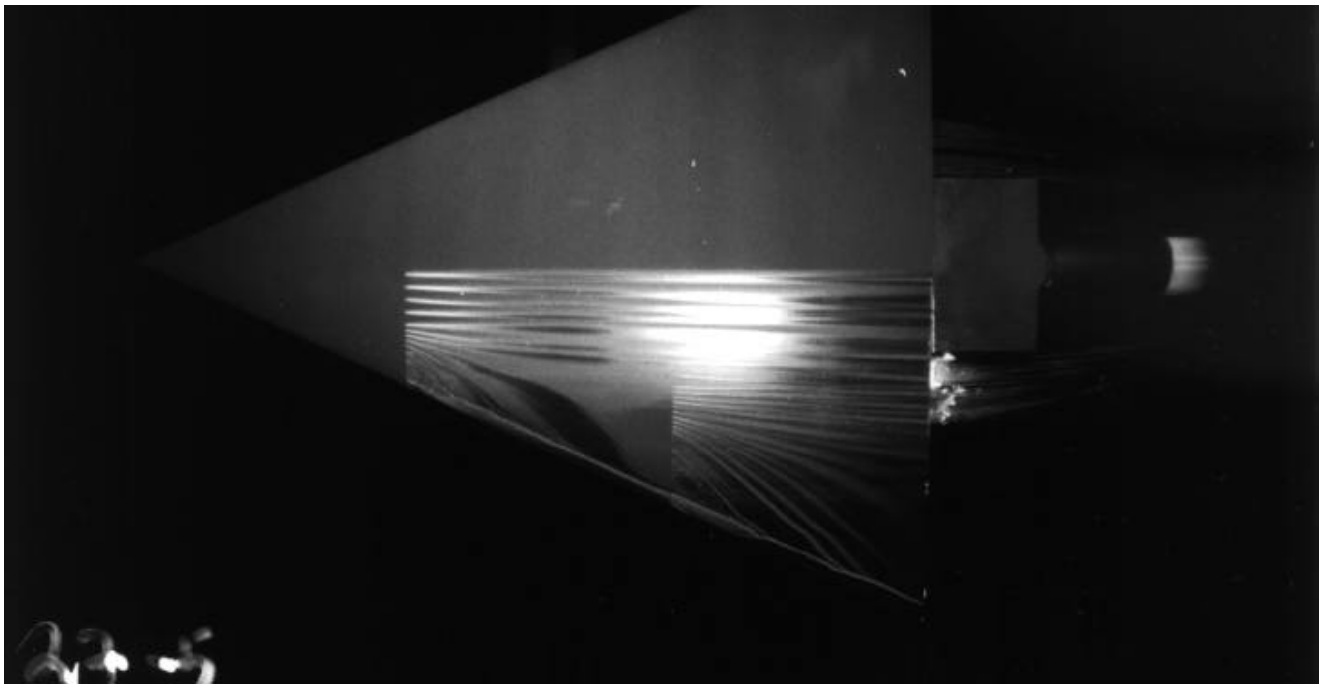

(f) $\alpha = 5.21°$.

Figure 20. Continued.

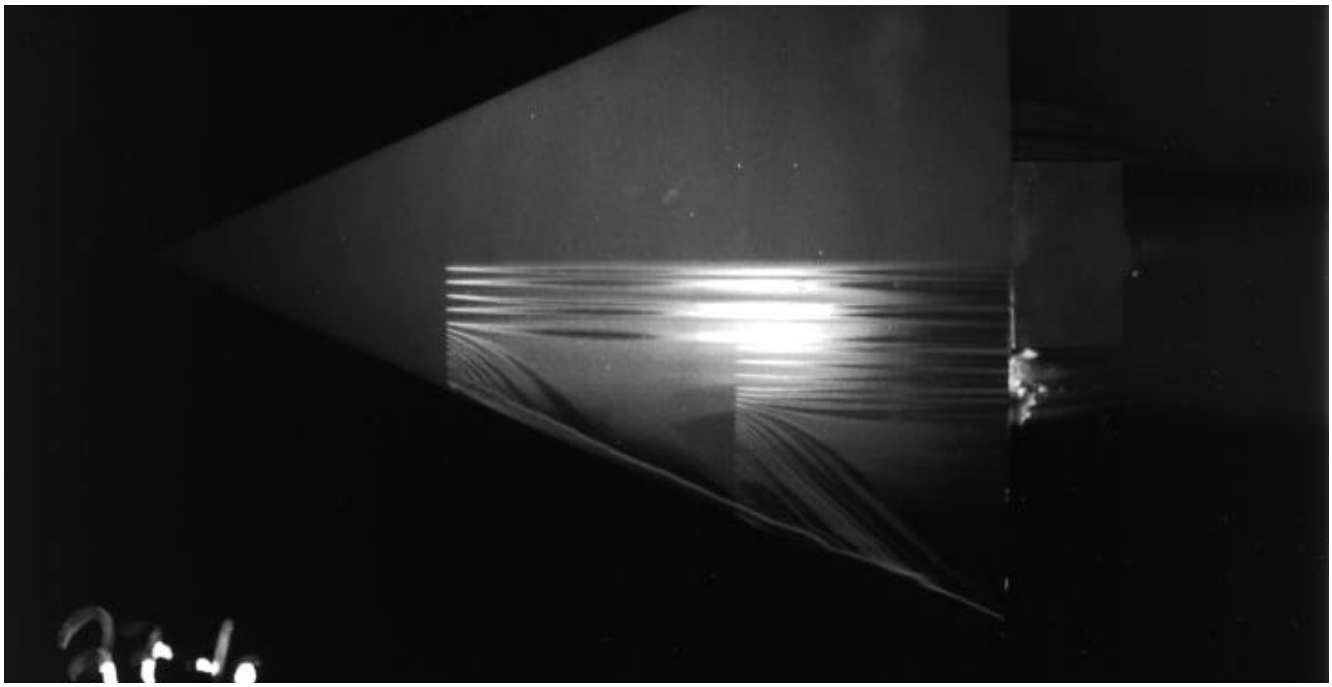

(g) $\alpha = 6.26°$.

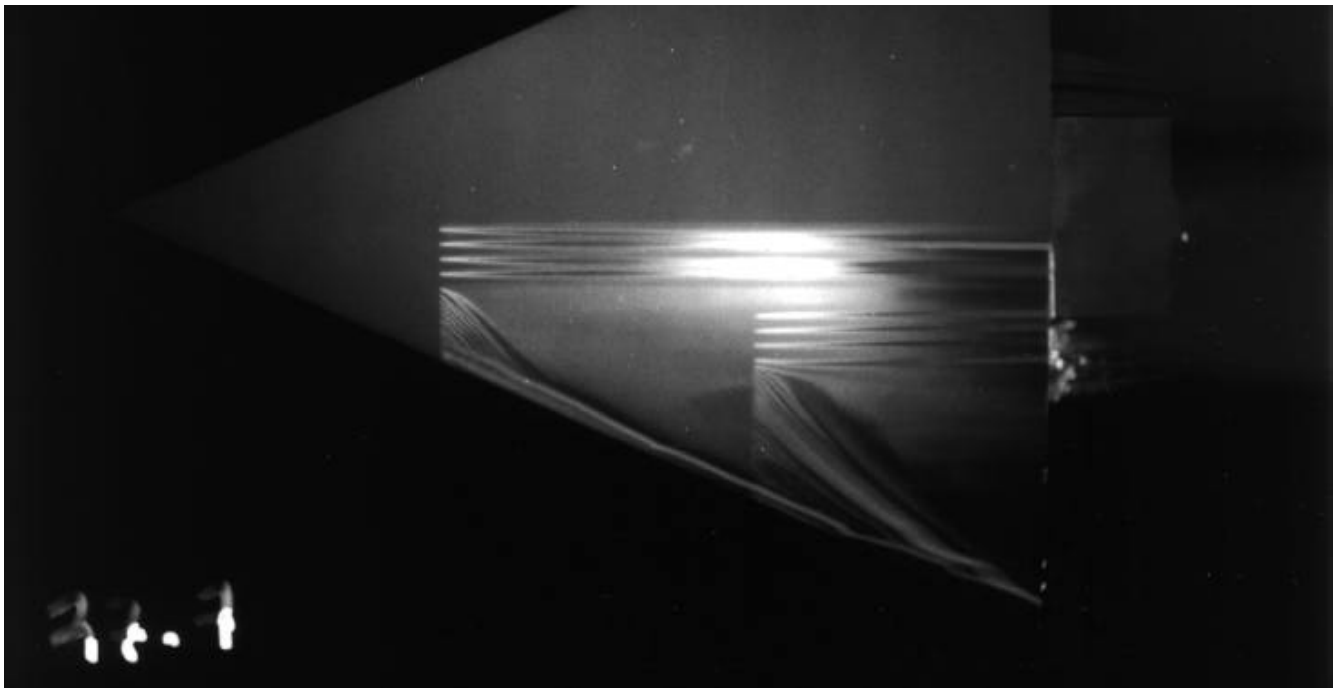

(h) $\alpha = 7.29°$.

Figure 20. Continued.

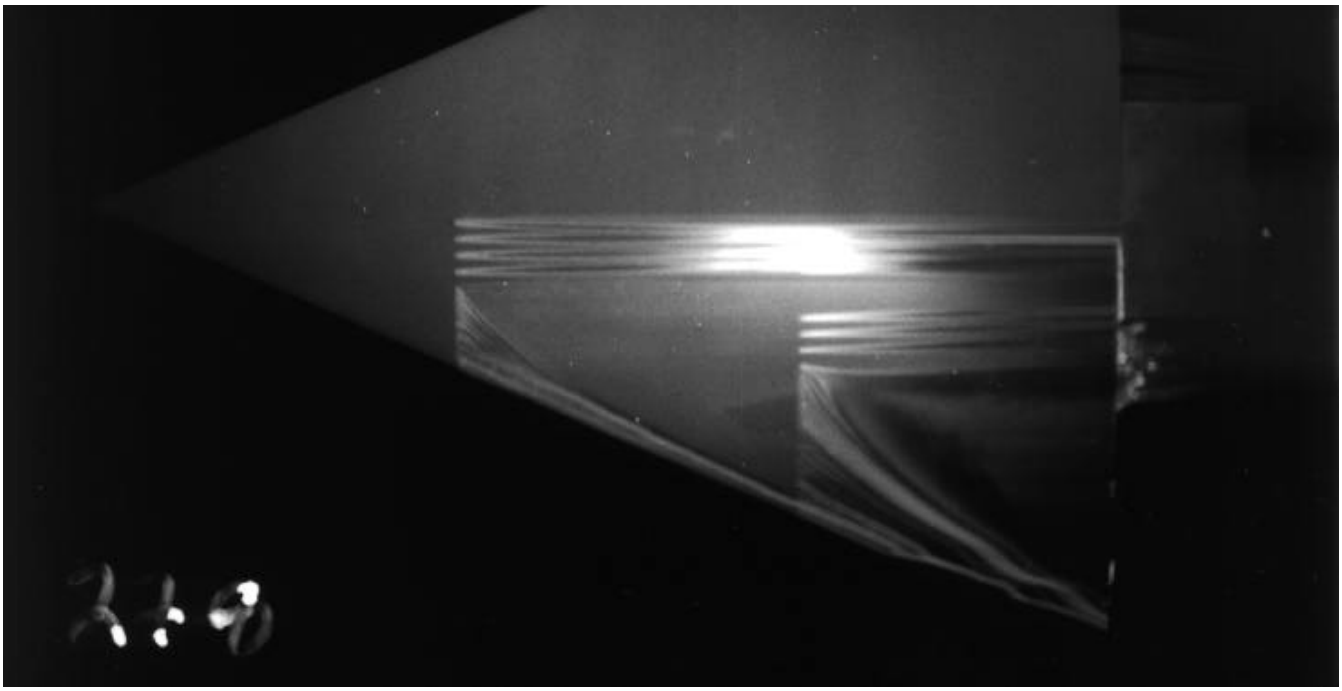

(i) $\alpha = 8.34°$.

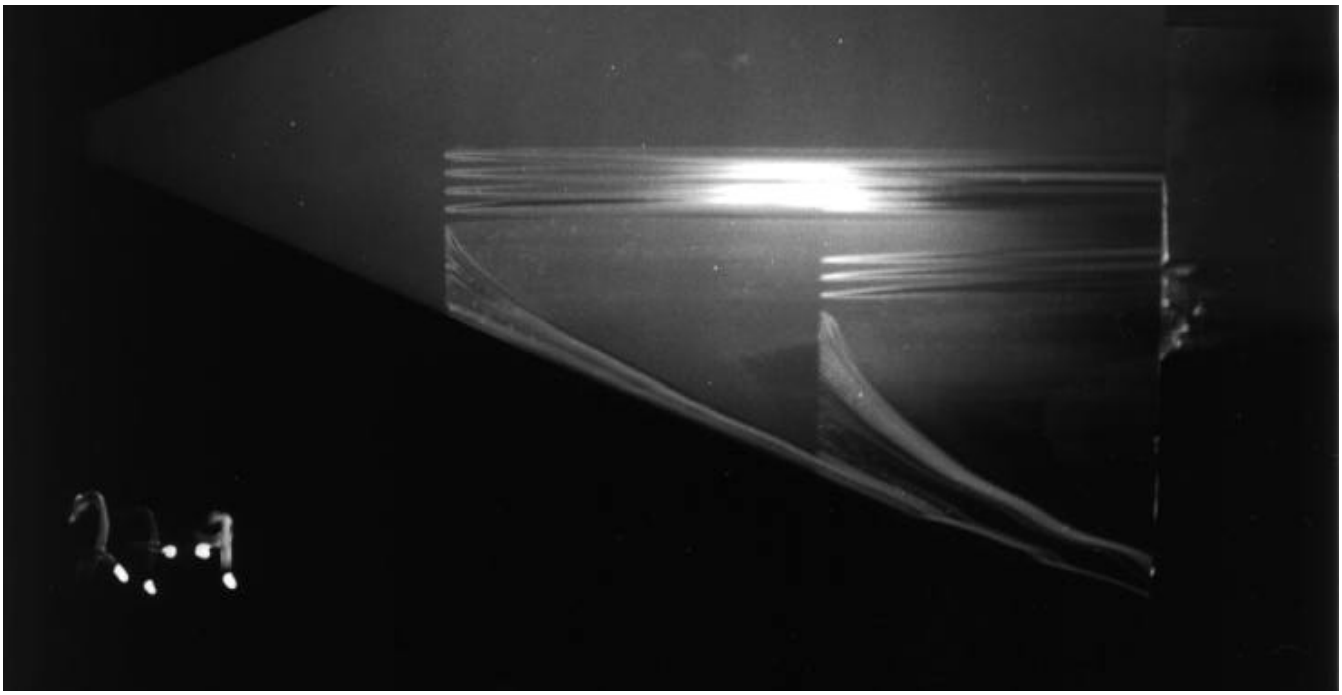

(j) $\alpha = 9.39°$.

Figure 20. Concluded.

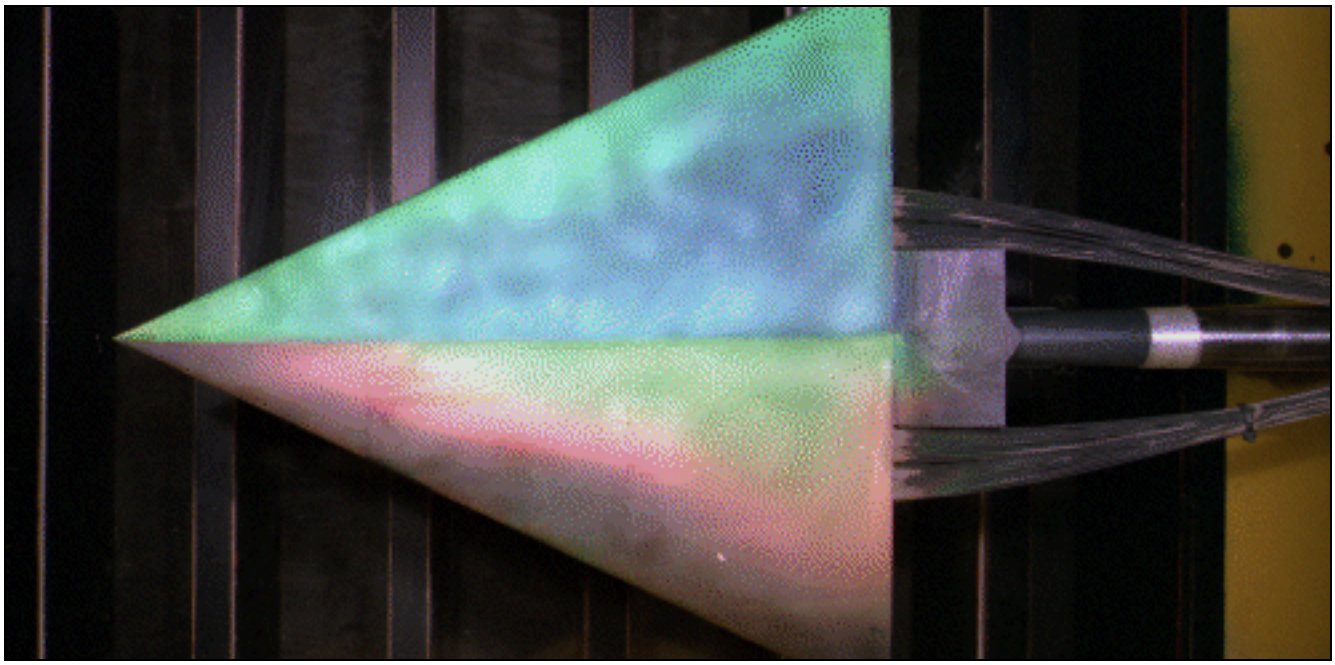

(a) $\alpha = 0°$.

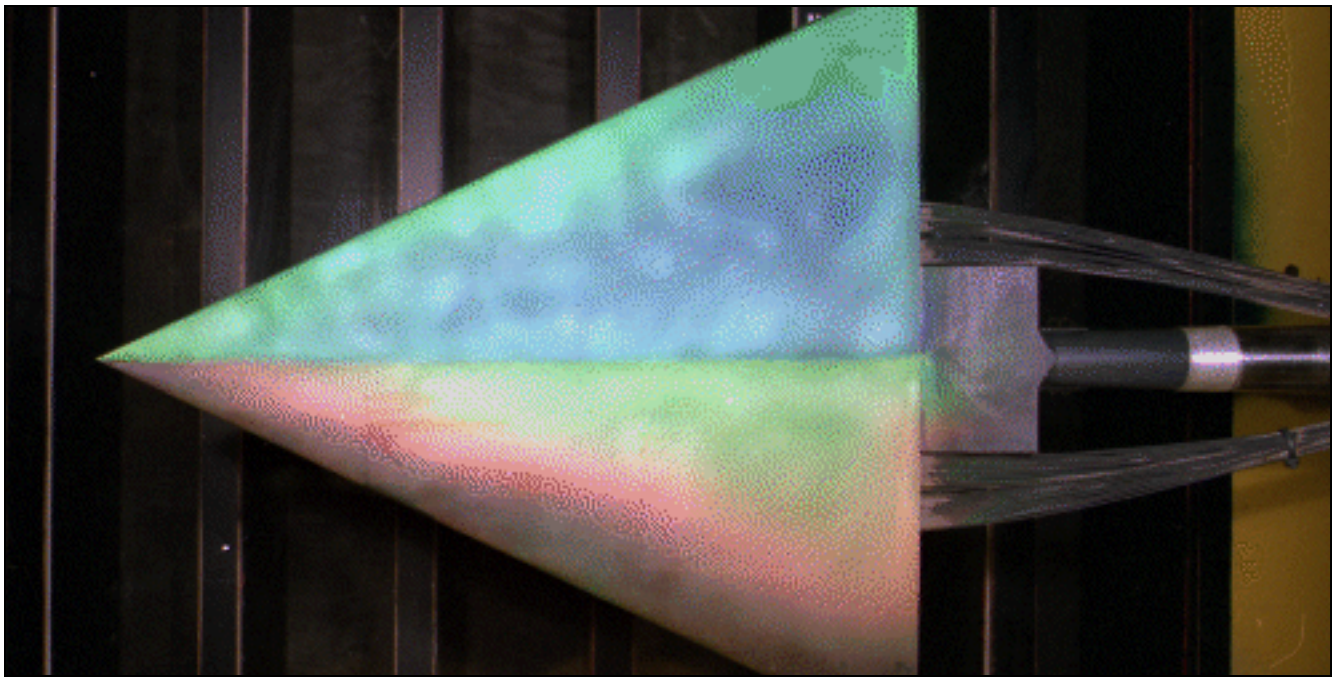

(b) $\alpha = 1.03°$.

Figure 21. Liquid-crystal photographs illustrating vortex growth with angle of attack on leeside of elliptical wing without transition grit at $M = 1.60$, $R = 2 \times 10^6$ ft^{-1}, and $T_o = 125°$F.

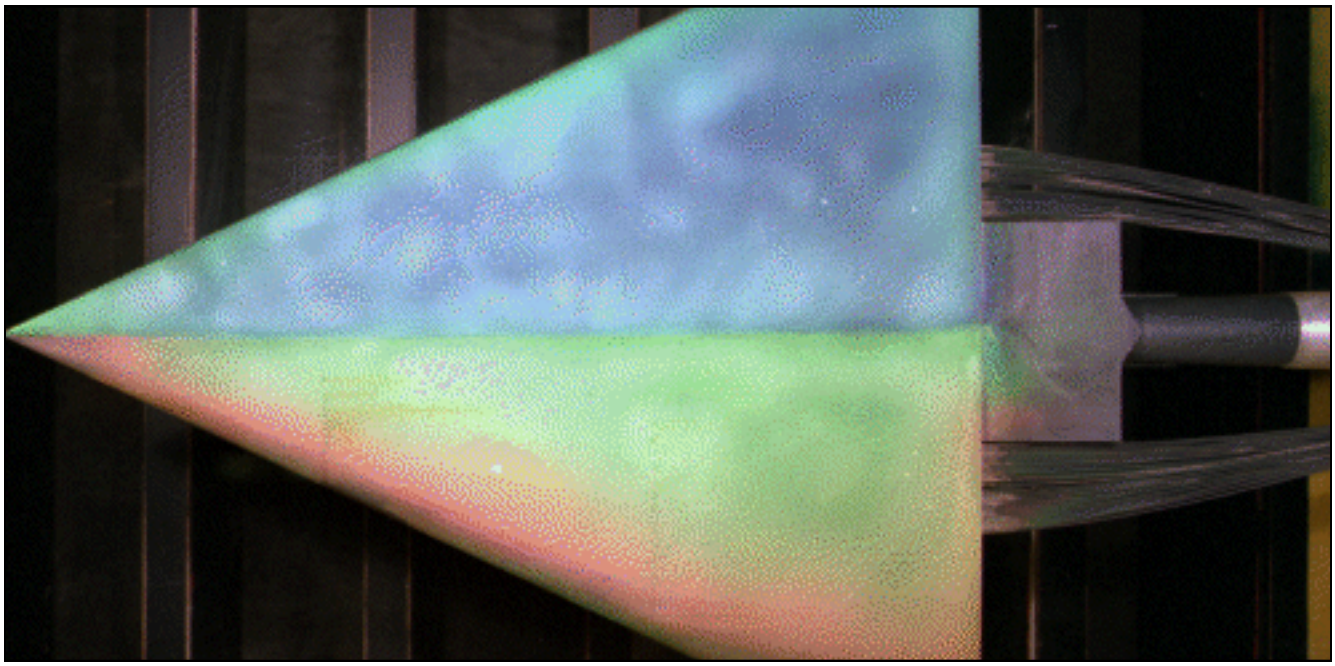

(c) $\alpha = 2.08°$.

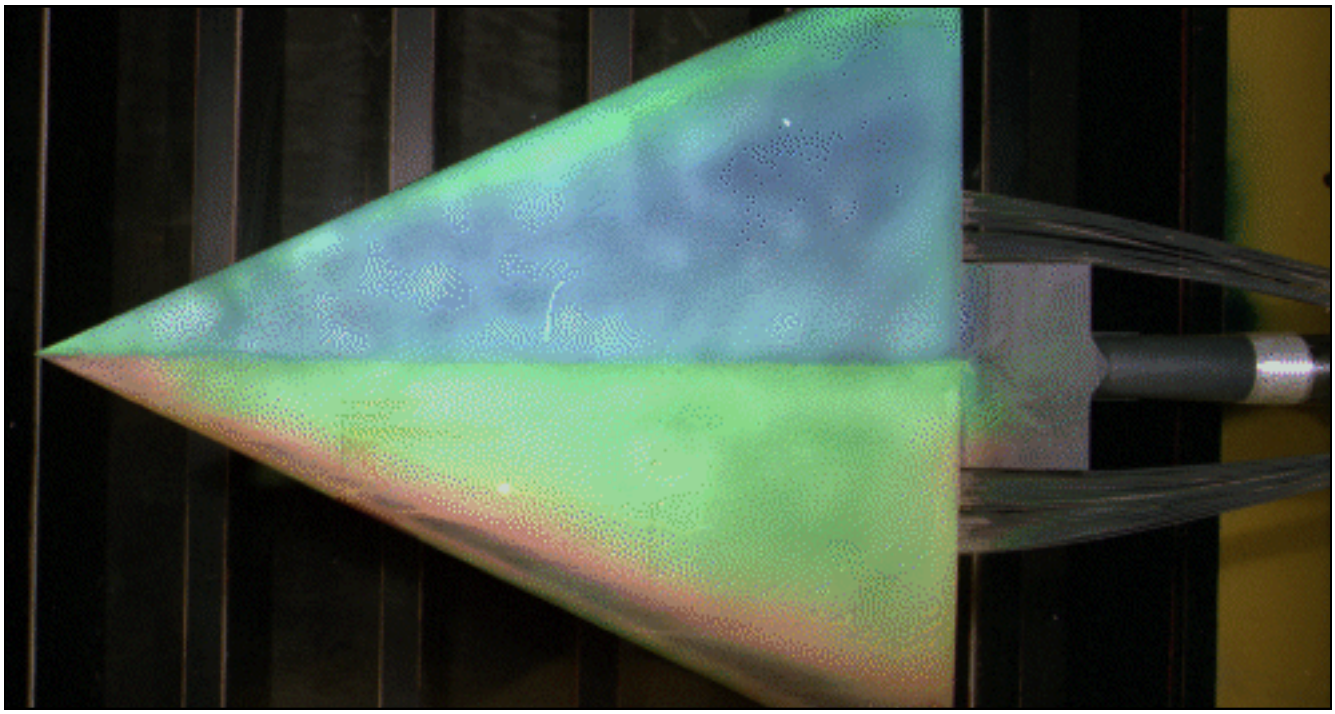

(d) $\alpha = 3.14°$.

Figure 21. Continued.

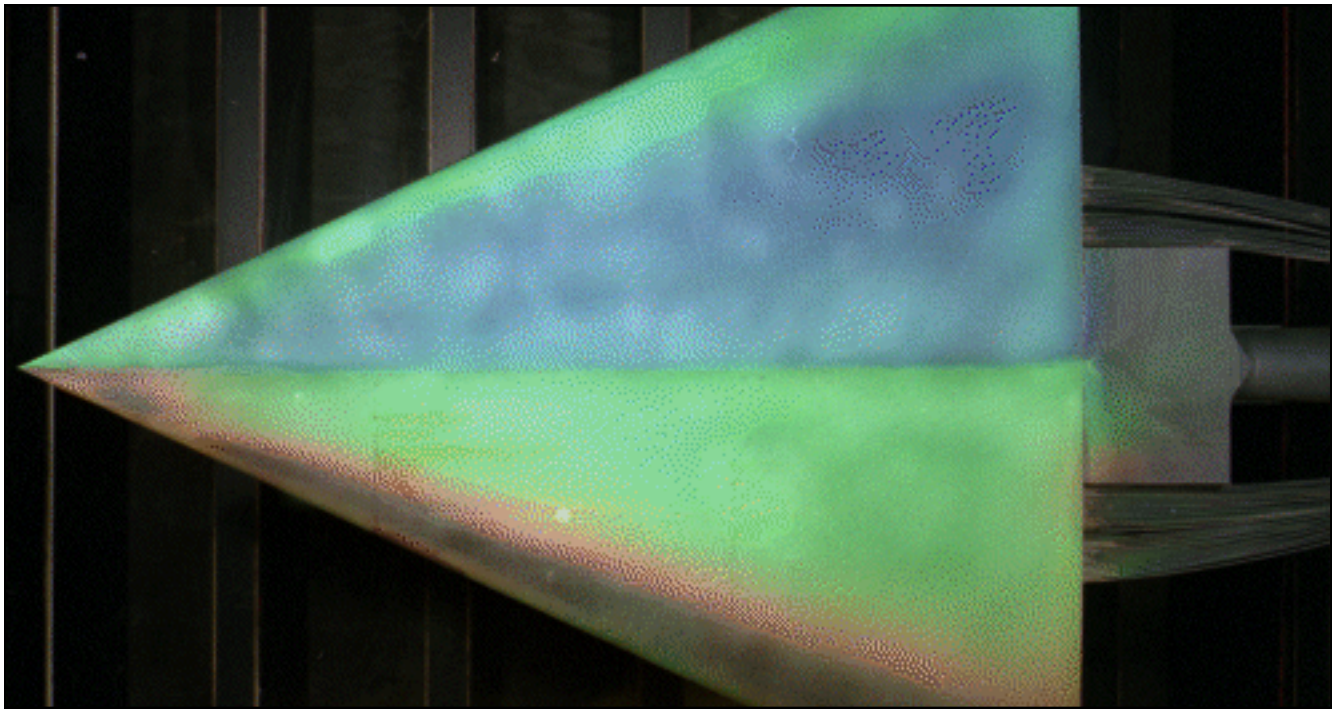

(e) $\alpha = 4.17°$.

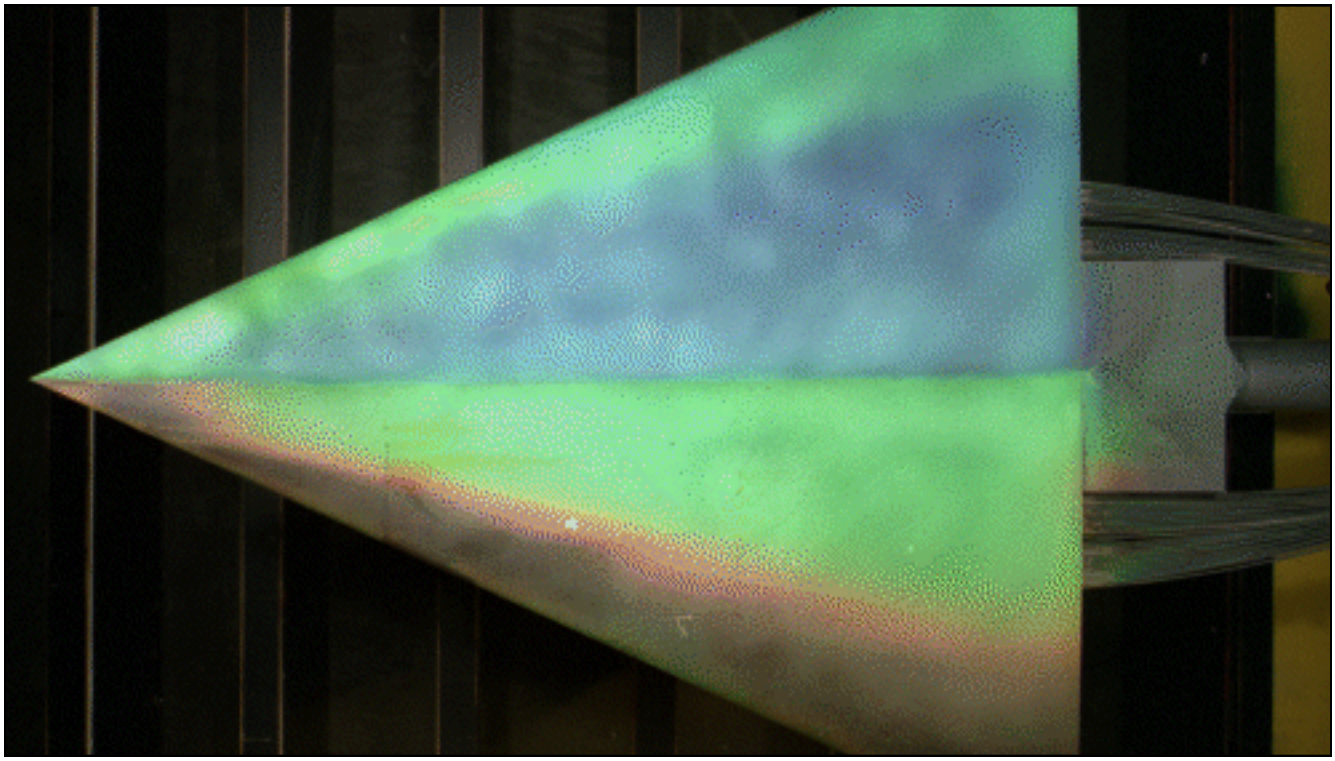

(f) $\alpha = 5.21°$.

Figure 21. Continued.

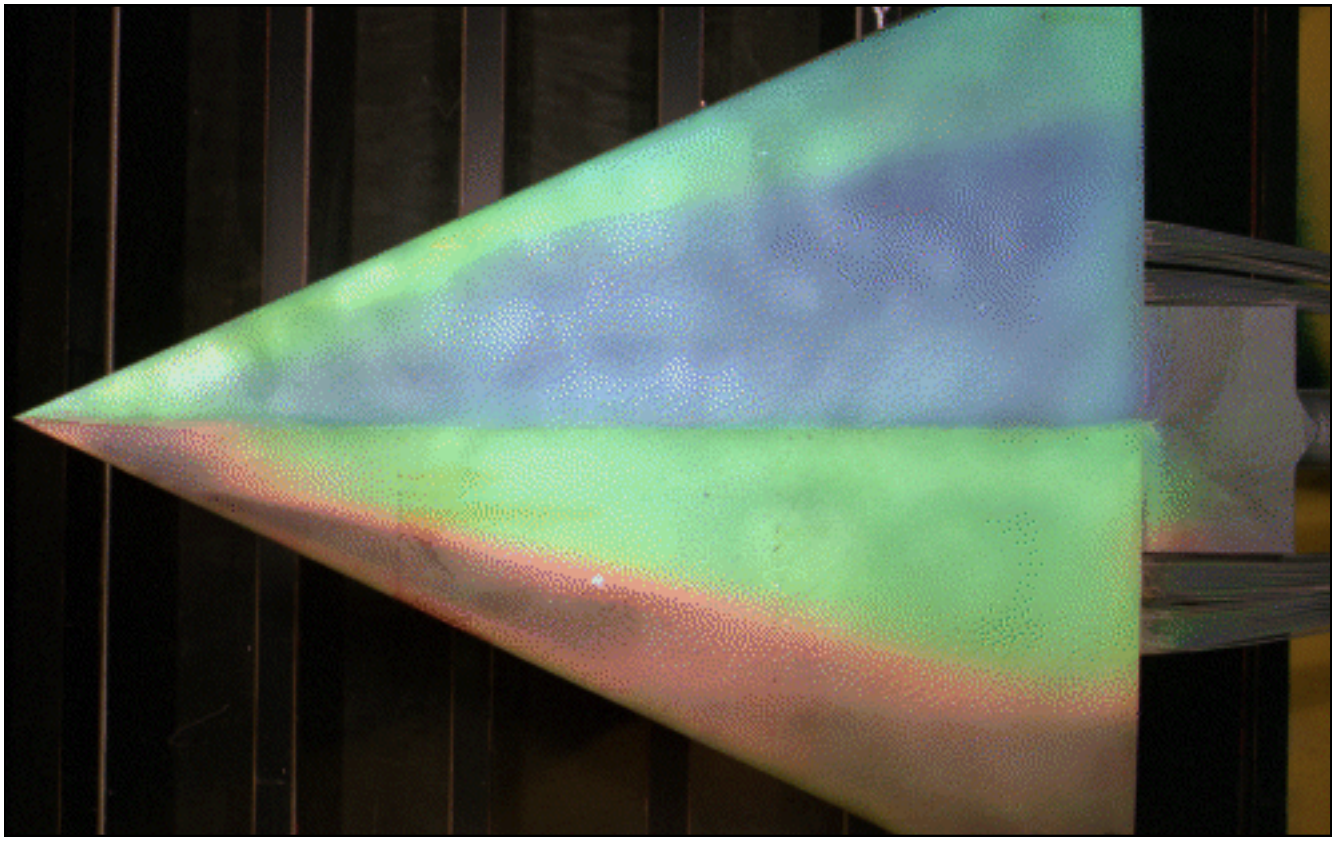

(g) $\alpha = 6.26°$.

Figure 21. Continued.

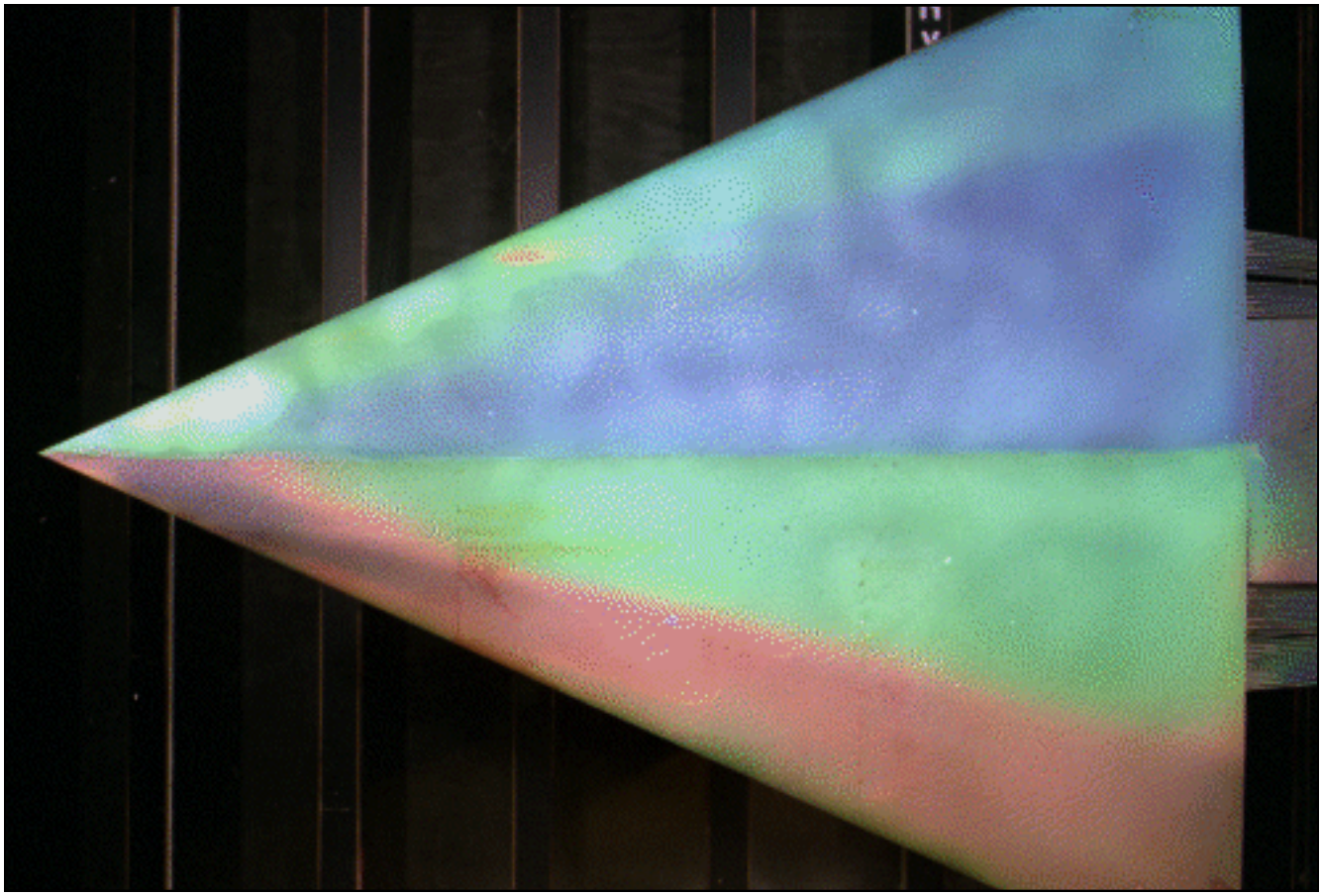

(h) $\alpha = 7.29°$.

Figure 21. Continued.

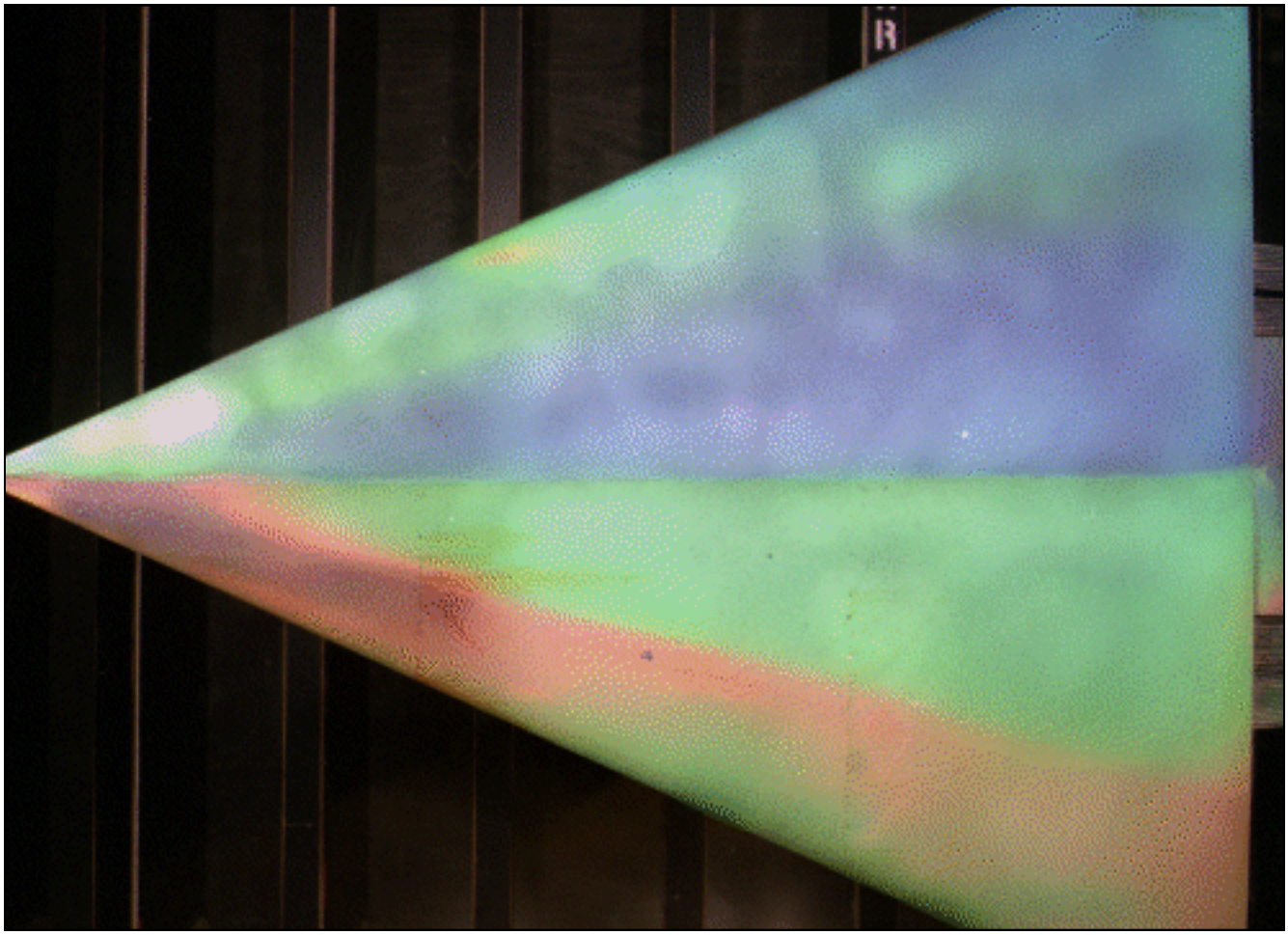

(i) $\alpha = 8.34°$.

Figure 21. Continued.

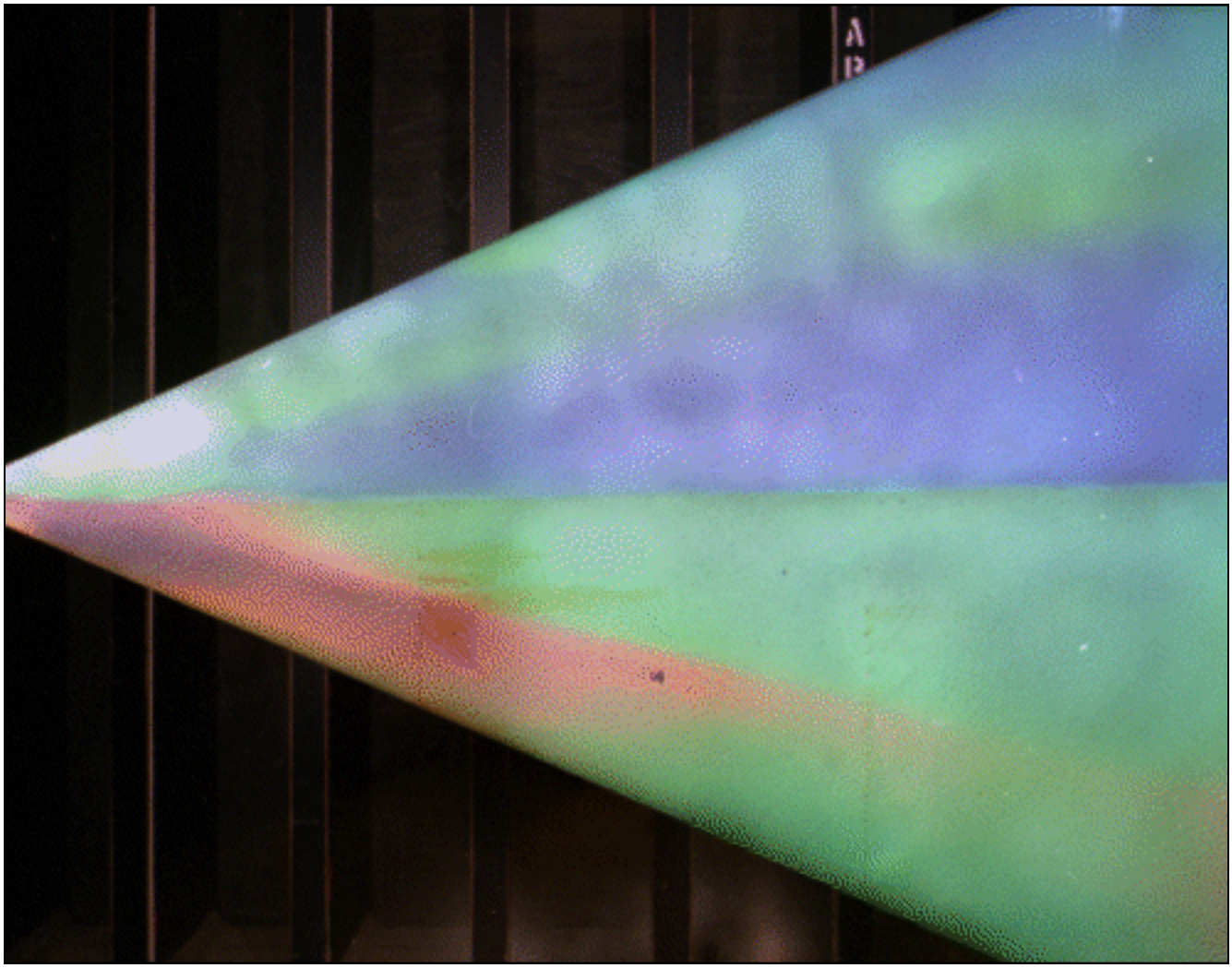

(j) $\alpha = 9.39°$.

Figure 21. Continued.

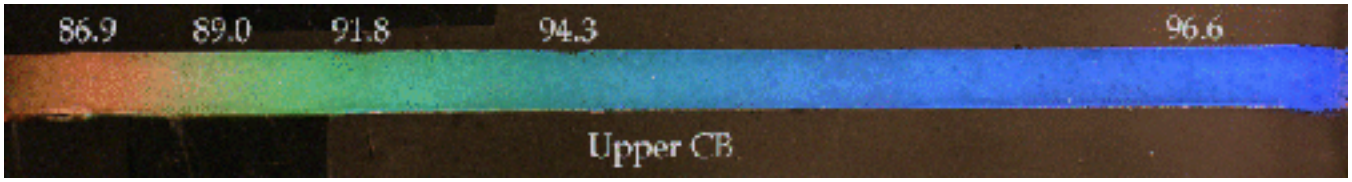

(k) Color scale bar for right side of delta wing (viewing wing from trailing edge). Temperature is in °F.

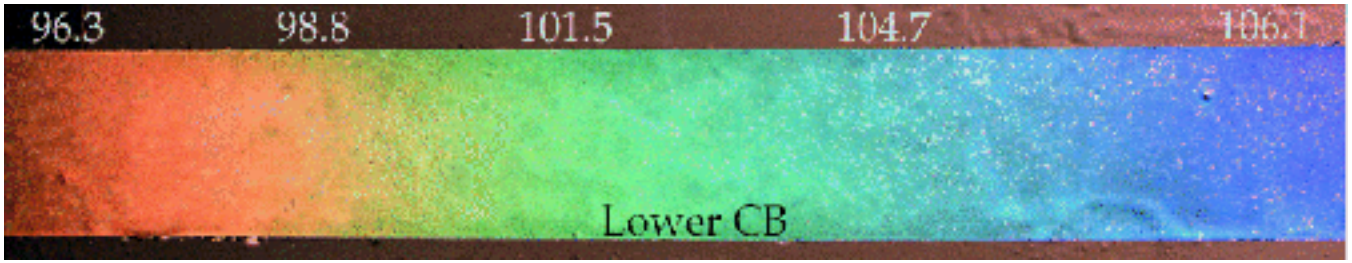

(l) Color scale bar for left side of delta wing (viewing wing from trailing edge). Temperature is in °F.

Figure 21. Concluded.

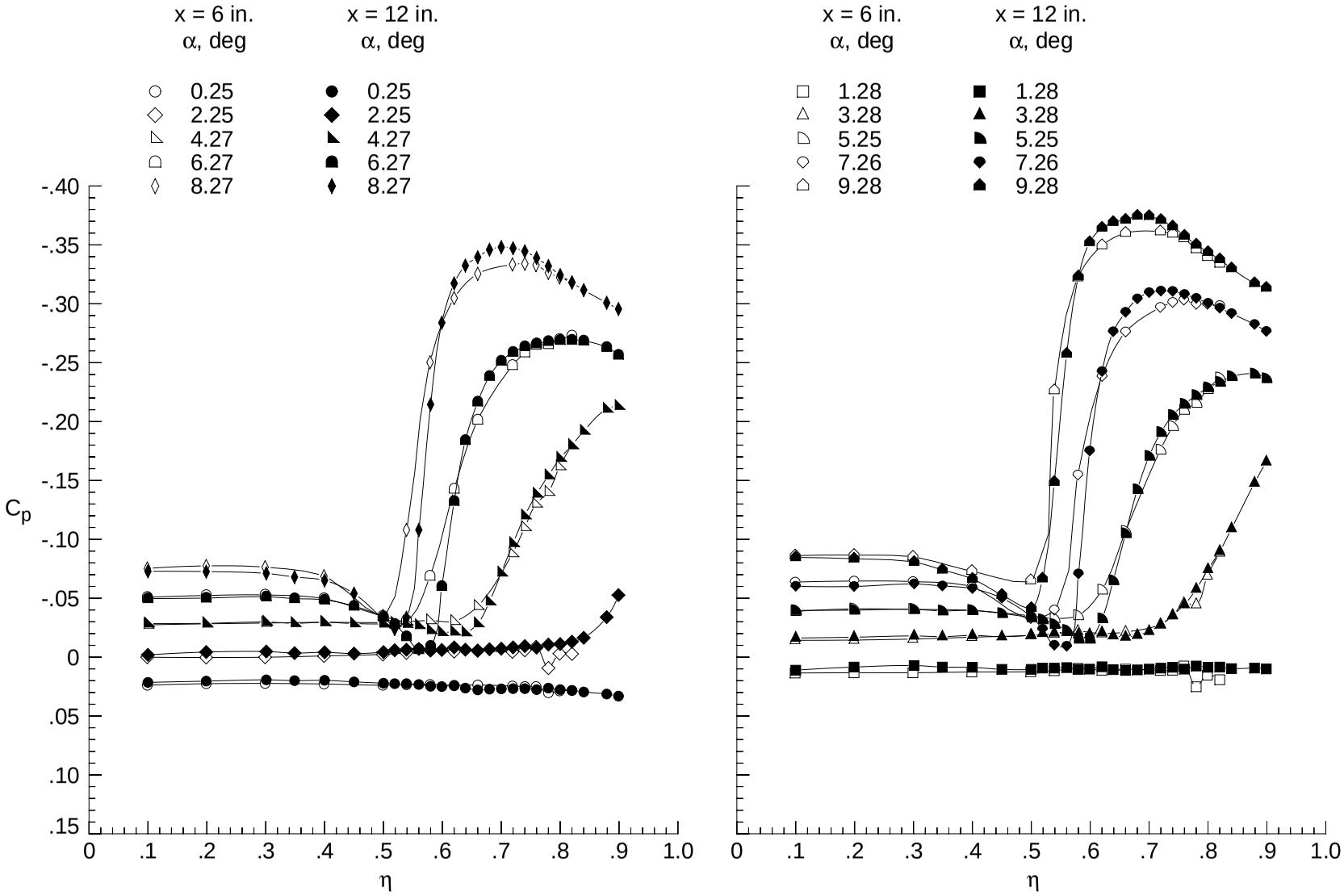

(a) Sharp wing.

Figure 22. Evaluation of flow conicity over upper surface of each delta wing without transition grit at $M = 1.60$ and $R = 2 \times 10^6$ ft^{-1}.

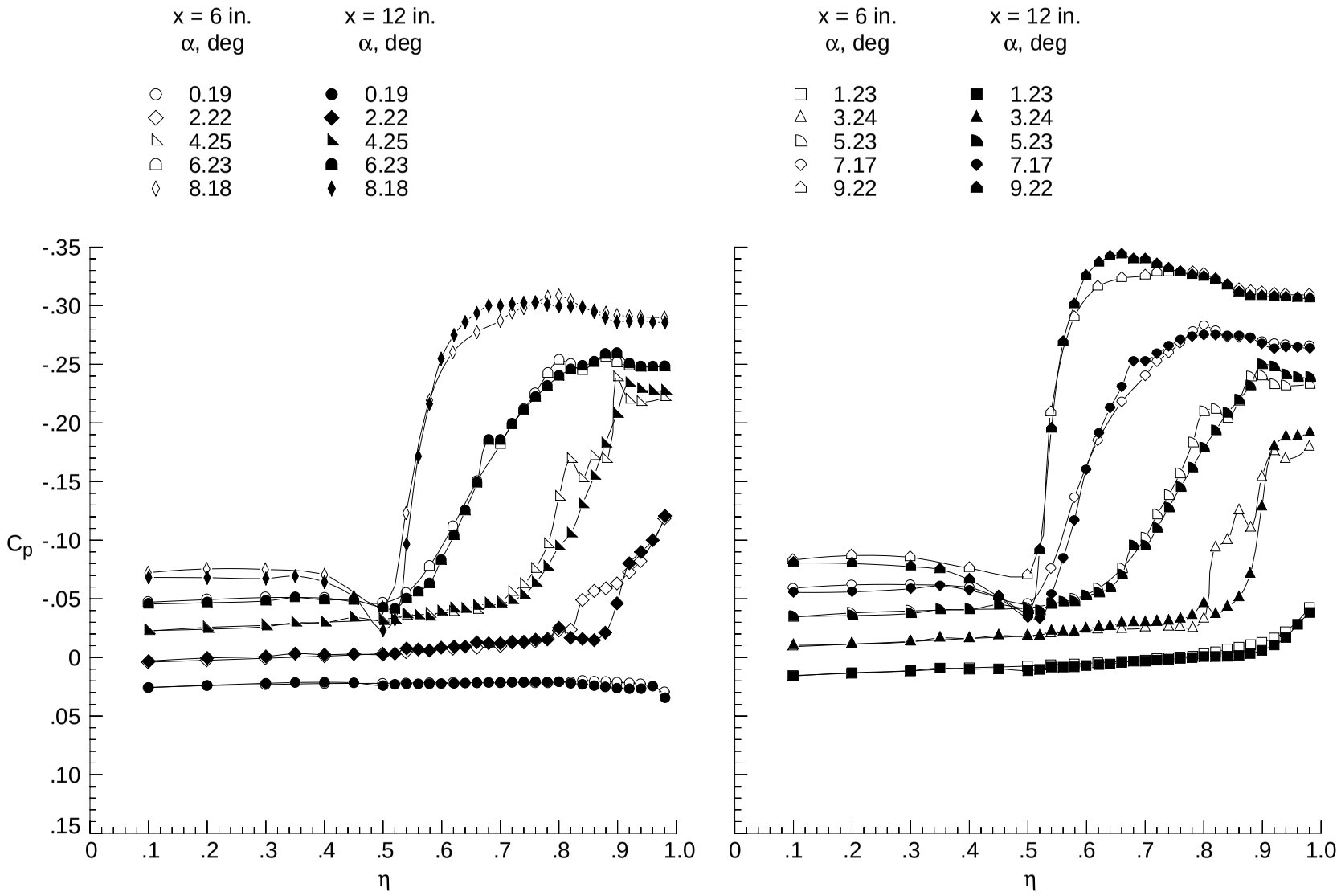

(b) Elliptical wing.

Figure 22. Continued.

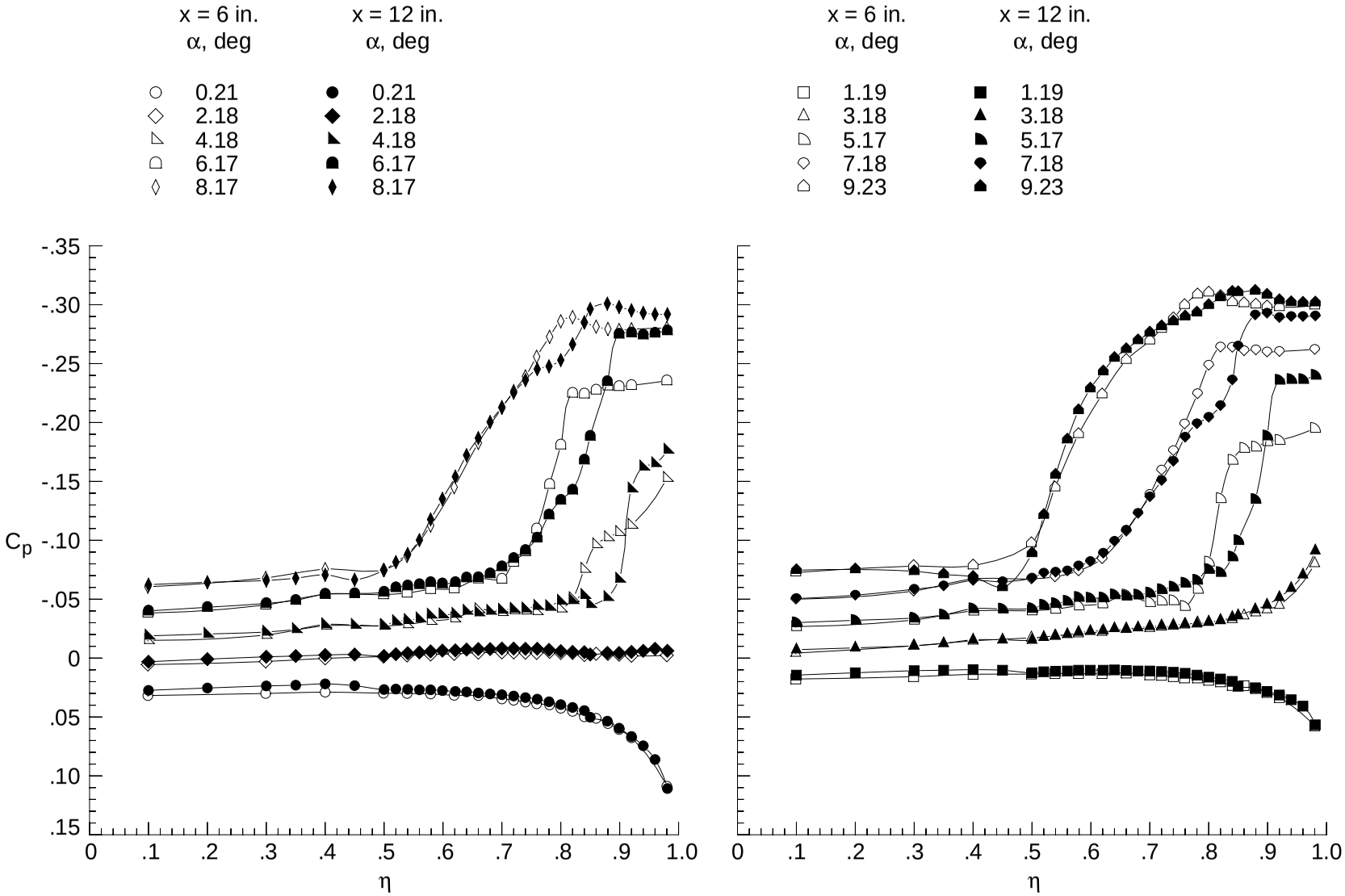

(c) Cambered wing.

Figure 22. Concluded.

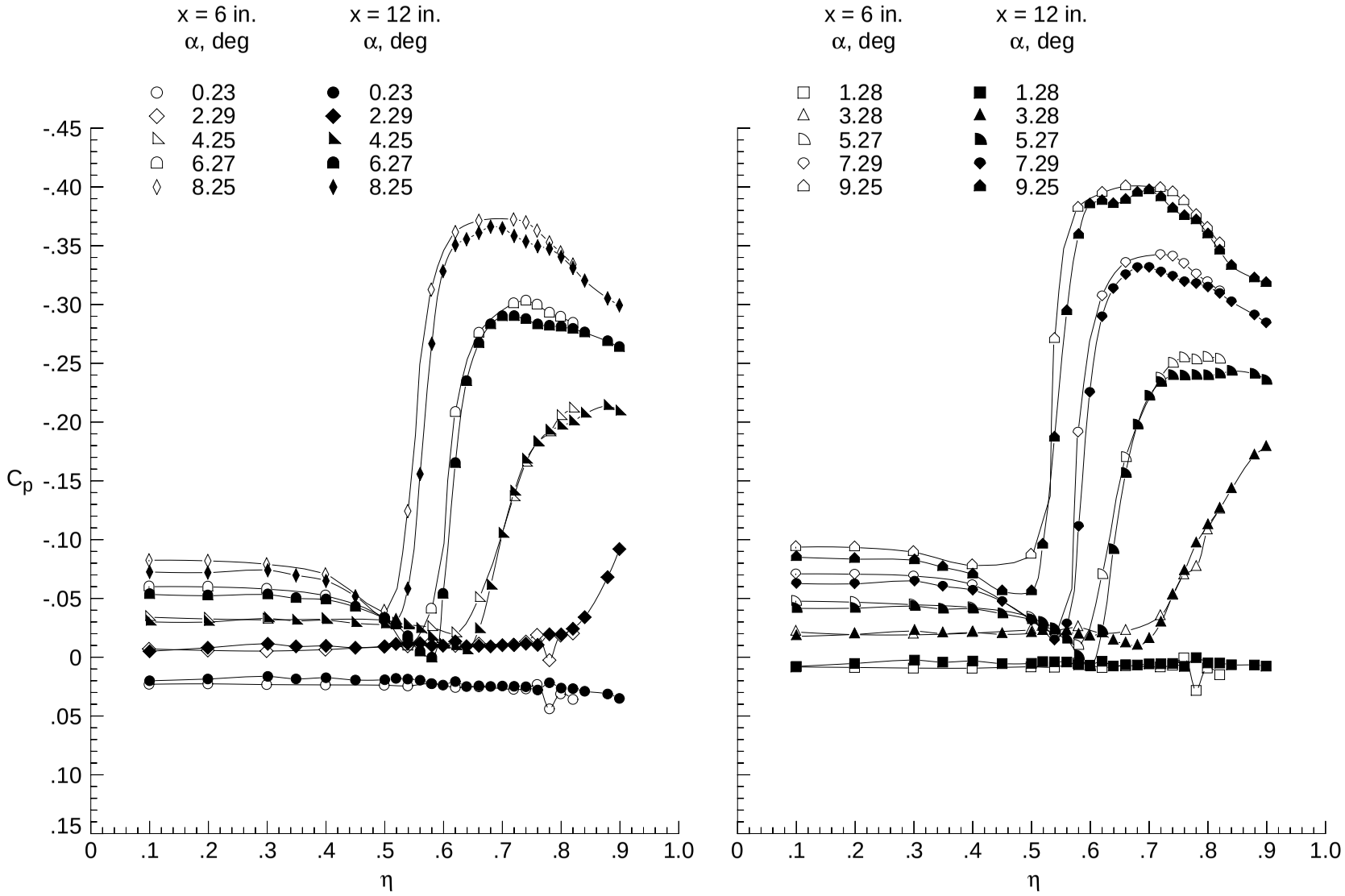

(a) Sharp wing.

Figure 23. Evaluation of flow conicity over upper surface of each delta wing without transition grit at $M = 1.60$ and $R = 5 \times 10^6$ ft^{-1}.

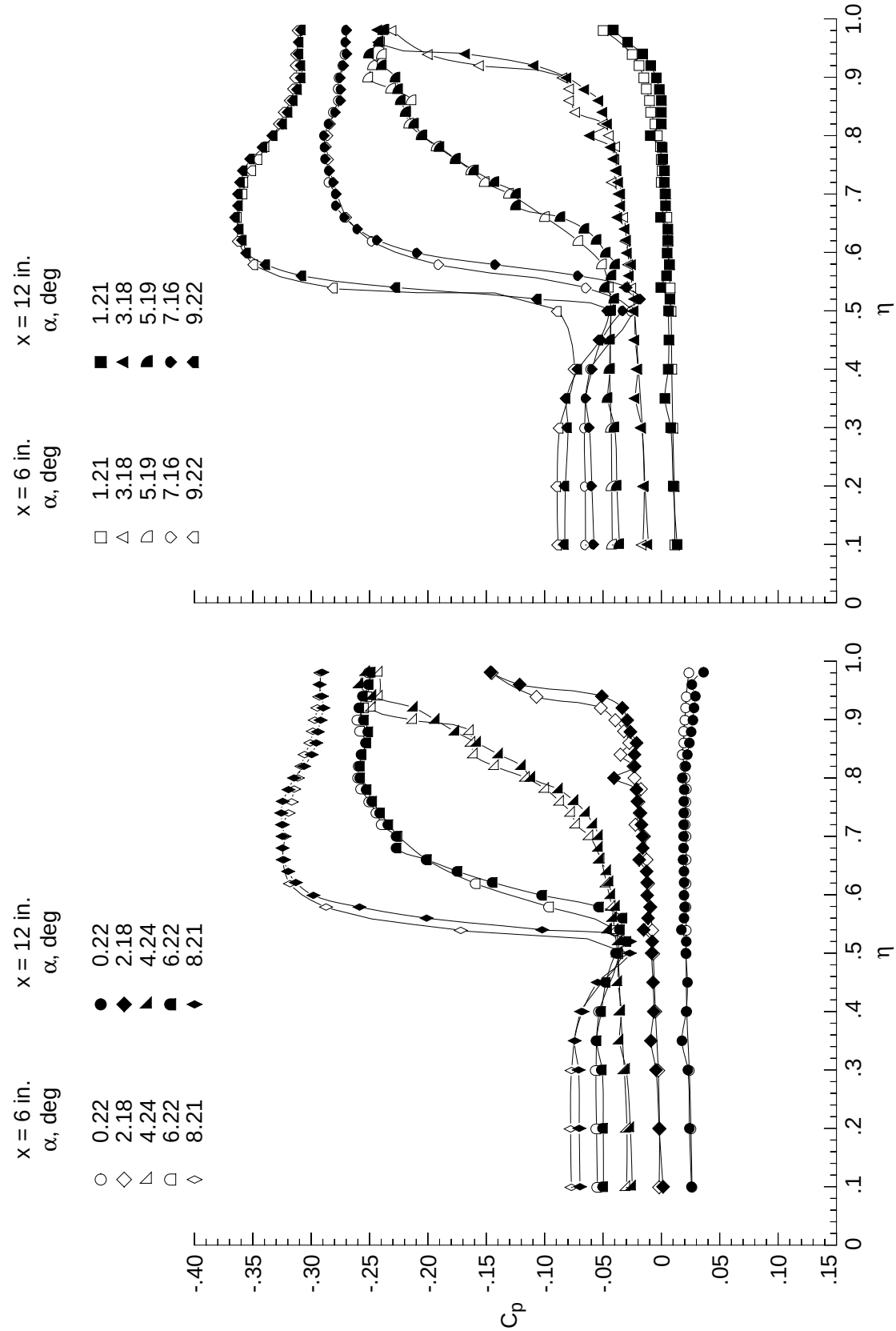

(b) Elliptical wing.

Figure 23. Continued.

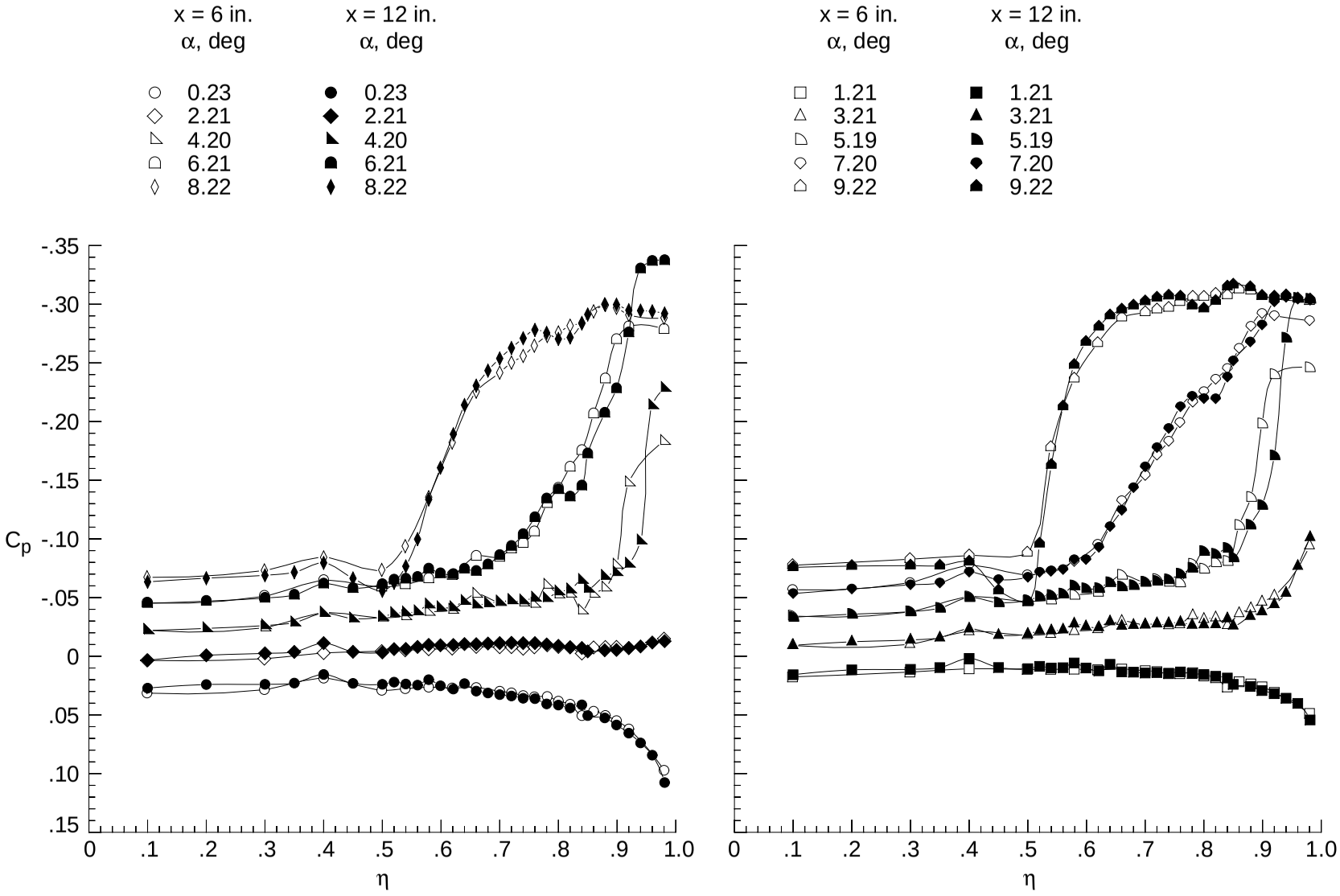

(c) Cambered wing.

Figure 23. Concluded.

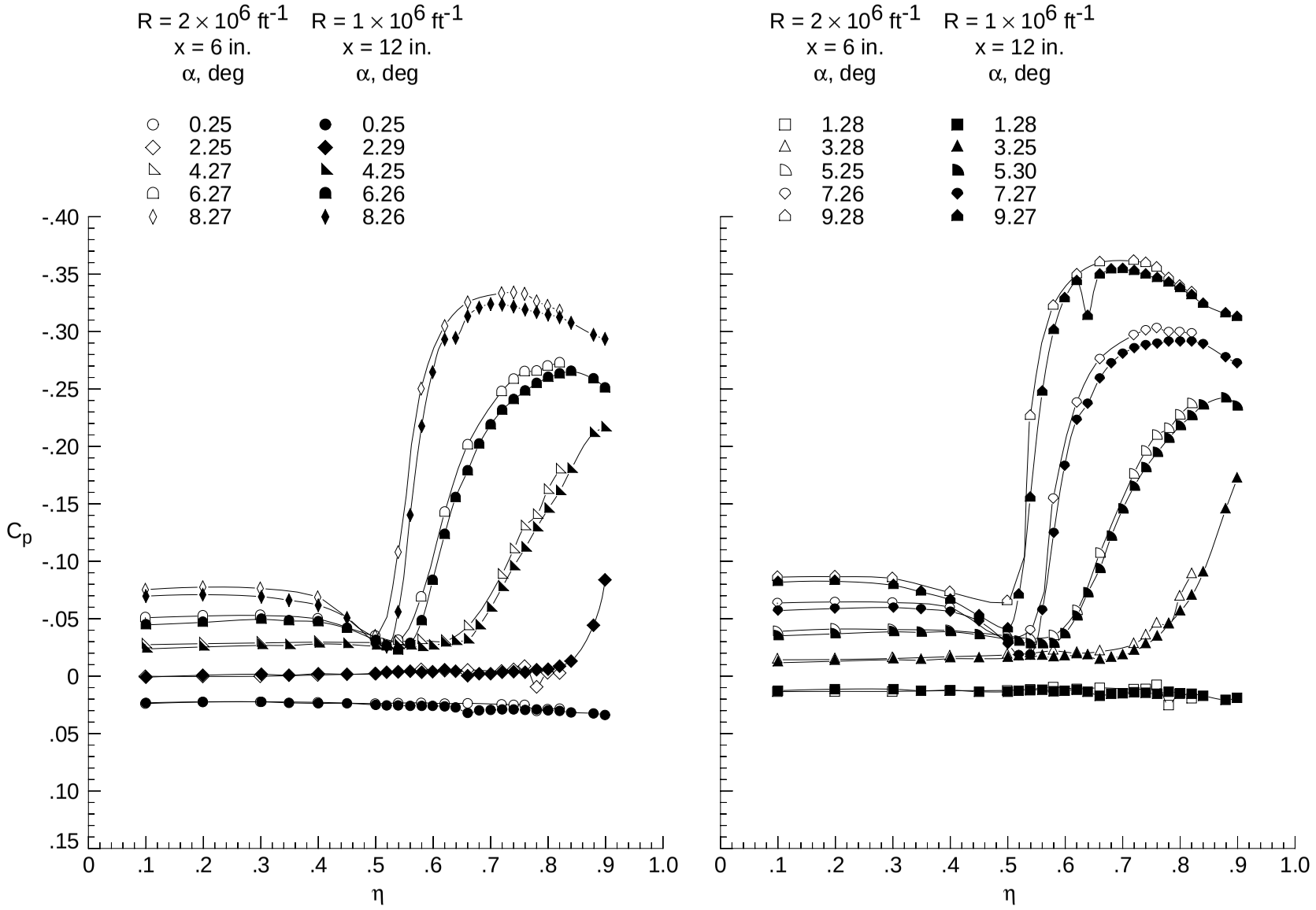

(a) Sharp wing data at $R_x = 1 \times 10^6$.

Figure 24. Effect of longitudinal position on upper surface-pressure coefficient distribution of delta wing without transition grit at $M = 1.60$. Local Reynolds number is held constant.

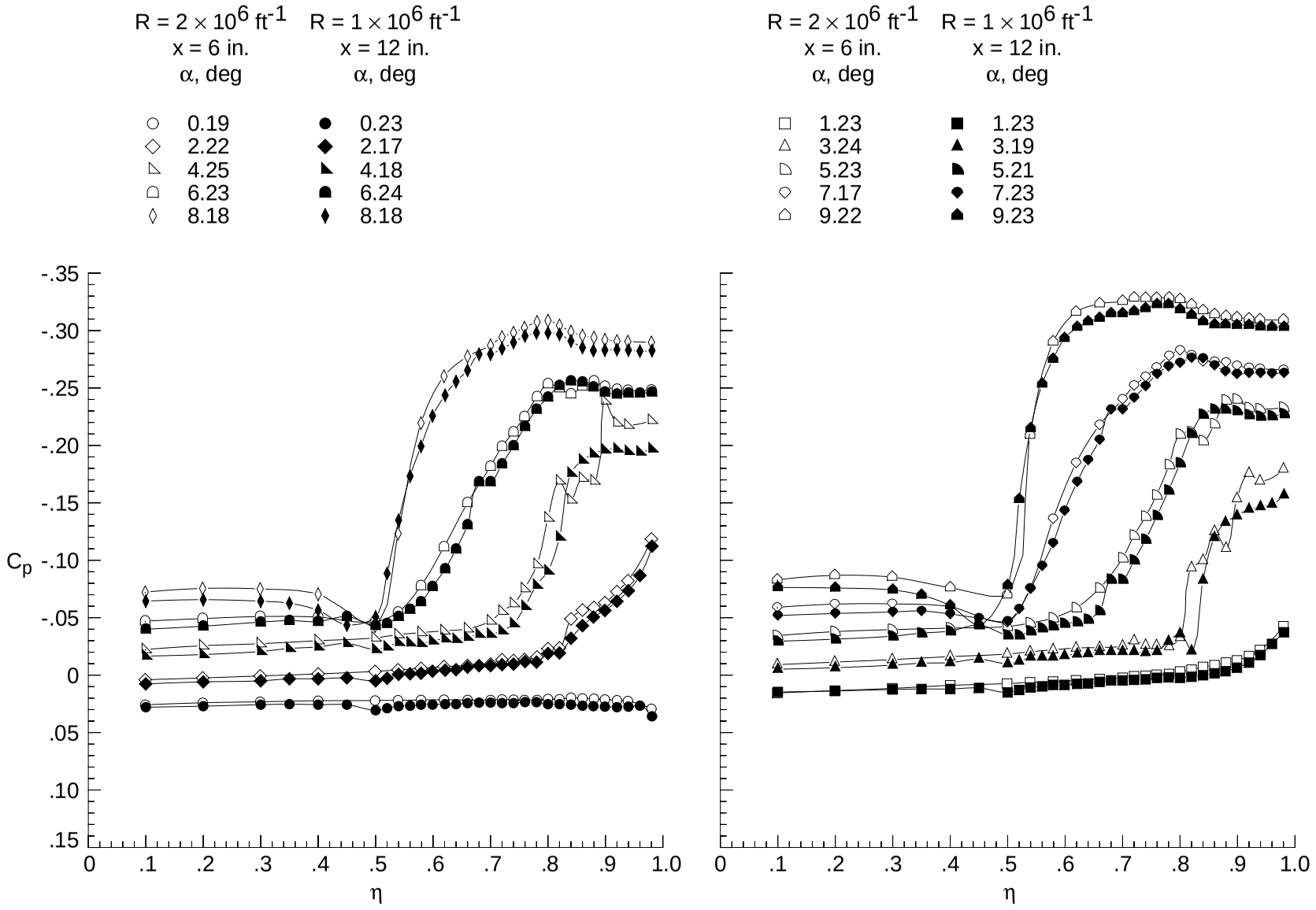

(b) Elliptical wing data at $R_x = 1 \times 10^6$.

Figure 24. Continued.

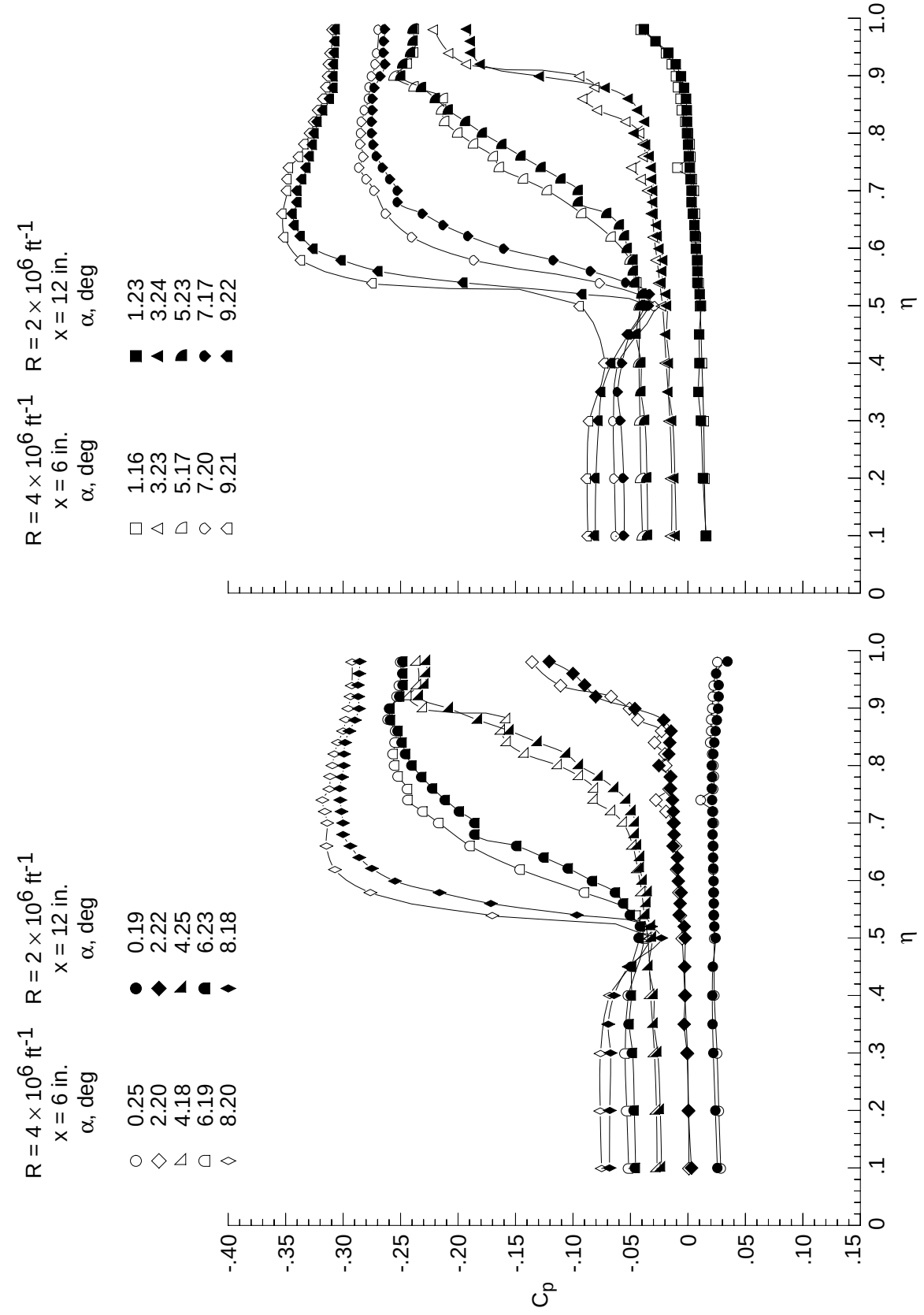

(c) Elliptical wing data at $R_x = 2 \times 10^6$.

Figure 24. Continued.

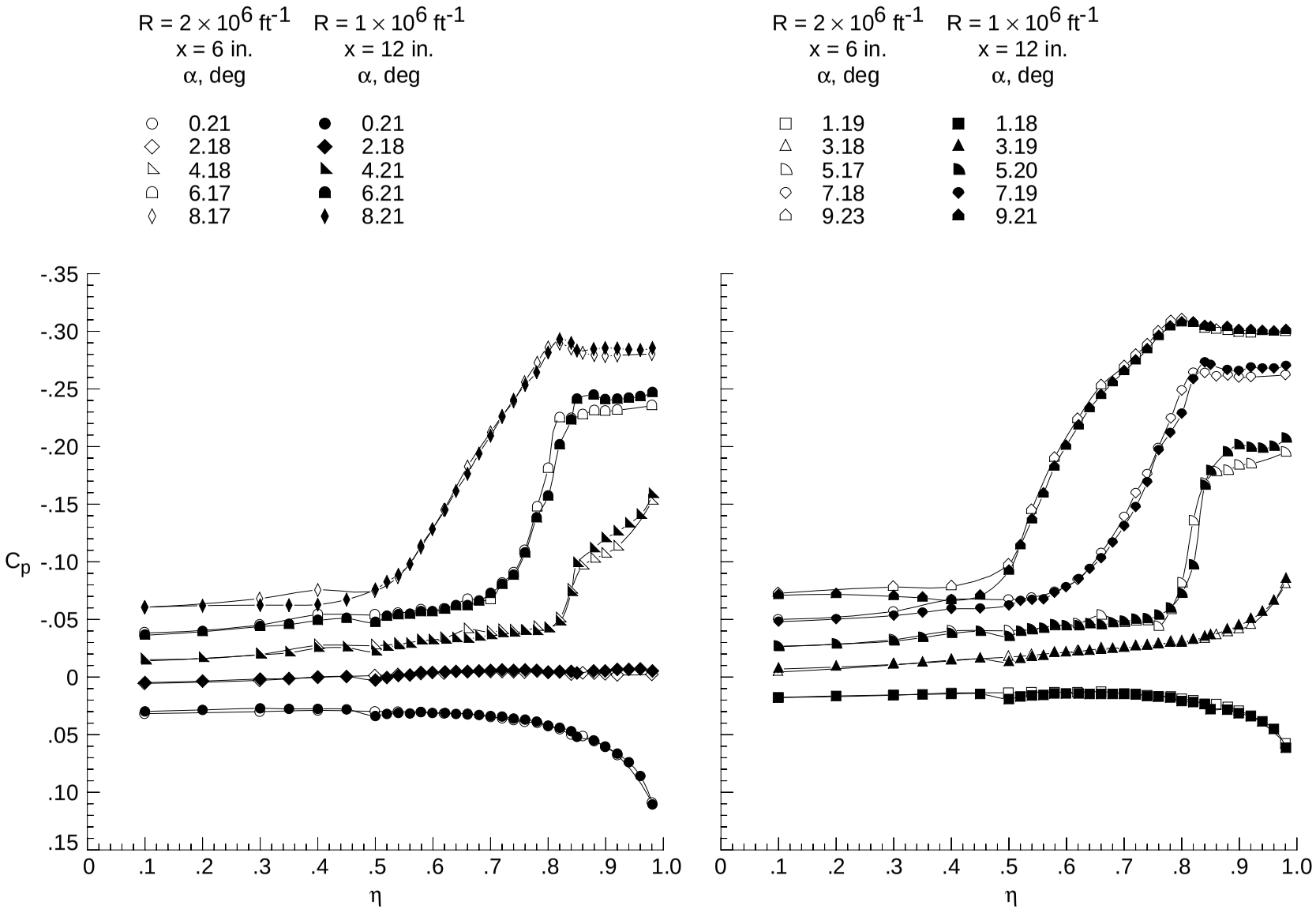

(d) Cambered wing data at $R_x = 1 \times 10^6$.

Figure 24. Concluded.

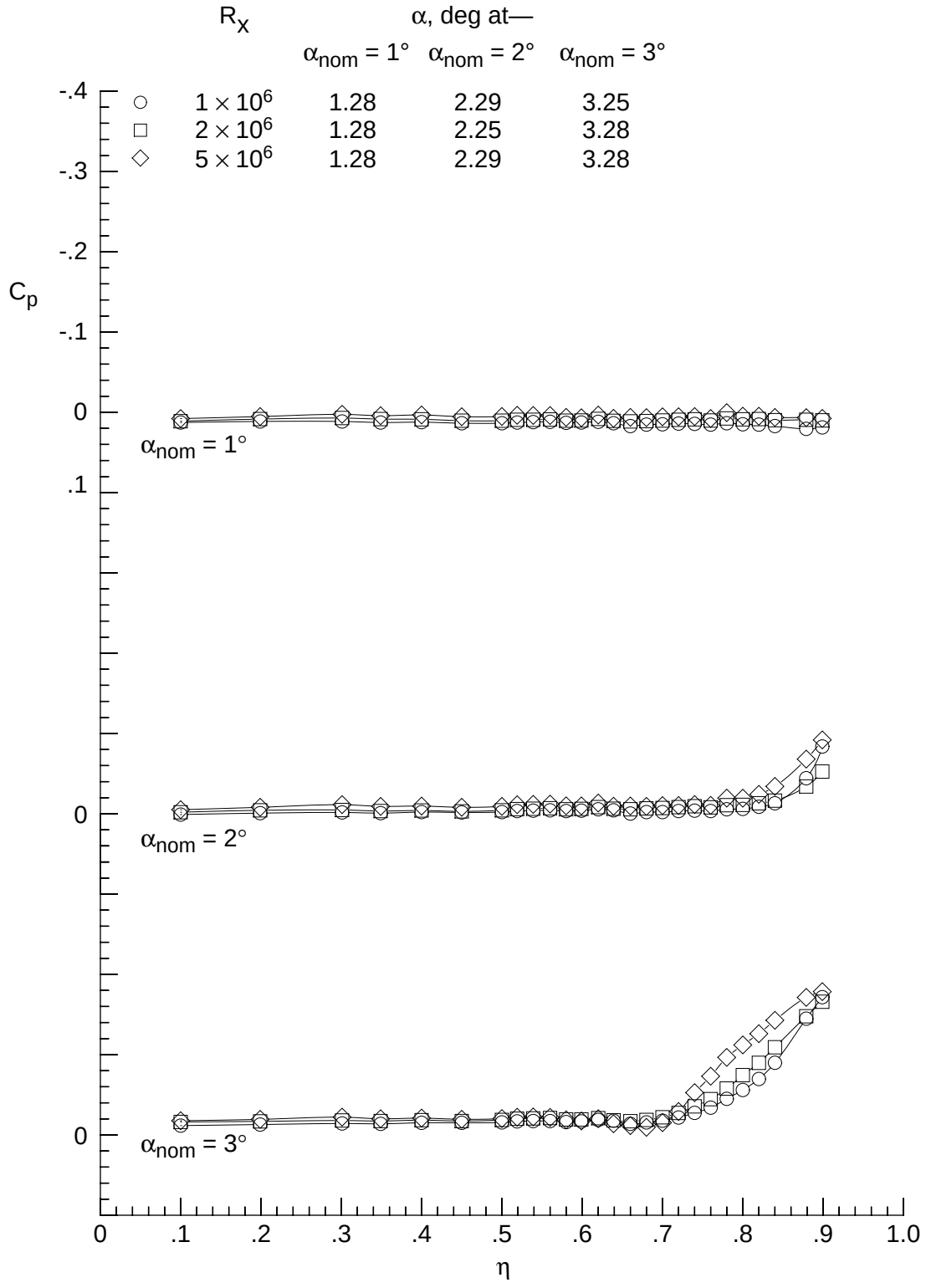

(a) α_{nom} = 1°, 2°, and 3°.

Figure 25. Effect of R_x on upper surface-pressure coefficient distribution for sharp wing without transition grit at x = 12 in. and M = 1.60.

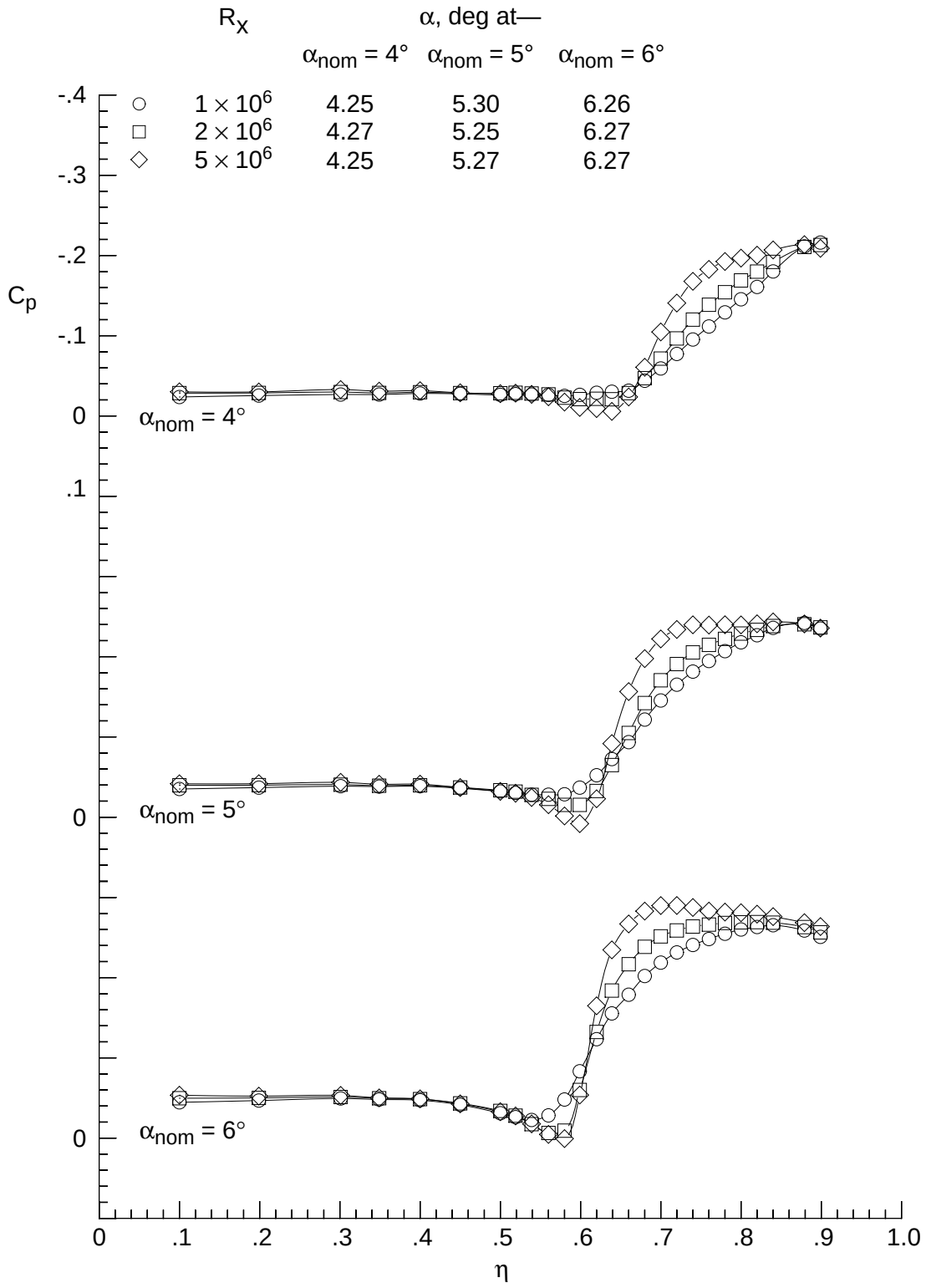

(b) α_{nom} = 4°, 5°, and 6°.

Figure 25. Continued.

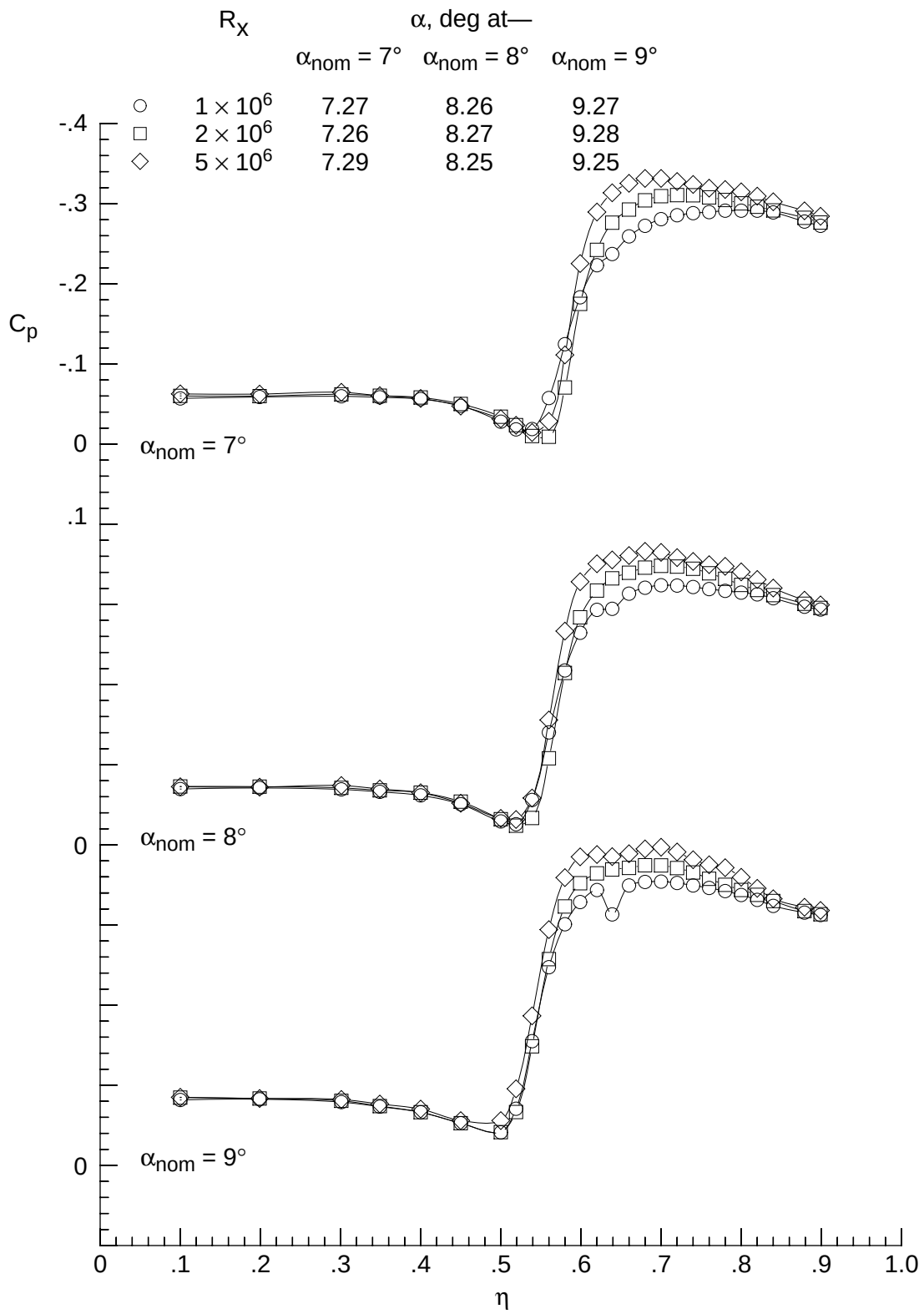

(c) α_{nom} = 7°, 8°, and 9°.

Figure 25. Concluded.

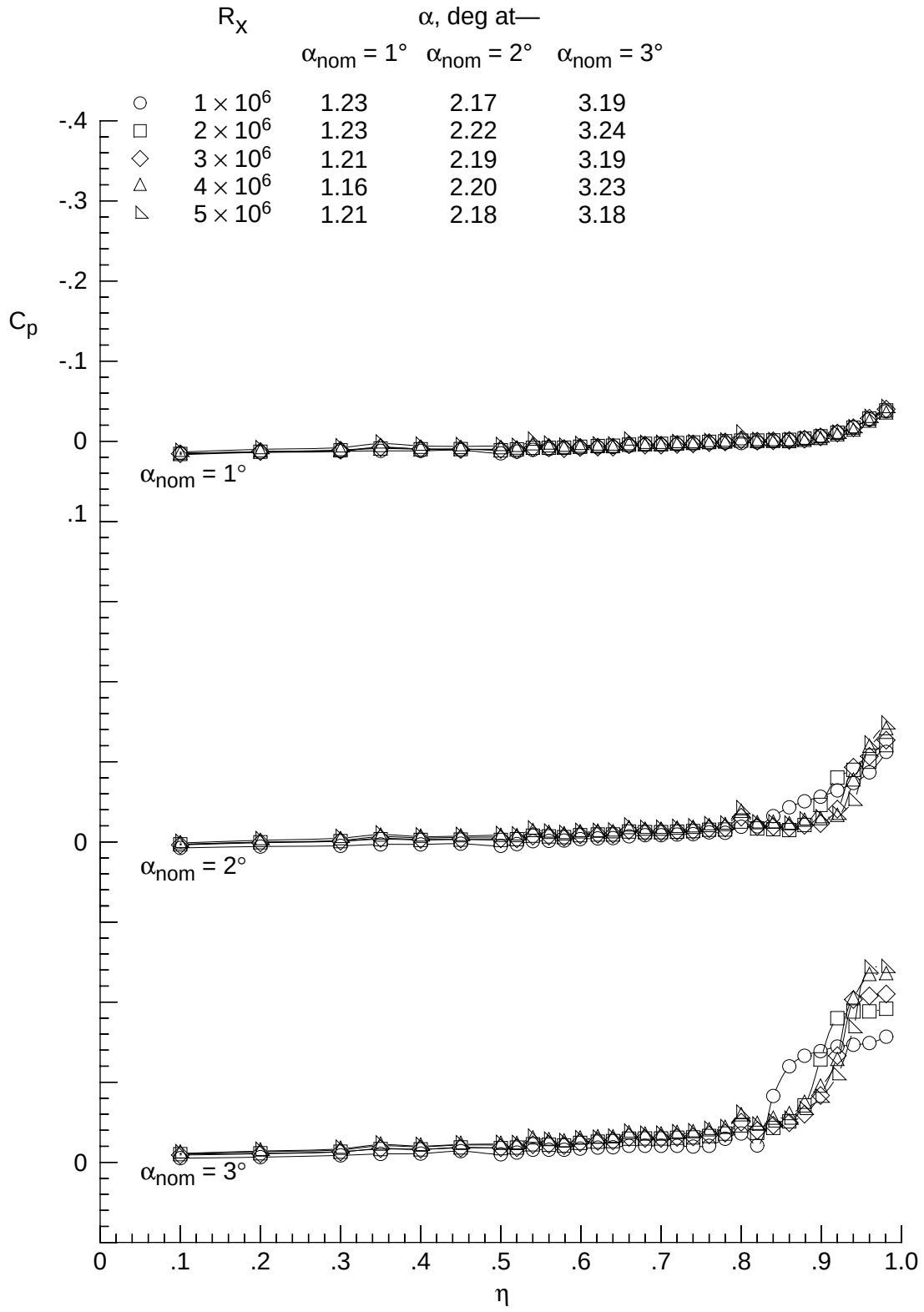

(a) α_{nom} = 1°, 2°, and 3°.

Figure 26. Effect of R_x on upper surface-pressure coefficient distribution for elliptical wing without transition grit at x = 12 in. and M = 1.60.

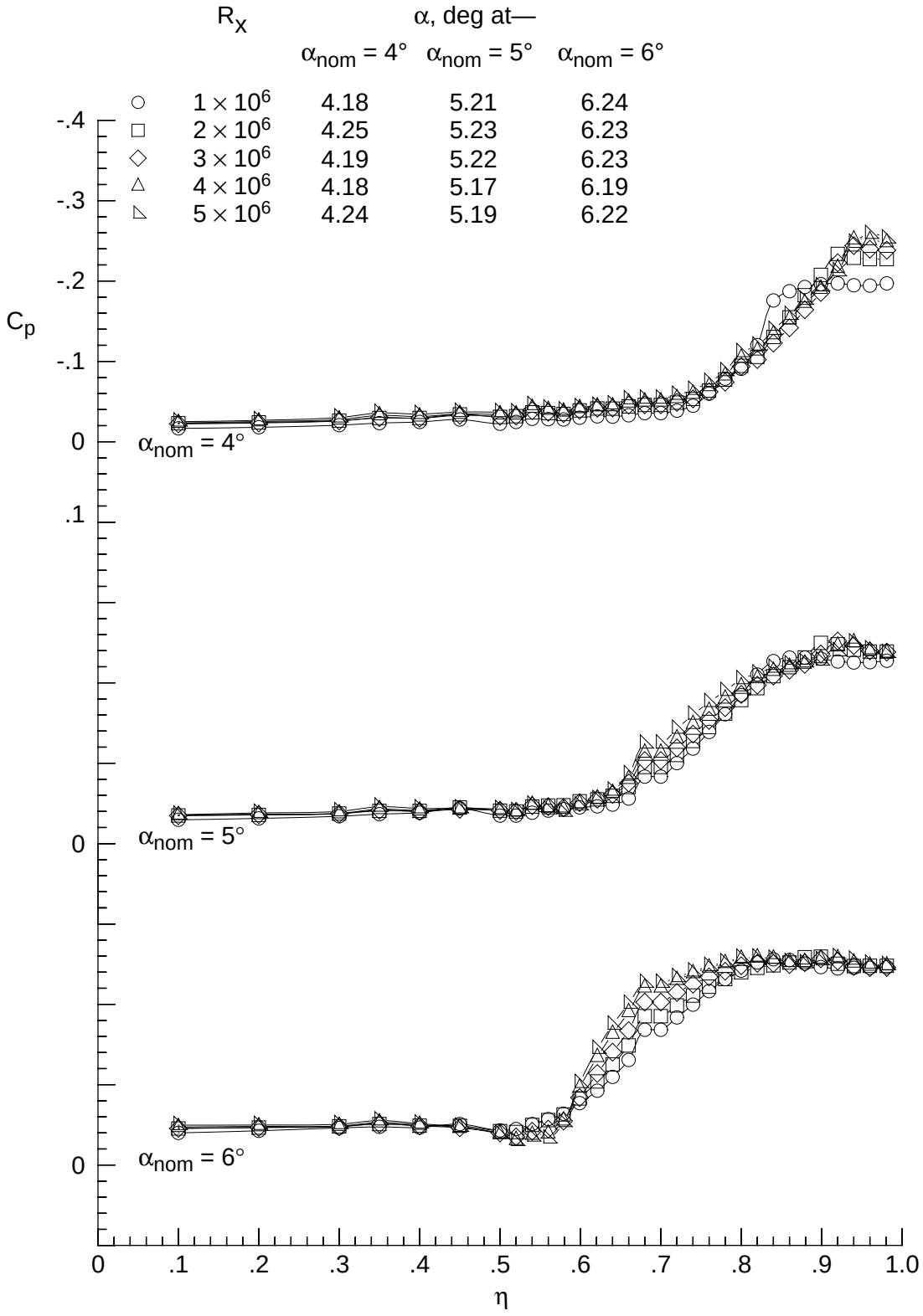

(b) α_{nom} = 4°, 5°, and 6°.

Figure 26. Continued.

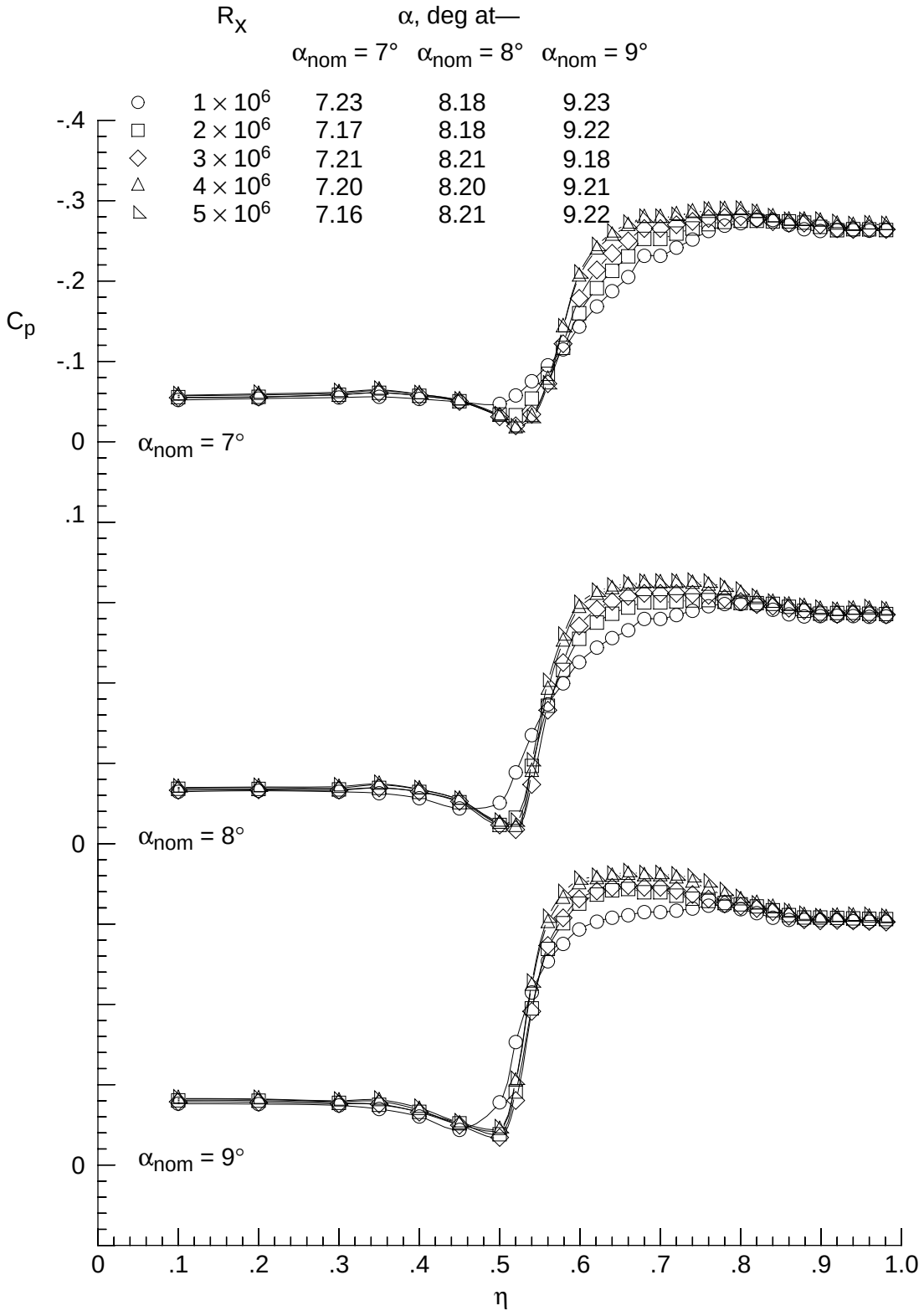

(c) α_{nom} = 7°, 8°, and 9°.

Figure 26. Concluded.

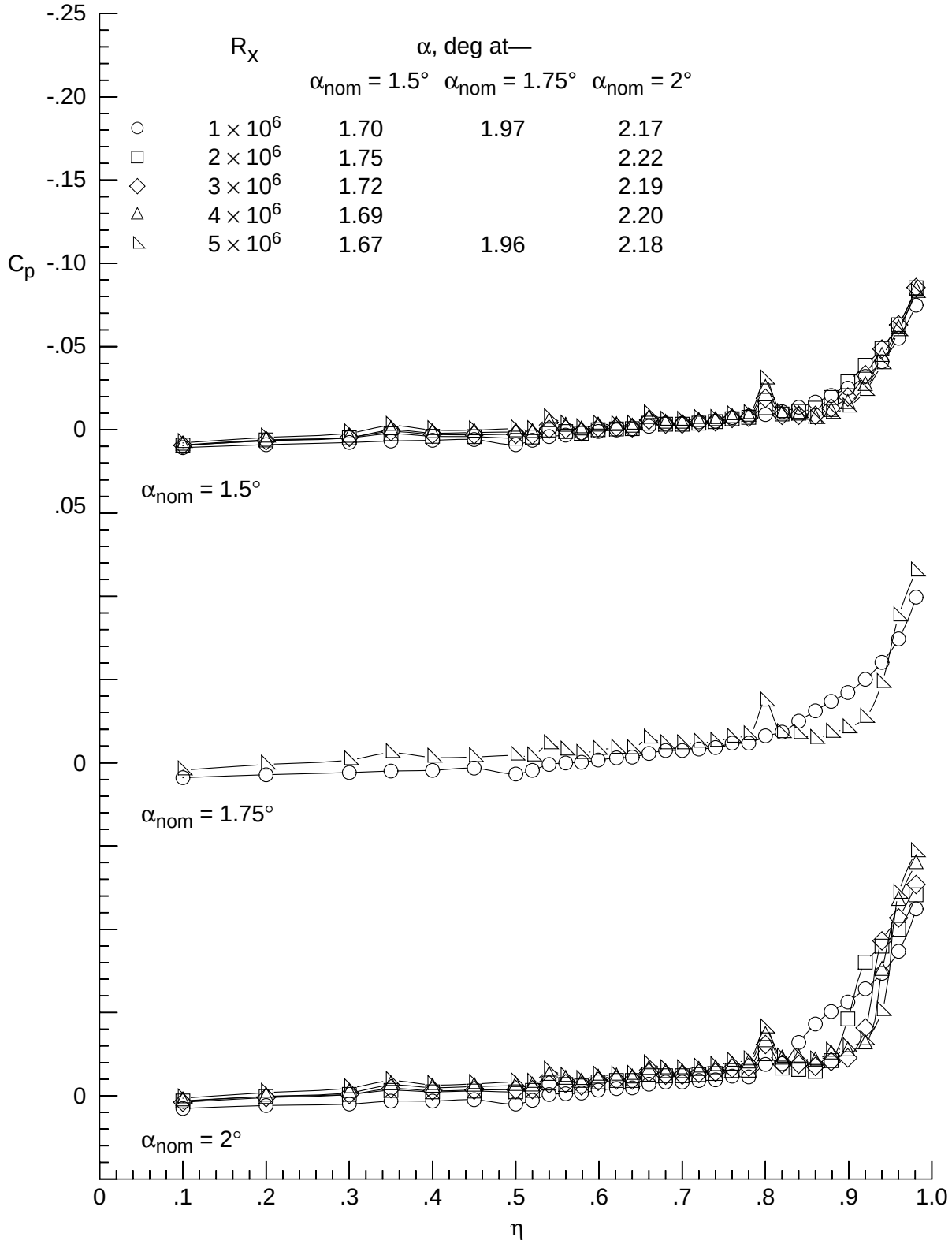

(a) α_{nom} = 1.5°, 1.75°, and 2°.

Figure 27. Effect of R_x on onset of leading-edge separation for elliptical wing without transition grit at x = 12 in. and M = 1.60.

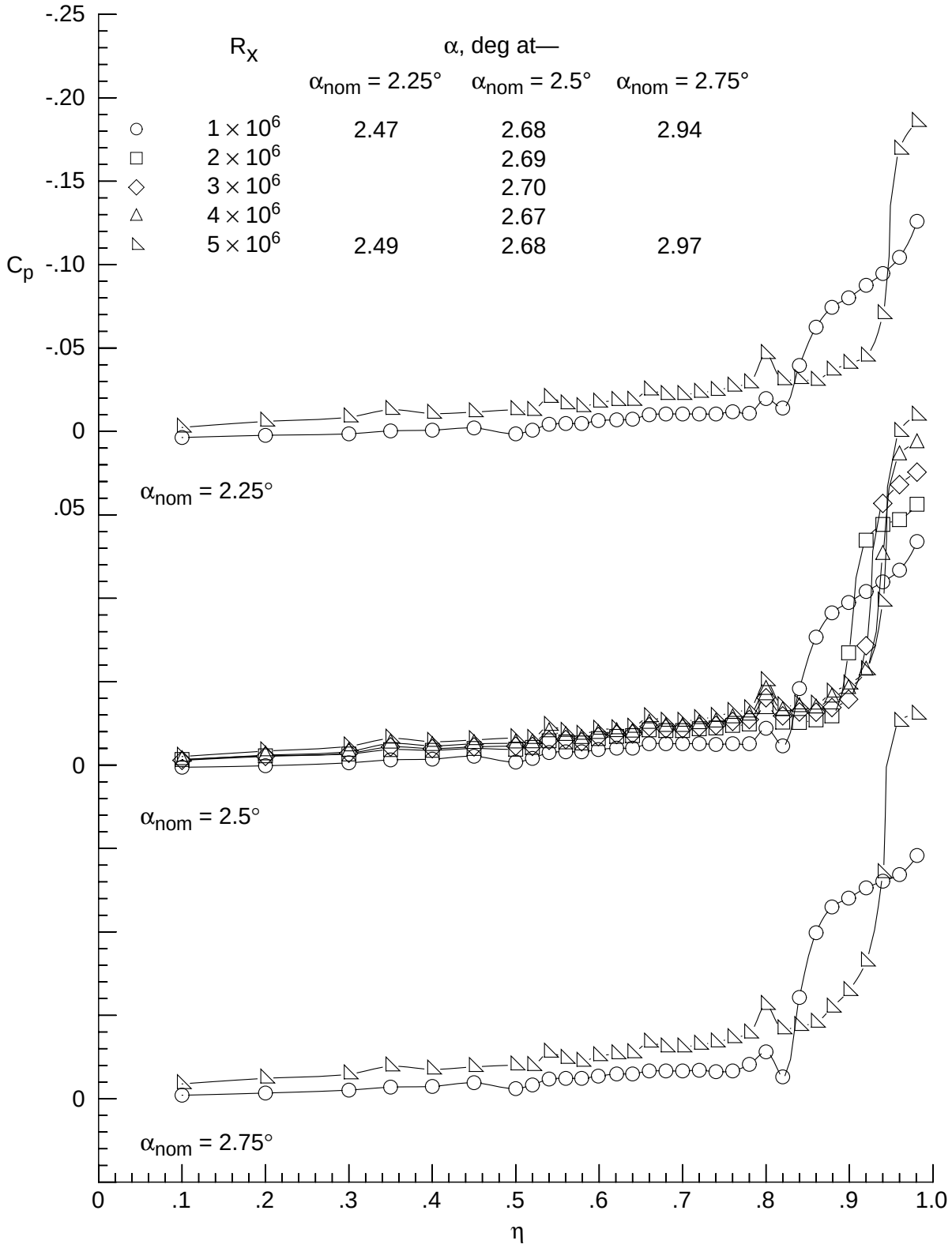

(b) α_{nom} = 2.25°, 2.5°, and 2.75°.

Figure 27. Concluded.

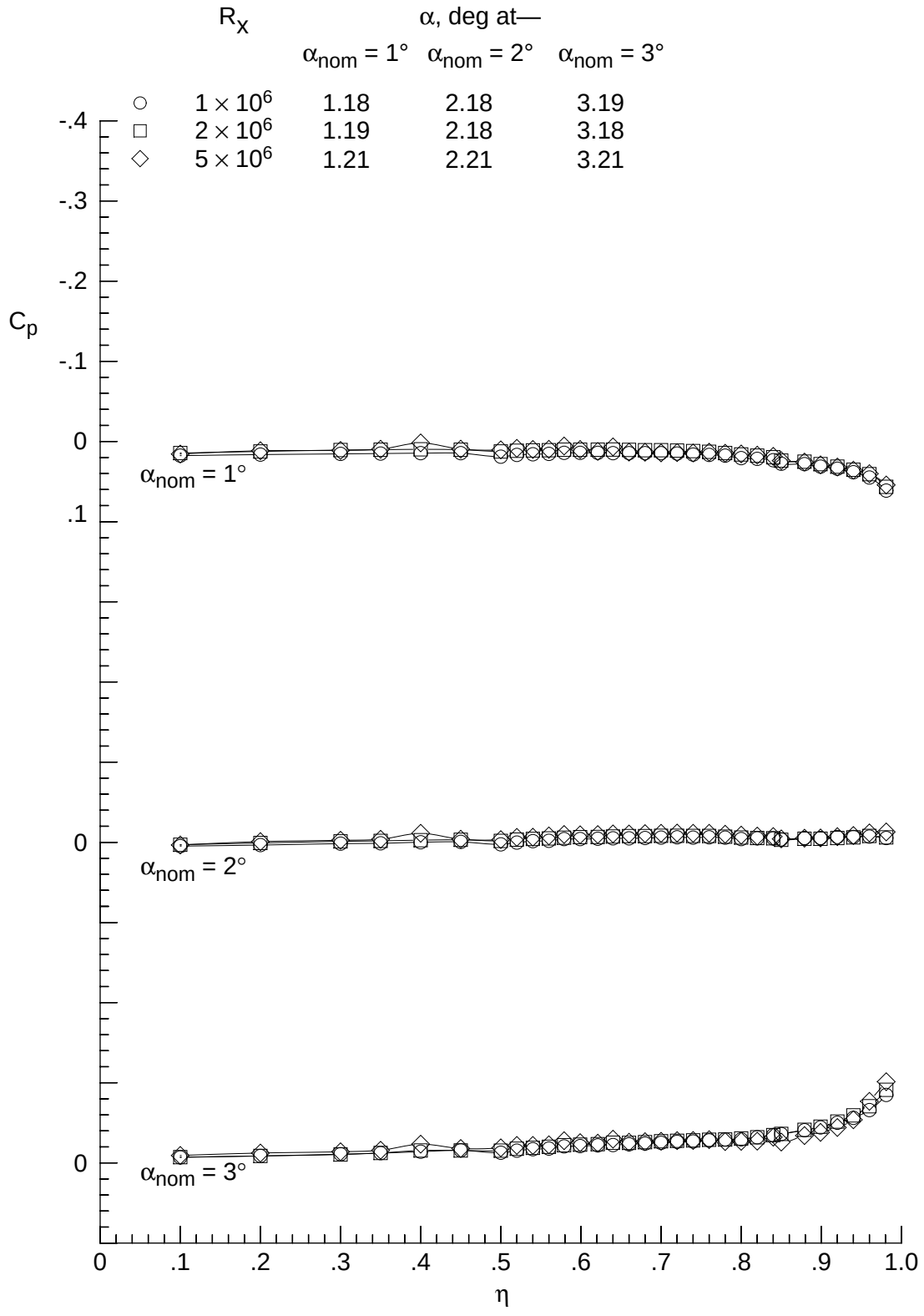

(a) α_{nom} = 1°, 2°, and 3°.

Figure 28. Effect of R_x on upper surface-pressure coefficient distribution for cambered wing without transition grit at x = 12 in. and M = 1.60.

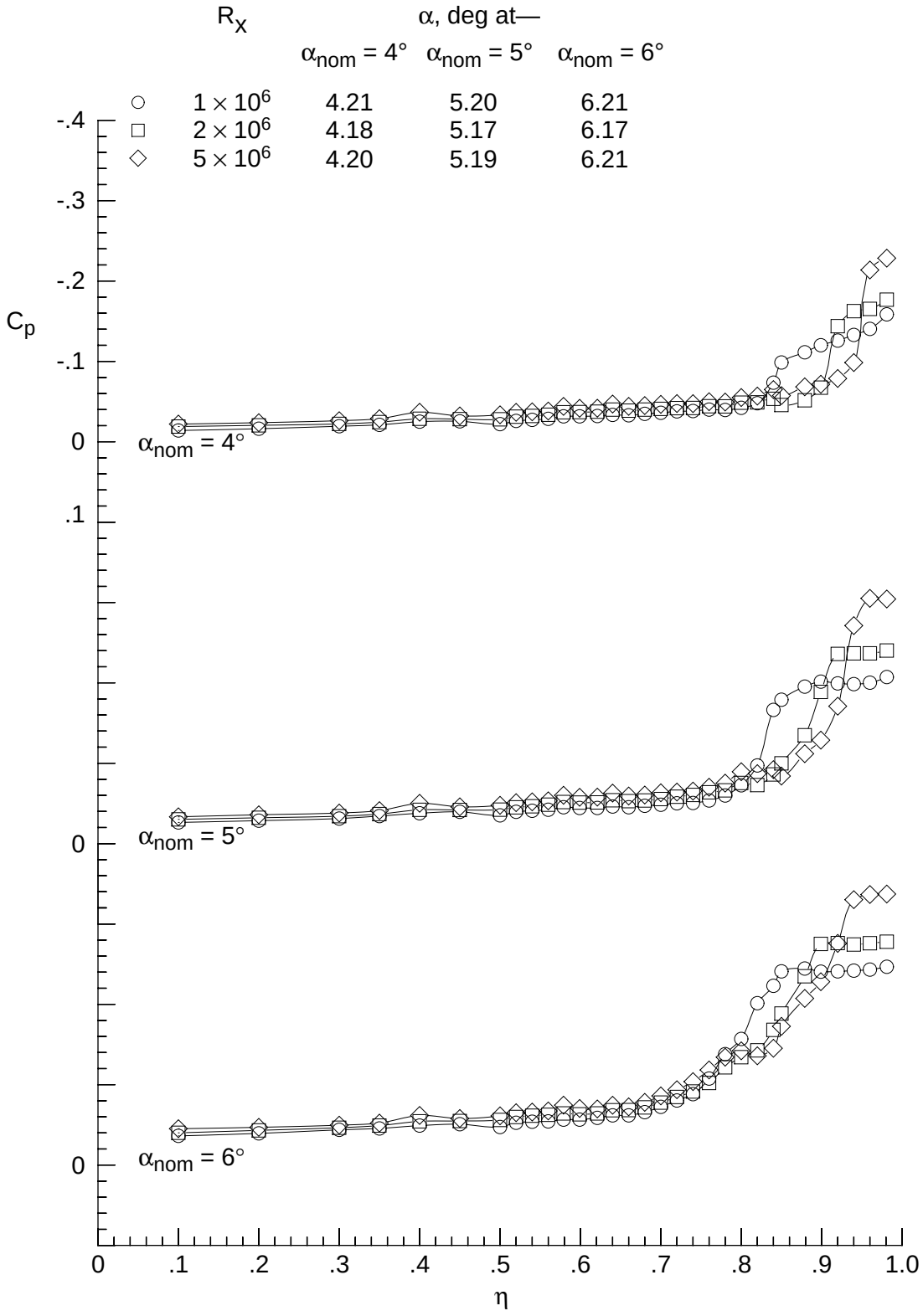

(b) α_{nom} = 4°, 5°, and 6°.

Figure 28. Continued.

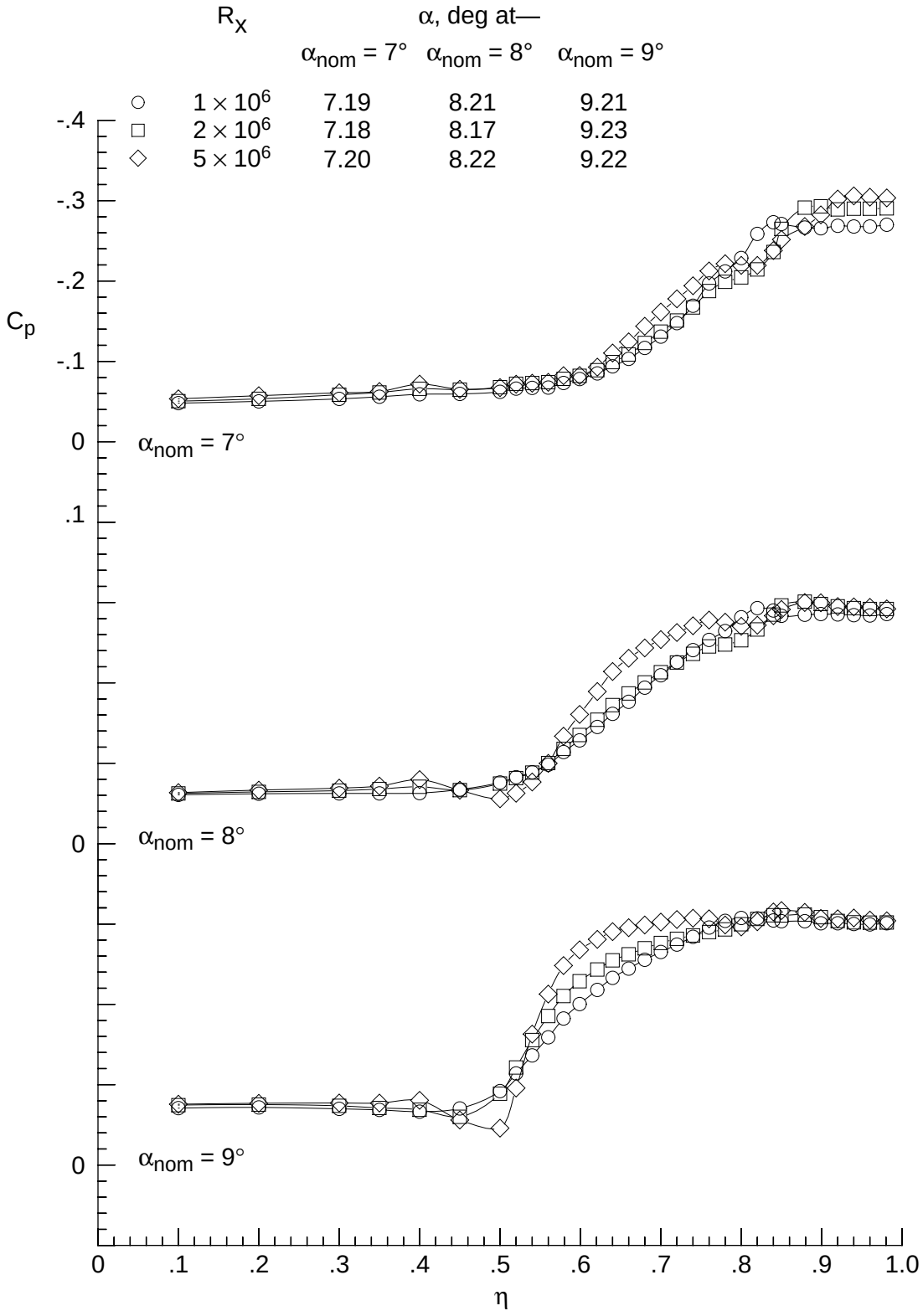

(c) α_{nom} = 7°, 8°, and 9°.

Figure 28. Concluded.

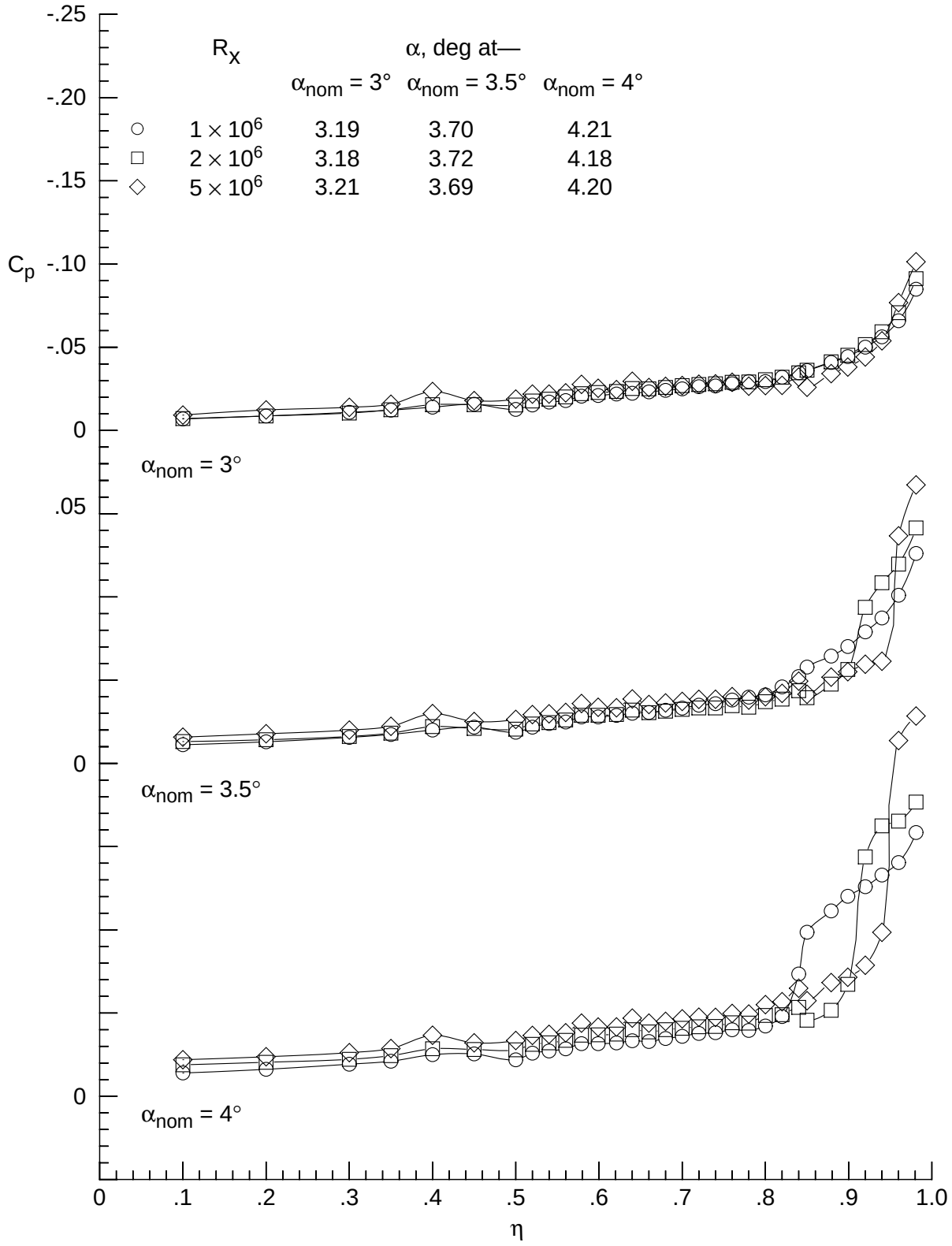

Figure 29. Effect of R_x on onset of leading-edge separation for cambered wing without transition grit at x = 12 in. and M = 1.60.

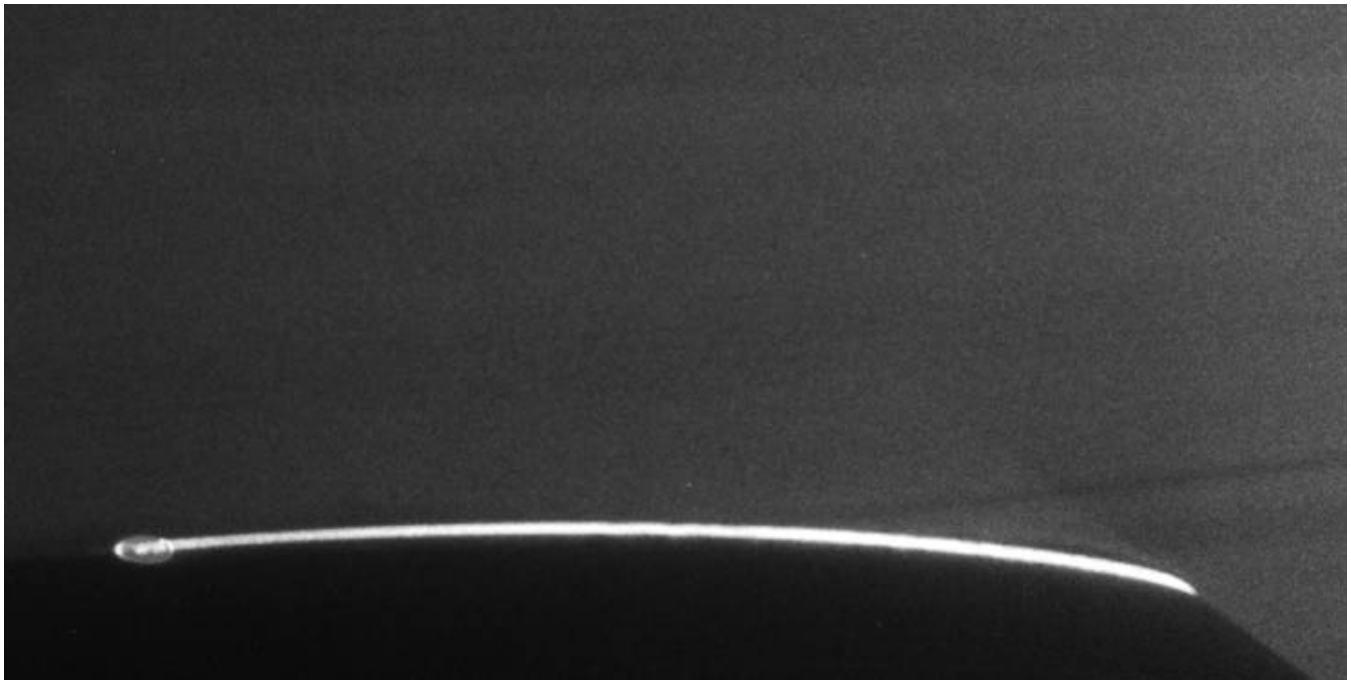

(a) $R_x = 1 \times 10^6$ and $\alpha = 5.20°$.

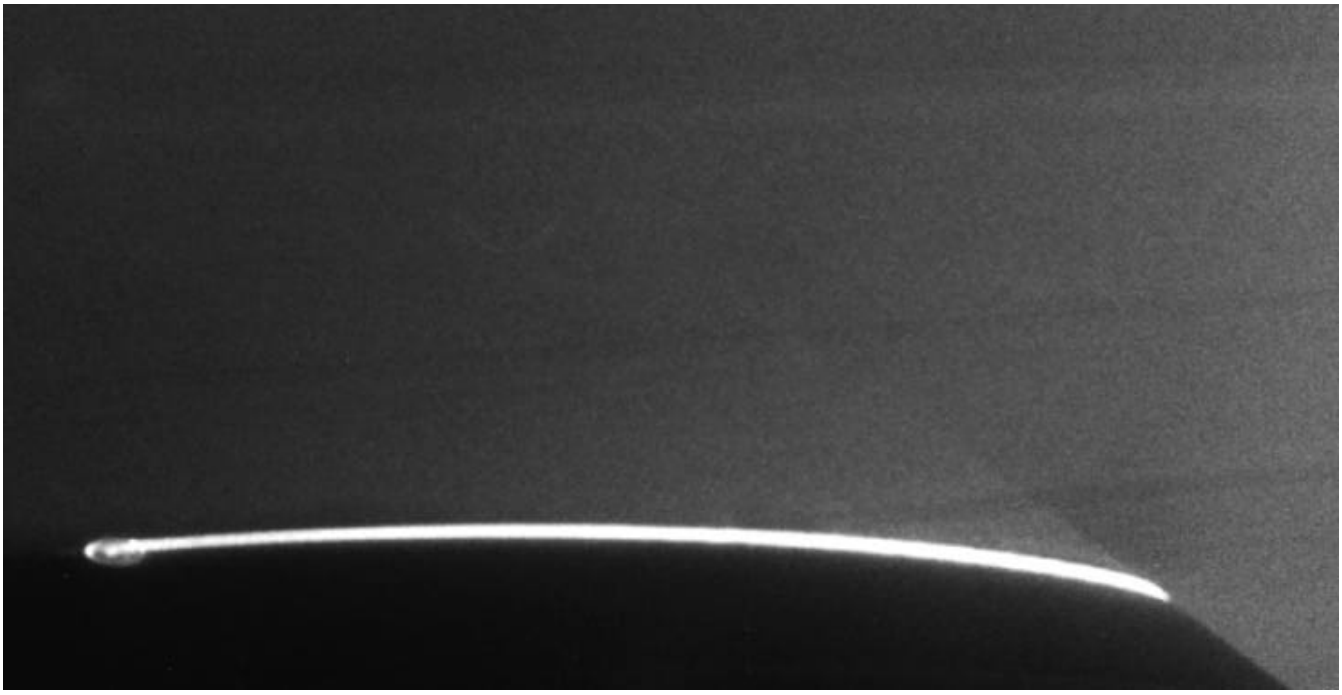

(b) $R_x = 2 \times 10^6$ and $\alpha = 5.20°$.

Figure 30. Vapor-screen photographs illustrating effect of R_x on flow structure over leeside of cambered wing without transition grit at x = 12 in., $\alpha_{nom} = 5°$, and M = 1.60.

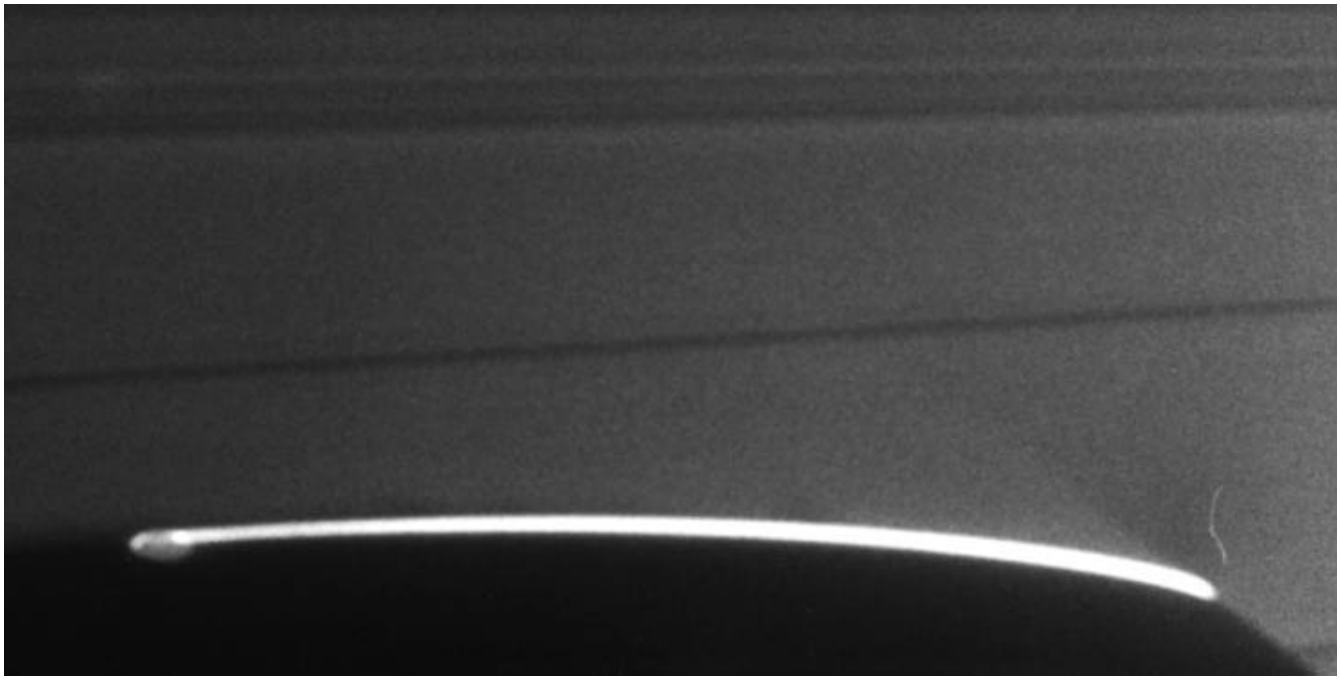

(c) $R_x = 5 \times 10^6$ and $\alpha = 5.20°$.

Figure 30. Concluded.

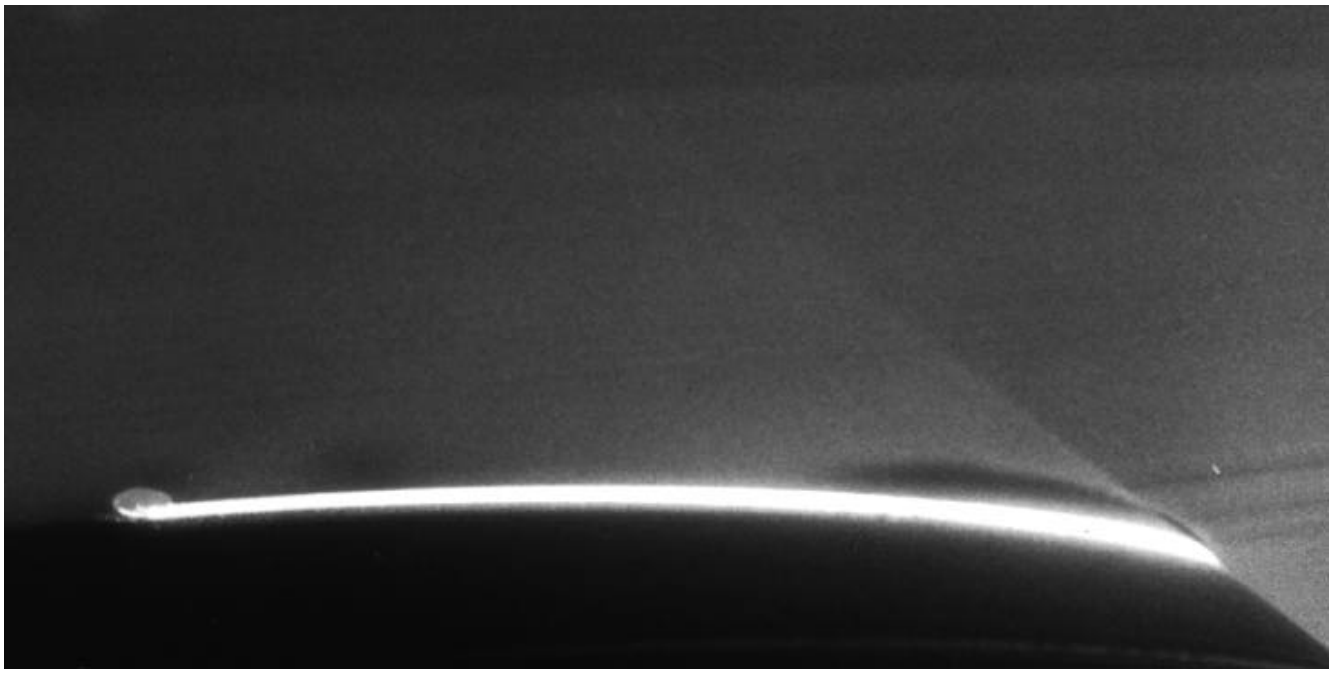

(a) $R_x = 1 \times 10^6$ and $\alpha = 8.20°$.

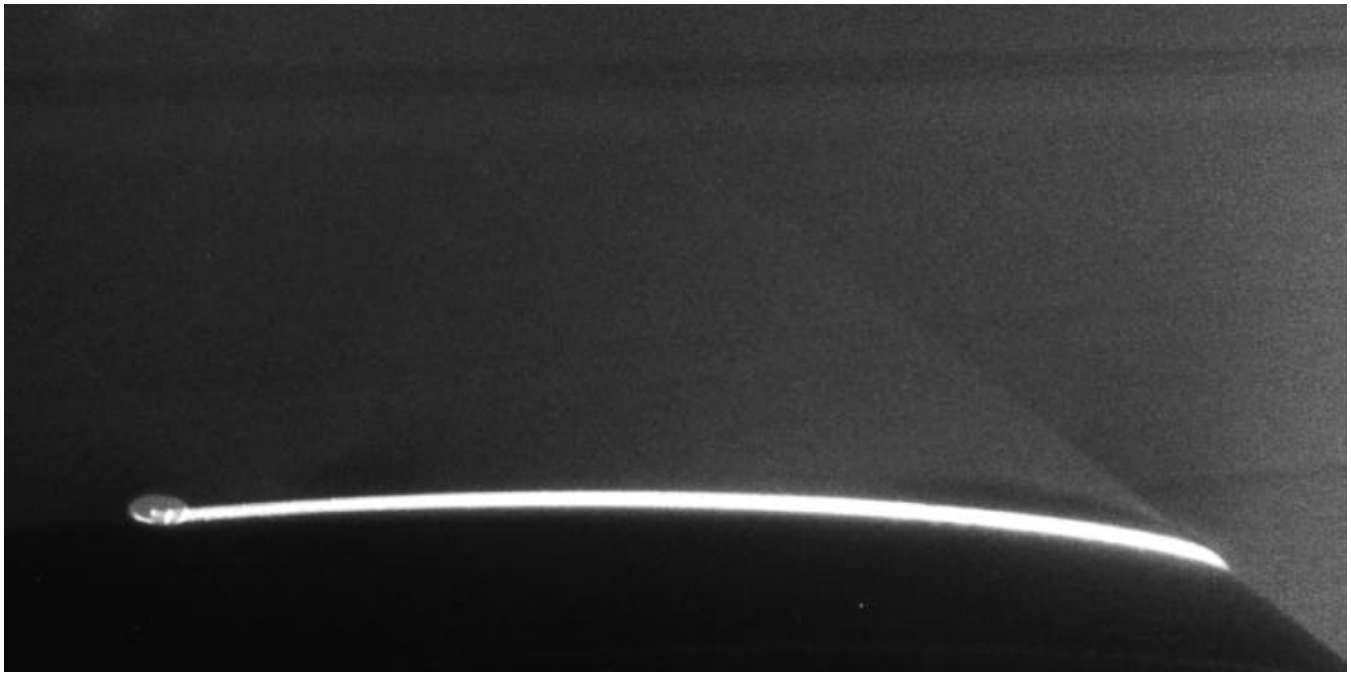

(b) $R_x = 2 \times 10^6$ and $\alpha = 8.20°$.

Figure 31. Vapor-screen photographs illustrating effect of R_x on flow structure over leeside of cambered wing without transition grit at x = 12 in., $\alpha_{nom} = 8°$, and M = 1.60.

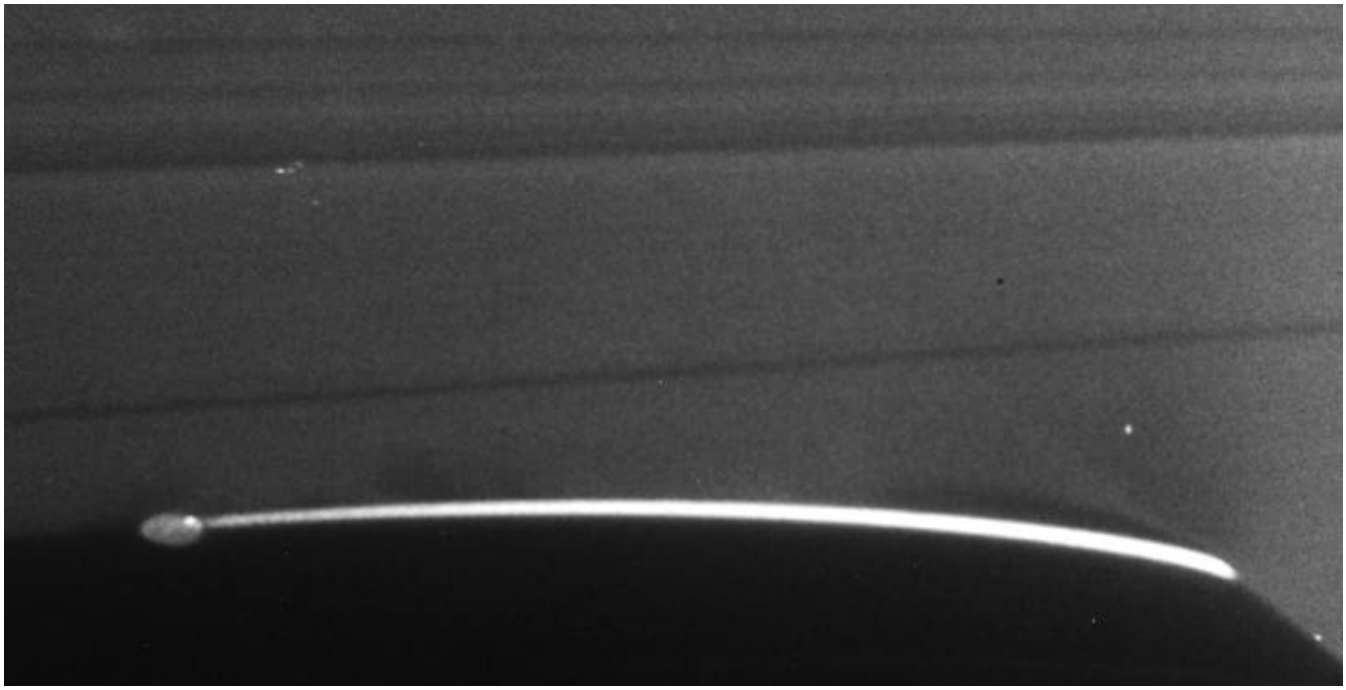

(c) $R_x = 5 \times 10^6$ and $\alpha = 8.20°$.

Figure 31. Concluded.

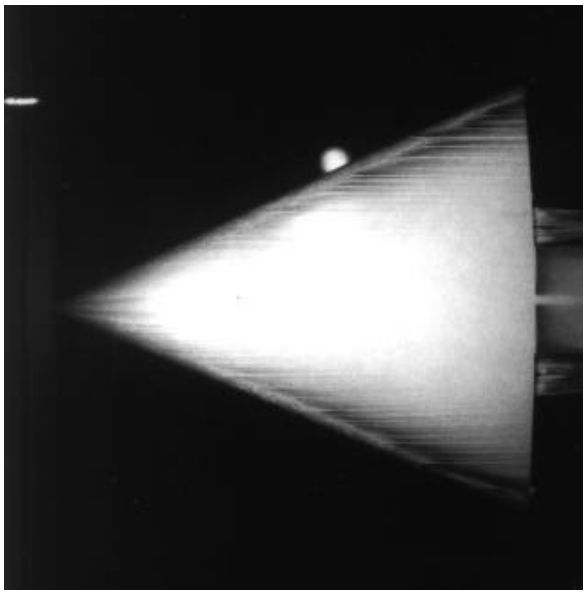

(a) $R = 1 \times 10^6$ ft^{-1} and $\alpha = 4.06°$.

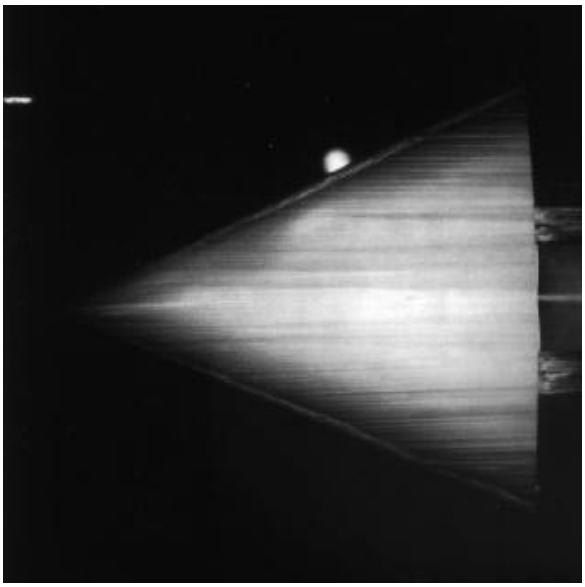

(b) $R = 2 \times 10^6$ ft^{-1} and $\alpha = 4.17°$.

(c) $R = 5 \times 10^6$ ft^{-1} and $\alpha = 4.34°$.

Figure 32. Painted-oil-flow photographs illustrating effect of Reynolds number on flow structure on leeside of cambered wing without transition grit at $\alpha_{nom} = 4°$ and $M = 1.60$.

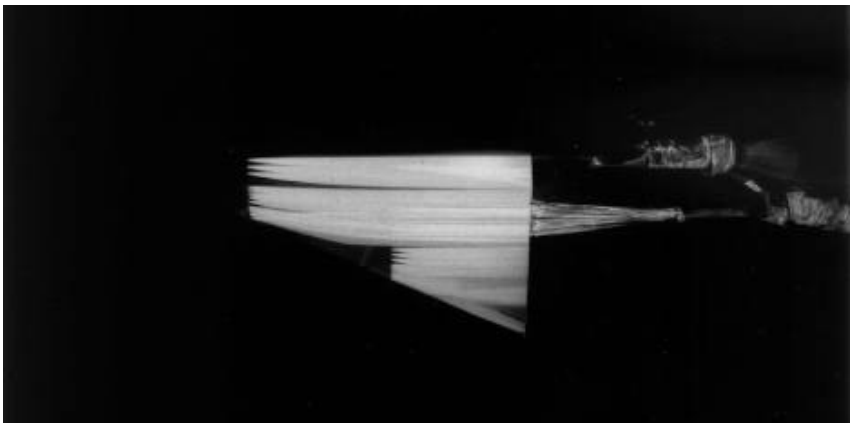

(a) $R = 1 \times 10^6$ ft^{-1} and $\alpha = 4.00°$.

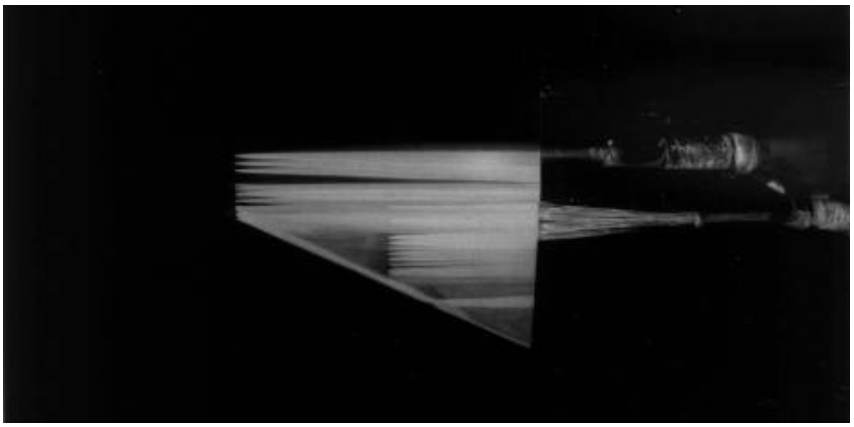

(b) $R = 2 \times 10^6$ ft^{-1} and $\alpha = 4.00°$.

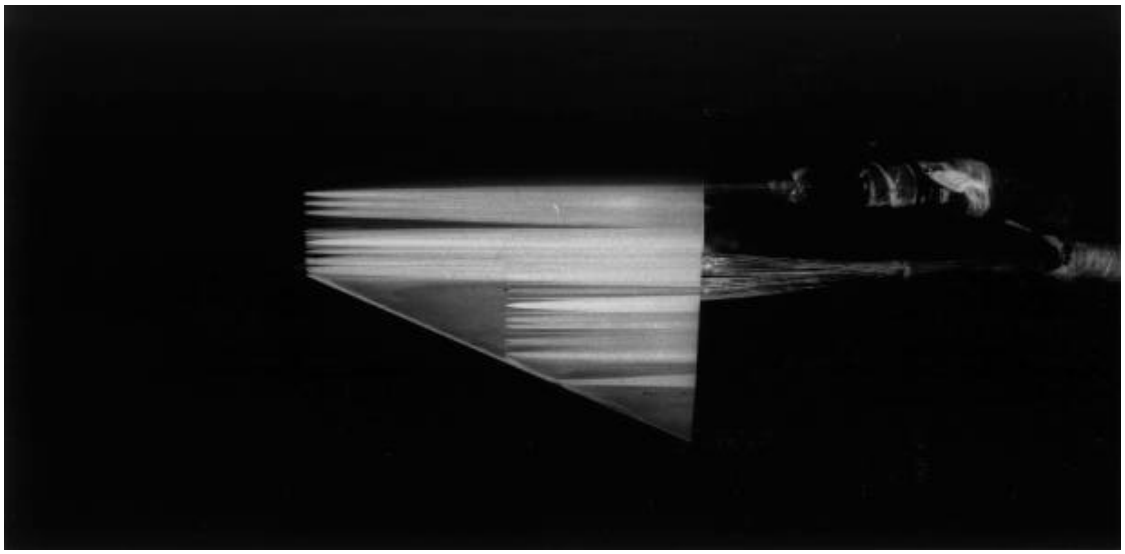

(c) $R = 5 \times 10^6$ ft^{-1} and $\alpha = 4.00°$.

Figure 33. Injected-oil-flow photographs illustrating effect of Reynolds number on flow structure on leeside of cambered wing without transition grit at $\alpha_{nom} = 4°$ and $M = 1.60$.

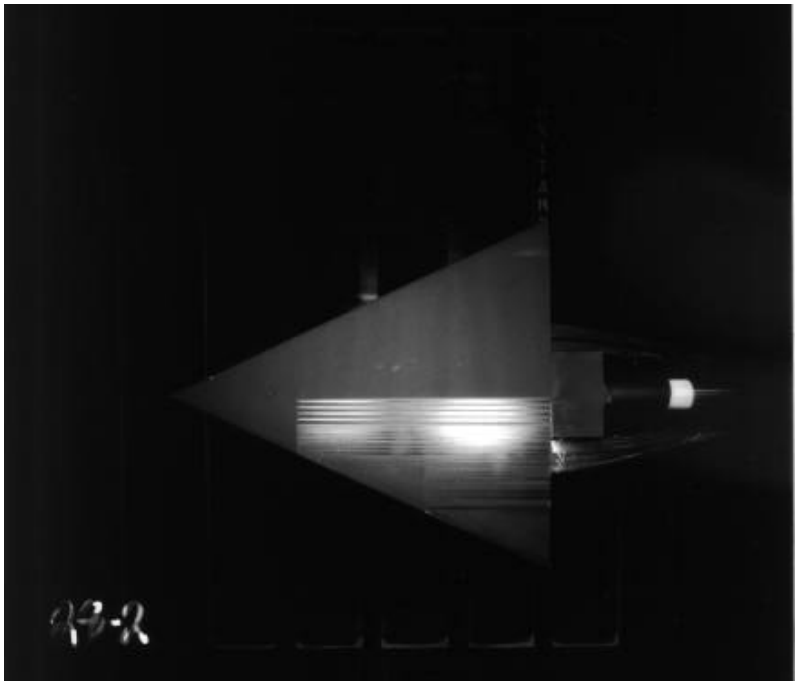

(a) $\alpha = 2.17°$.

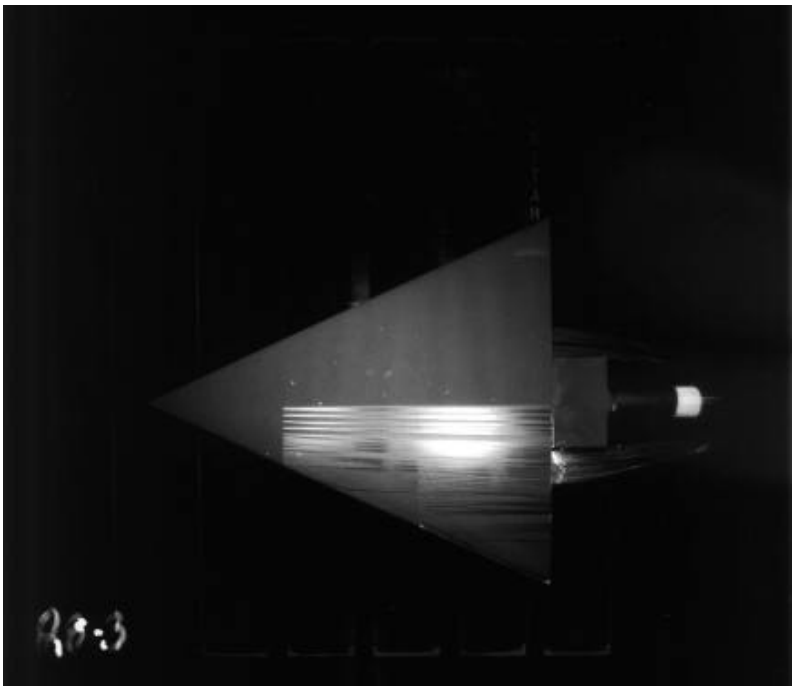

(b) $\alpha = 3.25°$.

Figure 34. Injected-oil-flow photographs of leeside of elliptical wing without transition grit at $\alpha_{nom} = 2°$ and 3°, $M = 1.60$, and $R = 5 \times 10^6$ ft^{-1}.

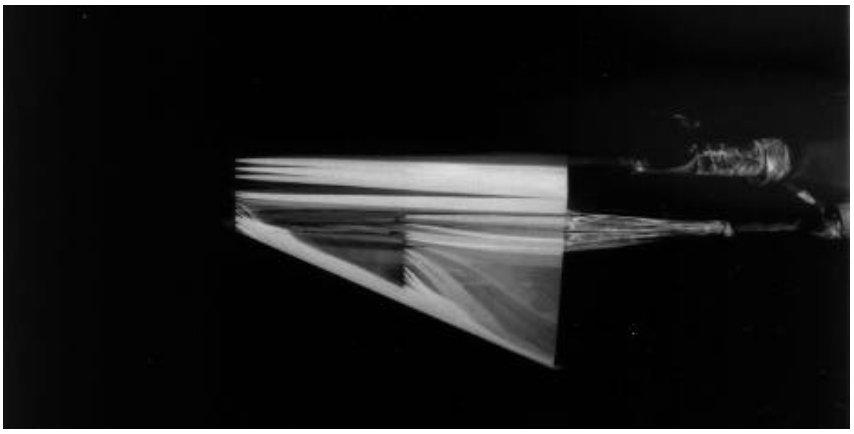

(a) $R = 1 \times 10^6$ ft^{-1} and $\alpha = 8.00°$.

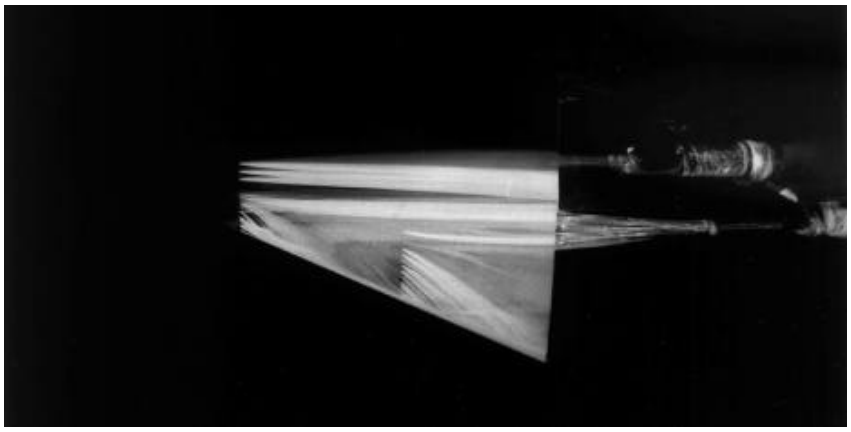

(b) $R = 2 \times 10^6$ ft^{-1} and $\alpha = 8.00°$.

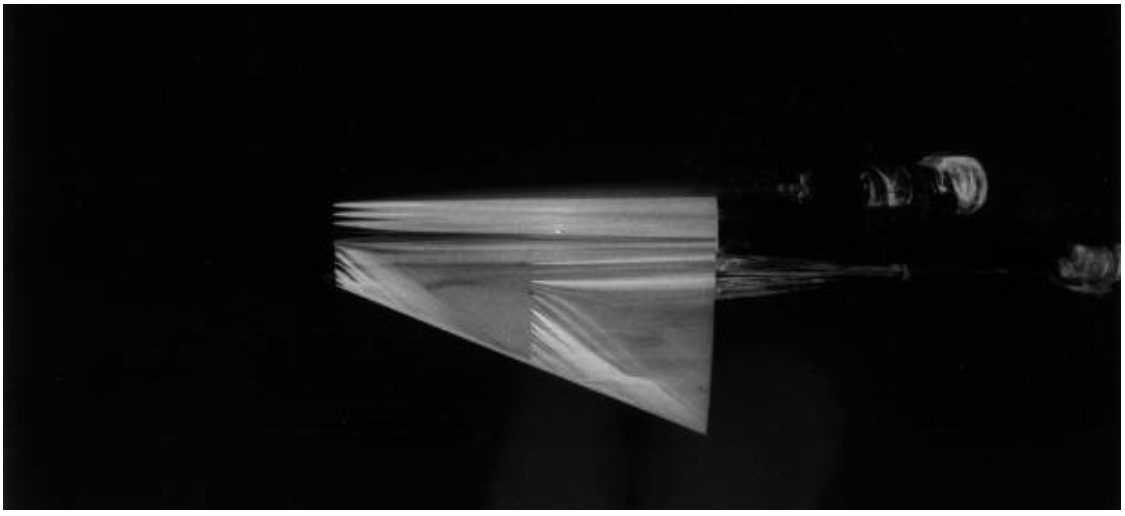

(c) $R = 5 \times 10^6$ ft^{-1} and $\alpha = 8.00°$.

Figure 35. Injected-oil-flow photographs illustrating effect of Reynolds number on flow structure on leeside of cambered wing without transition grit at $\alpha_{nom} = 8°$ and $M = 1.60$.

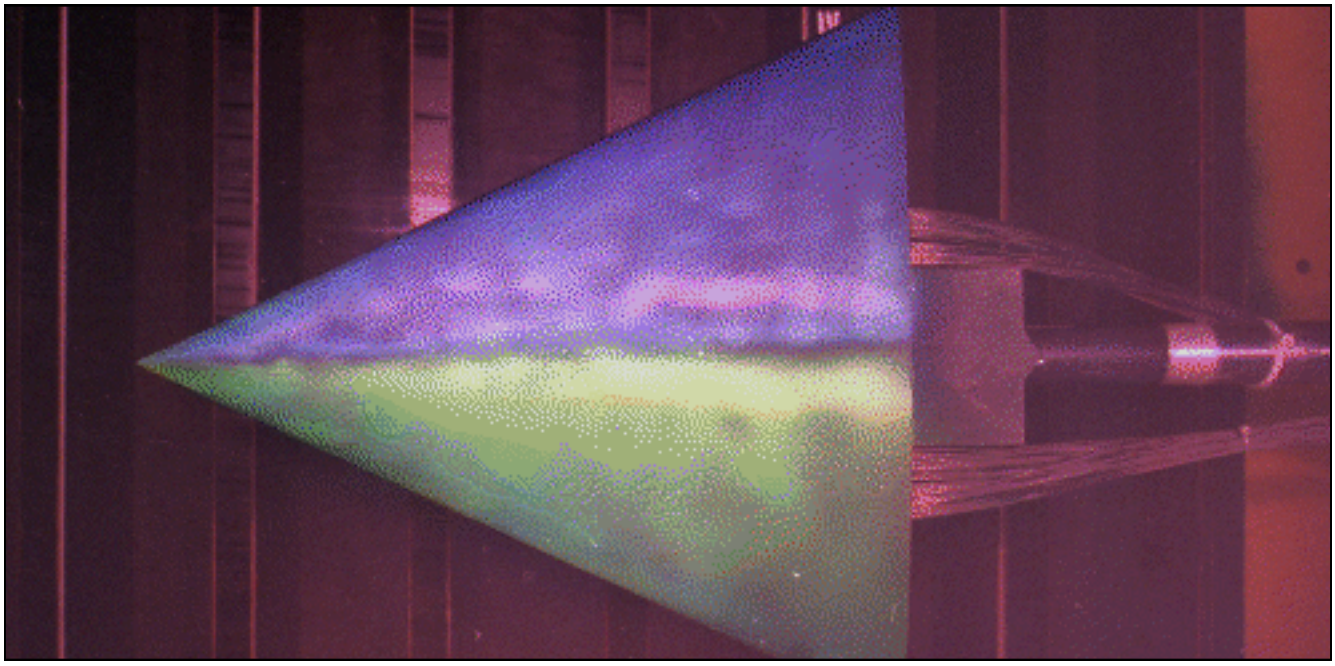

(a) $\alpha = 0°$.

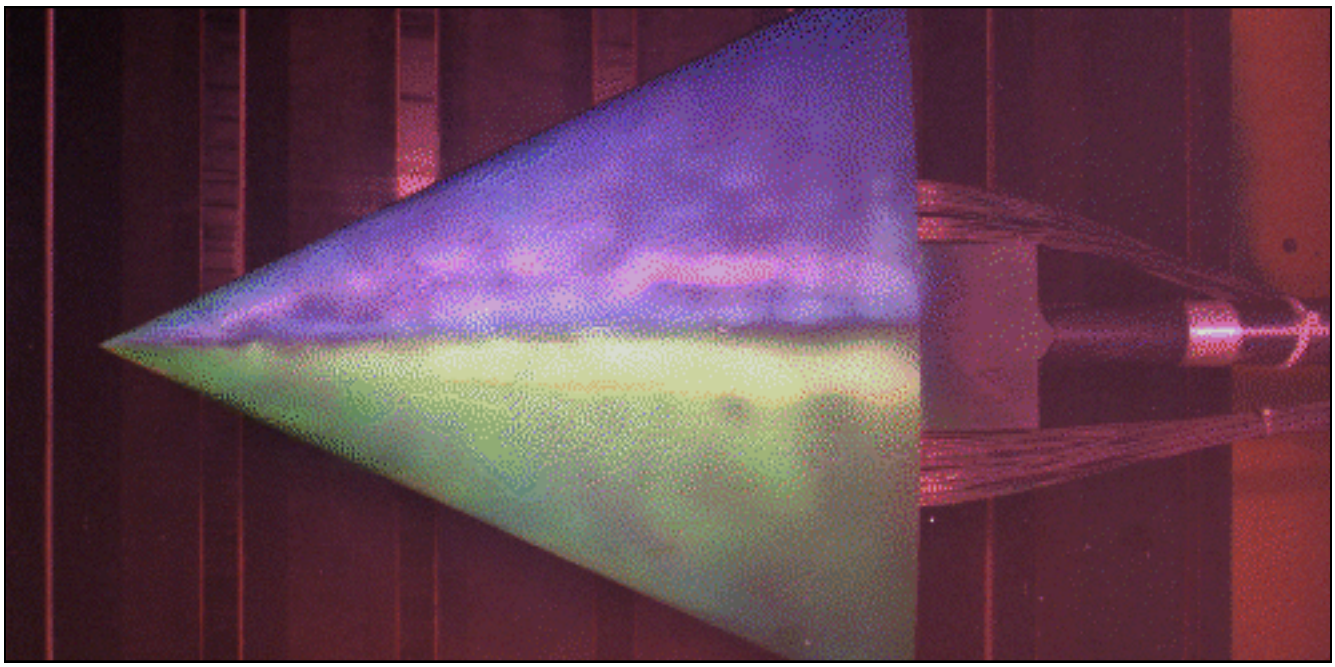

(b) $\alpha = 1.10°$.

Figure 36. Liquid-crystal photographs illustrating vortex growth with angle of attack on leeside of elliptical wing without transition grit at $M = 1.60$, $R = 5 \times 10^6$ ft^{-1}, and $T_o = 125°$F.

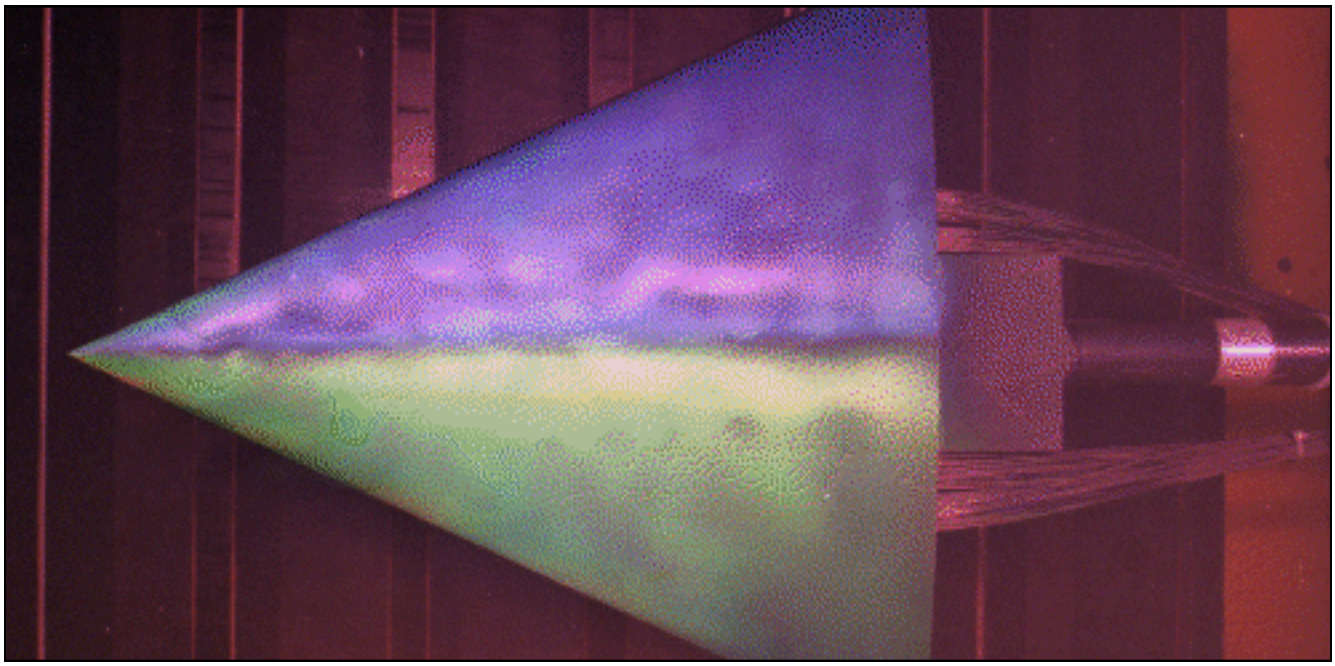

(c) $\alpha = 2.17°$.

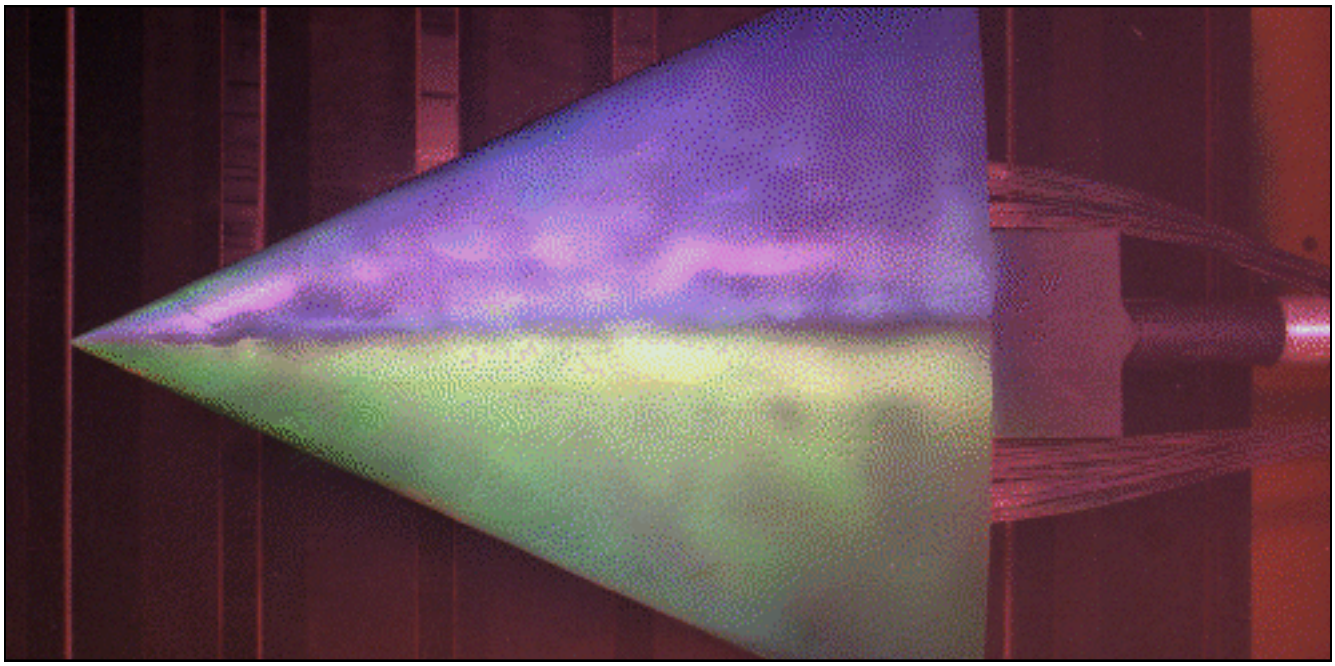

(d) $\alpha = 3.25°$.

Figure 36. Concluded.

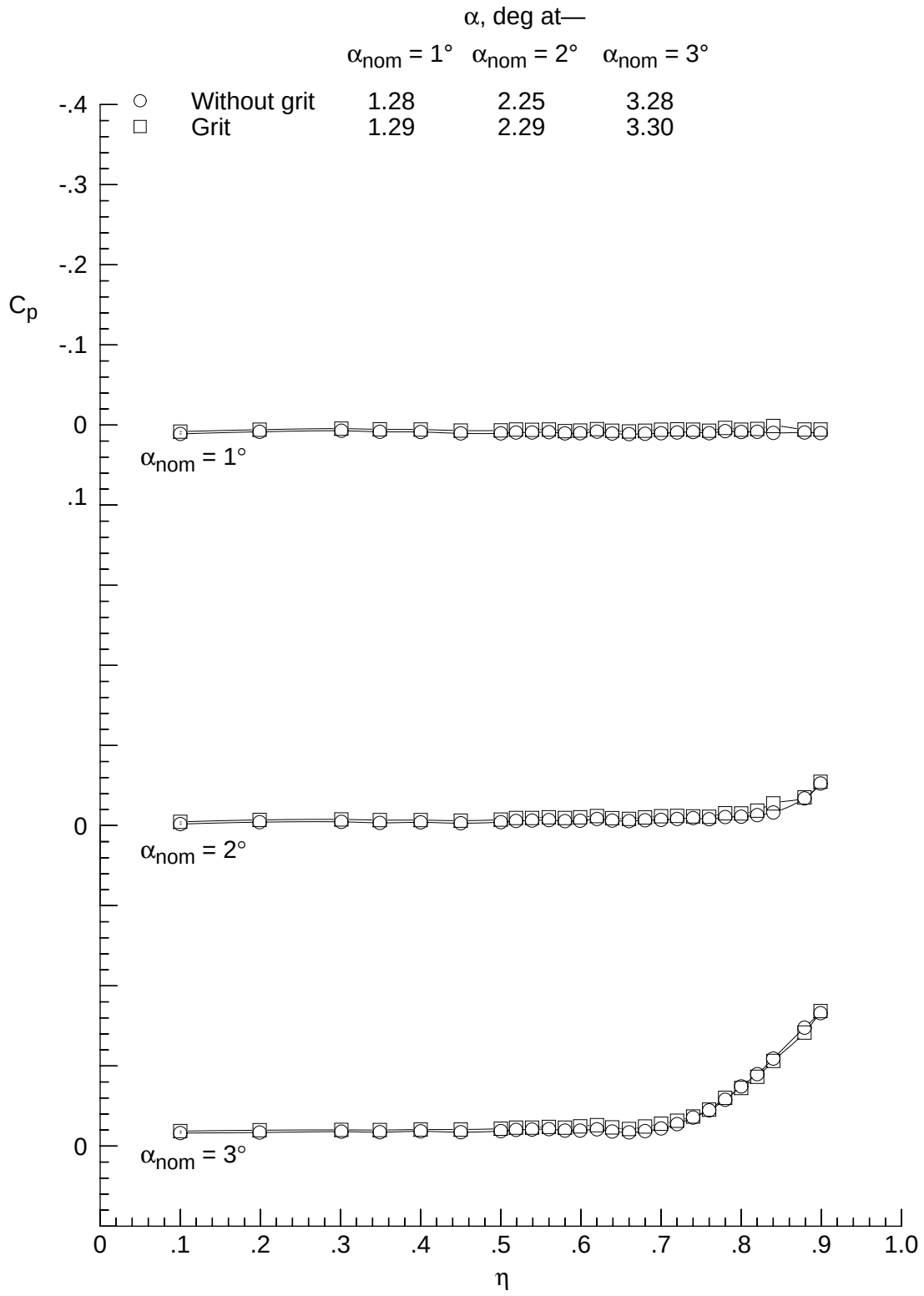

(a) α_{nom} = 1°, 2°, and 3°.

Figure 37. Effect of transition grit on upper surface-pressure coefficient distribution for sharp wing at x = 12 in., M = 1.60, and $R = 2 \times 10^6$ ft^{-1}.

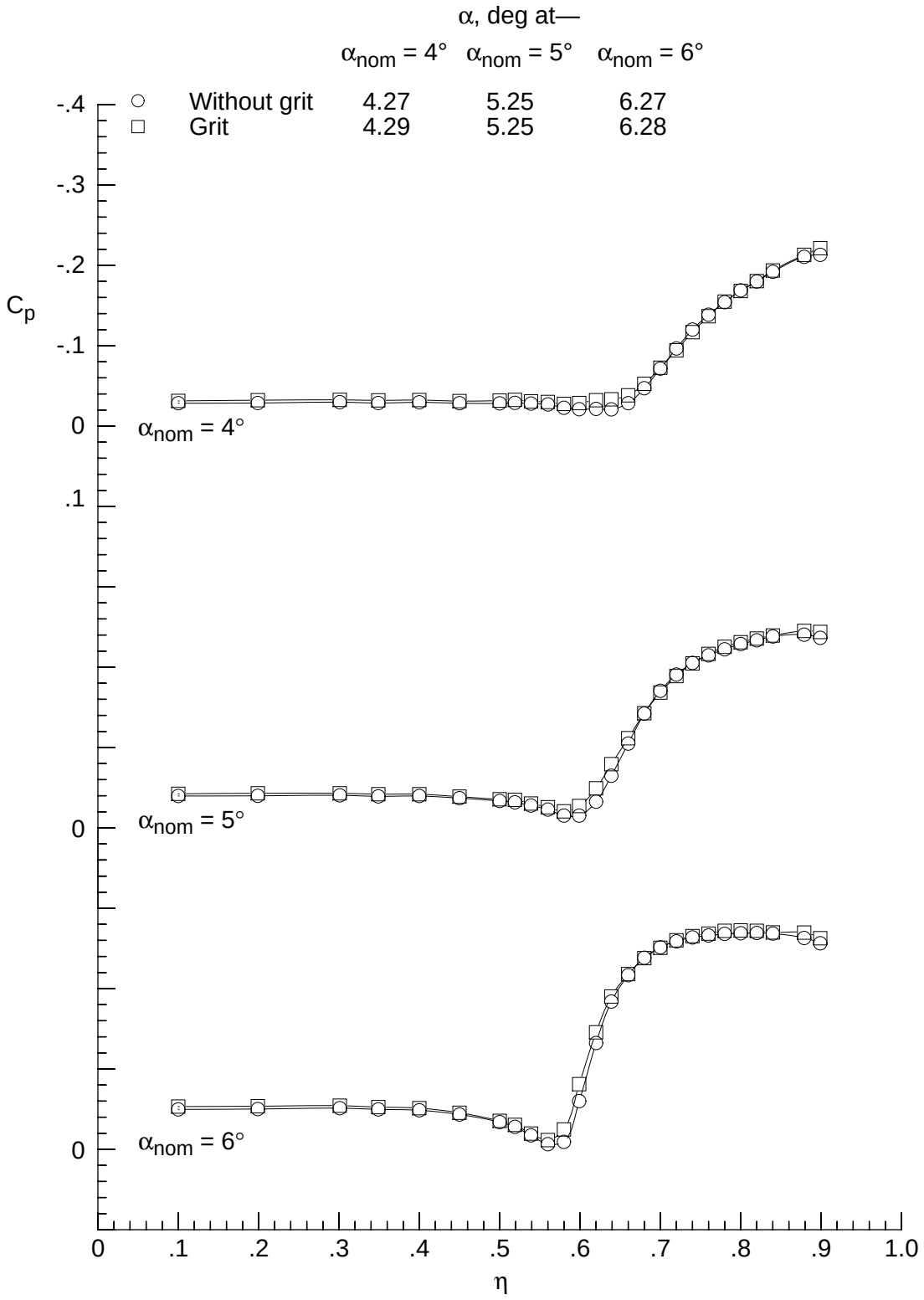

(b) α_{nom} = 4°, 5°, and 6°.

Figure 37. Continued.

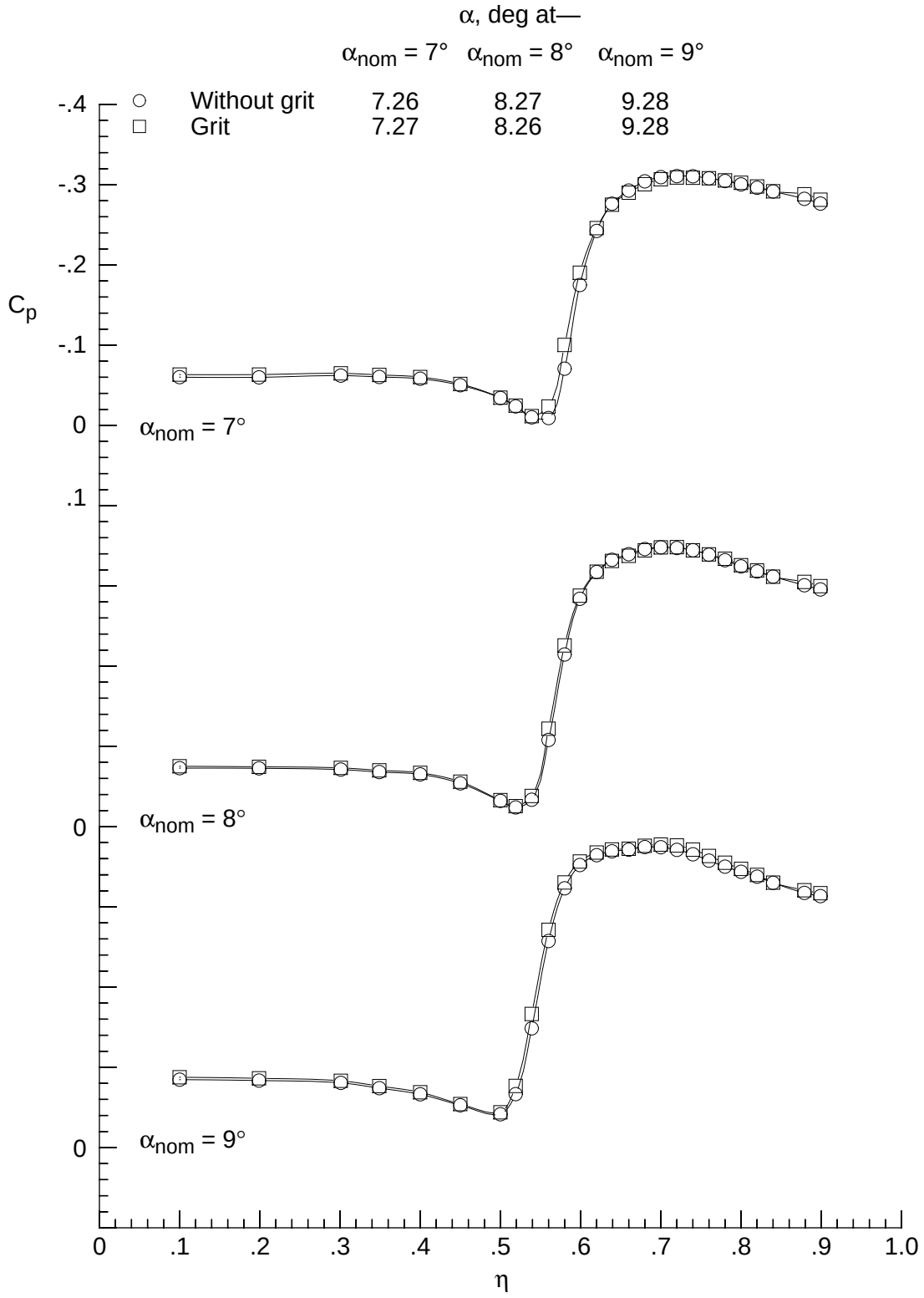

(c) α_{nom} = 7°, 8°, and 9°.

Figure 37. Concluded.

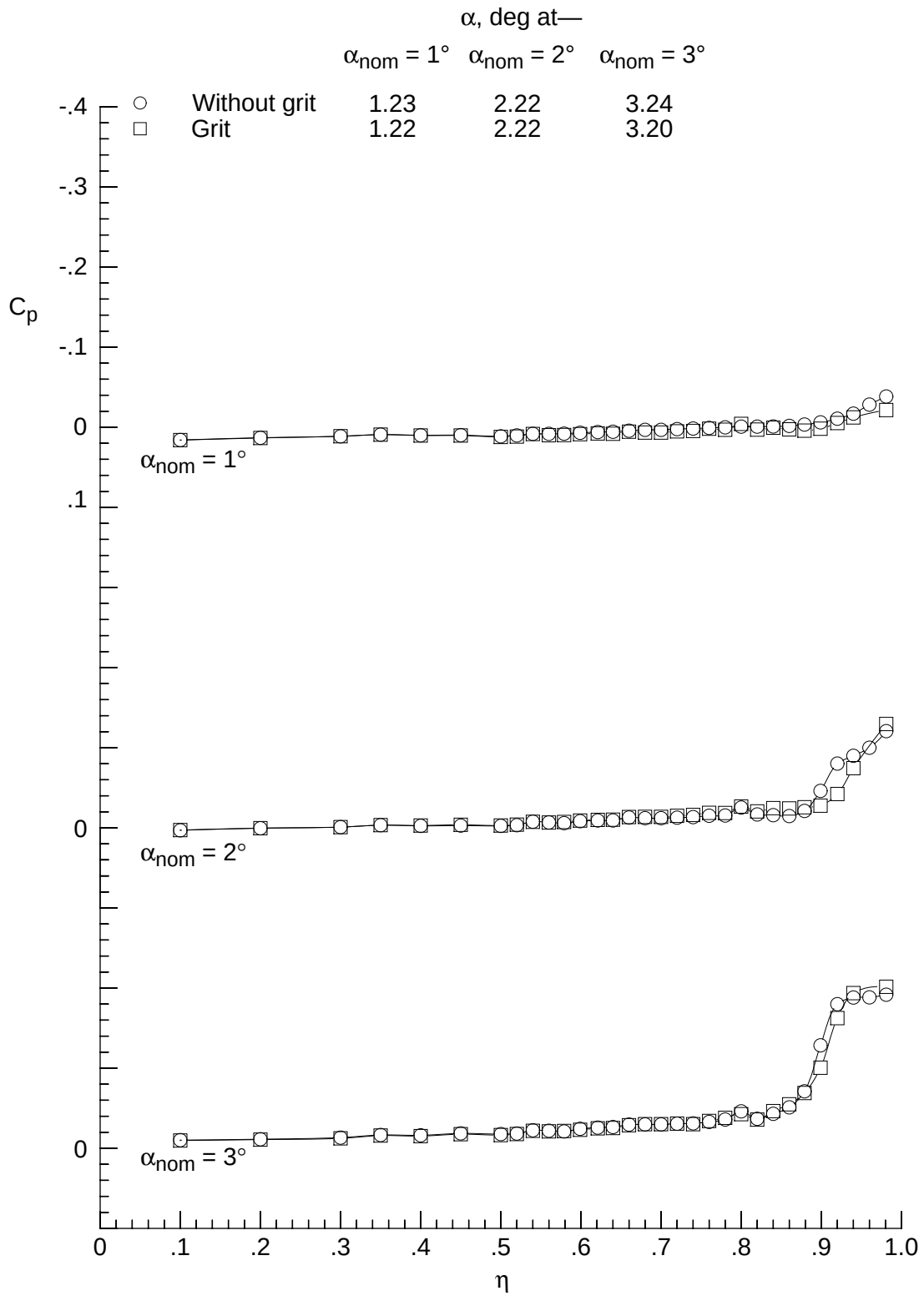

(a) α_{nom} = 1°, 2°, and 3°.

Figure 38. Effect of transition grit on upper surface-pressure coefficient distribution for elliptical wing at x = 12 in., M = 1.60, and $R = 2 \times 10^6$ ft^{-1}.

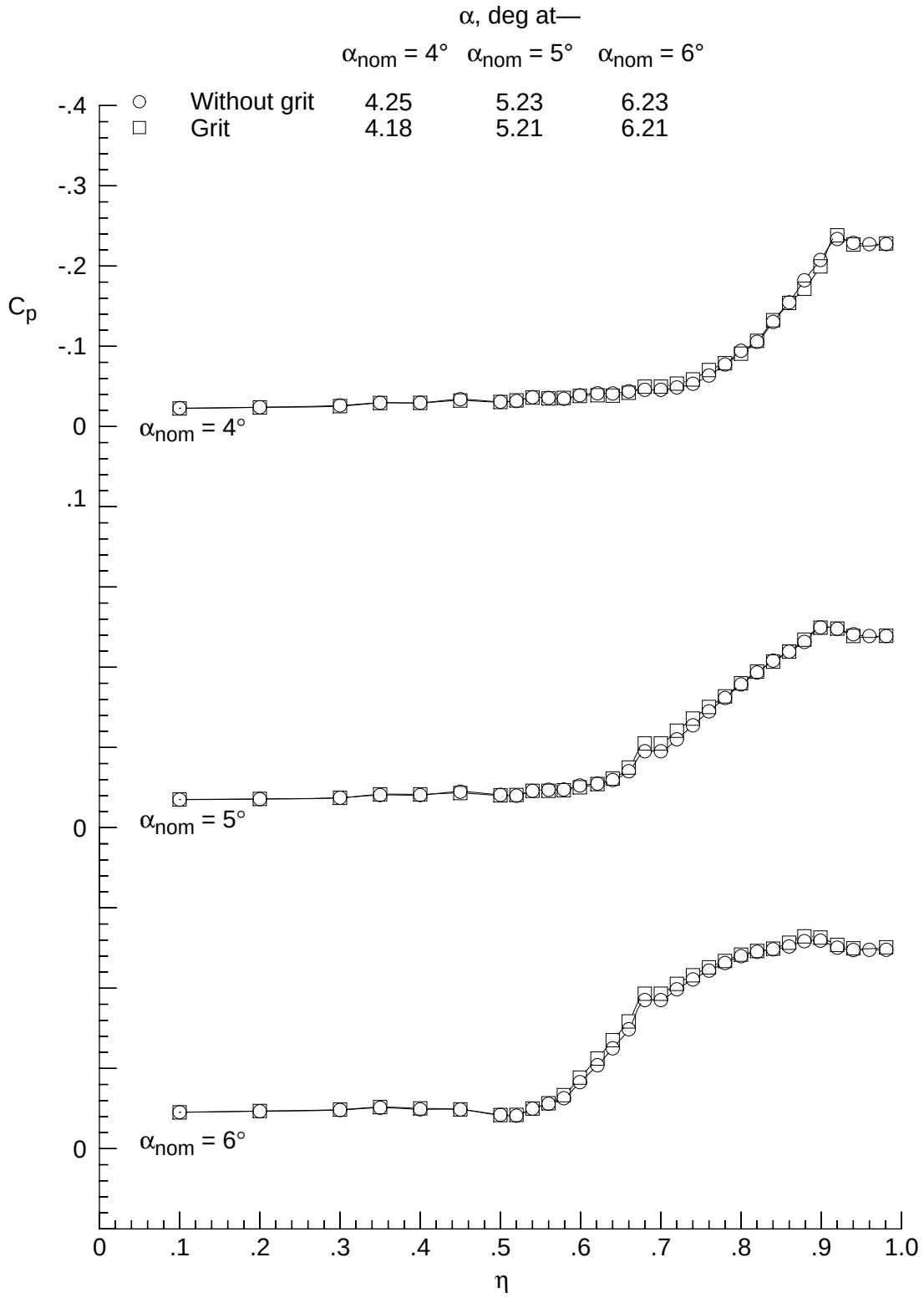

(b) α_{nom} = 4°, 5°, and 6°.

Figure 38. Continued.

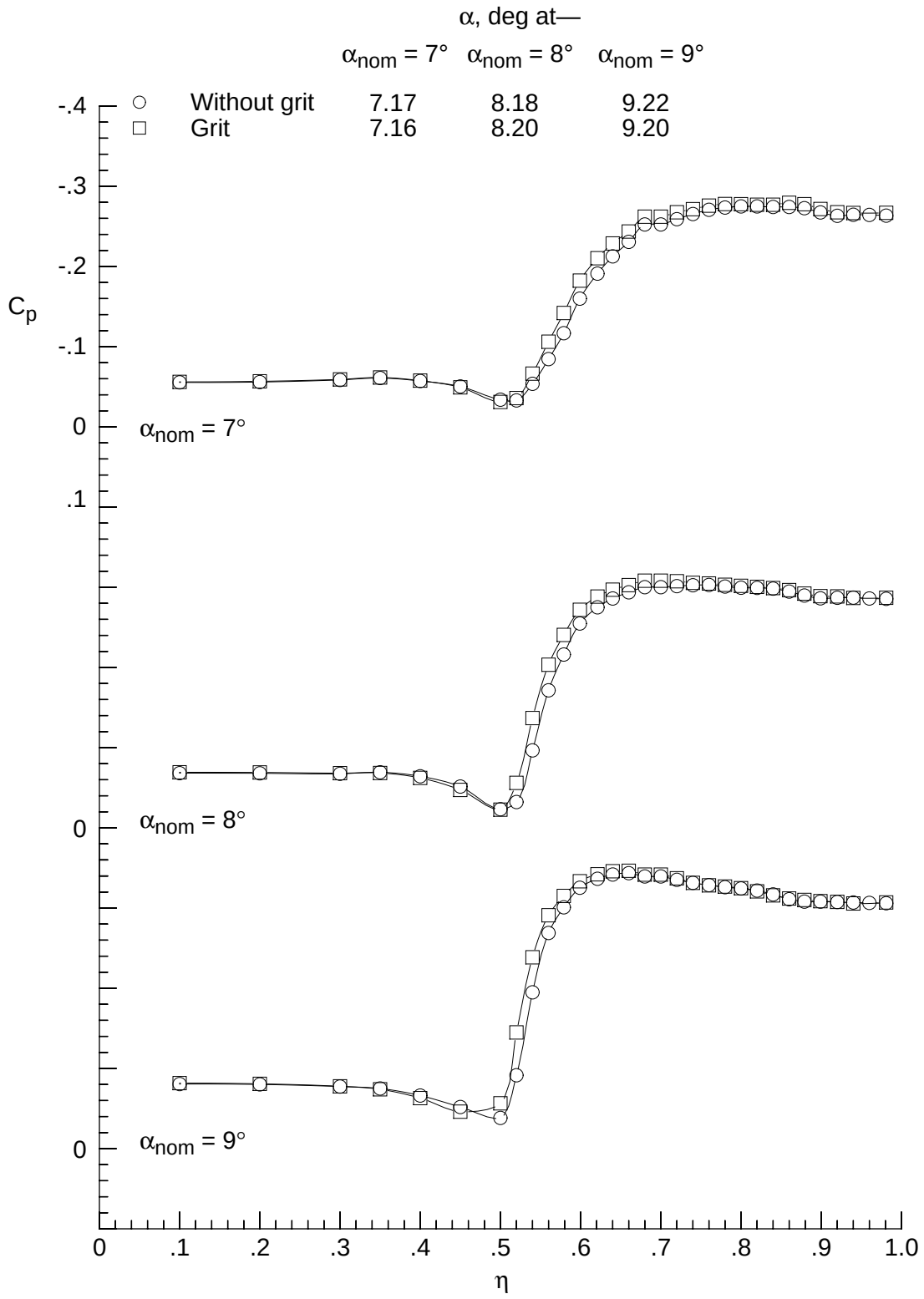

(c) α_{nom} = 7°, 8°, and 9°.

Figure 38. Concluded.

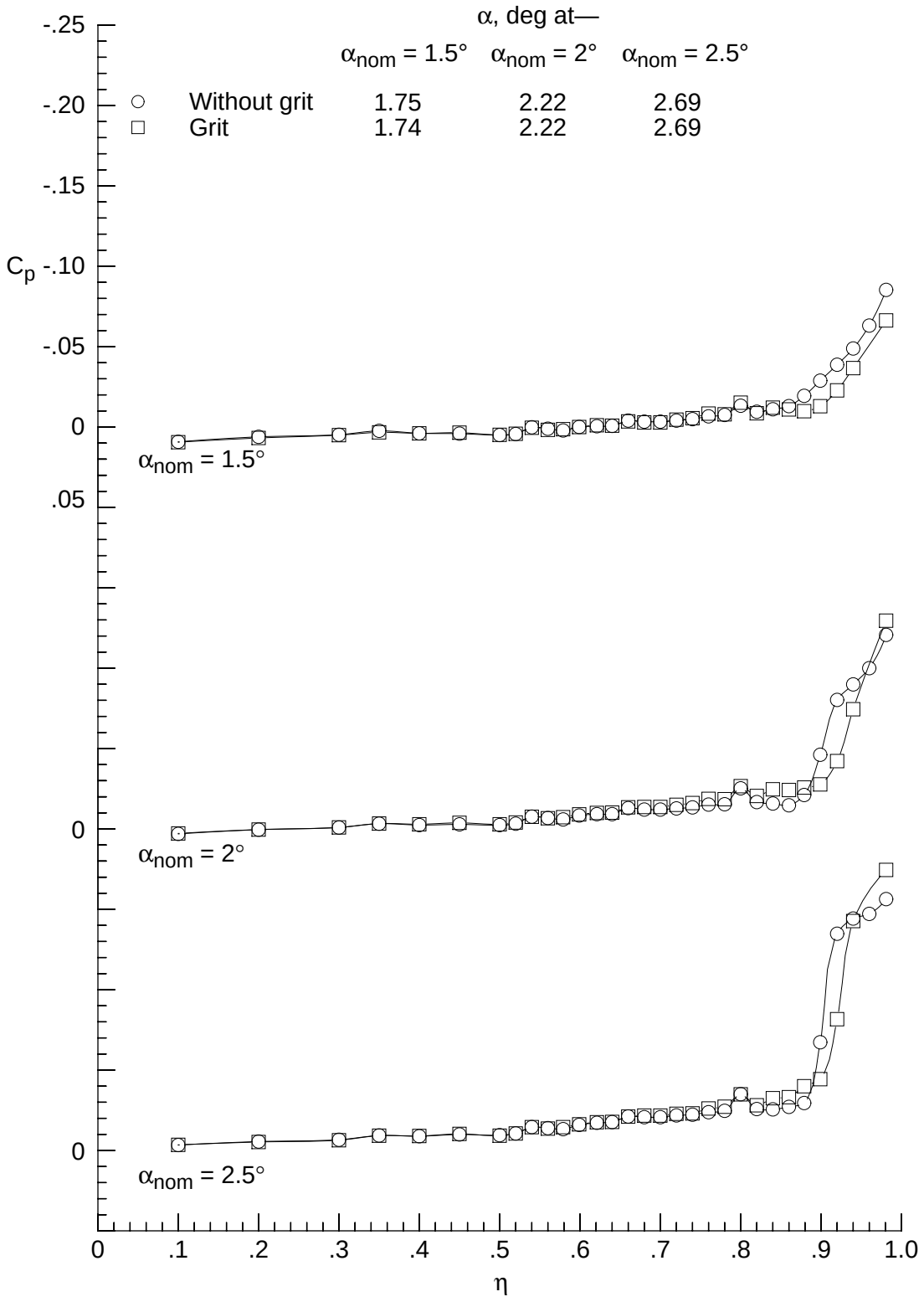

Figure 39. Effect of transition grit on onset of leading-edge separation for elliptical wing at $x = 12$ in., $M = 1.60$, and $R = 2 \times 10^6$ ft^{-1}.

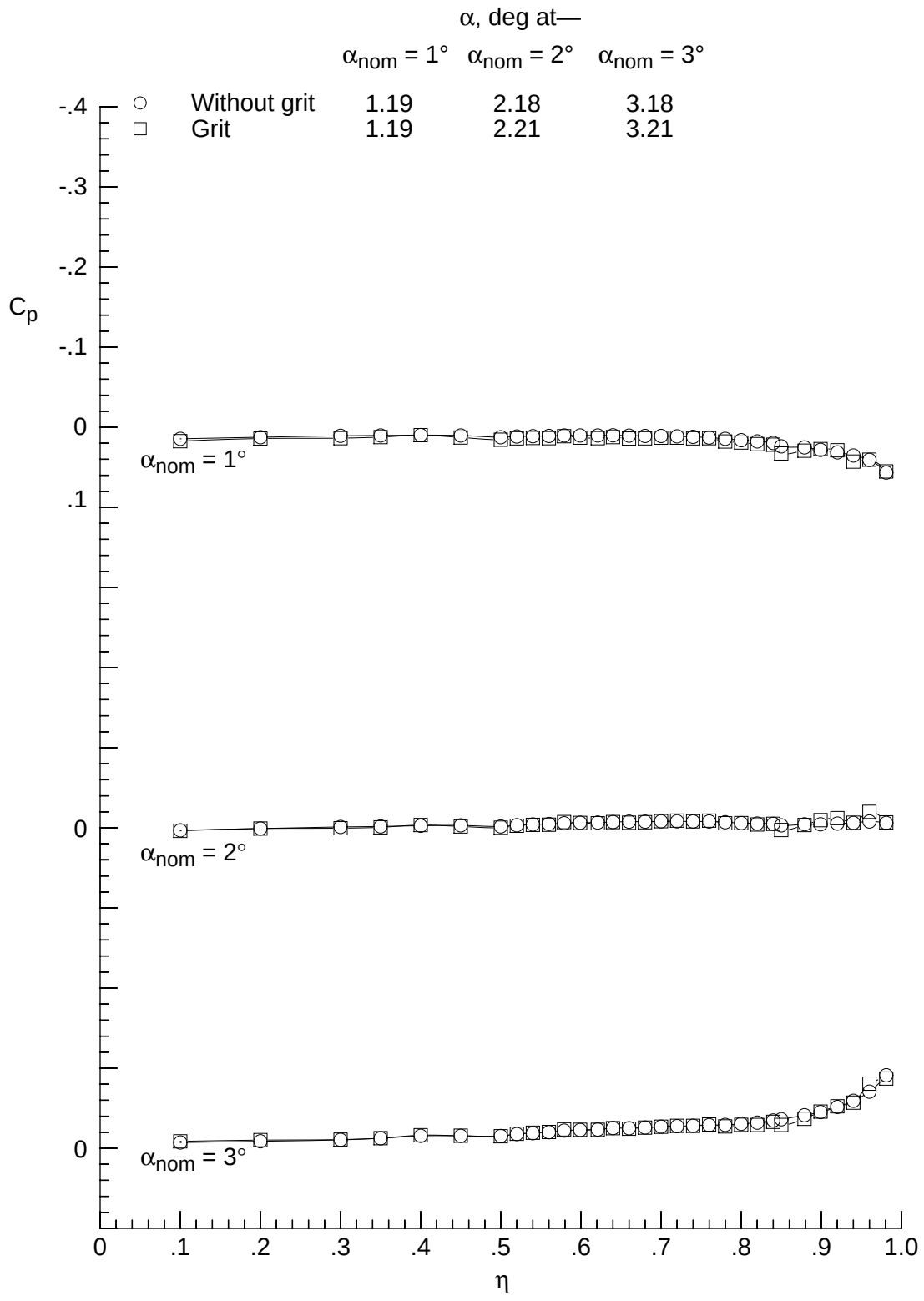

(a) α_{nom} = 1°, 2°, and 3°.

Figure 40. Effect of transition grit on upper surface-pressure coefficient distribution for cambered wing at x = 12 in., M = 1.60, and $R = 2 \times 10^6$ ft^{-1}.

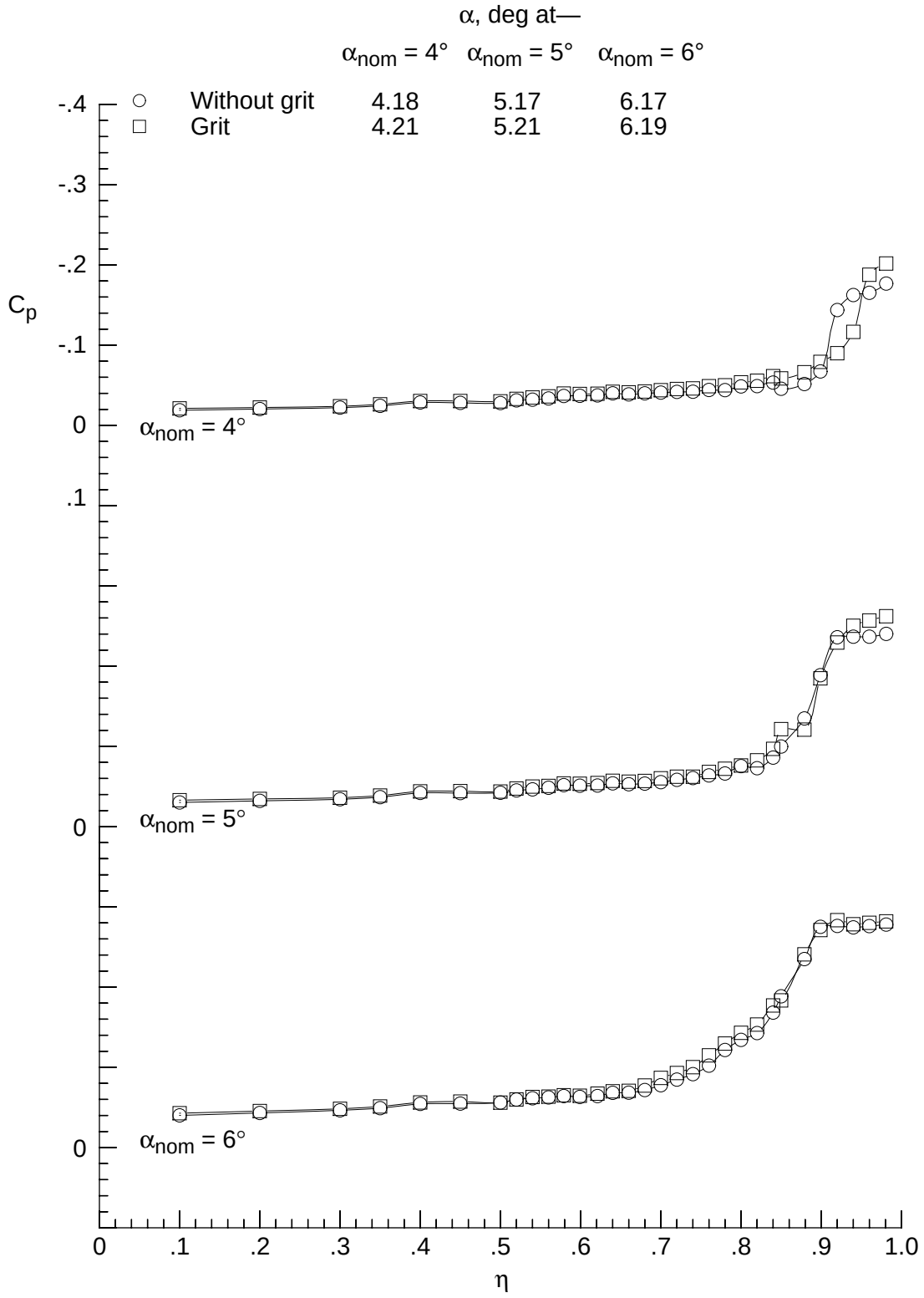

(b) α_{nom} = 4°, 5°, and 6°.

Figure 40. Continued.

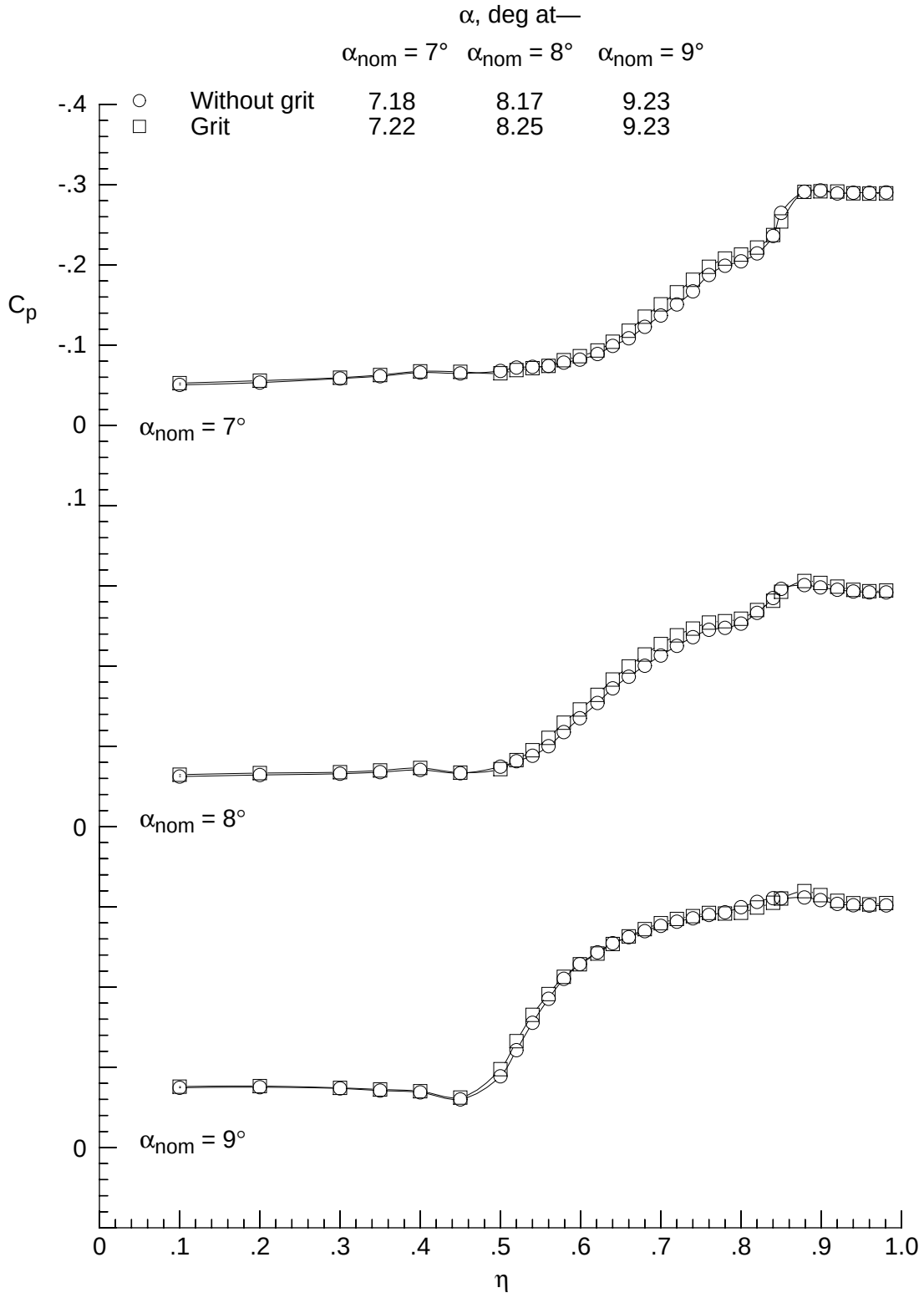

(c) α_{nom} = 7°, 8°, and 9°.

Figure 40. Concluded.

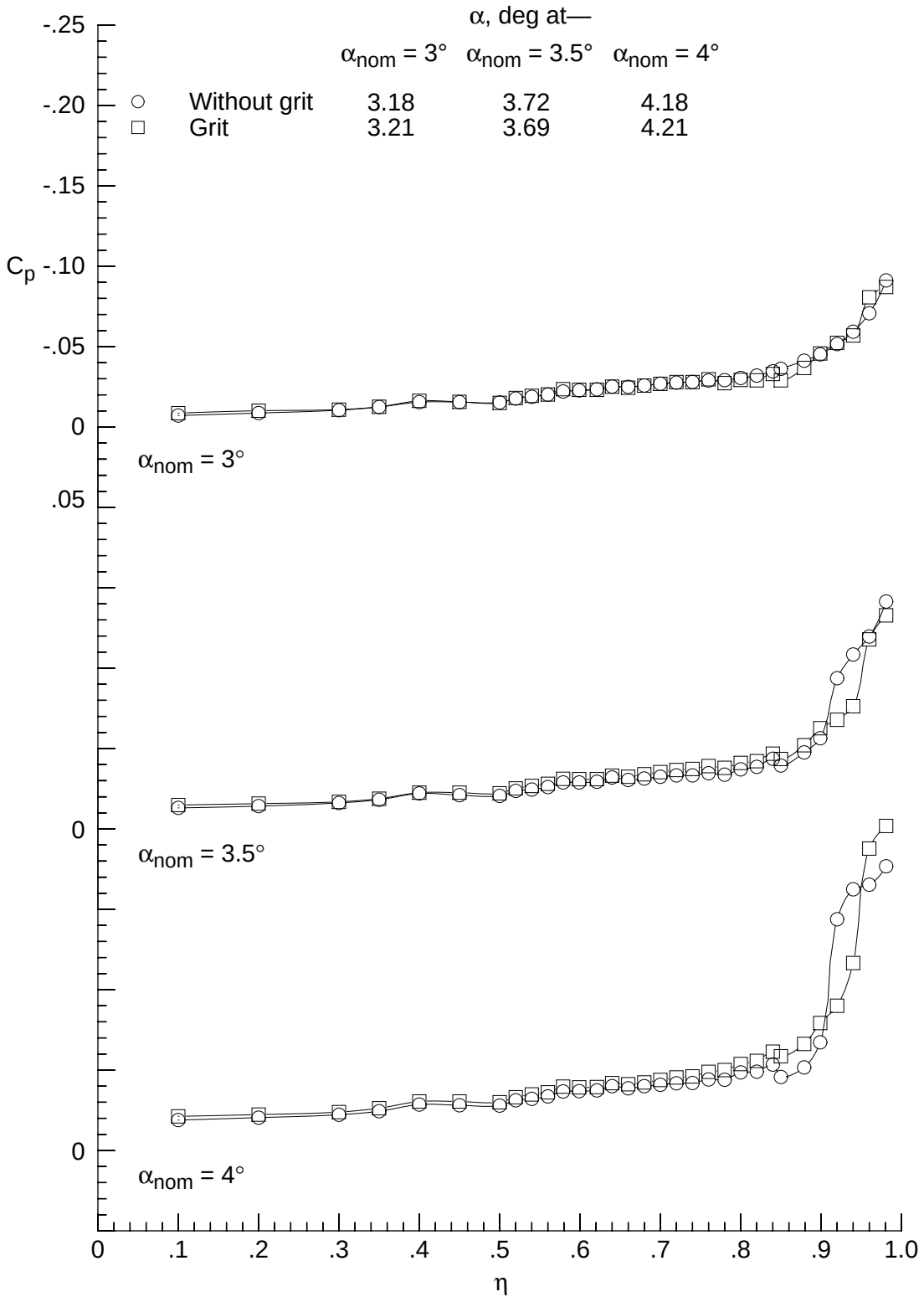

Figure 41. Effect of transition grit on onset of leading-edge separation for cambered wing at x = 12 in., M = 1.60, and $R = 2 \times 10^6$ ft^{-1}.

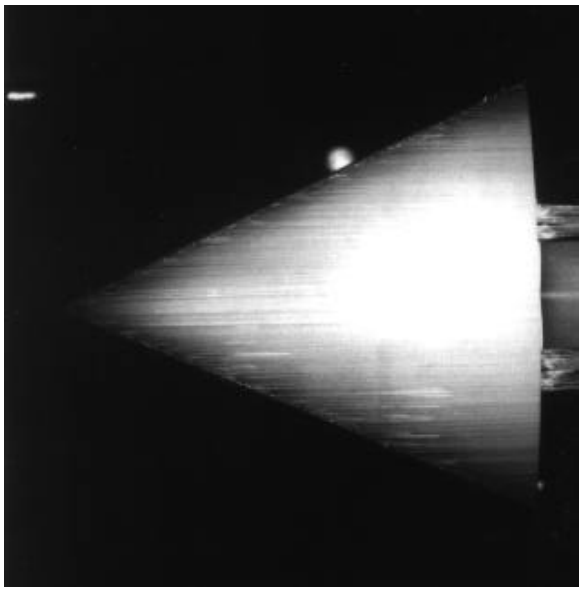

Figure 42. Painted-oil-flow photograph of leeside of cambered wing with transition grit at $\alpha = 4.17°$, $M = 1.60$, and $R = 2 \times 10^6$ ft^{-1}.

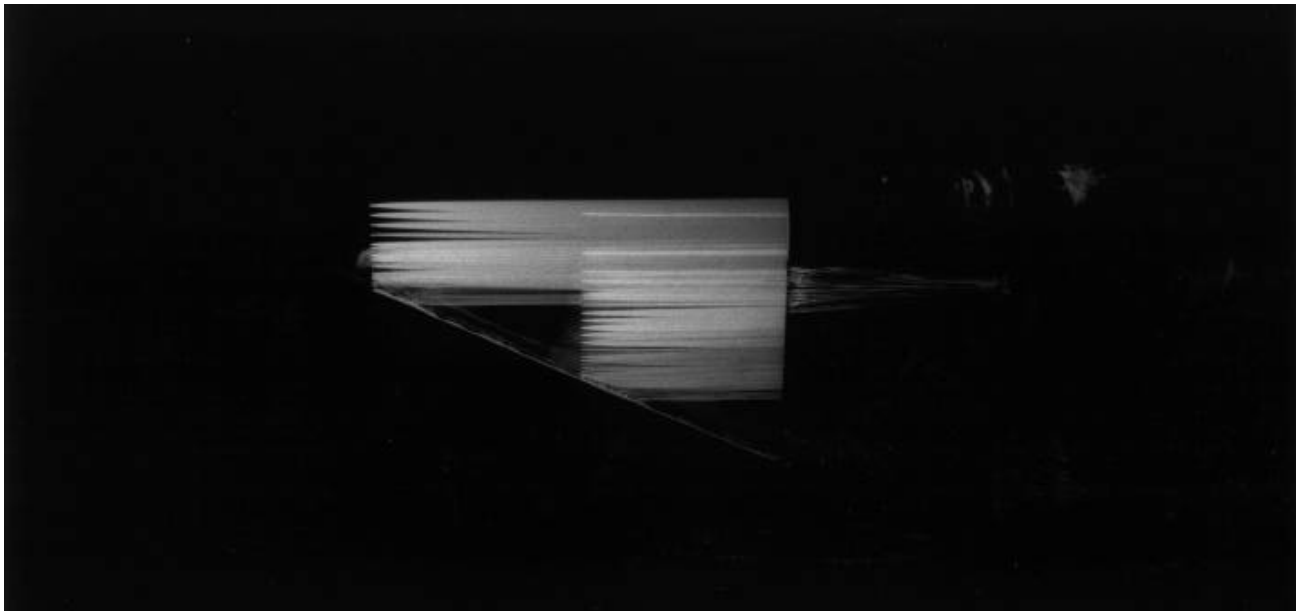

Figure 43. Injected-oil-flow photograph of leeside of cambered wing with transition grit at $\alpha = 4.00°$, $M = 1.60$, and $R = 2 \times 10^6$ ft^{-1}.

Appendix A

Analytical Expressions for Cross-Sectional Shapes of Delta Wing Models

The three cross-sectional shapes that were tested can be expressed analytically. The equations given in this appendix are in terms of y and z normalized by the local semispan (η and ζ, respectively). The equation defining the sharp cross-sectional shape is as follows for the upper surface:

$$\zeta = 0.05 - 0.05\eta \tag{A1}$$

for the lower surface

$$\zeta = -0.05 + 0.05\eta \tag{A2}$$

The equation defining a 20:1 ellipse is as follows for the upper surface:

$$\zeta = 0.05\sqrt{1-\eta^2} \tag{A3}$$

for the lower surface:

$$\zeta = -0.05\sqrt{1-\eta^2} \tag{A4}$$

To obtain a conical cambered geometry, a spanwise circular-arc camber was imposed on the elliptical cross-section geometry in the cross-flow plane. The equation for a circular arc with the center at $y = 0$, $z = z_1$ is as follows:

$$z = z_1 + \sqrt{(r_c)^2 - y^2} \tag{A5}$$

where r_c, the radius of curvature, is

$$r_c = s/\theta_c \tag{A6}$$

where s is the arc length and θ_c is the angle of camber in radians. A given condition is that at $y = 0$, z would equal 0. Therefore, z_1 would equal r_c. Thus, the equation for the camber line is

$$z = \frac{s}{\theta_c} + \sqrt{\left(\frac{s}{\theta_c}\right)^2 - y^2} \tag{A7}$$

Instead of the arc length, the semispan $b/2$ was used in generating the cambered geometry. Thus, the equation for the camber line is as follows:

$$z = \frac{(b/2)}{\theta_c} + \sqrt{\left(\frac{b/2}{\theta_c}\right)^2 - y^2} \tag{A8}$$

The equation defining the camber line in terms of η and ζ is as follows:

$$\zeta = \frac{1}{\theta_c} + \sqrt{\left(\frac{1}{\theta_c}\right)^2 - (\eta)^2} \tag{A9}$$

The angle of camber selected was −10°. The cambered cross-section equations are derived by adding the camber line equation (eq. (A9)) to the elliptical cross-section equations (eqs. (A3) and (A4)). The equations for the cambered cross section in terms of η and ζ are as follows for the upper surface:

$$\zeta = 0.05\sqrt{1-\eta^2} - 5.72958 + \sqrt{32.8281 - \eta^2} \tag{A10}$$

for the lower surface:

$$\zeta = (-0.05)\sqrt{1-\eta^2} - 5.72958 + \sqrt{32.8281 - \eta^2} \tag{A11}$$

As stated before, the arc length was set equal to the semispan. However, the arc length of the camber line would be greater than the semispan. The angle of camber θ_c can be corrected by taking the derivative of the camber line equation (eq. (A5)) with respect to z. Solving for $\partial y/\partial z$ yields

$$\frac{\partial y}{\partial z} = \frac{z - z_1}{y} = \frac{1}{\tan(\theta_c)} \tag{A12}$$

The angle of camber can be determined by using the known values of y and z at the end of the camber line. At the trailing edge, the following conditions apply: $y = 8.3935$, $z = -0.7381$, and $z_1 = 48.0912$. The correct angle of camber is –9.75°.

Appendix B

Determination of Flow Angle

The flow angularity that exists in both test sections of UPWT is described in reference 9 and is illustrated in figure 7. A positive flow angularity indicates that the flow is deflected upward in the test section. The data in reference 9 were used to develop unpublished flow angularity charts for each test section over a range of Mach numbers and Reynolds number. However, in actual practice, the flow angle is determined by obtaining force or pressure data with the model upright ($\phi = 0°$) and inverted ($\phi = 180°$) at several angles of attack. The data for both upright and inverted runs are plotted with angle of attack. A straight line is faired through the data for each run with emphasis on $-2° < \alpha < 2°$. The increment between the two faired lines is twice the flow angle θ_f.

In this study, two approaches were used to determine θ_f. In the first approach, individual pressure measurements were used to calculate θ_f. In the second approach, all pressure data at each x station were integrated to determine C_N. The C_N was then used to calculate θ_f. The pressure data in this study were obtained on the elliptical wing at $M = 1.60$ and $R = 1 \times 10^6$, 2×10^6, 3×10^6, 4×10^6, and 5×10^6 ft^{-1}. The $R = 1 \times 10^6$ and 5×10^6 ft^{-1} data were obtained without transition grit on the elliptical wing. The $R = 2 \times 10^6$, 3×10^6, and 4×10^6 ft^{-1} data were obtained with transition grit inboard of the leading edge of the elliptical wing.

Figure B1 gives an example of the method for determining θ_f with individual pressure measurements. Figure B1 shows the measured pressure coefficient from the orifice A on the lower surface at $x = 6$ in. and $\eta = 0.20$ plotted with angle of attack at $\phi = 0°$ and $180°$ for $R = 1 \times 10^6$ ft^{-1}. Also shown are the faired lines for both the upright and the inverted runs. The increment between the two faired lines is twice the flow angle, θ_f. Table B1 shows θ_f determined with this approach for six individual orifices at $M = 1.60$ and $R = 1 \times 10^6$, 2×10^6, 3×10^6, 4×10^6, and 5×10^6 ft^{-1}. Three pressure orifices were located at the forward station ($x = 6$ in.) and three were located at the aft station ($x = 12$ in.). At each station, one pressure orifice was located on the lower surface and two pressure orifices were located on the upper surface. The data in table B1 show that flow angle is dependent upon chordwise location. The flow angle decreases about 0.25° between $x = 6$ in. to $x = 12$ in. at the lower Reynolds numbers. The data at $x = 12$ in. indicate a dependency on Reynolds number, which results in flow angle increases with increasing Reynolds number. Also note that the variation of θ_f with x becomes smaller with an increase in Reynolds number.

Figure B2 shows an example of the second approach for determining θ_f. This approach uses C_N, which is calculated by integrating all the measured pressures at a given x station. Figure B2 shows the calculated values of C_N plotted with angle of attack for $x = 6$ in. and $\phi = 0°$ and 180° at $R = 1 \times 10^6$ ft^{-1}. Also shown are the faired lines for both the upright and the inverted runs. The increment between the two faired lines is twice the flow angle, θ_f. Table B2 shows θ_f determined with this approach for $x = 6$ and 12 in. at $M = 1.60$ and $R = 1 \times 10^6$, 2×10^6, 3×10^6, 4×10^6, and 5×10^6 ft^{-1}. Table B2 shows that the trends in the θ_f data are similar to those observed in the θ_f data obtained from individual pressure measurements. However, the change in θ_f with a variation in x or Reynolds number is approximately 0.1° or less, which is smaller than that observed in the θ_f data obtained from individual pressure measurements.

The two approaches for determining θ_f yielded similar trends in θ_f with respect to x and Reynolds number. Reference 9 documents a dependency of flow angle on x location in the test section. However, the variation of flow angle with x is very slight in the region of test section where the model is located. Reference 9 does not document a dependency of θ_f on Reynolds number. The approach using the calculated force data yielded smaller variations in θ_f with changes in x or Reynolds number than the approach using individual pressure measurements. The usual choice in determining flow angle at UPWT is force data. Because of these two observations, the calculated force data were used to determine θ_f. The data in table B2 were averaged so that the flow angle that was applied to all data was 0.4°.

Table B1. Flow Angles From Individual Pressure Measurements

Location				θ_f, deg at R, ft^{-1}, of—				
Orifice	Surface	x, in.	η	1×10^6	2×10^6	3×10^6	4×10^6	5×10^6
A	Lower	6	0.2	0.50	0.50	0.45	0.48	0.35
B	Upper	6	0.1	0.45	0.45	0.45	0.45	0.52
C	Upper	6	0.2	0.50	0.45	0.46	0.46	0.58
D	Lower	12	0.2	0.20	0.28	0.30	0.35	0.40
E	Upper	12	0.1	0.22	0.30	0.35	0.38	0.40
F	Upper	12	0.2	0.22	0.25	0.33	0.40	0.40

Table B2. Flow Angles From Integrated Force Data

x, in.	θ_f, deg at R, ft^{-1}, of—				
	1×10^6	2×10^6	3×10^6	4×10^6	5×10^6
6	0.45	0.45	0.40	0.40	0.38
12	0.30	0.35	0.38	0.42	0.40

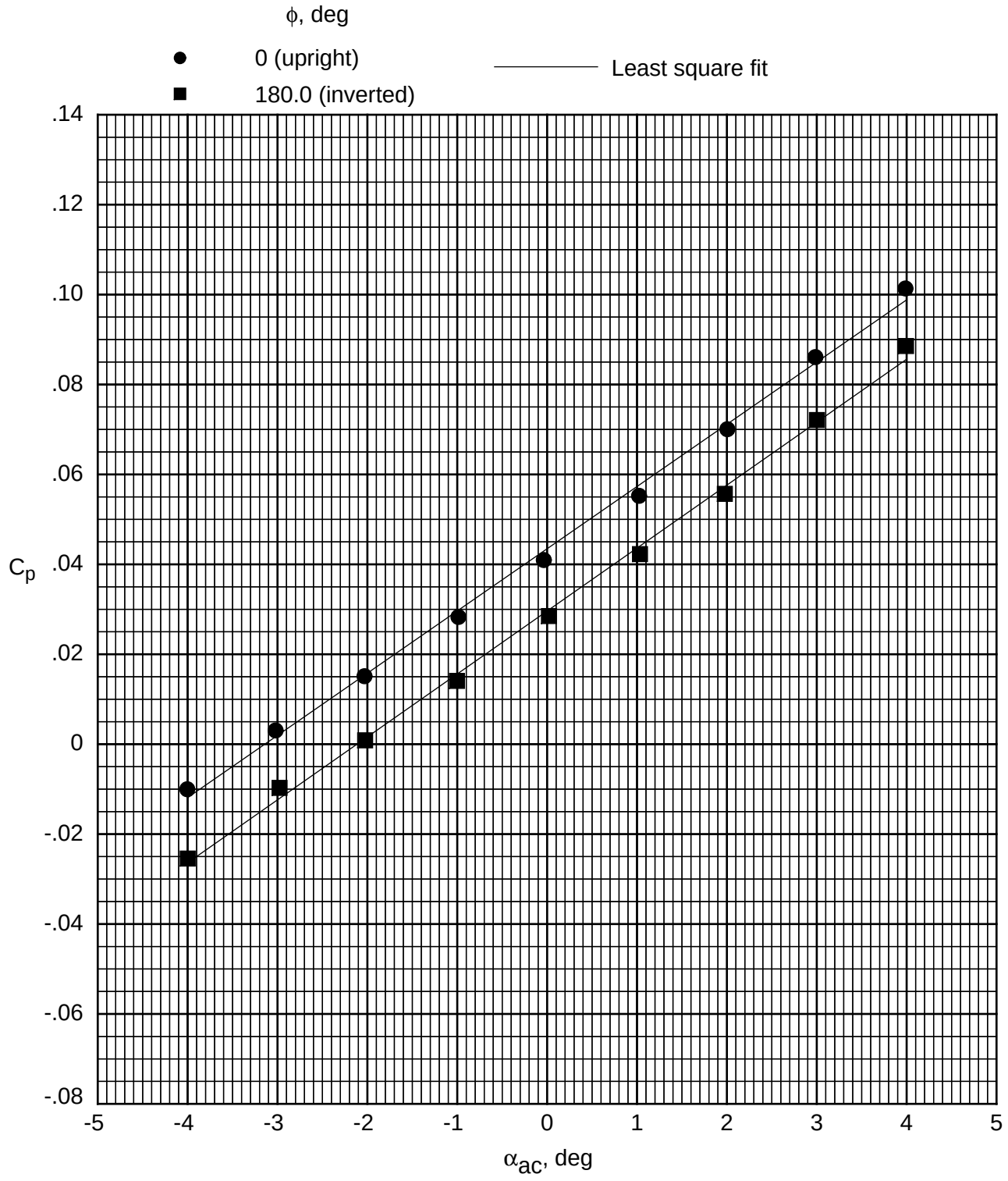

Figure B1. Example of method used to determine θ_f with individual pressure data from orifice A (lower surface, x = 6 in., η = 0.2) on elliptical wing without grit at $R = 1 \times 10^6$ ft^{-1}.

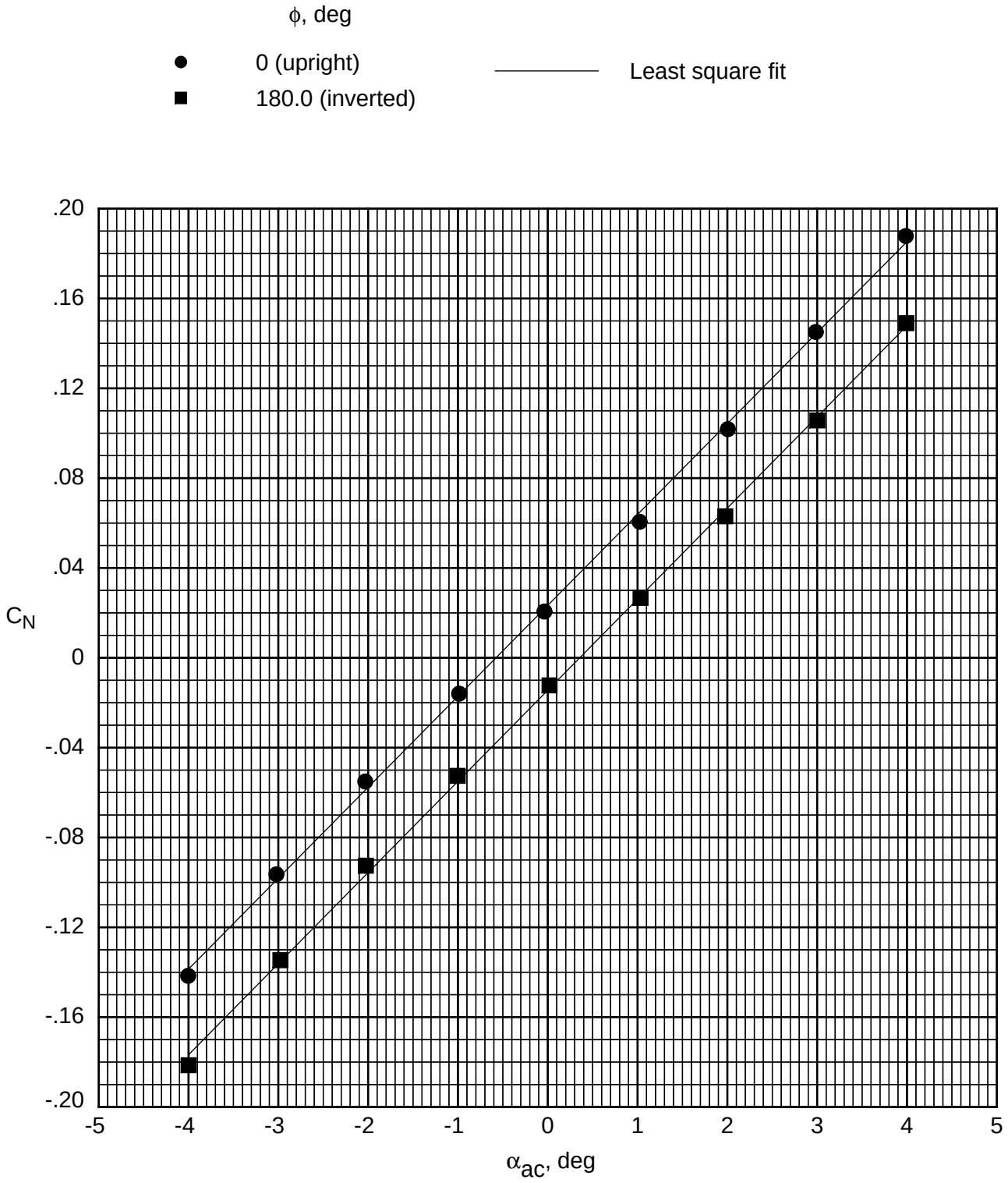

Figure B2. Example of method to determine θ_f with C_N obtained by integrating pressure data at $x = 6$ in. on elliptical wing without grit at $R = 1 \times 10^6$ ft^{-1}.

Appendix C

Description of CD-ROM

This appendix gives a description of the process used to transfer the experimental data recorded with photography into digital form. The digital data are stored on a CD-ROM disc that conforms to the ISO 9660 standard.

Scanning

The four flow-visualization techniques used to obtain data on the three delta wing models were the vapor-screen, painted-oil-flow, injected-oil-flow, and liquid-crystal techniques. The flow-visualization data were obtained by photography. The photographic images were digitized by using two standard charge coupled device (CCD) based scanners. Scanning resolution was selected to balance the need to represent the detailed flow field information and the requirement that all images would be distributed on one 650 MB CD-ROM disc. Table C1 summarizes the scanning process. The scanned images were stored in the TIFF format.

The vapor-screen data were digitized by scanning the 70-mm negatives with a flatbed scanner capable of scanning color images. The flatbed scanner has a resolution of 600 dots/in. (dpi) and uses a three-color fluorescent lamp system and a CCD image sensor. This equipment generates an image that has 8 bits per channel. The image size varies, but is usually 720 columns by 504 rows. To scan the negatives, it was necessary to specify their contrast level to achieve an accurate image.

The flatbed scanner is limited to three contrast settings. For some of the images, it was not possible to obtain optimal contrast because of the discrete nature of the contrast levels and the large variations in opacity of the negatives. When a suboptimal result was obtained, the image was automatically scaled to effectively increase the contrast. To determine those scans that were suboptimal, a region of the image that should have been gray level zero, or black, was probed. If the region was not reading an average gray level less than 30, the image was linearly scaled, with common data analysis software, between the average region value and the maximum image brightness value of 255. The integrity of each image was visually verified after scaling by comparison with photographic prints.

In addition to adjusting the contrast, two other corrections for the scanned vapor-screen technique images were necessary. The first correction was to invert the scanned image so that the final product was similar to a photographic print. This correction was done with common data analysis software. The second correction was to remove artifact lines—bright scan lines that propagated along the vertical, or subscan, direction in the scanned images. A procedure was developed that would detect an artifact line and replace it with a line equal to the average of the scan lines to the left and the right of the artifact line. Proper removal of these artifact lines was verified after processing was completed.

The liquid-crystal images were digitized by scanning the 70-mm negatives with a tabletop scanner which can scan color images. This tabletop scanner probes with a triband phosphor fluorescent lamp and measures the data with a 6000 element linear CCD array. The scanner was driven from a commercial image manipulation software package on a Macintosh computer system. Twenty-four-bit (three color planes of eight bits per plane) images were produced and the images on the CD-ROM are 24 bits as well. The negatives were scanned at 350 dpi resolution, which produced images that are 637 columns by 619 rows. The scanning software was used to convert the negative scan into a positive image by sensing and removing the orange mask present in color negatives.

The 70-mm negatives of the injected-oil-flow technique and the 4 in. by 5 in. positives of the painted-oil-flow technique were also scanned by the tabletop color scanner with a 6000 element linear CCD array. Both sets of images were scanned at 350 dpi resolution with the scanner producing 8-bit gray scale images. Again, the scanning software generated a positive from negatives of the injected-oil-flow technique by inverting the image. The size of all the injected-oil-flow images is 619 pixels $\times$ 637 pixels, while the painted-oil-flow image size is 622 pixels $\times$ 520 pixels.

Image Display

The digitized images were carefully reviewed after scanning. The gray levels in the scanned digital images accurately represent the flow-field information in the traditional positive prints. However, each monitor and printing device has a unique way of presenting the same digital gray level information. A sample image is given in figure C1 to illustrate this point. The image in figure C1(a) is displayed on a monitor that has a display $\gamma = 1.0$, while the image in figure C1(b) is displayed on a monitor with $\gamma = 1.7$. The parameter γ is a measure of the contrast response of the display; γ values greater or less than 1.0 will expand or compress the dark or bright end of the display range. Generally, γ values are different for each system and monitor, so image displays between monitors are not consistent even though the same digital image file is used. References 20–22 discuss the standardization of monitors so that image display is consistent between computer systems. It is suggested that an image display be adjusted so the model surface is essentially all black and there is a visible transition between the model and the flow field.

The above observations are also true with printers. Printers vary in the number of gray levels they can produce and the maximum resolution that can be printed. These two factors determine the fidelity of the image and adjustments may be needed to obtain a realistic print of the digital images.

In addition to being aware of system, printer, and monitor variations, there is another factor to consider when displaying 24-bit images on monitors that do not have full color capability. Ideally, the liquid-crystal images would be displayed on a monitor capable of displaying 24-bit images. Otherwise, the image must be quantized from 24 to 8 bits before displaying. Quantization is a procedure that will produce a pseudocolored image with 8 bits of data that have coloring similar to the 24-bit image. There are many different quantization schemes and some image display software packages will have a quantization code that is used automatically. The color range in the image is usually an input into a quantization algorithm. Therefore, it is suggested that the calibration images (the images containing the temperature scales to the colors viewed in the data images) be pasted into a data image file before quantization. If the flow-field image and the calibration images are quantized independently, comparisons of colors in the quantized data image to colors in the quantized calibration images may be invalid. References 23 to 24 contain more detailed discussion of quantization methods.

The CD-ROM

The CD-ROM distributed with this paper conforms to the ISO 9660 standard. Included on the CD are the images mentioned in the scanning section, a table of pressure data, and a description of header size and image dimensions for each TIFF image file. The remainder of this section will discuss the directory structure, image file format, image format conversion, and available software for three commonly used computer systems: UNIX, PC with DOS, and Macintosh.

The root directory of the CD-ROM contains three directories: PRESSDAT, IMAGES, and FILEINFO. The README file in each directory provides information on the contents of that directory. A schematic of the directory hierarchy is given in figure C2 and table C2 contains a brief description of each directory.

Pressure data files and formats. The files in the PRESSDAT directory are stored as ASCII files. Figure C3 shows the two formats in which the pressure data are given. Figure C3(a) shows a table format where, for a given condition, each pressure measurement is listed with its location on the wing. Table C3 contains the file name convention for the tabulated pressure data files.

Appendix D gives a detailed description of the variables found in each pressure file and a summary of the pressure data. Figure C3(b) shows a listing of all pressures and flow conditions for each data point. The pressure-listing file name on the CD-ROM is PRESS.LST. The pressure-listing data identifies each pressure measurement by the variable name CP# (tables 2 to 4). The pressure-listing file does not contain the location of each pressure. Tables 2 to 4 contain the location on the wing and the corresponding CP# for each pressure measurement. Thus, for plotting purposes, the pressure-listing data must be used with a curve definition file that gives the location for each pressure. Figure C4 shows a portion of the curve definition file, which is named CURDEF on the CD-ROM. The first curve defined in figure C4 is identified as curve “ellu1a” and is the pressure distribution on the upper surface of the elliptical wing at $x = 6$ in. for runs 4–21. The η location for each pressure measurement is given in the “xlist” section and the corresponding variable name for each pressure measurement from the pressure-listing file is given in the “ylist” section.

Image files and formats. The image files in the IMAGES directory are stored in a directory hierarchy that indicates the wing type, transition grit application, the flow-visualization technique, R, and T_o. The directory hierarchy is given in figure C2. A brief description of each directory is given in table C2. The file name for each image indicates the previously mentioned conditions as well as the angle of attack, while adhering to the DOS 8.3 file naming convention. Table C4 contains a description of the file name convention that was used on the CD-ROM.

Images are stored in the tagged image file format (TIFF). The TIFF files on this CD have some finite amount of supplemental information stored at the beginning of the file (often called a header) followed by the image information stored in sequential rows. If software that reads either one of these formats is unavailable, it is possible to read the TIFF images as raw data into most image display software packages. To read an image as raw data, the length of the header and the number of rows and columns in the image must be known. For all of the TIFF files, this information is provided in the file, FILESIZE.TXT under the FILEINFO directory.

The calibration images (the images containing the temperature scales to the colors viewed in the data images) for the liquid-crystal data are contained in the root directory. The file names are LEFTCB and RIGHTCB referring, respectively, to the left and right side of the wing when looking upstream of the model from the trailing edge.

UNIX workstation systems. There are many conversion and display routines written for UNIX workstations. Below is a listing of software that can be used to convert and display the TIFF images. The software is available by anonymous file transfer. The FTP directories listed are the current locations, but they are subject to change. Restrictions on the use and licensing for any of the software may be obtained from the associated documentation.

Conversion:

Software: imtools

Developer: San Diego Supercomputing Center (SDSC)

FTP site: ftp.sdsc.edu

Directory location: pub/sdsc/graphics/imtools

Description: Software that will read and write a variety of formats. The software, at this writing, only runs on UNIX based machines, but will write and read some typical PC and Macintosh formats.

Software: pbmplus

Developer: Jef Poskanzer

FTP site: ftp.x.org

Directory location: R5contrib

Description: Software that will read and write a variety of formats.

Display:

Software: ImageMagick

Developer: John Cristy, E. I. du Pont de Nemours and Company, Incorporated

FTP site: export.lcs.mit.edu

Directory location: contrib/applications/ImageMagick

Software: xv version 2.21

Developer: John Bradley, Grasp Laboratory at U. Penn.

FTP site: edhs1.gsfc.nasa.gov

Directory location: pub/freeware/unix/src/xv

Description: Software to display images on X compatible windowing environments. This software also has built-in quantization code and provides some flexibility on the method used to quantize 24-bit images.

PC with DOS systems. There are many conversion and display routines written in DOS for PC or PC-compatible systems using DOS. Listed below are a package, pbmplus, that can convert images and a package, imdisp, that can be used to display images. These are available by anonymous file transfer (FTP) at the sites given in each package description. The FTP directories listed are the current locations, but they are subject to change. Restrictions on the use and licensing for any of the software may be obtained from the associated documentation.

Conversion:

Software: pbmplus

Developer: Jef Poskanzer

FTP site: wuarchive.wustl.edu

Directory location: SimTel/msdos/graphics

Description: Image format conversion tools that read and write a large variety of image formats.

Display:

Software: imdisp

Developer: Jet Propulsion Laboratory (JPL)

FTP site: oak.oakland.edu

Directory location: simtel/msdos/graphics

Description: Written at JPL to display planetary data. It provides support for a very large variety of PC graphics cards (EGA, CGA, and VGA). The software will read and write out the special image formats used to distribute planetary data; however, the TIFF images can be read in as raw data with the header and size information as previously discussed. The package also provides some limited image processing and enhancement capabilities.

Macintosh systems. There are several display packages for the Macintosh systems that also have extensive image processing capabilities. Some of these packages are listed below along with anonymous file transfer sites from which the user can download the binaries for each package. Most of the packages listed have additional output formats and can also serve as conversion software. The FTP directories listed are the current locations, but they are subject to change. Restrictions on the use and licensing of any of the software may be obtained from the associated documentation.

Software: NIH Image

Developer: NIH

FTP site: zippy.nimh.nih.gov

Directory location: pub/nih-image

Description: This is a general purpose image processing package for the Macintosh. It can read 8-bit images only.

Software: JPEGView 3.3

Developer: Aaron Giles, Cornell University

FTP site: edhs1.gsfc.nasa.gov

Description: Can read and display (if hardware is capable) 24-bit and 8-bit TIFF files

Directory location: pub/freeware/mac

Table C1. Scanning Summary

Flow-visualization technique	Film type	Scanning resolution, dpi	Image size (pixels)		Pixel depth, bits
			Columns	Rows	
Vapor screen	70-mm black and white negatives	600	Variable	Variable	8
Liquid crystal	70-mm color negatives	350	673	619	24
Painted oil flow	4 in. by 5 in. self-developing film	350	622	520	8
Injected oil flow	70-mm black and white negatives	350	619	637	8

Table C2. Description of Directories on CD-ROM

Directory	Description
IMAGES.INF	Directory containing information on images.
PRESSDAT	Directory containing pressure data.
IMAGES	Directory containing all scanned images.
SNWING	Subdirectory containing all scanned images for sharp wing without transition grit.
ENWING	Subdirectory containing all scanned images for elliptical wing without transition grit.
EYWING	Subdirectory containing all scanned images for elliptical wing with transition grit.
CNWING	Subdirectory containing all scanned images for cambered wing without transition grit.
CYWING	Subdirectory containing all scanned images for cambered wing with transition grit.
IMAGES/??WING/ V_SCREEN	Subdirectory containing all vapor-screen images for configuration associated with IMAGES/??WING directory (where ??WING is SNWING, ENWING, EYWING, CNWING, or CYWING directory).
IMAGES/??WING/ I_OILFLO	Subdirectory containing all injected-oil-flow images for configuration associated with IMAGES/??WING directory.
IMAGES/??WING/ P_OILFLO	Subdirectory containing all painted-oil-flow images for configuration associated with IMAGES/??WING directory.
IMAGES/??WING/ LIQ_CRY	Subdirectory containing all liquid-crystal images for configuration associated with IMAGES/??WING directory.
IMAGES/??WING/ *_*/R1	Subdirectory containing data at $R = 1 \times 10^6$ ft^{-1} associated with IMAGES/??WING/*_* directory (where *_* is V_SCREEN, I_OIFLO, P_OILFLO, or LIQ_CRY directory).
IMAGES/??WING/ *_*/R2	Subdirectory containing data at $R = 2 \times 10^6$ ft^{-1} associated with IMAGES/??WING/*_* directory.
IMAGES/??WING/ *_*/R5	Subdirectory containing data at $R = 5 \times 10^6$ ft^{-1} associated with IMAGES/??WING/*_* directory.
IMAGES/??WING/ LIQ_CRY/R#/T120	Subdirectory containing liquid-crystal data at T_o = 120°F. Configuration and free-stream Reynolds number condition is that associated with IMAGES/??WING/LIQ_CRY/R# directory (where R# is R1, R2, or R5 directory).
IMAGES/??WING/ LIQ_CRY/R#/T125	Subdirectory containing liquid-crystal data at T_o = 125°F. Configuration and free-stream Reynolds number condition is that associated with IMAGES/??WING/Liq_cry/R# directory.
IMAGES/??WING/ LIQ_CRY/R#/T130	Subdirectory containing liquid-crystal data at T_o = 130°F. Configuration and free-stream Reynolds number condition is that associated with IMAGES/??WING/Liq_cry/R# directory.

Table C3. Description of Tabulated Pressure Data File Names on CD-ROM

[Tabulated Pressure File Name - 1 2 **PRESS . TAB**]

File name characters	Description
1 - Model geometry	S ... Sharp wing E ... Elliptical wing C ... Cambered wing
2 - Grit	N ... No transition grit applied Y ... Transition grit applied
Example: ENPRESS.TAB	File for all pressures for elliptical wing with no transition grit

Table C4. Description of Image File Names on CD-ROM

[Image File Name - 1 2 3 4 **T** 5 _ _ **. A** 6 _]

File name characters	Description
1 - Model geometry	S ... Sharp wing E ... Elliptical wing C ... Cambered wing
2 - Grit	N ... No transition grit applied Y ... Transition grit applied
3 - Flow visualization technique	V ...Vapor screen P ... Painted oil flow I ... Injected oil flow L ... Liquid crystal
4 - Freestream Reynolds number	1 ... $R = 1 \times 10^6$ ft^{-1} 2 ... $R = 2 \times 10^6$ ft^{-1} 5 ... $R = 5 \times 10^6$ ft^{-1}
T 5 _ _ - T_o	T120 ... T_o = 120°F T125 ... T_o = 125°F T130 ... T_o = 130°F
A 6 _ - α_{nom}	A00 ... α_{nom} = 0° A10 ... α_{nom} = 1.0° A15 ... α_{nom} = 1.5° . . . A90 ... α_{nom} = 9.0°
Example: ENV2T125.A50	Image file for vapor-screen photograph of elliptical wing without grit at $R = 2 \times 10^6$ ft^{-1}, T_o = 125 °F, and α_{nom} = 5.0°. All image data were obtained at x = 12 in.

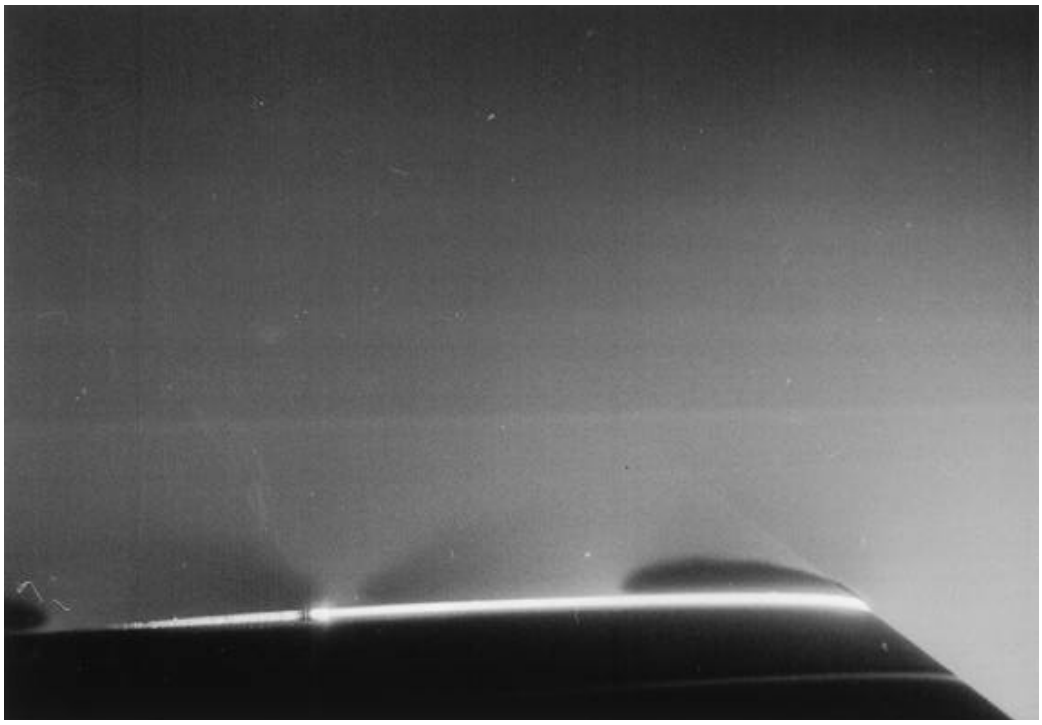

(a) $\gamma = 1.0$.

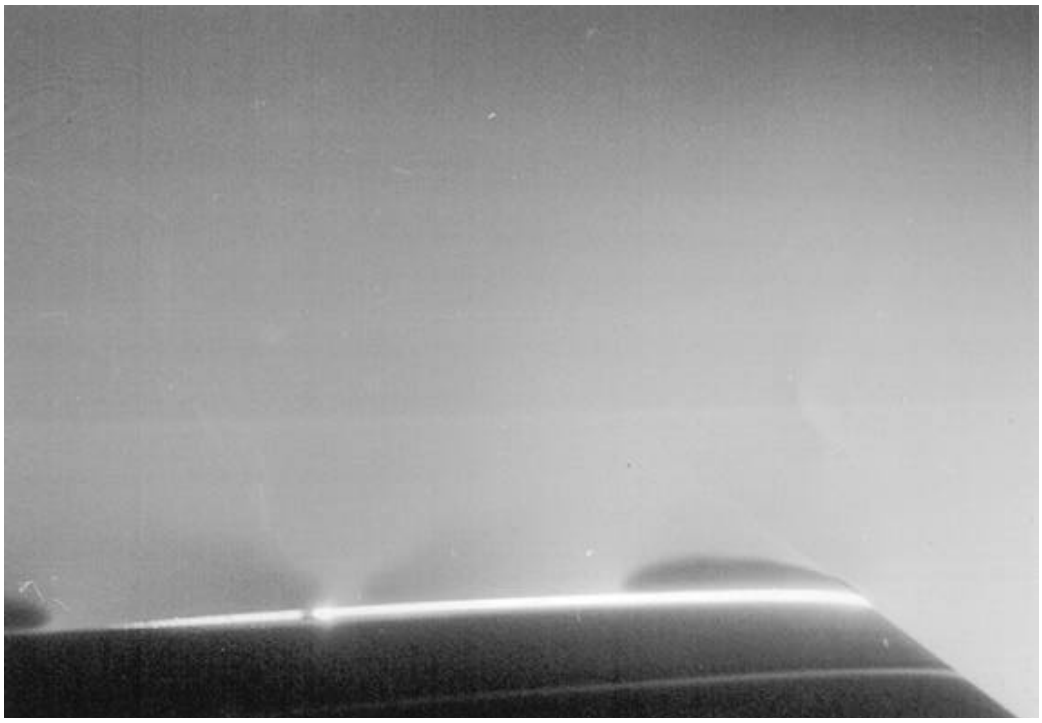

(b) $\gamma = 1.7$.

Figure C1. Comparison of same image from different display systems.

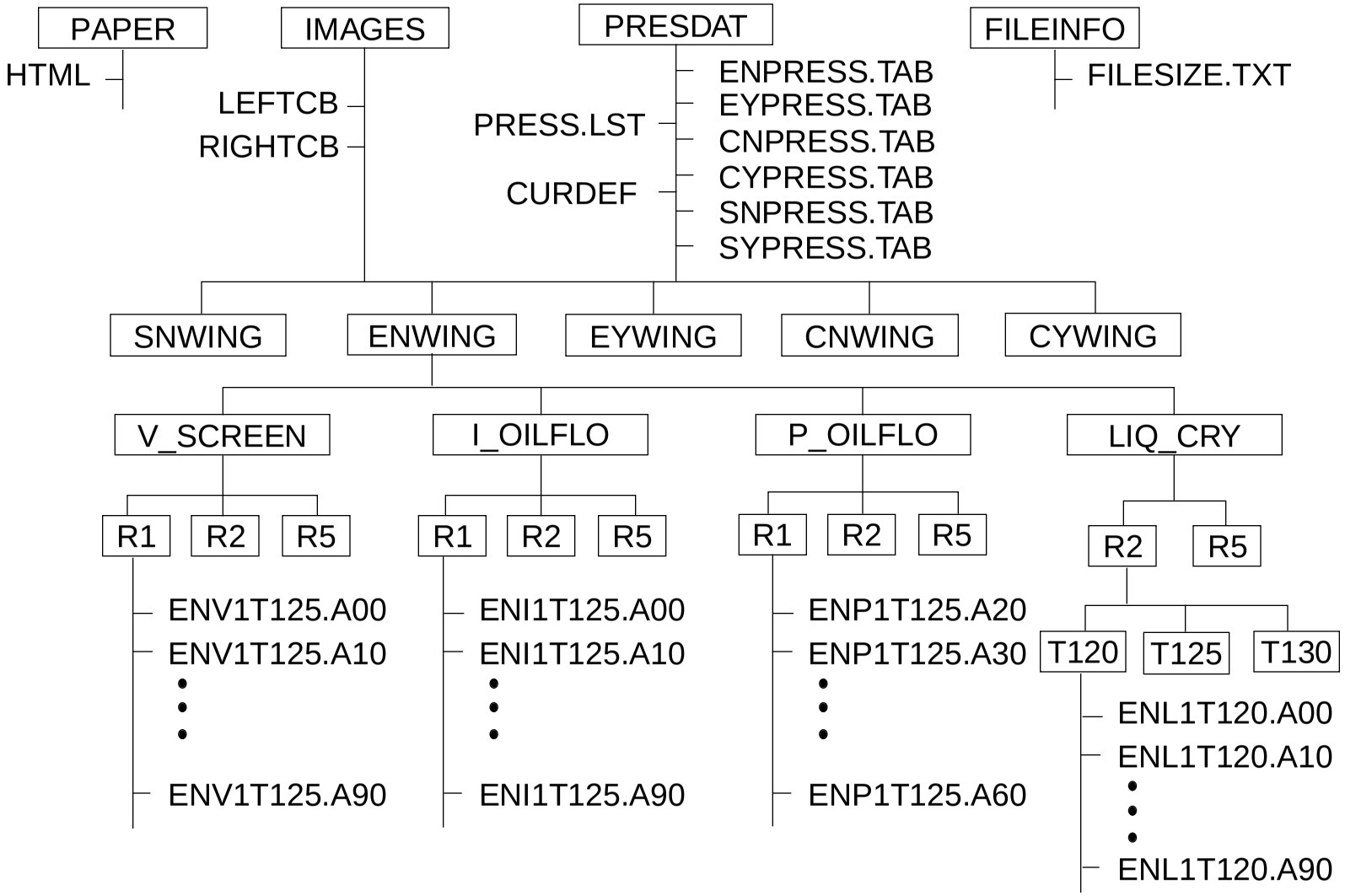

Figure C2. Schematic of directory hierarchy on CD-ROM.

MACH = 1.60 Q = 227.6 PINF = 127.0 R/FT = 1.00
PHI = -0.08 FLOW ANGLE = 0.40

X/C = 0.333, UPPER SURFACE

ETA	CP	ETA	CP	ETA	CP	ETA	CP
0.099	0.0718	0.579	0.0749	0.759	0.0859	0.880	0.1027
0.199	0.0701	0.619	0.0767	0.781	0.0890	0.899	0.1084
0.299	0.0692	0.660	0.0784	0.800	0.0899	0.920	0.1155
0.400	0.0709	0.700	0.0811	0.820	0.0925	0.939	0.1252
0.499	0.0727	0.720	0.0824	0.840	0.0943	0.980	0.1670
0.539	0.0740	0.740	0.0842	0.860	0.0983		

X/C = 0.333, LOWER SURFACE

ETA	CP	ETA	CP	ETA	CP	ETA	CP
0.200	0.0031	0.500	-0.0009	0.700	0.0009	0.850	-0.0547
0.400	0.0017	0.600	-0.0031	0.799	-0.0516	0.900	-0.0626

X/C = 0.667, UPPER SURFACE

ETA	CP	ETA	CP	ETA	CP	ETA	CP
0.100	0.0679	0.540	0.0749	0.700	0.0811	0.860	0.0991
0.200	0.0679	0.560	0.0749	0.720	0.0820	0.879	0.1044
0.300	0.0679	0.579	0.0753	0.740	0.0837	0.899	0.1102
0.350	0.0683	0.599	0.0767	0.760	0.0846	0.920	0.1185
0.400	0.0692	0.621	0.0771	0.780	0.0868	0.940	0.1287
0.450	0.0705	0.640	0.0780	0.800	0.0894	0.960	0.1423
0.500	0.0767	0.660	0.0784	0.820	0.0921	0.981	0.1754
0.520	0.0753	0.680	0.0802	0.840	0.0956		

X/C = 0.667, LOWER SURFACE

ETA	CP	ETA	CP	ETA	CP	ETA	CP
0.200	-0.0049	0.550	-0.0084	0.700	-0.0146	0.850	-0.0221
0.400	-0.0027	0.600	-0.0093	0.750	-0.0159	0.900	-0.0847
0.450	-0.0036	0.650	-0.0146	0.800	-0.0207	0.950	-0.1045

(a) Table format.

Figure C3. Formats in which surface-pressure coefficient data are stored on CD-ROM.

RUN	POINT	MACH	Q	ALPHA	R/FT
PINF	CP1	CP2	CP3	CP4	CP5
CP6	CP7	CP8	CP9	CP10	CP11
CP12	CP13	CP14	CP15	CP16	CP17
CP18	CP19	CP20	CP21	CP22	CP23
CP24	CP33	CP34	CP35	CP36	CP37
CP38	CP39	CP40	CP41	CP42	CP43
CP44	CP45	CP46	CP47	CP48	CP49
CP50	CP51	CP52	CP53	CP54	CP55
CP56	CP57	CP58	CP59	CP60	CP61
CP66	CP67	CP68	CP69	CP70	CP71
CP72	CP73	CP74	CP75	CP76	CP77
CP78	CP79	CP80	CP81	CP82	CP83
CP84	CP85	CP86	CP87	CP88	CP89
CP90	CP91				
0.40000E+01	0.10400E+03	0.16000E+01	0.22688E+03	-0.30213E+01	0.99229E+00
0.12661E+03	0.30589E-02	0.17365E-02	-0.90805E-03	-0.31119E-02	0.85502E-03
-0.51596E-01	-0.54681E-01	-0.62615E-01	0.99999E+01	-0.62174E-01	-0.53157E-02
-0.48749E-02	-0.26711E-02	-0.35526E-02	0.99999E+01	-0.84011E-02	-0.92826E-02
-0.14572E-01	-0.14572E-01	-0.15894E-01	-0.20743E-01	-0.22065E-01	-0.84653E-01
-0.10449E+00	0.71818E-01	0.70055E-01	0.69174E-01	0.70937E-01	0.72700E-01
0.74022E-01	0.74904E-01	0.76667E-01	0.78430E-01	0.81074E-01	0.82397E-01
0.84160E-01	0.85923E-01	0.89008E-01	0.89890E-01	0.92534E-01	0.94297E-01
0.98264E-01	0.10267E+00	0.10840E+00	0.11545E+00	0.12515E+00	0.99999E+01
0.16702E+00	0.67851E-01	0.67851E-01	0.67851E-01	0.68292E-01	0.69174E-01
0.76667E-01	0.75344E-01	0.74904E-01	0.74904E-01	0.75344E-01	0.76667E-01
0.77107E-01	0.77989E-01	0.78430E-01	0.80193E-01	0.81074E-01	0.81956E-01
0.83719E-01	0.84601E-01	0.86804E-01	0.89449E-01	0.92093E-01	0.95620E-01
0.99146E-01	0.10443E+00	0.11016E+00	0.11854E+00	0.12868E+00	0.14234E+00
0.17540E+00	0.70496E-01				
0.40000E+01	0.10500E+03	0.16000E+01	0.22682E+03	-0.20316E+01	0.99514E+00
0.12657E+03	0.15113E-01	0.13790E-01	0.12027E-01	0.10263E-01	0.76179E-02
0.56379E-03	-0.47268E-02	-0.12663E-01	0.99999E+01	-0.10899E-01	0.45317E-02

(b) Pressure listing format.

Figure C3. Concluded.

```
*
* ********************************************************
*           Curve Definition File
* ********************************************************
* ************************************************
* Elliptic wing for Runs 4-21, upper surface, x=6”
* ************************************************
*
curve ellu1a
xlist
0.099 0.199 0.299 0.4 0.499 0.539 0.579 0.619
0.66 0.7 0.72 0.74 0.759 0.781 0.8 0.82
0.84 0.86 0.88 0.899 0.92 0.939 0.98
ylist
CP33 CP34 CP35 CP36 CP37 CP38 CP39 CP40
CP41 CP42 CP43 CP44 CP45 CP46 CP47 CP48
CP49 CP50 CP51 CP52 CP53 CP54 CP56
*
* ************************************************
* Elliptic wing for runs 22-32, upper surface, x=6”
* ************************************************
*
curve ellu1b
xlist
0.099 0.199 0.299 0.4 0.499 0.539 0.579 0.619
0.66 0.7 0.72 0.74 0.759 0.781 0.8 0.82
0.84 0.86 0.88 0.92 0.939 0.98
ylist
CP33 CP34 CP35 CP36 CP37 CP38 CP39 CP40
CP41 CP42 CP43 CP44 CP45 CP46 CP47 CP48
CP49 CP50 CP51 CP53 CP54 CP56
```

Figure C4. Example of curve definition file for pressure data.

Appendix D

Surface-Pressure Coefficient Data

The surface-pressure coefficient data (referred to hereafter as pressure data) are referenced to the free-stream dynamic pressure q. The pressure data are presented in figures D1 to D22. The pressure data for each row of orifices on the upper and the lower surface are presented for each configuration. For example, figure D1 presents the surface-pressure coefficient data for the sharp wing without grit at $R = 1 \times 10^6$ ft^{-1} and angles of attack from 0.25° to 9.27° in approximately 0.5° increments. Table D1 presents an index to the data and the wind-tunnel conditions for each figure.

The surface-pressure coefficient data are also presented on the CD-ROM in a simple pressure-listing format and a table format. The pressure-listing format presents a row of pressures for each data point. For plotting purposes, the pressure-listing file must be used with a curve definition file, which gives the location of each pressure for a given run. The curve definition file is also located on the CD-ROM. The pressure data are also stored on the CD-ROM in table format where, for a given condition, each pressure measurement is listed with its location on the wing. Appendix C contains the details on the pressure data files and CD-ROM. Table D1 presents, for each run, the test conditions and the CD-ROM file that contains the tabulated pressure data. Tables 6 to 11 contain a point and α index to the pressure data. All surface-pressure coefficient data were taken at $\beta = 0°$ and $T_o = 125°$F.

Table D1. Index to Figures D1 to D22 and Tabulated Data at M = 1.60 and T_o = 125°F on CD-ROM

Figure	Pressure data table file name	Configuration	Run	R, million/ft	θ_f, deg	ϕ, deg
D1	SNPRESS.TAB	Sharp wing without grit	40	1	0.4	0
D2	SNPRESS.TAB	Sharp wing without grit	41	2	0.4	0
D3	SNPRESS.TAB	Sharp wing without grit	42	5	0.4	0
D4	SYPRESS.TAB	Sharp wing with grit	43	1	0.4	0
D5	SYPRESS.TAB	Sharp wing with grit	44	2	0.4	0
D6	SYPRESS.TAB	Sharp wing with grit	45	5	0.4	0
	ENPRESS.TAB	Elliptical wing without grit	4[a]	1	0	0
	ENPRESS.TAB	Elliptical wing without grit	5[a]	1	0	180.0
D7	ENPRESS.TAB	Elliptical wing without grit	6	1	0.4	0
D8	ENPRESS.TAB	Elliptical wing without grit	7	2	0.4	0
D9	ENPRESS.TAB	Elliptical wing without grit	8	3	0.4	0
D10	ENPRESS.TAB	Elliptical wing without grit	10	4	0.4	0
	ENPRESS.TAB	Elliptical wing without grit	13[a]	5	0	0
	ENPRESS.TAB	Elliptical wing without grit	11[a]	5	0	180.0
D11	ENPRESS.TAB	Elliptical wing without grit	14	5	0.4	0
D12	EYPRESS.TAB	Elliptical wing with grit	22	1	0.4	0
	EYPRESS.TAB	Elliptical wing with grit	23[a]	2	0	0
	EYPRESS.TAB	Elliptical wing with grit	24[a]	2	0	180.0
D13	EYPRESS.TAB	Elliptical wing with grit	25	2	0.4	0
	EYPRESS.TAB	Elliptical wing with grit	26[a]	3	0	0
	EYPRESS.TAB	Elliptical wing with grit	27[a]	3	0	180.0
D14	EYPRESS.TAB	Elliptical wing with grit	28	3	0.4	0
	EYPRESS.TAB	Elliptical wing with grit	30[a]	4	0	0
	EYPRESS.TAB	Elliptical wing with grit	31[a]	4	0	180.0
D15	EYPRESS.TAB	Elliptical wing with grit	32	4	0.4	0
D16	EYPRESS.TAB	Elliptical wing with grit	29	5	0.4	0
D17	CNPRESS.TAB	Cambered wing without grit	36	1	0.4	0
D18	CNPRESS.TAB	Cambered wing without grit	34	2	0.4	0
	CNPRESS.TAB	Cambered wing without grit (Unacceptable dew point)	33	5	0.4	0
D19	CNPRESS.TAB	Cambered wing without grit	35	5	0.4	0
D20	CYPRESS.TAB	Cambered wing with grit	37	1	0.4	0
D21	CYPRESS.TAB	Cambered wing with grit	38	2	0.4	0
D22	CYPRESS.TAB	Cambered wing with grit	39	5	0.4	0

[a]Data used in determining θ_f.

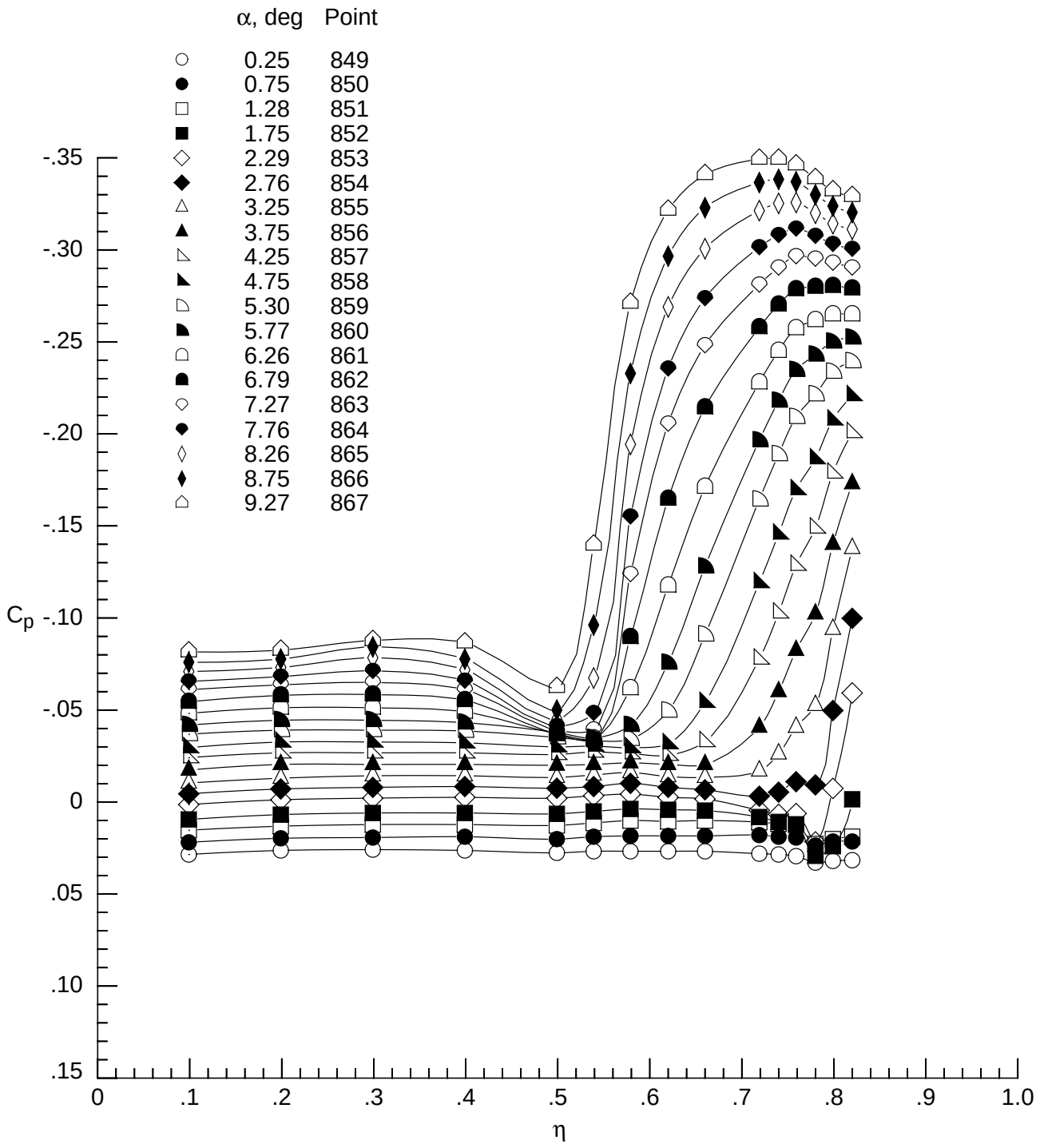

(a) Upper surface at x = 6 in.

Figure D1. Surface-pressure coefficient data for sharp wing without transition grit at M = 1.60 and $R = 1 \times 10^6$ ft^{-1} for run 40.

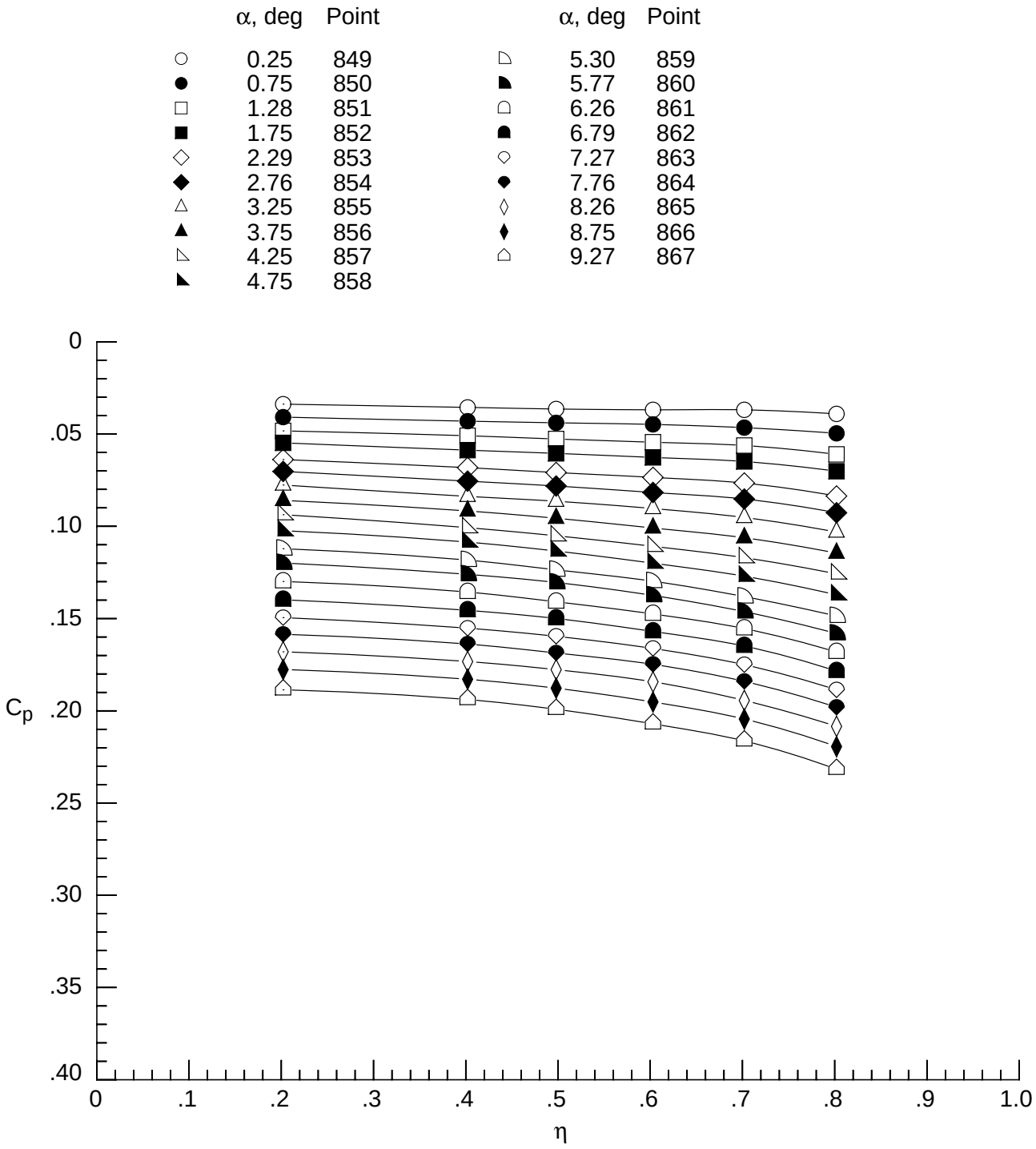

(b) Lower surface at x = 6 in.

Figure D1. Continued.

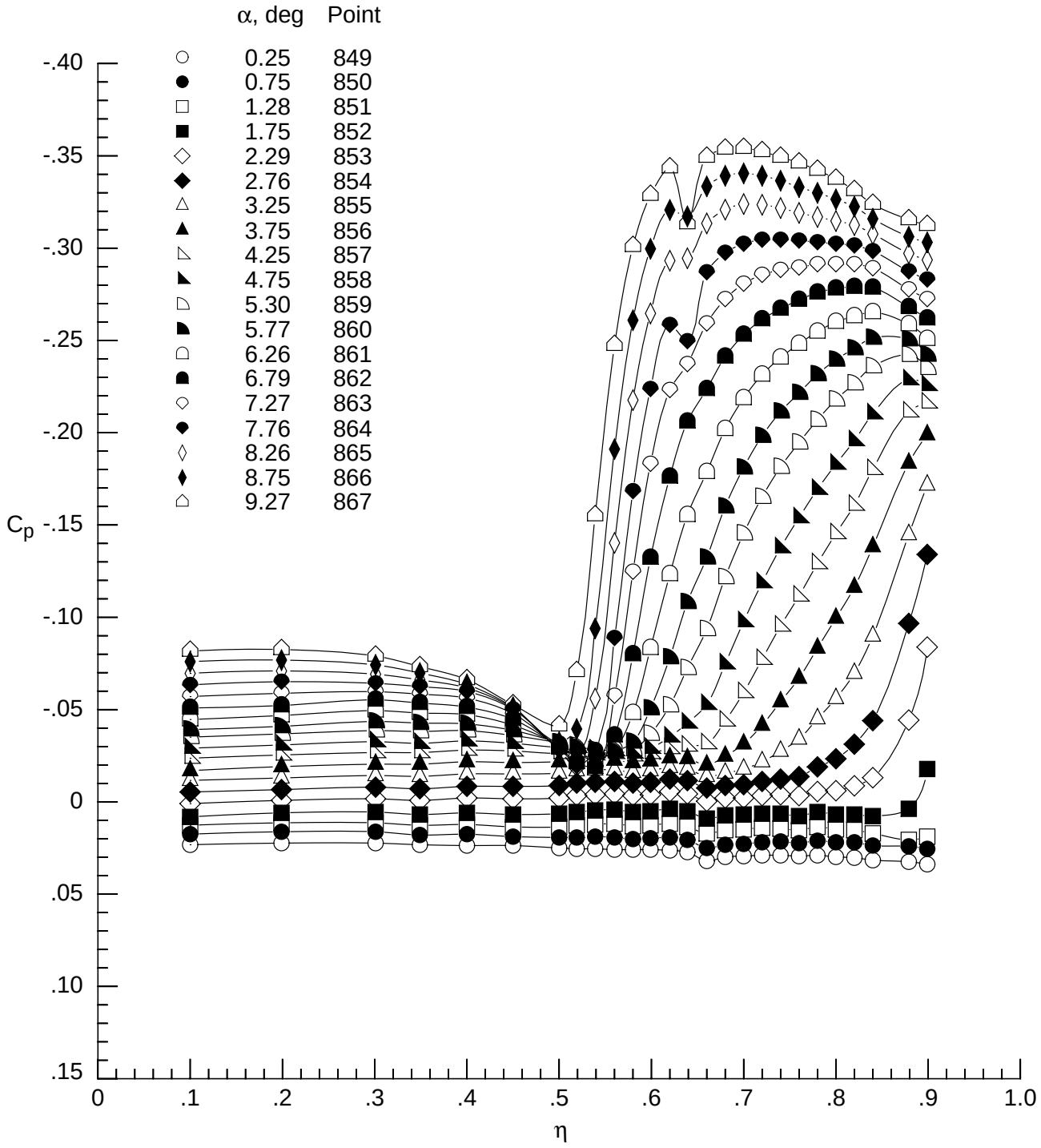

(c) Upper surface at x = 12 in.

Figure D1. Continued.

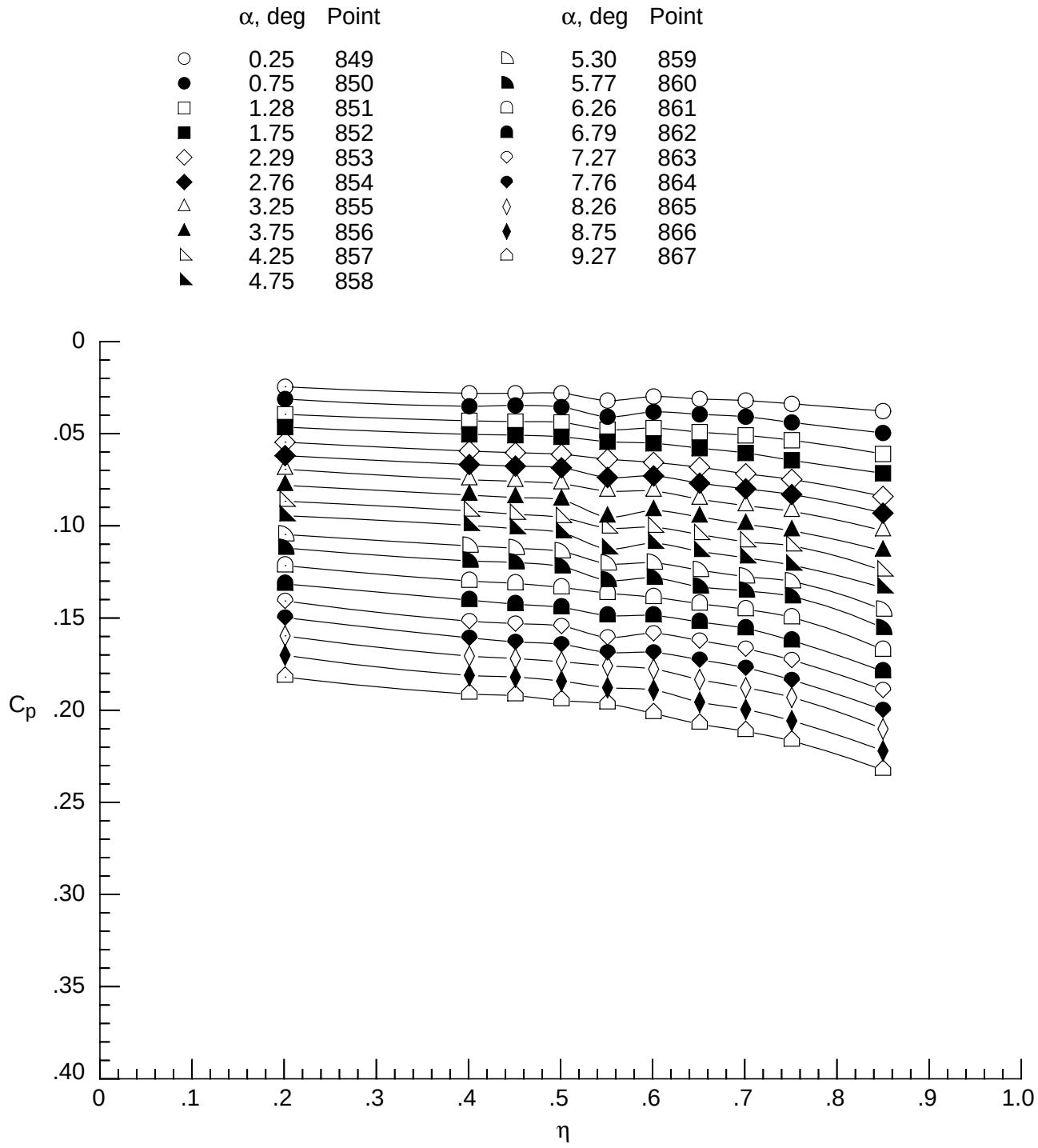

(d) Lower surface at x = 12 in.

Figure D1. Concluded.

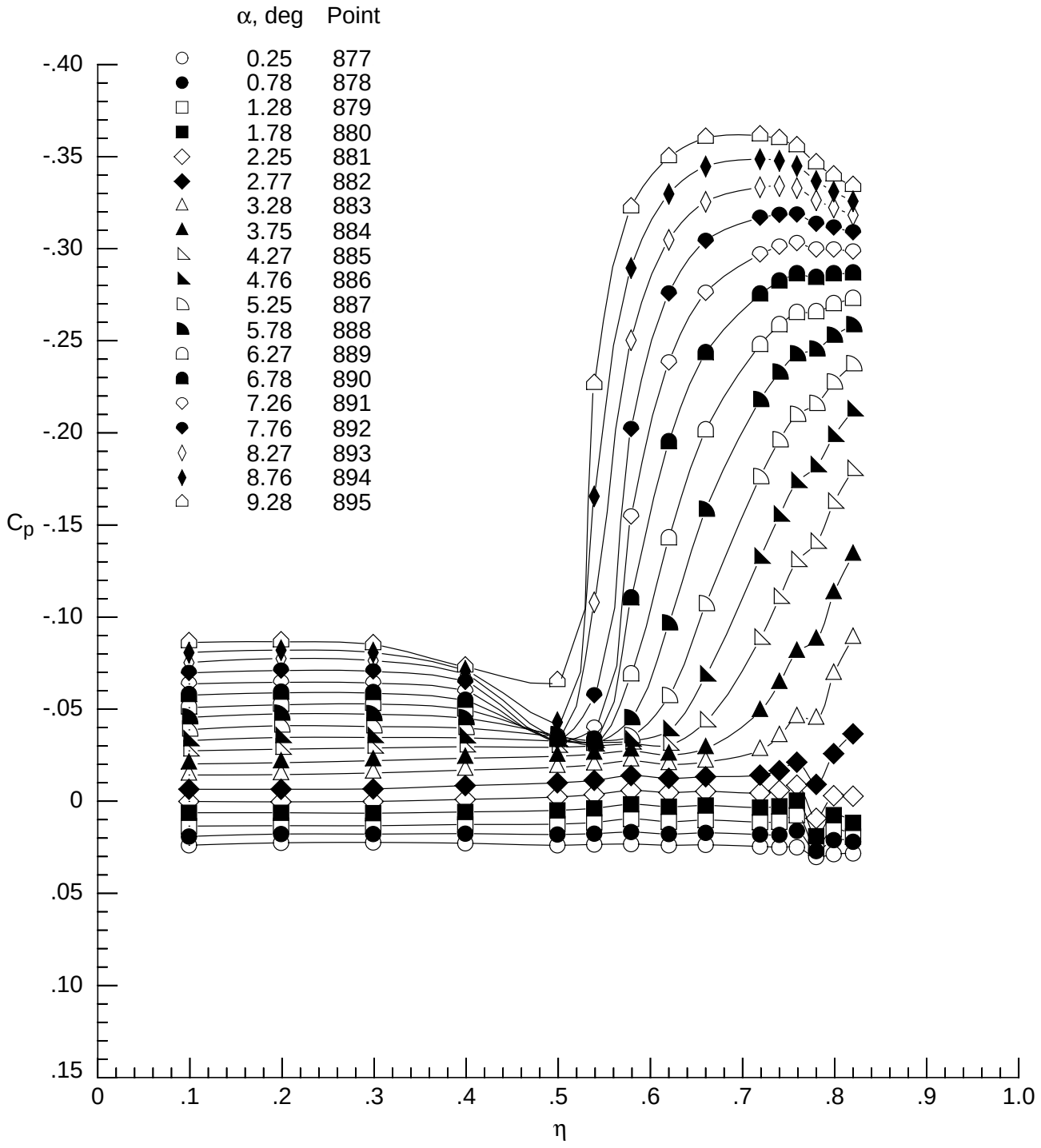

(a) Upper surface at x = 6 in.

Figure D2. Surface-pressure coefficient data for sharp wing without transition grit at M = 1.60 and $R = 2 \times 10^6$ ft^{-1} for run 41.

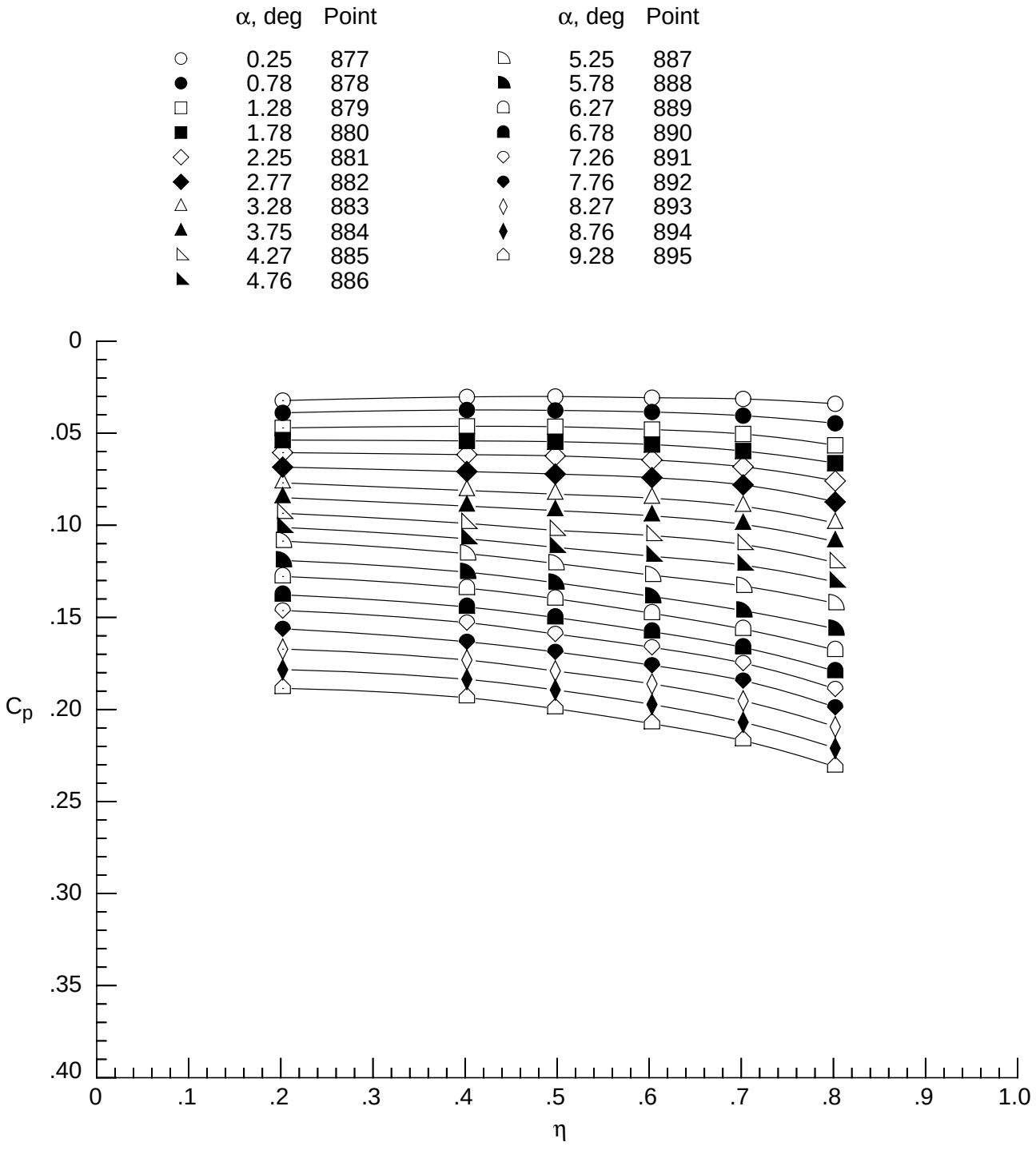

(b) Lower surface at x = 6 in.

Figure D2. Continued.

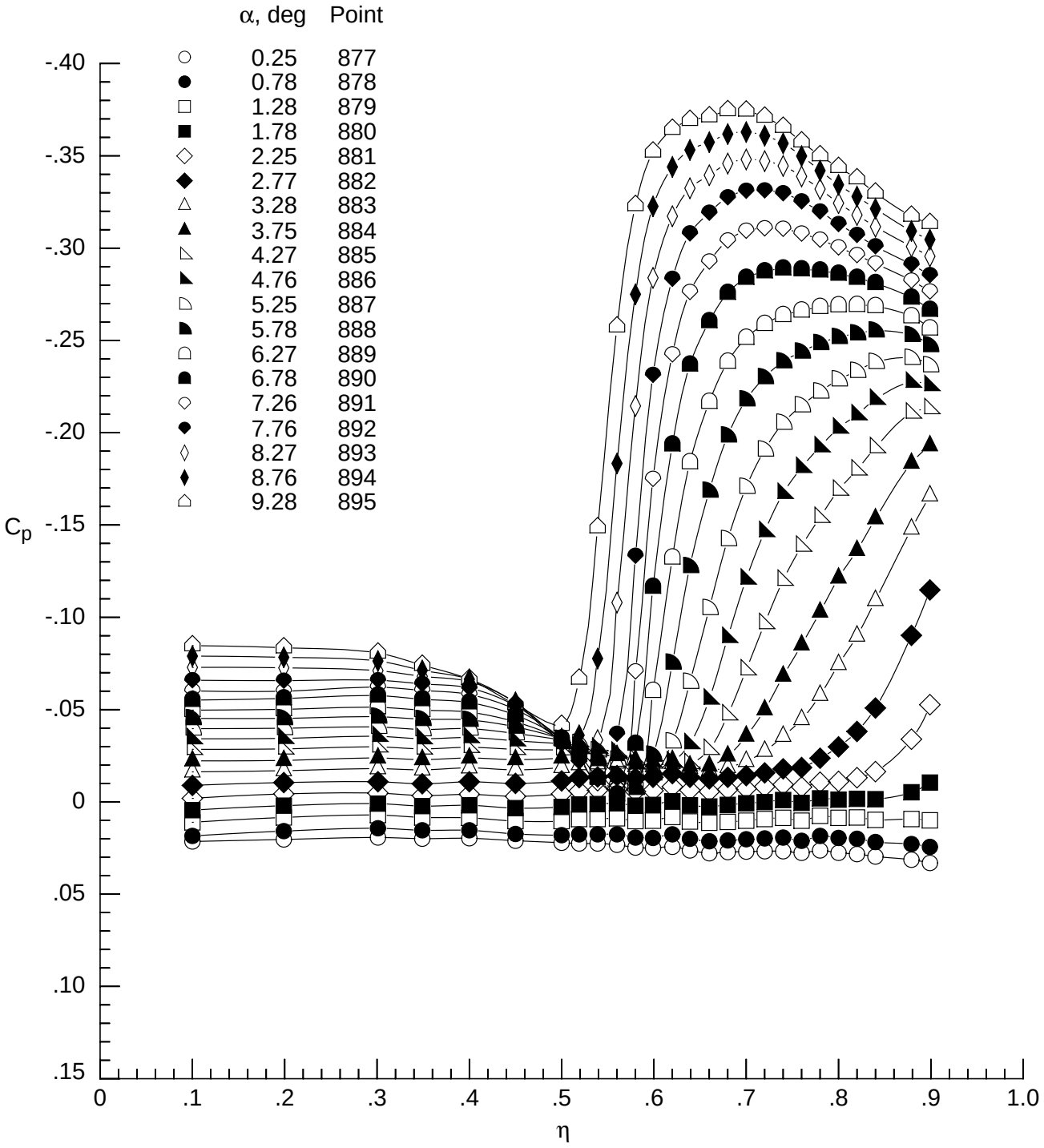

(c) Upper surface at x = 12 in.

Figure D2. Continued.

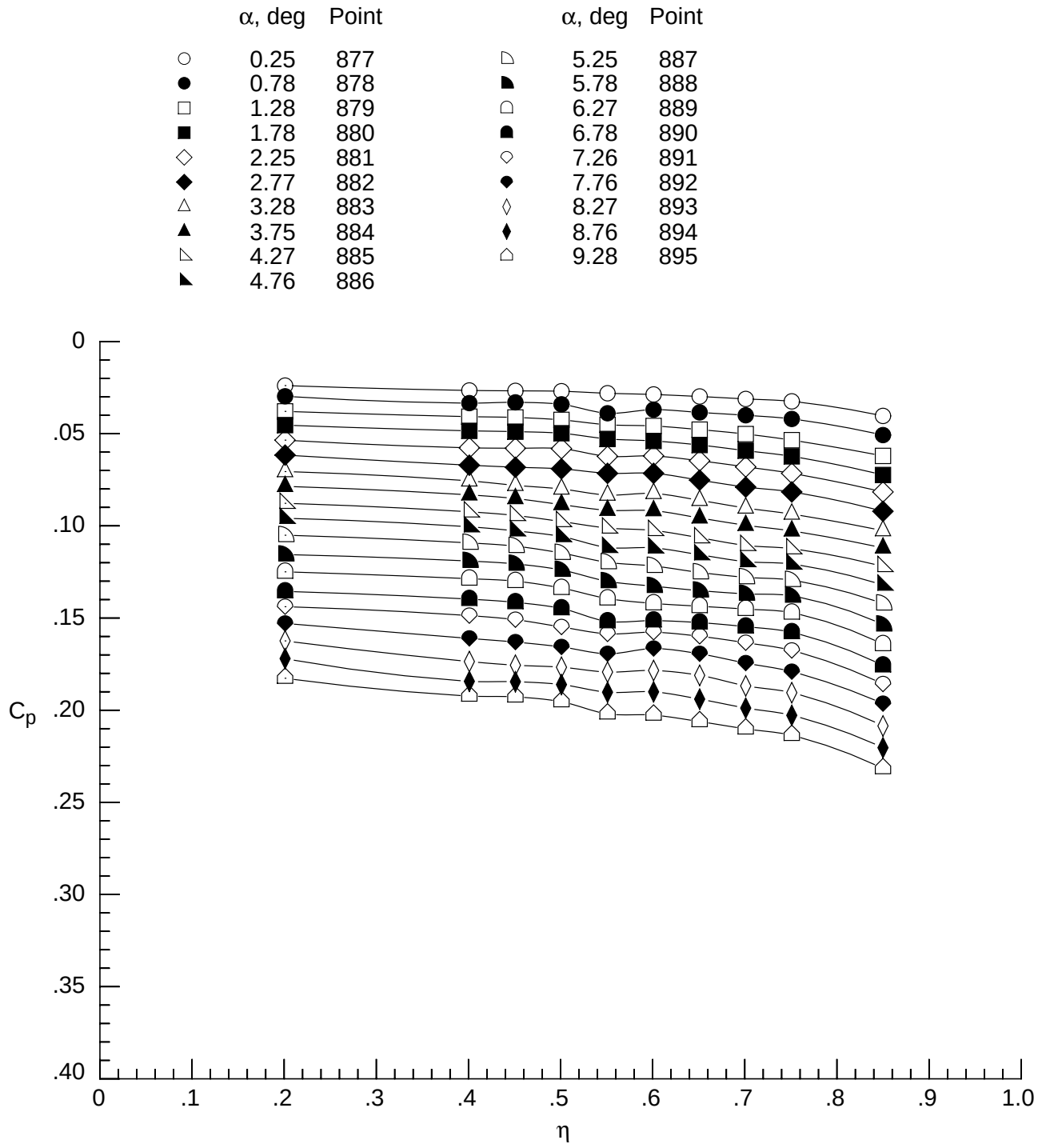

(d) Lower surface at x = 12 in.

Figure D2. Concluded.

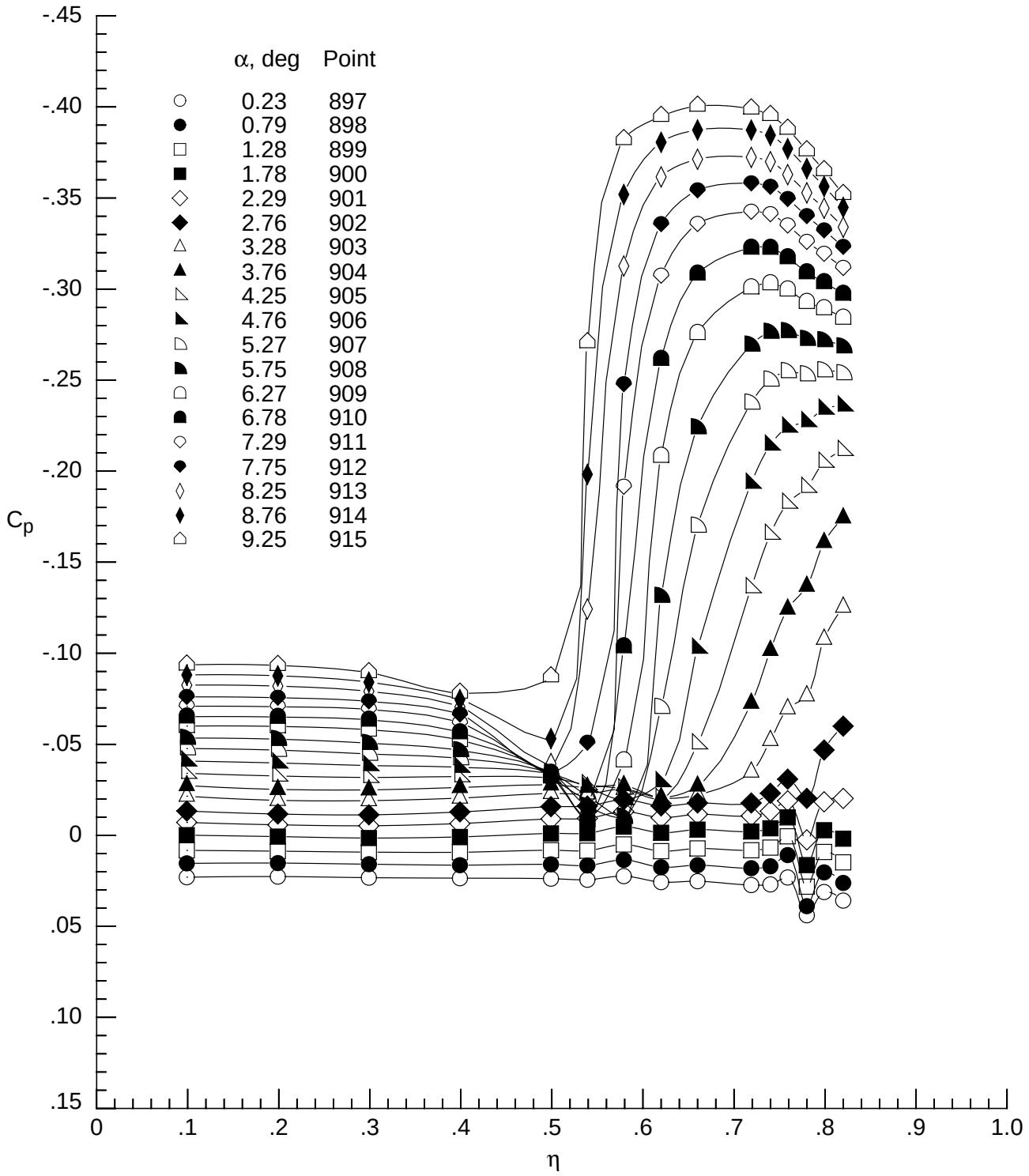

(a) Upper surface at x = 6 in.

Figure D3. Surface-pressure coefficient data for sharp wing without transition grit at M = 1.60 and $R = 5 \times 10^6$ ft^{-1} for run 42.

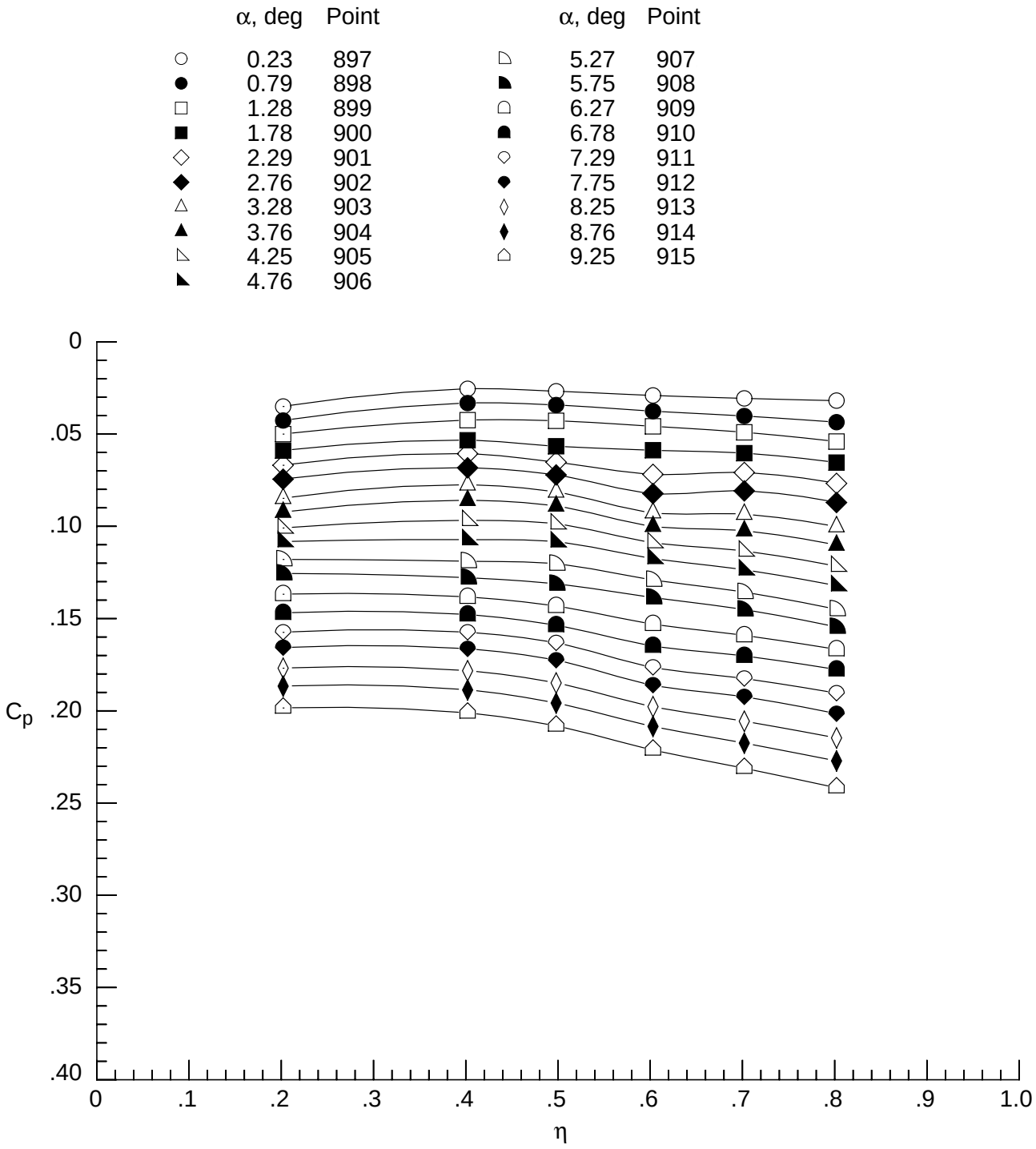

(b) Lower surface at x = 6 in.

Figure D3. Continued.

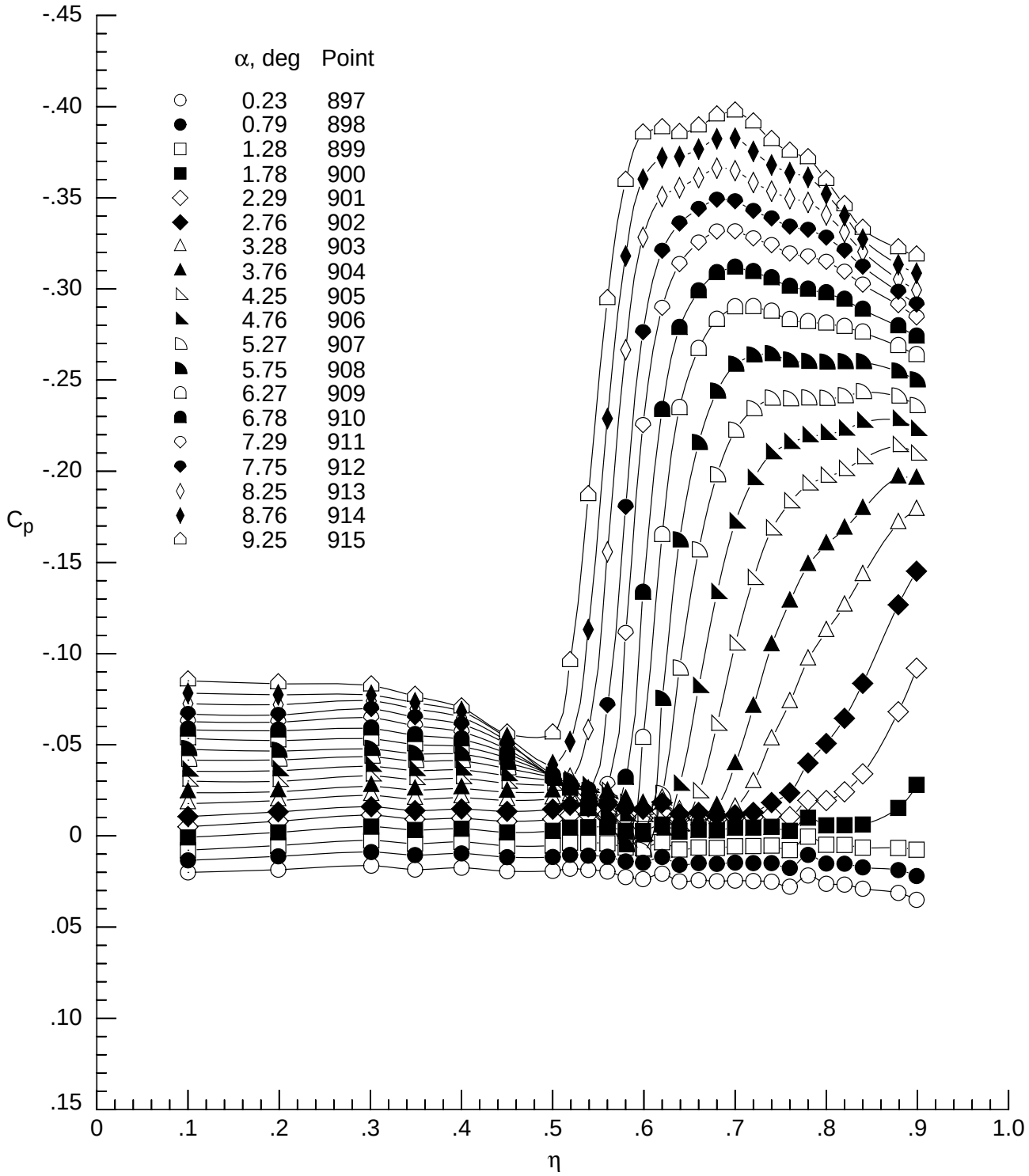

(c) Upper surface at x = 12 in.

Figure D3. Continued.

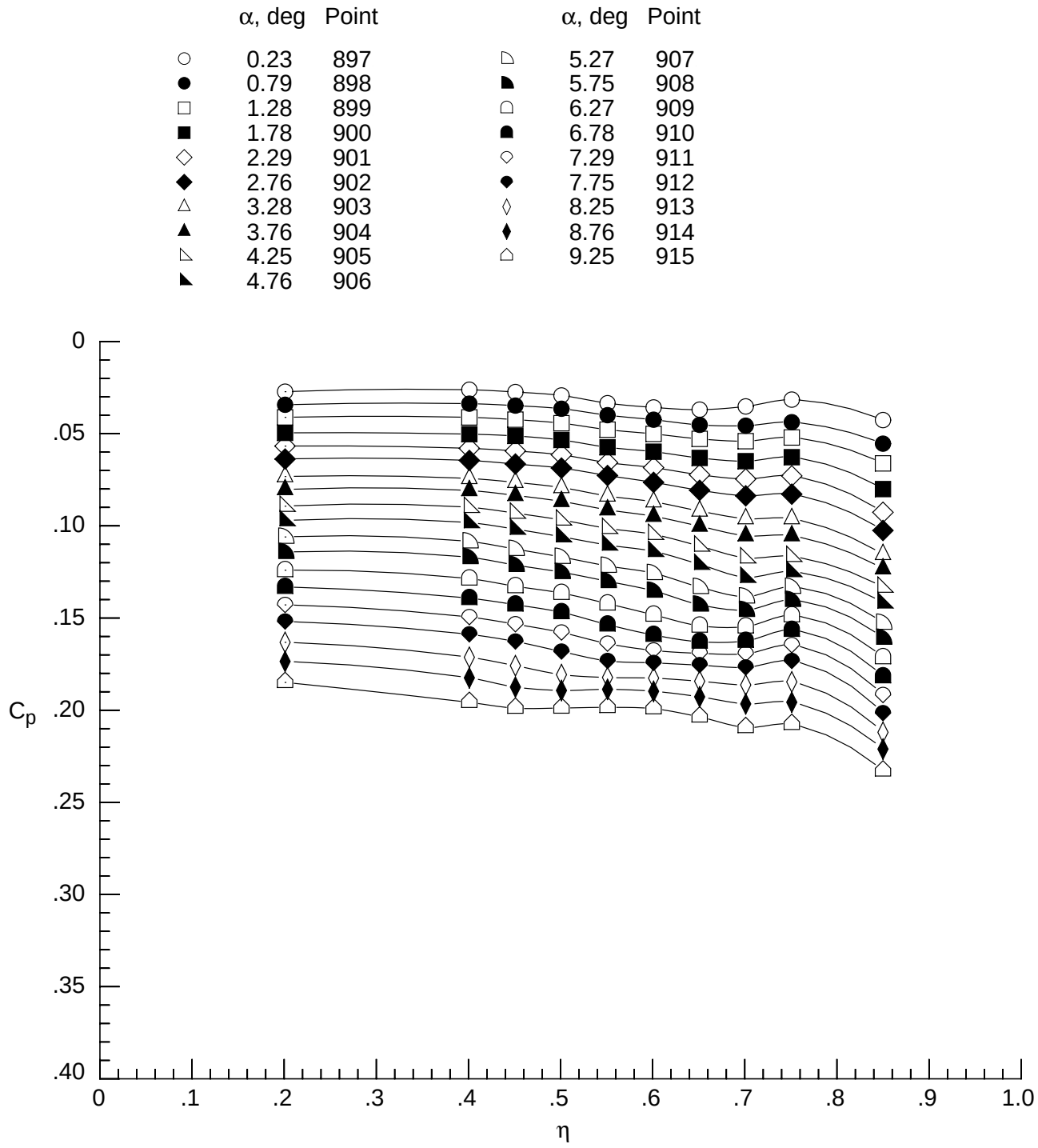

(d) Lower surface at x = 12 in.

Figure D3. Concluded.

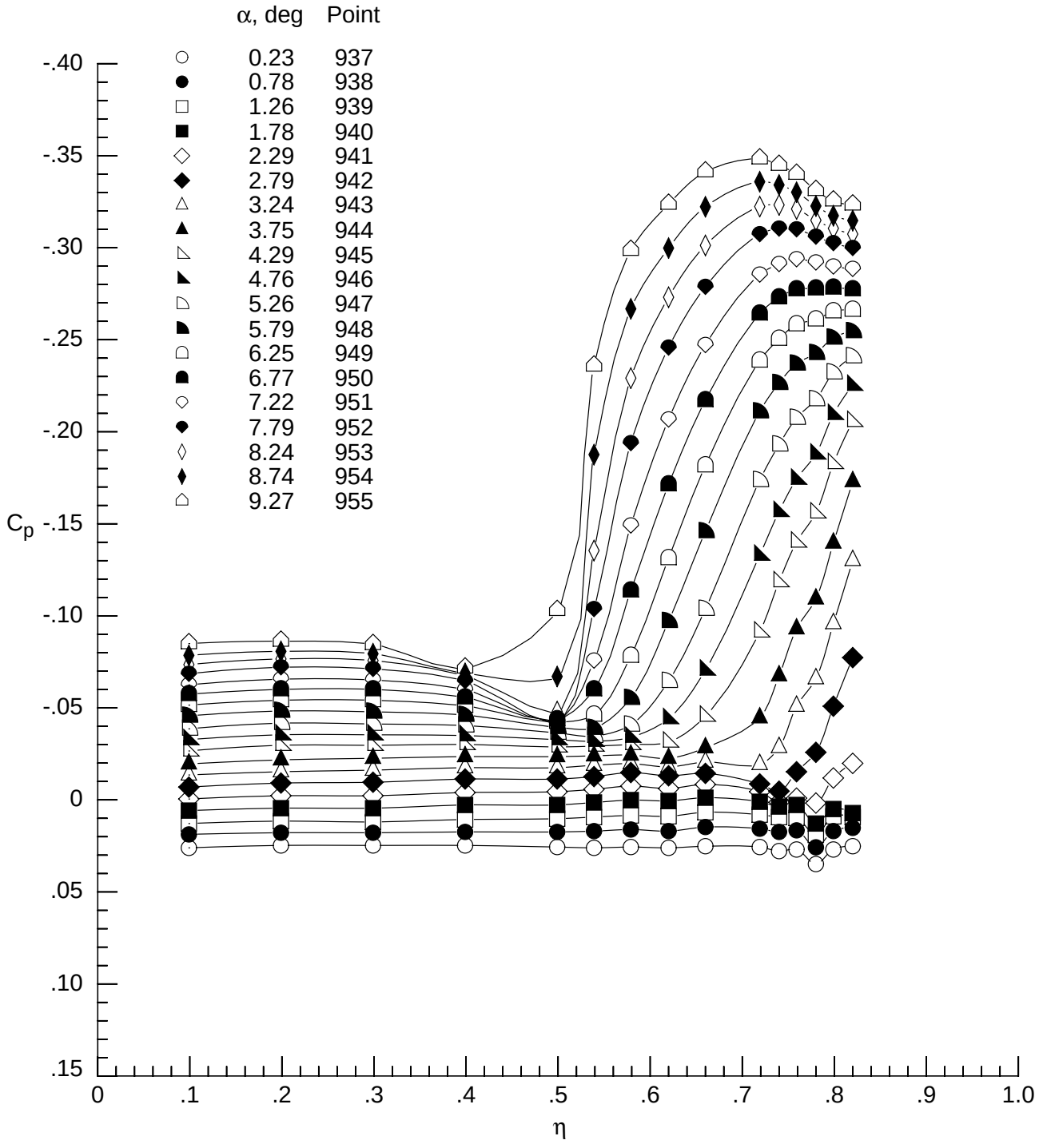

(a) Upper surface at x = 6 in.

Figure D4. Surface-pressure coefficient data for sharp wing with transition grit at $M = 1.60$ and $R = 1 \times 10^6$ ft^{-1} for run 43.

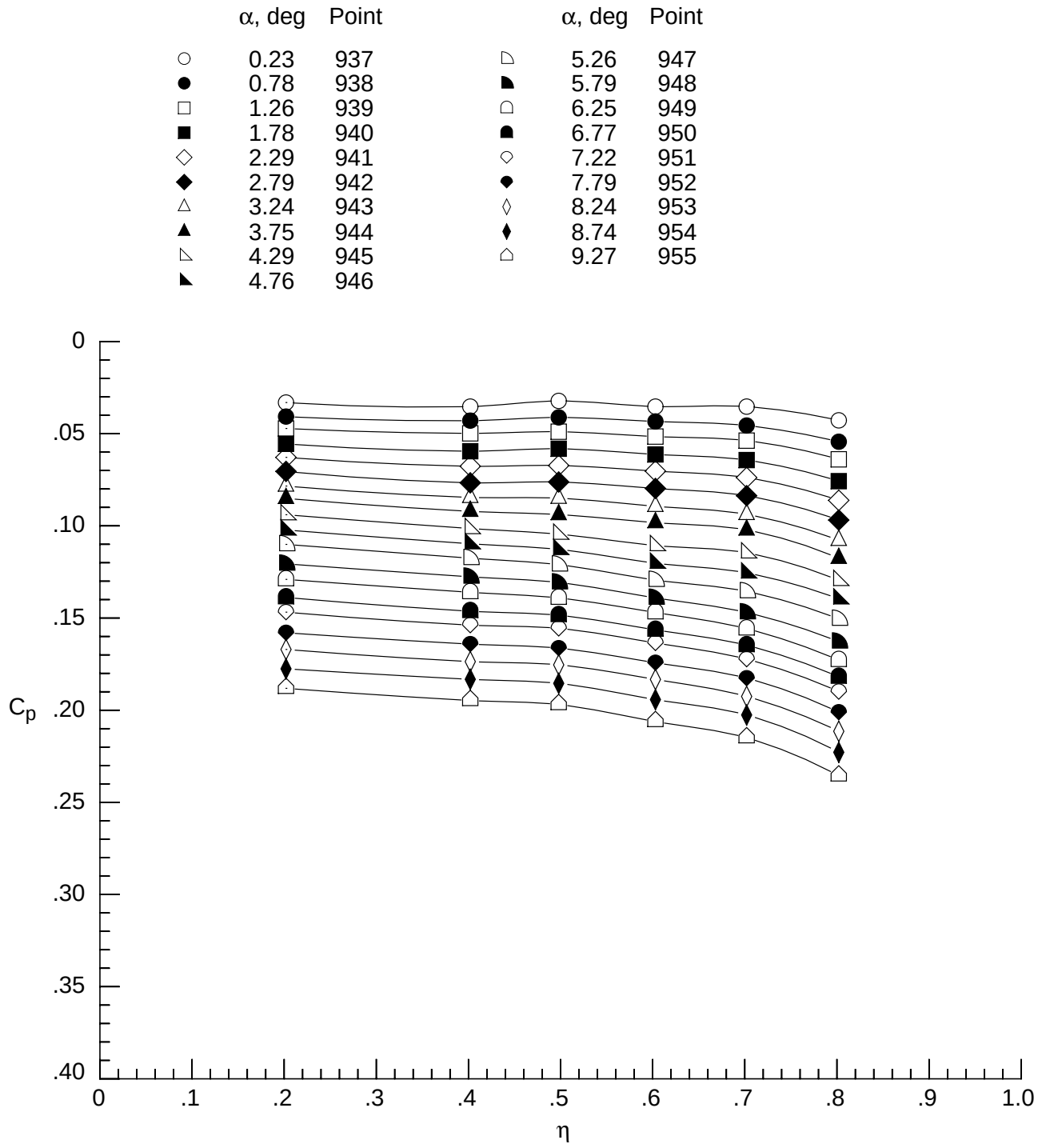

(b) Lower surface at x = 6 in.

Figure D4. Continued.

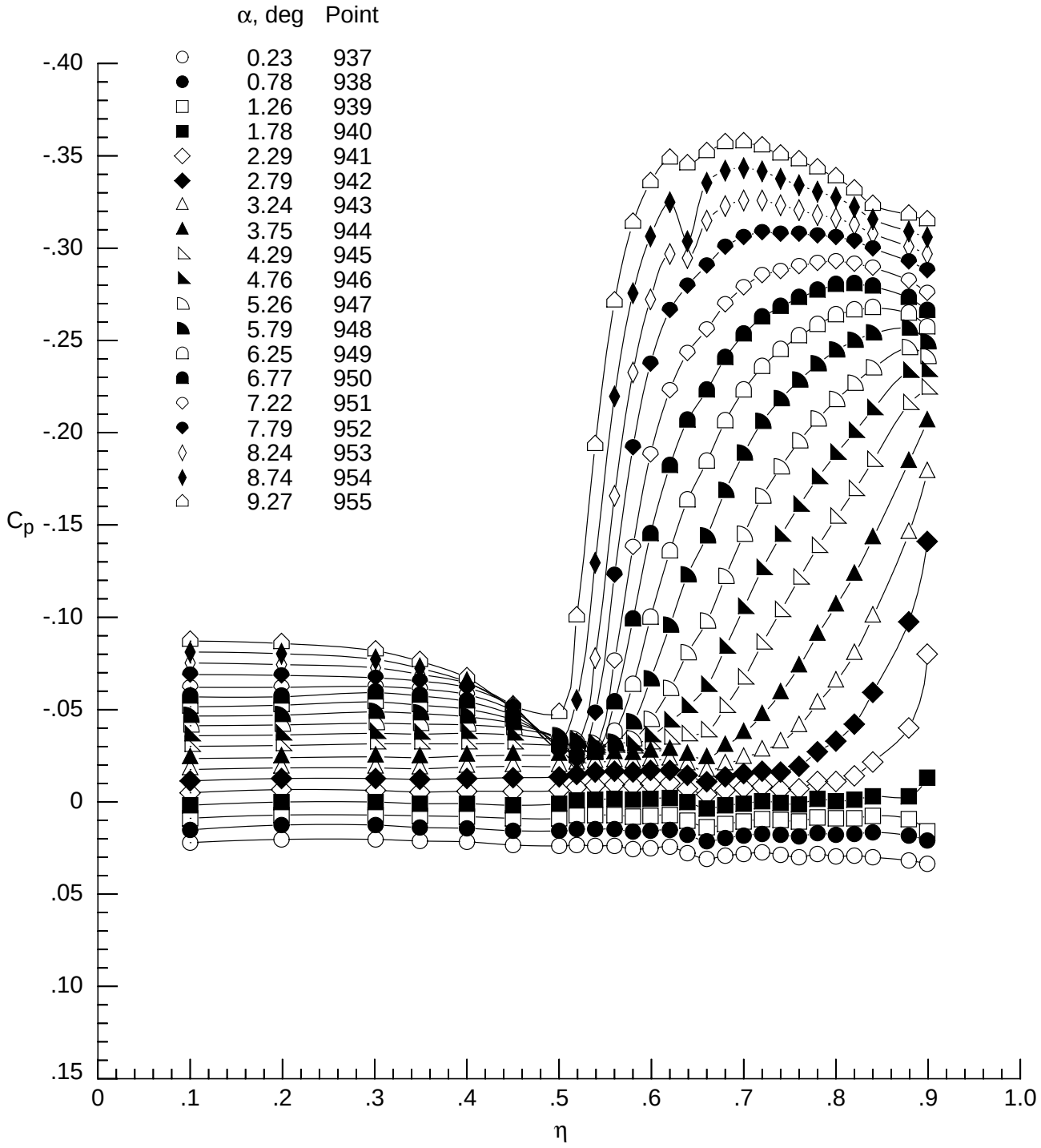

(c) Upper surface at x = 12 in.

Figure D4. Continued.

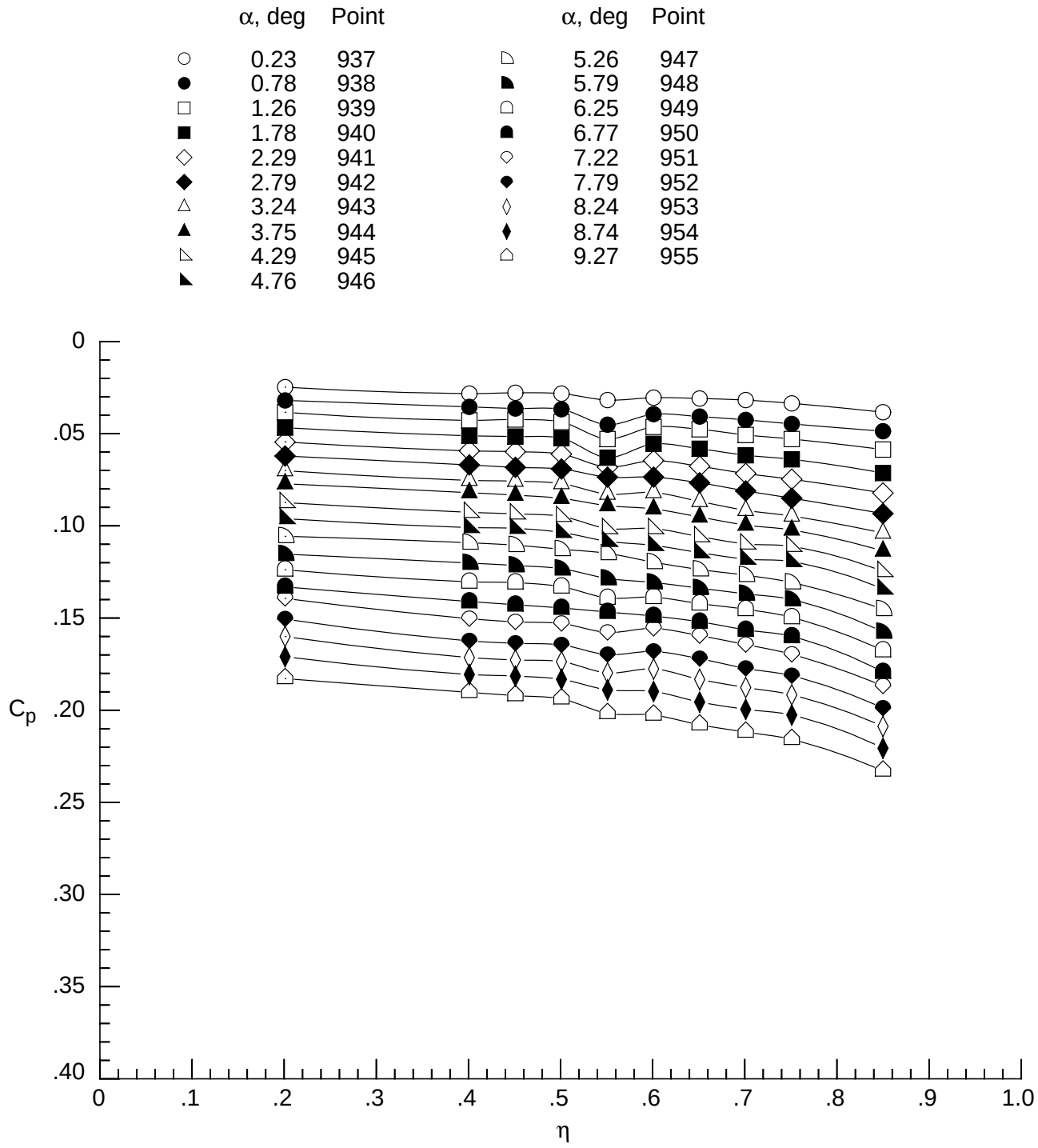

(d) Lower surface at x = 12 in.

Figure D4. Concluded.

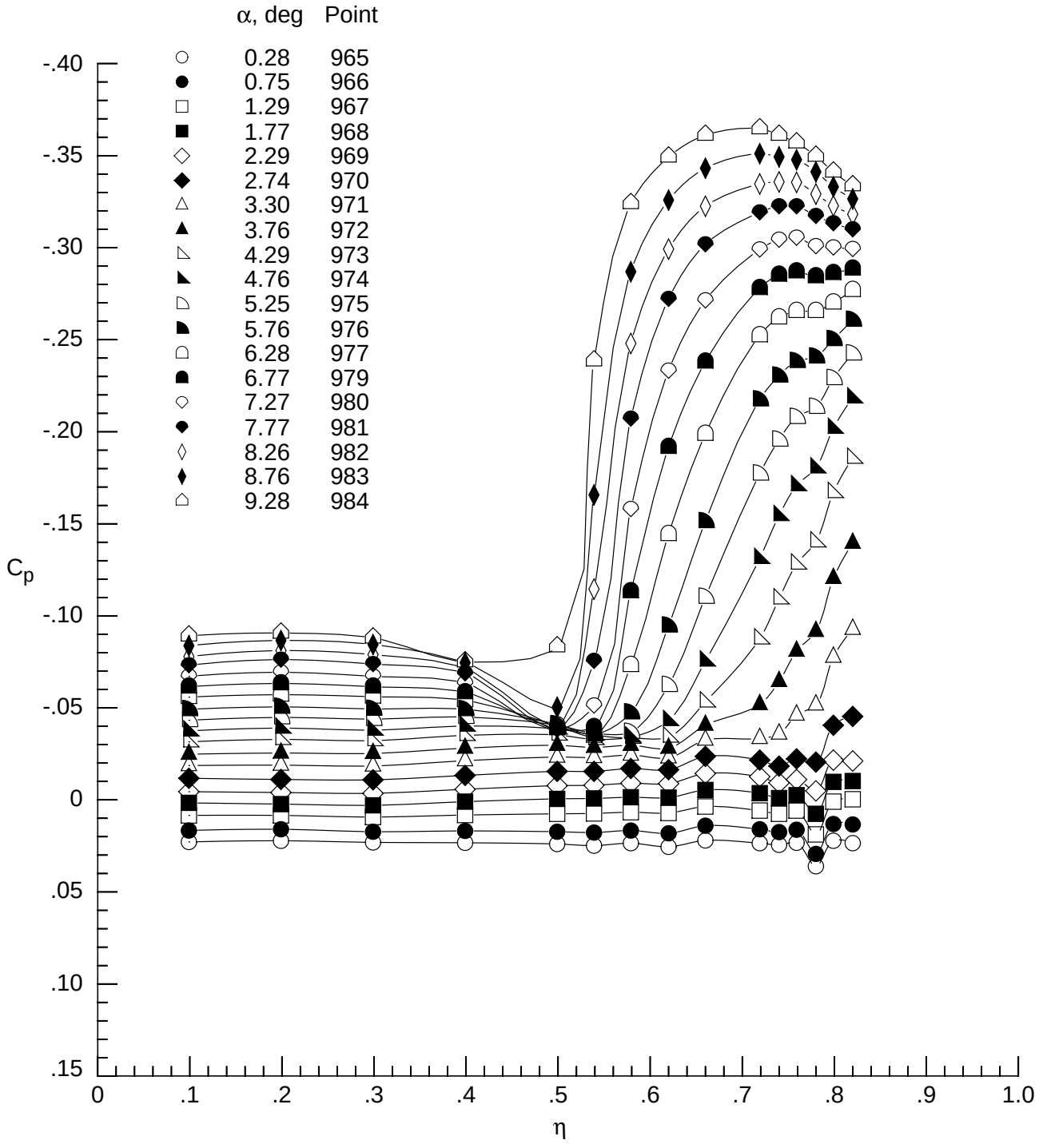

(a) Upper surface at x = 6 in.

Figure D5. Surface-pressure coefficient data for sharp wing with transition grit at $M = 1.60$ and $R = 2 \times 10^6$ ft^{-1} for run 44.

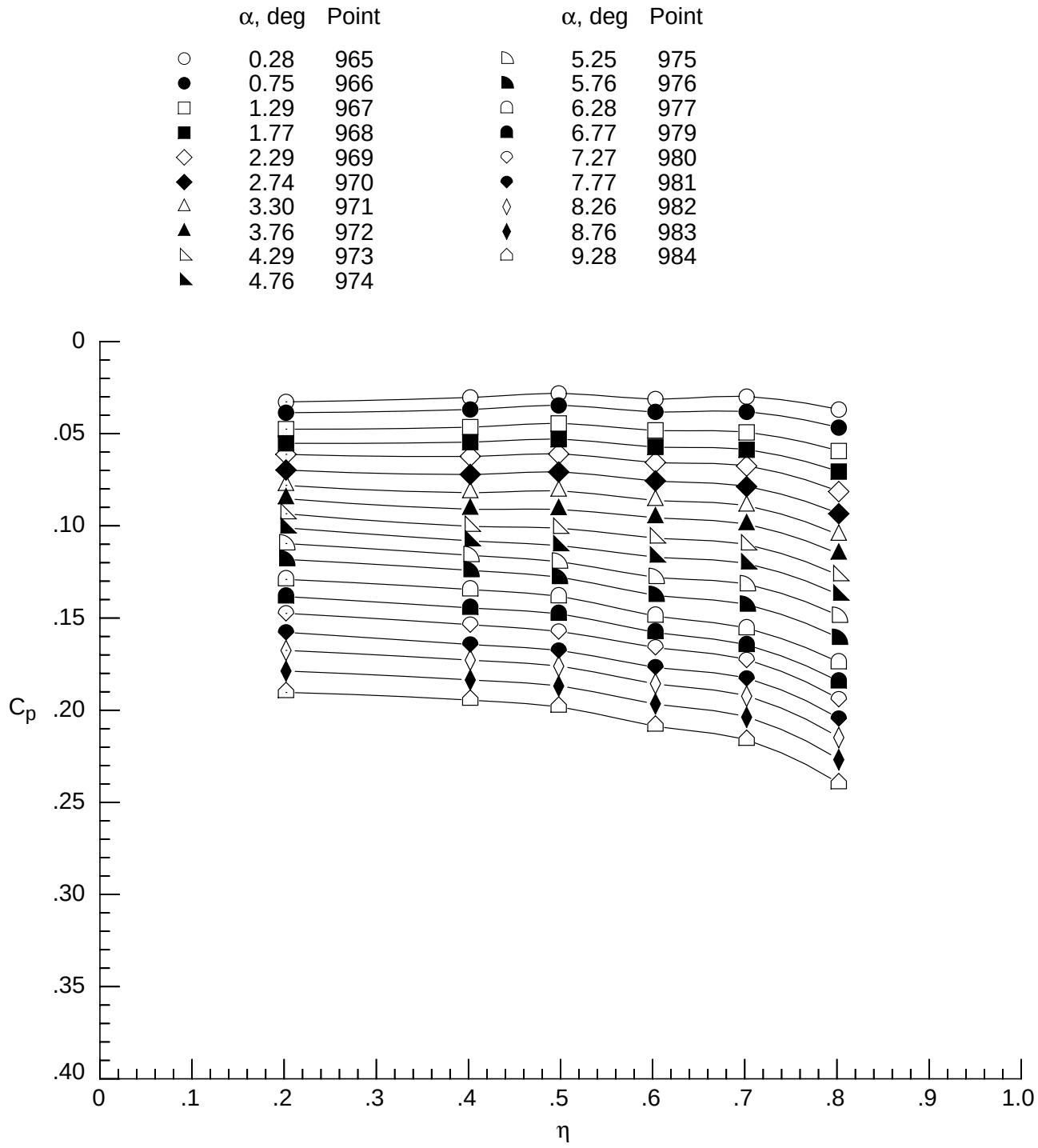

(b) Lower surface at x = 6 in.

Figure D5. Continued.

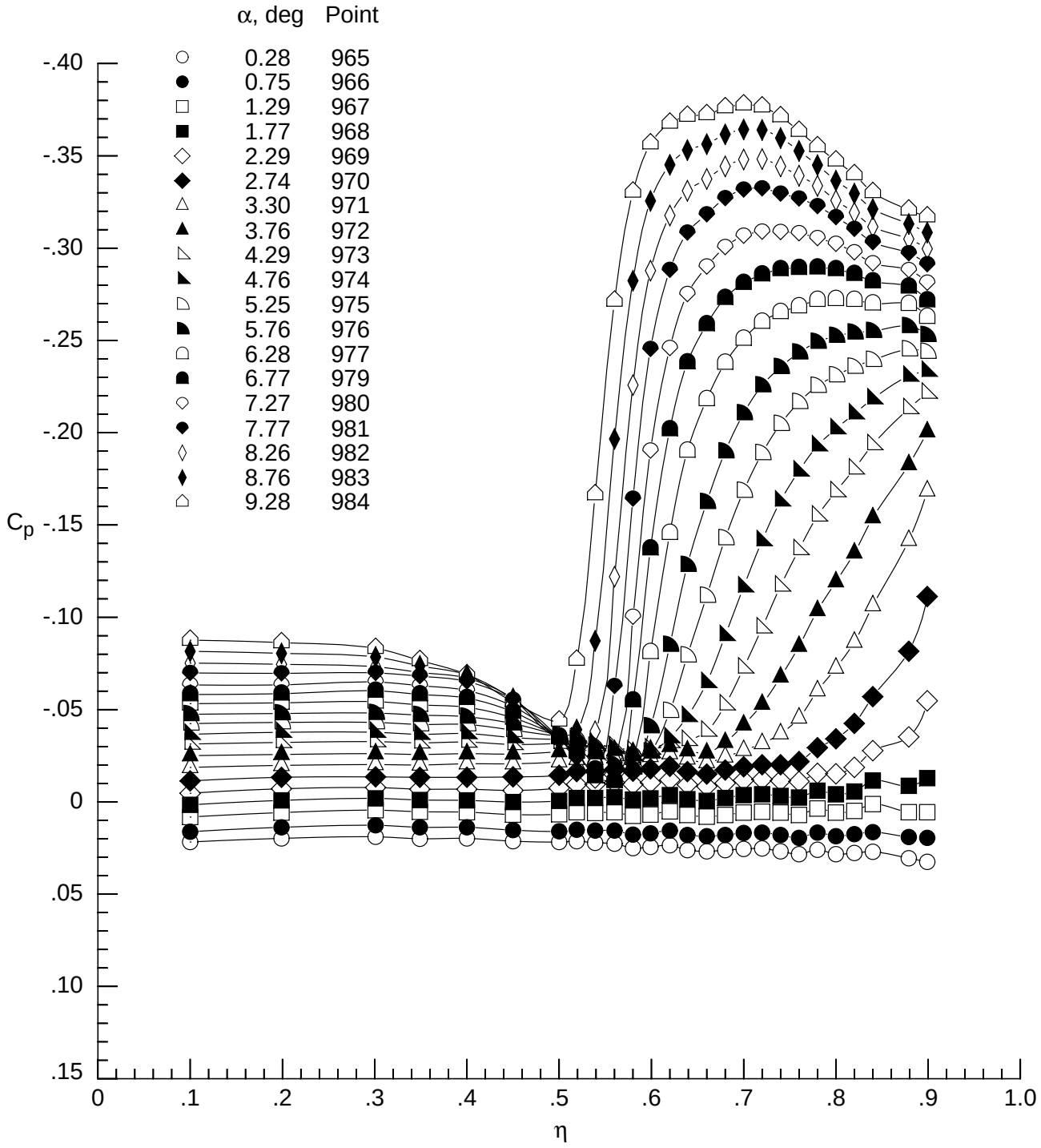

(c) Upper surface at x = 12 in.

Figure D5. Continued.

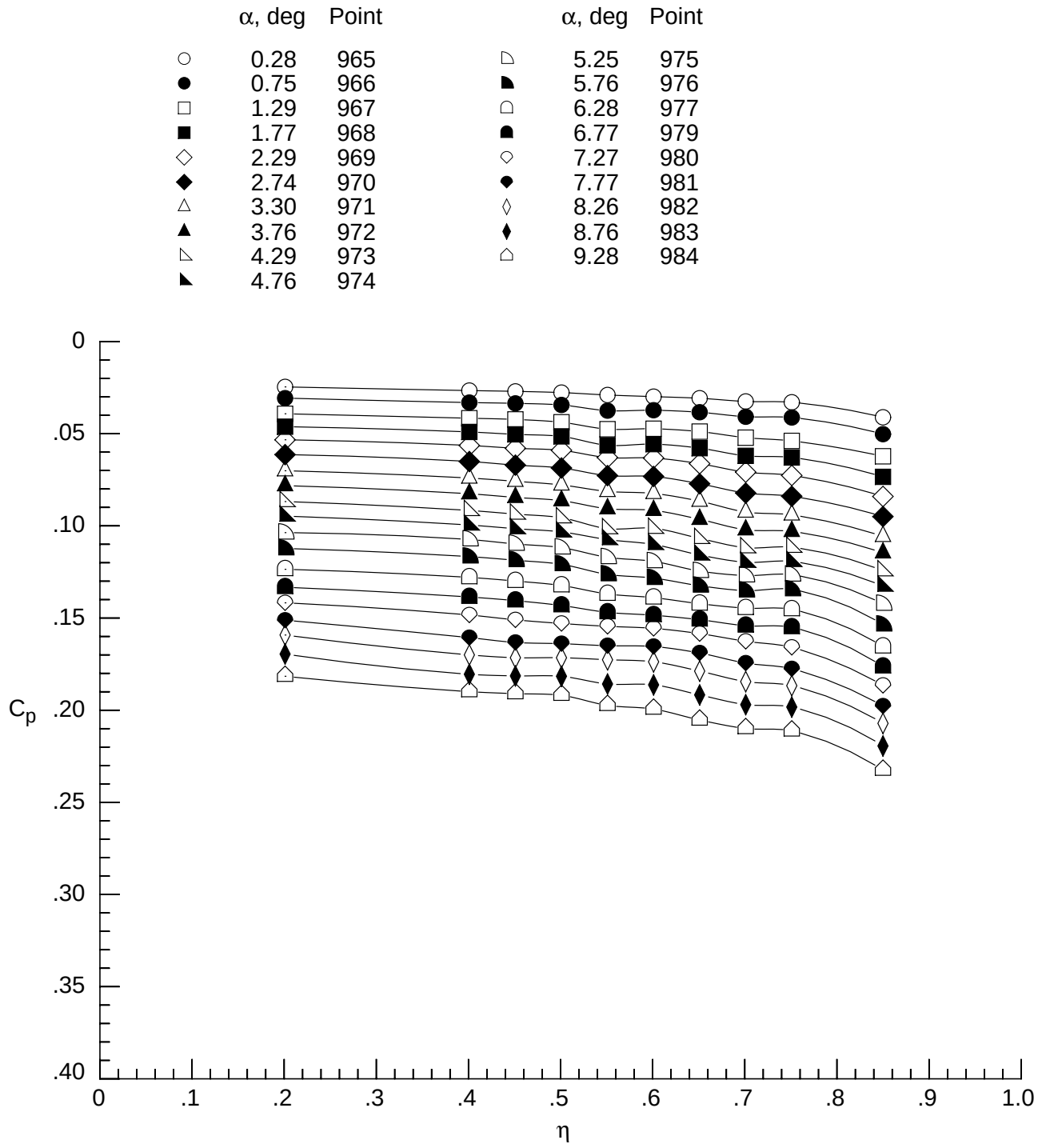

(d) Lower surface at x = 12 in.

Figure D5. Concluded.

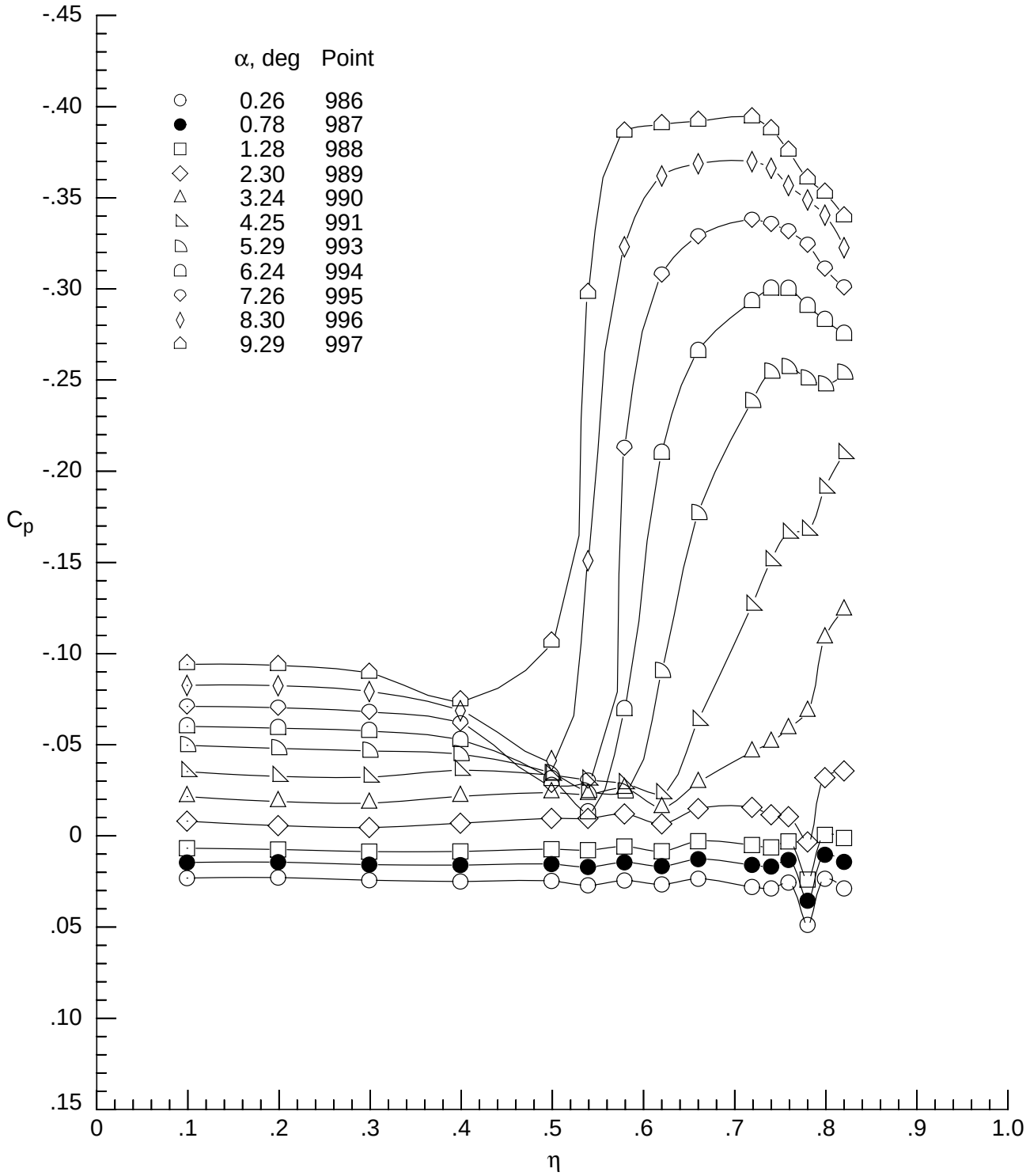

(a) Upper surface at x = 6 in.

Figure D6. Surface-pressure coefficient data for sharp wing with transition grit at $M = 1.60$ and $R = 5 \times 10^6$ ft^{-1} for run 45.

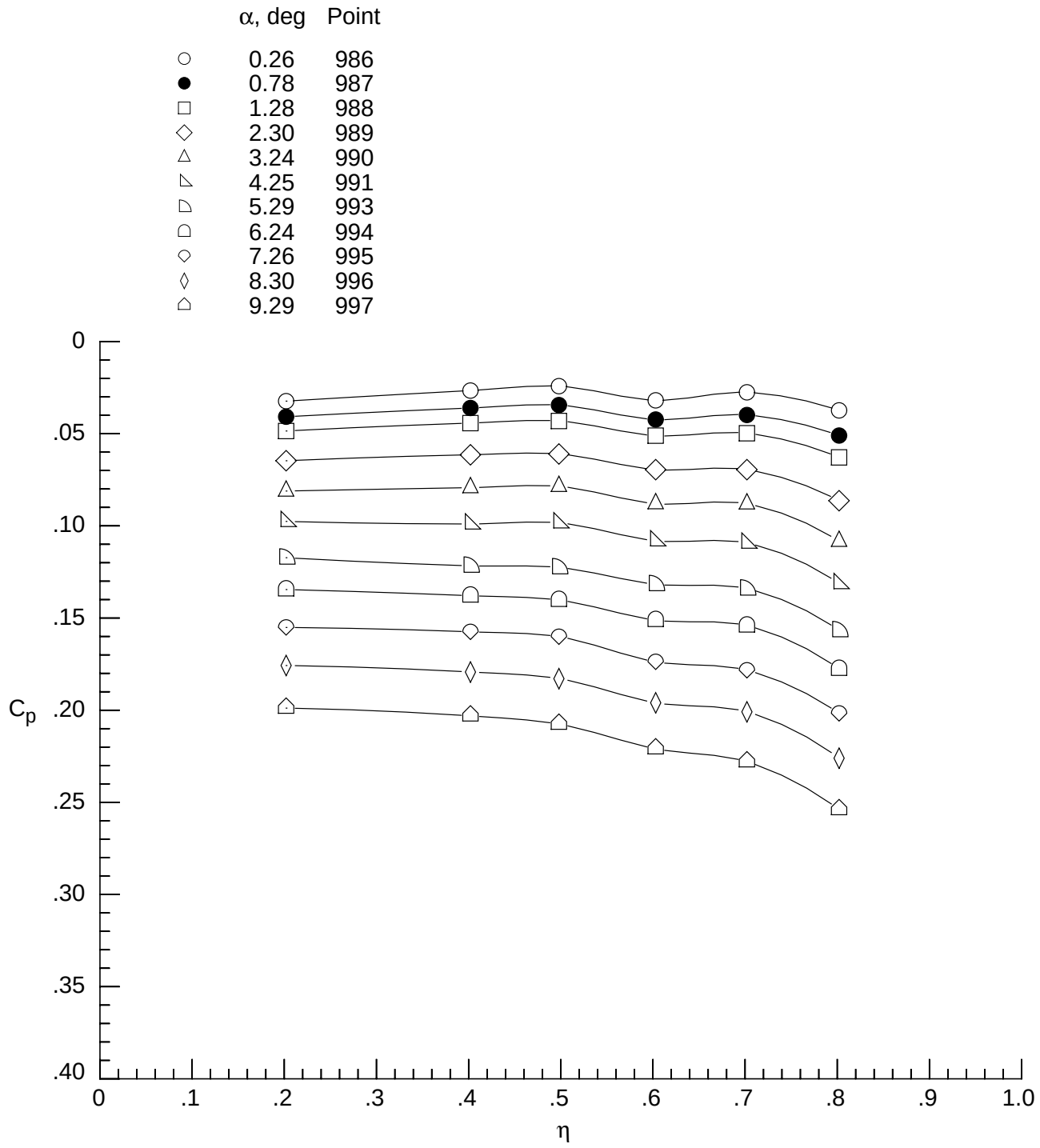

(b) Lower surface at x = 6 in.

Figure D6. Continued.

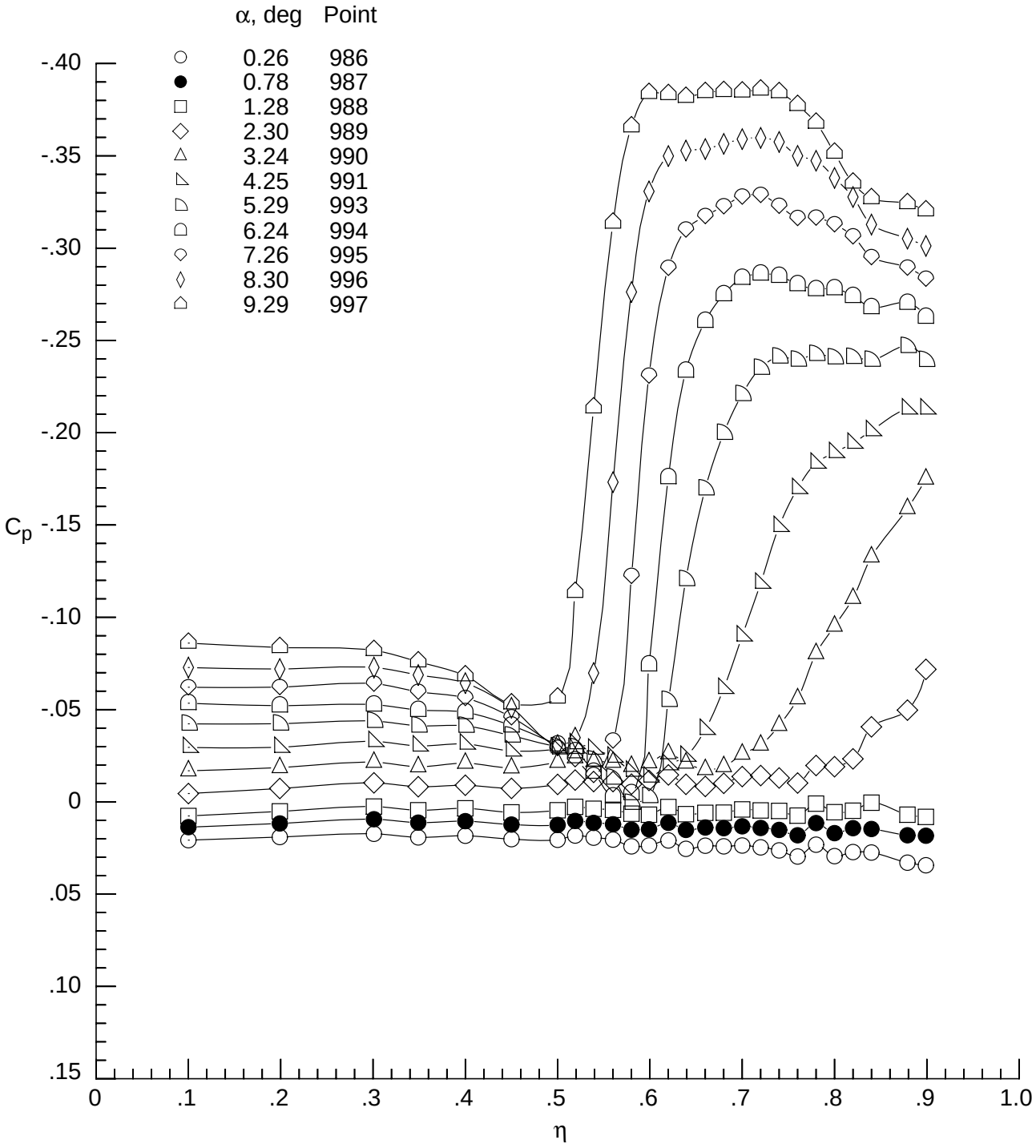

(c) Upper surface at x = 12 in.

Figure D6. Continued.

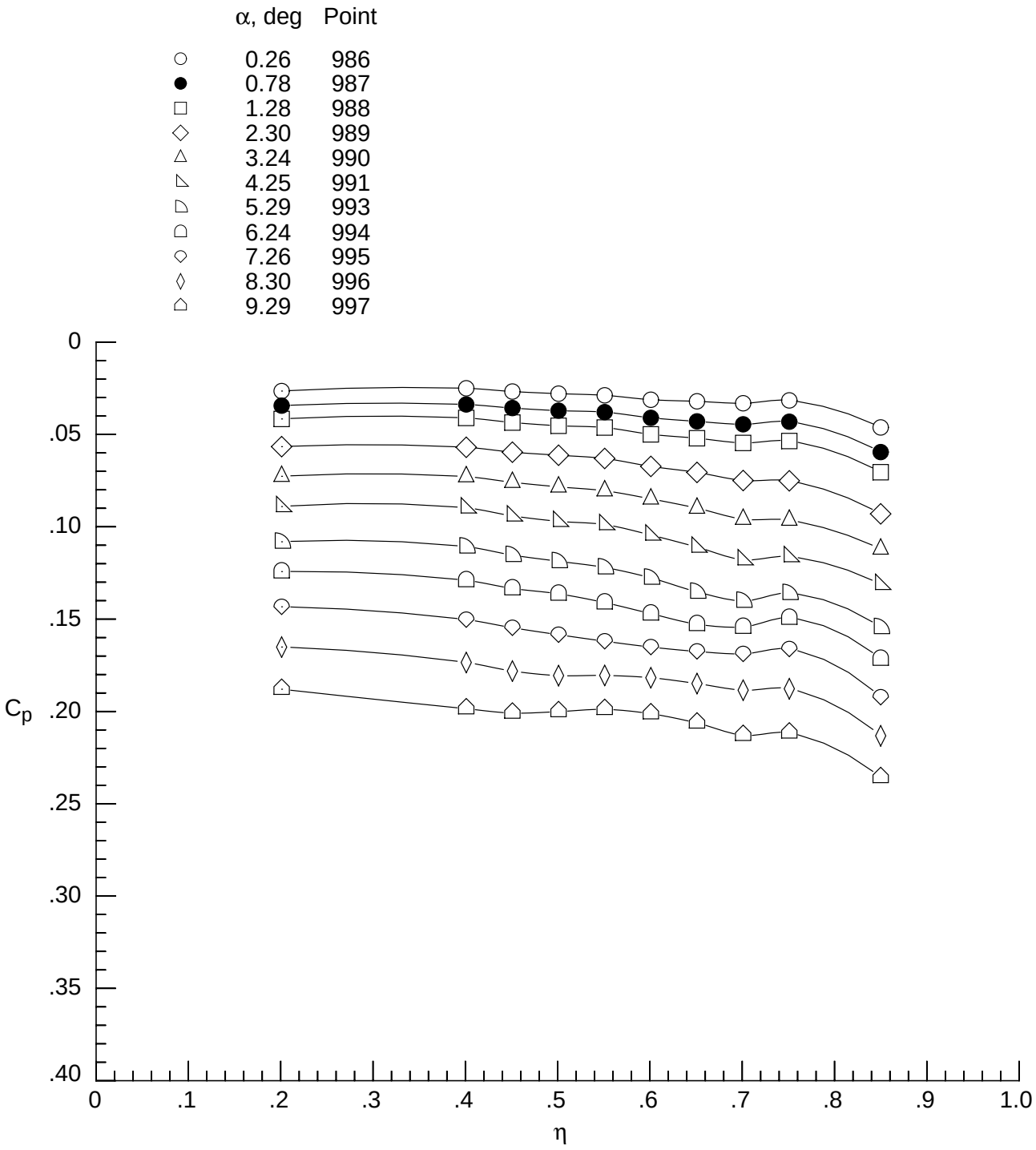

(d) Lower surface at x = 12 in.

Figure D6. Concluded.

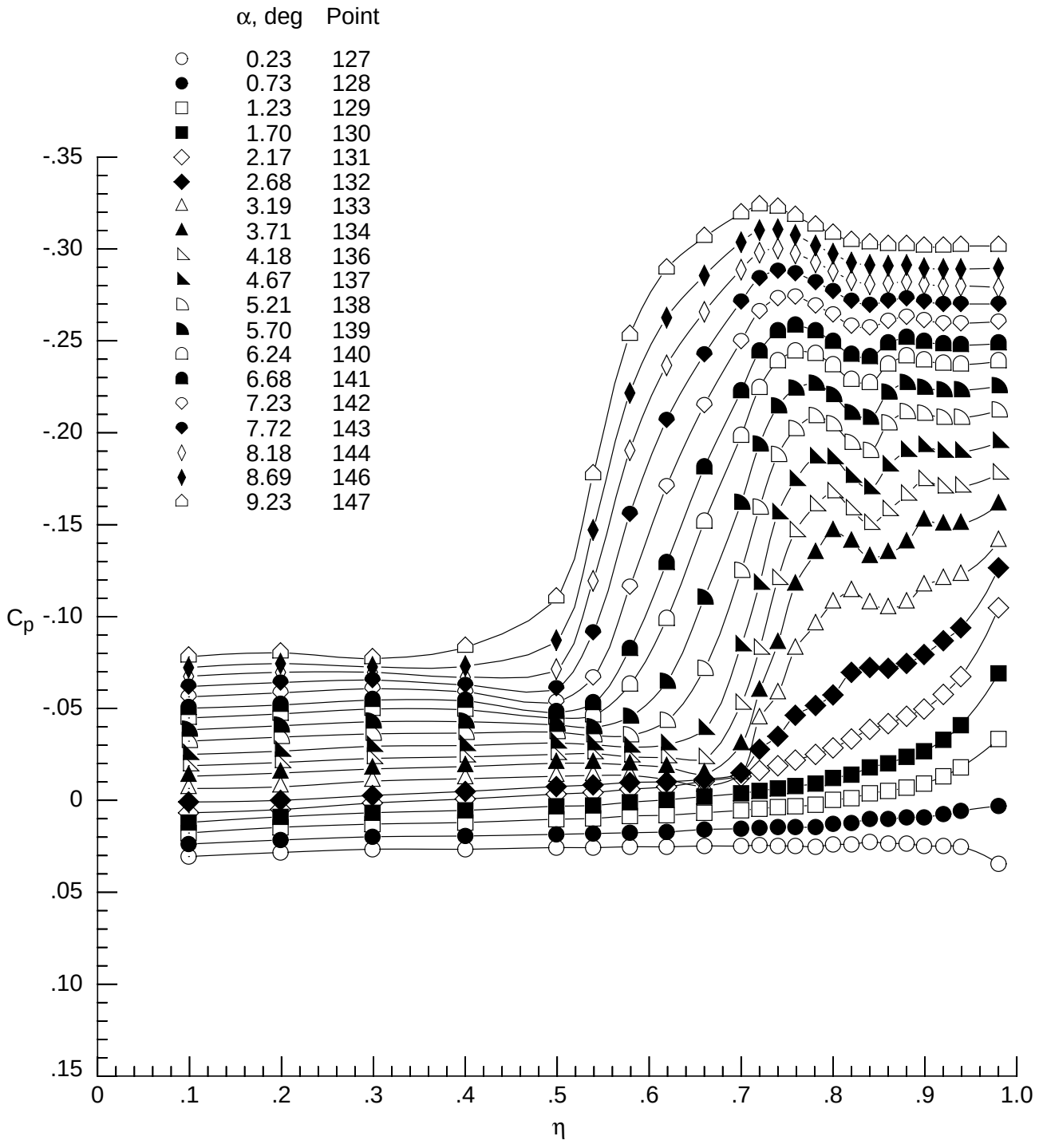

(a) Upper surface at x = 6 in.

Figure D7. Surface-pressure coefficient data for elliptical wing without transition grit at M = 1.60 and $R = 1 \times 10^6$ ft^{-1} for run 6.

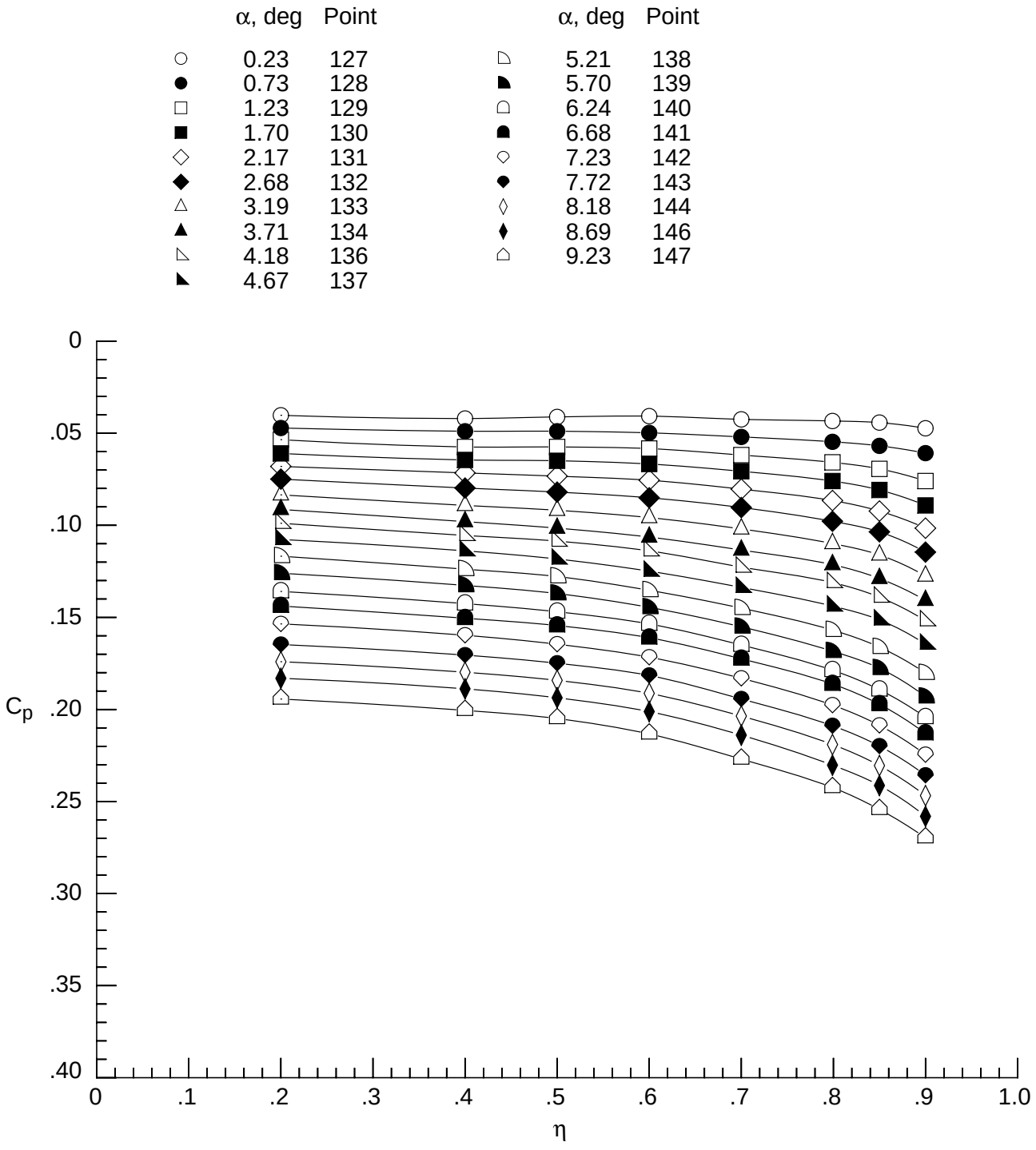

(b) Lower surface at x = 6 in.

Figure D7. Continued.

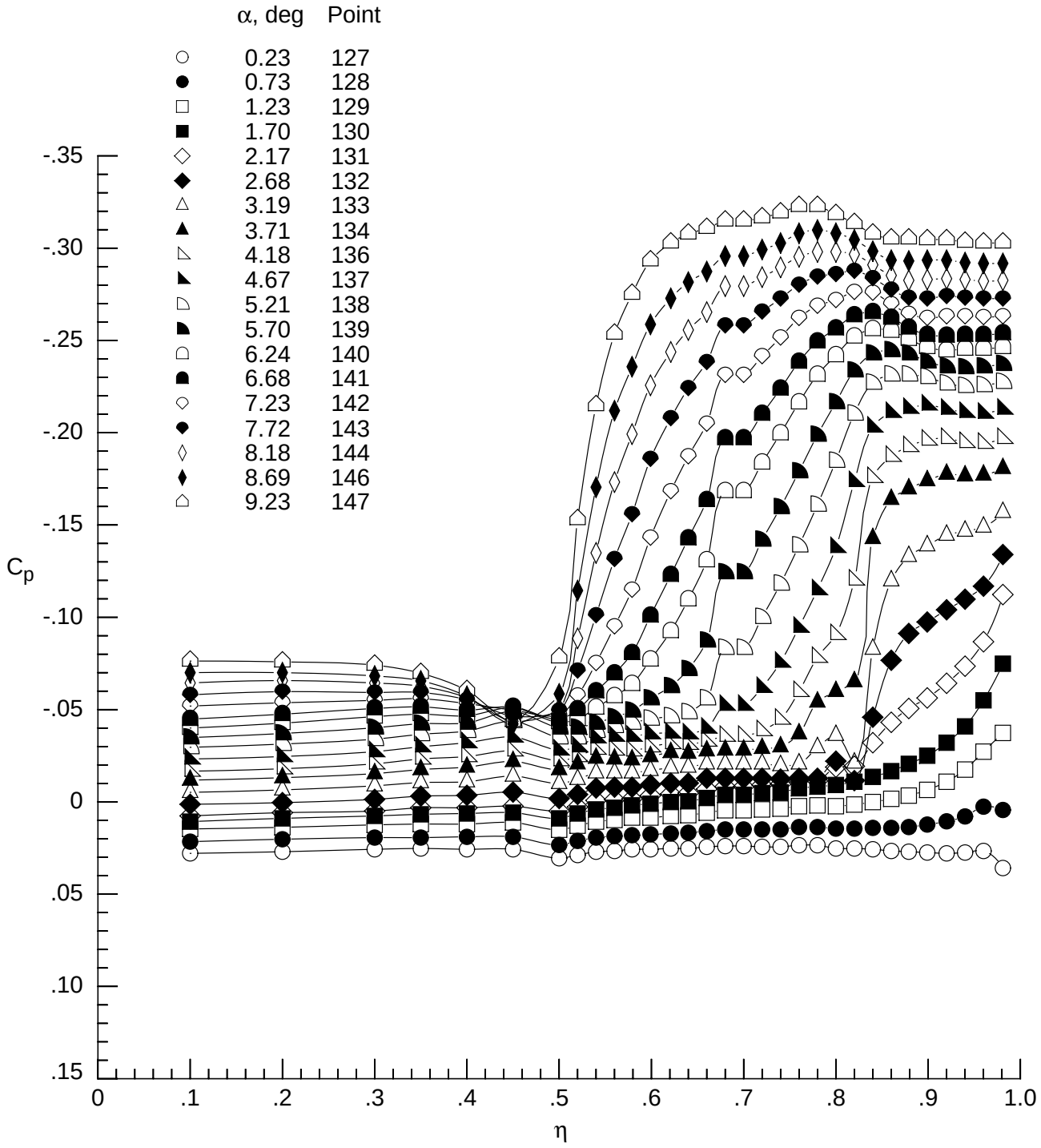

(c) Upper surface at x = 12 in.

Figure D7. Continued.

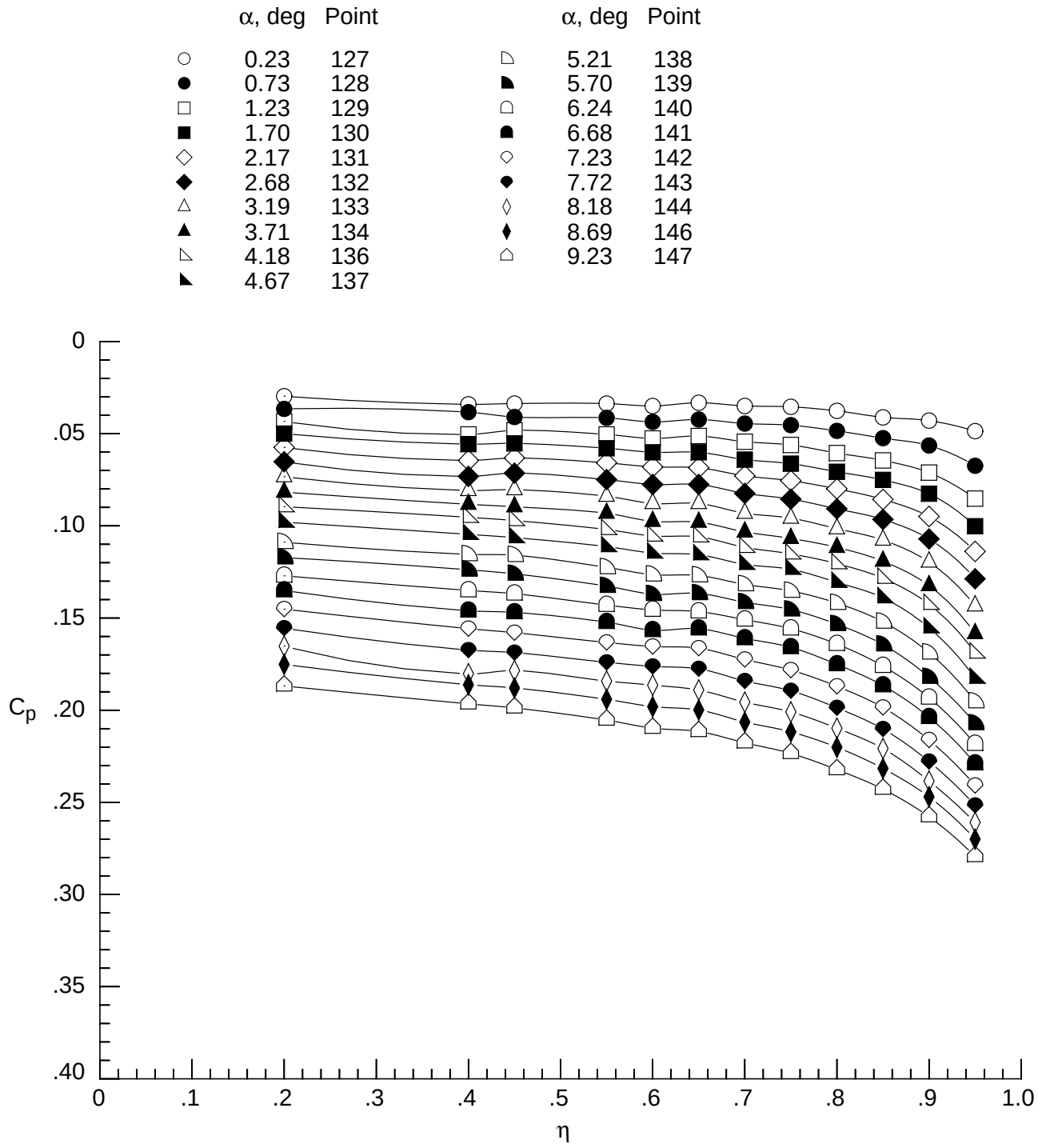

(d) Lower surface at x = 12 in.

Figure D7. Concluded.

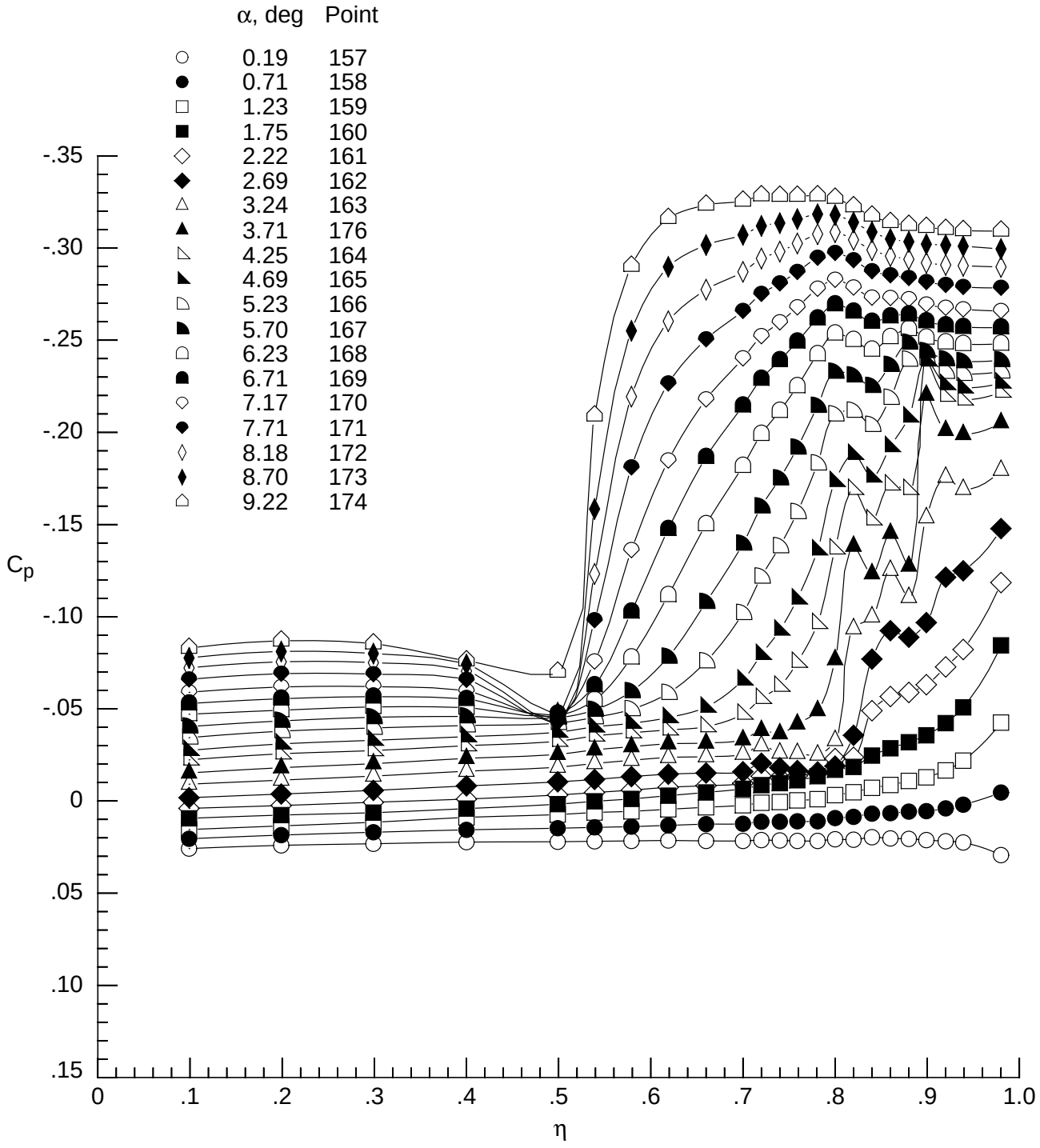

(a) Upper surface at x = 6 in.

Figure D8. Surface-pressure coefficient data for elliptical wing without transition grit at M = 1.60 and $R = 2 \times 10^6$ ft^{-1} for run 7.

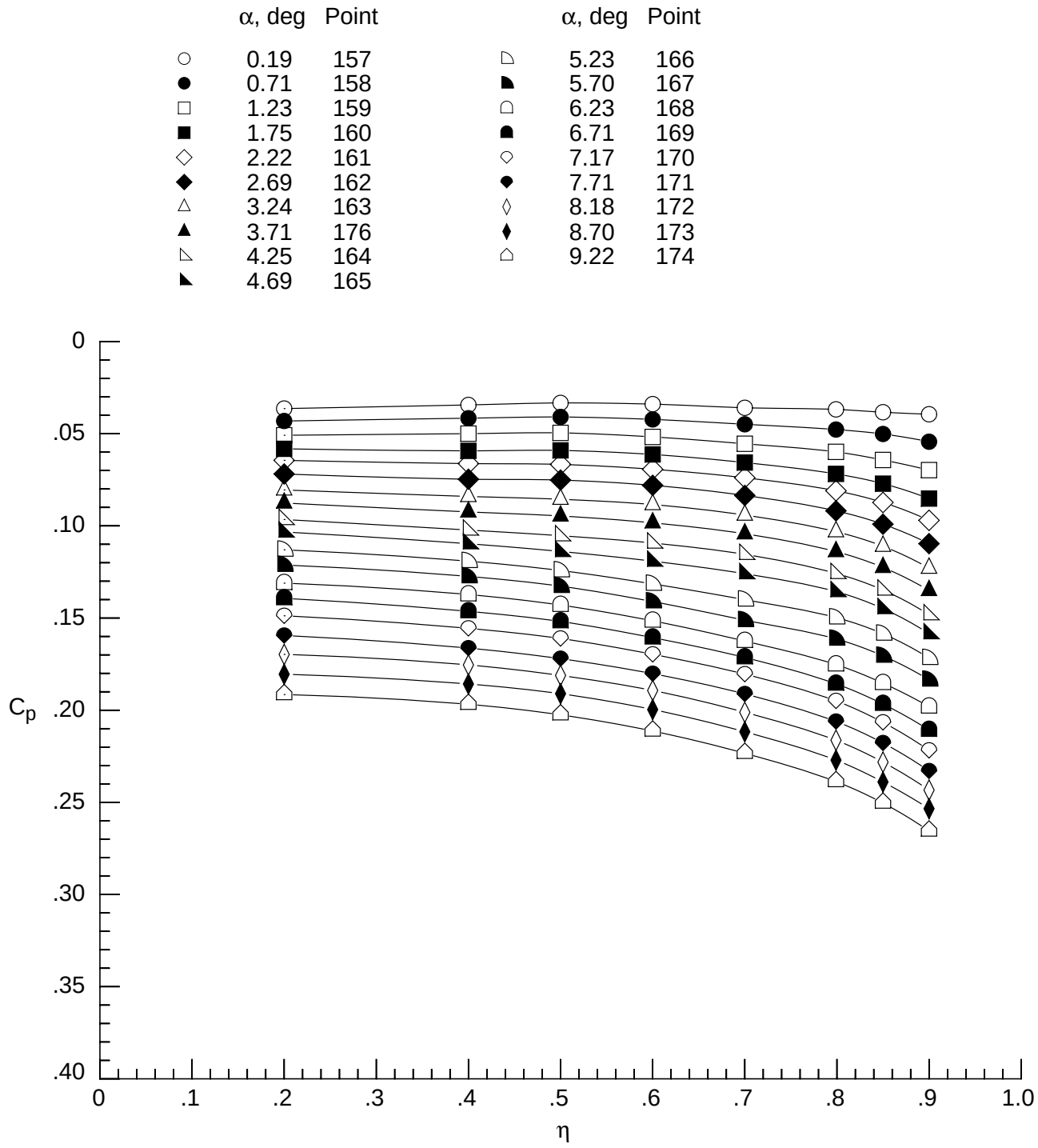

(b) Lower surface at x = 6 in.

Figure D8. Continued.

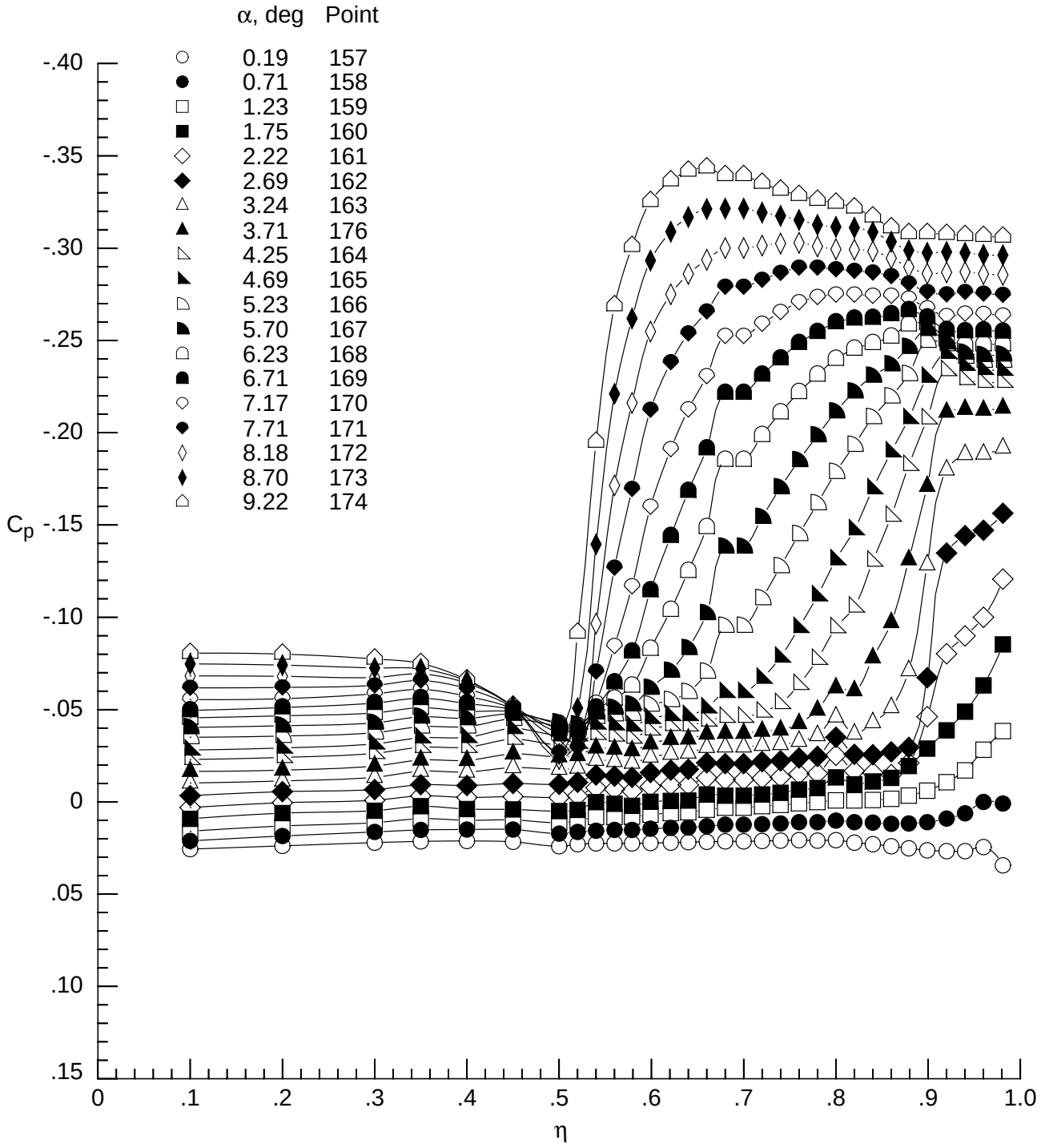

(c) Upper surface at x = 12 in.

Figure D8. Continued.

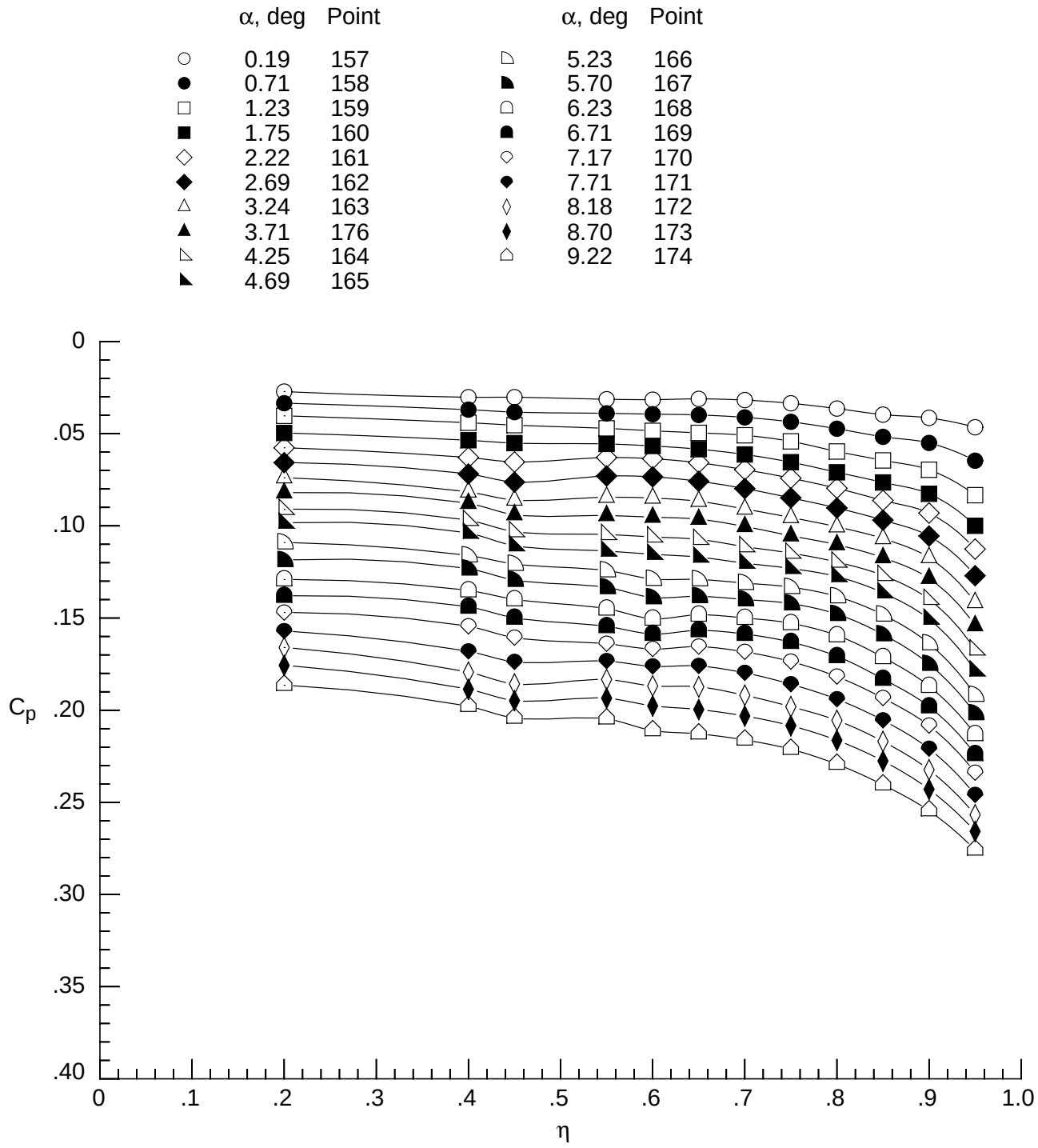

(d) Lower surface at x = 12 in.

Figure D8. Concluded.

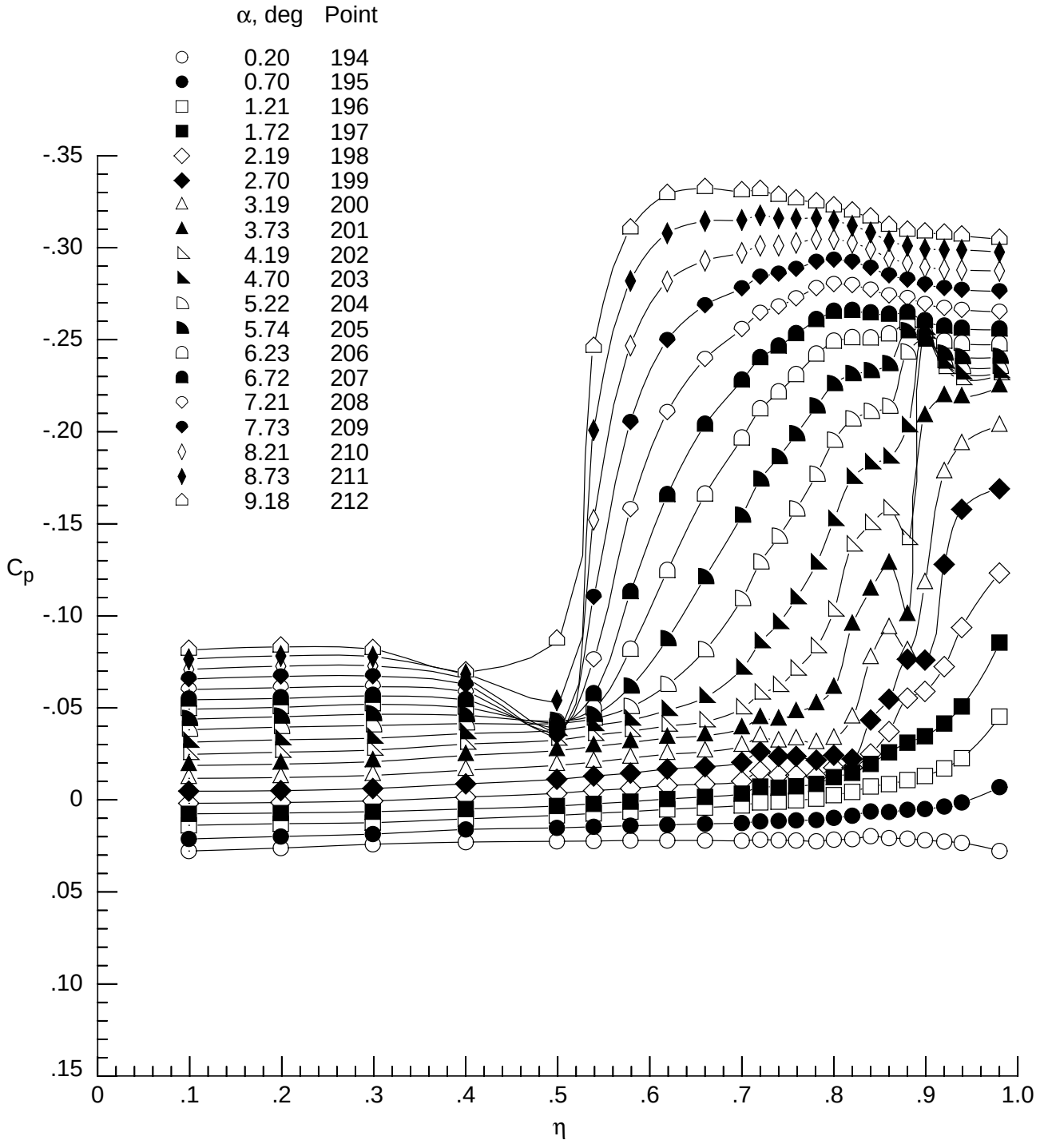

(a) Upper surface at x = 6 in.

Figure D9. Surface-pressure coefficient data for elliptical wing without transition grit at M = 1.60 and $R = 3 \times 10^6$ ft^{-1} for run 8.

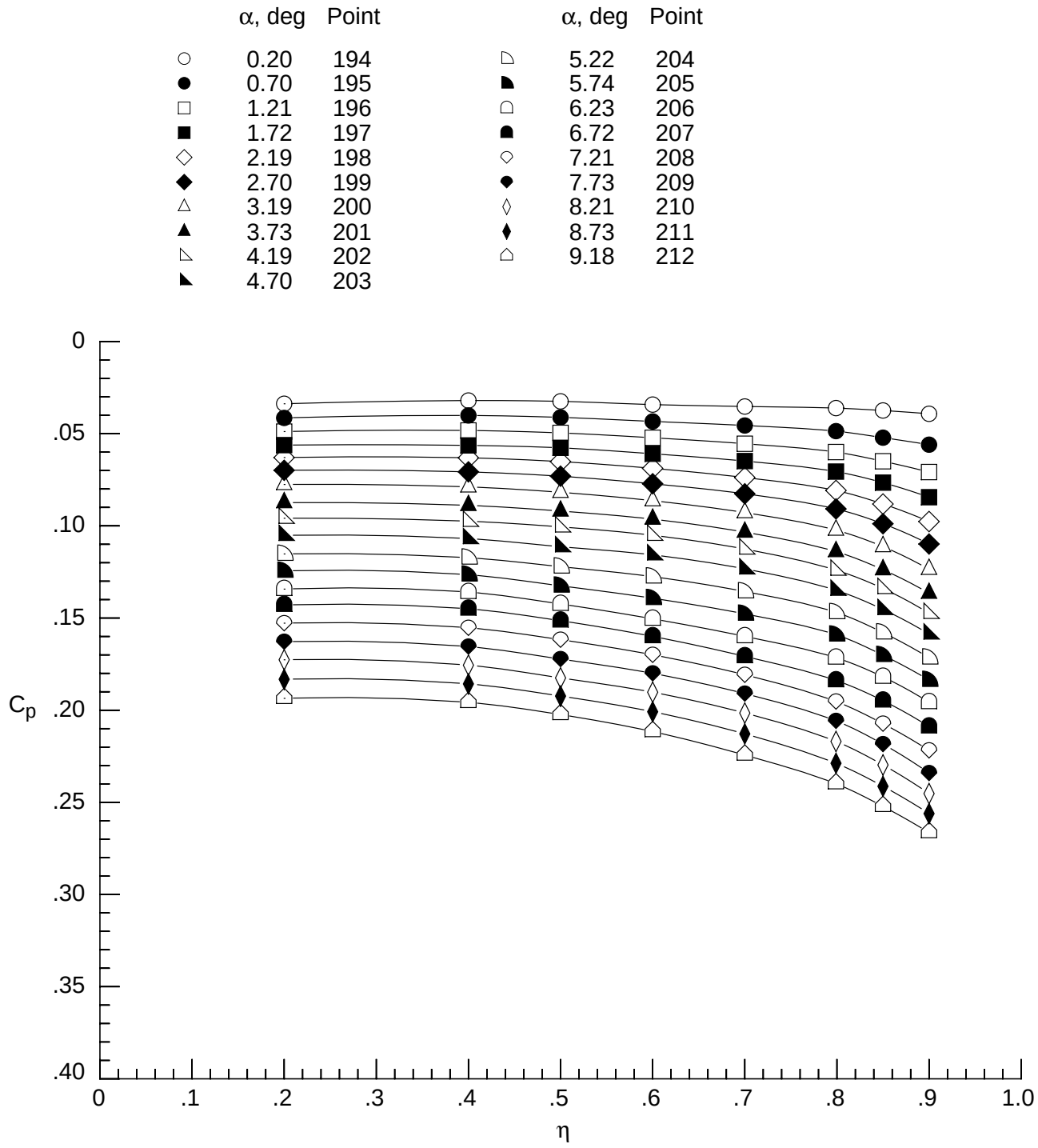

(b) Lower surface at x = 6 in.

Figure D9. Continued.

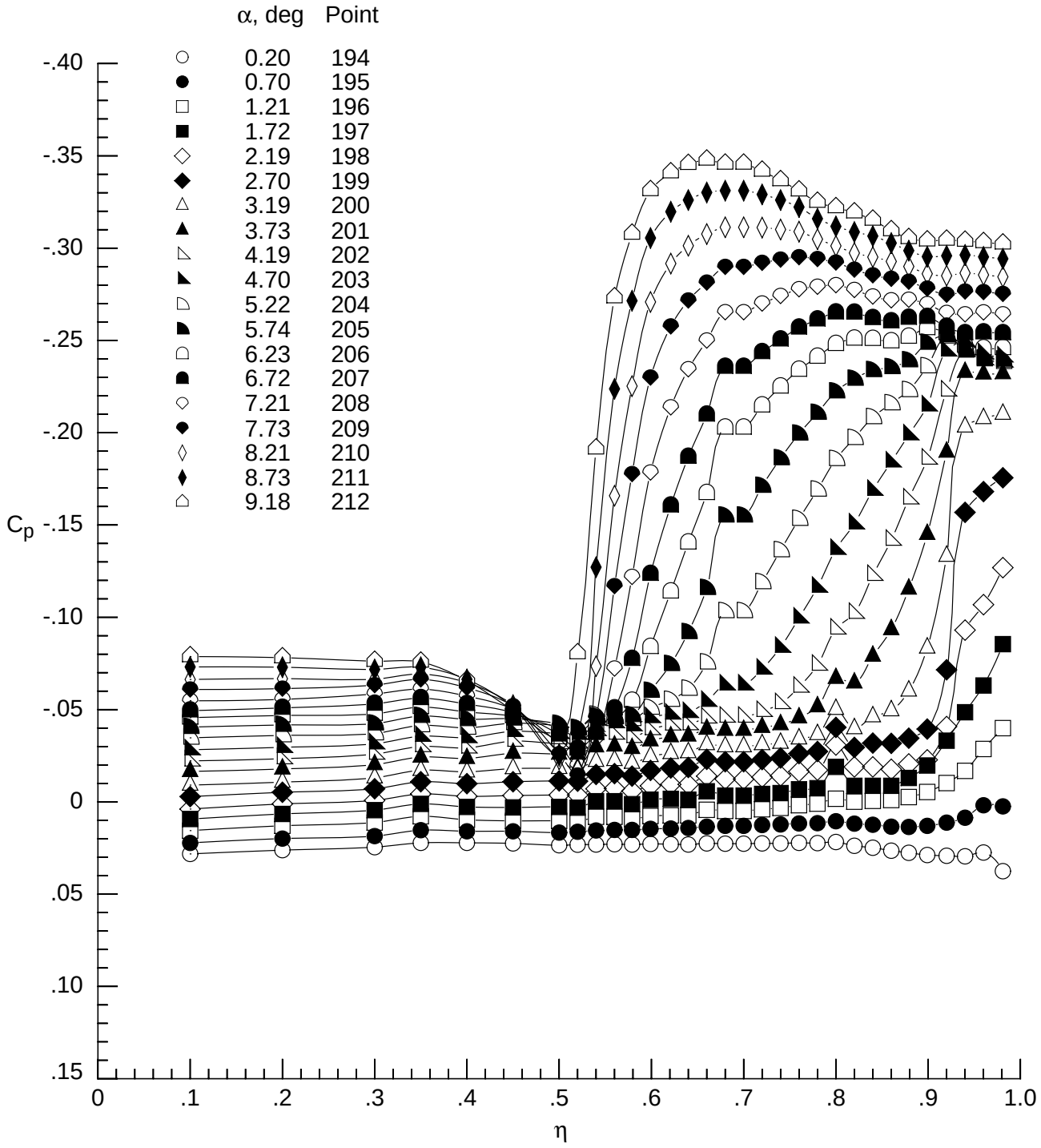

(c) Upper surface at x = 12 in.

Figure D9. Continued.

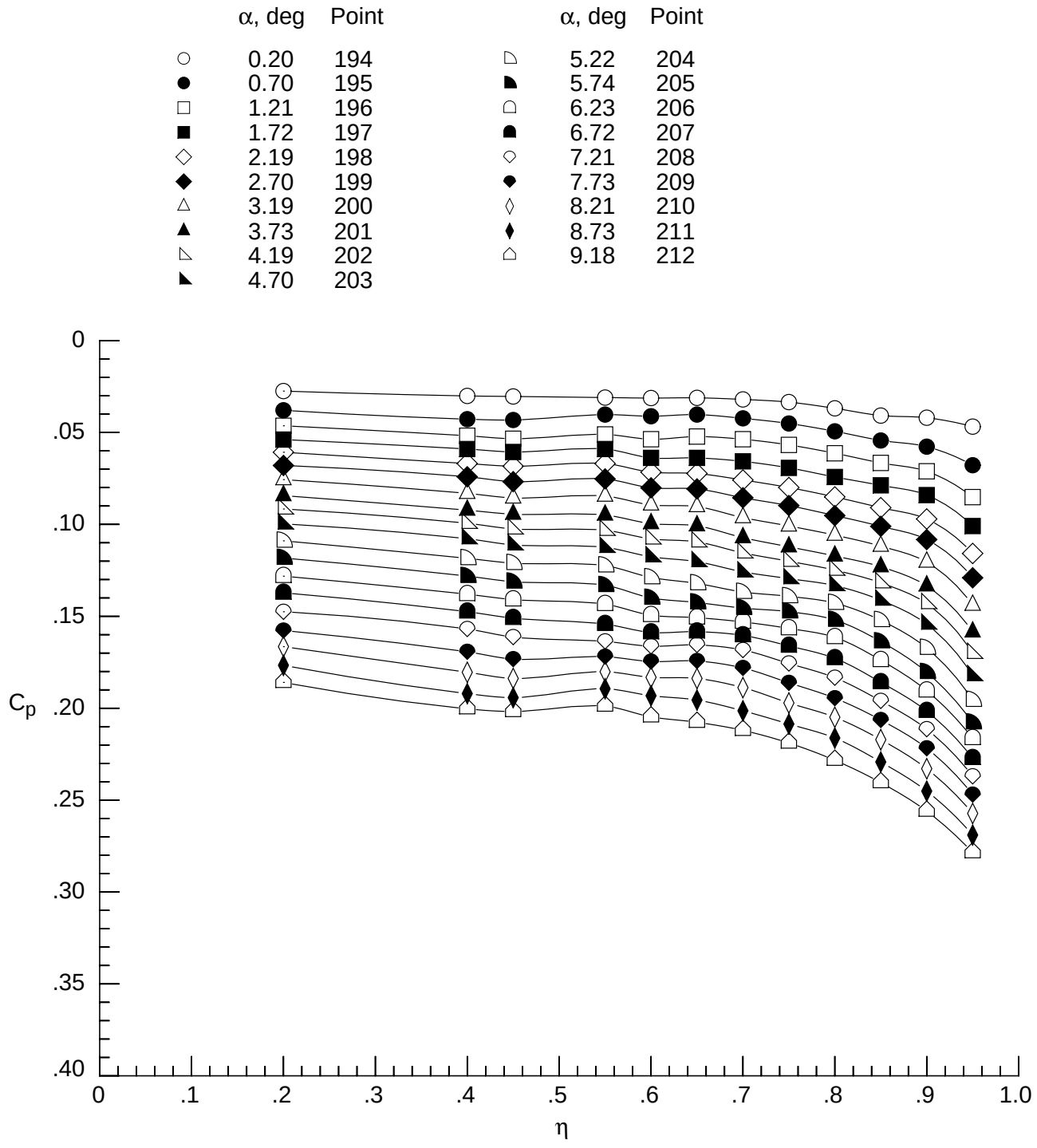

(d) Lower surface at x = 12 in.

Figure D9. Concluded.

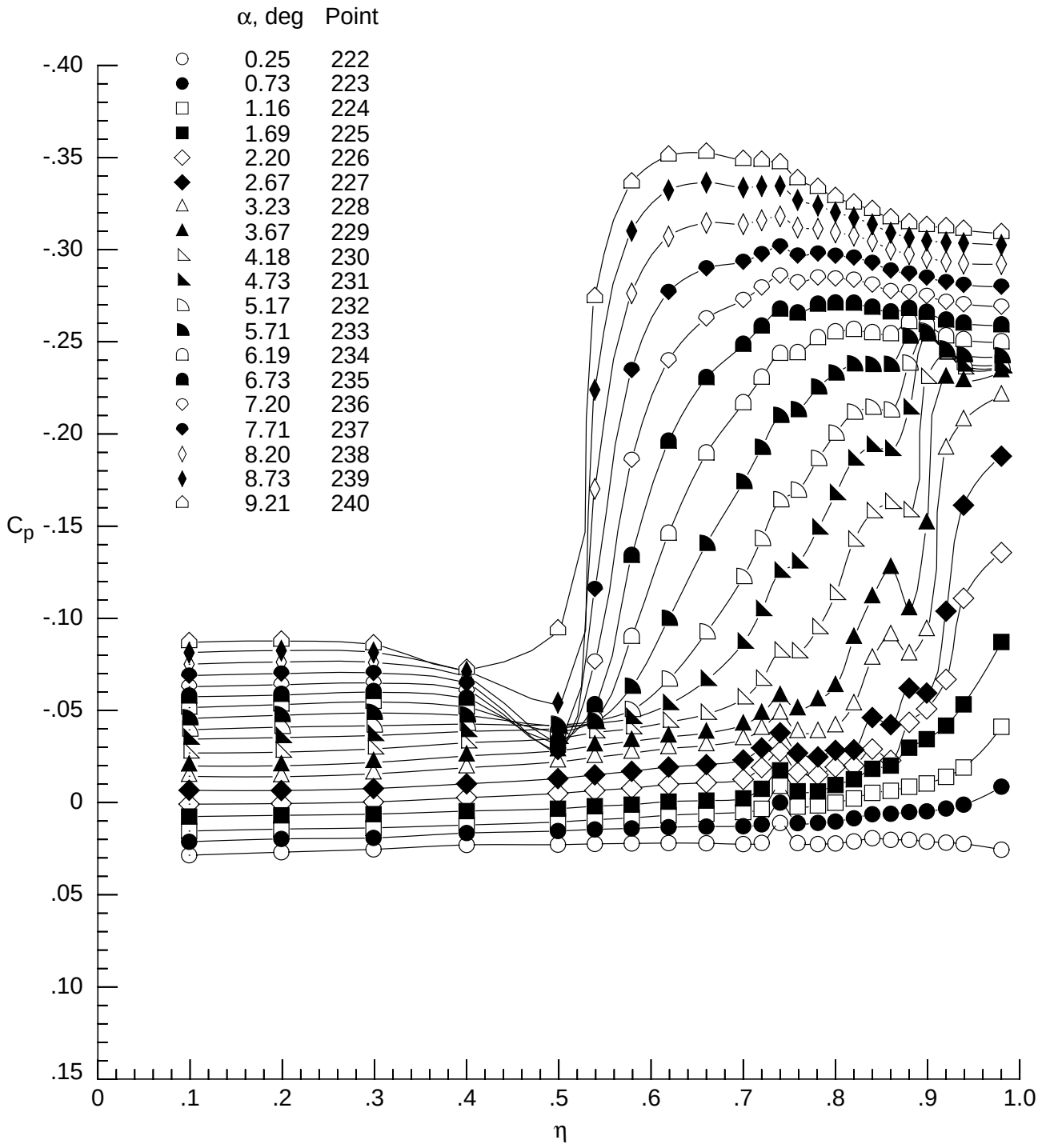

(a) Upper surface at x = 6 in.

Figure D10. Surface-pressure coefficient data for elliptical wing without transition grit at M = 1.60 and $R = 4 \times 10^6$ ft^{-1} for run 10.

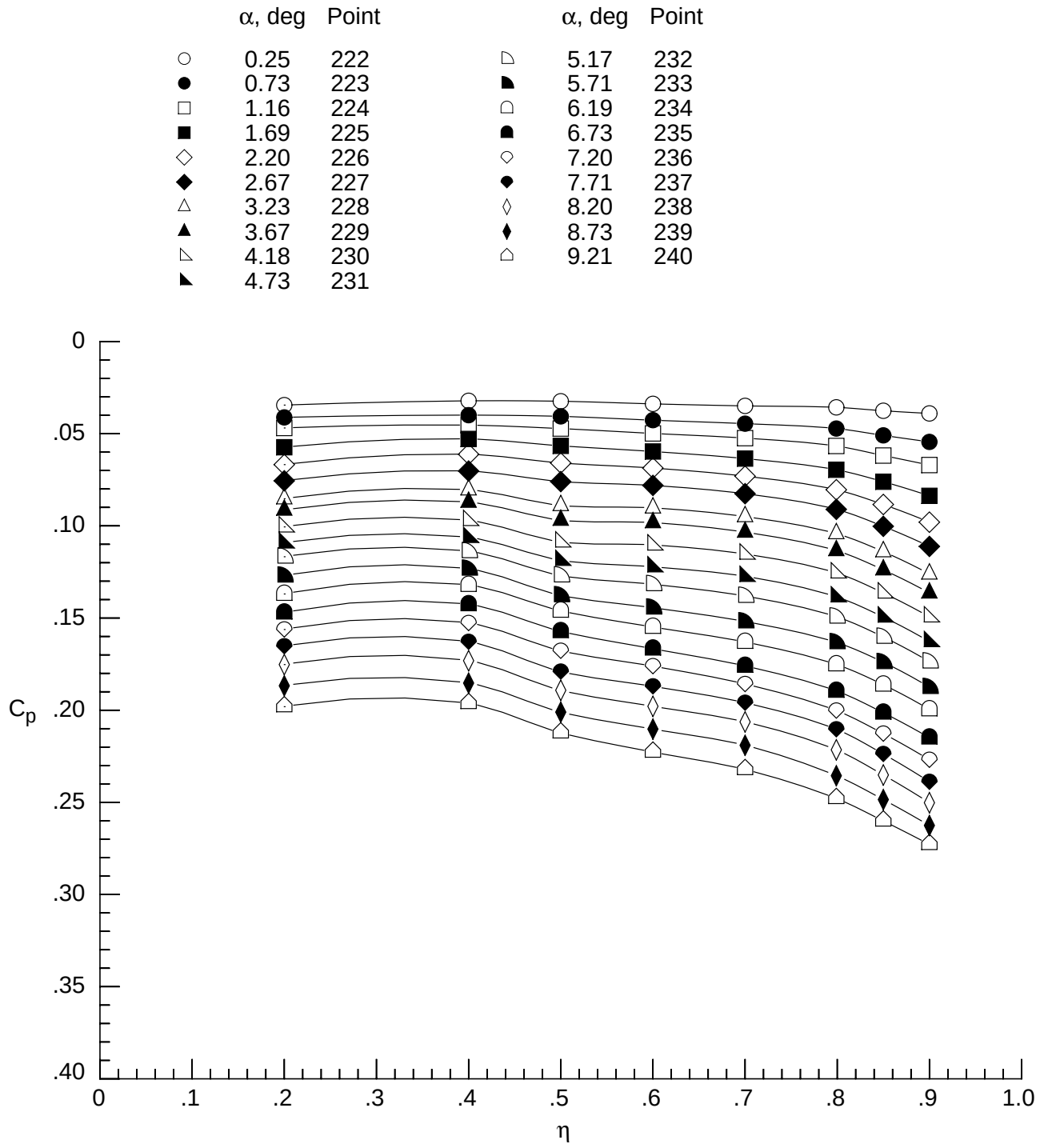

(b) Lower surface at x = 6 in.

Figure D10. Continued.

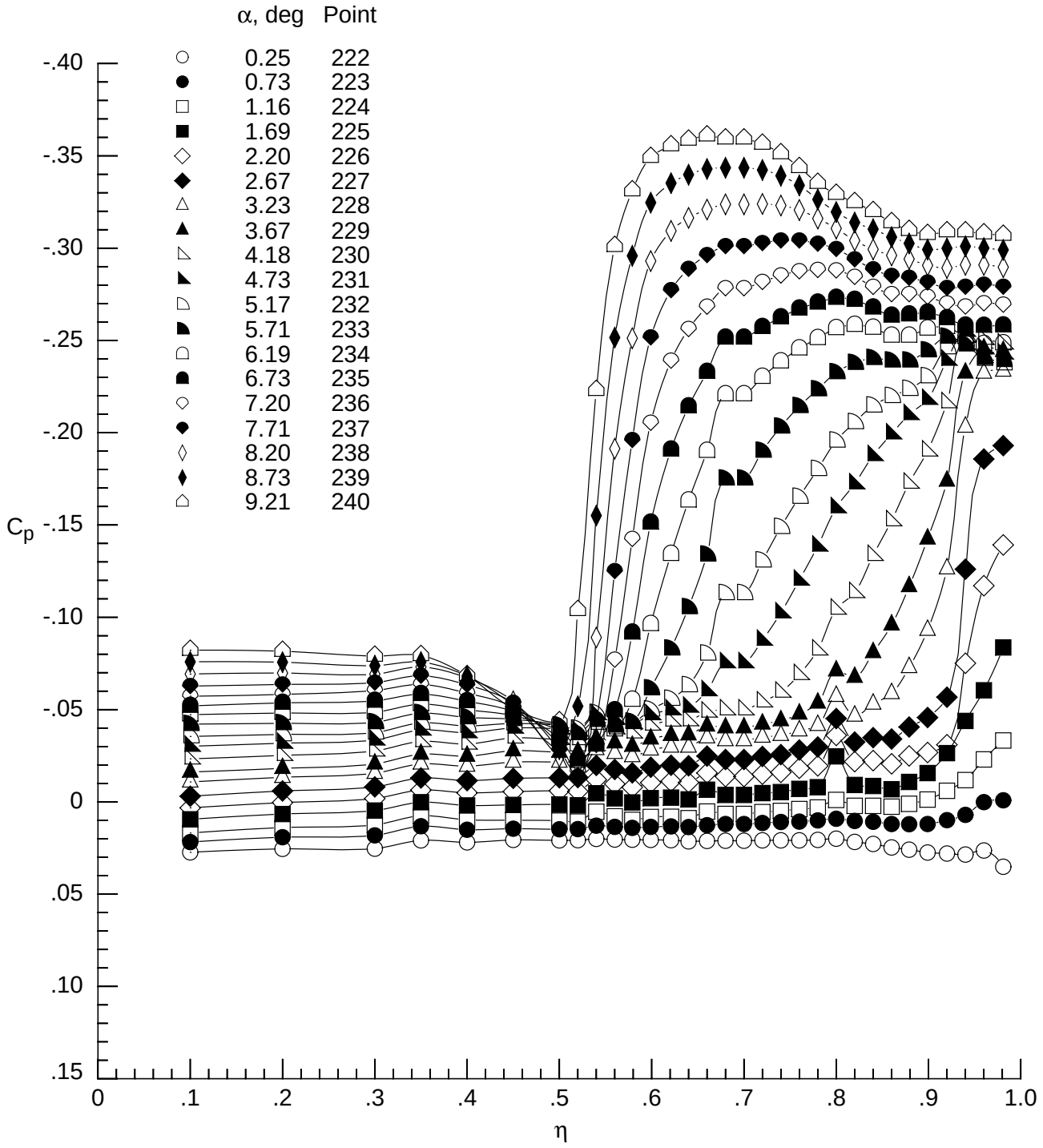

(c) Upper surface at x = 12 in.

Figure D10. Continued.

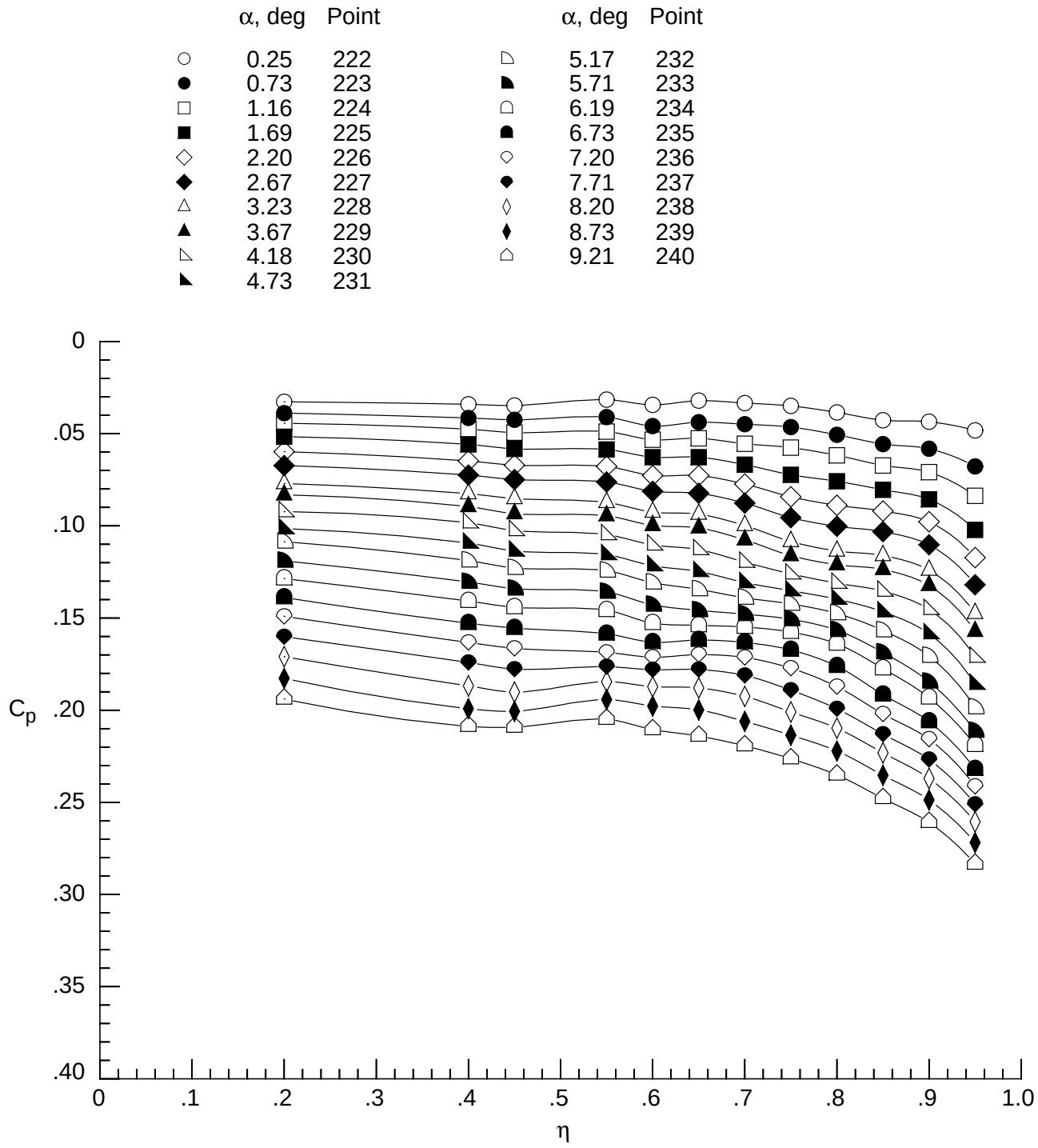

(d) Lower surface at x = 12 in.

Figure D10. Concluded.

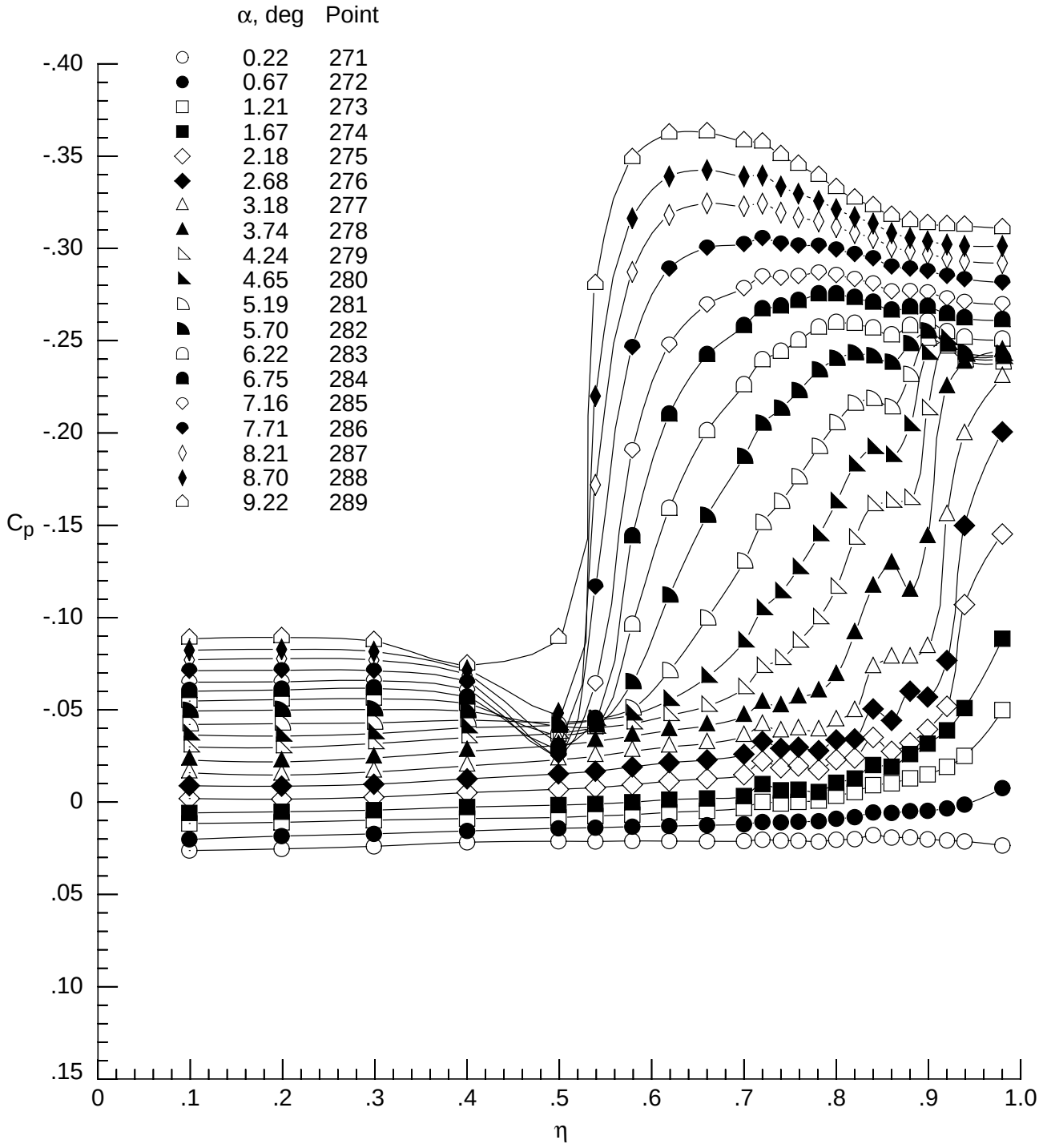

(a) Upper surface at x = 6 in.

Figure D11. Surface-pressure coefficient data for elliptical wing without transition grit at M = 1.60 and $R = 5 \times 10^6$ ft^{-1} for run 14.

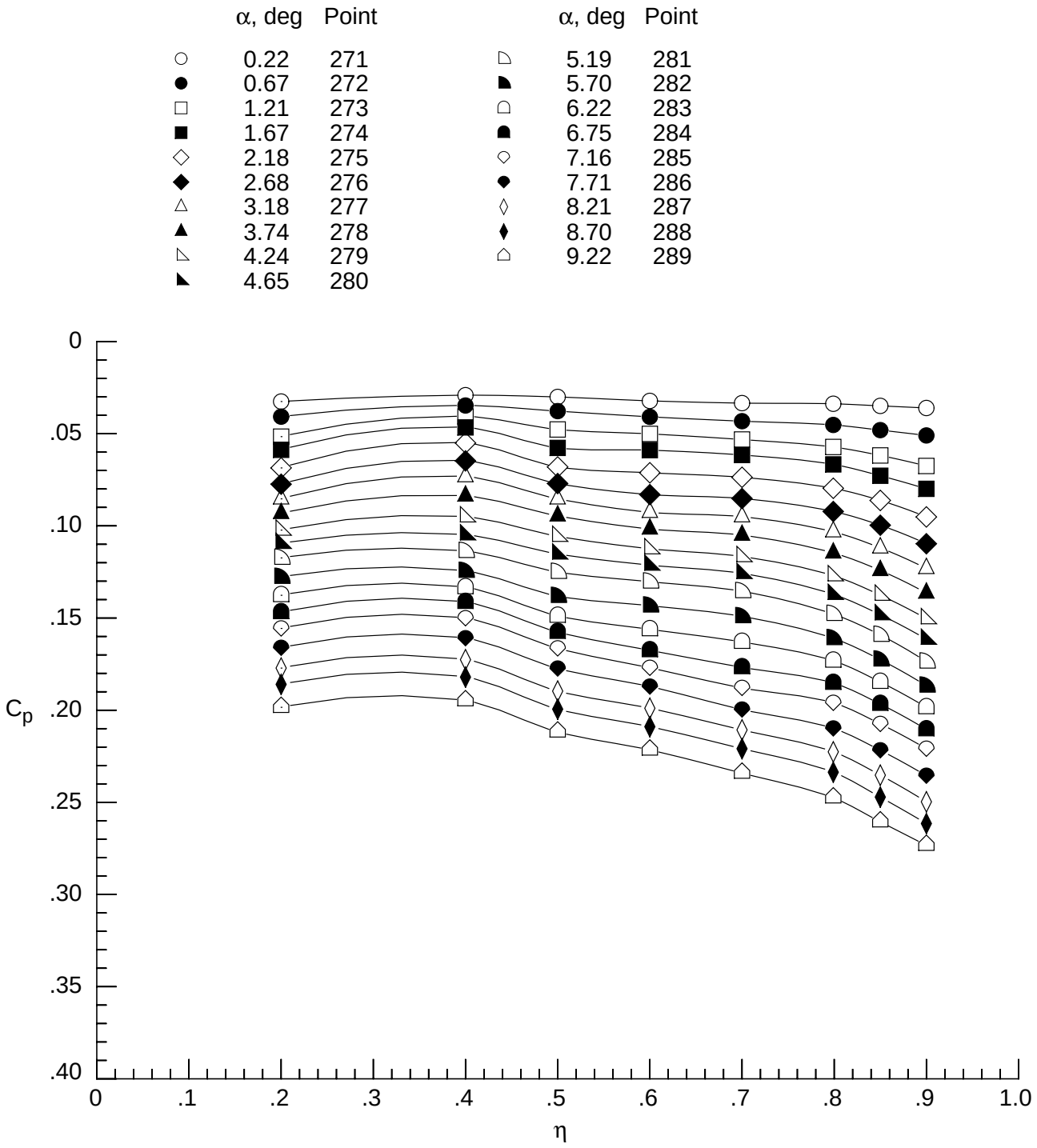

(b) Lower surface at x = 6 in.

Figure D11. Continued.

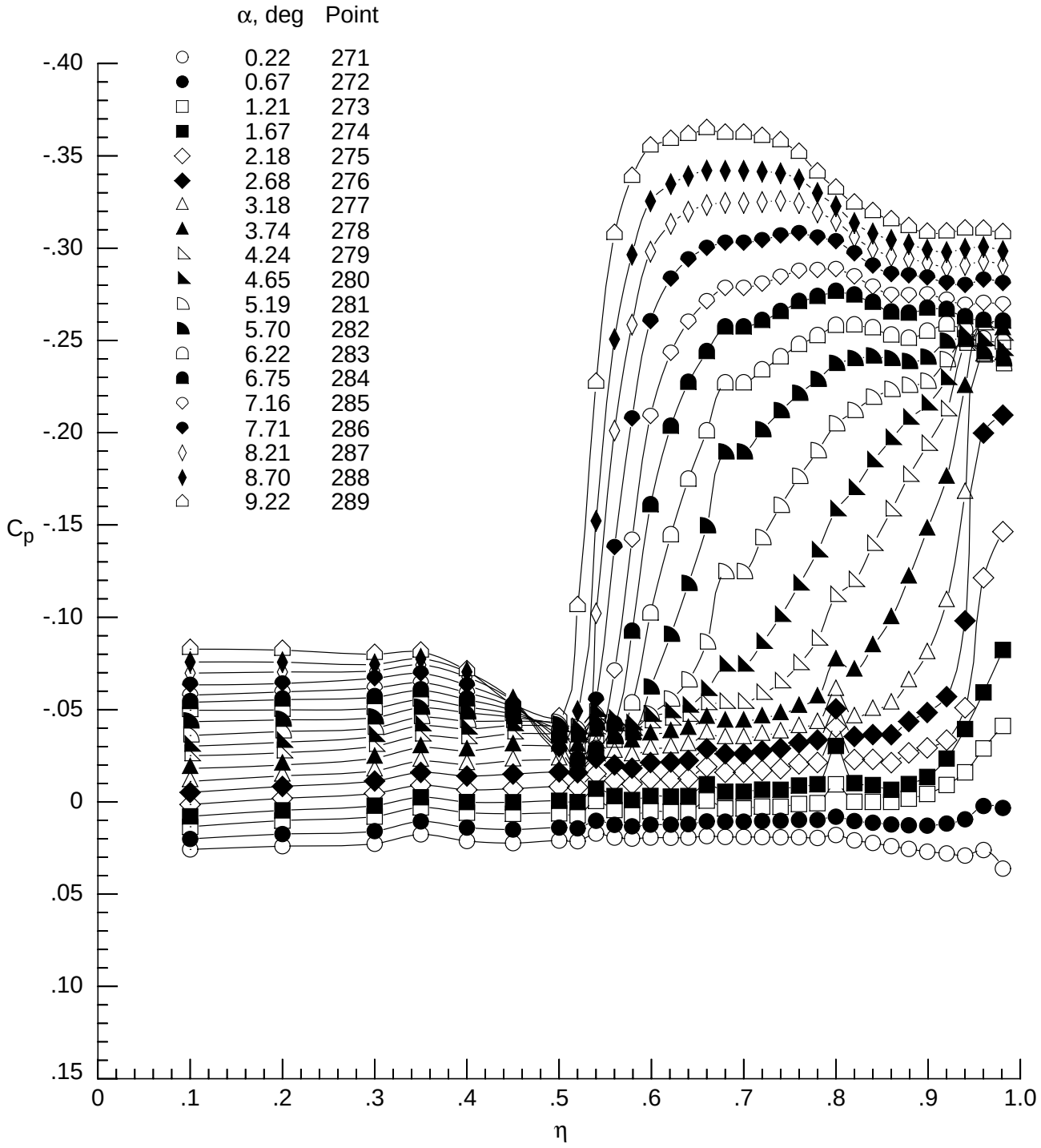

(c) Upper surface at x = 12 in.

Figure D11. Continued.

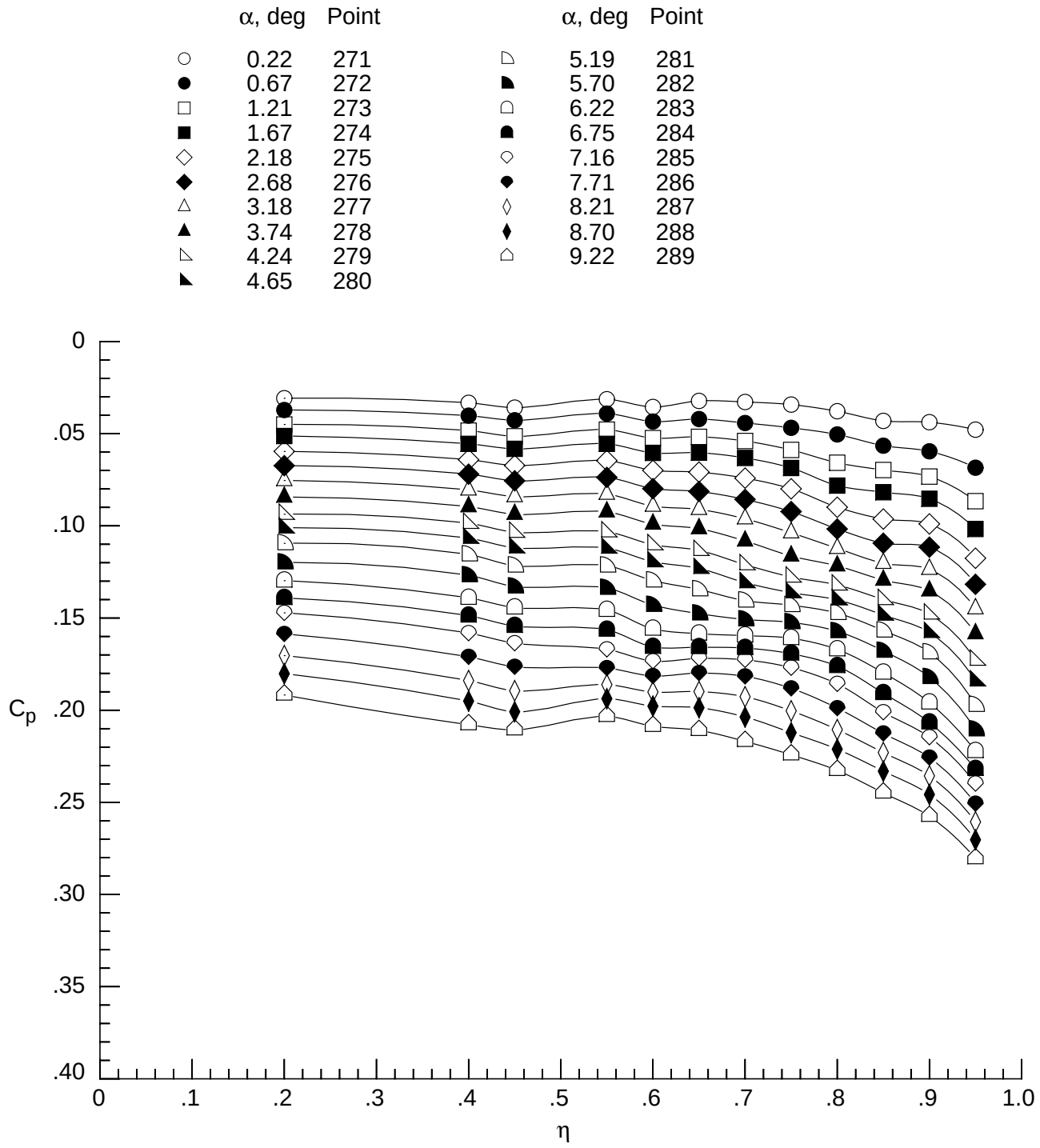

(d) Lower surface at x = 12 in.

Figure D11. Concluded.

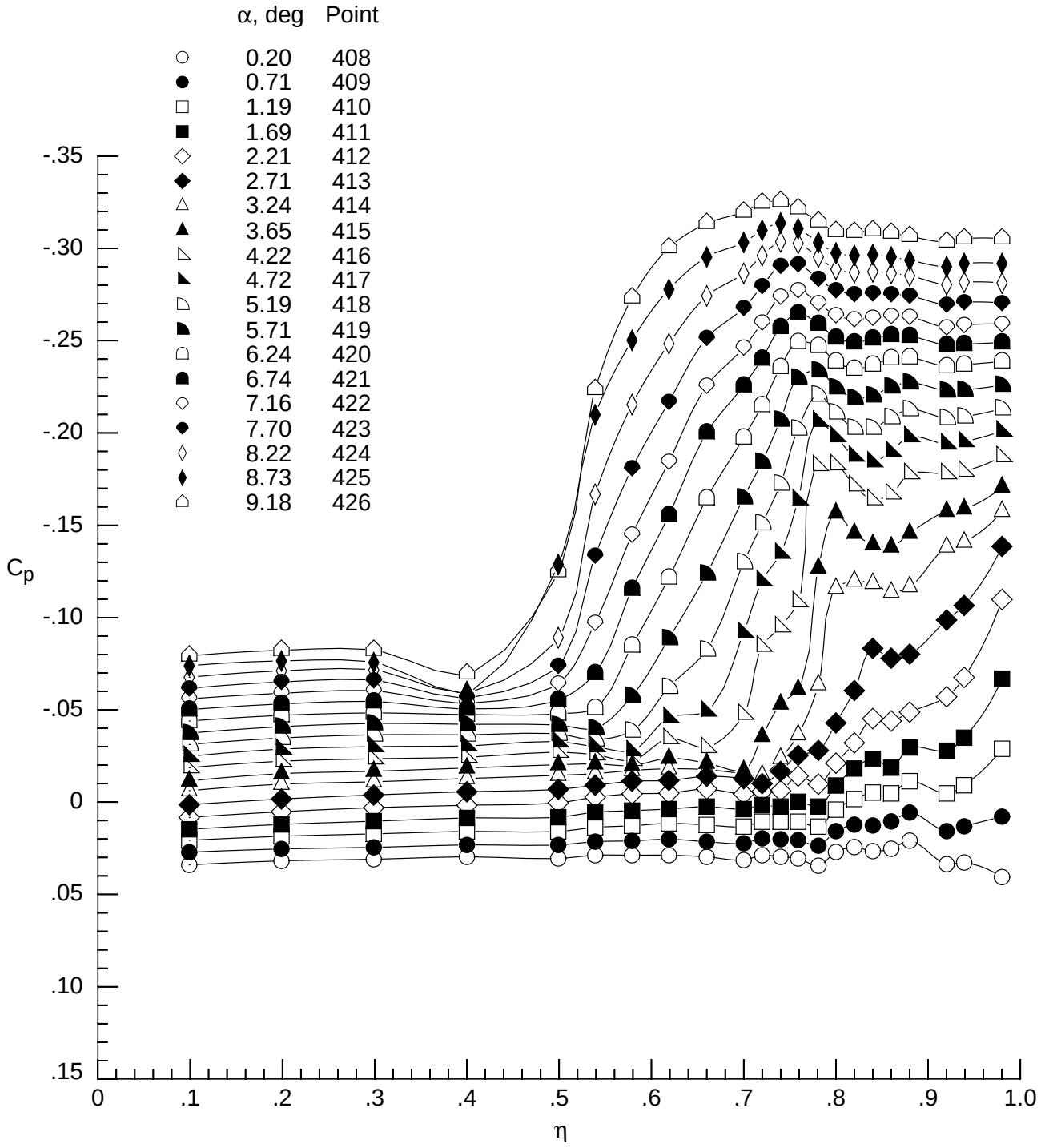

(a) Upper surface at x = 6 in.

Figure D12. Surface-pressure coefficient data for elliptical wing with transition grit at M = 1.60 and $R = 1 \times 10^6$ ft^{-1} for run 22.

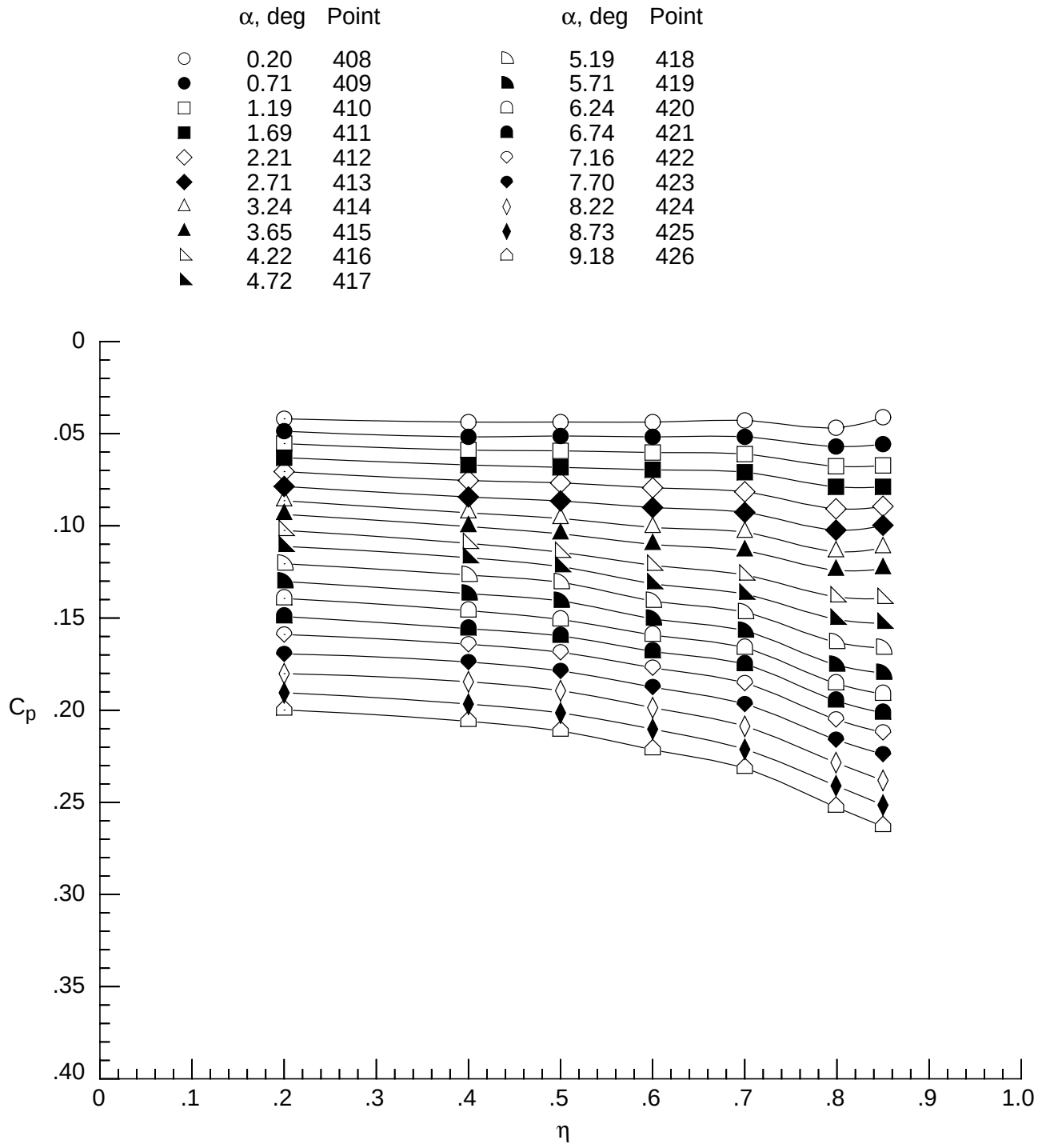

(b) Lower surface at x = 6 in.

Figure D12. Continued.

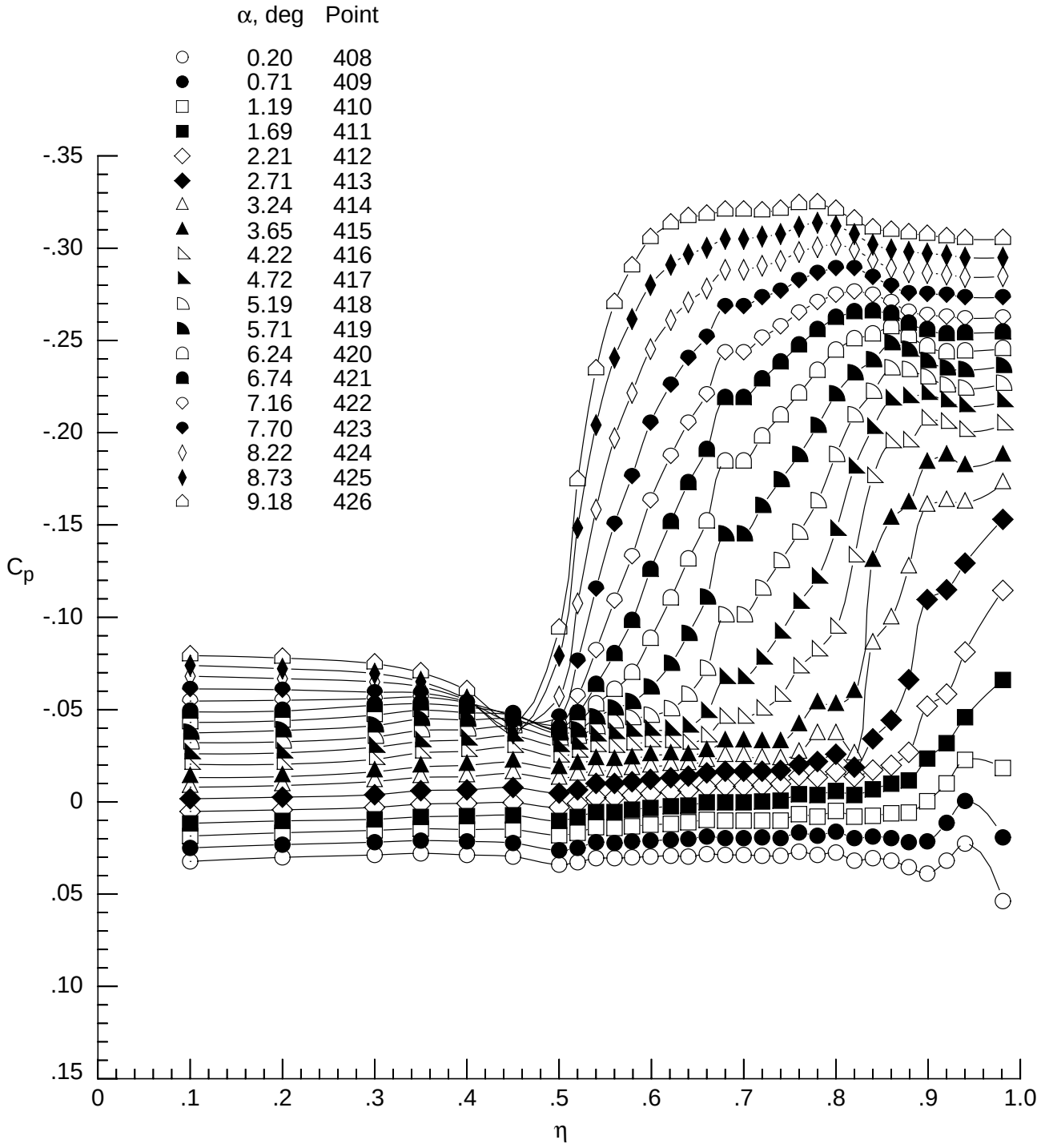

(c) Upper surface at x = 12 in.

Figure D12. Continued.

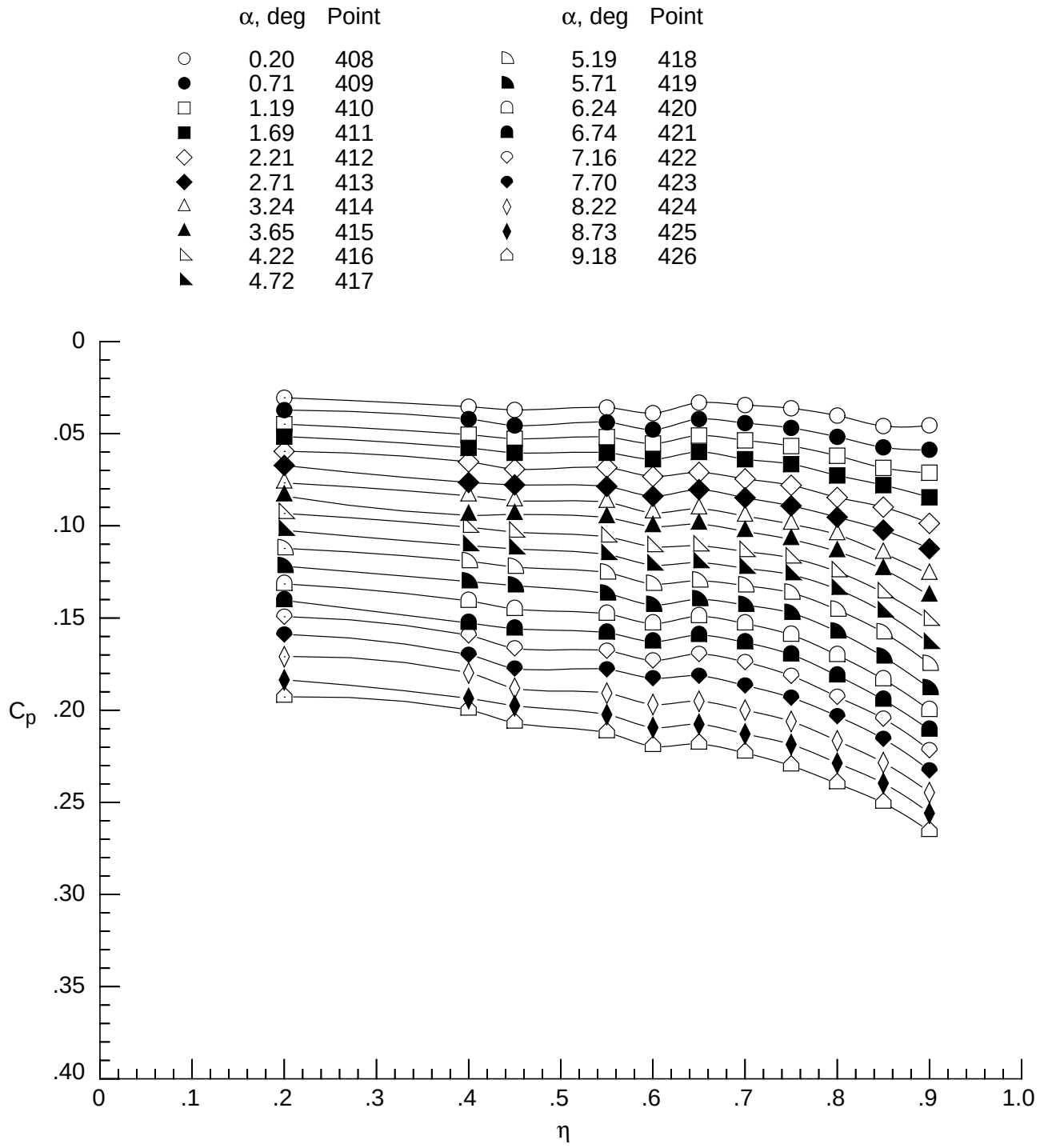

(d) Lower surface at x = 12 in.

Figure D12. Concluded.

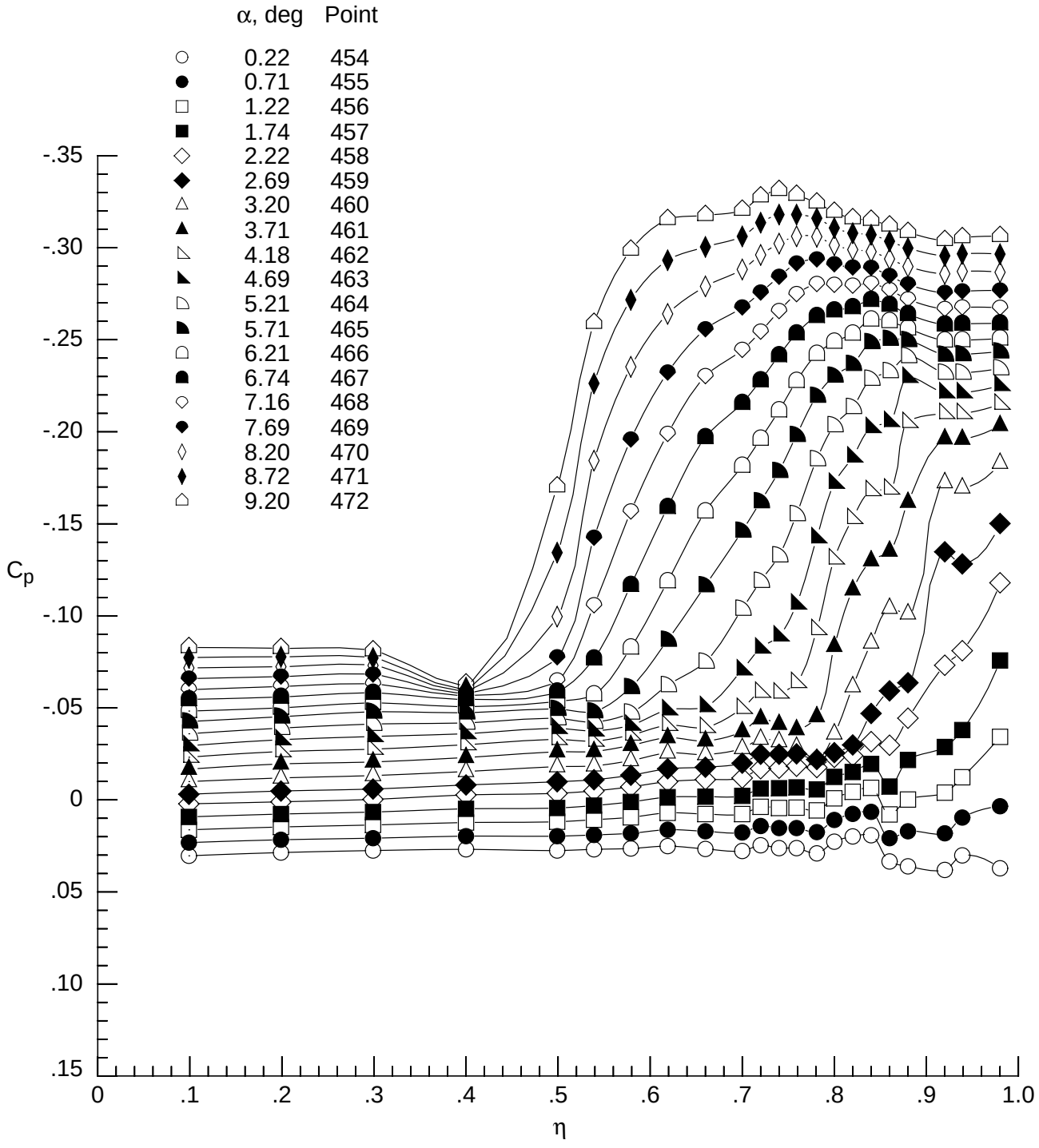

(a) Upper surface at x = 6 in.

Figure D13. Surface-pressure coefficient data for elliptical wing with transition grit at M = 1.60 and $R = 2 \times 10^6$ ft^{-1} for run 25.

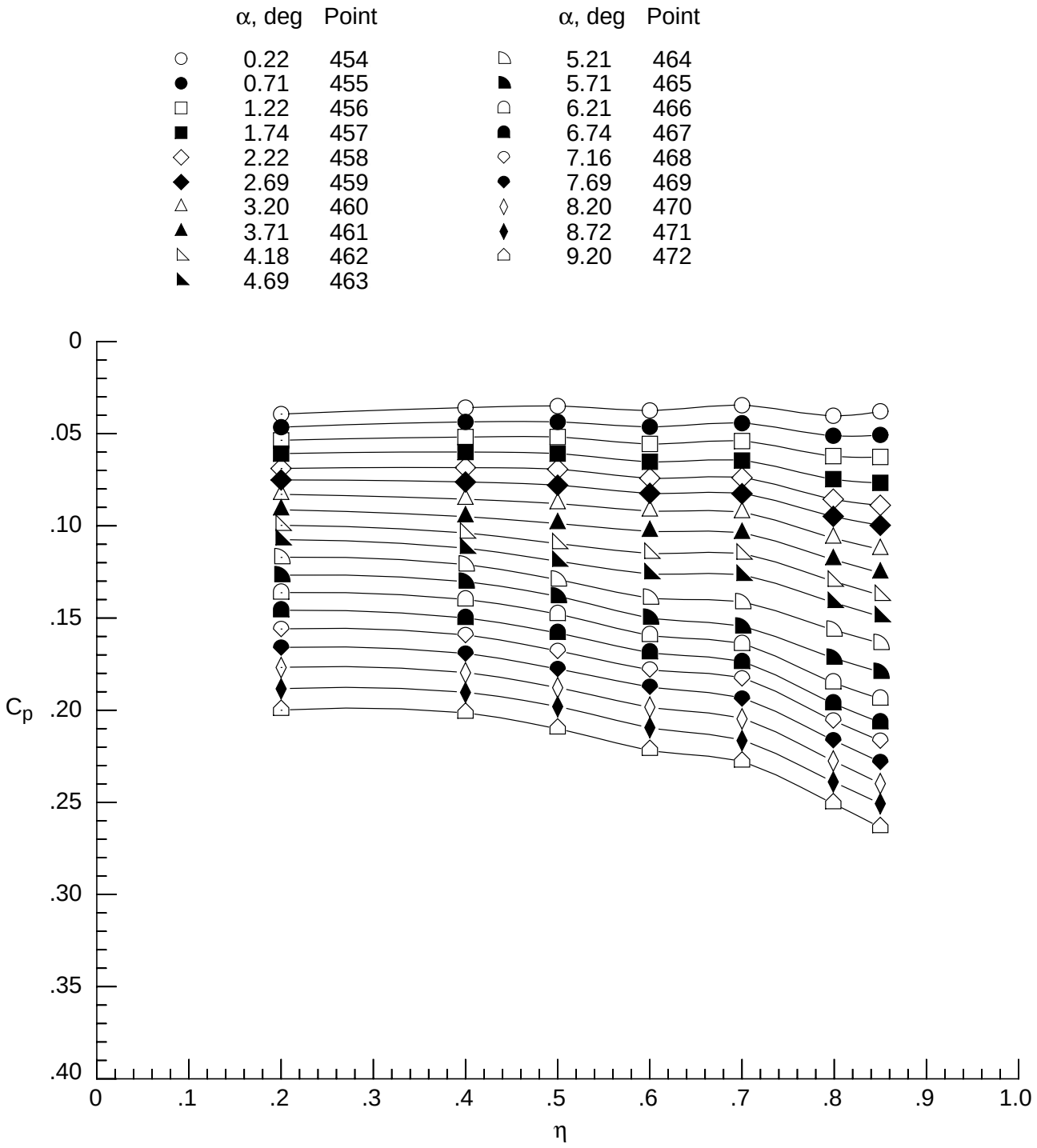

(b) Lower surface at x = 6 in.

Figure D13. Continued.

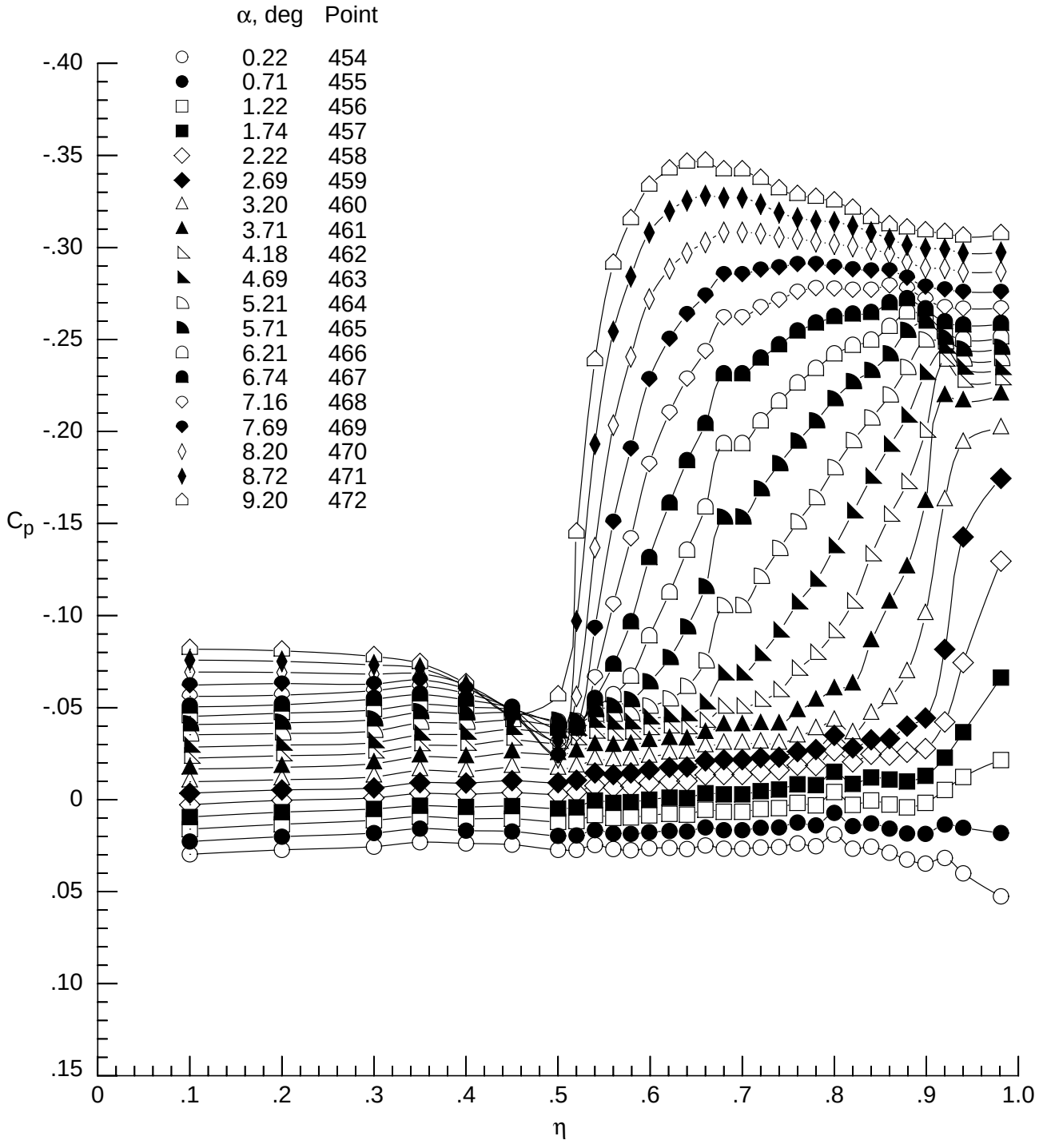

(c) Upper surface at x = 12 in.

Figure D13. Continued.

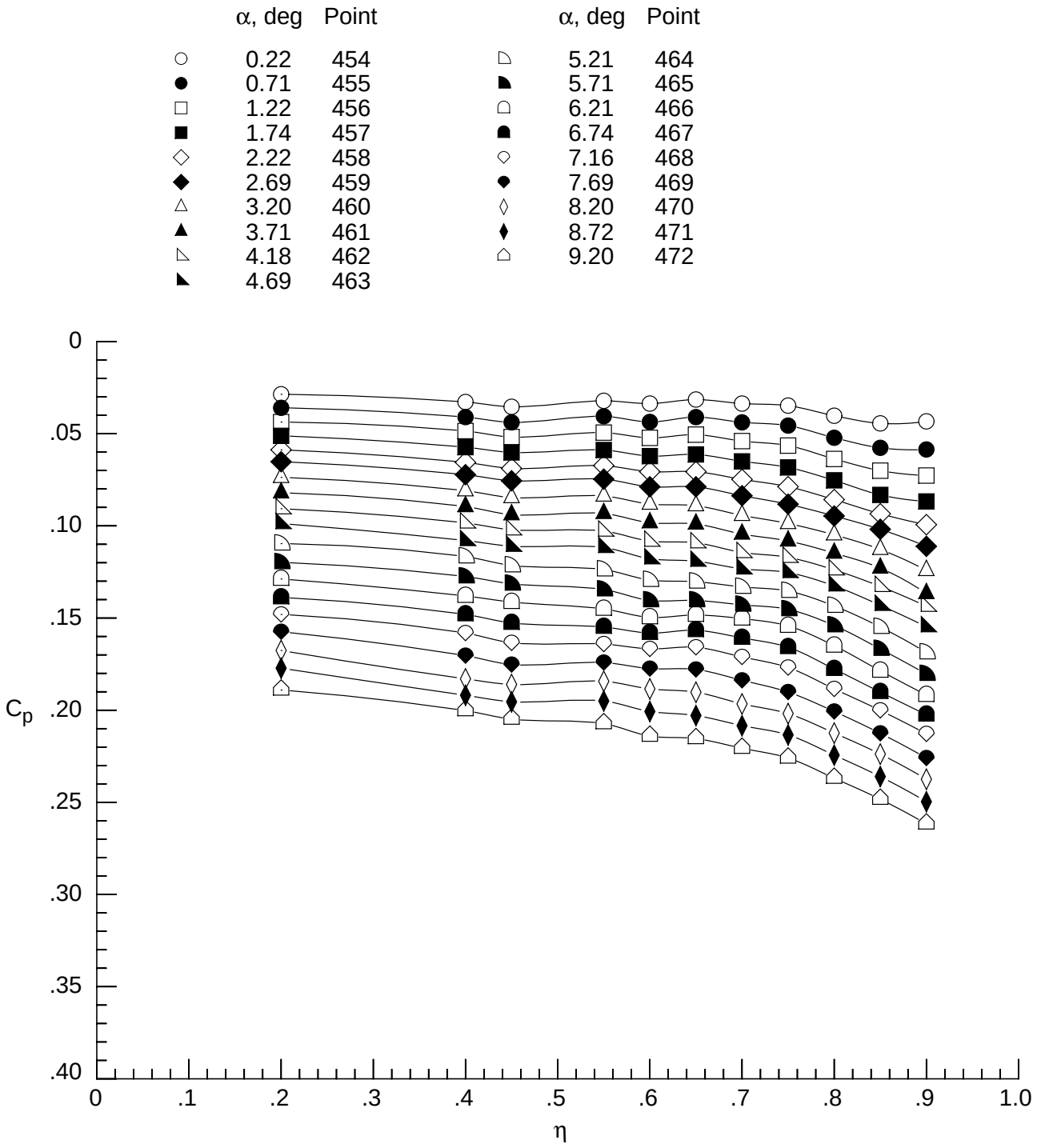

(d) Lower surface at x = 12 in.

Figure D13. Concluded.

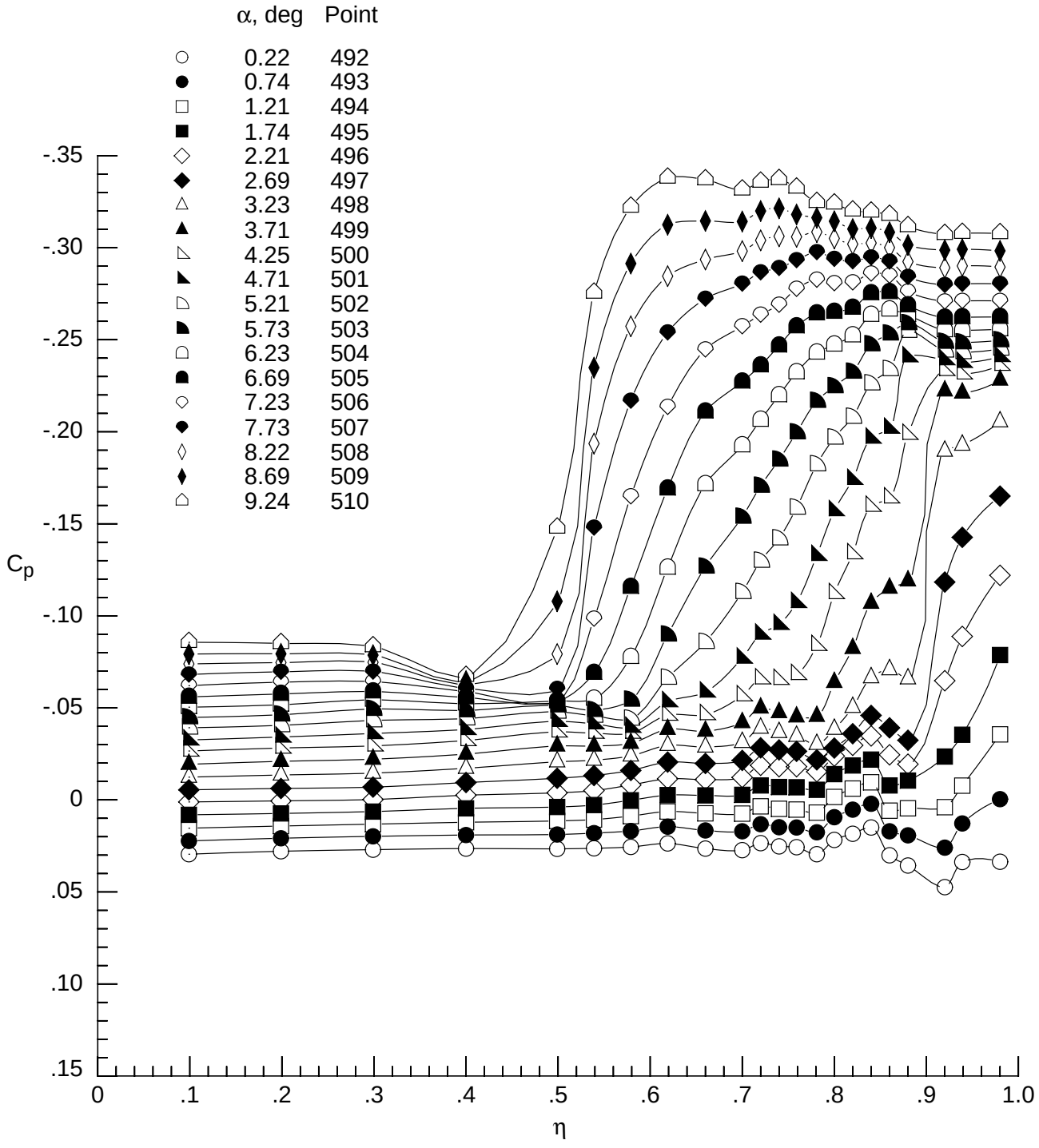

(a) Upper surface at x = 6 in.

Figure D14. Surface-pressure coefficient data for elliptical wing with transition grit at M = 1.60 and $R = 3 \times 10^6$ ft^{-1} for run 28.

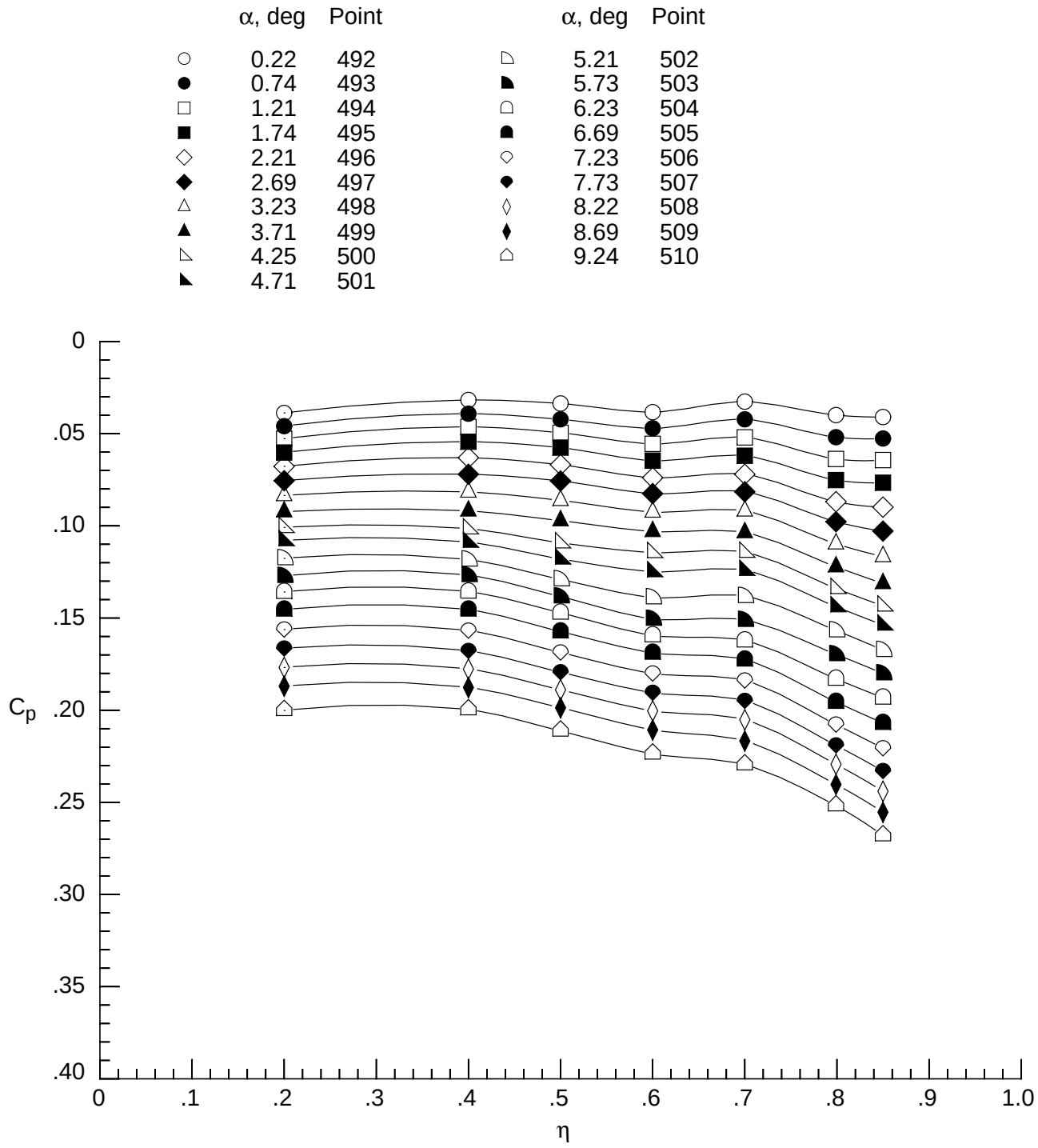

(b) Lower surface at x = 6 in.

Figure D14. Continued.

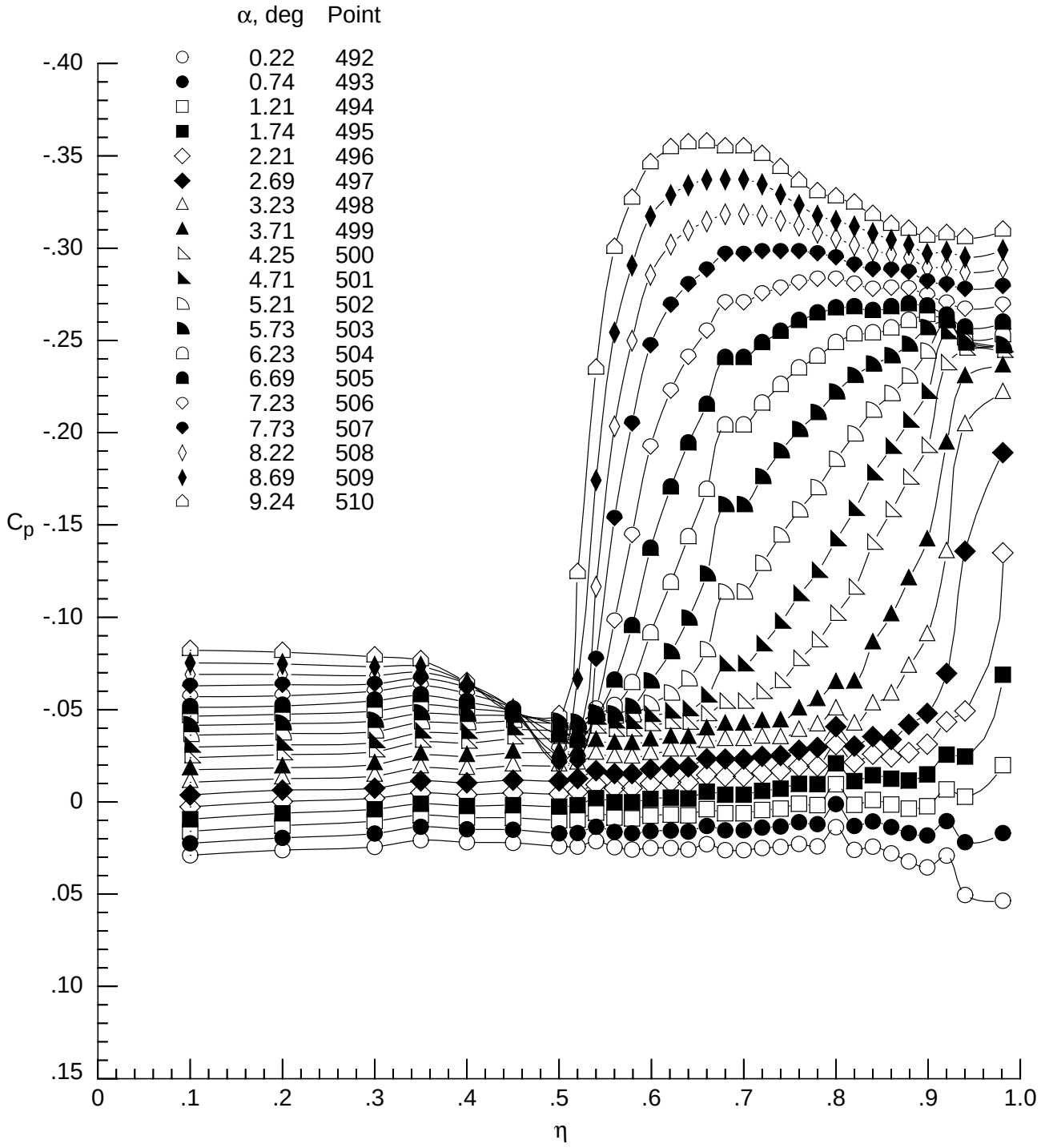

(c) Upper surface at x = 12 in.

Figure D14. Continued.

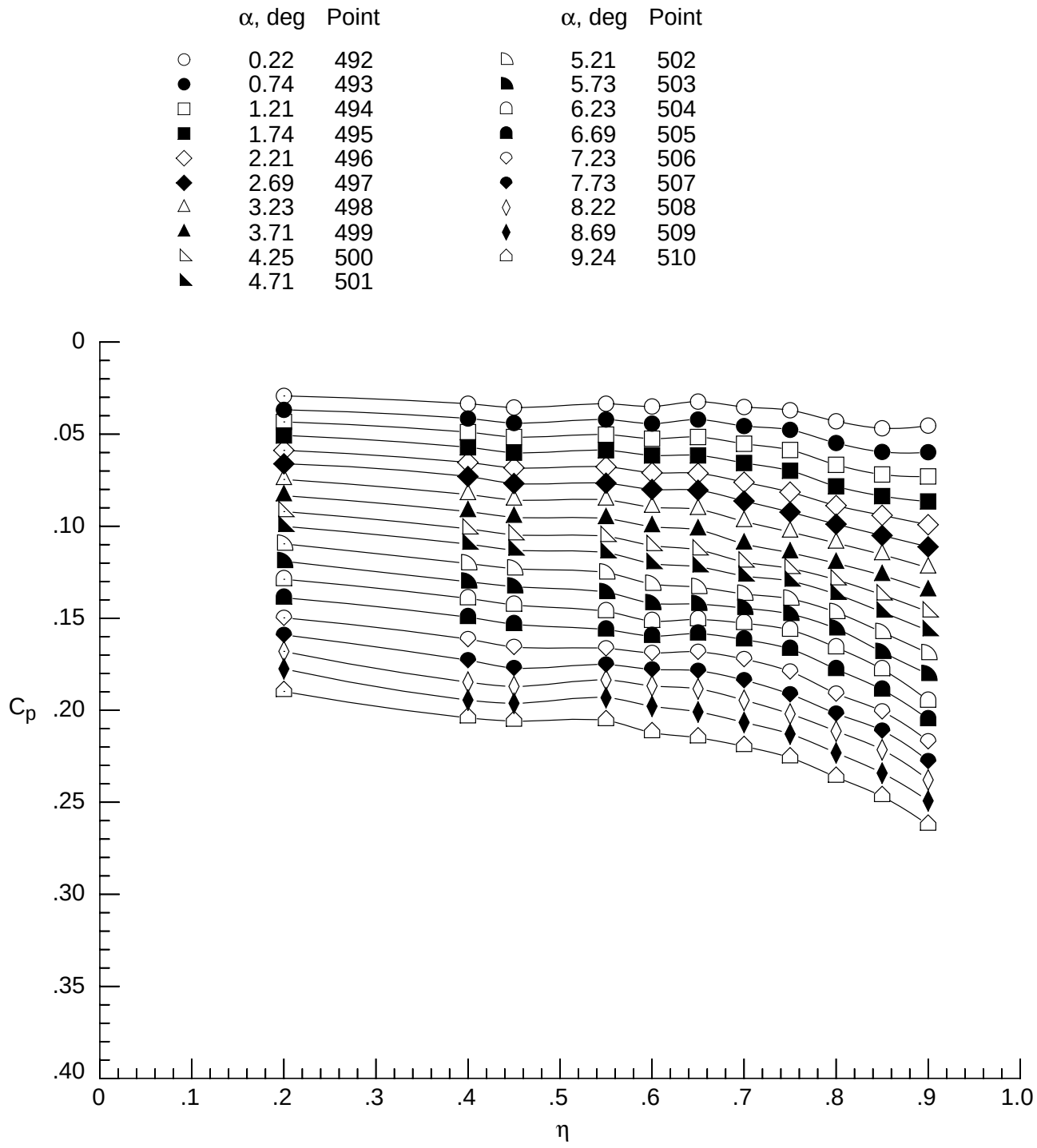

(d) Lower surface at x = 12 in.

Figure D14. Concluded.

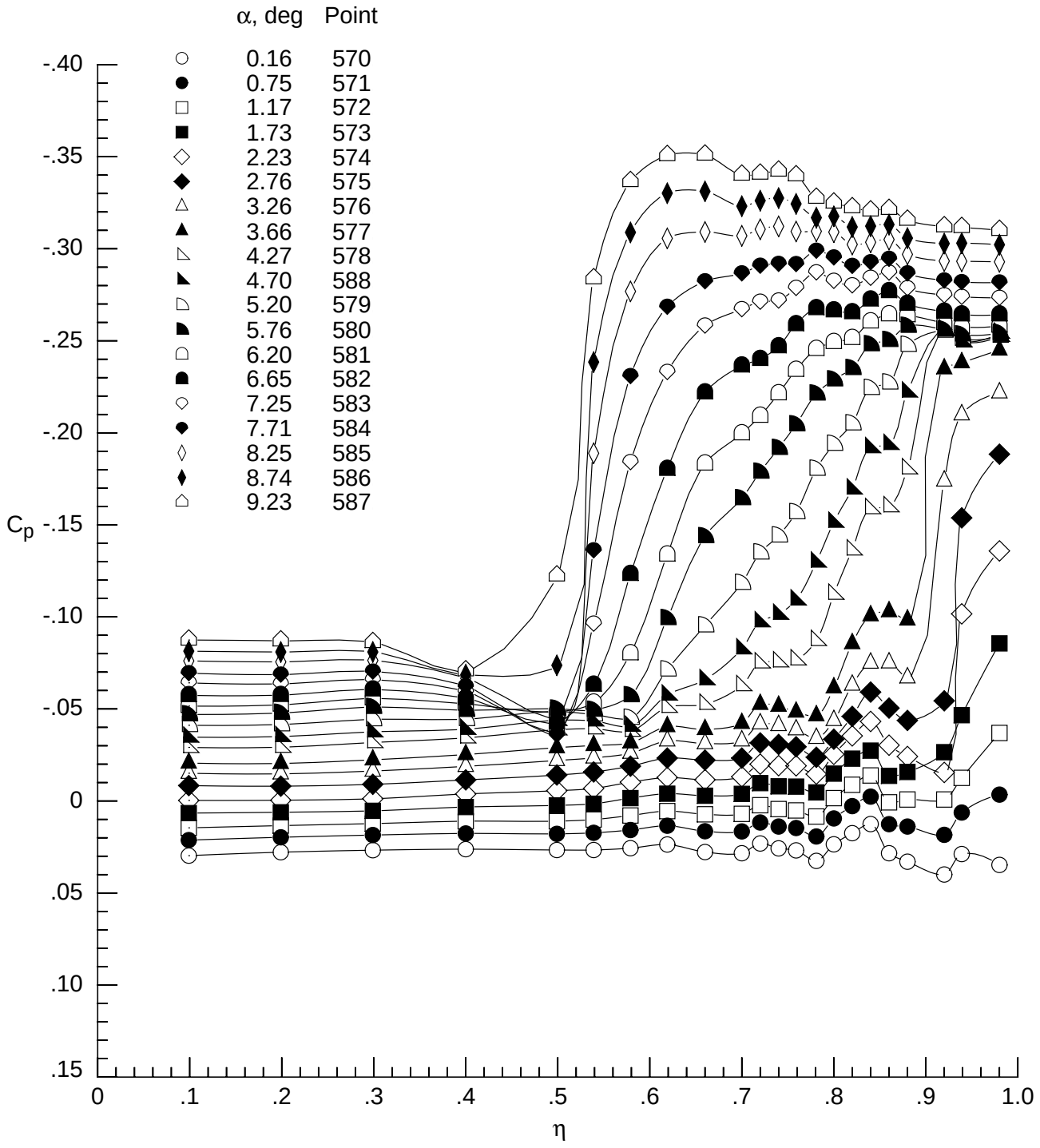

(a) Upper surface at x = 6 in.

Figure D15. Surface-pressure coefficient data for elliptical wing with transition grit at M = 1.60 and $R = 4 \times 10^6$ ft^{-1} for run 32.

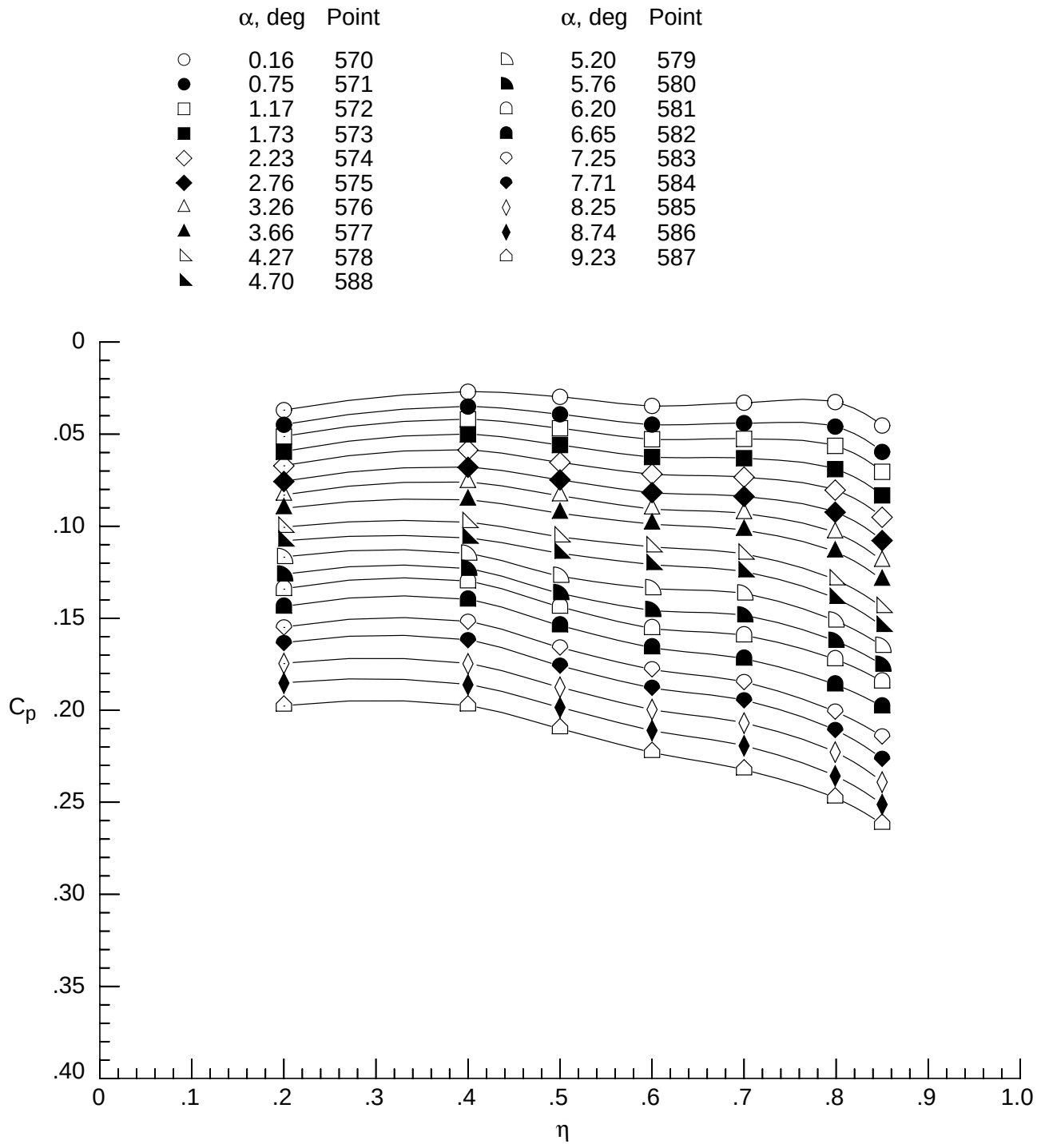

(b) Lower surface at x = 6 in.

Figure D15. Continued.

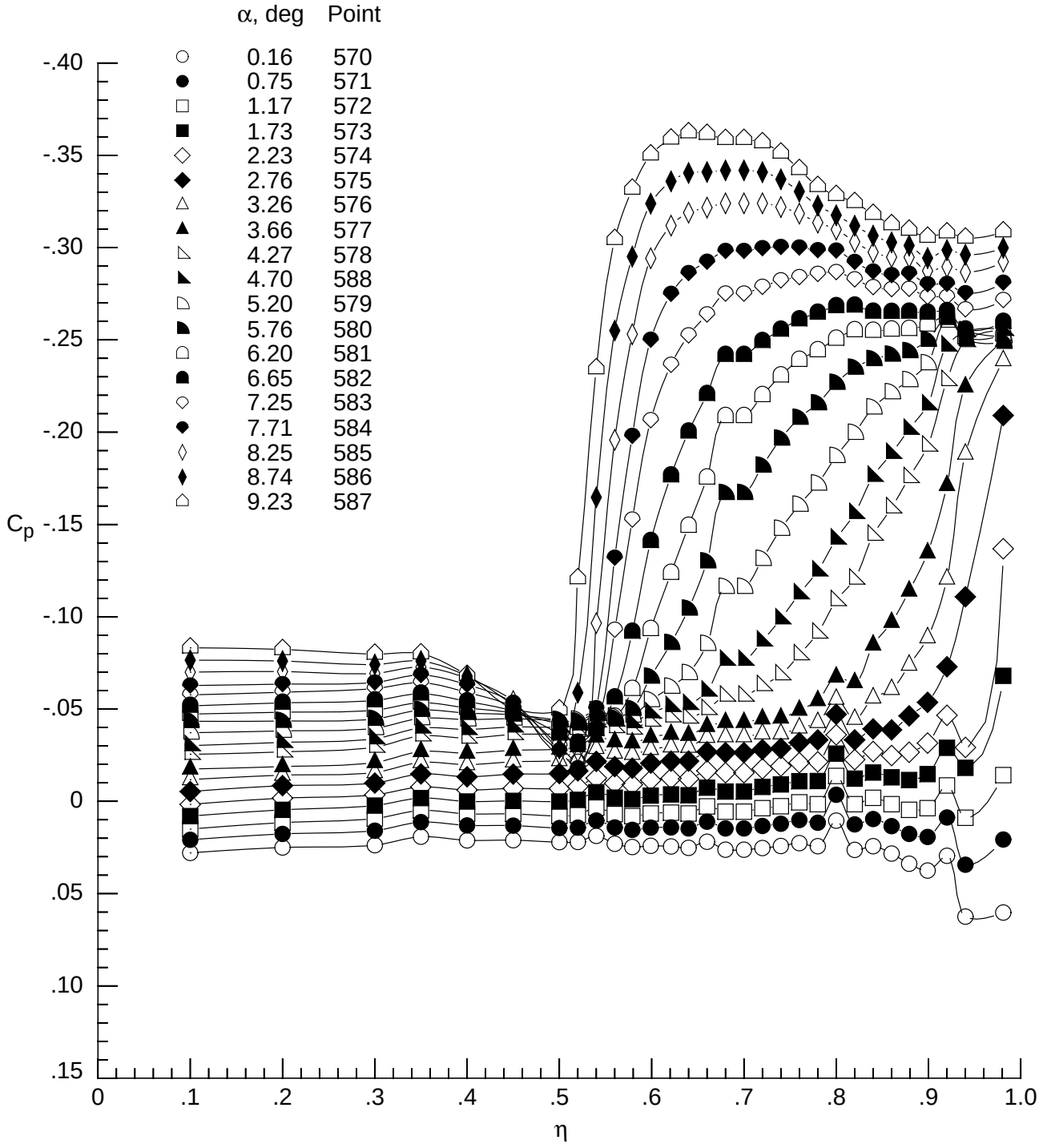

(c) Upper surface at x = 12 in.

Figure D15. Continued.

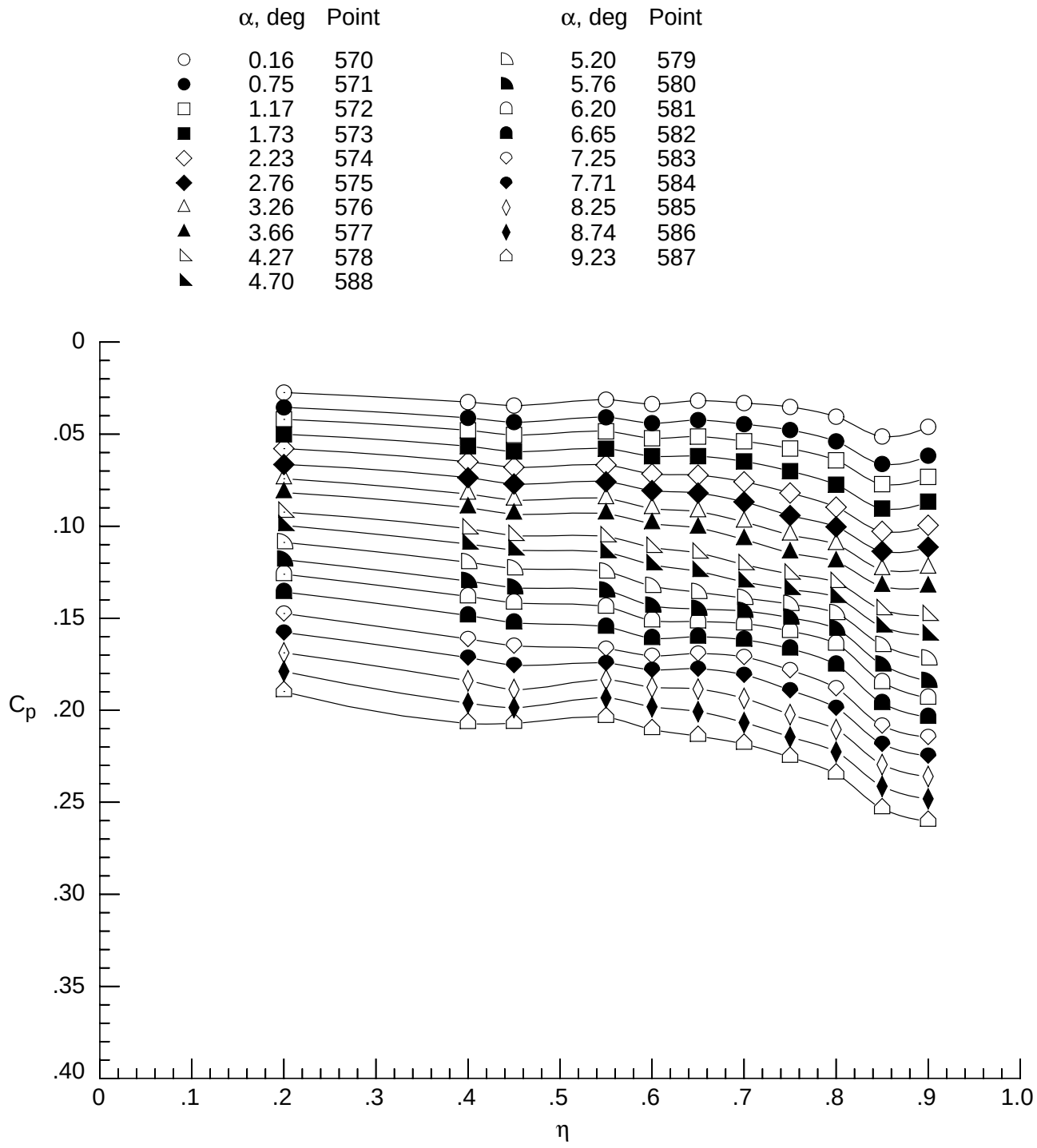

(d) Lower surface at x = 12 in.

Figure D15. Concluded.

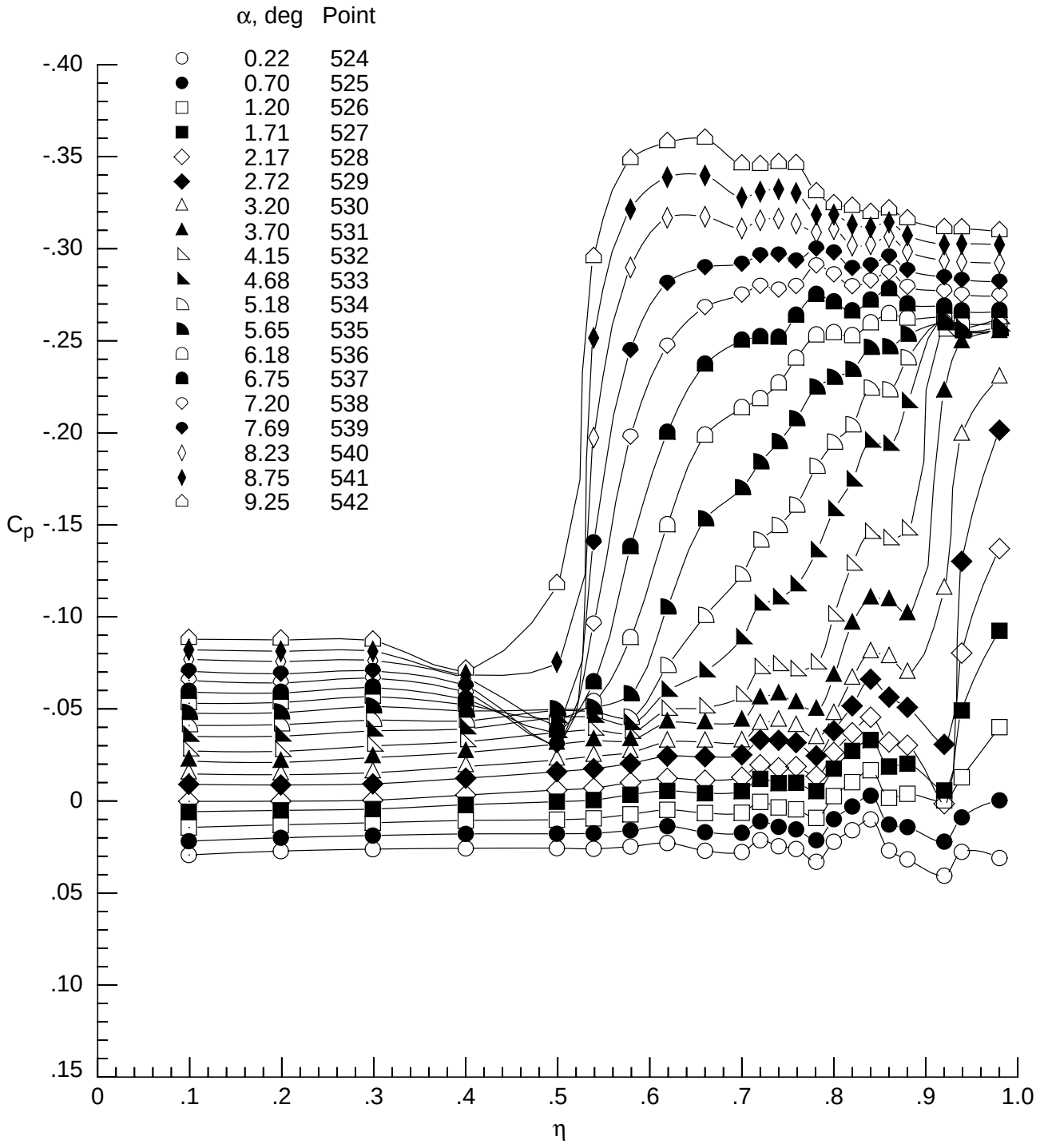

(a) Upper surface at x = 6 in.

Figure D16. Surface-pressure coefficient data for elliptical wing with transition grit at M = 1.60 and $R = 5 \times 10^6$ ft^{-1} for run 29.

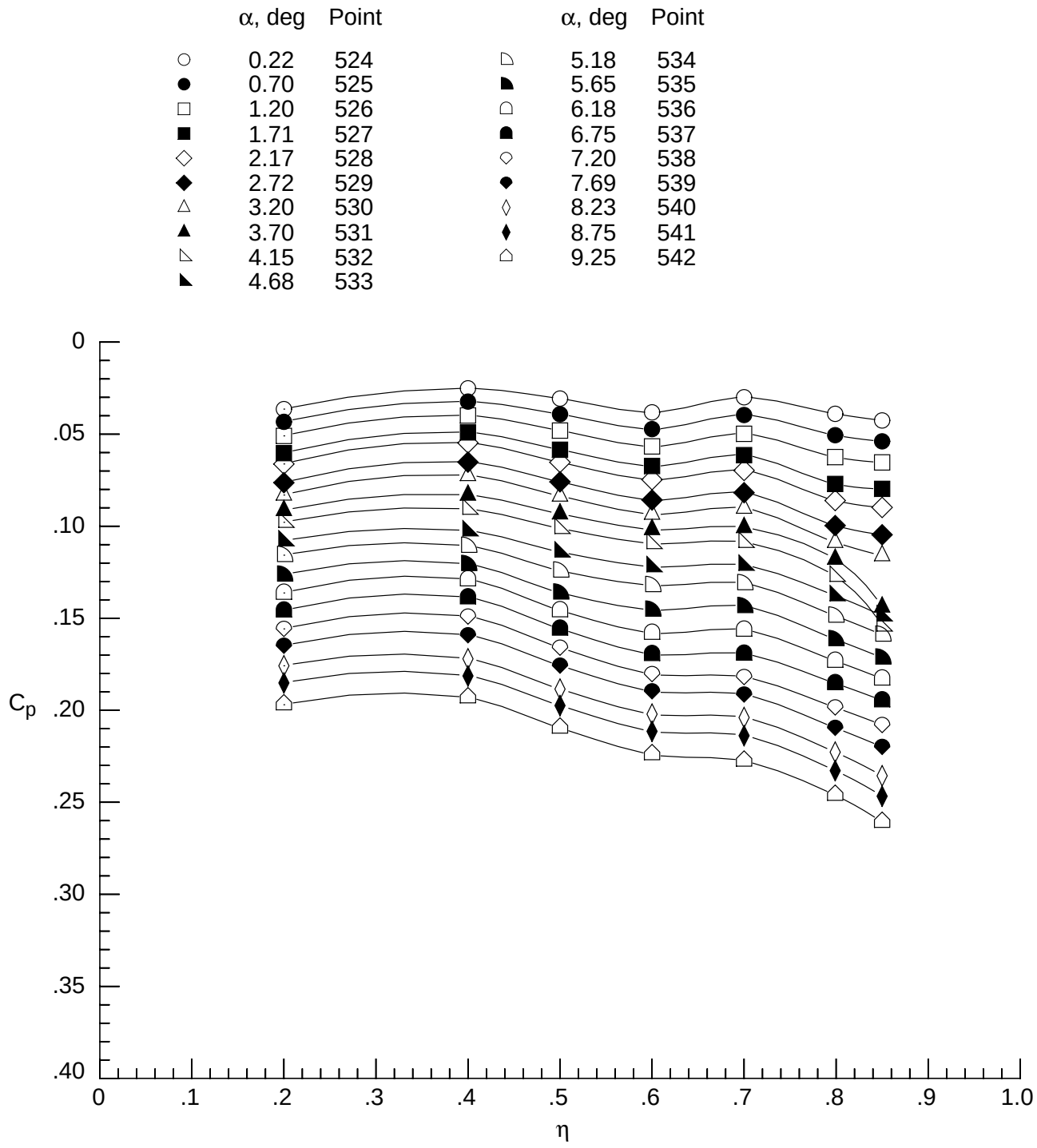

(b) Lower surface at x = 6 in.

Figure D16. Continued.

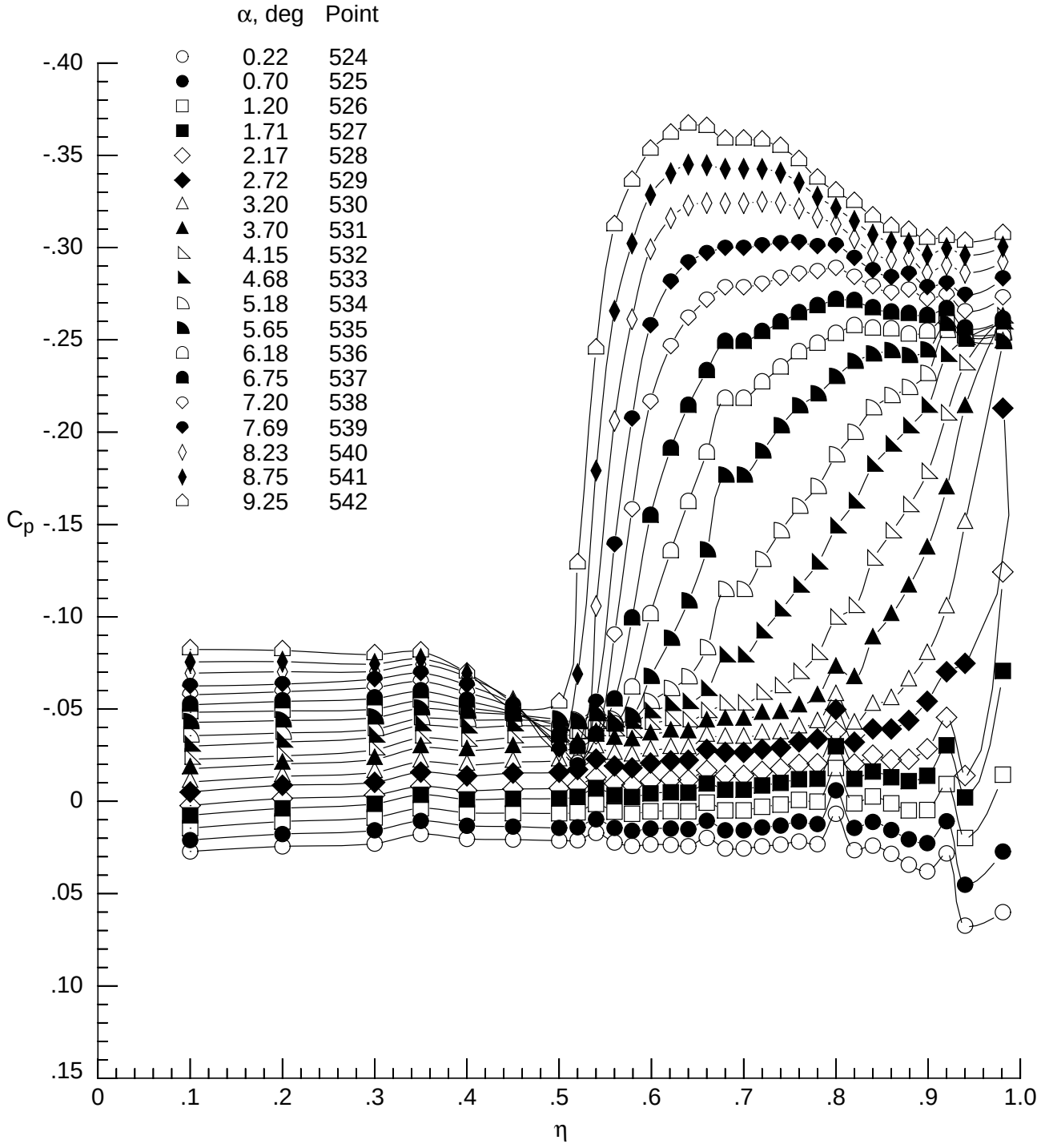

(c) Upper surface at x = 12 in.

Figure D16. Continued.

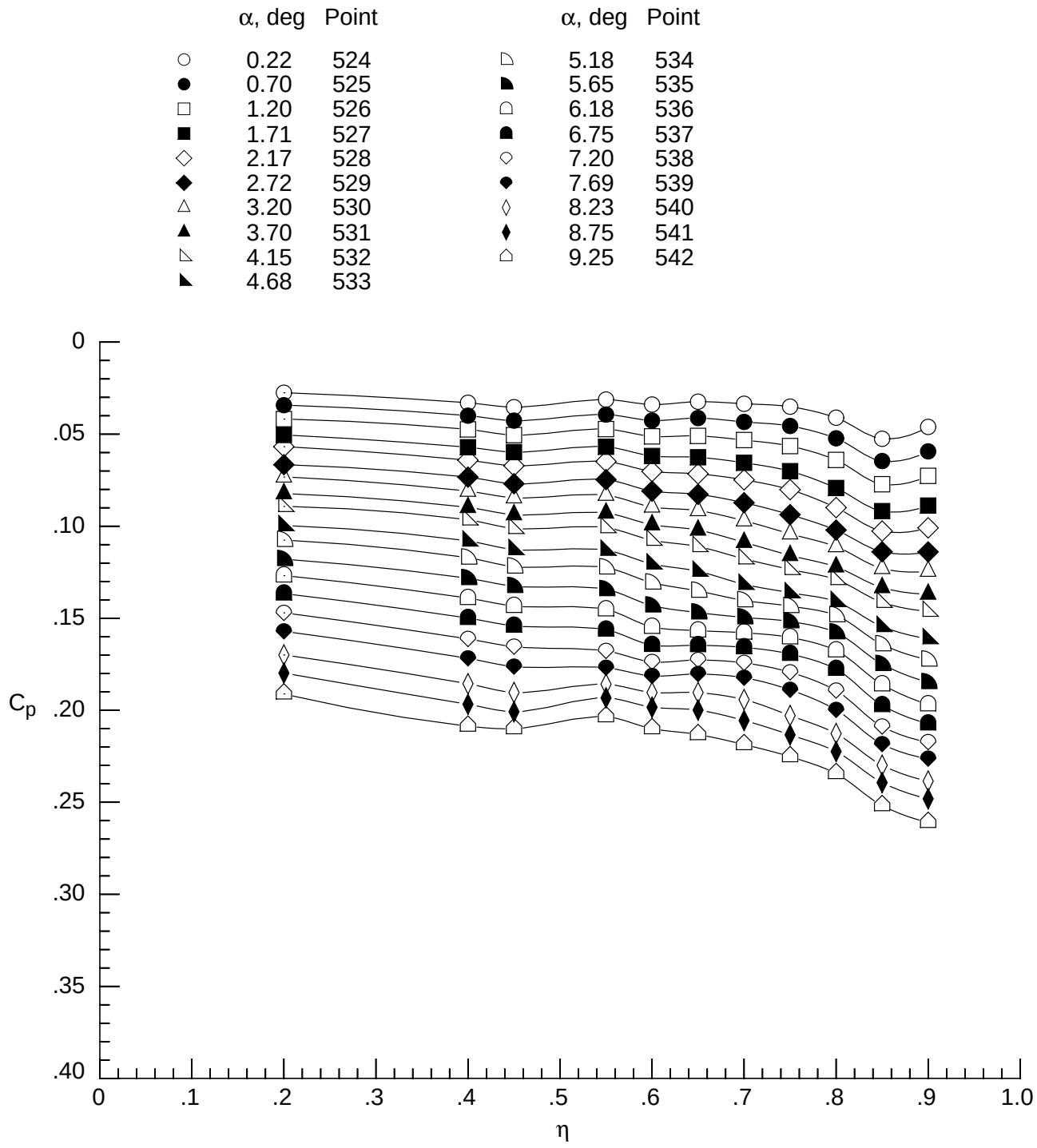

(d) Lower surface at x = 12 in.

Figure D16. Concluded.

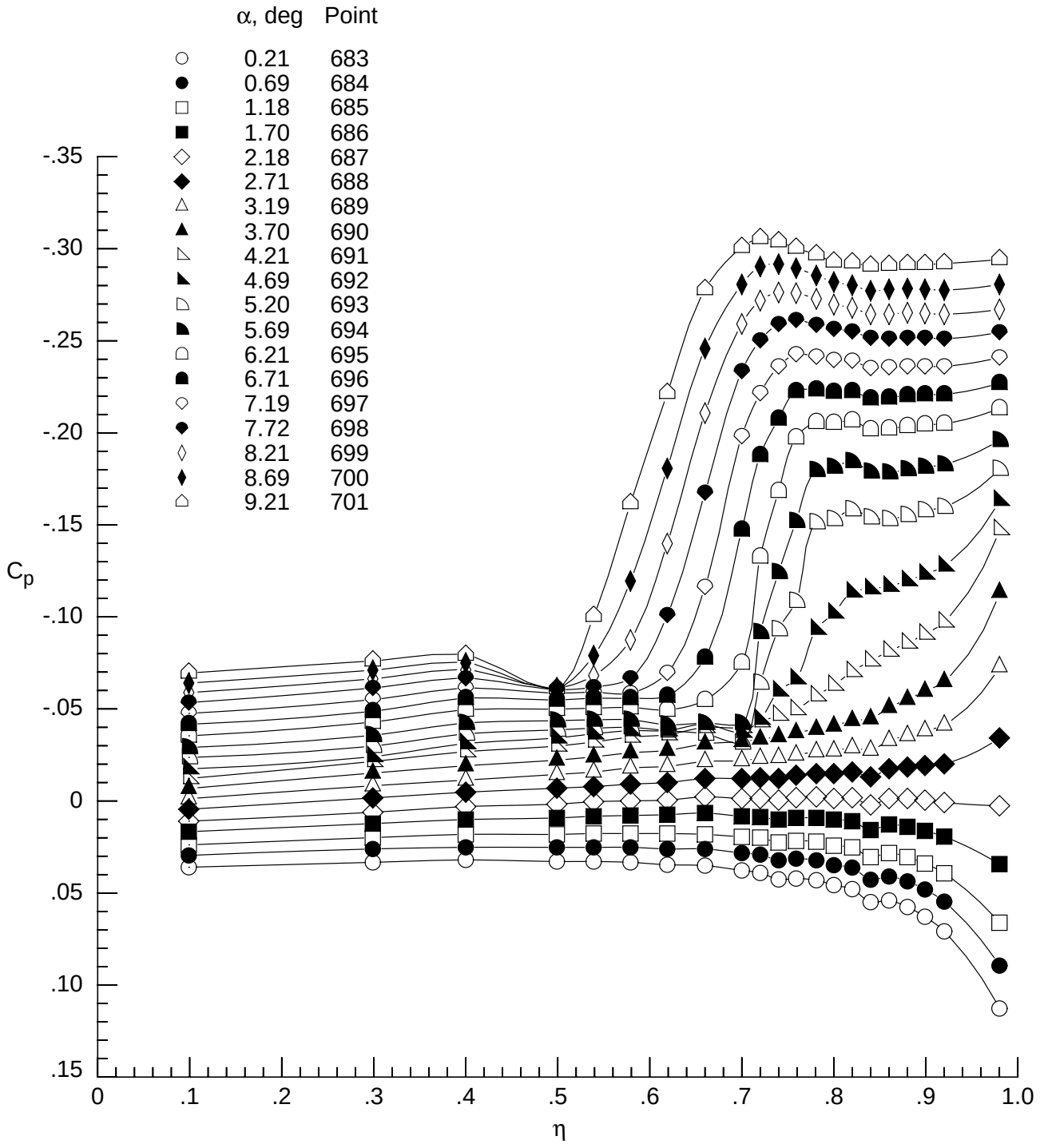

(a) Upper surface at x = 6 in.

Figure D17. Surface-pressure coefficient data for cambered wing without transition grit at $M = 1.60$ and $R = 1 \times 10^6$ ft^{-1} for run 36.

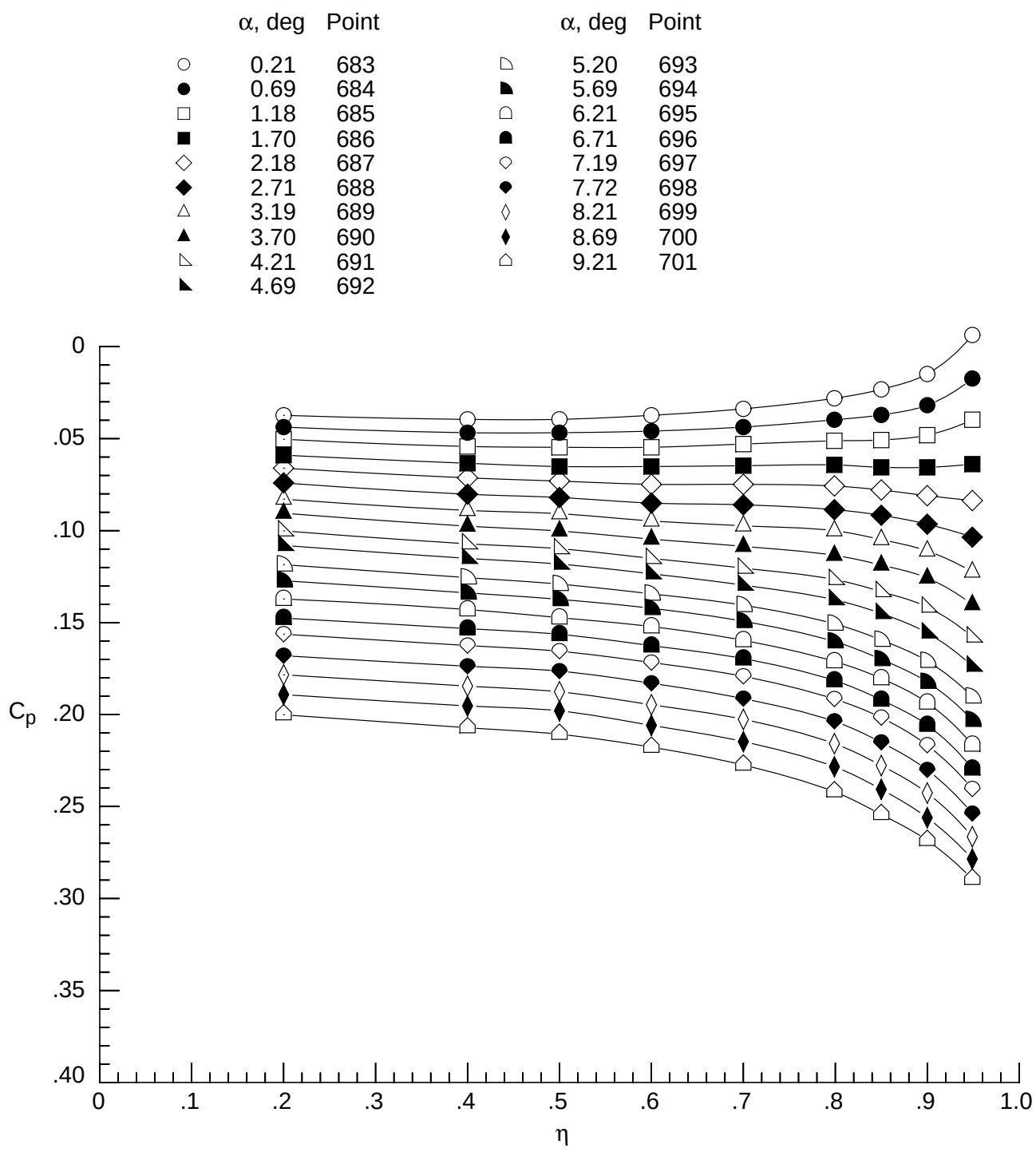

(b) Lower surface at x = 6 in.

Figure D17. Continued.

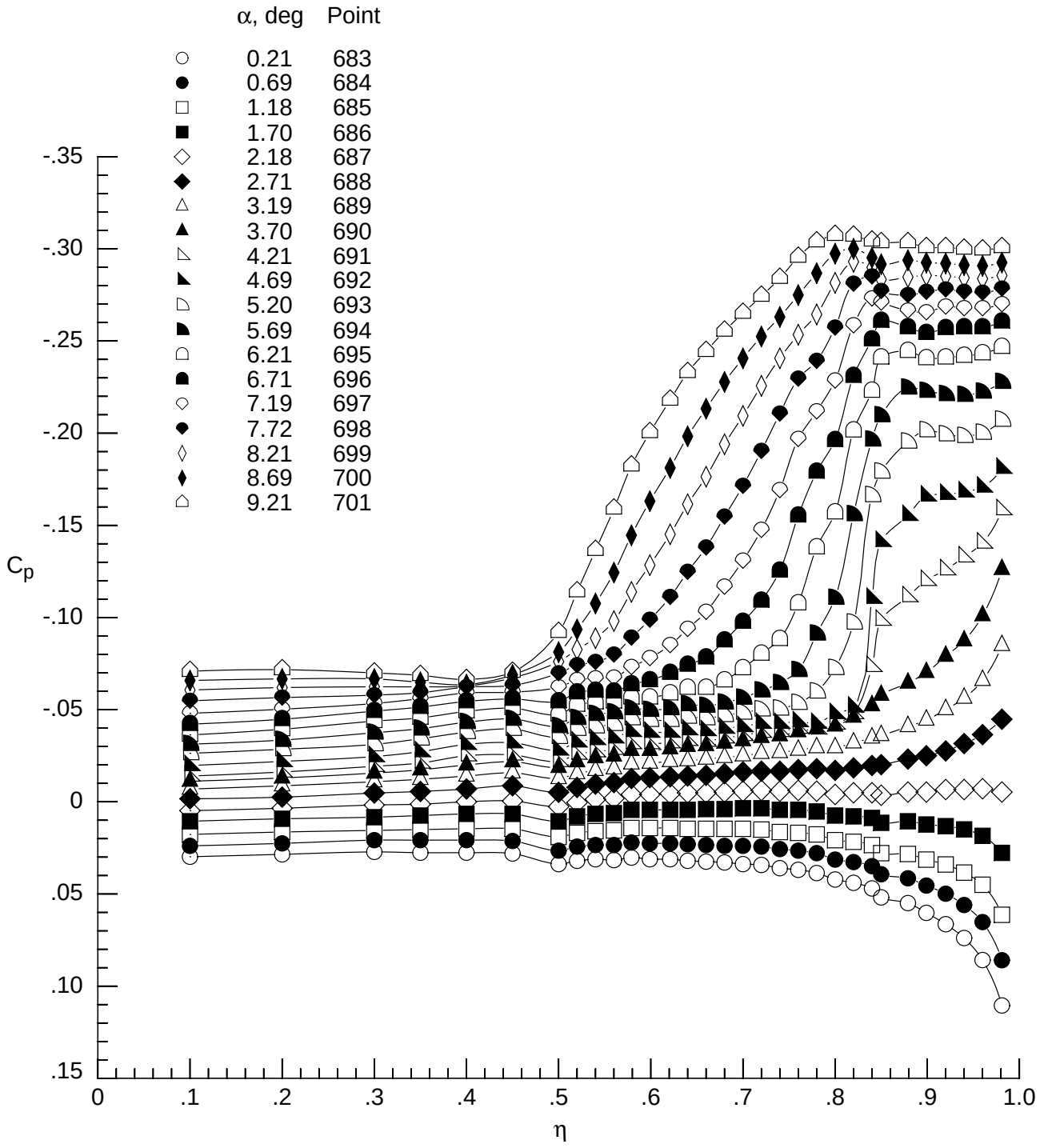

(c) Upper surface at x = 12 in.

Figure D17. Continued.

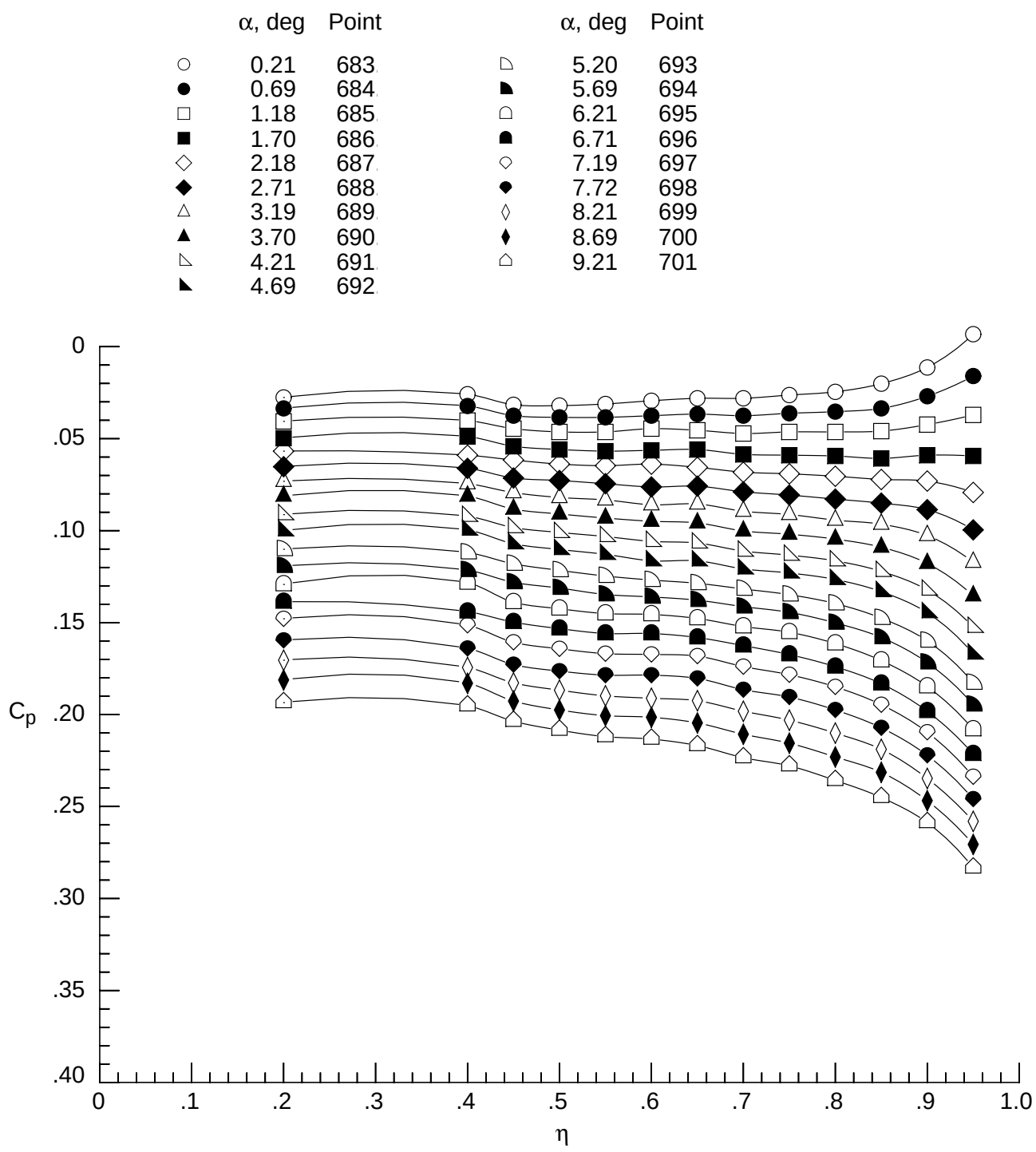

(d) Lower surface at x = 12 in.

Figure D17. Concluded.

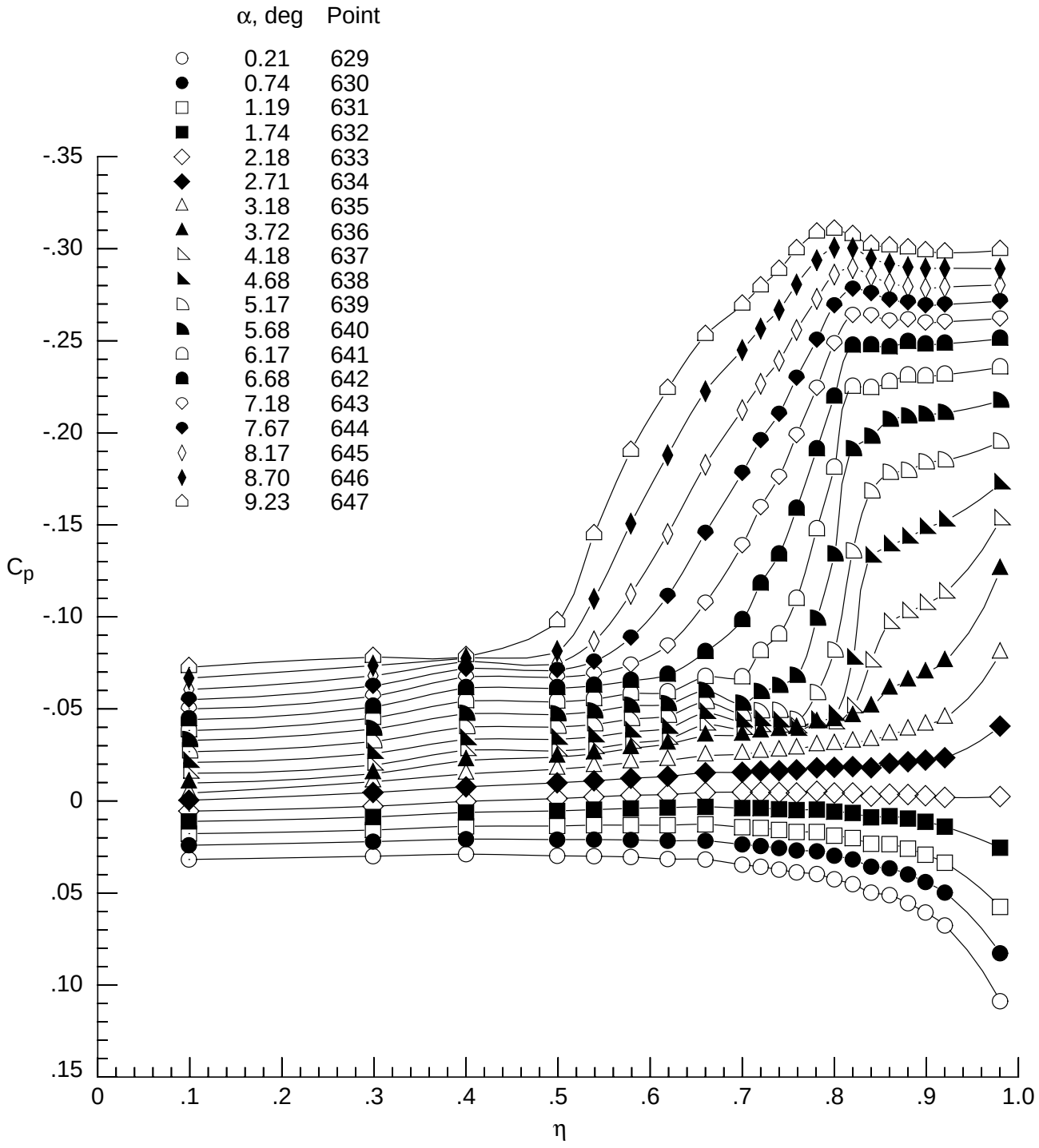

(a) Upper surface at x = 6 in.

Figure D18. Surface-pressure coefficient data for cambered wing without transition grit at $M = 1.60$ and $R = 2 \times 10^6$ ft^{-1} for run 34.

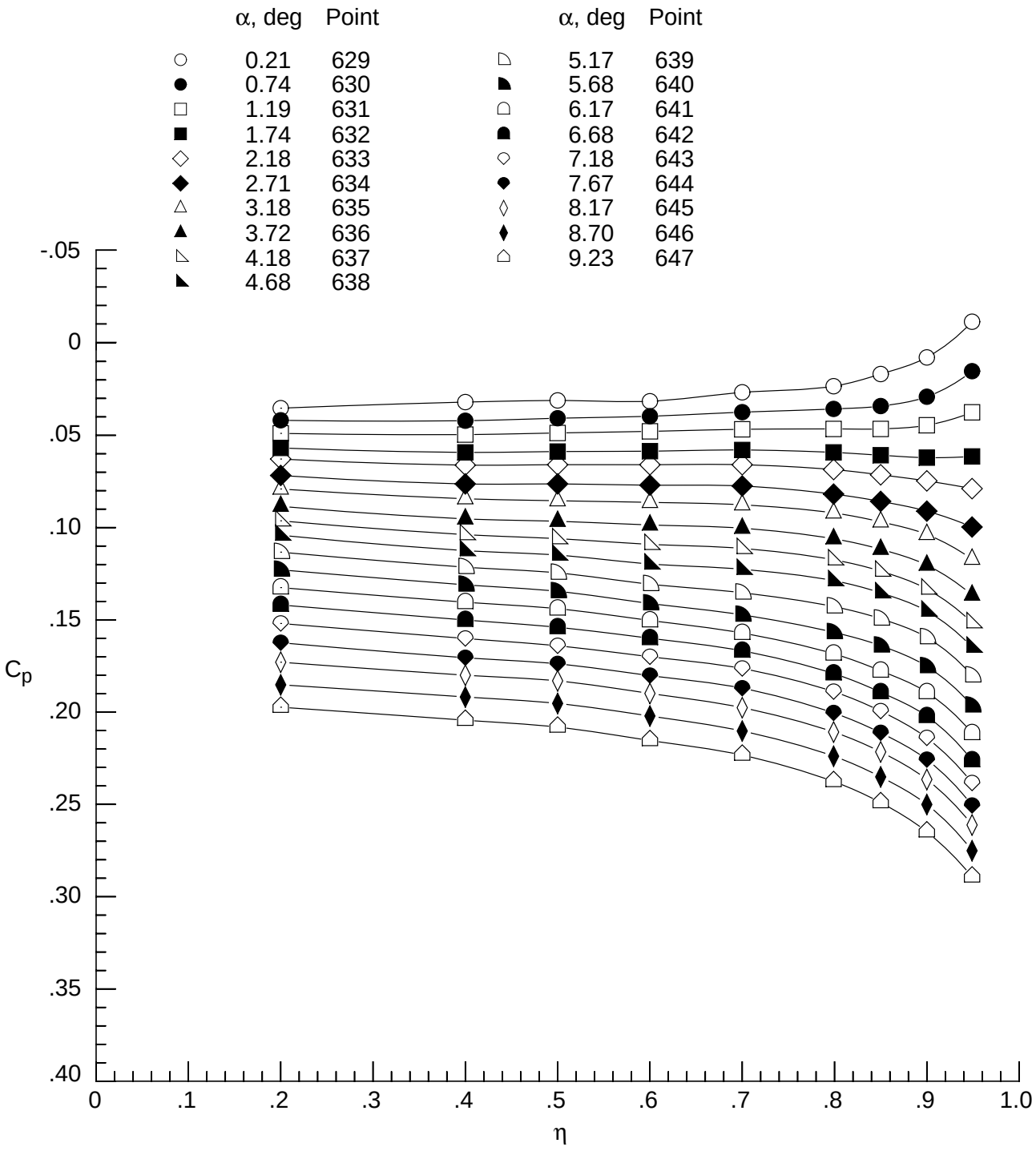

(b) Lower surface at x = 6 in.

Figure D18. Continued.

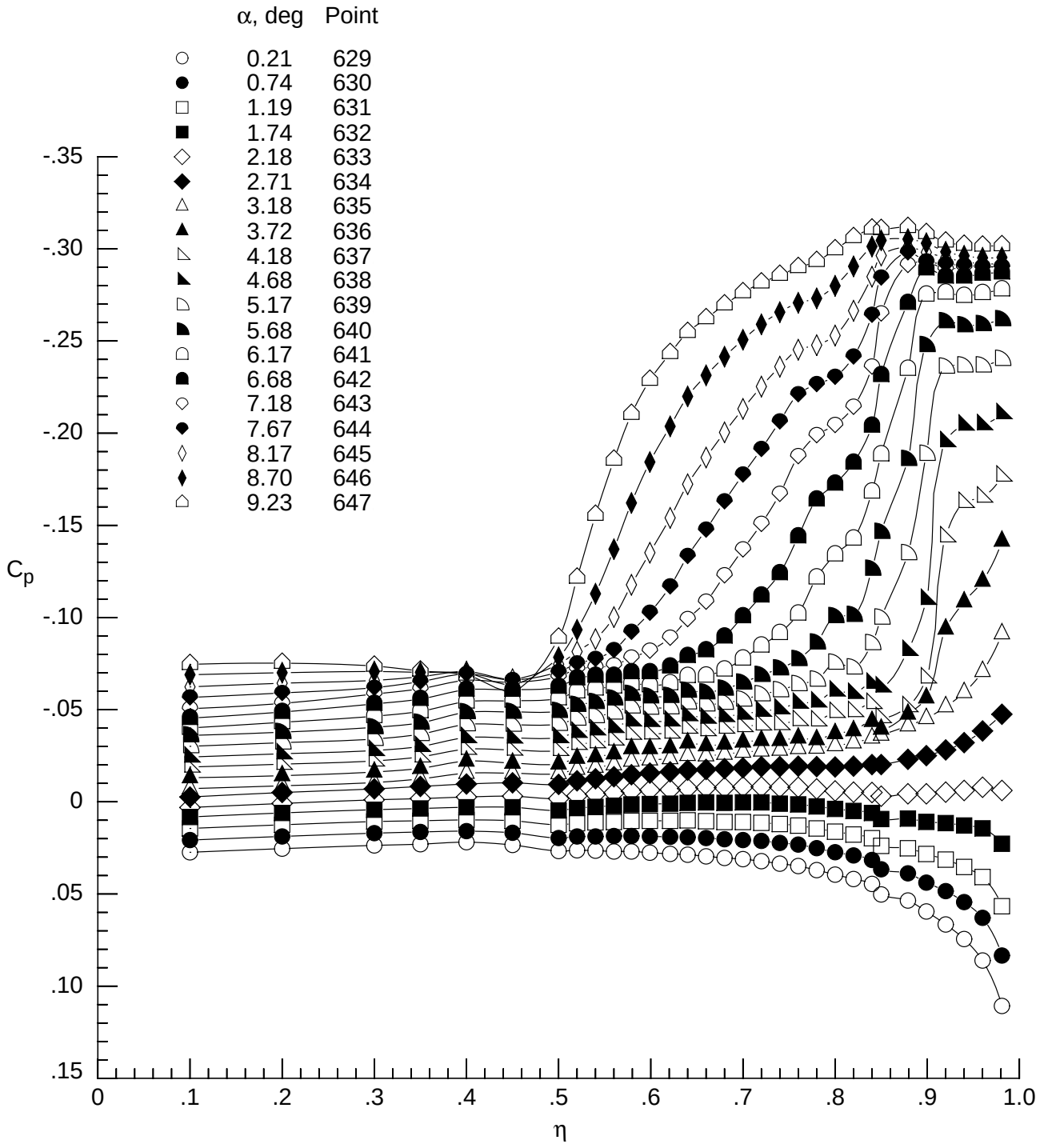

(c) Upper surface at x = 12 in.

Figure D18. Continued.

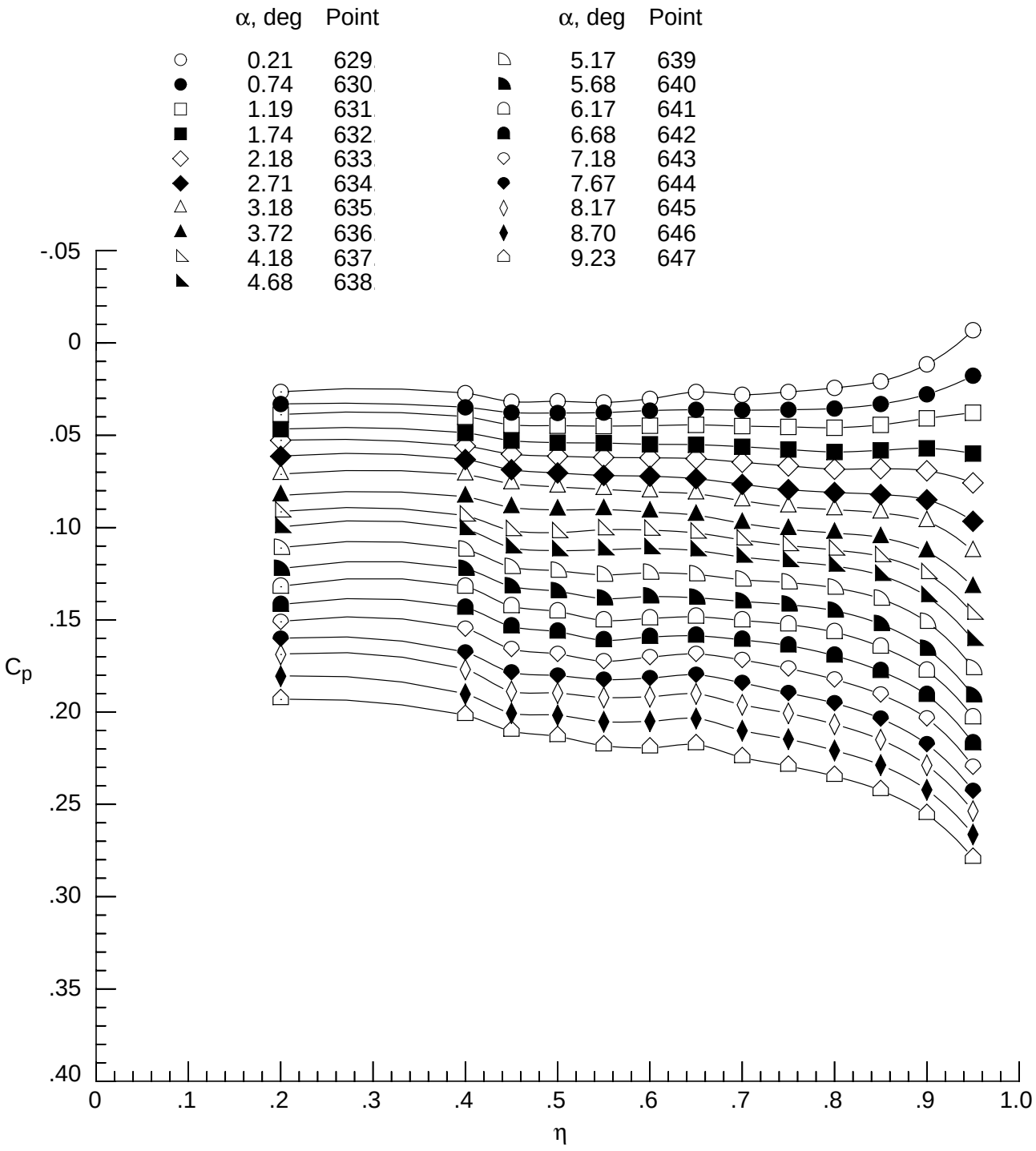

(d) Lower surface at x = 12 in.

Figure D18. Concluded.

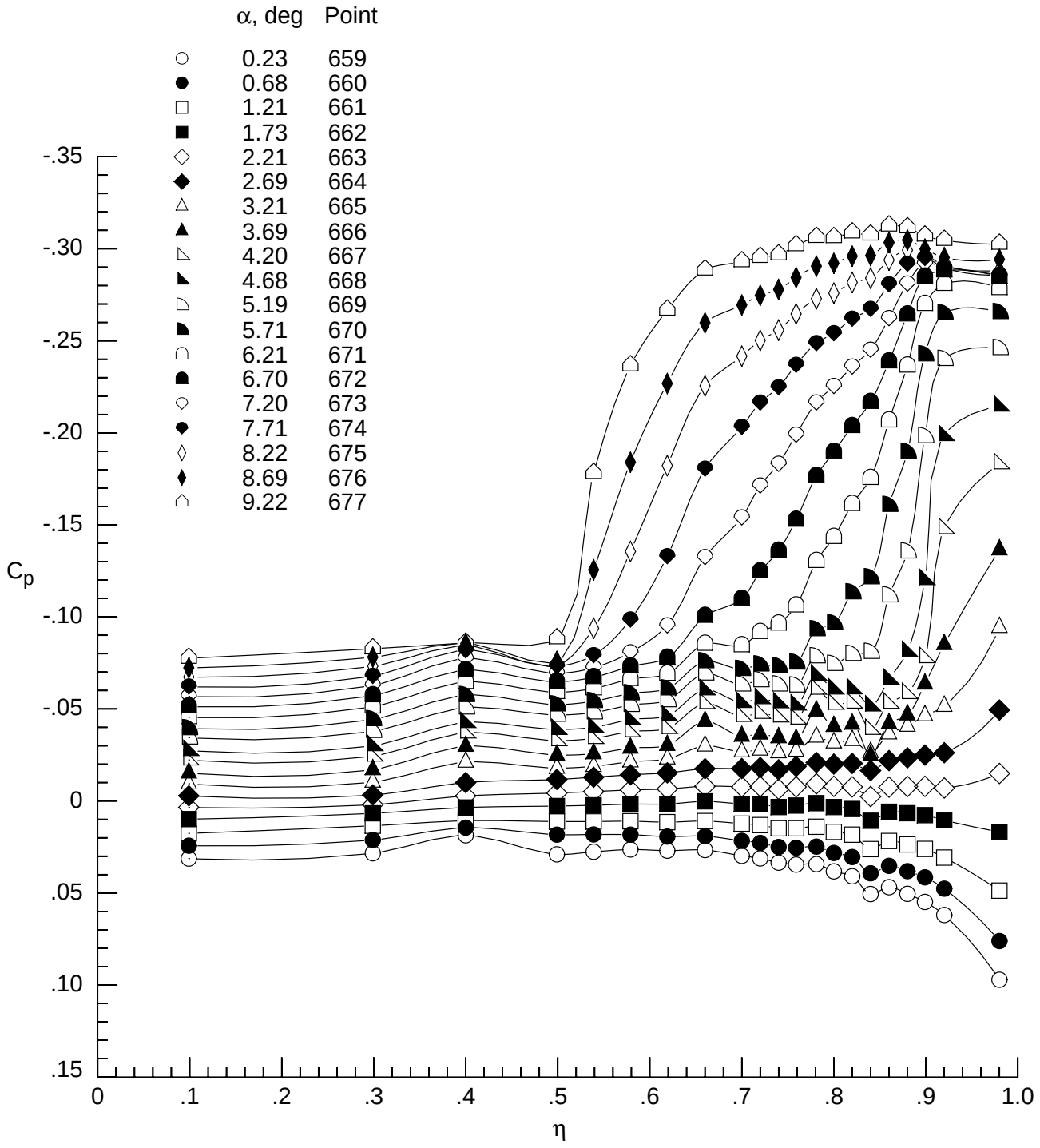

(a) Upper surface at x = 6 in.

Figure D19. Surface-pressure coefficient data for cambered wing without transition grit at $M = 1.60$ and $R = 5 \times 10^6$ ft^{-1} for run 35.

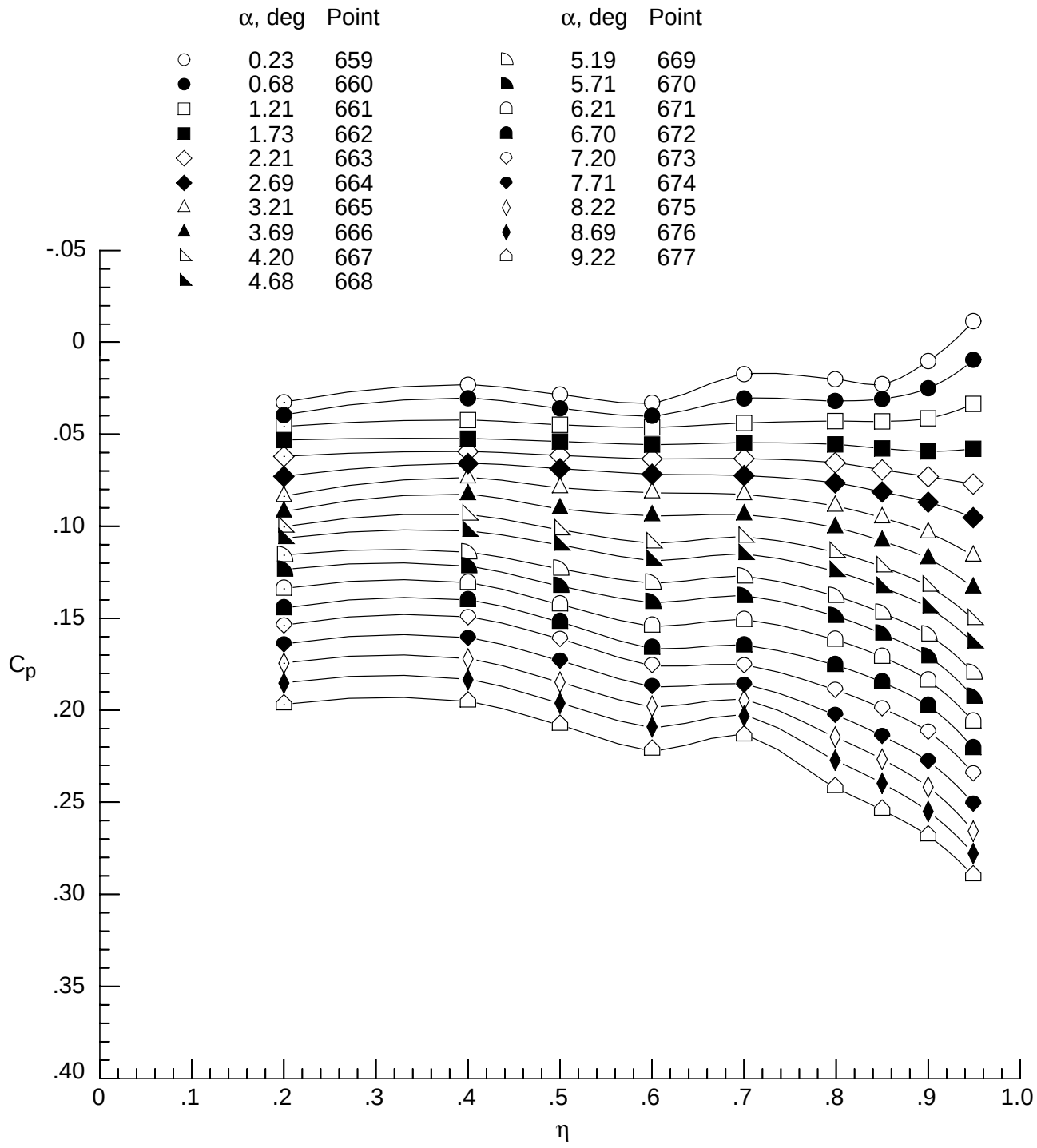

(b) Lower surface at x = 6 in.

Figure D19. Continued.

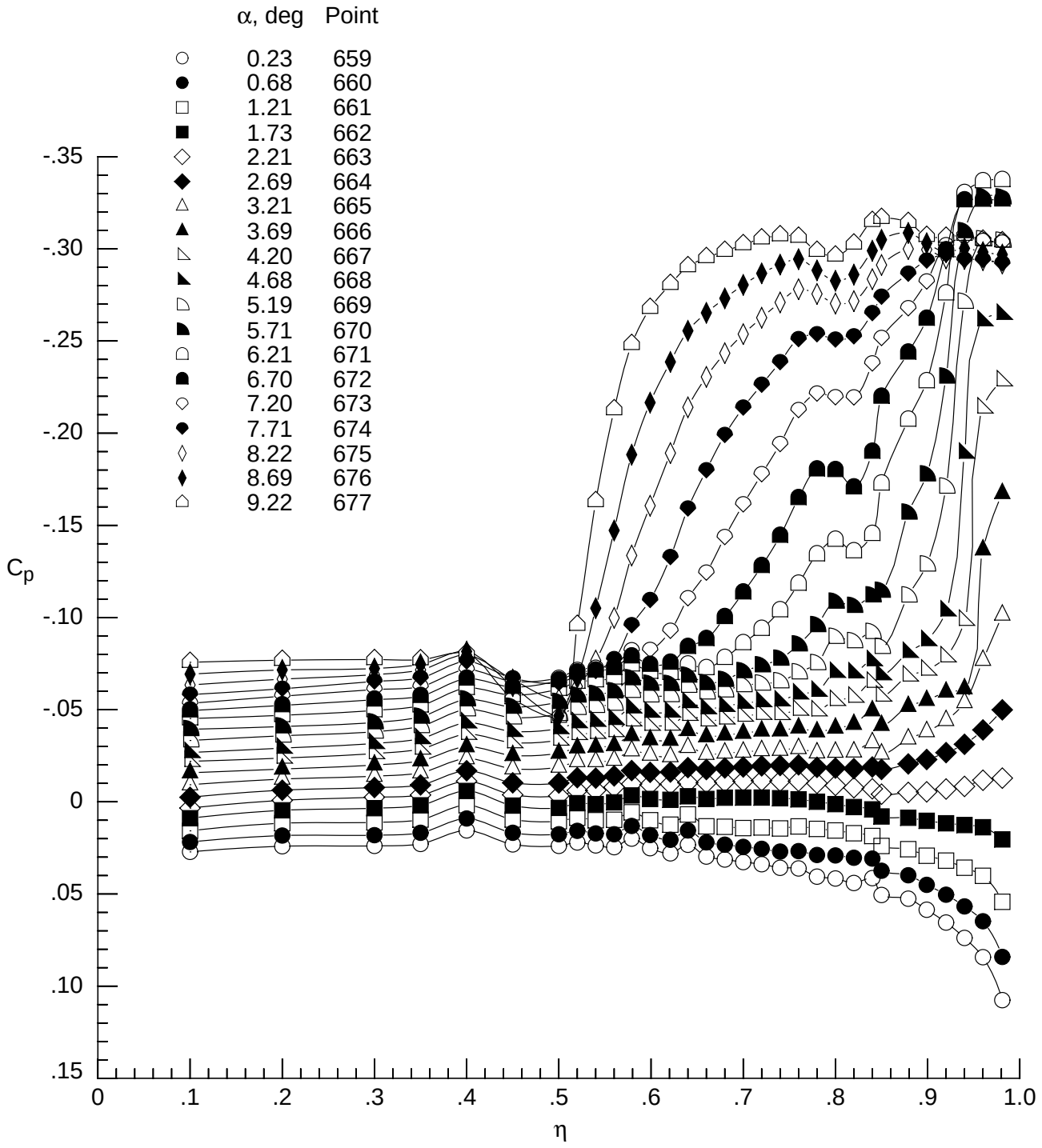

(c) Upper surface at x = 12 in.

Figure D19. Continued.

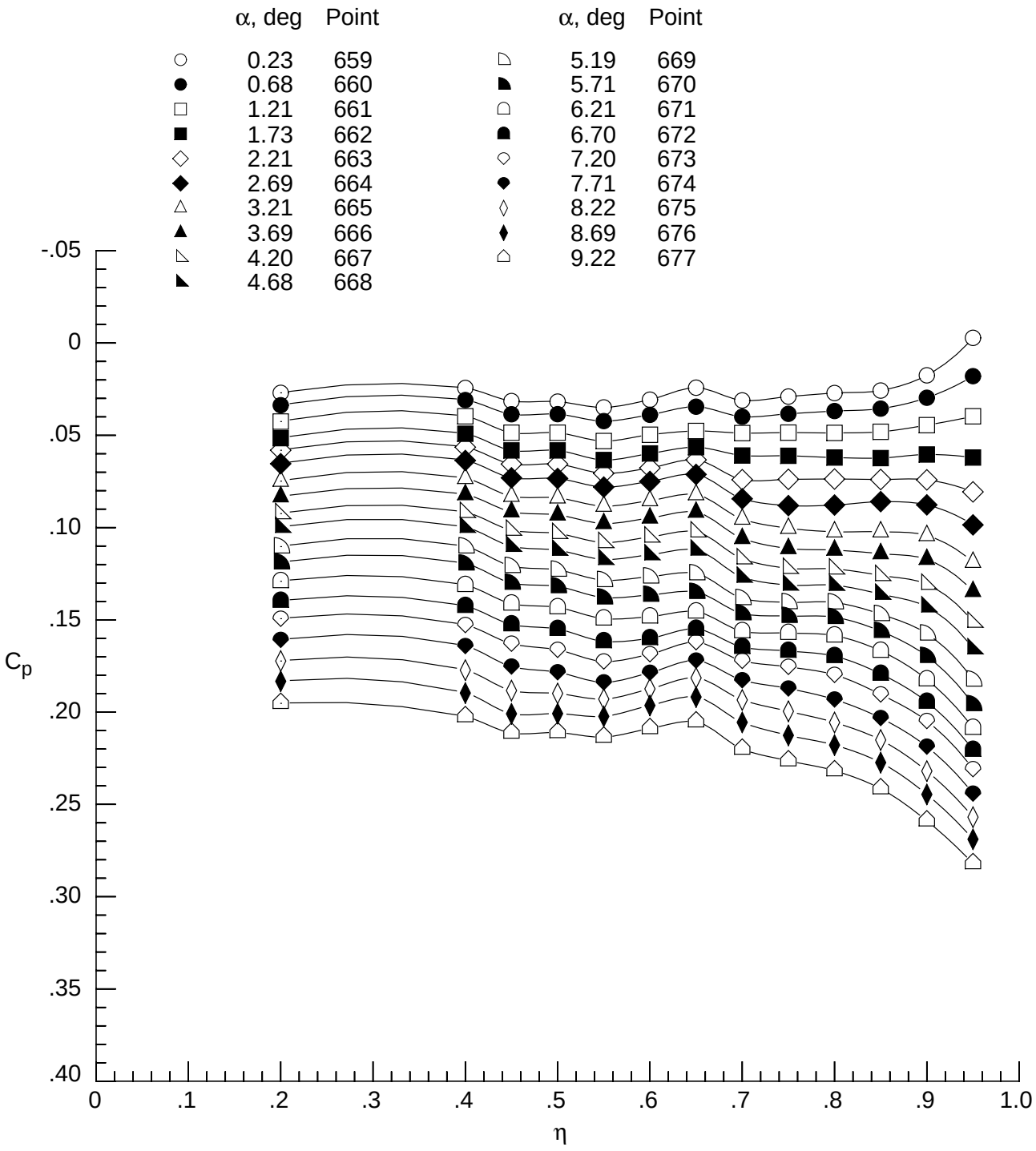

(d) Lower surface at x = 12 in.

Figure D19. Concluded.

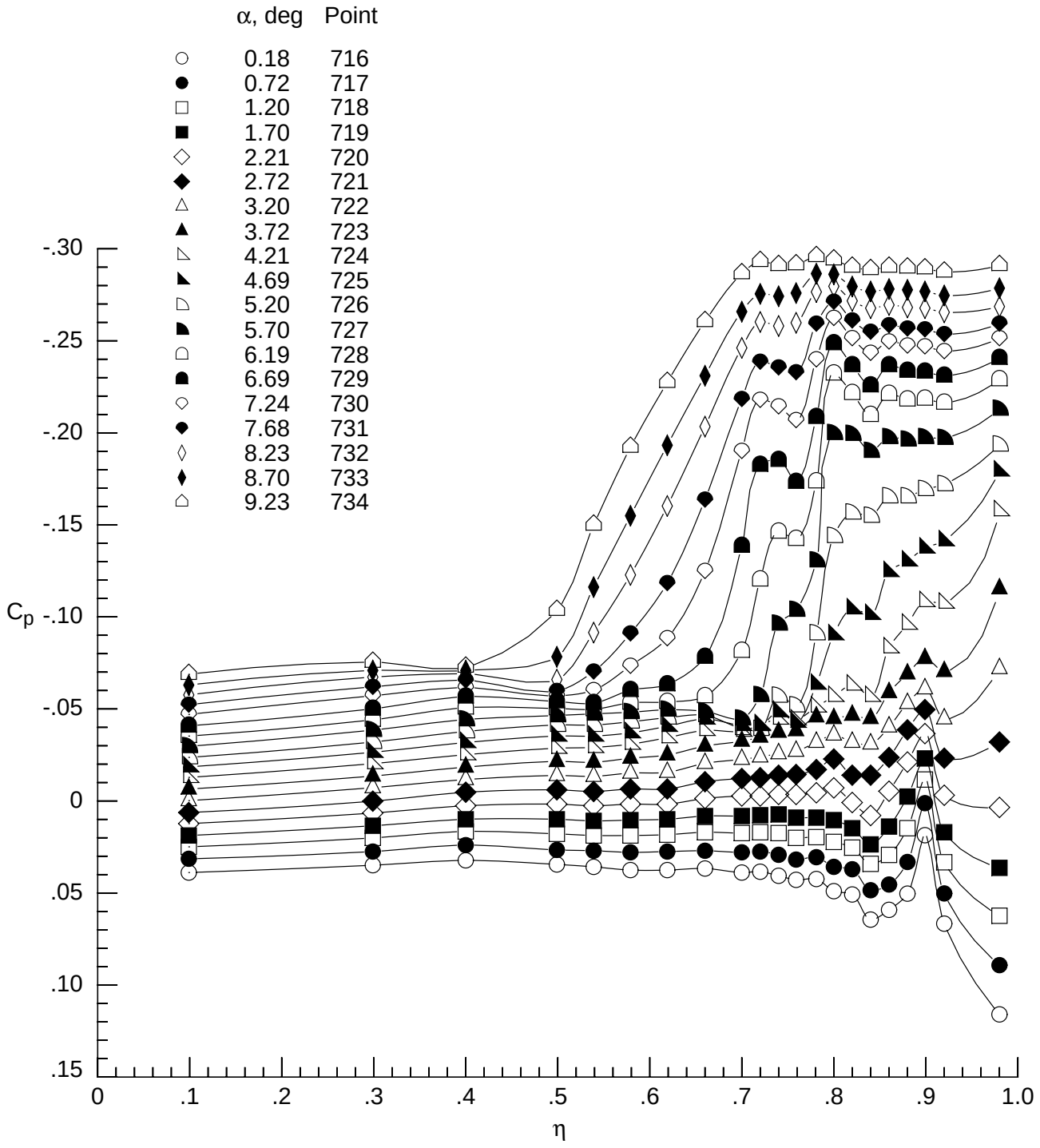

(a) Upper surface at x = 6 in.

Figure D20. Surface-pressure coefficient data for cambered wing with transition grit at M = 1.60 and $R = 1 \times 10^6$ ft^{-1} for run 37.

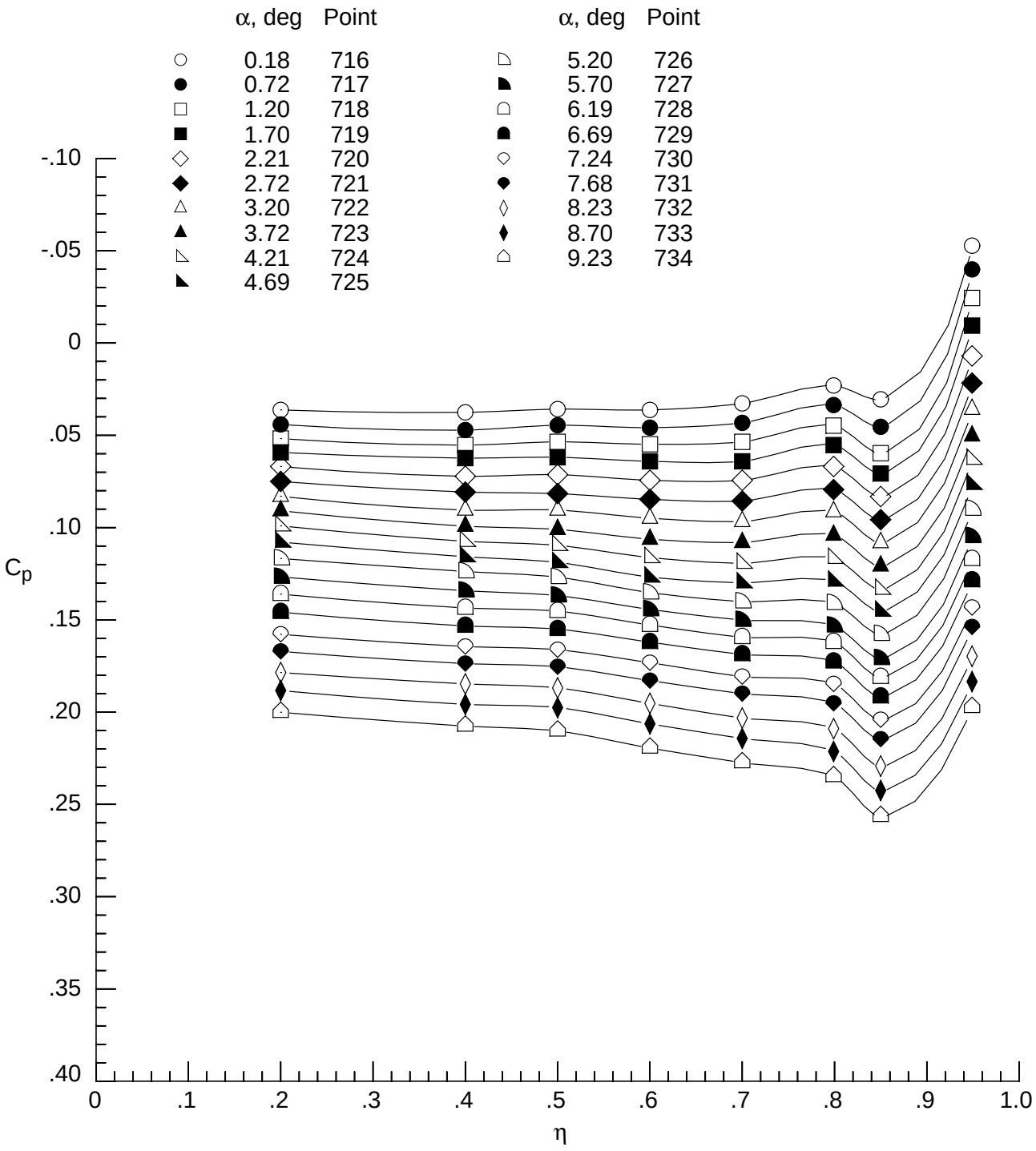

(b) Lower surface at x = 6 in.

Figure D20. Continued.

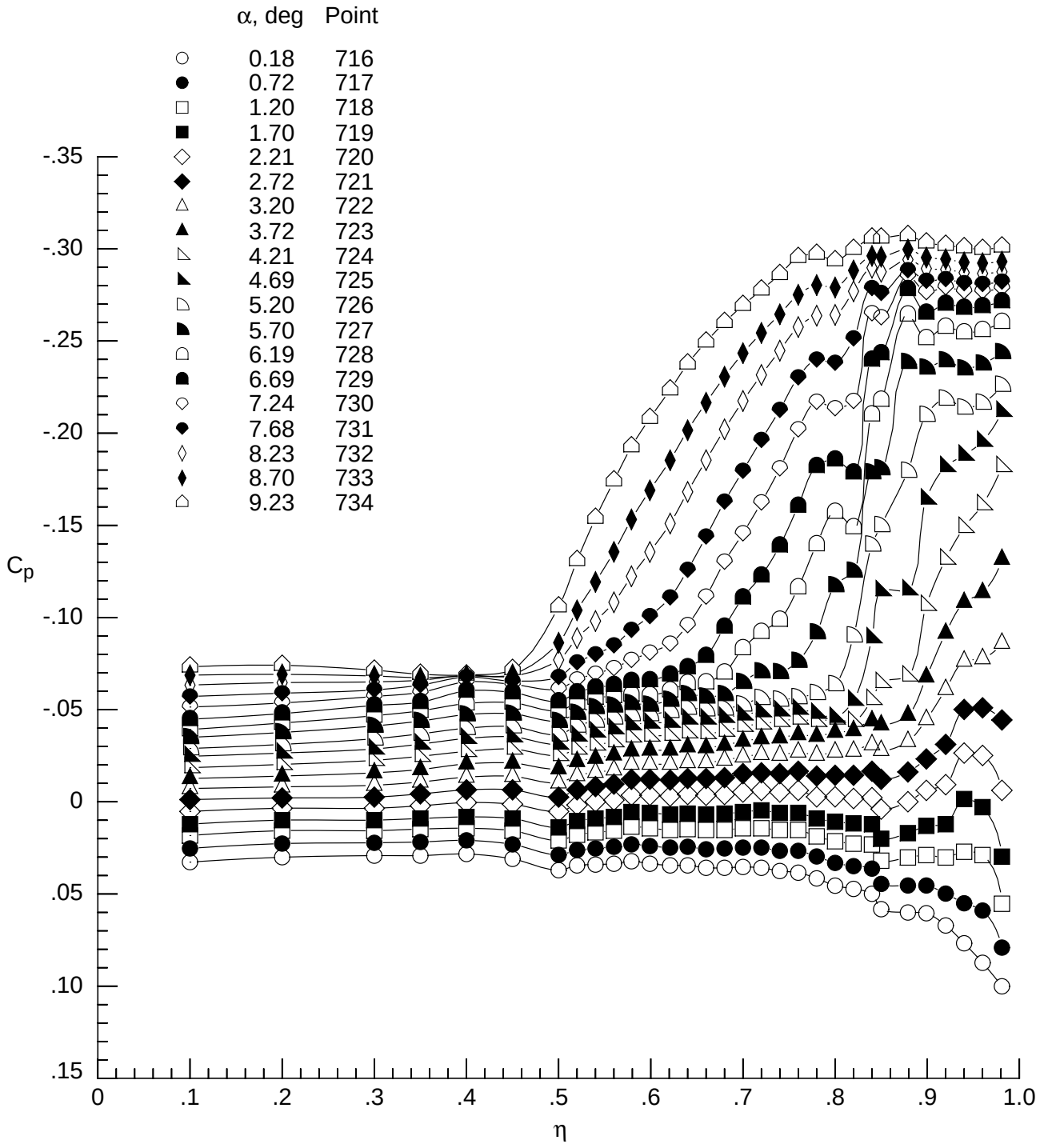

(c) Upper surface at x = 12 in.

Figure D20. Continued.

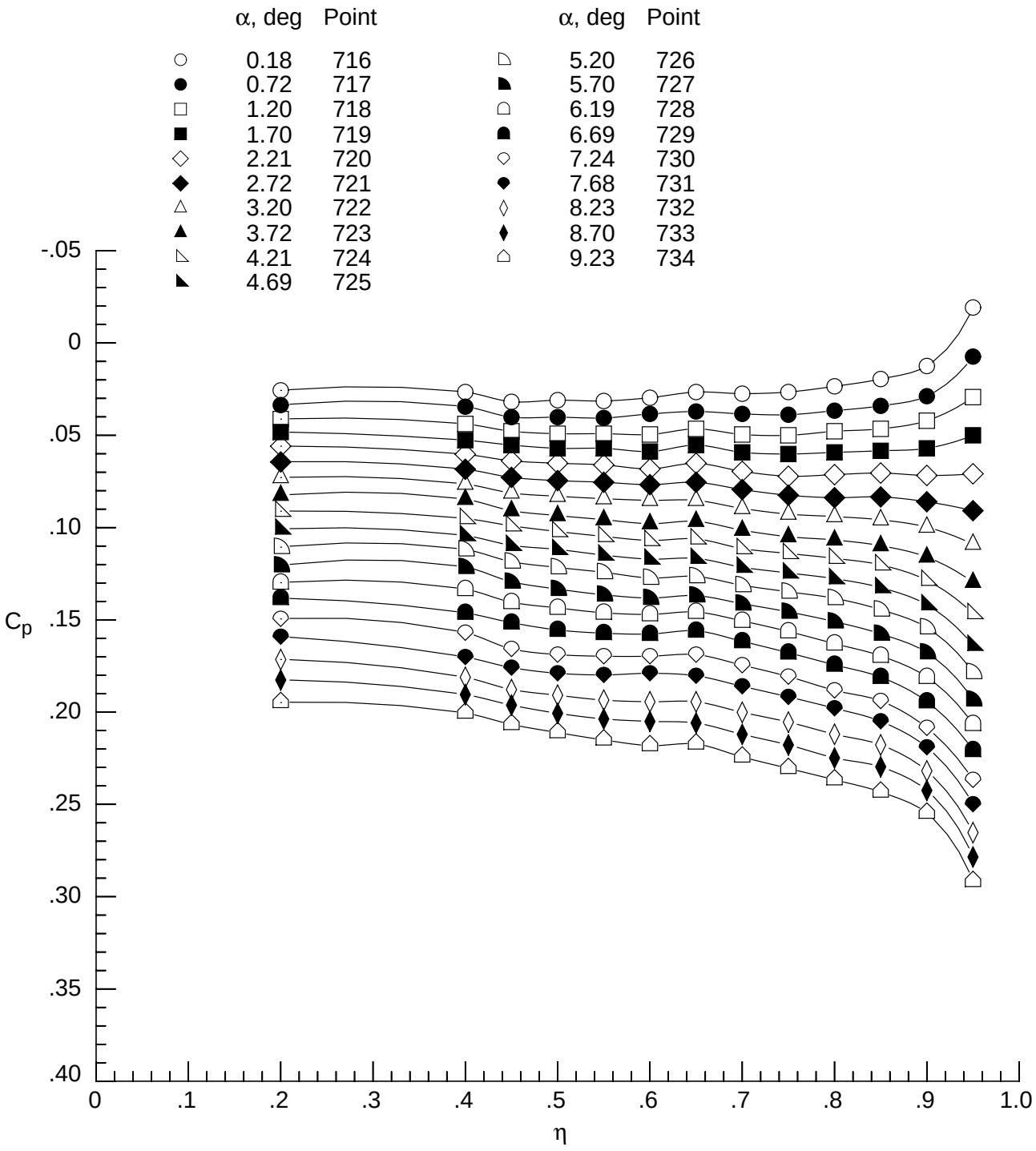

(d) Lower surface at x = 12 in.

Figure D20. Concluded.

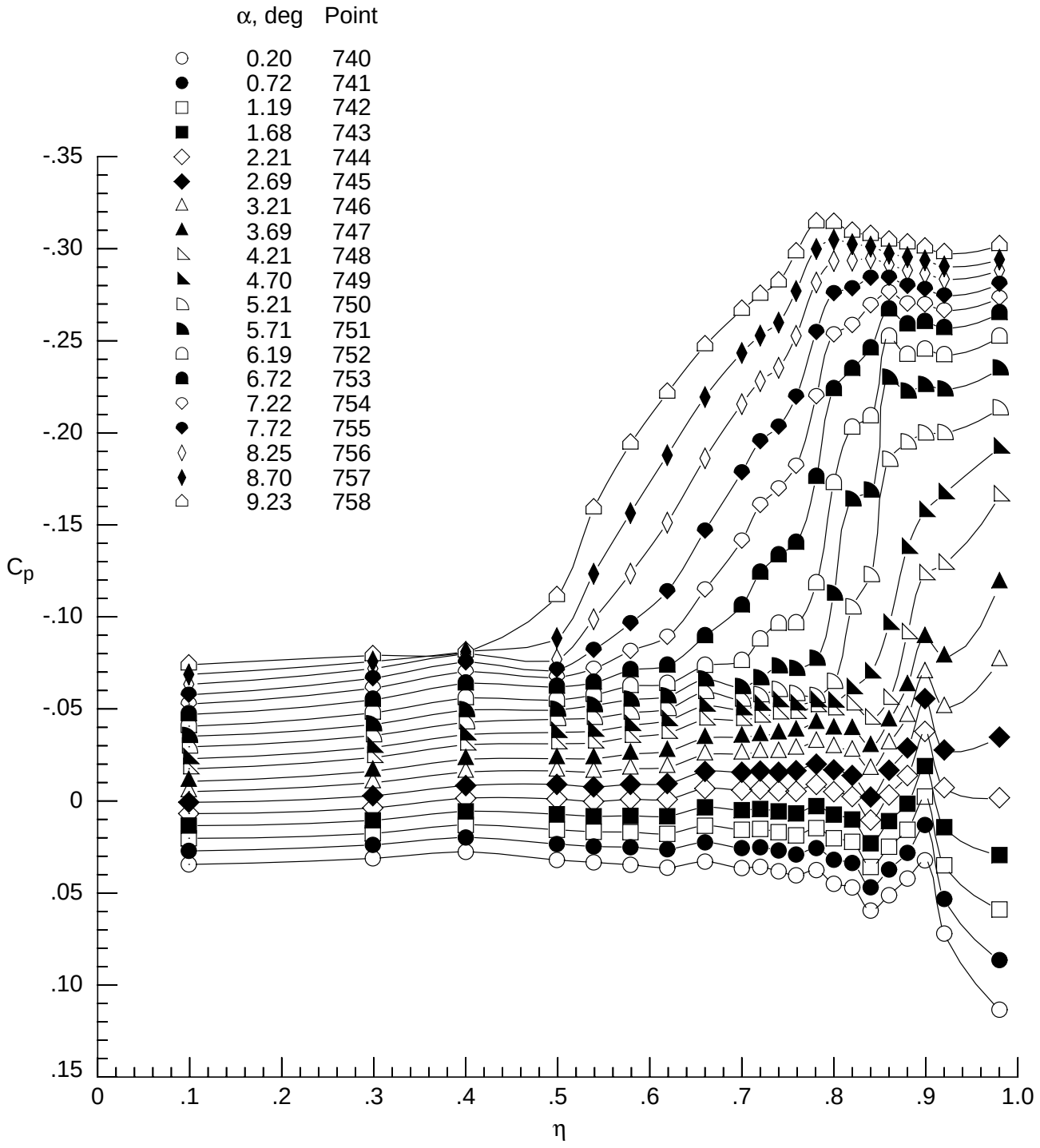

(a) Upper surface at x = 6 in.

Figure D21. Surface-pressure coefficient data for cambered wing with transition grit at M = 1.60 and $R = 2 \times 10^6$ ft^{-1} for run 38.

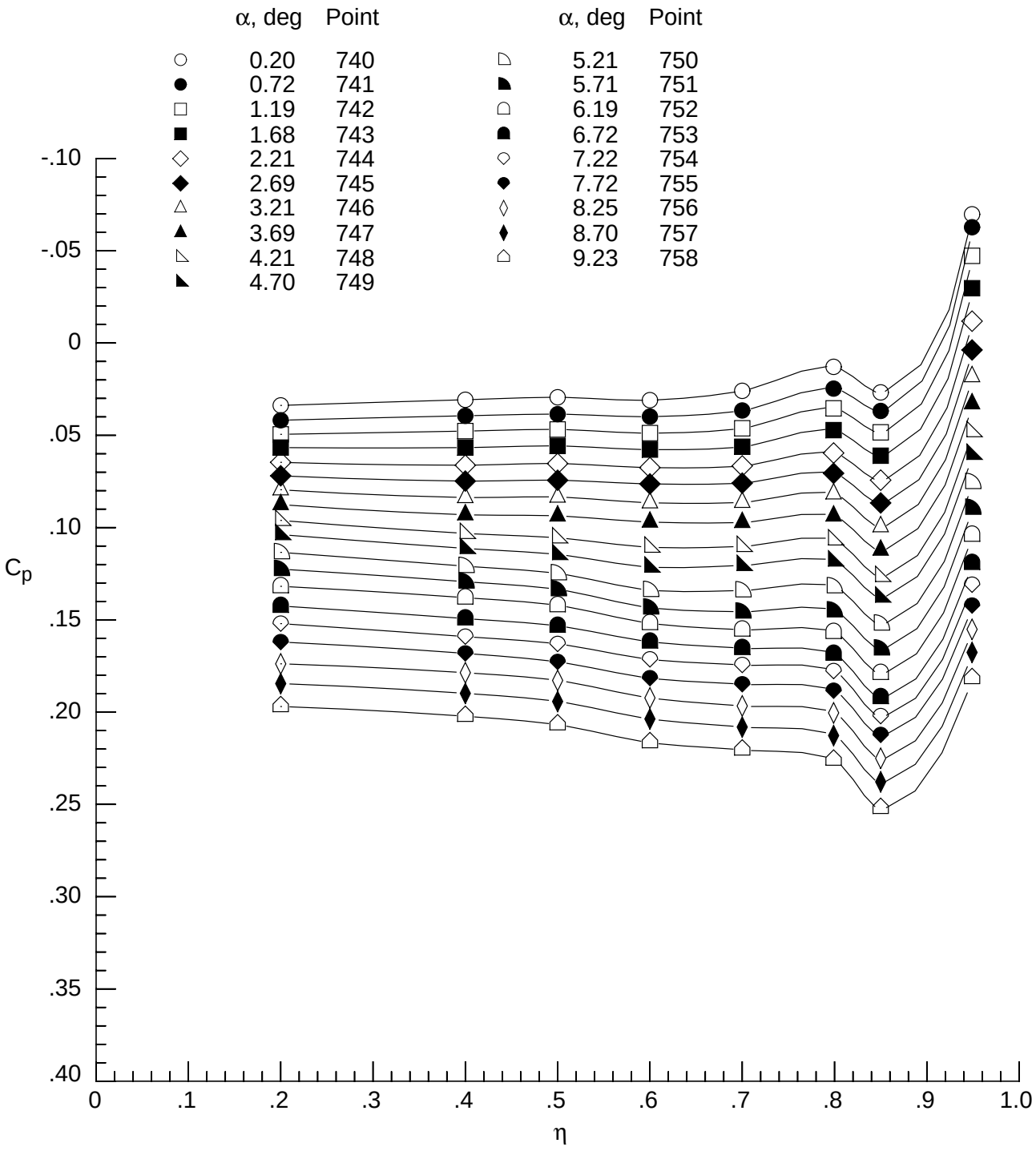

(b) Lower surface at x = 6 in.

Figure D21. Continued.

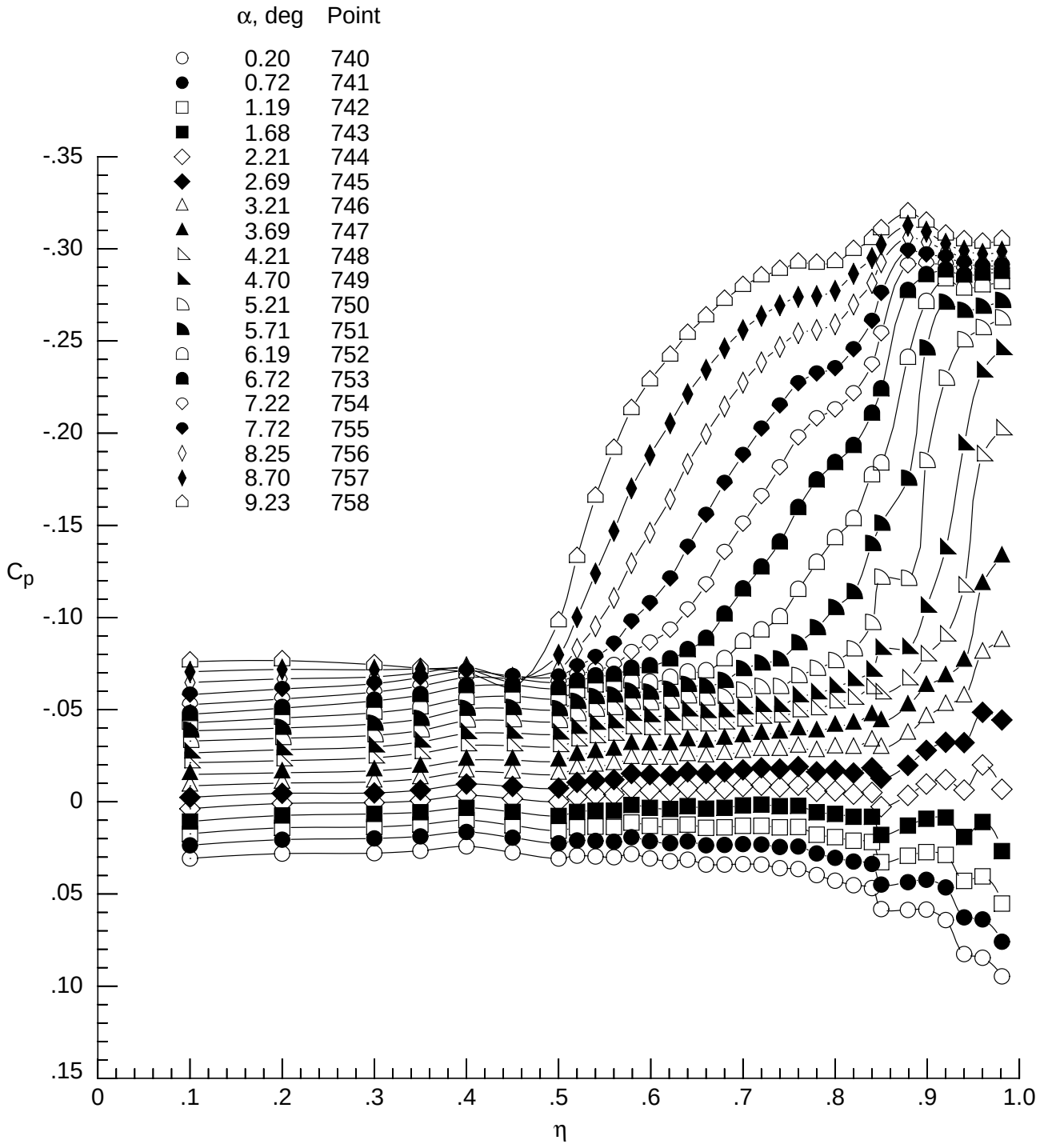

(c) Upper surface at x = 12 in.

Figure D21. Continued.

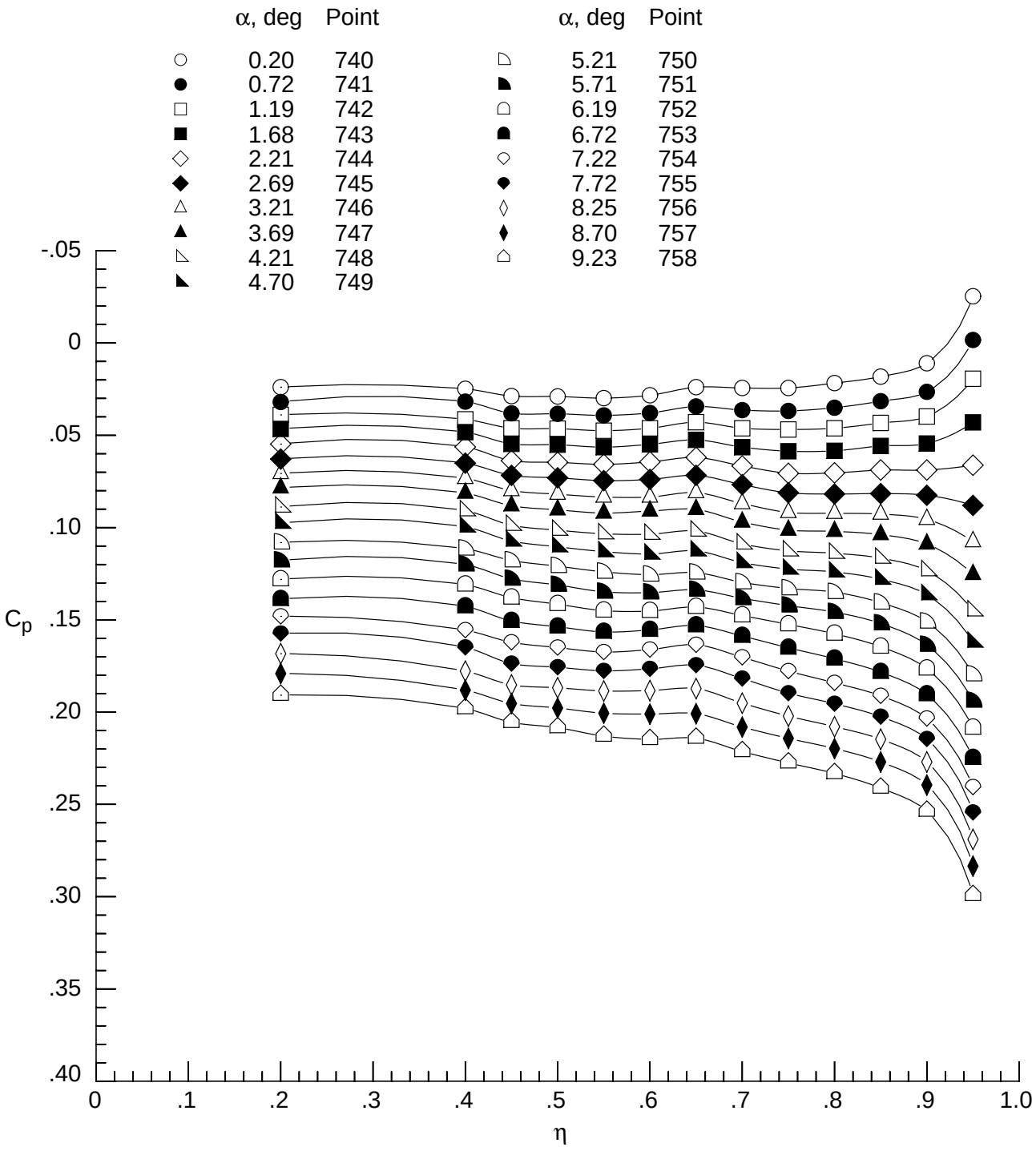

(d) Lower surface at x = 12 in.

Figure D21. Concluded.

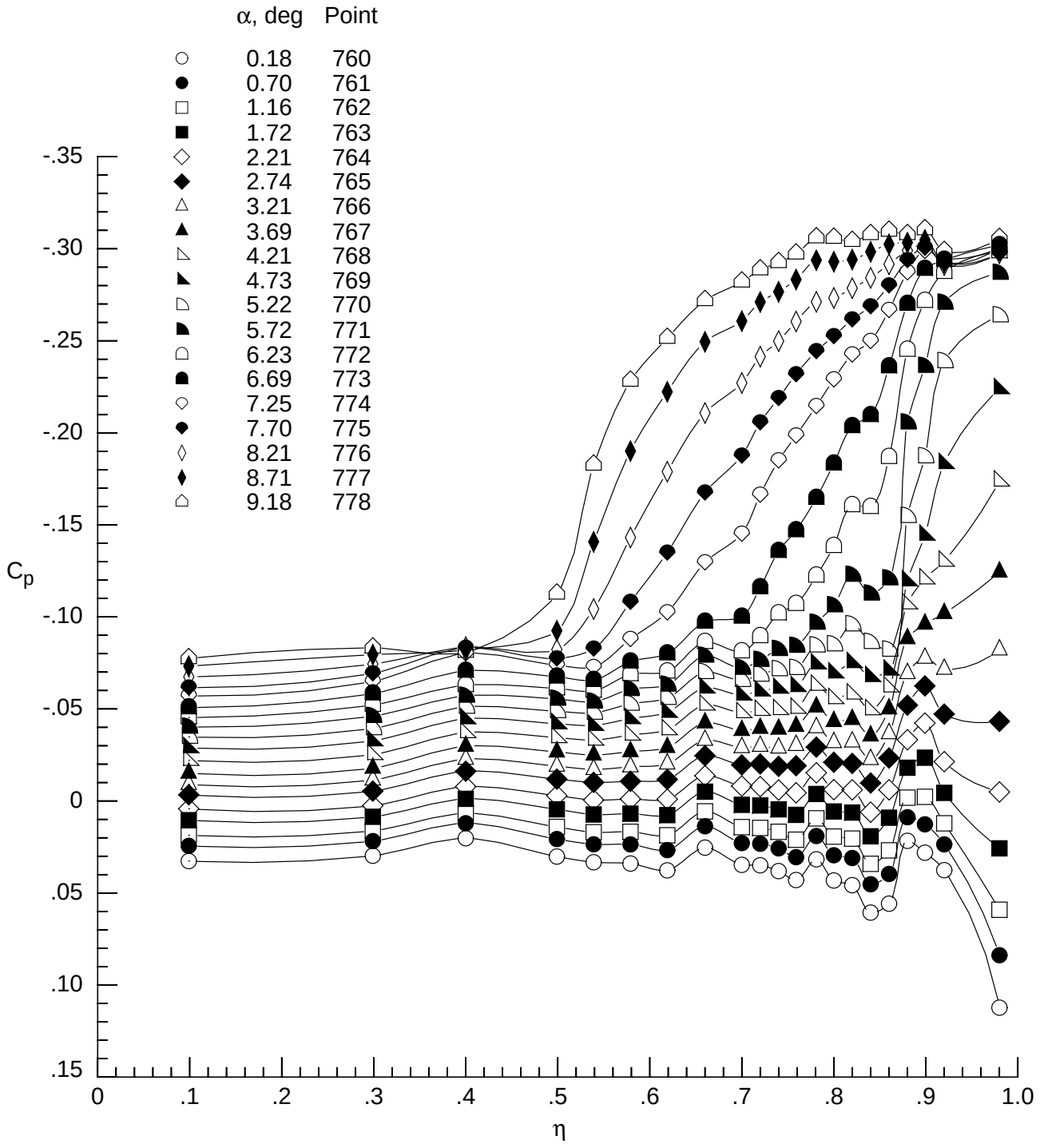

(a) Upper surface at x = 6 in.

Figure D22. Surface-pressure coefficient data for cambered wing with transition grit at M = 1.60 and $R = 5 \times 10^6$ ft^{-1} for run 39.

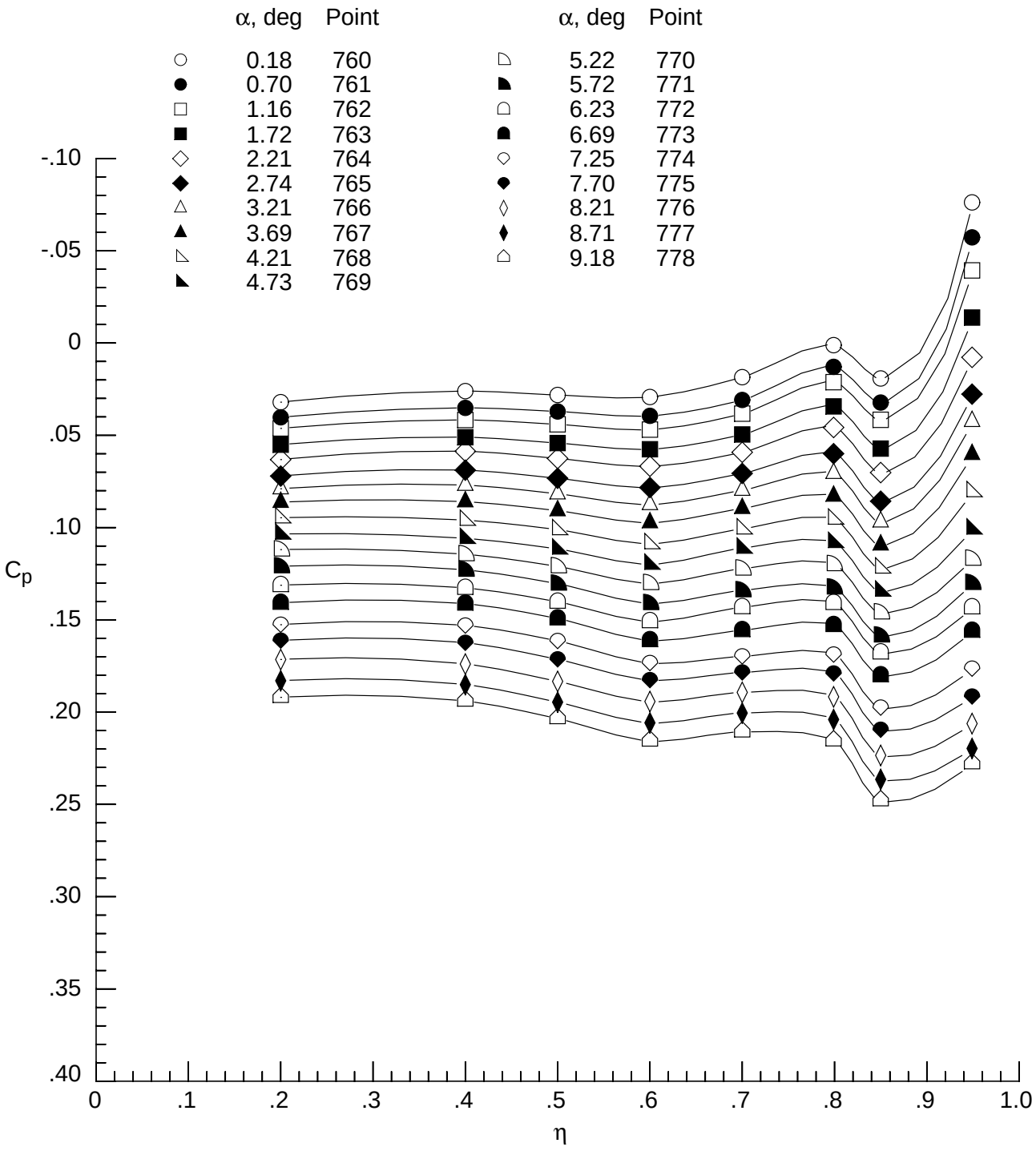

(b) Lower surface at x = 6 in.

Figure D22. Continued.

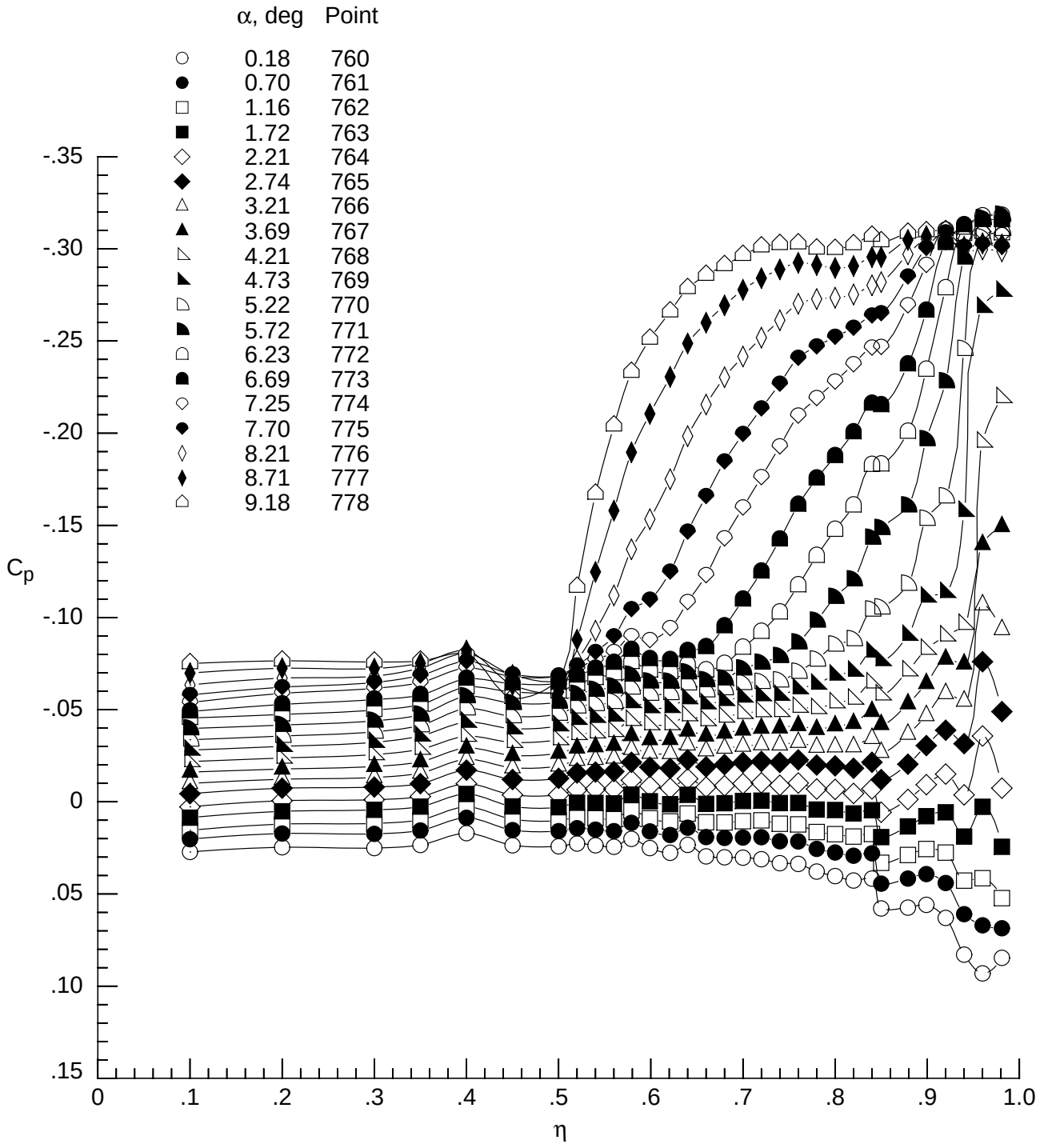

(c) Upper surface at x = 12 in.

Figure D22. Continued.

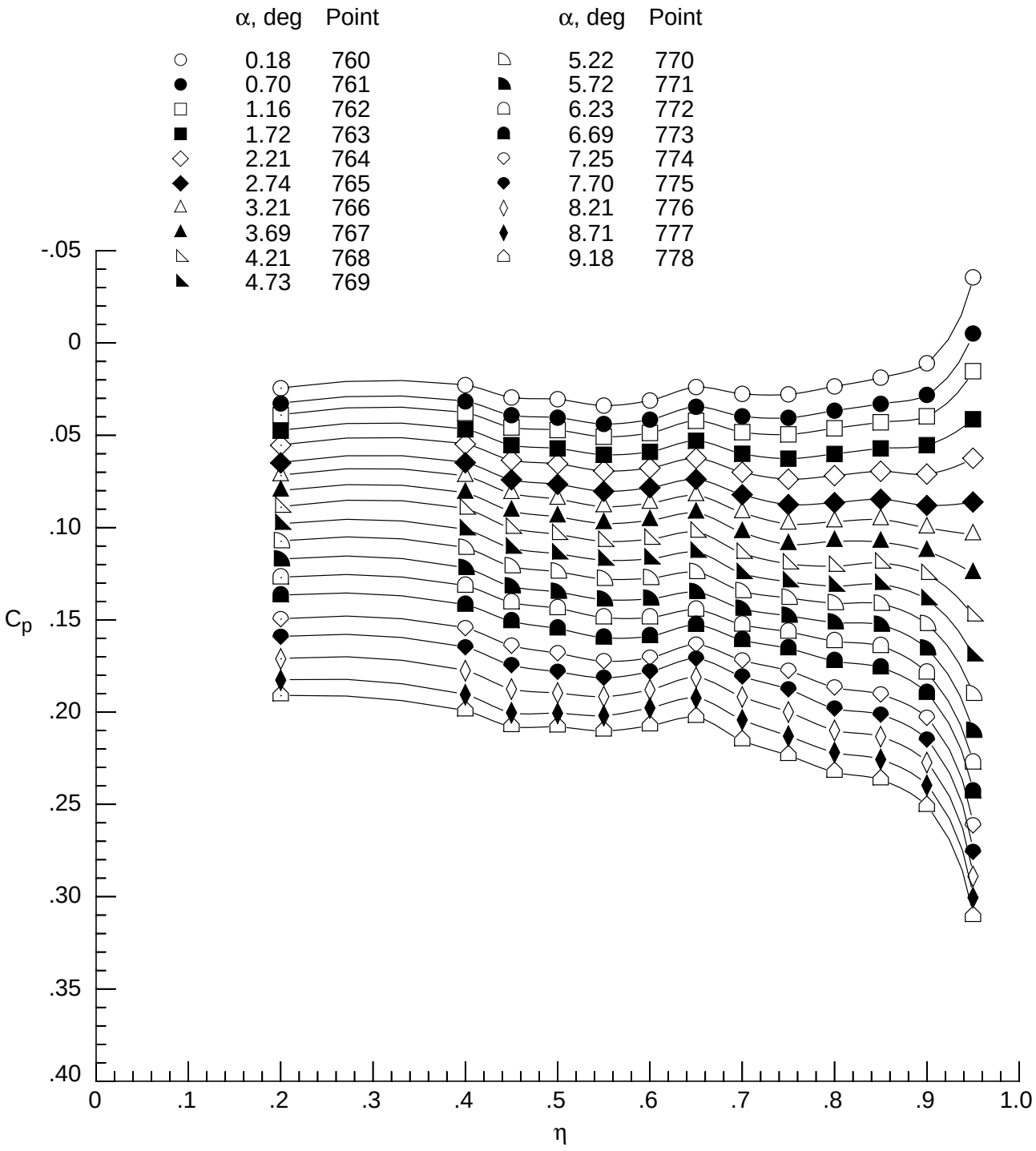

(d) Lower surface at x = 12 in.

Figure D22. Concluded.

References

1. Stanbrook, A.; and Squire, L. C.: Possible Types of Flow at Swept Leading Edges. *Aeronaut. Q.*, vol. XV, pt. 1, Feb. 1964, pp. 72–82.

2. Whitehead, A. H.: Lee-Surface Vortex Effects Over Configurations in Hypersonic Flow. AIAA-72-77, 1972.

3. Szodruch, Joachim; and Ganzer, Uwe: On the Lee-Side Flow Over Delta Wings at High Angle of Attack. *High Angle of Attack Aerodynamics*, AGARD-CP-247, 1979, pp. 21-1–21-7.

4. Szodruch, Joachim: *Lee Side Flow for Slender Delta Wings of Finite Thickness.* NASA TM-75753, 1980.

5. Miller, David S.; and Wood, Richard M.: *Lee-Side Flow Over Delta Wings at Supersonic Speeds.* NASA TP-2430, 1985.

6. Seshadri, S. N.; and Narayan, K. Y.: *Lee-Surface Flow Over Delta Wings at Supersonic Speeds.* TM AE 8610, National Aeronautical Lab. (Bangalore, India), Sept. 1986.

7. Covell, Peter F.; and Wesselmann, Gary F.: Flow-Field Characteristics and Normal-Force Correlations for Delta Wings From Mach 2.4 to 4.6. AIAA-89-0026, Jan. 1989.

8. Szodruch, Joachim G.: *Leeward Flow Over Delta Wings at Supersonic Speeds.* NASA TM-81187, 1980.

9. Jackson, C. M., Jr.: *Description and Calibration of the Langley Unitary Plan Wind Tunnel.* NASA TP-1905, 1981.

10. Braslow, Albert L.; and Knox, Eugene C.: *Simplified Method for Determination of Critical Height of Distributed Roughness Particles for Boundary-Layer Transition at Mach Numbers From 0 to 5.* NACA TN-4363, 1958.

11. Braslow, Albert L.; Hicks, Raymond M.; and Harris, Roy V., Jr.: *Use of Grit-Type Boundary-Layer-Transition Trips on Wind-Tunnel Models.* NASA TN D-3579, 1966.

12. Stallings, Robert L., Jr.; and Lamb, Milton: *Effects of Roughness Size on the Position of Boundary-Layer Transition and on the Aerodynamic Characteristics of a 55° Swept Delta Wing at Supersonic Speeds.* NASA TP-1027, 1977.

13. McMillin, S. N.; Pittman, James L.; and Thomas, James L.: Computational Study of Incipient Leading-Edge Separation on a Supersonic Delta Wing. *J. Aircr.* vol. 29, Mar.–Apr. 1992, pp. 203–209.

14. Gray, G. W., ed.: *Thermotropic Liquid Crystals*. Critical Reports on Applied Chemistry, Volume 22, John Wiley & Sons, Inc., 1987.

15. Holmes, Bruce J.; Gall, Peter D., Croom, Cynthia C.; Manuel, Gregory S.; and Kelliher, Warren C.: *A New Method for Laminar Boundary Layer Transition Visualization in Flight—Color Changes in Liquid Crystal Coatings.* NASA TM-87666, 1986.

16. Parmar, D. S.; Singh, Jag J.; and Eftekhari, Abe: A Shear Sensitive Monomer-Polymer Liquid Crystal System for Wind Tunnel Applications. *Rev. Sci. Inst.* vol. 63, Jan. 1992, pp. 225–229.

17. Ireland, P. T.; and Jones, T. V.: Response Time of a Surface Thermometer Employing Encapsulated Thermochromic Liquid Crystals. *J. Phys. E: Sci. Instrum.*, vol. 20, no. 10, Oct. 1987, pp. 1195–1199.

18. Schlichting, Hermann (J. Kestin, transl.): *Boundary-Layer Theory.* Seventh ed., McGraw-Hill Book Co., 1979.

19. McMillin, S. Naomi; Thomas, James L.; and Murman, Earll M.: *Navier-Stokes and Euler Solutions for Lee-Side Flows Over Supersonic Delta Wings—A Correlation With Experiment.* NASA TP-3035, 1990.

20. Cromartie, Robert C.; Johnston, R. Eugene; Pizer, Stephen M.; and Rogers, Diane: *Standardization of Electronic Display Devices Based on Human Perception*. TR88-002, Univ. of North Carolina, 1988.

21. Johnston, R. E.; Zimmerman, J. B.; Rogers, D. C.; and Pizer, S. M.: Preceptual Standardization. *SPIE*, vol. 236, 1985, pp. 44–50.

22. Pizer, S. M.; Johnsont, R. E.; Zimmerman, J. B.; and Chan, F. H.: Contrast Perception With Video Displays. *1st International Conference and Workshop on Picture Archiving*, Part 1, A. J. Duerinckx, ed., SPIE, vol. 318, Jan. 1982, pp. 223–230.

23. Dixit, Sudhir S.: Quantization of Color Images for Display/Printing on Limited Color Output Devices. *Comput. & Graph.*, vol. 15, no. 4, 1991, pp. 561–567,

24. Pearson, D. E.: *Transmission and Display of Pictorial Information.* John Wiley & Sons, Inc., 1975.

REPORT DOCUMENTATION PAGE

Form Approved
OMB No. 0704-0188

Public reporting burden for this collection of information is estimated to average 1 hour per response, including the time for reviewing instructions, searching existing data sources, gathering and maintaining the data needed, and completing and reviewing the collection of information. Send comments regarding this burden estimate or any other aspect of this collection of information, including suggestions for reducing this burden, to Washington Headquarters Services, Directorate for Information Operations and Reports, 1215 Jefferson Davis Highway, Suite 1204, Arlington, VA 22202-4302, and to the Office of Management and Budget, Paperwork Reduction Project (0704-0188), Washington, DC 20503.

1. AGENCY USE ONLY *(Leave blank)*	2. REPORT DATE	3. REPORT TYPE AND DATES COVERED
	December 1996	Technical Memorandum

4. TITLE AND SUBTITLE
Surface-Pressure and Flow-Visualization Data at Mach Number of 1.60 for Three 65° Delta Wings Varying in Leading-Edge Radius and Camber

5. FUNDING NUMBERS
WU 505-59-53-05

6. AUTHOR(S)
S. Naomi McMillin, James E. Byrd, Devendra S. Parmar,
Gaudy M. Bezos-O'Connor, Dana K. Forrest, and Susan Bowen

7. PERFORMING ORGANIZATION NAME(S) AND ADDRESS(ES)
NASA Langley Research Center
Hampton, VA 23681-0001

8. PERFORMING ORGANIZATION REPORT NUMBER
L-17443

9. SPONSORING/MONITORING AGENCY NAME(S) AND ADDRESS(ES)
National Aeronautics and Space Administration
Washington, DC 20546-0001

10. SPONSORING/MONITORING AGENCY REPORT NUMBER
NASA TM-4673

11. SUPPLEMENTARY NOTES
McMillin, Bezos-O'Connor, and Forrest: Langley Research Center, Hampton, VA; Byrd: Lockheed Engineering & Sciences Company, Hampton, VA; Parmar: Old Dominion University, Norfolk, VA; Bowen: Computer Sciences Corporation, Hampton, VA.

12a. DISTRIBUTION/AVAILABILITY STATEMENT
Unclassified–Unlimited
Subject Category 02
Availability: NASA CASI (301) 621-0390

12b. DISTRIBUTION CODE

13. ABSTRACT *(Maximum 200 words)*

An experimental investigation of the effect of leading-edge radius, camber, Reynolds number, and boundary-layer state on the incipient separation of a delta wing at supersonic speeds was conducted at the Langley Unitary Plan Wind Tunnel at Mach number of 1.60 over a free-stream Reynolds number range of 1×10^6 to 5×10^6 ft^{-1}. The three delta wing models examined had a 65° swept leading edge and varied in cross-sectional shape: a sharp wedge, a 20:1 ellipse, and a 20:1 ellipse with a −9.750 circular camber imposed across the span. The wings were tested with and without transition grit applied. Surface-pressure coefficient data and flow-visualization data are electronically stored on a CD-ROM. The data indicated that by rounding the wing leading edge or cambering the wing in the spanwise direction, the onset of leading-edge separation on a delta wing can be raised to a higher angle of attack than that observed on a sharp-edged delta wing. The data also showed that the onset of leading-edge separation can be raised to a higher angle of attack by forcing boundary-layer transition to occur closer to the wing leading edge by the application of grit or the increase in free-stream Reynolds number.

14. SUBJECT TERMS
Delta wings; Supersonic; Vortical flows; Leading-edge separation; Leeside flows

15. NUMBER OF PAGES
265

16. PRICE CODE
A12

17. SECURITY CLASSIFICATION OF REPORT	18. SECURITY CLASSIFICATION OF THIS PAGE	19. SECURITY CLASSIFICATION OF ABSTRACT	20. LIMITATION OF ABSTRACT
Unclassified	Unclassified	Unclassified	